

AD628385



CLEARINGHOUSE
FOR FEDERAL SCIENTIFIC AND
TECHNICAL INFORMATION

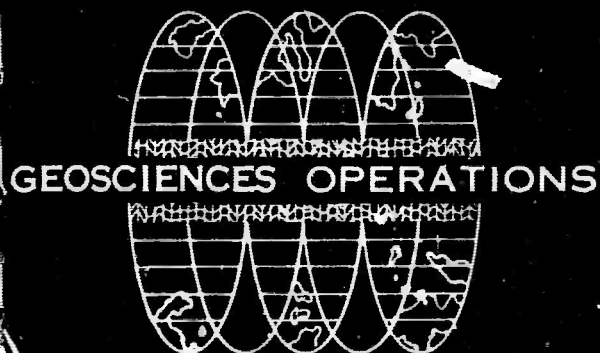
Hardcopy

Microfilm

\$39.20 \$1.75 396 pp as

ARCHIVE COPY

Code 1



TEXAS INSTRUMENTS
INCORPORATED
SCIENCE SERVICES DIVISION

6000 LEMMON AVENUE
D. BOX 5621 • DALLAS, TEXAS

DISCLAIMER NOTICE

THIS DOCUMENT IS THE BEST
QUALITY AVAILABLE.

COPY FURNISHED CONTAINED
A SIGNIFICANT NUMBER OF
PAGES WHICH DO NOT
REPRODUCE LEGIBLY.

BASIC RESEARCH IN CRUSTAL STUDIES

FINAL REPORT

Stanley J. Laster, Program Manager
FL 7-5411, Ext. 317

Milo M. Backus, Project Scientist
FL 7-5411, Ext. 319

TEXAS INSTRUMENTS INCORPORATED
Science Services Division
P. O. Box 5621
Dallas, Texas 75222

Contract AF 49(638)-1244
Date of Contract: 1 September 1963
Contract Expiration Date: 30 November 1965

Prepared for

AIR FORCE OFFICE OF SCIENTIFIC RESEARCH
Washington, D C 20333

Sponsored by
ADVANCED RESEARCH PROJECTS AGENCY
ARPA Order No. 292-63
Project Code 3810, 25 March 1963

31 December 1965

Request for additional copies by agencies of the Department of Defense, their contractors, or other government agencies should be directed to

DEFENSE DOCUMENTATION CENTER (DDC)
CAMERON STATION
ALEXANDRIA, VIRGINIA 22314

Department of Defense contractors must be established for DDC services or have their "need-to-know" certified by the cognizant military agency of their project or contract.

All other persons and organizations should apply to the

Clearinghouse for Federal Scientific and
Technical Information (CFSTI)
Sills Building
5285 Port Royal Road
Springfield, Virginia 22151

ABSTRACT

The work performed under Contract AF 49(638)-1244 falls into four tasks: (1) single-layer models; (2) multilayer models; (3) models with layer thickness variation; and (4) experimental studies using field data.

The single-layer studies included theoretical investigation of normal and leaking modes, studies of the practical aspects of frequency-wavenumber analysis and investigation of mode separation by multichannel filtering. The importance of leaking modes has been well-established and their use for interpretation greatly enhanced by mode separation to obtain detailed dispersion curves.

Theoretical and analog model investigations for two layers over a half-space showed the difficulty in directly observing an intermediate velocity layer using frequencies of 0.5 cps or less. However, such a layer implicitly affects the dispersion curves for low-order modes. Direct evidence (refractions, plateaus in the dispersion curves) becomes important near 1.0 cps.

Analog model investigations of a model having a dipping M-discontinuity showed a wide range of phase velocities for ray events, as predicted. The true refraction velocity was measured using phase velocity differences and was found to be in agreement with known values. Measurement of leaking-mode dispersion curves at various points in the model showed the utility of the "local" dispersion representation. These curves may be used to measure average dip.

Experimental studies of field data showed the usefulness of velocity filtering as an interpretive aid. Correlation statistics for small events showed that only about 50 percent of the energy arriving between the first arrival and surface waves is predictable. For events at small distance ($\Delta < 30$ km), Rayleigh-mode dispersion curves were measured. These suggested low near-surface velocities extending to a depth of 1/2-km. It was found that receiving arrays inline with the shot are necessary for adequate dispersion measurements.

BASIC RESEARCH IN CRUSTAL STUDIES
Final Report

The principal authors of this report are

Section I	Milo M. Backus Stanley J. Laster
Appendix A	Stanley J. Laster Joe G. Foreman A. Frank Linville
B	A. Frank Linville Stanley J. Laster
C	Stanley J. Laster A. Frank Linville
D	Hugh K. Harris Joe G. Foreman
E	Stanley J. Laster A. Frank Linville
F	Terry W. Harley Renner Hofmann Stanley J. Laster
G	A. Frank Linville Stanley J. Laster

Prepared for
Air Force Office of Scientific Research
Washington, D. C. 20333

TABLE OF CONTENTS

Section	Title	Page
	ABSTRACT	i
I	SUMMARY	1
	A. TASK 1	1
	B. TASK 2	3
	C. TASK 3	5
	D. TASK 4	6

LIST OF APPENDIXES

A	THEORETICAL INVESTIGATION OF MODAL SEISMOGRAMS FOR A LAYER OVER A HALF-SPACE
B	NUMERICAL EXPERIMENTS IN THE ESTIMATION OF FREQUENCY WAVENUMBER SPECTRA OF SEISMIC EVENTS USING LINEAR ARRAYS
C	APPLICATION OF MULTICHANNEL FILTERING FOR THE SEPARATION OF DISPERSIVE MODES OF PROPAGATION
D	WAVE PROPAGATION IN A 2-LAYERED MODEL OF THE EARTH'S CRUST
E	ANALOG MODEL STUDIES OF WAVE PROPAGATION IN A CRUST WITH A DIPPING INTERFACE
F	MULTICHANNEL PROCESSING APPLIED TO THE ANALYSIS OF REFRACTION SEISMOGRAMS RECORDED AT TONTO FOREST SEISMOLOGICAL OBSERVATORY
G	NEAR-SURFACE DISPERSION STUDIES AT TONTO FOREST SEISMOLOGICAL OBSERVATORY

BLANK PAGE

SECTION I

SUMMARY

The work performed under the present contract was divided into four tasks. These are defined as follows:

- Task 1: Develop and demonstrate a quantitative understanding of the seismic arrivals for propagation in a simple low-velocity layer over a half-space
- Task 2: Develop and demonstrate a quantitative understanding of the seismic arrivals for propagation in simple multilayered models of the earth's crust
- Task 3: Develop an understanding of the effects of crustal thickness variation on the properties of the seismograms
- Task 4: Utilize actual data from the three station network of arrays in an attempt to separate and identify later arrivals and the higher-order modes propagating from earthquakes and explosions in the general range of 1 to 1000 km

The bulk of the technical effort was expended on Task 1 and 4 because the performance of Tasks 2 and 3 depended on theoretical results and computer programs developed under Task 1. Also, in addition to its intrinsic importance, Task 4 was closely related to Task 3. Results of the various studies will be discussed in the following paragraphs.

A. TASK 1

A single-layer 2-dimensional analog model with a 2-cm brass layer overlying a steel half-space was constructed. Seismograms obtained in digital form for this model are shown in Figures 11.1 and 11.2 of Appendix A. These seismograms clearly indicate the dominance of the fundamental Rayleigh mode and the shear modes and show observable early-arriving leaking modes. Theoretical studies using the elastic parameters of this model also show the importance of the leaking modes. The fundamental difficulty associated with theoretical studies of leaking modes is their mathematical representation by complex poles on a many-sheeted Riemann surface. There are several ways to implement this representation, but we have chosen to keep frequency a real variable while letting wavenumber assume complex values. The fact that the pole is

complex implies attenuation, and this particular representation focuses attention on attenuation (of a single frequency) with distance. Typical theoretical attenuation curves are shown in Figure 3.2 of Appendix A. The net result of attenuation is a frequency-dependent loss of energy into the half-space. A comparison of the power spectra of the leaking and normal modes is shown in Figure 5.5 of Appendix A for a source-receiver distance of 50 cm (25 times the layer thickness). For this distance, the leaking modes are not negligible compared to the normal modes, but attenuation causes their spectra to be sharply peaked in frequency.

A concept which has great importance in regard to modal propagation is the transfer function. A linear filter which operates on a given mode at one distance to produce the same mode a unit distance farther from the source can be determined. This transfer function has uniform unit amplitude in frequency (for normal modes) and a phase shift dependent on the dispersion characteristics of the mode. Typical examples of such functions are shown in Figure 6.2 of Appendix A. The transfer function is useful even in materials with varying layer thickness since it depends on the local structure between the two receivers but is relatively independent of complications between the source and near receiver. Finally, one might note that experimental dispersion measurements are really based on estimating the transfer function or its complex frequency spectrum.

Another phase of the theoretical single-layer studies was the computation of single-mode seismograms. Since all the modes except the fundamental Rayleigh mode have low-frequency cutoff points (and also high-frequency cutoff points in the case of leaking modes), it is found that the individual modes are not physically realizable but instead have nonvanishing motion before time zero. Only the sum of all the modes, plus the two branch line integrals, is required to be realizable as it represents the complete solution. The sum of the theoretical modes, when properly bandlimited (Appendix A Figures 10.1 and 10.2), are quite similar to the experimental seismograms.

The presence of more than one mode in the experimental seismograms complicates the interpretation. Frequency-wavenumber spectral analysis is one promising technique for determining the modal characteristics and measuring the relative excitation of the various modes. In theory, this technique yields the 2-dimensional power spectrum of the seismic disturbance, but numerous difficulties arise in practice. The chief problems result from the use of a finite-length spatial array. This gives rise to sidelobes whereby a strong spectral peak can corrupt the spectral estimate in other regions of the frequency-wavenumber plane. In the estimation of spectra of transient signals, another difficulty arises because of spatial nonstationarity. It is found that the chief expression of

the higher modes of propagation arises from their crosscorrelation with the Rayleigh mode. This information is difficult to interpret, however, and it is more desirable to average over an ensemble of correlations to eliminate nonstationarity. This gives a more reasonable spectral estimate but less indications of the higher modes (Appendix B, Figures 9 and 10). Use of a space-lag window such as the Bartlett window gives the strongest but least precise estimate of the higher modes (Appendix B, Figure 11). In general, it is found that frequency-wavenumber analysis yields the general location of the various modes but cannot give precise dispersion curves.

A more sophisticated method for estimating dispersion curves uses multichannel filter techniques to first separate the modes. Filter systems were designed on the basis of crude correlation statistics (time domain) or crosspower spectra (frequency domain) of the various modes. These may be obtained either theoretically or indirectly from frequency-wavenumber spectra of Appendix B. Figure 18 of Appendix C shows the wavenumber response at two frequencies for a typical filter system which was designed to pass the M_{12} shear mode while suppressing all others. The filter systems were applied to both theoretical and experimental seismograms from the single-layer model. Results are shown in Appendix C, Figures 19 through 28. In general, filter systems designed in the time domain were found to be slightly better than those designed in the frequency domain, probably because of the transient behavior of the former filters. Each mode was estimated at two output distances. The dispersion curves could then be measured from the phase of the crosspower spectra between these two distances. In Appendix C, results for the theoretical seismograms are shown in Figure 37 and for experimental seismograms in Figure 38. These are particularly striking for the shear modes since they are overlapped both in frequency and arrival time by the Rayleigh mode.

In designing a second set of processors, use was made of the relation between the horizontal and vertical components of motion at each receiver site. In this case, results were excellent for the theoretical data but poor for the experimental seismograms. The difficulty was traced to the finite size of the receiver crystal on the analog model, coupled with the sensitive dependence of the Rayleigh-wave motion on receiver depth. These difficulties would not occur in practice, but a similar problem would arise if one attempted to apply one filter system to data from sources at a range of depths. In general, the mode separation technique appears to be very useful and should be evaluated using actual field data.

B. TASK 2

A 2-dimensional analog model with 2-layer crust over a half-space was built. The upper crustal layer was made of brass, the intermediate layer of monel and the half-space of steel. Monel is a useful

modeling material because it has a velocity intermediate between brass and steel. The parameters of this model are given in Table 3 of Appendix D. Letting 1 cm scale to 20 km yields a crustal thickness of 40 km.

Theoretical computations were made for all modes lying below a frequency of 1 Mc/sec (scaling to ~ 0.74 cps). This gave 7 leaking modes and 10 normal modes. Dispersion curves, attenuation functions, excitation functions and, finally, seismograms were computed for each mode. One purpose of the study was to determine the effects produced by the intermediate layer. The most obvious evidence for the existence of the intermediate layer is found in the dispersion curves. The shear modes show well-defined group velocity maxima at phase velocity plateaus near the velocity of shear waves in monel (Appendix D, Figures 1 to 6). These could be experimentally observed if the group velocity were determined directly from the seismograms. However, if the phase velocity were first determined and then the group velocity obtained indirectly by differentiation, the effect might be masked. The phase velocity curves are quite flat over broad frequency ranges, and small errors would greatly affect the derivative used in computing the group velocity. There are less well-defined plateaus in the leaking-mode phase velocity curves near the velocity for compressional waves in monel (Appendix D, Figure 7). In some instances, however, the attenuation is quite high near these plateaus so that the observance of P-pulses refracted along the top of the monel also depends on the relative excitation of the modes as a function of frequency.

It is natural to compare the distribution of dispersion curves with frequency for this model with that of the single-layer model considered previously. In both cases, the total crustal layering is 2 cm thick. One means of comparison, appropriate for low frequency, would be to replace the 2-layer model by an equivalent 1-layer model which could be chosen to have the same total layer thickness (2 cm) but a higher average velocity. However, it is more convenient to consider a thinner all-brass layer. Then, the dispersion curves for the equivalent model can be obtained from those of the 1-layer model simply by stretching the frequency axis. This simple artifice shows that there should be greater separation in frequency for the modes in the 2-layer model than in the 1-layer model. (Compare Figure 3.1, Appendix A, and Figure 7, Appendix D.)

The seismograms are shown in Appendix D, Figure 16. A sufficient number of modes is present to show some hint of pulse formation. However, it is difficult to identify a given "pulse" on traces that are 20 cm apart because the pulses change shape rapidly with distance. However, events having about the velocity of compressional waves in monel can be seen.

The experimental seismograms for the 2-crustal layer model are shown in Appendix D, Figure 8 through 15. These show some significant deviations from the theoretical predictions. The PL_{22} mode seems to be strongly excited, but its dominant frequency is about 95 kc/s instead of 120 kc/s. Experimental determination of dispersion (Appendix D, Figures 61 through 63) shows this more clearly for both the PL and shear modes. In terms of our crude equivalent 1-layer model, the analog model appears to have a "thicker" layer than the theoretical model. This is probably due in some measure to an imperfect bond between the various materials. However, the bond is sufficiently strong that distinct events refracted along the top of the steel are seen.

C. TASK 3

A 2-dimensional analog model with a single brass crustal layer having a dipping boundary was investigated. The underlying half-space was of stainless steel. Layer thickness varied from 3 to 6 cm over a distance of 244 cm. The source was located at 33 cm from the 3-cm end of the model, so regions of the model were appropriate to both ray and modal propagation. Experimental seismograms for these two cases are shown in Appendix E, Figures 5 through 11.

The chief prediction of the theory for ray propagation above a dipping boundary is the presence of a range of phase velocities for critically refracted events. In particular, events recorded updip from the source will have a phase velocity higher than the true velocity in the refractor, while the reverse is true for events recorded downdip. In addition, the multiple reflections of the primary refraction will have different velocities, depending on the number and location of the reflected legs. Theoretical and experimental travel-time curves showing these effects are shown in Appendix E, Figures 12 and 13. The difference in phase velocity for a given event, measured updip and downdip, can be used to measure the true velocity below the refracting interface. Similar results can be obtained using the phase velocities for two different but identifiable events measured in a single direction. Examples of this are given in Appendix E. Additional information concerning the velocities of layers above the refractor allows computation of the dip. Amplitude measurements for this model, while behaving as predicted, show considerable scatter (Appendix E, Figure 16.)

The most convenient representation of modal propagation in a model with a dipping interface ignores the dip completely; instead, it represents the layer thickness variation by a sequence of plane-parallel layered models, each valid for a small range of distance. This allows computation of a dispersion curve for each model in the sequence, so we can associate with the dipping interface model a dispersion curve which is a function of distance. Measured dispersion curves at a number of source-

receiver distances then allows measurement of layer thickness and averaged dip. Dispersion curves measured for the leaking modes of propagation are shown in Appendix E, Figure 18 through 20. Theoretical curves for the appropriate layer thickness are shown for comparison; the agreement is quite good. Since only a single leaking mode of propagation was strongly excited, the problem was simplified. As long as the thickness variations occur over several wavelengths, this method can be used for modal propagation in models with nonplane boundaries.

D. TASK 4

Experimental studies were conducted using data recorded from the cross array at Tonto Forest Seismological Observatory. These data consisted of recordings of nuclear events detonated in Nevada, quarry blasts and U.S. Geological Survey calibration shots. The data were divided into two categories, based primarily on distances from TFO. The more distant events have all the characteristics of seismic refraction seismograms, while the near events ($\Delta < 30$ km) show near-surface modal propagation with indications of dispersion. The two sets of data were treated separately.

Two nuclear events (Appendix F, Figures 4 and 5) were used, both of which had very high signal-to-ambient-noise ratio. These events showed clearly the P_n and P_g refracted events and their multiples, but there was no indication of P^* . On one of the records, S_g also was seen. Because of the high quality of these recordings, velocity filtering was applied in an attempt to separate various overlapping events and, in particular, to bring out P^* if it were present (Appendix F, Figure 18). No indication of P^* was found. Following P_g , however, there were certain low-velocity events which probably represent scattered energy generated by P_g . This energy was not apparent on the unprocessed record. Velocity filtering applied to the broadside array (perpendicular to the travel path) showed that the P_n event and its multiples traveled directly along a line from source to receiver. While this was true also for some of the P_g events, there was observation of events traveling with P_g velocity that arrived from a direction slightly south of the line connecting source and receiver. It is assumed that these events were laterally refracted by the mechanism of varying sediment thickness.

Recordings of U.S. Geological Survey shots (Appendix F, Figures 7 through 15) showed a poorer signal-to-ambient-noise ratio than the nuclear events because the decrease in epicentral distance did not offset the vast difference in effective charge size. In general for these events, fewer well-defined secondary arrivals were observed and the signal-generated noise was more of a problem. This may have been partly due to the higher frequency content of the seismograms. The experiments were aimed at improving data quality to a point that later events could be picked. Also, there were efforts to determine the coherence or

predictability of the data from trace to trace in order to evaluate the importance of the scattered energy. It was found that velocity filtering and data-dependent prewhitening ("deconvolution") aided in picking later arrivals from a small USGS shot (Appendix F, Figures 20 through 24). To confirm the validity of this, the same events could be picked on a larger quarry blast from the same area.

Single-channel prediction studies showed that only 50 percent of the energy arriving between the first arrival and the surface waves is predictable. This could be caused by several coherent events with different velocities (or from different sources) arriving during this time, or it could be that about half the energy in this frequency range (2-5 cps) is spatially random. Multichannel prediction studies showed about the same percentage prediction, so the latter hypothesis seems more tenable. A reasonable mechanism for this random energy would be scattering of early arrivals from a large number of inhomogeneities in the immediate vicinity of the array.

The outstanding difficulty which remains in interpreting these refraction records is the problem of identifying later events with ray paths. In the usual case, crusts beneath the source and the receiver are different so that the seismogram contains two different sets of multiply reflected events superimposed upon one another. The strongest evidence for complicated velocity structure within the crust is the observation that very few of the many later events show time intervals large enough to allow reflection between the surface and the M-discontinuity.

The local USGS events (Appendix G, Figures 2 through 4) show compressional arrivals, shear arrivals and a well-defined Rayleigh train. Frequency-wavenumber spectra of these events (Appendix G, Figure 7 and 9) indicated a Rayleigh velocity of 2.8 km/sec and there was some indication of dispersion. The frequency spectrum is strongly peaked at 1.0 to 2.0 cps. Events whose travel paths were inline with the array were found to give frequency-wavenumber spectra which were reasonable in the sense that they could be interpreted in terms of an arrival with well-defined velocity, its sidelobes, and its aliases (Appendix G, Figure 13). Events whose travel paths made a large angle with the array gave 2-dimensional spectra with energy seemingly randomly distributed in wave-number (Appendix G, Figure 21).

Rayleigh-wave dispersion was measured by using correlation statistics of the Rayleigh mode on adjacent traces. From these, a filter was computed to predict one trace from the other. Since only one mode was present with any measurable power, this filter represented the transfer function for that mode and dispersion curves could be computed from the phase response of the filter. Results computed by this method are

shown in Appendix G, Figures 27 and 35. Again, it was found that the data from shots inline with the array gave reasonable results while those not inline gave uninterpretable dispersion results. The cause of this behavior was traced to the very rough topography in the area between the array and the shots. For inline shots, the phase difference between two receivers at a given frequency depends on the subsurface structure between the two receivers but is independent of the structure between the source and near receiver. This remains true for noninline shots if there are no inhomogeneities. In the present case, however, the topography is so rough (Appendix G, Figures 38 through 41) that the phase difference is due primarily to differences in the source-receiver path and depends only slightly on the structure between receivers.

The usable results showed very similar dispersion curves for the southwest, northwest and northeast ends of the array. Although a unique structure cannot be determined from such a small amount of data, the dispersion results were in agreement with theoretical curves for a model having a single layer 0.5 km thick and a P-velocity of 4.8 km/sec. The underlying material would have a compressional velocity of 5.9 km/sec. Results from the southeast end of the array showed lower velocities. These could be obtained by making the P-velocity in the single-layer model 4.5 km/sec.

Results seem to be correct but are not in agreement with observed surface geology. The southeast and southwest ends of the array lie on granite and would be expected to have a higher velocity than the northwest and northeast ends which lie on sediments. The cause of this disagreement is not known.

In summary, we may say that computer processing, particularly velocity filtering, has improved the interpretability of the field data. Frequency-wavenumber spectra have also proved useful for analysis. However, two outstanding problems remain. One is the problem of identifying later arrivals with specific ray paths. This probably can be solved only by having more observatories closer together. Second is the problem of scattered energy corrupting later events. Here, the best solution seems to be more receivers closer together. Then these can be processed on a subarray basis to remove scattered energy. It is worthwhile to note that both problems will be greatly alleviated by facilities such as the Large Aperture Seismic Array in Montana.

APPENDIX A

THEORETICAL INVESTIGATION OF MODAL SEISMOGRAMS FOR A LAYER OVER A HALF-SPACE

**THEORETICAL INVESTIGATION OF MODAL
SEISMOGRAMS FOR A LAYER
OVER A HALF-SPACE**

BY

**STANLEY J. LASTER, JOE G. FOREMAN,
AND A. FRANK LINVILLE**

Reprinted for private circulation from
GEOPHYSICS
Vol. XXX, No. 4, August, 1965

THEORETICAL INVESTIGATION OF MODAL SEISMOGRAMS FOR A LAYER OVER A HALF-SPACE†

STANLEY J. LASTER*, JOE G. FOREMAN*, AND A. FRANK LINVILLE*

The use of normal modes to represent the propagation of elastic waves at large horizontal offset is well known. By addition of the relevant leaky modes, the mode theory is shown to be useful for representation of the seismograms at shorter range. A theoretical model consisting of a 2-cm brass layer over a steel half-space is considered. Dispersion curves and excitation functions are computed for the first four normal modes and the first three PL modes. Attenuation as a function of frequency also is computed for the PL modes. A suite of seismograms is computed for the distance range 50-70 cm, showing each mode individually and their sum (the total seismogram). It is found that, for the distances used, the individual modes do not approximate transients with a definite "arrival" time. Only their sum is required to exhibit this physical behavior. In addition, at short distances, the dispersion of a single mode is not visually obvious although the dispersion curve may be recovered by use of Fourier transform methods. Determination of the dispersion curves from the total seismogram is more difficult and requires some separation of the modes, as they overlap in frequency and velocity. This work shows the preponderance of the leaky modes in the early part of the seismogram and indicates their importance in the later part of the seismogram for short horizontal offset.

INTRODUCTION

This study deals with the application of mode theory to the study of elastic wave propagation in a model consisting of a single layer overlying a half-space. The application of mode theory to such problems is not new; however, such investigations usually are not carried past the point of computing dispersion curves and excitations for the normal modes. The novel features of the present study are the inclusion of the relevant leaky modes and computation of actual seismograms. This was done as a part of a broader study of separation of the various modes for the purpose of measuring dispersion, attenuation, and excitation from experimental data.

A unique characteristic of a "mode" of propagation is the frequency-phase velocity (or frequency-wavenumber) relationship. The phase velocity, as defined here, is simply the apparent resultant velocity between closely spaced recesses. Another parameter of interest is the group velocity, defined as the average velocity of travel (for each frequency) in the sense of total distance traveled divided by elapsed time. Two or more modes may partially overlap in frequency, phase velocity, and group velocity, but no two modes agree completely in the dependence of phase and group velocity on frequency. If all the

physical constants of a plane-layered model are known, the frequency-phase velocity relations (dispersion curves) may be computed theoretically. The next section gives a brief résumé of how this may be done.

MODE-THEORY RESUME

Consider the problem of elastic wave propagation in plane layers above a half-space. Let \mathbf{u} be the vector whose components are u_r and u_h , the vertical and horizontal component of displacement. There will be defined for each layer and half-space the quantities: ϕ , a scalar potential; and ψ , a vector potential; such that $\mathbf{u} = \nabla\phi + \nabla \times \psi$. For the two-dimensional problem considered here, ψ has only one nonzero component. The equations of motion of the elastic solid are satisfied identically if

$$\nabla^2\phi = \frac{1}{\alpha^2} \frac{\partial^2\phi}{\partial t^2} \text{ and}$$

$$\nabla^2\psi = \frac{1}{\beta^2} \frac{\partial^2\psi}{\partial t^2} \text{ (P- and S-wave equations).}$$

Here, α and β are the P- and S-wave velocities in the layer. The appropriate boundary conditions are continuity of the stresses and displacements across each interface and vanishing of the stresses

† Presented at the 34th Annual International SEG Meeting, Los Angeles, California, November 19, 1964. Manuscript received by the Editor December 22, 1964.

* Texas Instruments, Incorporated, Dallas, Texas.

at the free surface. We take x to be the horizontal coordinate and z to be the vertical coordinate, with z positive downward. The normal stress across an interface ($z = \text{constant}$) is

$$T_{zz} = \lambda \left(\frac{\partial u_h}{\partial x} + \frac{\partial u_v}{\partial z} \right) + 2\mu \frac{\partial u_v}{\partial z},$$

while the shearing stress across the interface in the direction of propagation is

$$T_{zx} = \mu \left(\frac{\partial u_v}{\partial x} + \frac{\partial u_h}{\partial z} \right),$$

where μ, λ are Lamé's constants. In the two-dimensional problem, there is no shearing stress perpendicular to the direction of propagation.

The problem is solved formally by applying successive Fourier transform to eliminate the time t and the distance x .¹ This introduces the angular frequency ω and the "angular" wave-number k , respectively (either or both may be complex). One may interpret the transformation process physically as a decomposition of the disturbances into plane waves.

After transformation, the wave equations are solved quite easily to give

$$\begin{aligned} \phi &= P e^{i\eta z} + Q e^{-i\eta z}, & \nu &= (\omega^2/\alpha^2 - k^2)^{1/2}, \\ \psi &= C e^{i\eta z} + D e^{-i\eta z}, & \eta &= (\omega^2/\beta^2 - k^2)^{1/2}. \end{aligned}$$

Since the quantities η and ν are square roots, the solution is not complete until the signs of the radicals are specified. We arbitrarily take the imaginary part of ν, η to be positive on the "physical" Riemann sheet. (Similar results will be obtained if the opposite choice is taken.) Specification of these signs introduces two natural barriers (or "branch" lines) in the complex k plane.

The quantities P, Q, C, D are constants of integration. The transformed boundary conditions form a system of linear algebraic equations for the determination of these constants, and the actual evaluation is carried out by using Haskell's (1953) matrix method. The final transformed solution for the elastic displacement vector is of the form

$$\mathbf{U}(\omega, k, z) = \frac{\mathbf{A}(\omega, k, z)}{\Delta(\omega, k)},$$

¹ Note that there is nothing to tell us which transform to perform first and that we could have taken the alternative choice.

where the function Δ is determinant of the system of linear equations. The formulas for Δ and \mathbf{A} have been given in detail by Harkrider (1964). In order to evaluate leaky modes, his expressions must be programmed in complex arithmetic. The time-distance solution ("seismogram") of the boundary problem is, by Fourier inversion,

$$\mathbf{u}(t, x, z) = \frac{1}{4\pi^2} \int_{-\infty}^{\infty} e^{i\omega t} \int_{-\infty}^{\infty} \frac{\mathbf{A}(\omega, k)}{\Delta(\omega, k)} e^{-ikx} dk d\omega.$$

It is important to note that (1) $\mathbf{A}(\omega, k, z)$ is a function of the type of source and receiver, i.e., the radiation pattern and location of the source and the response and location of the receiver, as well as the model parameters, (2) the horizontal distance x appears only in the exponent e^{-ikx} , and (3) $\Delta(\omega, k)$ is independent of the source and receiver; it is purely a function of the model parameters, i.e., α_i, β_i, h_i , and ρ_i .

The inner integral may be evaluated most conveniently by contour integration, the evaluation being carried out for each value of ω . The dominant contributions are due to the poles of the integrand which occur at $\Delta(\omega, k) = 0$. This defines a set of dispersion curves $k_j(\omega)$ or, more commonly, $c_j(f)$ where $f = \omega/2\pi$ and $c = \omega/k$.

For real values of ω and with cuts taken in the k plane defined as above, the only poles lie on the real k axis. The remaining contribution to the integral then consists of the two line integrals beginning at branch points of the integrand and extending to infinity, as shown in Figure 1. For large source-receiver distances, the pole contributions dominate the branch-line contributions. This can be shown by asymptotic expansion about the branch points to yield two simple "blunt" pulses which are intimately connected with pure P and S waves in the half-space. While these blunt pulses represent most of the energy in the branch-line integral, such an approximation is misleading. The integrand along the branch line does not decay monotonically away from the branch point but has occasional smooth peaks which contribute early-arriving, oscillatory events.

In their original form, the oscillatory events are difficult to evaluate; the most convenient procedure is to reroute the lines of integration in such a manner that the integrand is, insofar as possible, a rapidly decaying function.

In the process of moving the lines of integra-

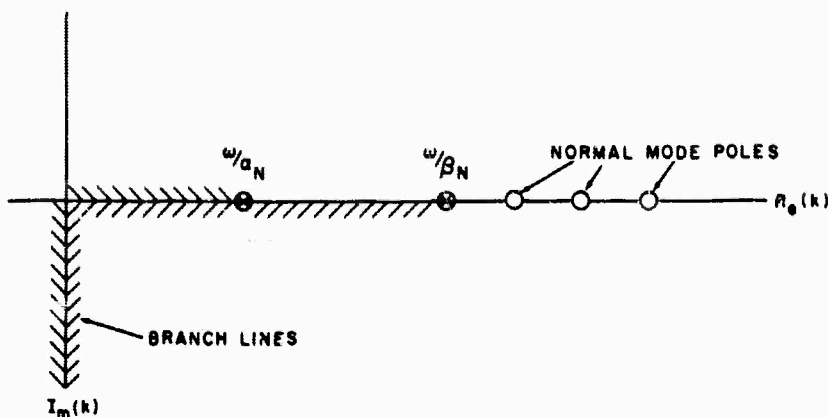


FIG. 1. Schematic diagram of fourth quadrant of complex k plane showing normal mode poles and original branch lines. The path of integration is just above and parallel to the real axis.

tion, new poles, for which $k(\omega)$ is a complex number, are uncovered. These poles yield the damped, oscillatory disturbances which correspond to high-velocity reflected refractions and slowly moving near-vertical reflections, collectively called leaky modes. The damping results from loss of energy into the half-space rather than from dissipation.

The improved branch lines are shown in Figure 2. Note that the branch points move as ω changes. The path of a single pole (mode) relative to the branch point is shown as a function of frequency. The pole emerges from the forbidden domain as a PL mode, crosses again into a forbidden do-

main, and finally emerges on the real axis as a shear mode. The path of integration is slightly above and parallel to the real axis. The remaining branch line integrals are quite small and will be ignored in the remainder of this paper.

The contribution to the inner integral due to a single pole (one "mode") is

$$\frac{A(\omega, k, z)}{\frac{\partial \Delta}{\partial k} \bigg|_{\omega}} e^{-ik(\omega)z},$$

where $k(\omega)$ may be complex.

Let $k(\omega) = k_r - i\tau$ (for the normal modes, $\tau=0$)

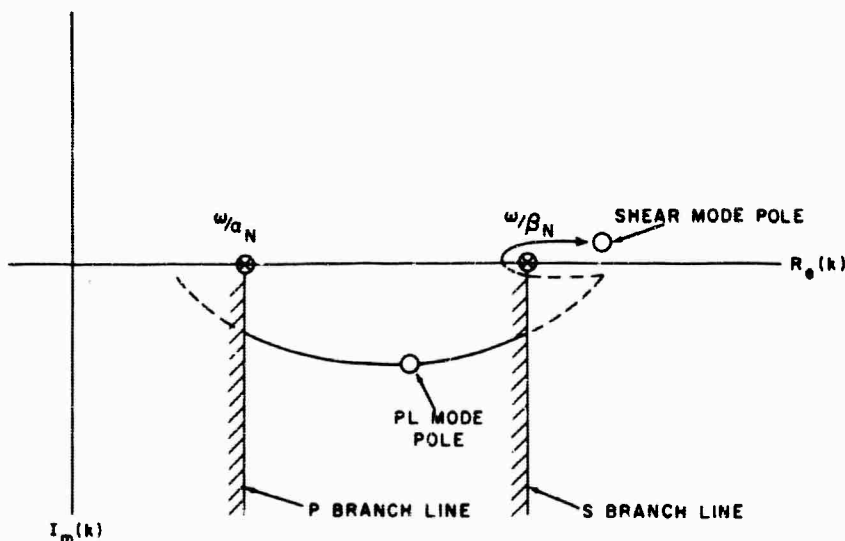


FIG. 2. Schematic diagram of fourth quadrant of complex k plane showing poles and simplified branch lines. The path of integration is just above and parallel to the real axis.

and

$$\frac{\mathbf{A}(\omega, k(\omega), z)}{\left. \frac{\partial \Delta}{\partial k} \right|_{\omega}} e^{-i(\omega)z}$$

be denoted by $\mathbf{H}(\omega)$.

$\mathbf{H}(\omega)$, the complex frequency spectrum of the given mode at the source, is called the excitation function and is generally a smooth, slowly varying function of ω . In particular, $\mathbf{H}(\omega)$ will not have poles. The integral may now be written

$$u(t, x, z) = \frac{1}{2\pi} \int_{-\infty}^{\infty} \mathbf{H}(\omega) e^{i(\omega t - k_r x)} d\omega.$$

This integral cannot be evaluated in closed form. There are several methods for approximating the result. It is often useful to use methods by which the analytic behavior of the function can be determined without resorting to numerical methods. In this instance, asymptotic approximations to the integral may be used which are valid for large source-receiver distances or large times after the source disturbance has been initiated. Two such methods closely related to each other are the method of stationary phase and the method of steepest descents. For convenience, the former usually is used, the angular frequency ω being taken real.

The stationary-phase method utilizes the knowledge that $e^{i(\omega t - k_r x)}$, unlike $\mathbf{H}(\omega)$, is a rapidly varying function of ω . Therefore, the dominant part of the integral comes from the region where the phase $\theta = \omega t - k_r x$ is stationary, i.e., where $d\theta/d\omega = 0$. Erdelyi (1955) shows that contributions from stationary points, if present, are of order $t^{-1/2}$. Contributions from end points of the region of integration contribute terms of order t^{-1} . For large t , the latter may be neglected in favor of the former. Defining the group velocity to be $U \equiv x/t$, then $1 - (dk_r/d\omega) U = 0$ or $U = d\omega/dk_r$. In addition, we will define the phase velocity by $c = \omega/k_r$, so that the phase of the exponential can be written $\omega[t - (x/c)]$.

It is noted here that the identification of $d\omega/dk_r$ with the group velocity is a direct result of using the stationary-phase approximation (the same result holds for the saddle point method) and is valid only insofar as the integrand satisfies the prerequisite conditions. If we approximate

θ by the first two terms of its Taylor series

$$\theta = \theta(\omega_0) + (\omega - \omega_0) \left. \frac{d\theta}{d\omega} \right|_{\omega_0} + \frac{(\omega - \omega_0)^2}{2} \left. \frac{d^2\theta}{d\omega^2} \right|_{\omega_0} + \dots$$

then

$$\theta \approx \theta(\omega_0) + \frac{(\omega - \omega_0)^2}{2} \theta_0''$$

at the stationary point. Assuming that $\mathbf{H}(\omega)$ varies slowly near ω_0 , the integral becomes

$$u(t, x, z) \approx \frac{\mathbf{H}(\omega_0)}{2\pi} e^{i\theta_0} \int_{-\infty}^{\infty} e^{i\theta_0'' t (\omega - \omega_0)^2/2} d\omega$$

with

$$\theta_0'' = -x \left. \frac{d^2 k_r}{d\omega^2} \right|_{\omega_0}.$$

The final result is

$$u(t, x, z) = \text{Re} \left[\left(2\pi x \left. \frac{d^2 k_r}{d\omega^2} \right|_{\omega_0} \right)^{-1/2} \mathbf{H}(\omega_0) \cdot e^{i(\omega_0 t - k_r x \pm \pi/4)} \right];$$

the plus or minus sign in the exponential is taken to agree with the sign of θ_0'' .

Use of the real part follows from the symmetry properties of the real and imaginary parts of $\mathbf{H}(\omega)$. This approximate formula does not hold near the Airy Phase, where $\theta_0'' = 0$.

This approximate solution has some remarkable implications. For the moment, consider the distance x fixed. Then the group velocity U is determined by the time t at which it is desired to make an observation and, from the dispersion curves, a frequency ω_0 is determined. This tells us that, near time t , the seismogram approximates a sine wave of frequency ω_0 . Alternatively, the signal spectrum in a small frequency band centered at ω_0 is determined to a high degree of approximation by the signal time function measured in a small time interval centered about t . This is a direct result of dispersion and is valid only for large values of t . This also explains the success of the method for measuring dispersion

by the method of visual correlations of peaks and troughs on the seismograms.

For moderate distances and times (approximately 10-15 layer thicknesses), the stationary phase approximation may be worse than is realized. This manifests itself in a number of ways. First, the time interval necessary to determine the spectrum near ω_0 becomes larger. In particular, this means that, for short distances, long time samples are necessary to determine adequate experimental dispersion curves. The ability to follow an "event" (peak or trough) across an array of seismograms may not be significant because it may not be possible to determine the "frequency" of the event with sufficient accuracy. A second failure results from the neglect of the end-point contributions to the integral. The end-point terms, because of the coefficient involved, may be as large as the $t^{-1/2}$ term. Consider, for instance, the shear modes, each of which has a low-frequency cutoff. This "end point" contributes waves traveling at the velocity of shear waves in the half-space. For times before the arrival of the refracted shear waves, there is no stationary point but the end points still contribute nonvanishing motion. This may be stated differently. Because the spectra of the normal modes (except the fundamental) vanish over finite frequency bands, the time functions cannot be transients. Only at large distances do they ap-

proximate transients. A single normal mode is not in the strict sense a physically realizable entity; however, this is not required. Only the sum of all modes (and branch line integrals) must behave physically.

Because of these difficulties, direct numerical integration based on sampled data theory, may prove more satisfactory for computing seismograms, at least for short distances.

DISPERSION, ATTENUATION, AND EXCITATION FUNCTIONS FOR A LAYER OVER A HALF-SPACE

Theoretical solutions were evaluated for a simple crustal model consisting of a single layer overlying an infinitely deep half-space. The parameters of the layer are taken to be those of brass, while the parameters of the half-space are those appropriate to steel (see the following table). This model, designated H-1, is based on an existing analog model.

Elastic parameters of model H-1

Material	P Velocity	S Velocity	Density Ratio	Layer Thickness
Half-hard brass	3.83 mm/ μ s	2.14	1.0	20 mm
Cold rolled steel	5.49	3.24		∞

(Note that velocities in mm/ μ s are numerically equal to velocities in km/sec.)

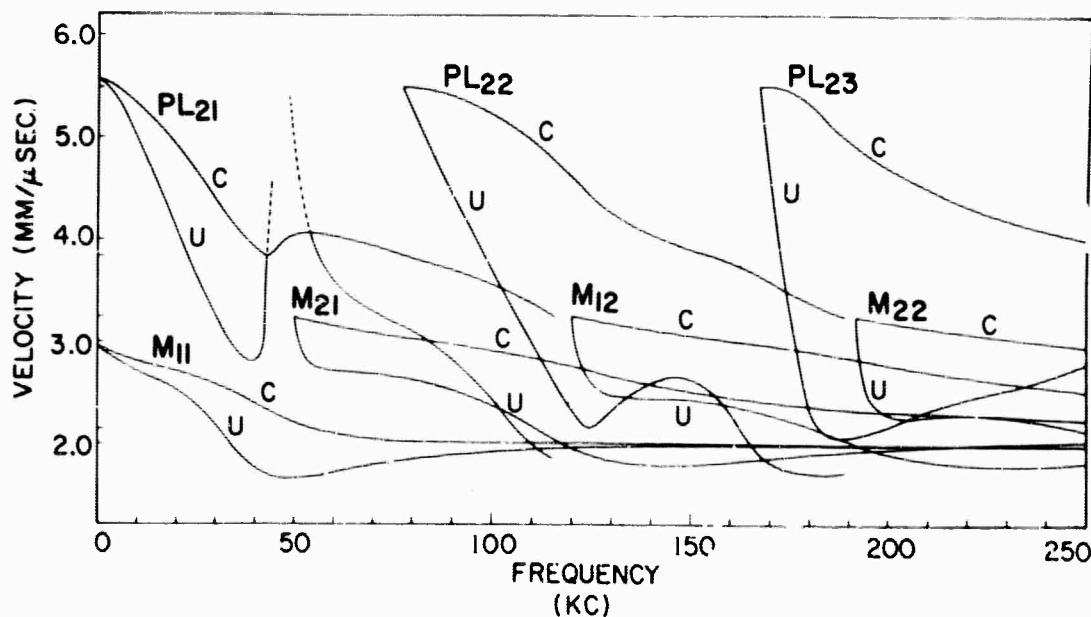


FIG. 3.1. Dispersion curves for the dominant normal and leaky modes in model H-1.

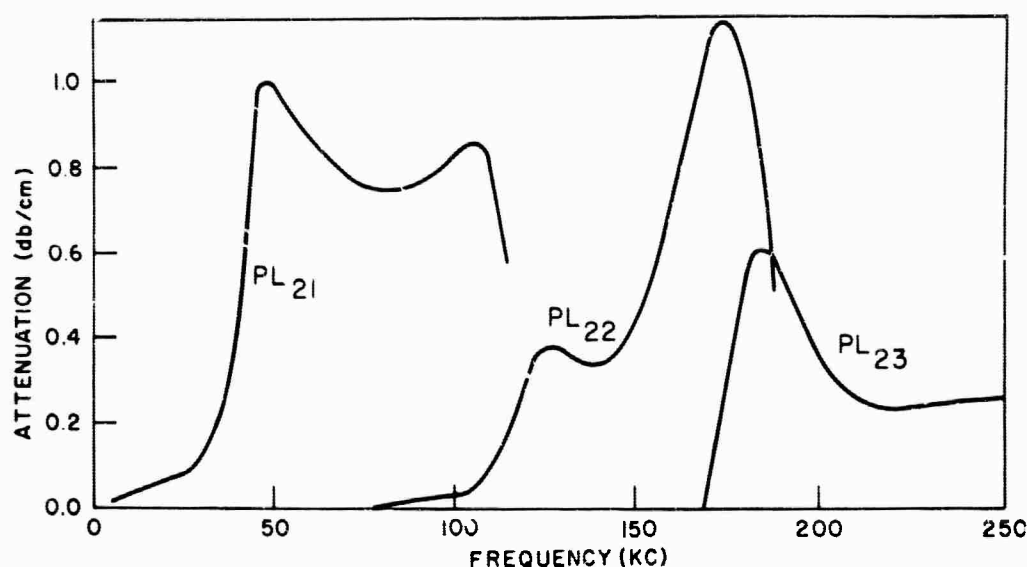


FIG. 3.2. Attenuation as a function of frequency for the first three *PL* modes.

Seven significant modes of propagation were anticipated in the frequency range of interest (0–250 kc/sec)—three leaky (*PL*) and four normal (trapped) modes. The *PL* modes represent early-arriving refracted events which have been multiply reflected between the base of the layer and the free surface, while the normal modes contain mainly shear and Rayleigh energy. The theoretical dispersion curves are shown in Figure 3.1. The very steep group velocity curves of the leaky modes indicate that these modes have an almost sinusoidal appearance.

The name convention for the M_{1j} and M_{2j} modes is based on analogy with the normal modes of an infinite free plate. The modes of a free plate have displacement distributions which are either symmetrical (M_{1j}) or antisymmetrical (M_{2j}) with respect to the median plane of the plate. When, as in the present investigation, the plate is bounded to a half-space, the motion is only approximately symmetrical or antisymmetrical. The *PL* modes, with the exception of PL_{21} , are the mathematical continuations for frequencies below cutoff of the M_{2j} shear modes.

The attenuations of the leaky modes are shown in Figure 3.2. Each of these curves begins with a very low attenuation but increases rapidly. Each mode has one or more peaks in the attenuation function. An attenuation of 1.0 db/cm indicates a decay to 10 percent of original amplitude while traveling through 20 cm.

For completeness, an additional set of leaky

modes is mentioned—the so-called “Organ Pipe” modes (Rosenbaum, 1960). These fall into two categories— Σ modes and π modes. (The present name convention conforms with that of Gilbert, 1963.) The Σ modes are extensions below cutoff of the M_{1j} shear modes (with one exception discussed below). These are composed primarily of near-vertically reflected shear waves. The π modes are not extensions of realizable shear modes but consist primarily of near-vertically reflected compressional waves. The locations of typical Σ and π modes in the complex k plane are shown in Figure 4.1, and the dispersion curves for the first four of these modes is shown in Figure 4.2. The attenuation is very high, being on the order of 7 db/cm, with minimum value of 1.5 db/cm. However, for the model investigated, the attenuation decreases with mode number for the Σ modes. Because of the high attenuation, the Organ Pipe modes are important only from a mathematical standpoint for the present study.

The strange appearance of the dispersion curves for the Organ Pipe modes appears to be a characteristic of the method of computation that has been used, i.e., real frequency, complex wave-number. If the original Fourier transforms are performed in the reverse order and the wavenumber taken to be real, the Organ Pipe dispersion curves have a more reasonable shape. In particular, the phase velocity becomes infinite for specific frequencies (real part) as would be expected for vertically bouncing waves (Gilbert, 1963). Fi-

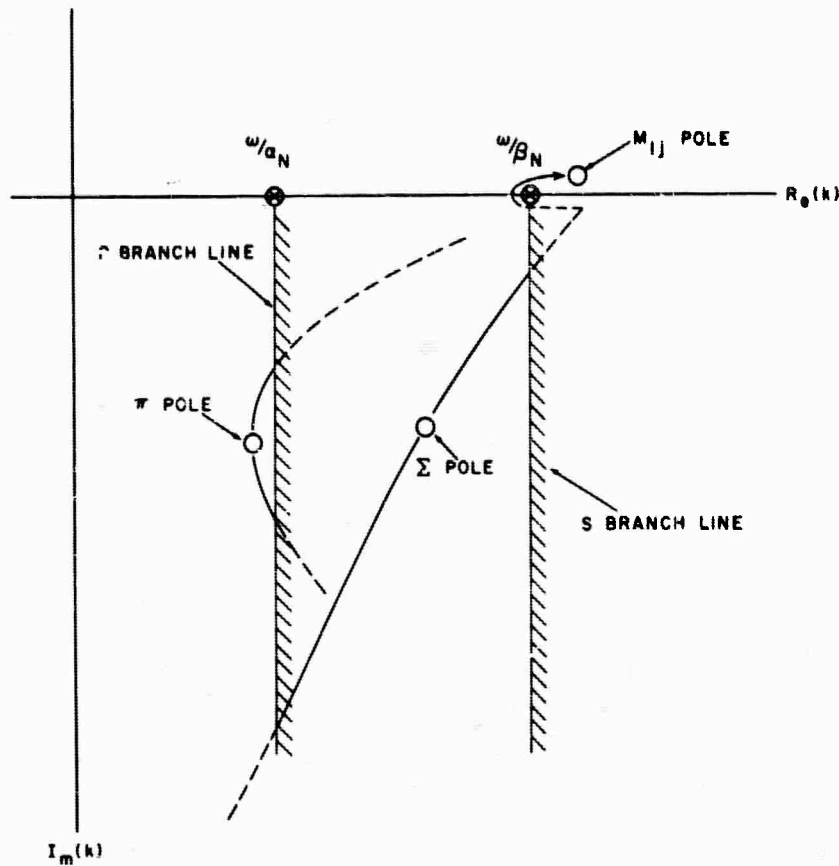


FIG. 4.1. Schematic diagram of fourth quadrant of complex k plane showing typical motions of π and Σ mode poles as functions of frequency.

nally, with this alternate representation, Σ_1 becomes the extension of M_{12} and PL_{21} the extension of M_{21} . This indicates that the two modes actually intersect at some point in the doubly complex k, ω plane. An indication of this is shown in Figure 4.3. The solid curves are the paths of the PL_{21} and Σ_1 poles found by taking the frequency real and finding the complex wavenumber root of the secular equation. The dashed curves are similarly computed by taking wavenumber real and finding the complex frequency root. It can be seen that various segments of the original curves are paired differently in the latter case. Solutions for arbitrary complex frequencies near the real frequency axis have shown the two sets of curves approaching a point of intersection. At that point, $\Delta(k, \omega) = 0$ has a double root and the function $k(\omega)$ has a branch point. The nearness of this point to the real ω axis is the cause of the exceptional behavior of PL_{21} at about 50 kc/sec in Figure 3.1. It might also be mentioned that the high theoretical group velocity PL_{21} at 50 kc

should not be taken too seriously since the integrand of the frequency integral no longer satisfies the conditions for the validity of a stationary phase approximation. Near the peak in the attenuation function, the theoretical curve no longer represents the group velocity.

Once the elastic disturbance has been initiated, the individual modes propagate independently of each other. The propagation of each mode is determined by its dispersion curve, while the relative amplitude of the various modes depends on the model parameters and the source-receiver configuration. The spectral excitation functions for the first four normal modes are shown in Figures 5.1 and 5.2. These curves were computed for a receiver and vertical force source both located at the free surface of the brass layer ($z=0$). These excitation functions are independent of horizontal source-receiver distance as long as that distance is great enough for the mode theory to be valid. The Rayleigh (M_{11}) mode has approximately ten times the amplitude of the other modes

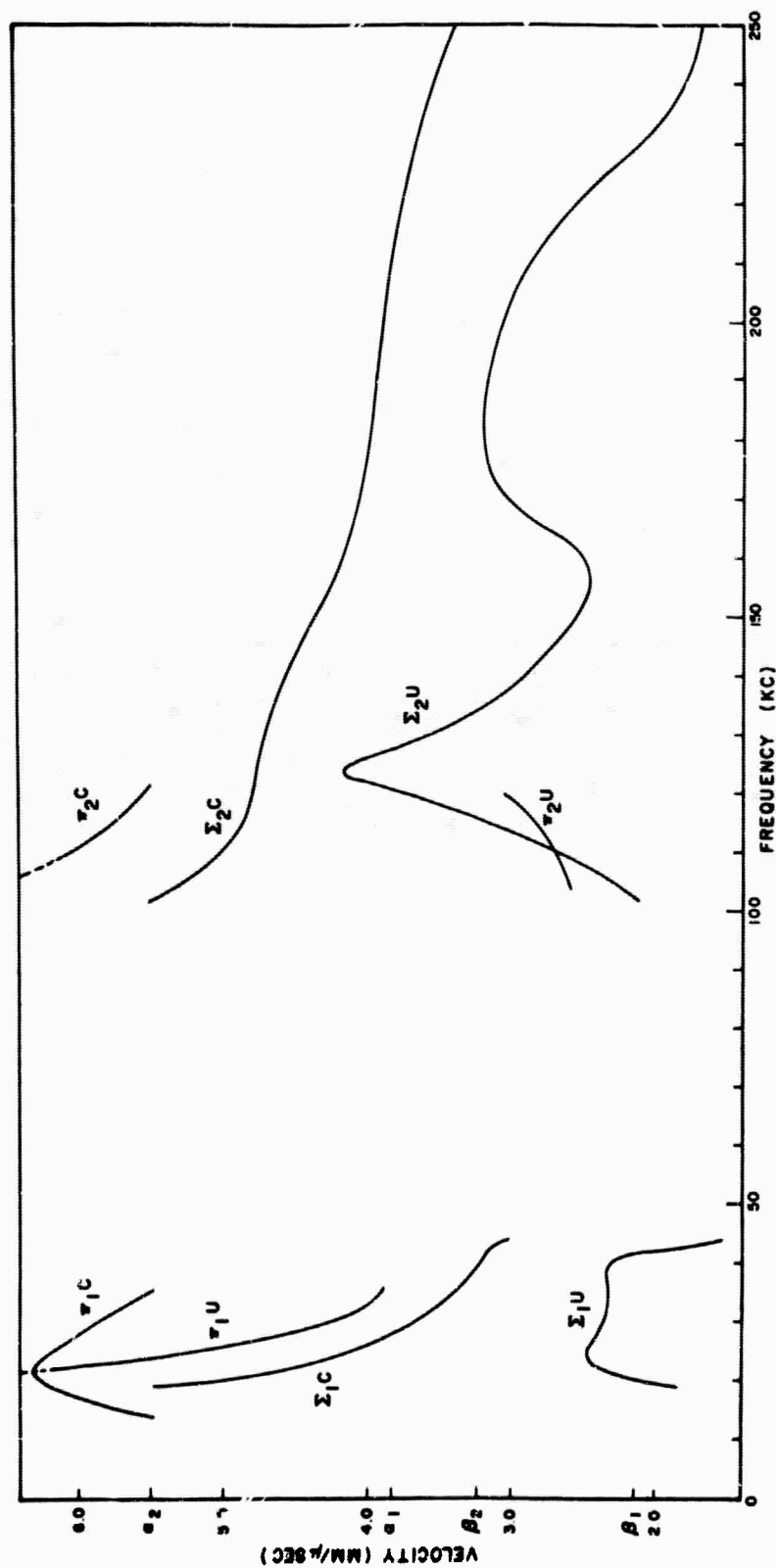


FIG. 4.2. Dispersion curves for the Organ Pipe modes Σ_1 , Σ_2 , π_1 , and π_2 in model H-1.

though the peaks in the spectra occur at different frequencies. In all four modes, the vertical displacement is significantly greater than the horizontal displacement. There is a $\pi/2$ phase difference between horizontal and vertical displacement at every frequency.

The excitation amplitudes for the three *PL* modes also have been computed for the source and receiver on the surface. The amplitudes are shown in Figures 5.3 and 5.4. The *PL* excitation

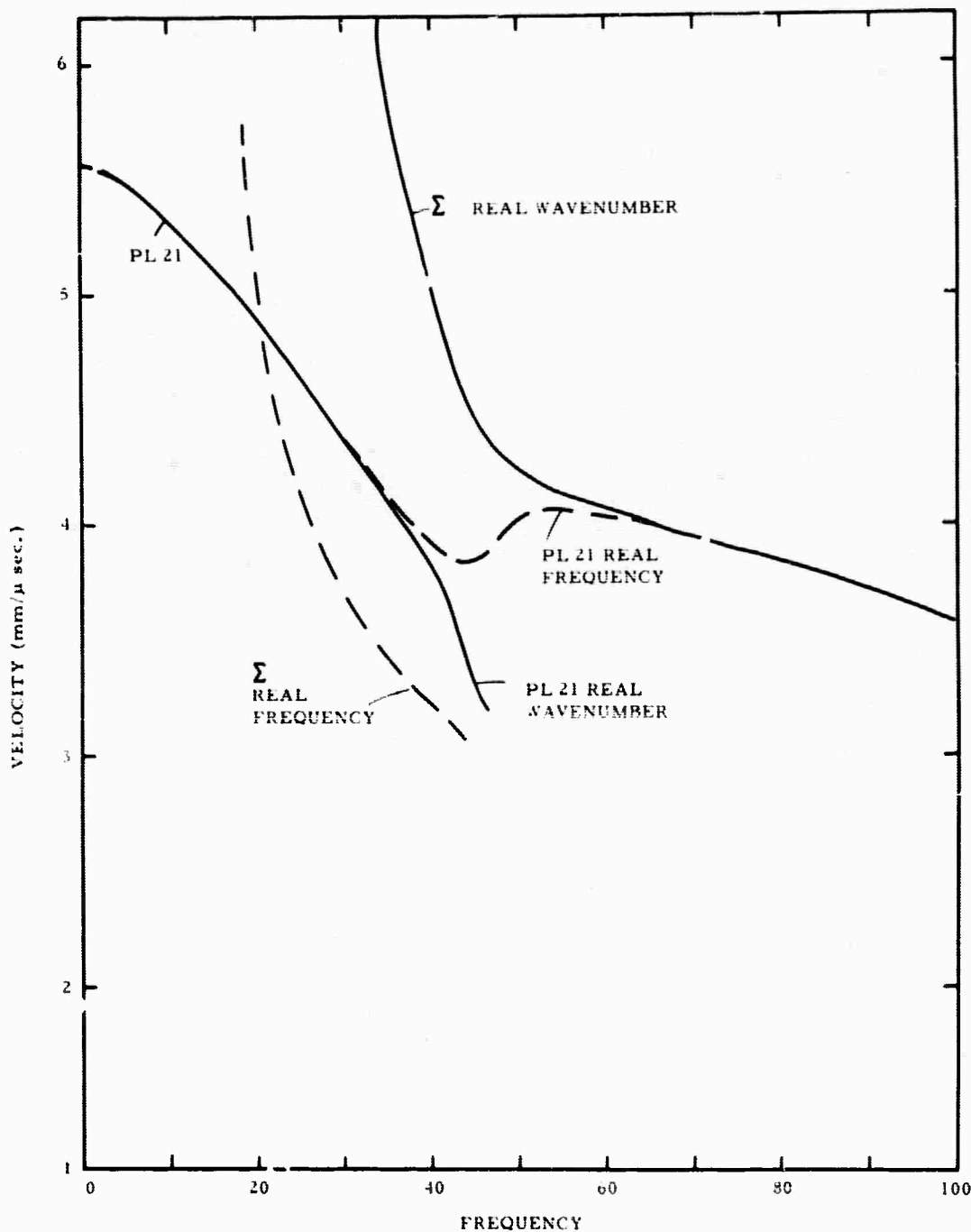
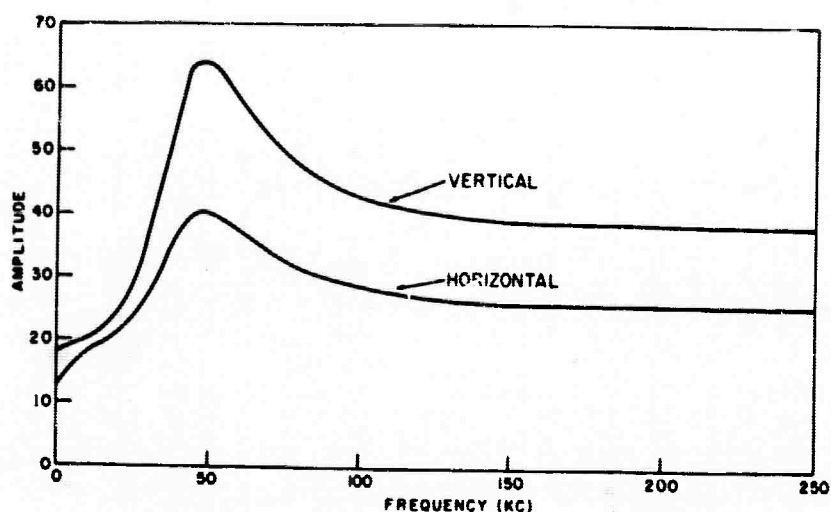


FIG. 4.3. Dispersion curves for the lowest order leaky modes. The dashed curve shows the path of PL_{21} and Σ_1 for real frequency and complex wavenumber. The solid curves show the corresponding PL_{21} and Σ_1 paths for complex frequency and real wavenumber. An intersection in the doubly complex frequency-wavenumber plane is indicated.

RAYLEIGH MODE

FIG. 5.1. Spectral excitation functions for the Rayleigh mode M_{11} .

functions are complex, so the phase difference between horizontal and vertical displacements is different at each frequency. The low-frequency end of each mode begins with low amplitude and, with increasing frequency, builds up, giving a series of maxima and minima. The frequencies at which the excitation minima occur coincide with the frequencies of group velocity maxima and attenuation minima; i.e., frequency bands having low excitation amplitude propagate with high velocity and decay slowly with distance. The converse is true for excitation maxima. At moderate distance, the effects of attenuation and excitation are offsetting, producing a very complicated seismogram.

It is difficult to adequately compare the amplitudes of the leaky modes and the shear modes unless the effects of attenuation are considered. In Figure 5.5, the relative power for vertical displacement in the various modes is shown for a source-receiver distance of 50 cm. It is seen that, at their spectral peaks, the modes PL_{21} and PL_{22} have about the same power density as the shear modes. Also, it is seen that the cumulative effect of attenuation in the leaky modes is to produce highly peaked spectra. Once again, this indicates a very sinusoidal-appearing arrival.

HORIZONTAL TRANSFER FUNCTION FOR NORMAL AND LEAKY MODES

The description of modal propagation is particularly simple for propagation between two

identical receivers on the surface of the model. One may speak of a "transfer function" which operates on single mode at one distance to change it into the same mode at greater distance. The transfer function for the total seismogram, however, is very complicated and depends on the source and source-receiver distance. For normal modes in a two-dimensional model, the frequency domain transfer function is a pure phase distortion which tends to stretch out the seismogram in time. If this function is represented as $e^{i\theta}$, the phase shift θ is given by

$$\theta(f) = -\frac{2\pi f}{c(f)} \Delta x.$$

The phase velocity $c(f)$ is obtained from the theoretically determined dispersion curves (Figure 3.1). If the behavior of a mode is known in propagating through a unit distance, it is clear that its behavior everywhere on the surface of a plane-layered model can be determined easily. For leaky modes, the transfer function contains an additional factor $e^{-\tau x}$ where $\tau(f)$ is the frequency-dependent attenuation.

The modal transfer functions also have a simple interpretation in models with crustal thickness variation. The transfer function between two receivers for a single mode is relatively independent of complications in the path between the source and near receiver but depends strongly on the local layering in the vicinity of the two re-

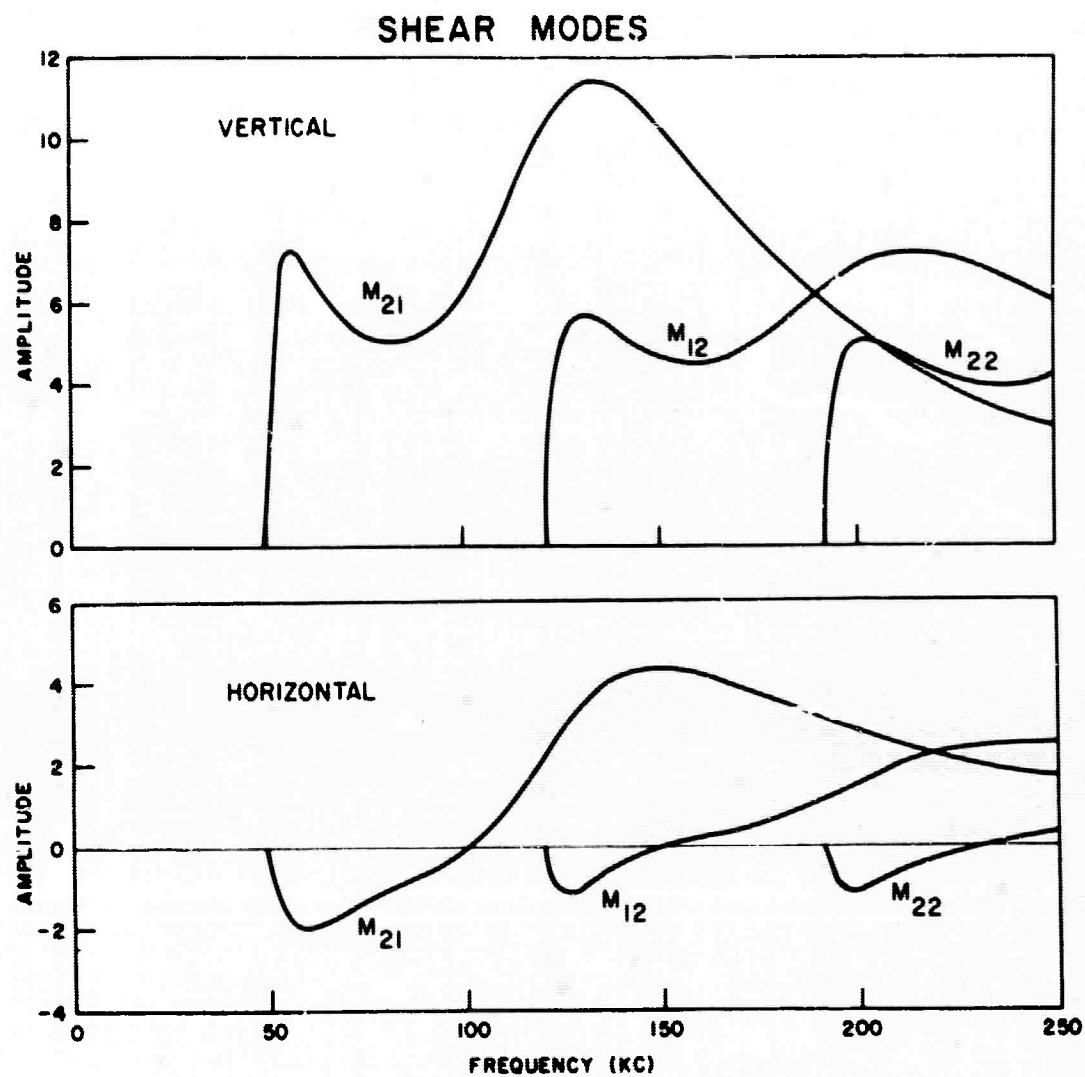


FIG. 5.2. Spectral excitation functions for the first three shear modes.

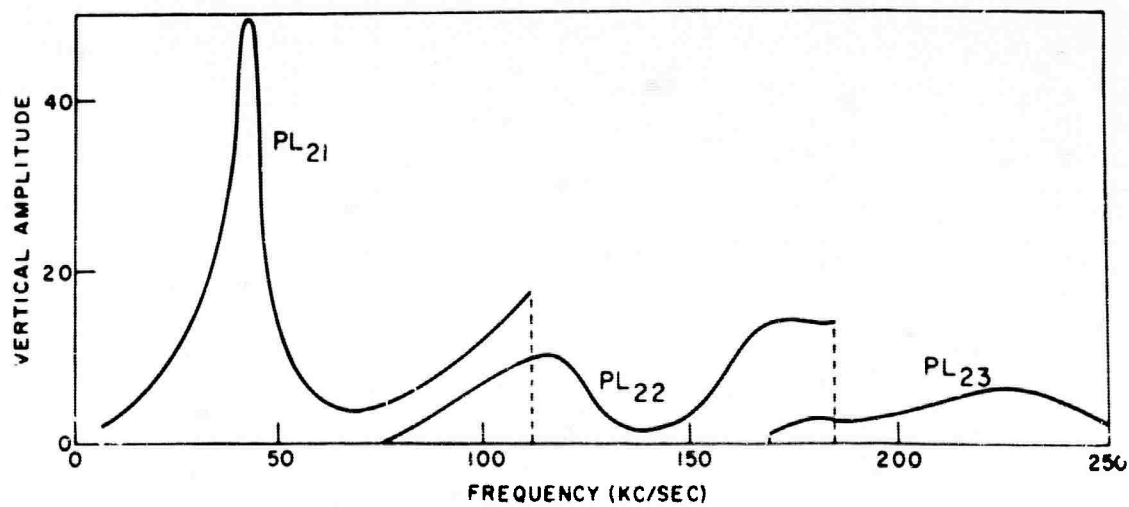


FIG. 5.3. Vertical excitation functions for the first three *PL* modes.

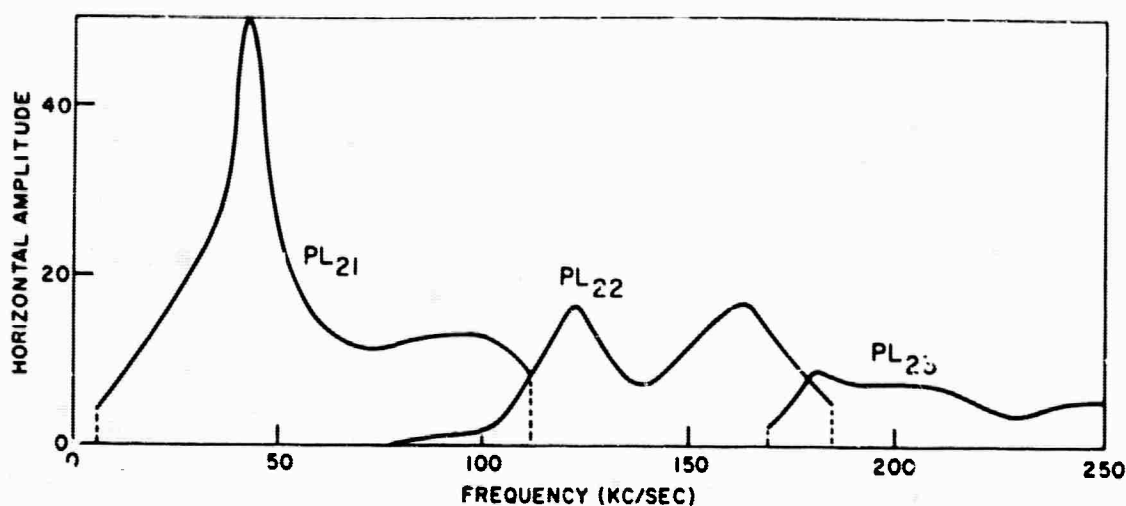


FIG. 5.4. Horizontal excitation functions for the first three PL modes.

ceivers. Experimental dispersion information contained in such a transfer function thus may be interpreted in terms of local crustal structure.

Transfer functions are more useful when represented in the time domain. This may be accomplished by performing the inverse Fourier transform operation on the frequency spectrum. One difficulty does arise, however. Consider, for example, M_{12} (Figure 5.2). The idealized amplitude spectrum is flat over the frequency band of

interest at zero outside. The inverse transform of this, with the phase spectrum discussed above, gives a very long, ringing time function. The frequencies readily observable in the time function are the cutoff frequencies of the spectrum; however, since the mode does not contain energy outside the band of interest, it is of no importance how the amplitude response of the transfer function behaves there. Therefore, the amplitude function was modified (Figure 6.1) before computing the time function. The resulting transient transfer functions are shown in Figure 6.2. These short, well-behaved filter operators, when applied to the appropriate mode at some distance, yield the same mode one unit distance farther away from the source. The unit of distance here is one cm. The phase information contained in the dispersion curve is not visually apparent in the time functions. As a final check, the direct Fourier transforms of the transfer functions were computed and the phase velocities recalculated from the phase spectrum. Excellent agreement was obtained.

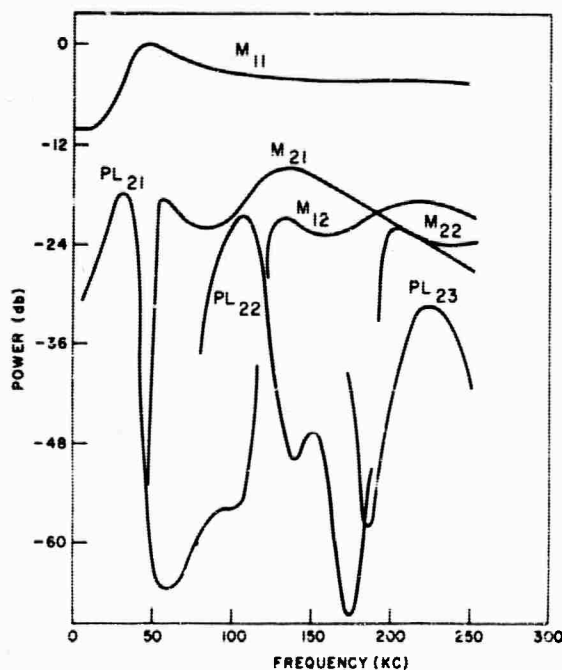


FIG. 5.5. Relative vertical power spectra of leaky and normal modes at 50 cm distance from source.

THEORETICAL SEISMOGRAMS FOR A LAYER OVER A HALF-SPACE

Using the dispersion curves and the surface excitation functions, theoretical seismograms were computed for the leaky and normal modes. The inverse Fourier transform was performed numerically for the distance 50 to 70 cm in two-cm increments using 2.5 kc frequency increments in the summation. On the basis of sampled data theory, this yields 400 μ s of independent time

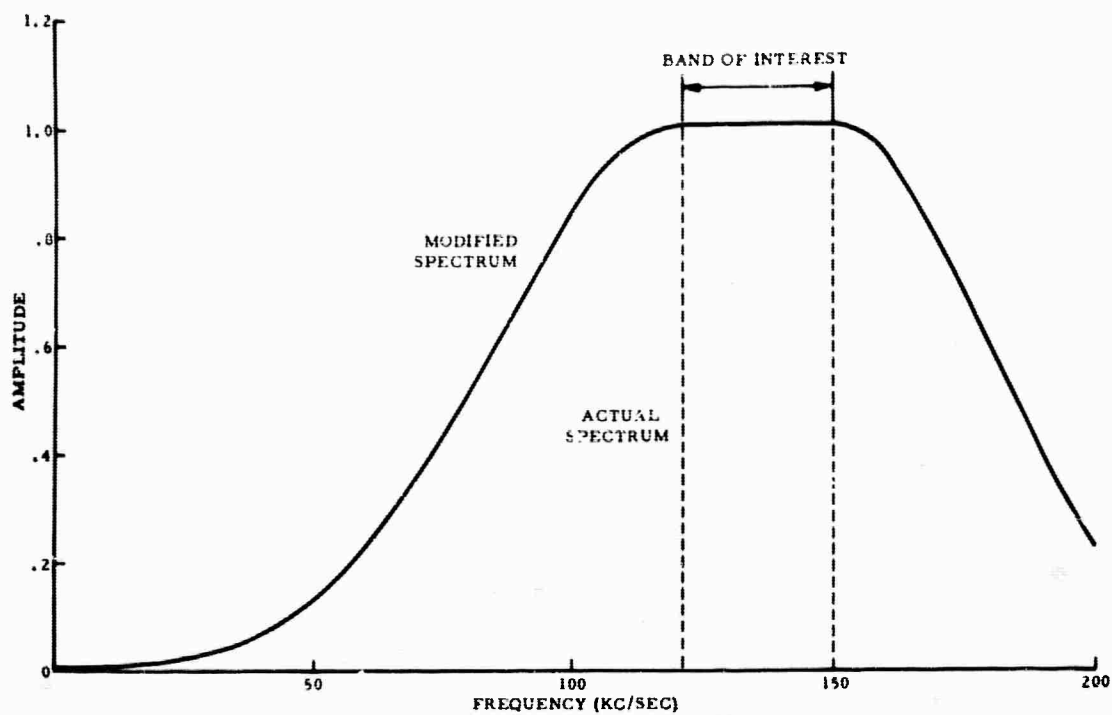


FIG. 6.1. Idealized and modified amplitude spectra for the transfer function of shear mode M_{12} . The idealized spectrum is shown in dotted lines.

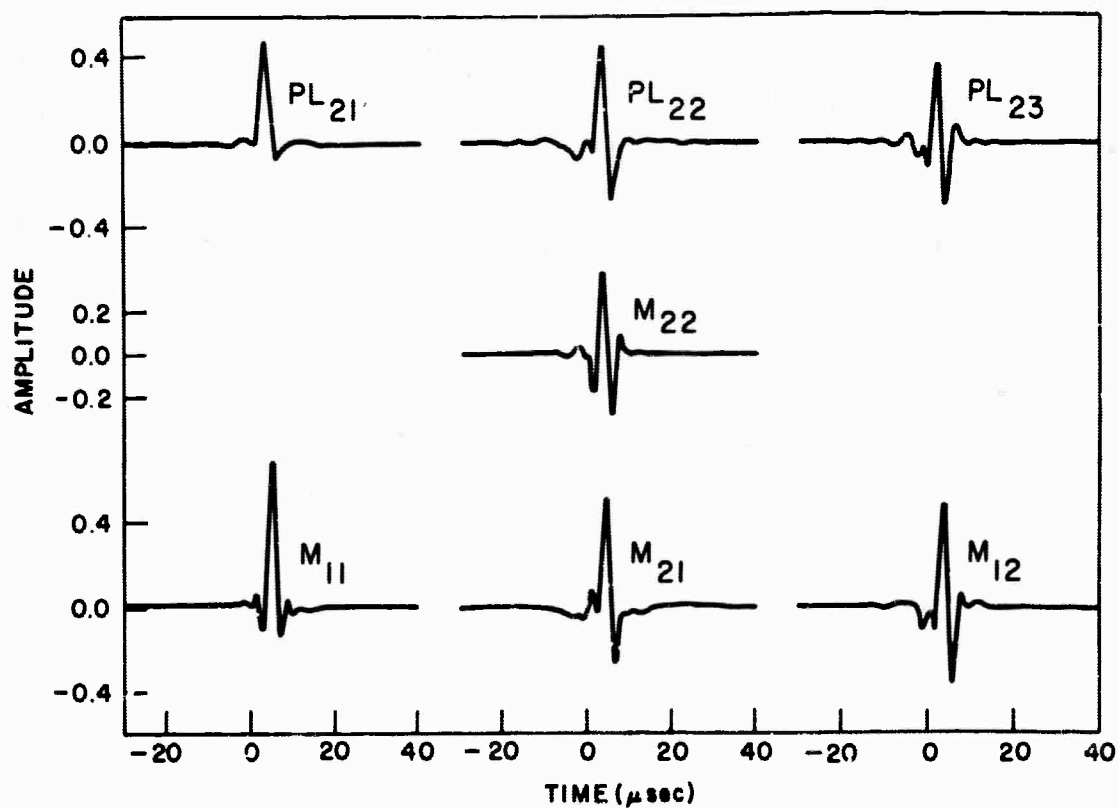


FIG. 6.2. Transfer functions between station one cm apart for the dominant leaky and normal nodes in model H-1. Note that for this short distance a two-sided operator is necessary. All operators are shown to be 71 μ sec long. However 400 μ sec were used for M_{11} and PL_{21} because of their low-frequency content.

data. A study of the group velocity curves shows that this should be sufficient for distances of 50 to 70 cm. The vertical traces for 51 cm to 69 cm (in two-cm increments) were computed by applying the modal transfer functions to the directly integrated traces. The seismograms are presented in Figures 7.1 to 7.14. The source time function, assumed to be a zero phase band-limited impulse (0-250 kc/sec), was implicitly included by truncation in the frequency domain.

Seismograms for the first shear mode (Figure 7.2) show the effects on the seismograms of subsidiary group velocity maxima and minima. The motion begins with very small amplitude but begins to develop a pulse-like appearance at the time appropriate to the group-velocity maximum near 65 kc. The succeeding high amplitudes correspond to the group-velocity minimum at 60 kc. The maxima and minima are very slight in this case, forming almost an inflection point on the curve. If this pulse were interpreted experimentally as the first shear arrival, the value assigned to the shear velocity would be too low. This particular pulse, which also occurs in the higher

modes with lower and lower group velocity, is related to the leaky interface pulse found in a model consisting of two half-spaces (Gilbert and Laster, 1962b).

The particle motion associated with M_{21} is also of some interest. For a source and receiver on the surface, the vertical motion excitation function has no nodes (as a function of frequency), while the horizontal motion excitation has one node. Thus, at low frequencies (corresponding to the early-arriving pulse), the motion is prograde elliptical while, for late-arriving high frequencies, the motion is retrograde. An example of this is shown in Figure 8; the abscissa being the horizontal displacement and the ordinate the vertical displacement. The curve shown is the locus of a point on the surface of the model.

The dominant group velocity minimum also gives rise to a pulslike event occurring at the end of the seismogram. This high-amplitude pulse is called the Airy phase. Pekeris (1948) has shown that the point of maximum amplitude occurs somewhat before the time associated with minimum group velocity. Strictly speaking, pulses

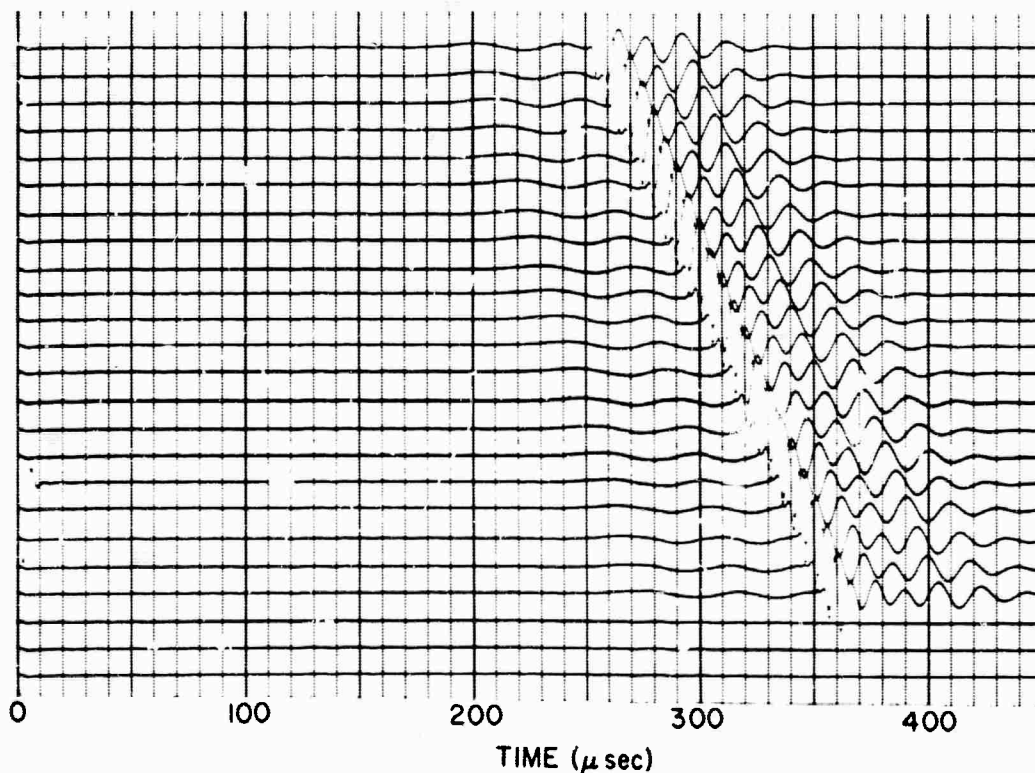


FIG. 7.1. Theoretical vertical seismogram for the Rayleigh mode M_{11} in the distance range 50 to 70 cm. The smallest time markers are 10 μ sec apart. The successive traces are one cm apart. Gain -24 db.

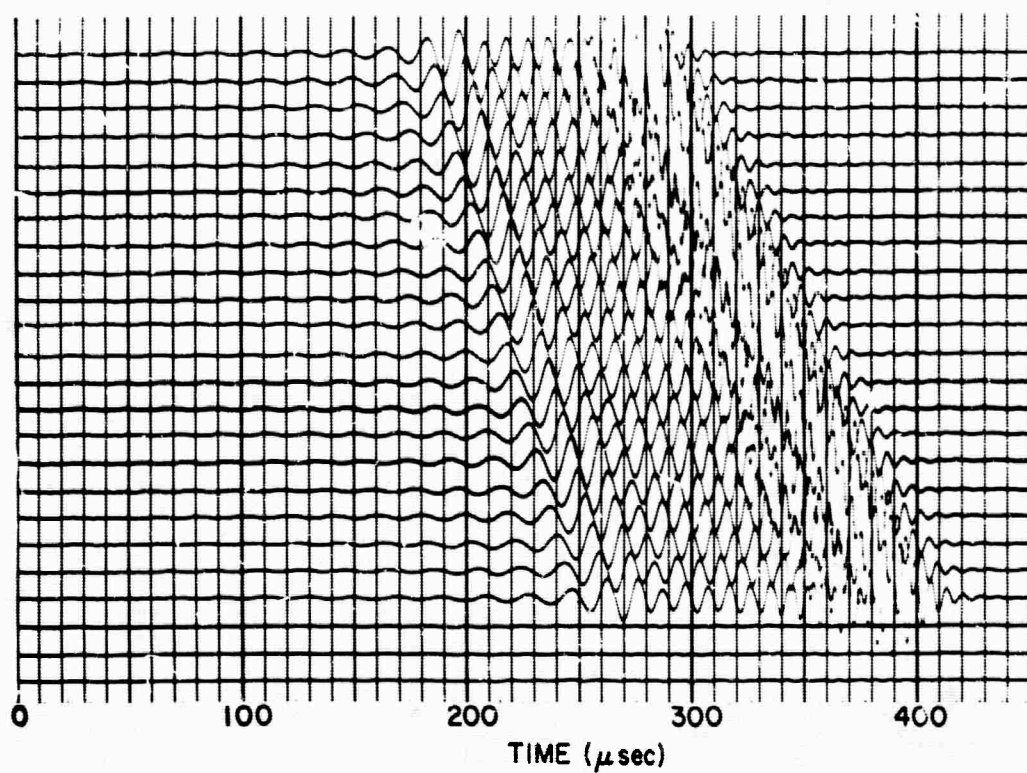


FIG. 7.2. Theoretical vertical seismogram for the shear mode M_{21} in the distance range 50 to 70 cm. The smallest time markers are 10 μ sec apart. The successive traces are one cm apart. Gain 0 db.

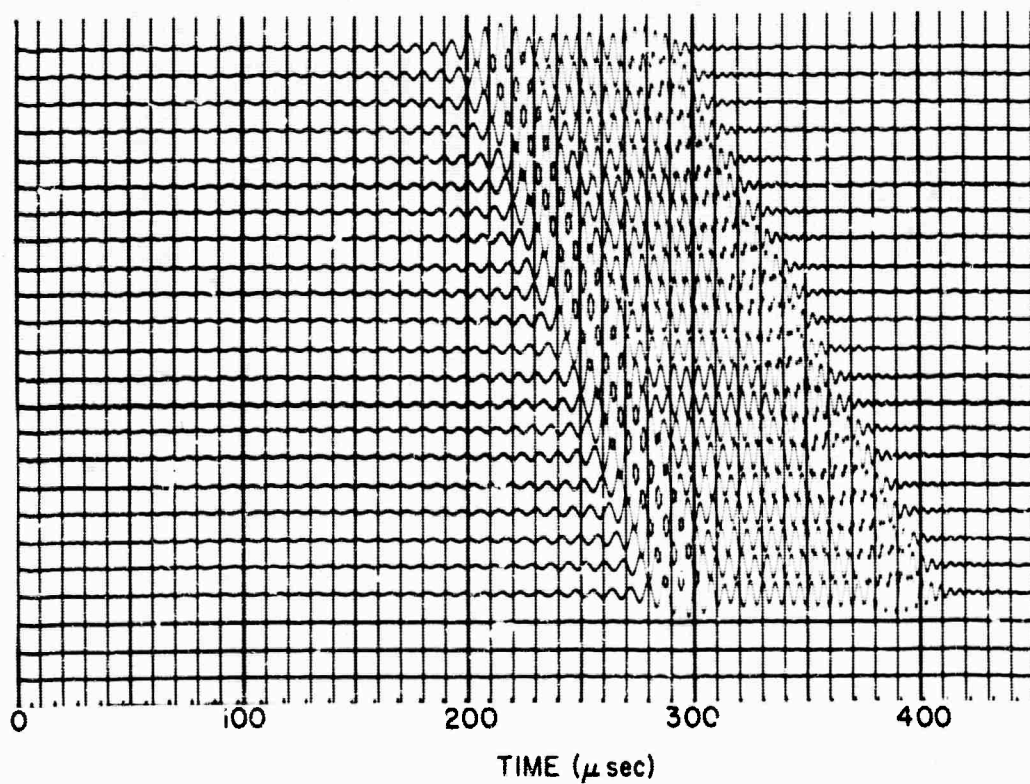


FIG. 7.3. Theoretical vertical seismogram for the shear mode M_{12} in the distance range 50 to 70 cm. The smallest time markers are 10 μ sec apart. The successive traces are one cm apart. Gain 0 db.

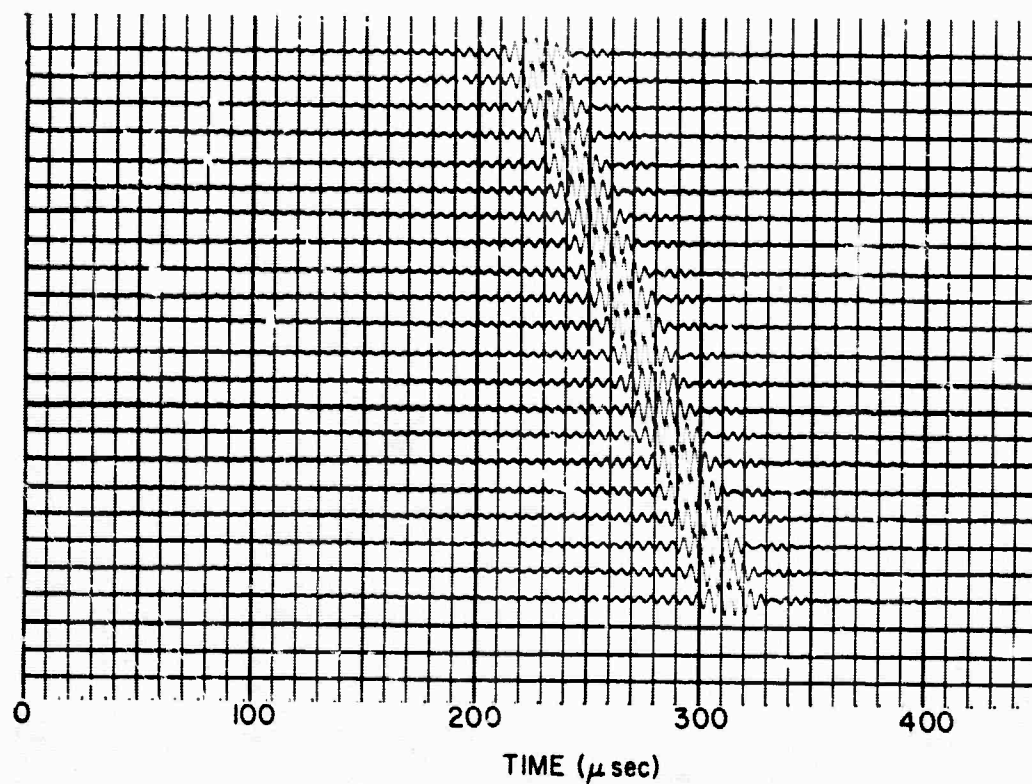


FIG. 7.4. Theoretical vertical seismogram for the shear mode M_{22} in the distance range 50 to 70 cm. The smallest time markers are 10 μ sec apart. Gain 0 db.

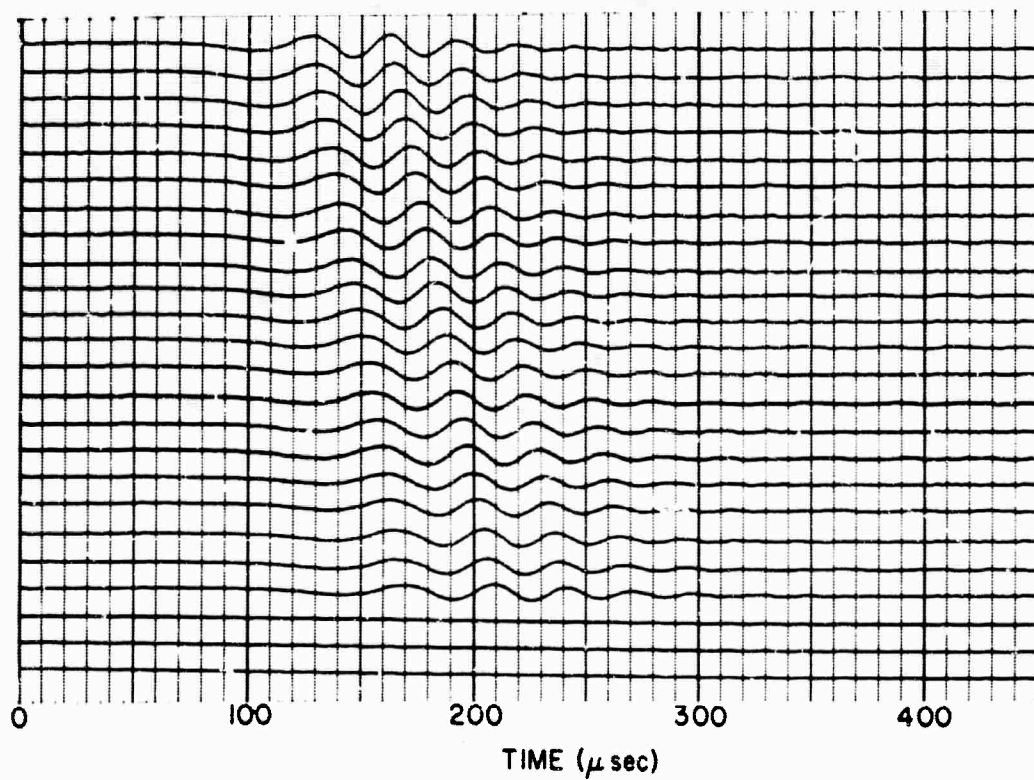


FIG. 7.5. Theoretical vertical seismogram for the leaky mode PL_{21} in the distance range 50 to 70 cm. The smallest time markers are 10 μ sec apart. The successive traces are one cm apart. Gain 0 db.

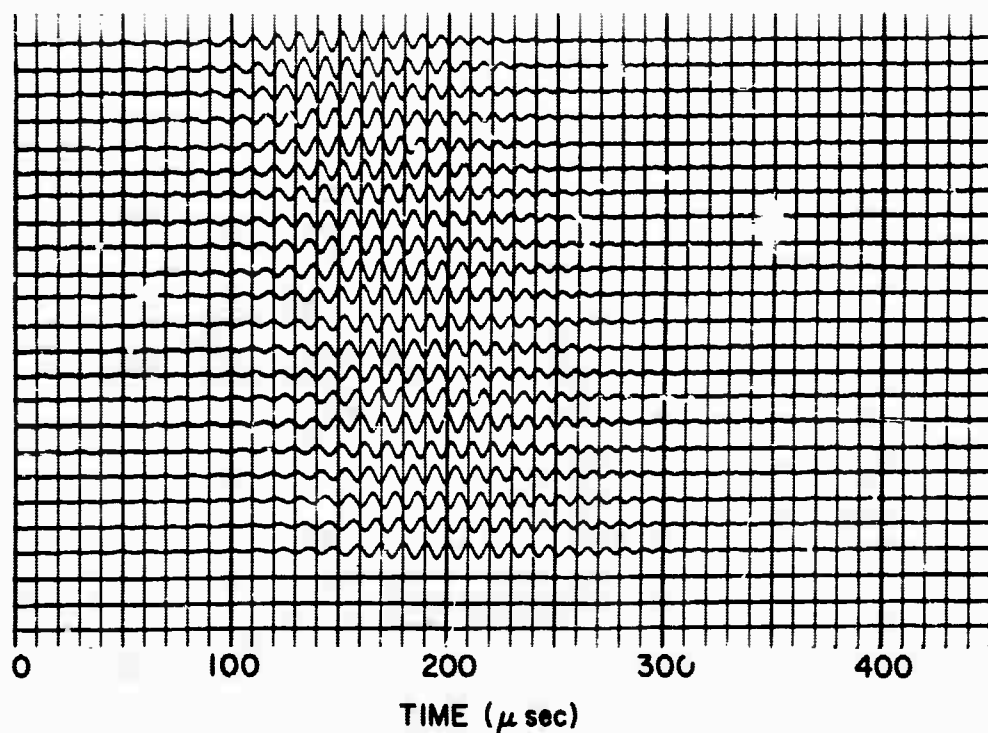


FIG. 7.6. Theoretical vertical seismogram for the leaky mode PL_{22} in the distance range 50 to 70 cm. The smallest time markers are 10 μ sec apart. The successive traces are one cm apart. Gain 0 db.

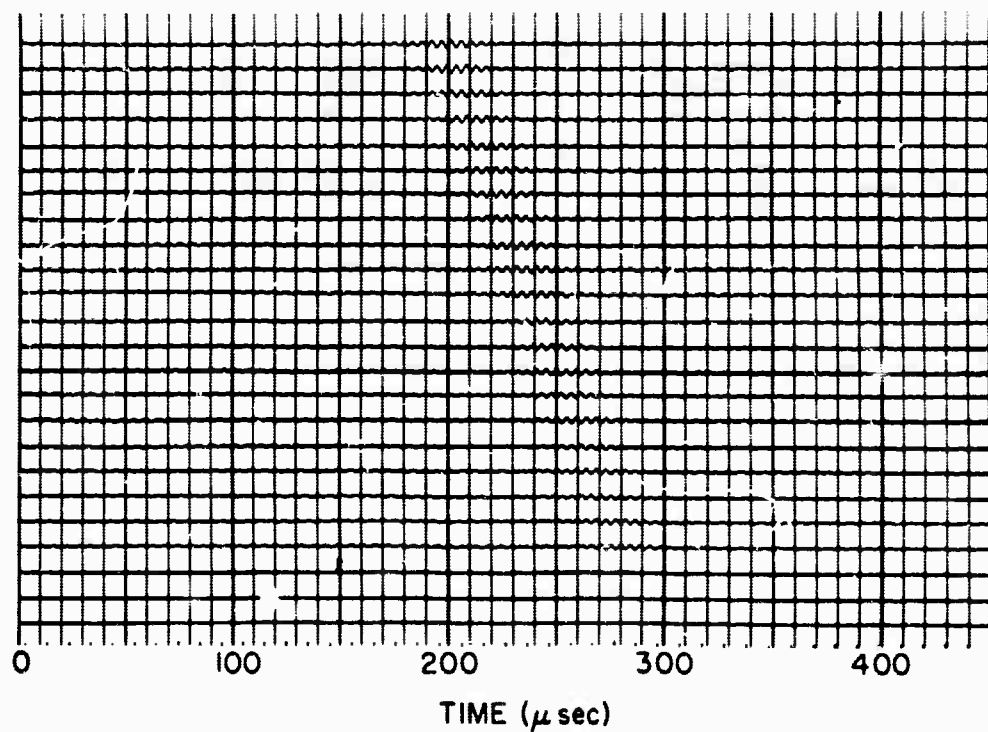


FIG. 7.7. Theoretical vertical seismogram for the leaky mode PL_{23} in the distance range 50 to 70 cm. The smallest time markers are 10 μ sec apart. The successive traces are one cm apart. Gain 0 db.

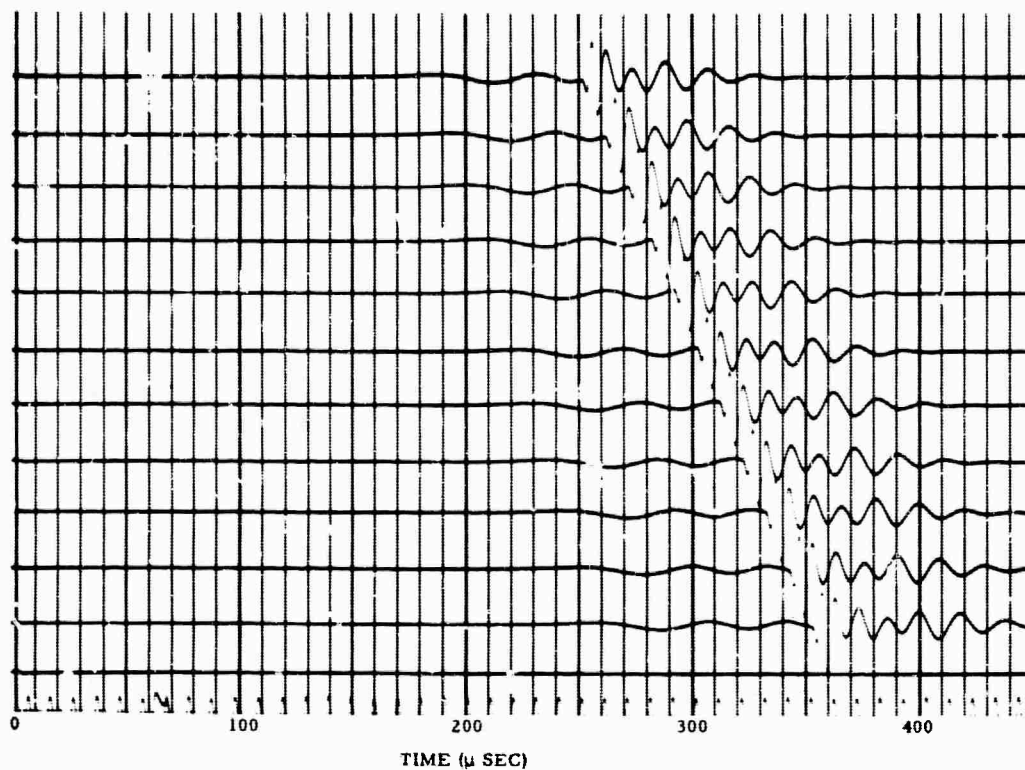


FIG. 7.8. Theoretical horizontal seismogram for the Rayleigh mode M_{11} in the distance range 50 to 70 cm. The smallest time markers are 10 μ sec apart. Distance between successive traces is two cm. Gain -20 db.

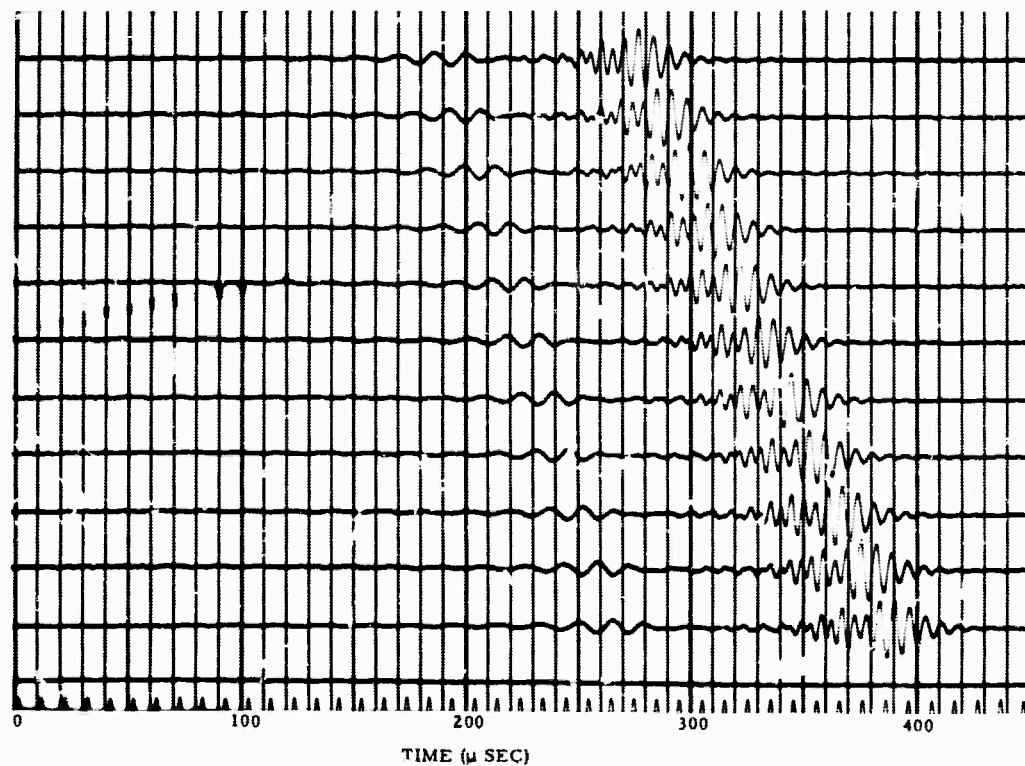


FIG. 7.9. Theoretical horizontal seismogram for the shear mode M_{21} in the distance range 50 to 70 cm. The smallest time markers are 10 μ sec apart. Distance between successive traces is two cm. Gain 0 db.

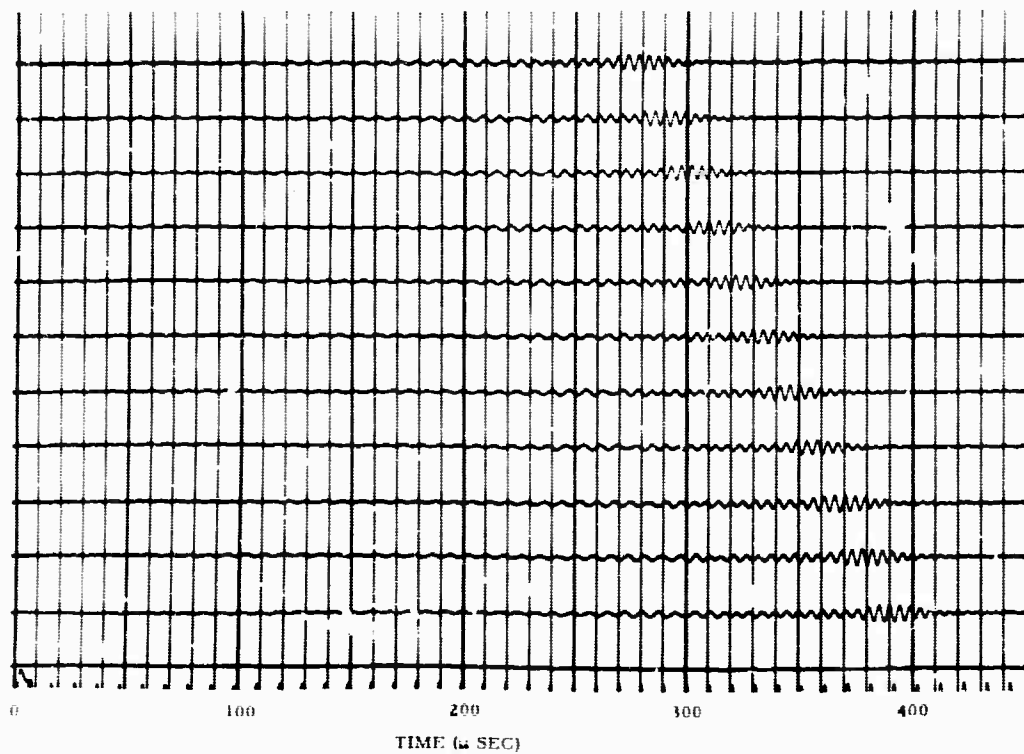


FIG. 7.10. Theoretical horizontal seismogram for the shear mode M_{12} in the distance range 50 to 70 cm. The smallest time markers are 10 μ sec apart. Distance between successive traces is two cm. Gain 0 db.

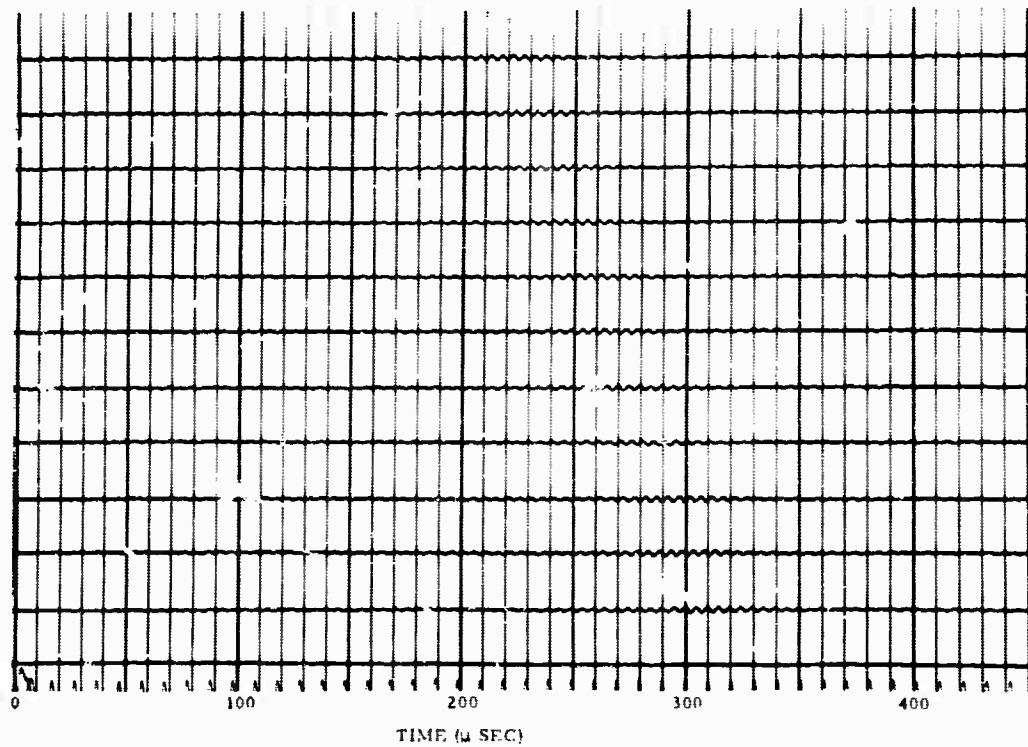


FIG. 7.11. Theoretical horizontal seismogram for the shear mode M_{22} in the distance range 50 to 70 cm. The smallest time markers are 10 μ sec apart. Distance between successive traces is two cm. Gain 0 db.

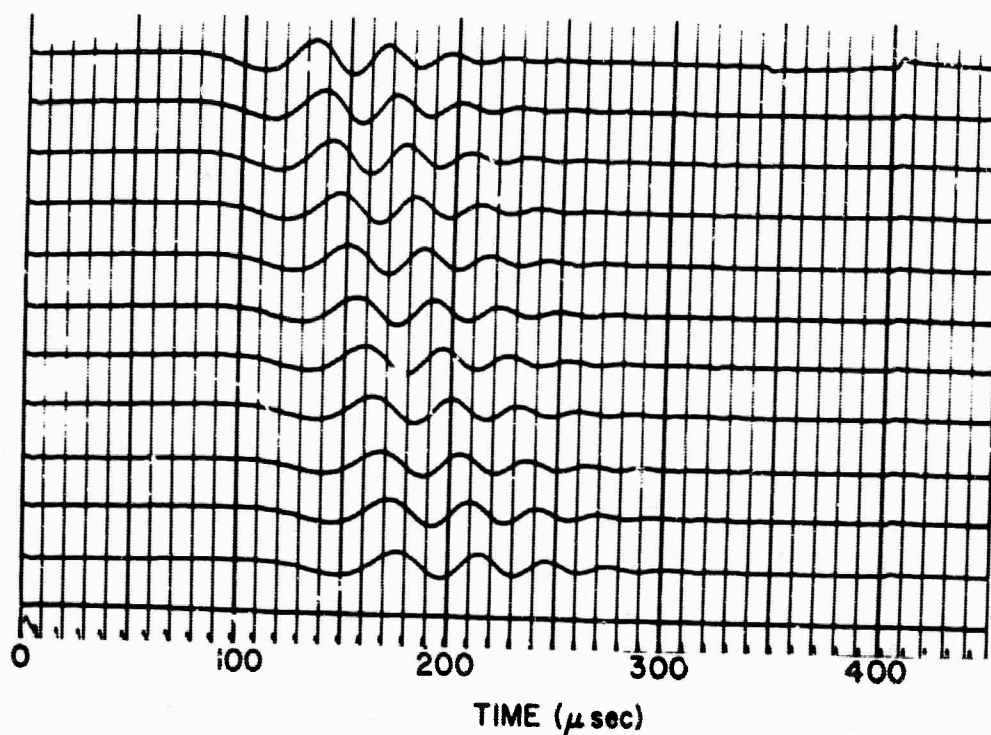


FIG. 7.12. Theoretical horizontal seismogram for the leaky mode PL_{21} in the distance range 50 to 70 cm. The smallest time markers are $10 \mu\text{sec}$ apart. Distance between successive traces is two cm. Gain 0 db.

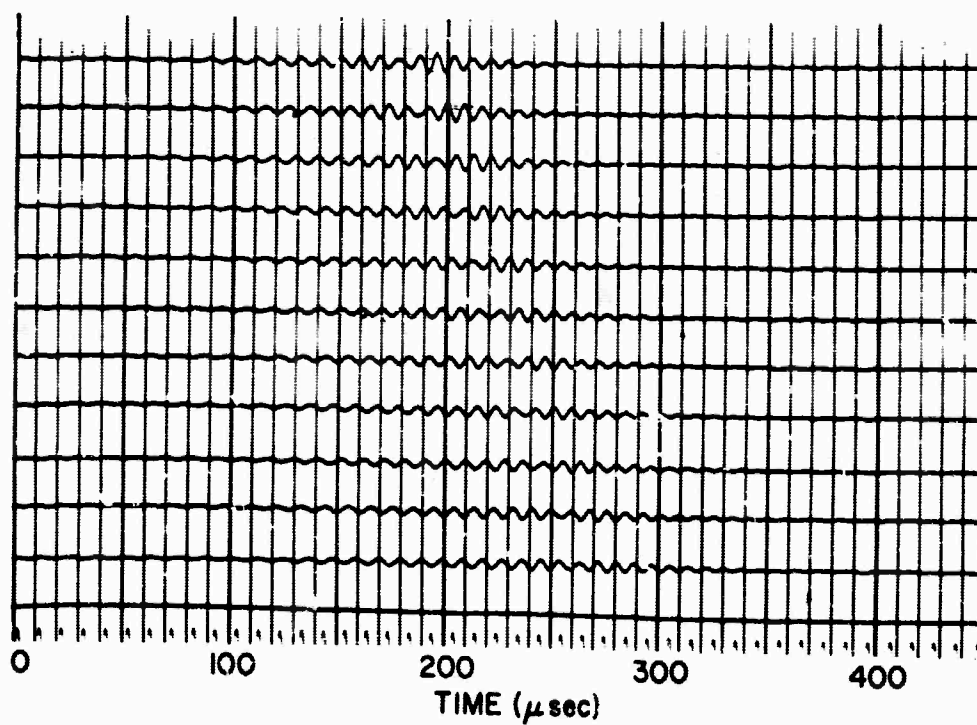


FIG. 7.13. Theoretical horizontal seismogram for the leaky mode PL_{22} in the distance range 50 to 70 cm. The smallest time markers are $10 \mu\text{sec}$ apart. Distance between successive traces is two cm. Gain 0 db.

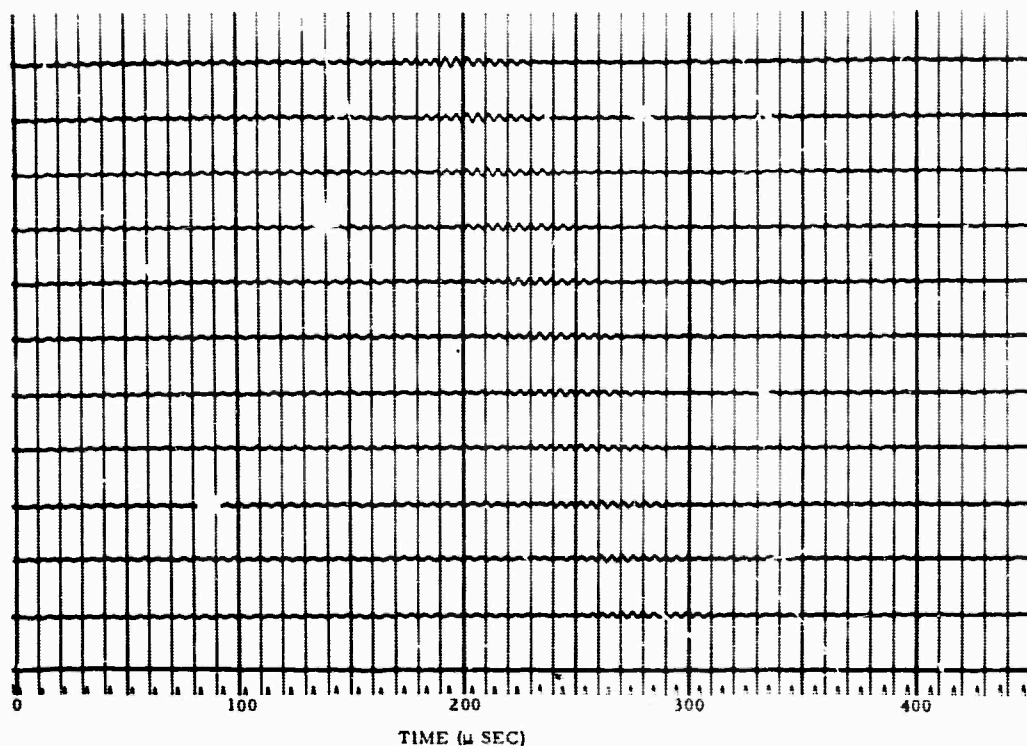


FIG. 7.14. Theoretical horizontal seismogram for the leaky mode PL_{23} in the distance range 50 to 70 cm. The smallest time markers are 10 μ sec apart. Distance between successive traces is two cm. Gain 0 db.

associated with every maximum and minimum can be called Airy phases. The Airy phase associated with a group-velocity maximum behaves like the time reverse of the Airy phase associated with a minimum, having a relatively sharp onset and an indistinct trailing edge.

The first shear mode also shows a striking example of the nontransient behavior discussed above. There is no sharp onset, and the almost constant frequency oscillation is visible even at time zero.

Despite the group-velocity maxima and minima, the leaky-mode seismograms are relatively simple. This is a result of the spectral peaking brought on by attenuation. The PL_{21} mode has enough low-frequency content to show measurable dispersion. This is the "Continental" PL mode of Oliver (1964). The PL_{22} mode is commonly seen in analog model studies (Gilbert and Laster, 1962a). The horizontal motion is somewhat more complicated than the vertical, and dispersion is not visually obvious. The PL_{22} mode is only slightly excited, and the measurable arrivals occur considerably later than the predicted arrival time.

The individual modes were summed to obtain

PARTICLE MOTION FOR M_{21}

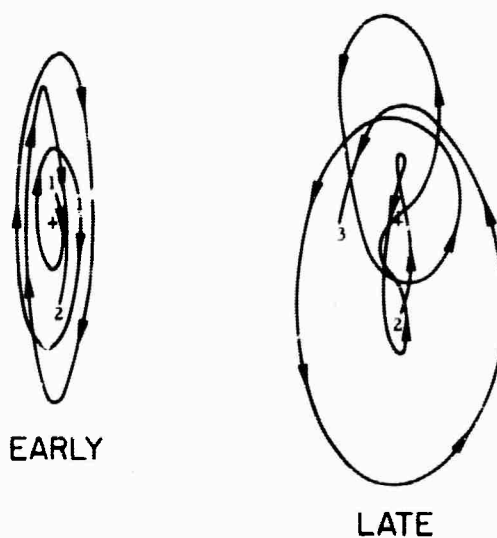


FIG. 8. Particle motion for unfiltered shear mode M_{21} at 50 cm from the source. Seismograms shown in Figures 7.2 and 7.9. The seismogram starts at point labelled 1 and ends at point labelled 3. The left and right figures connect at point 2.

the total seismograms (exclusive of the branch-line integral and the small Organ Pipe modes). The broad-band seismograms are shown in Figures 9.1 and 9.2. The most obvious events are the large, low-frequency energy bands of PL_{21} and M_{11} and the high-frequency pulse of M_{11} . For comparison with analog model experiments, the total seismograms have been filtered to approximate the model source spectrum (70–215 kc/sec). These seismograms are shown in Figures 10.1 and 10.2. For comparison, the analog model records are shown in Figures 11.1 and 11.2. Both sets of records show the PL_{22} mode to be the primary early arrival, a very complicated shear mode zone, and a distance dependent phasing at about the arrival time of the refracted shear. Also, it should be noted that a perfect transient behavior in the theoretical seismograms still has not been achieved.

DISPERSION MEASUREMENTS FROM THEORETICAL SEISMOGRAMS

Attempts were made to measure dispersion of PL_{22} using the theoretically computed total seismograms. In the first experiment, peaks and

troughs on the filtered vertical seismograms (Figure 10.1) were visually correlated across the distances 50 cm to 70 cm. The peaks were numbered on each trace, and the frequency was approximately given by

$$f_n(x) = \frac{1}{t_{n+1}(x) - t_{n-1}(x)}.$$

The phase velocity was obtained approximately from

$$c_n = \frac{x_2 - x_1}{t_n(x_2) - t_n(x_1)},$$

and the group velocity from

$$U_n = \frac{x}{t_n(x)}.$$

The resulting points were plotted as shown in Figure 12.1. This method of measuring dispersion is quite crude as is seen from the results obtained.

A second, more sophisticated method also was used to estimate the dispersion curve. The seismogram was truncated just before the time of ar-

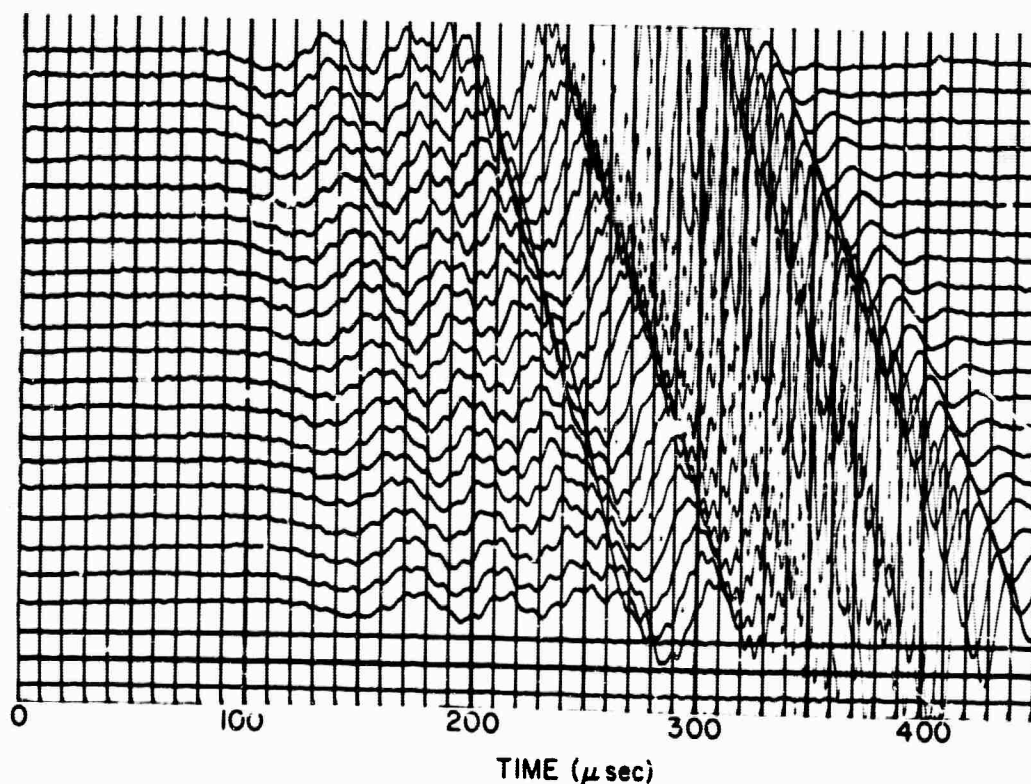


FIG. 9.1 Total horizontal seismograms for distance range 50 to 70 cm. The smallest time markers are 10 μ sec apart. The successive traces are one cm apart. Gain 0 db.

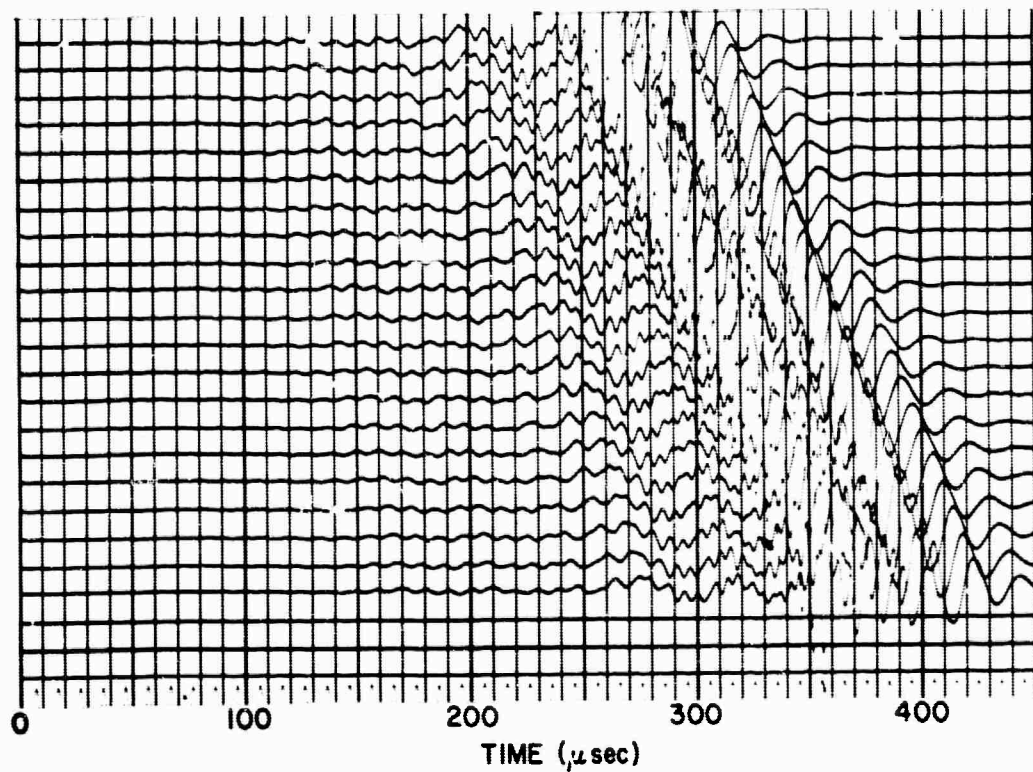


FIG. 9.2. Total vertical seismograms for distance range 50 to 70 cm. The smallest time markers are 10 μ sec apart. The successive traces are one cm apart. Gain 0 db.

FILTER H 215KK L 70KK

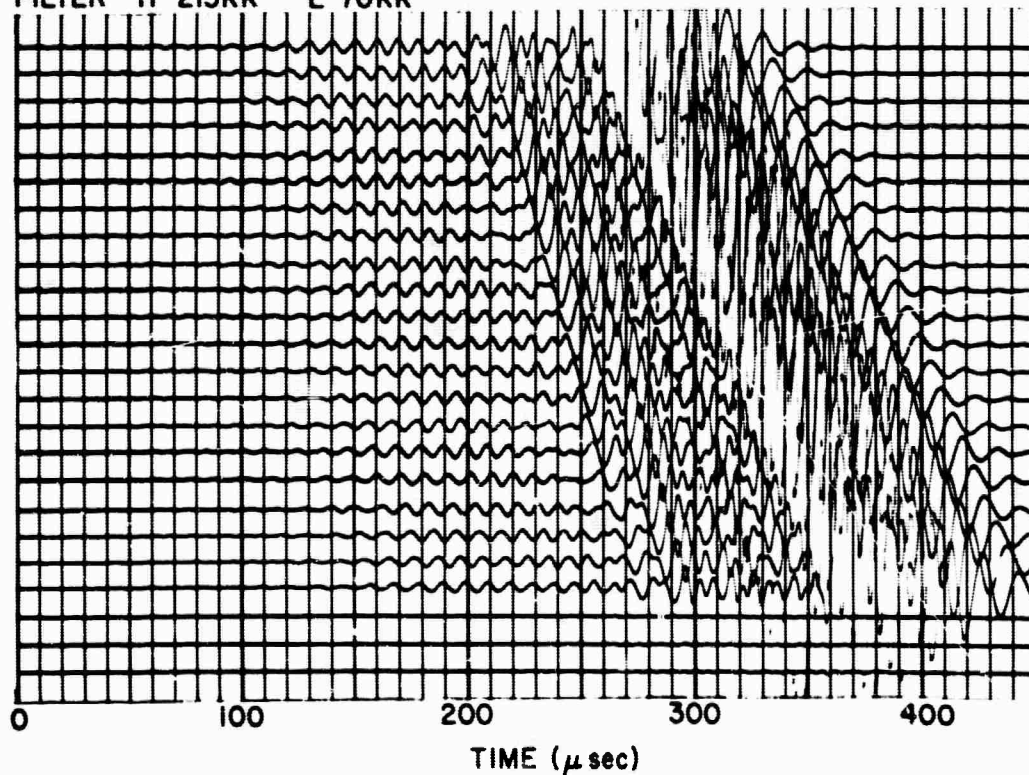


FIG. 10.1. Total vertical seismograms filtered to approximate analog model source (70-215 kc/sec passband). Small time markers are 10 μ sec apart. Distance range is 50 to 70 cm in one-cm increments. Gain 0 db.

FILTER H 215KK L 70KK

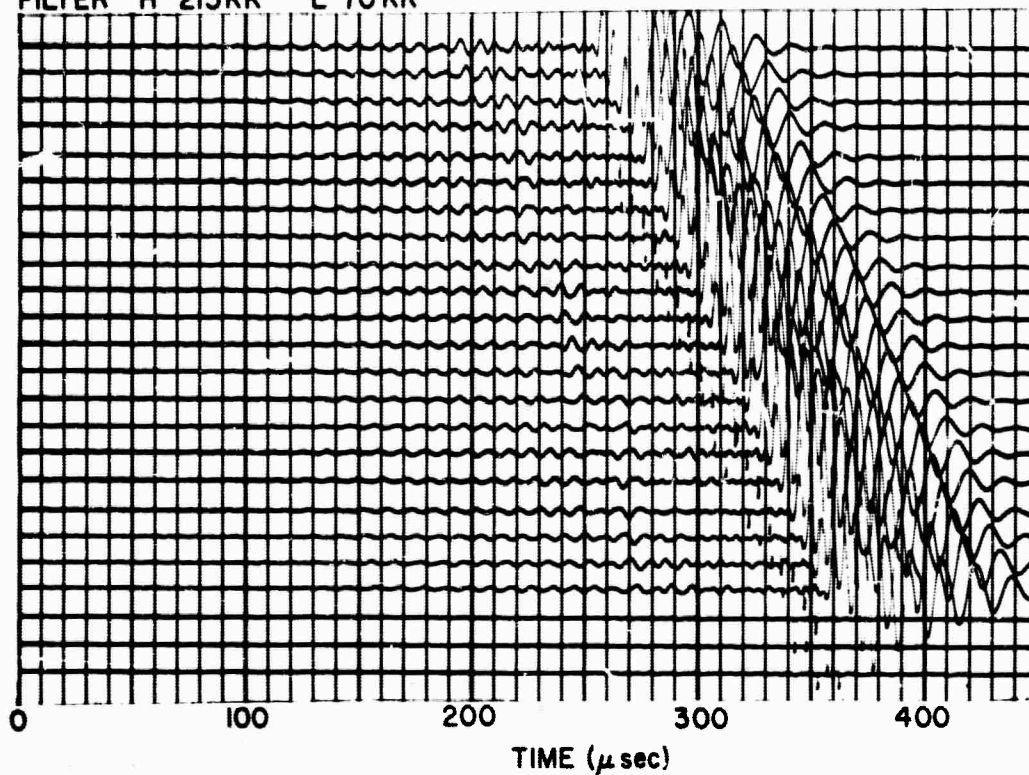


FIG. 10.2. Total horizontal seismograms filtered to approximate analog model source (70-215 kc/sec passband). Small time markers are 10 μ sec apart. Distance range is 50 to 70 cm in one-cm increments. Gain 0 db.

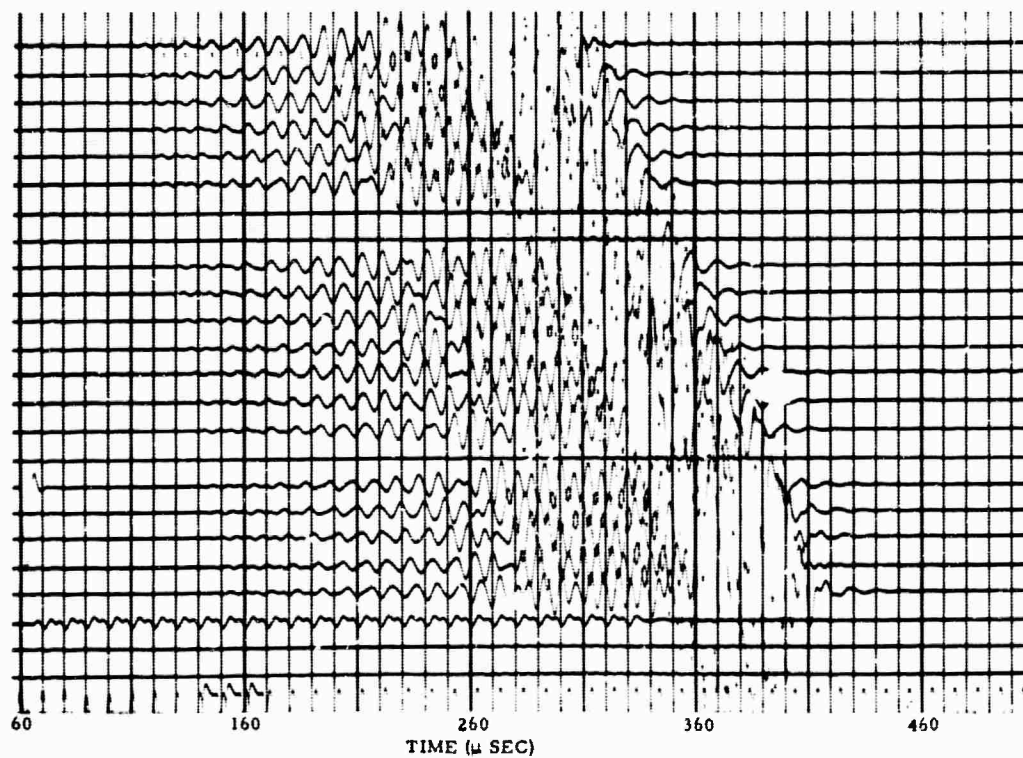


FIG. 11.1. Experimental vertical seismograms obtained from analog Model H-1. The distance range is 50 to 70 cm in one-cm increments. Small timing lines are 10 μ sec apart. Dead traces indicate arcs of anomalous amplitude, due perhaps to poor interface bonding or receiver coupling. Gain +10 db.

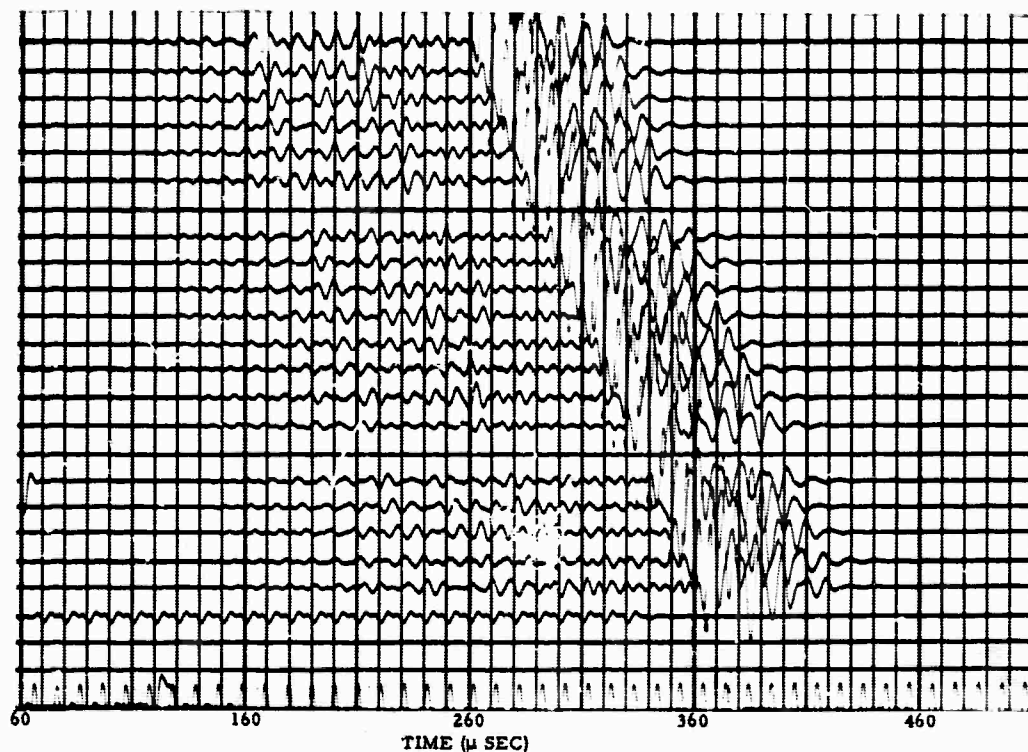


FIG. 11.2. Experimental horizontal seismograms obtained from an analog model H-1. The distance range is 50 to 70 cm in one-cm increments. Small timing lines are 10 μ sec apart. Dead traces indicate areas of anomalous amplitude, due perhaps to poor interface bonding or receiver coupling. Gain +10 db.

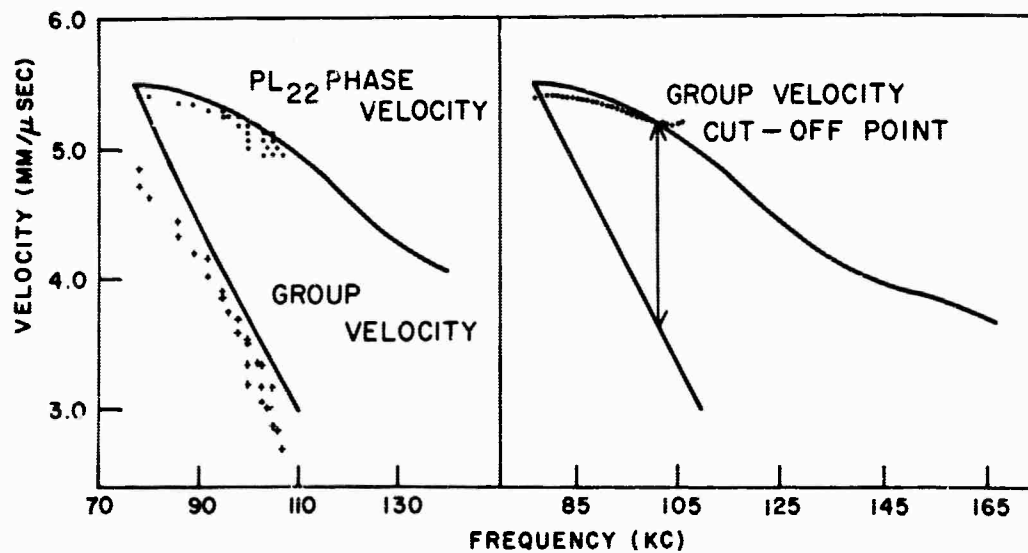


FIG. 12.1. (left) PL_{22} phase and group velocities determined from peak and trough method using entire vertical seismogram array.

FIG. 12.2. (right) PL_{22} phase velocities determined by crosscorrelation method using traces at 50 cm and 60 cm.

rival of the shear refraction. The crosscorrelation of the traces at 50 cm and 60 cm was computed and its Fourier transform calculated. If a single mode were present, the phase of this transform would be just the phase of a 10-cm transfer function and the phase velocity would be computed from the equation given in an earlier section of this paper. The results of making this assumption are shown in Figure 12.2. There is seen to be much less scatter than in the previous experiment, but errors of the order of two percent still occur. One would be quite pleased with this if the data were experimental. However, for the present data, there is no visible error when the isolated PL_{22} mode is used. The error seen in Figure 12.2 is due partly to truncation and partly to the presence of other modes at low power levels. If the array of seismograms was processed in such a way as to reduce all the modes except PL_{22} , the results would be improved greatly. In particular, truncation would no longer be necessary.

SUMMARY

The studies described here have shown the importance of the leaky modes compared to normal modes. The most important single function for the leaky modes is the attenuation. At large distances, the leaky modes tend to become more and more peaked about a single frequency. It is seen that none of the isolated modes has exact transient behavior. Only at large distances is this

approached. Finally, the utility of the transfer function representation of dispersion has been demonstrated. The transfer function for a given mode should be useful for describing local dispersion even in models with nonparallel boundaries.

ACKNOWLEDGMENT

This study was supported by the Air Force Office of Scientific Research under Contract AF 49(638)-1244.

REFERENCES

- Erdelyi, A., 1956, Asymptotic expansions: New York; Dover.
- Gilbert, F., and Laster, S., 1962a, Experimental investigation of PL modes in a single layer: *Bull. Seis. Soc. Am.*, v. 52, p. 59-66.
- Gilbert, F. and Laster, S., 1962b, Excitation and propagation of pulses on an interface: *Bull. Seis. Soc. Am.*, v. 52, p. 299-319.
- Gilbert, F., 1964, Propagation of transient leaking modes in a stratified elastic waveguide: *Rev. of Geophys.* v. 2, p. 123-153.
- Harkrider, D., 1964, Surface waves in multilayered elastic media I. Rayleigh and Love waves from buried sources in a multilayered elastic half-space: *Bull. Seis. Soc. Am.*, v. 54, p. 627-679.
- Haskell, N., 1953, The dispersion of surface waves on multi-layered solid media: *Bull. Seis. Soc. Am.*, v. 43, p. 17-34.
- Oliver, J., 1964, Propagation of PL waves across the United States: *Bull. Seis. Soc. Am.*, v. 54, p. 151-160.
- Pekeris, C. L., 1948, Theory of propagation of explosive sound in shallow water: *Propagation of Sound in the Ocean*: *Geol. Soc. Am. Memoir* 27.
- Rosenbaum, J., 1960, The long-time response of a layered elastic medium to explosive sound: *Jour. Geophys. Res.*, v. 66, p. 1445-1469.

APPENDIX B

NUMERICAL EXPERIMENTS IN THE ESTIMATION
OF FREQUENCY WAVENUMBER SPECTRA OF SEISMIC EVENTS
USING LINEAR ARRAYS

NUMERICAL EXPERIMENTS IN THE ESTIMATION
OF FREQUENCY WAVENUMBER SPECTRA OF SEISMIC EVENTS
USING LINEAR ARRAYS

by A. Frank Linville* and Stanley J. Laster*

Abstract

Studies in the measurement of frequency-wavenumber spectra of transient events have been conducted using theoretical and analog model data recorded along a 21-element, inline array. Straightforward numerical transformation, assuming space stationarity, gives good definition of the dominant (Rayleigh) mode, but little information concerning higher modes. The presence of spatial non-stationarity due primarily to cross-correlation between modes complicates the fine structure of the spectral estimate. Averaging over redundant space lags is necessary to remove this. Additional difficulties arise from side lobes due to use of the finite length array. The amplitude of the side lobes can be reduced by using a space lag window. In the present case this gives indications of the higher modes, but these indications are so ill defined as to be useless for determining dispersion. The effects of amplitude deviations between channels are also studied.

*Texas Instruments Incorporated, Dallas, Texas.

NUMERICAL EXPERIMENTS IN THE ESTIMATION
OF FREQUENCY WAVENUMBER SPECTRA OF SEISMIC EVENTS
USING LINEAR ARRAYS

by A. Frank Linville and Stanley J. Laster

I. Introduction

The most familiar representation of seismic wave propagation, in terms of plane or cylindrical waves, is based on the solution of linear partial differential equations by the use of Fourier transform techniques. Generally speaking, in models without lateral inhomogeneity the equations of motion of the elastic solid and the appropriate boundary conditions may be doubly transformed, with frequency and horizontal wavenumber replacing the time and horizontal range variables. The problem is then reduced to solving an ordinary differential equation dependent on the depth variable. While this may be difficult in practice, it presents no conceptual difficulty. The constants of integration are found from the solution of a system of algebraic equations to give the formal representation of the elastic disturbances in the frequency-wavenumber (f - k) domain. Even in the presence of lateral inhomogeneities, this "plane wave" approximation may be valid at high frequencies.

The chief practical difficulty arises because one wishes to compare the theoretical solution directly with the experiment, a step that requires the evaluation of two inverse transforms in order to return to the time-space domain. Because the resulting integrals cannot be expressed in terms of known integrals (except in rare cases), one is led to consider

approximate integration techniques, particularly asymptotic methods appropriate to high frequencies and large horizontal ranges. However, an alternative approach can be taken. One can operate on the experimental data to change it into a form suitable for direct comparison with the theoretical frequency-wavenumber representation. This has the distinct advantage that while the total effort expended is unchanged, the amount of effort expended on a given theoretical hypothesis (which may be incorrect) is greatly reduced. The present paper describes investigations of the problems associated with this estimation of the frequency-wavenumber spectra of experimental data. To simplify the computations and display of results only inline arrays are considered, but results using arrays of other geometry will be similar.

There are several obvious reasons for computing frequency-wavenumber spectra. If very good spectral estimates can be obtained, the dispersion curves for the earth model can be determined directly and are the raw data for the "inversion" techniques presently in use. The exact spectrum for a normal mode in an idealized model is a weighted Dirac delta function distributed along the dispersion characteristic in the frequency-wavenumber plane. The weighting factor is just the excitation function for the mode. Because of leakage, the idealized leaking mode spectrum is continuous but strongly peaked along the dispersion characteristic. In real models, it will be found that the spectra for both kinds of modes are continuous functions peaked along the dispersion curves. This is true because of inelastic attenuation and inhomogeneities in the model.

With the capabilities of the arrays presently in use, it is doubtful that dispersion curves can be determined directly from f-k spectra. In this case, the frequency-wavenumber analysis serves as an exploratory tool which can give quick estimates of the gross structure and serve as a guide for designing mode separation filters whose application can give precise estimates of the dispersion. (Lasier and Linville, 1966)

It is obvious that frequency-wavenumber spectra could be determined exactly if an infinitely long array and an unlimited time span were used for recording. In that case, a straightforward 2-dimensional (numerical) Fourier transform could be performed. Because of the necessity of sampling the data in space and time, alias points will be found in both frequency and wavenumber. This is not usually a significant problem since the unit cell in the frequency-wavenumber (f-k) plane can be made as large as desired by decreasing the sample spacing. This unit cell may be chosen in a number of ways, but here it will be defined such that the alias frequency and wavenumber are respectively

$$f_n = 1/2 \Delta t \quad \text{and} \quad k_n = 1/\Delta x \quad .$$

The necessity for using a finite time gate is not a strong restriction. If the seismic events are coherent propagating events from a well-defined source, there is significant motion in the neighborhood of a given receiver only near the arrival time of the wave train for that source-receiver distance. Short time gates may be used if the time origin is redefined at each receiver. When recording ambient noise, much longer time gates are necessary, but no conceptual difficulty occurs in obtaining this. However, in order to test the time stationarity of ambient noise many independent samples may be required.

The use of finite spatial arrays introduces most of the problems found in f-k analysis. With short arrays, it is no longer acceptable to perform straightforward Fourier transforms. The space-time signal obviously does not vanish outside the limits of the array* nor does it repeat itself in a periodic manner. Without recourse to statistical methods, it is difficult to characterize the behavior of the signal outside the array. The most useful statistical assumption endows the signal with the property of space stationarity, i.e., it is assumed that the crosscorrelation of time signals at two receivers depends only on the space separation of the receivers but not on their absolute location. That is, any group of seismometers specifies the signal correlation at any point which can be represented by a vector (direction and distance) between two seismometers in the array. For space stationary signals, it is necessary only to perform the 2-dimensional Fourier transform operation on a non-redundant set of crosscorrelations from the array; i.e. only one autocorrelation need be used, one crosscorrelation between receivers a unit distance apart, one crosscorrelation between receivers two samples apart, etc. Still, a truncation of the 2-dimensional correlation function occurs because only those space lags which correspond to separations less than or equal to the length of the array can be computed. This means that the f-k spectrum which we compute has been

*One exception to this does occur. When estimating the frequency-wavenumber response of multichannel (space-time) filter systems, the signal (impulse response of the filter system) obviously does vanish outside the limits of the array. Here straightforward two-dimensional Fourier transforms give the correct answer and expansion in correlation space is unnecessary.

obtained from the correct f-k spectrum of the infinite length, two-dimensional correlation function by implicit convolution with a window function (Blackman and Tukey, 1959).

Truncation in space (use of a finite array) and truncation in time correspond to multiplication by a lag window which is a step function in space-time. The double Fourier transform of the seismic disturbance is thus convolved with the spectral window function $\frac{\sin(\pi N k \Delta x)}{\sin(\pi k \Delta x)} \frac{\sin(\pi M f \Delta t)}{\sin(\pi f \Delta t)}$, where N is the number of elements in the array and M is the number of time points used. This convolution is undesirable, but results automatically from the use of a finite length array. It gives rise to side lobe effects whereby strong peaks in the two-dimensional spectrum influence the estimates in other regions of the f-k domain. In this paper the time functions used are long enough (250-500 time samples) that the factor $\frac{\sin(\pi M f \Delta t)}{\sin(\pi f \Delta t)}$ causes little difficulty. It has unit amplitude at $f = 0$ and at multiples of $f = \frac{1}{\Delta t}$. Elsewhere it has very small, closely spaced side lobes. The two arrays used in this paper have 21 and 12 elements with 1 cm spacing. This gives rise to side lobes with spacings of approximately .05/cm and .08/cm respectively.

A signal consisting of a single event with constant velocity V is represented by a Dirac delta function along the line $f = kV$ passing through the origin in the f-k domain. Estimation of the spectrum of this signal using a finite array and finite time span yields

$$F(f, k) = \int W(\sigma) U(f - kV + V\sigma) d\sigma,$$

where $W(k)$ is the spectral window due to truncating the array and $U(f)$

is the spectral window due to using a finite time span. Writing $V(f) = U(\frac{f}{V})$, we see that the expression for $F(f, k)$ is just the crosscorrelation between W and V , i.e.

$$F(f, k) = \Phi_{W, V}(\frac{f}{V} - k) = \int W(\sigma) V(\sigma + \frac{f - kV}{V}) d\sigma .$$

If an unlimited time span were used we would have $V = \delta(f)$, so $F(k, f) = W(k - \frac{f}{V})$. That is, the estimate of the single velocity signal would be just the spectral window of the finite array, rotated so that the central lobe lies along the line $f = kV$. If the length in time of the data is much longer than the array length, the spectral estimate will have approximately this form. In all practical cases W and V will have a similar appearance and the maximum of the crosscorrelation will be $\Phi_{W, V}(0)$. Thus the combined spectral window will possess a maximum or "central" lobe along the line $f = kV$. Also, side lobes will appear which are parallel to this line. Dispersive events are characterized by curved lines in the f - k plane, so the effects of the window are more difficult to assess.

We might note here that the side lobes arising from the use of a finite array are diffraction effects analogous to those encountered in optics due to light falling on a narrow slit. The aliases of the central lobe may also be considered as side lobes, but these are analogous to the higher order optical spectra produced by a diffraction grating, and are due to the periodic spacing of elements in the array. An unequally spaced array may have no true alias points (for example when the various receiver spacings are incommensurable), but "pseudo-alias" points usually occur if the spacings are even approximately equal. When, as in the present paper, the horizontal seismic wavelength

is greater than the inter-element spacing the diffraction effects predominate. However, if the wavelength is much shorter than the spacing, alias side lobes predominate and unequally spaced arrays are almost always required in practice.

II. The Data

The aforementioned technique was used to compute the frequency wavenumber spectra for two sets of data. The first of these was a set of theoretical seismograms computed for a model consisting of a single layer over a half-space, while the second consists of a set of analog model seismograms for the same model (Laster, Foreman, and Linville, 1965). The two sets of seismograms are shown in Figures 1 and 2. The Rayleigh mode dominates both sets of data. However, leaking modes and shear modes can be seen in the early portion of each record. The analog model data has a low frequency cutoff due to the model source spectrum, which explains the difference in appearance of the two sets of data.

The frequency wavenumber characteristics which one would ideally obtain for the theoretical data are shown in Figure 3. The same curves are also known to be approximately correct for the experimental data. These curves, of course, give no indication of the amplitude distribution along a characteristic (i.e., the excitation function). The latter information is shown in Figure 4.

III. Estimation of the Spectra

The initial frequency-wavenumber spectral estimates for the two data sets are shown in Figures 5 and 6.* The non-redundant correlations

*Note to Reader: Generous use of one or two colored pencils will make the f-k plots in this paper easier to interpret.

were obtained wherever possible by correlating with channel 1. For the experimental data dead traces prevented this for some space lags.

The array had 21 elements and was 20 cm long. Using the approximate scaling 20 km (real earth) = 1 cm (model), it is seen that this is a very large, 400-km array. The time sample was 1 μ sec (which scales to about 2 sec) and 500 time lags were used in the correlations. In Figure 5, which shows the spectra for the theoretically computed seismograms, the Rayleigh wave stands out sharply. The first alias of the Rayleigh mode can be seen starting at 200 kc and zero wavenumber. The other six modes are not well defined. It is questionable as to whether the subsidiary peaks represent the higher modes or side lobes of the Rayleigh mode produced by using a finite-length array.

The spectrum in Figure 6 was computed from the experimental analog model seismograms using the same array configuration. Here again, it is seen that the Rayleigh wave stands out sharply and that there is close agreement between the Rayleigh velocities in the experimental and theoretical models. No strong evidence is seen for identifying the higher modes in the experimental f-k spectrum.

To obtain some estimate of the Rayleigh side-lobe pattern, the frequency-wavenumber spectrum was computed for the Rayleigh mode alone using correlations computed from the theoretical Rayleigh mode seismograms. Again, 21 channels were used, but only 400 time lags were used instead of 500. This should produce negligible differences. The resulting spectrum is shown in Figure 7. It is similar to the spectrum for the total seismogram except for being somewhat smoother. Comparison of

Figures 5 and 7 permits determination of the effects of the higher modes. It is seen that the peaks near 55, 90 and 130 kc probably are real expressions of the first shear mode. Unfortunately, it is not possible to perform this same experiment for the experimental data because the isolated Rayleigh mode is not available.

It is obvious that the curvature of the Rayleigh f - k characteristic produces measurable effects, since the lines of equal power are not, in general, parallel to the dispersion characteristic. (The individual side lobes are not seen with the resolution used here.) The effects are most pronounced at low frequencies where the curvature is greatest. The low power troughs near 50 and 70 kcps were not expected. It was first thought that these are part of the side lobe structure associated with the peak in power at 60 kcps. This peak in power is the Airy Phase of the Rayleigh mode. Subsequent studies showed that this is not an adequate interpretation.

The real cause of these low power areas may still be questioned, but it is thought that they result from a disparity between the side lobe spacing and the spacing of the computed points in frequency and wavenumber. Thus, along a line of constant wavenumber, the first few frequency points sampled fell near side lobe peaks, but subsequent samples fell on the flanks of the lobes and finally in the valley between lobes. As this process was carried further, the sampled points began to rise up the flank of the next lobe and finally again fell on a peak. With the complicated side lobe structure found in the present examples, this can give rise to the kind of low power areas observed. It should be

noted that these low power regions do not occur in the spectra computed using shorter arrays, and thus having greater side lobe spacing. This suggests that the spacing of computed points in spectra from long arrays must be carefully chosen in order to yield a meaningful representation.

In order to see more clearly the effect of curvature on the side lobe pattern, the spectra for the Rayleigh mode and for the total theoretical seismogram were recomputed using a 12 element array (11 cm. long). These are shown in Figures 8 and 9. The side lobes are now readily apparent, but the overall pattern is scarcely affected, except for absence of the low power regions near 50 and 70 kc.

It is obvious that the techniques presented must be modified to observe adequately the higher modes. A number of points need to be considered. Probably the most successful method would be to process subarrays in such a fashion as to remove the Rayleigh wave (which has been seen to be well-defined). If a 4-channel subarray processor were used, five independent outputs could be obtained from the 21 elements whose f-k spectrum could be computed, but side lobes would still be a significant problem.

More direct approaches have been studied here using the entire array. First, it should be observed that the signal from a well-defined finite source is not stationary. This is true for three reasons: 1) because of cylindrical spreading, the crosscorrelations for a single mode depend not only on receiver separation but also on distance from the source; 2) besides cylindrical spreading, the leaking mode correlations are affected strongly by frequency-dependent leakage; 3) between the various normal and leaking modes, there is significant crosscorrelation which

is strongly dependent on source-receiver distance. All three effects may be removed by averaging the correlations for a given space lag over an ensemble of source-receiver distances. Thus, for a given array, all autocorrelations are averaged, all crosscorrelations between adjacent receivers are averaged, etc. This scheme suffers from the defect that, for a finite array, the number of correlations available for averaging decreases as the space lag (separation between receivers) is increased. An alternate but better approach is to average correlations for events from a number of different sources located at various distances from the array.

Both our experimental and theoretical data were obtained for a single source 50 cm from the near-end of the array. However, ensemble averaging can be simulated for the theoretical data since the correlations for the individual modes are available, having been computed from the individual mode seismograms. The individual mode correlations were averaged to obtain the "ensemble average correlations." Two simplifications occurred. First, the theoretical seismograms were computed for a 2-dimensional model so no cylindrical spreading occurred. Second, at the distance used, the leaking modes already are strongly peaked in spectrum and any additional leakage effect is small. This was, in fact, neglected. The f-k spectrum for the average or "uncoupled" correlations is shown in Figure 10. For reasons of economy, a 12-channel array (11 cm long) was used. Compare this with the spectrum for the total seismogram using the 12-channel array (Figure 9). The following conclusions may be drawn.

The average or uncoupled spectrum is much simpler than the "single-source" spectrum, particularly in the region where higher modes would be expected. There is little indication of the individual higher modes, but these are almost certainly obscured by the side lobes of the Rayleigh mode. Indeed, it seems likely that the only indication of the higher modes is in the smearing of the otherwise clean side-lobe pattern.

Although some indications of the higher modes are seen in the "single-source" spectrum, the data are very difficult to interpret in terms of dispersion curves. This indicates that the chief expression of the higher modes is found in the crosscorrelation between these modes and the Rayleigh mode. Computations have shown the crosscorrelation between higher modes and the Rayleigh mode to be an order of magnitude greater than the autocorrelations of the higher modes.

Obviously, the higher mode spectra could be interpreted more easily if they could be observed in the uncoupled spectrum. This suggests an attempt to reduce the side lobes of the Rayleigh mode. Such a reduction in side lobes is always gained at the expense of broadening the central peak. In the present case, we could accept some broadening because of the sharpness of the Rayleigh mode if there is sufficiently large separation between modes. Such a technique should not be used where two large events with small wavenumber separation are expected. Reduction of side lobes and resultant broadening of the central peak are achieved by using some lag window other than the simple step function (truncation). The window chosen here is the Bartlett window (Blackman and

Tukey, 1959), whereby the weight or significance attached to a crosscorrelation decreases linearly with increasing space lag (no change was made in the time window). It should be noted that this is the window obtained if one simply computed all possible crosscorrelations obtainable with the given array and summed correlations with the same space lag. For the Bartlett window the first side lobe is down 12 db compared to the central lobe height as opposed to 7 db for the step function (truncation window). But the Bartlett central lobe half-width (wavenumber distance between peak and half-power points) is about .030/cm as opposed to .017/cm for the truncation window. One unfortunate result of this is that the first side lobe is displaced farther in wavenumber from the central lobe. Thus while the side lobes of the Rayleigh mode will be reduced by using the Bartlett window, they will be moved nearer the shear modes, so that even more interference could result. However, in order to see if any improvement could be obtained, the window was applied to the theoretical data and the spectrum computed (Figure 11). The results were considerably better than anticipated. There is some reason to believe that the -12 to -18 db regions for frequencies above the central Rayleigh lobe may represent the higher modes. One reason for believing this is the absence of similar regions for frequencies below the central Rayleigh lobe. However, these regions of relatively high power are so broad as to be essentially useless for determining dispersion curves. However, such results would be useful for the design of mode separation processors. Other windows could be used, but similar results would be expected.

One final problem not previously touched upon is the problem of channel to channel equalization. All receivers in an array would not be expected to have identical response. In addition, the variable coupling to the ground and small scale local geologic inhomogeneities would tend to upset the predicted amplitude relation between channels. To test the effect of this on frequency-wavenumber analysis the correlations for the 12-channel array were scaled by the random weights shown in Table 1. This is similar to the effects observed in the analog model due to receiver coupling. The corresponding f-k spectrum is shown in Figure 12. Widely spaced peaks in power are observed. (This figure should be compared to Figure 10.) While the results were not as bad as had been expected, they are sufficiently in error to upset the higher mode structure of the estimated spectrum. An attempt was made to improve the experimental spectral estimate by using an empirical equalization technique. All channels were normalized to have the same total power. The recomputed spectral estimate is shown in Figure 13. Some improvement was noticed but the overall spectrum is only slightly changed. The equalization weights are shown in Table II.

It may be noted that ensemble averaging over correlations between various pairs of receivers would reduce this effect, while averaging the correlations between a fixed pair of receivers for events from various sources would maximize the effect. The best procedure seems to be equalization of the various receivers on a mean power or mean amplitude basis. It should be observed that, in practice, the observed gain difference may be frequency-dependent so that equalization requires a set of filter operators rather than a set of weights.

TABLE I

Random Scale Factors Applied to Theoretical Traces

Distance	Scale Factor
54	2.0
55	1.0
56	0.3
57	3.3
58	2.7
59	2.3
60	1.0
61	0.4
62	0.4
63	1.6
64	0.8
65	0.7

TABLE II

Equalization Factors for Experimental Data (21-Element Array)

Correlation	Equalization Weights
1X1	1.1025
1X2	1.2301
1X3	1.6784
1X4	1.1718
1X5	1.0778
1X6	1.6105
1X7	2.4249
1X8	1.8046
1X9	1.6826
1X10	1.6132
1X11	1.4099
1X12	1.0884
1X13	1.7938
1X14	1.8075
1X15	1.3593
1X16	1.1456
1X17	1.0754
1X18	1.0000
1X19	1.0098
1X20	1.2126
1X21	1.2033

IV. Summary

Because of the nature of the data used, the present study has dealt primarily with the estimation of the f - k spectra of small events (the higher modes) in the presence of a very large event (Rayleigh mode). Only events from a single well defined source were considered. The results partially apply to estimation of ambient noise spectrum, but some significant differences will occur which have not been considered in this paper.

The significance of the spectral window (side lobe structure) for a given array is well known. However, the present study has also indicated significant effects due to the action of the spectral window on the curved f - k characteristic of a dispersive event. In this case the trend of the side lobes will not in general be parallel to the central lobe.

A second effect of great importance is the non-stationarity of the total signal from a well defined source. The chief cause of this is crosscorrelation between modes. The dominant expression of the higher modes is found in their crosscorrelation with the Rayleigh mode. However, this is very difficult to interpret, so that such coupling should be eliminated wherever possible by ensemble averaging over ensembles of sources or receivers. For this reason an array with high redundancy is desirable.

Another effect, amplitude differences between channels, also can be overcome by averaging over redundant receivers. The effect of amplitude differences is similar to that obtained by applying a spatial lag window, although in this case the weights are random.

This may sometimes produce large anomalous peaks in the spectral estimate, though in the present case the effect was not so severe as expected.

Finally, the use of spatial lag windows was studied briefly. For the arrays shown here and the closely spaced signals, these windows were found to be undesirable. Indications of the higher modes are seen, but are so ill defined as to be useless for dispersion estimation. In fact, the primary reason for the assumption of space stationarity is to eliminate implicit use of one such window--the Bartlett window. On the basis of the present studies the assumption of space stationarity appears highly desirable, even if it must be justified by ensemble averaging.

V. Acknowledgment

This work was supported by the Air Force Office of Scientific Research under contract AF 49(638)-1244.

REFERENCES

- Blackman, R., and J. Tukey, 1959: The Measurement of Power Spectra
From the Point of View of Communications Engineering, Dover, New
York, New York.
- Laster, S. J., J. G. Foreman, and A. F. Linville, 1965, Theoretical
investigation of modal seismograms for a layer over a half-space:
Geophysics, v. 30, August, p. 571-596.
- Laster, S. J., and A. F. Linville, 1966, Application of multichannel
filtering for the separation of dispersive modes of propagation:
Journal of Geophysical Research, in press.

BLANK PAGE

Figure

Title

- 1 Theoretical vertical seismograms. The distance range is 50 to 70 cm.
- 2 Experimental vertical analog model seismograms. The distance range is 50 to 70 cm. Small timing lines represent 10 μ sec.
- 3 Frequency wavenumber characteristics of the theoretical modes.
- 4 Relative power spectra of the theoretical modes at 50 cm distance from the source.
- 5 Spectral estimate of theoretical data using 21-element array. The numbers within the contours represent decibels down from maximum amplitude.
- 6 Spectral estimate of experimental data using 21-element array. The numbers within the contours represent decibels down from maximum amplitude.
- 7 Spectral estimate of Rayleigh mode using 21-element array. The numbers within the contours represent decibels down from maximum amplitude.
- 8 Spectral estimate of Rayleigh mode using 12-element array. The numbers within the contours represent decibels down from maximum amplitude.
- 9 Spectral estimate of theoretical data using 12-element array. The numbers within the contours represent decibels down from maximum amplitude.
- 10 Spectral estimate of uncoupled theoretical data using 12-element array. The numbers within the contours represent decibels down from maximum amplitude.

Figure

Title

11. Spectral estimate of theoretical data using 12-element array with Bartlett spatial lag window. The numbers within the contours represent decibels down from maximum amplitude.
12. Spectral estimate of theoretical data using 12-element array and random receiver gains (see Table I). The numbers within the contours represent decibels down from maximum amplitude.
13. Spectral estimate of experimental data using 21-element array with equalization factors. The numbers within the contours represent decibels down from maximum amplitude.

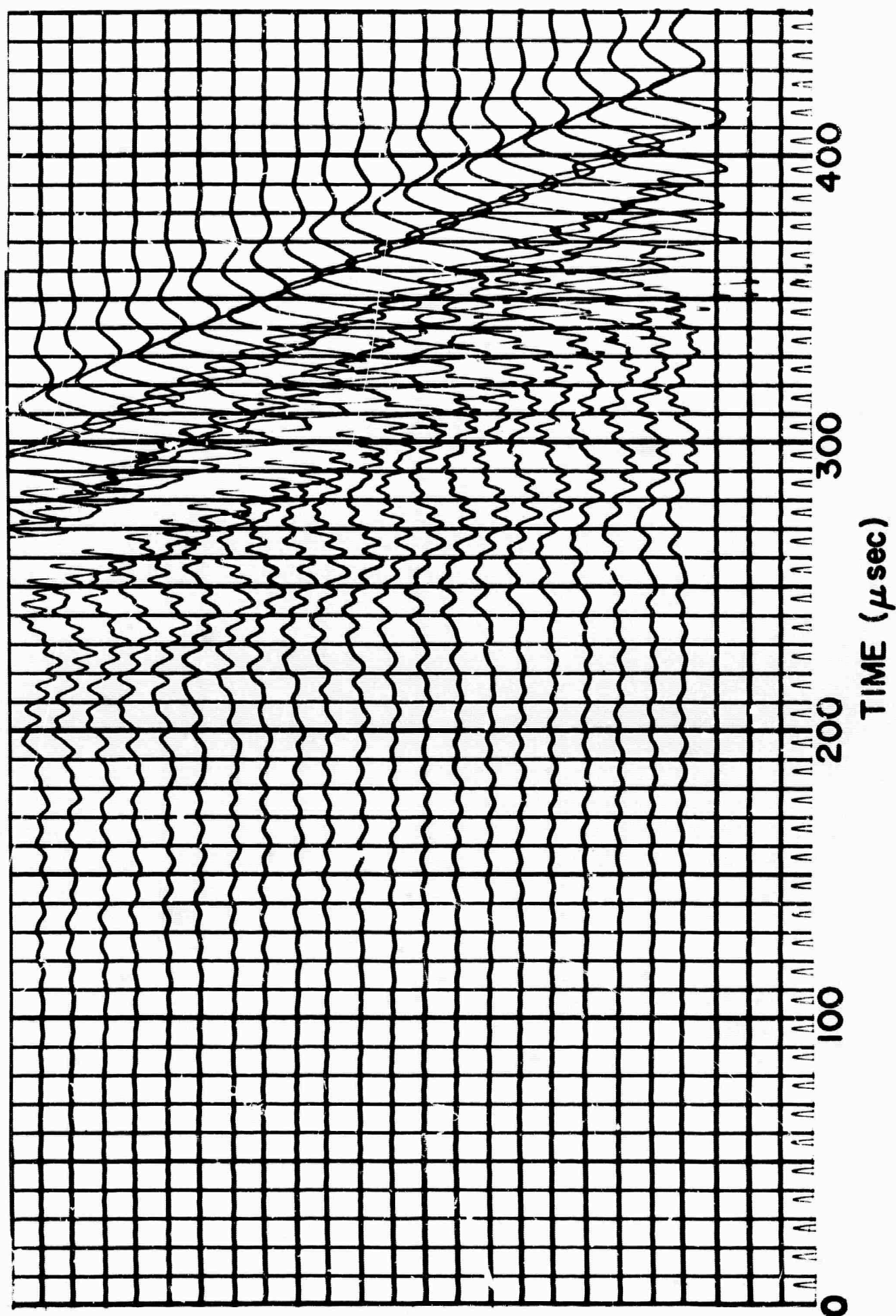


Figure 1. Theoretical Vertical Seismograms. The Distance Range is 50 to 70 cm.

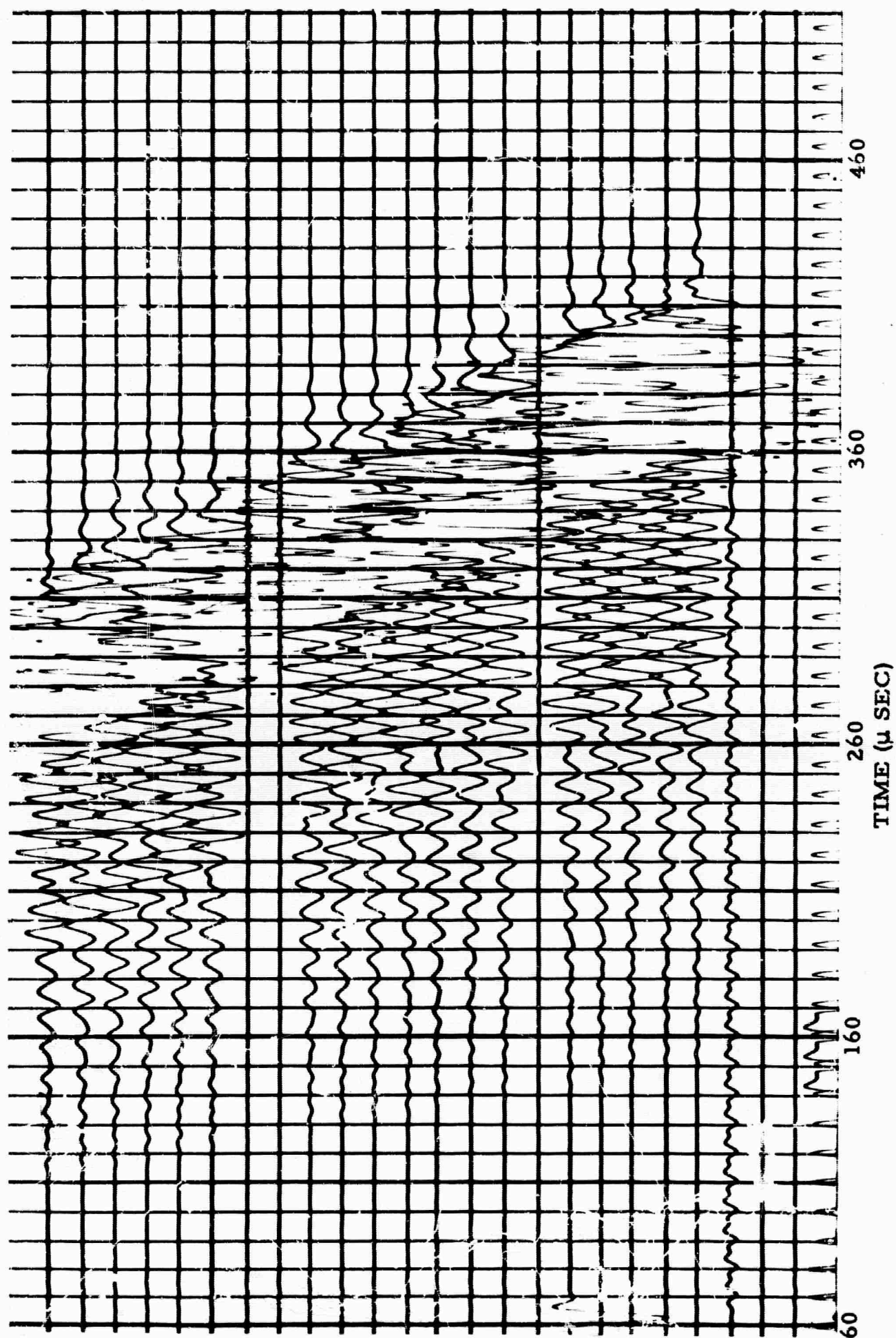


Figure 2. Experimental Vertical Analog Model Seismograms. The Distance Range is 50 to 70 cm. Small Timing Lines Represent 10 μ sec.

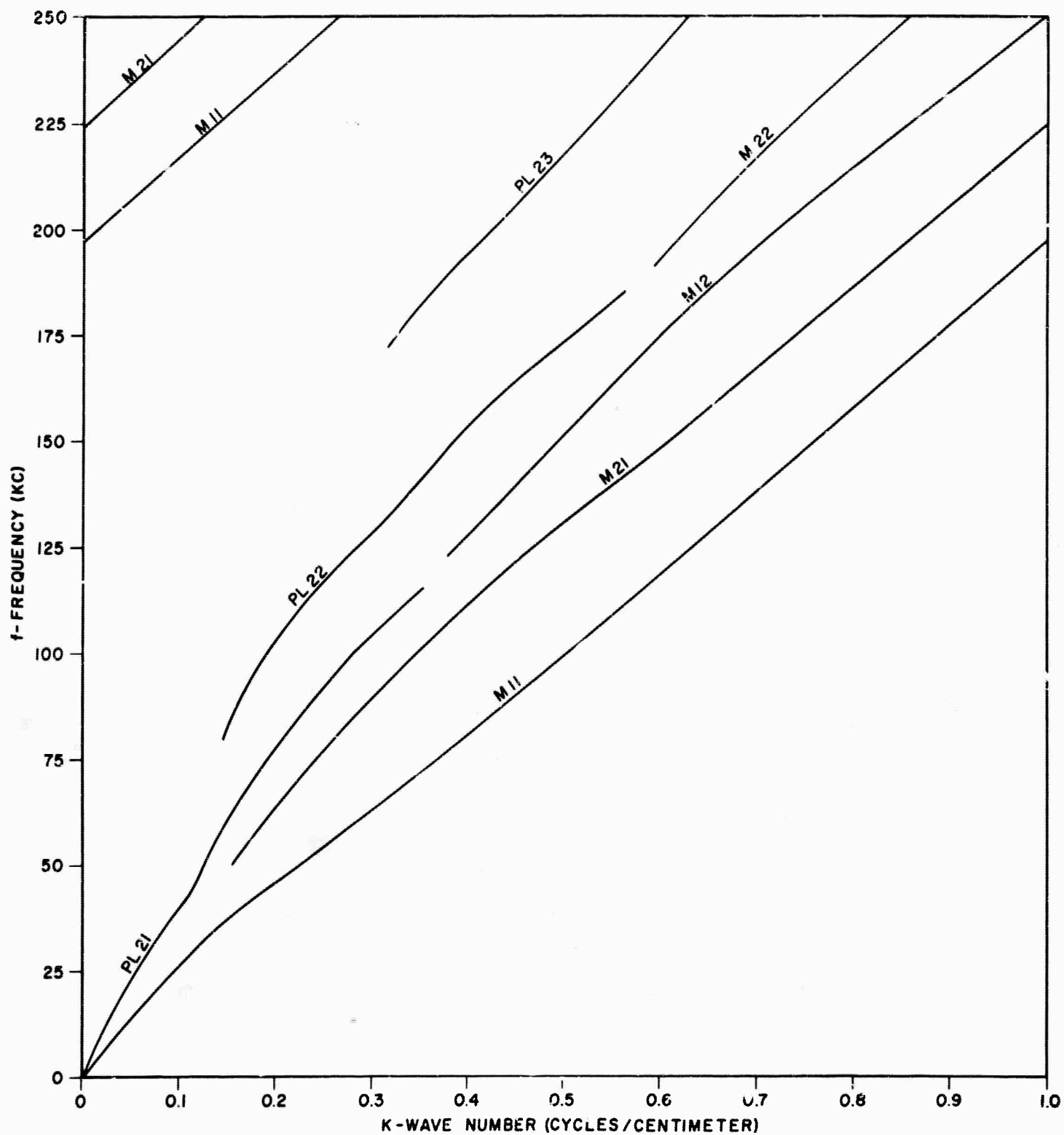


Figure 3. Frequency Wavenumber Characteristics of the Theoretical Modes

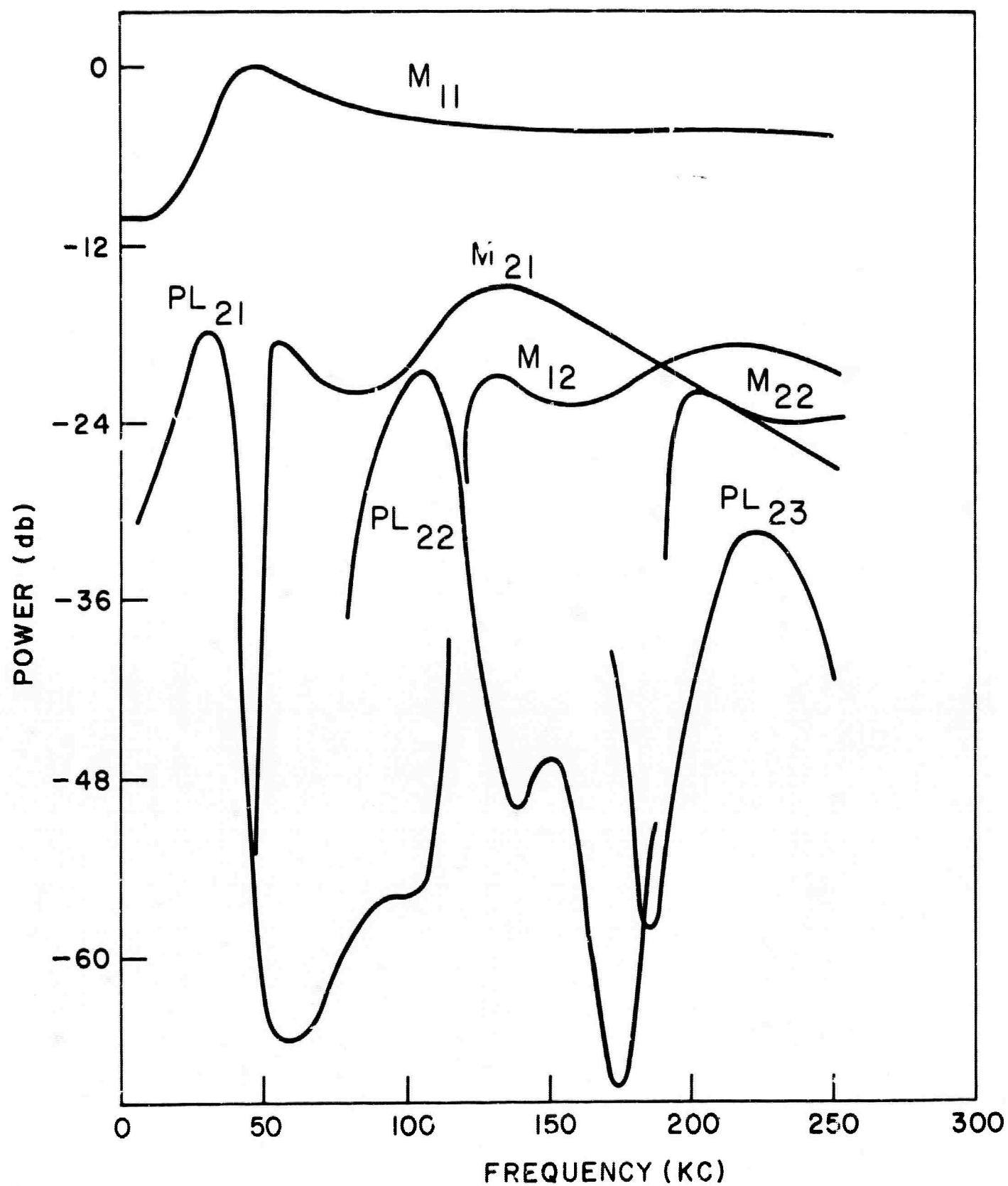


Figure 4. Relative Power Spectra of the Theoretical Modes at 50 cm Distance from the Source

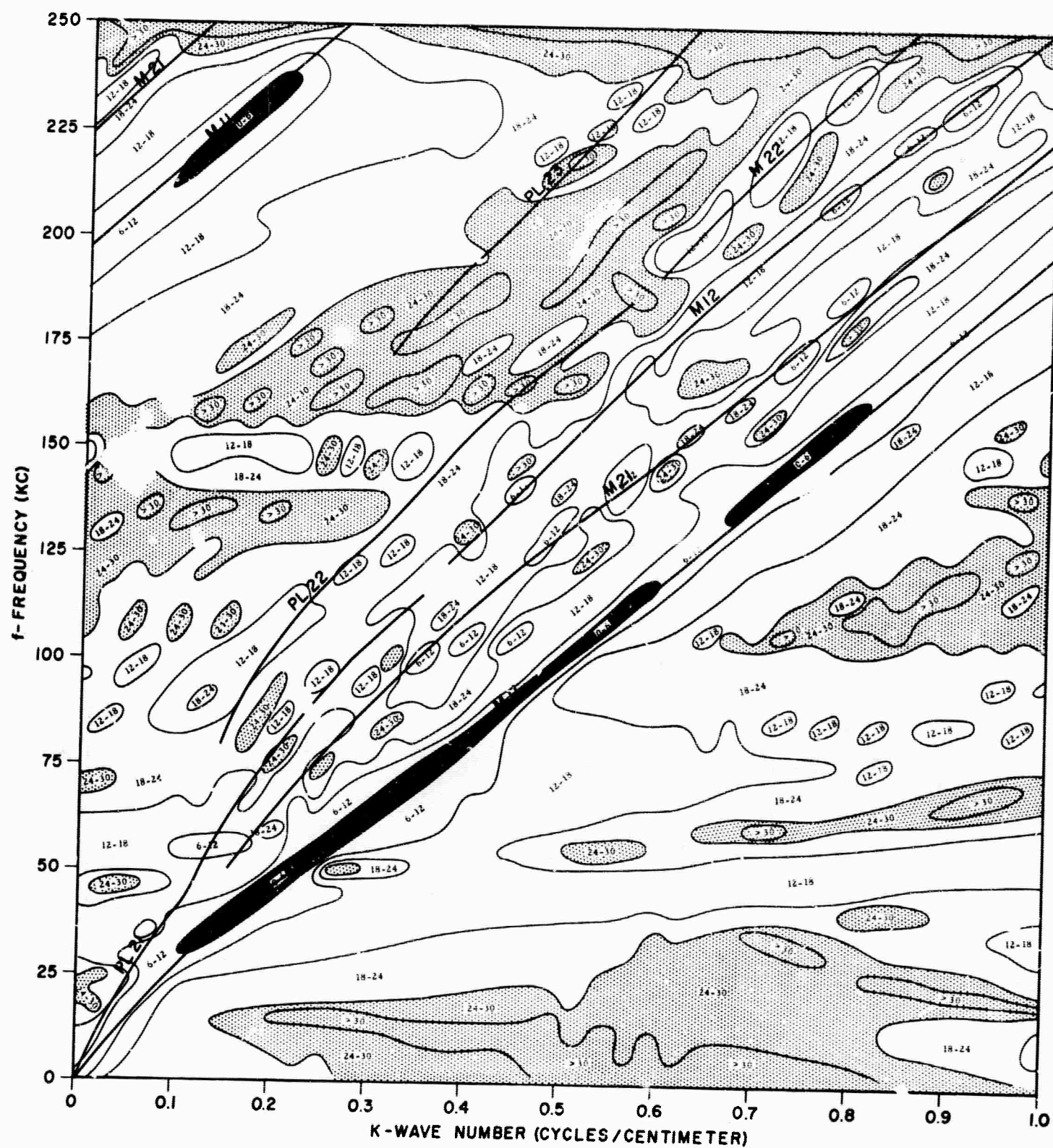


Figure 5. Spectral Estimate of Theoretical Data Using 21-Element Array. The numbers within the contours represent decibels down from Maximum Amplitude.

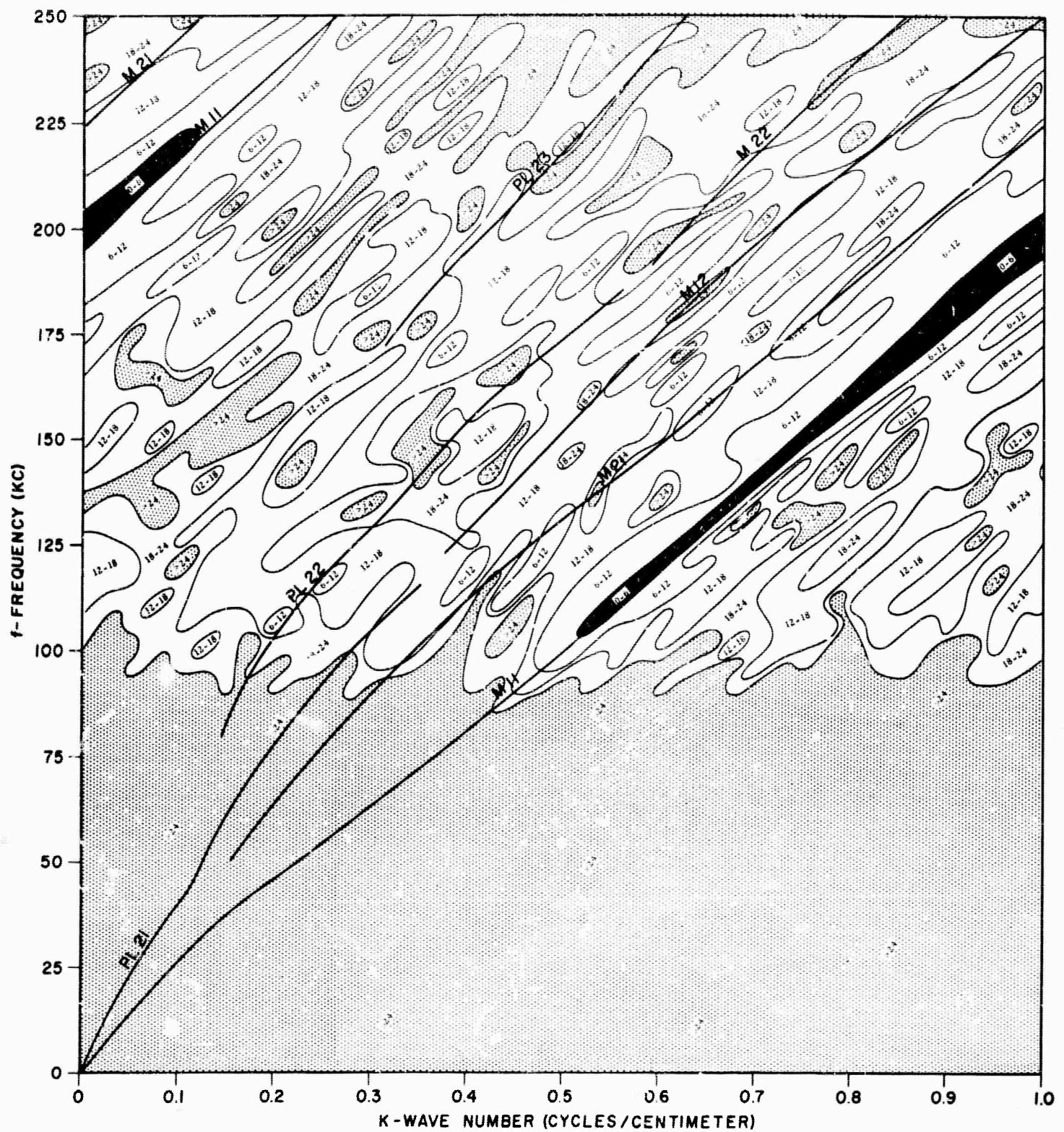


Figure 6. Spectral Estimate of Experimental Data Using 21-Element Array. The Numbers within the Contours Represent Decibels Down from Maximum Amplitude.

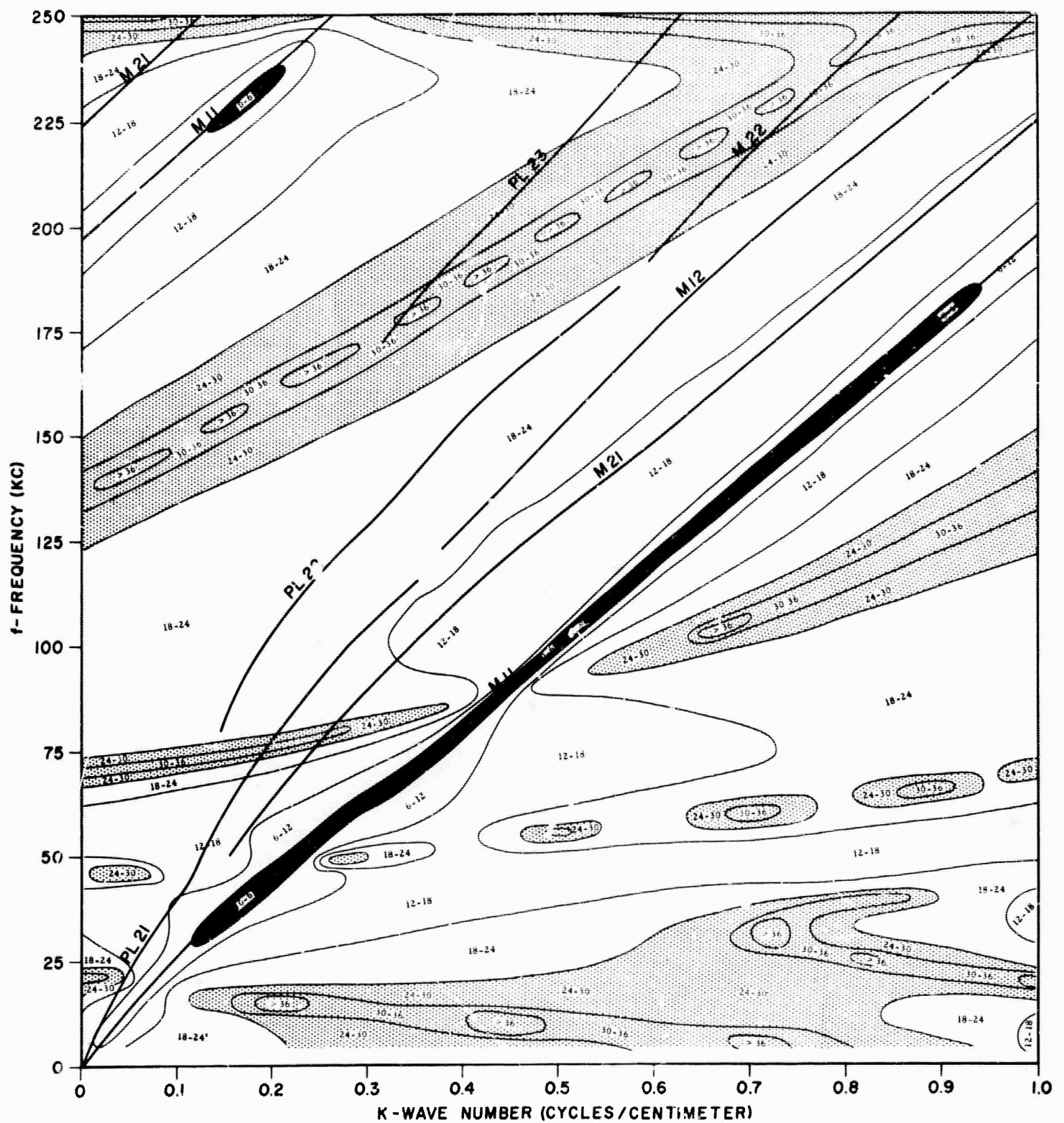


Figure 7. Spectral Estimate of Rayleigh Mode Using 21-Element Array. The Numbers within the Contours Represent Decibels Down from Maximum Amplitude.

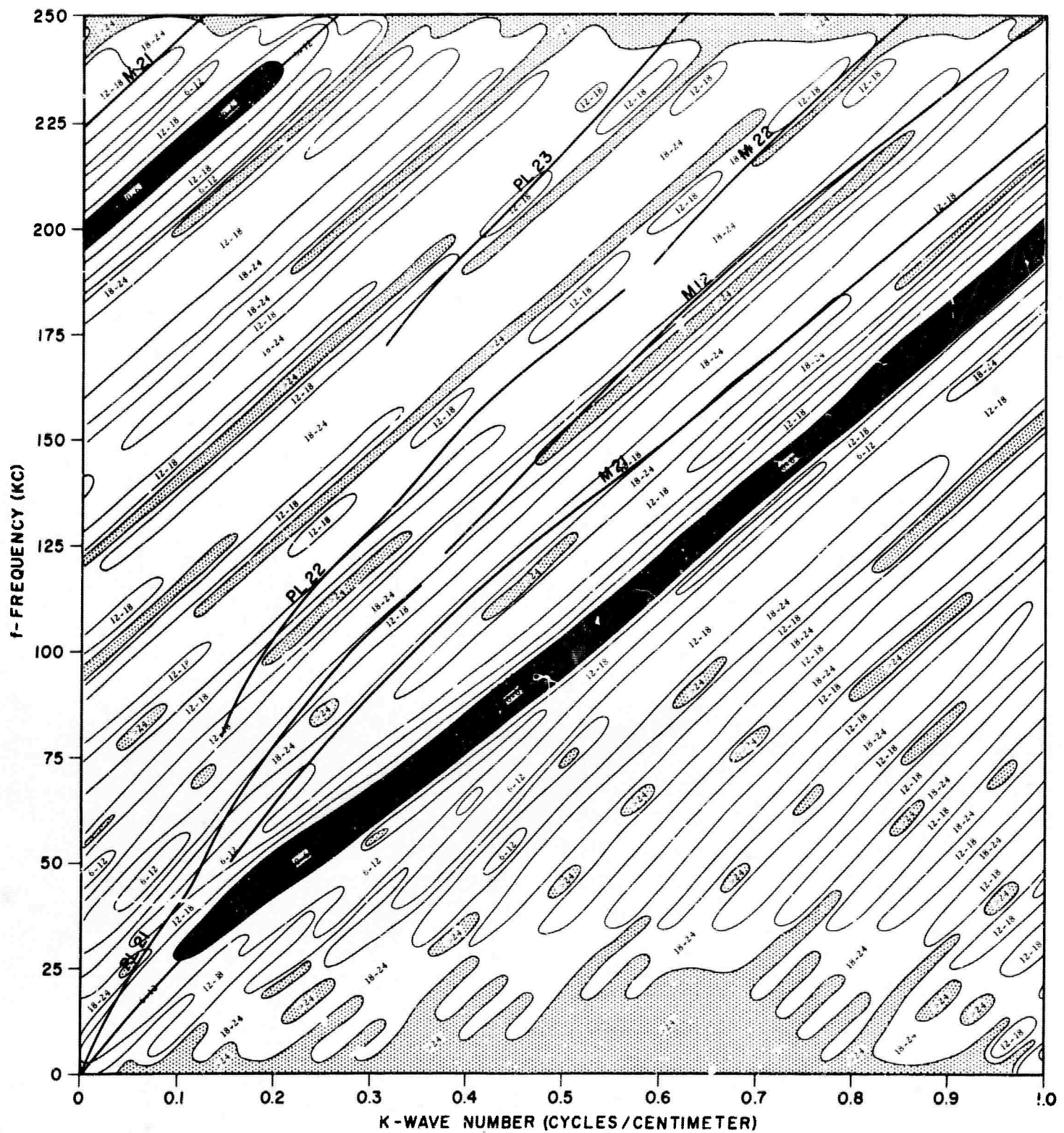


Figure 8. Spectral Estimate of Rayleigh Mode Using 12-Element Array.
The Numbers within the Contours Represent Decibels Down from
Maximum Amplitude.

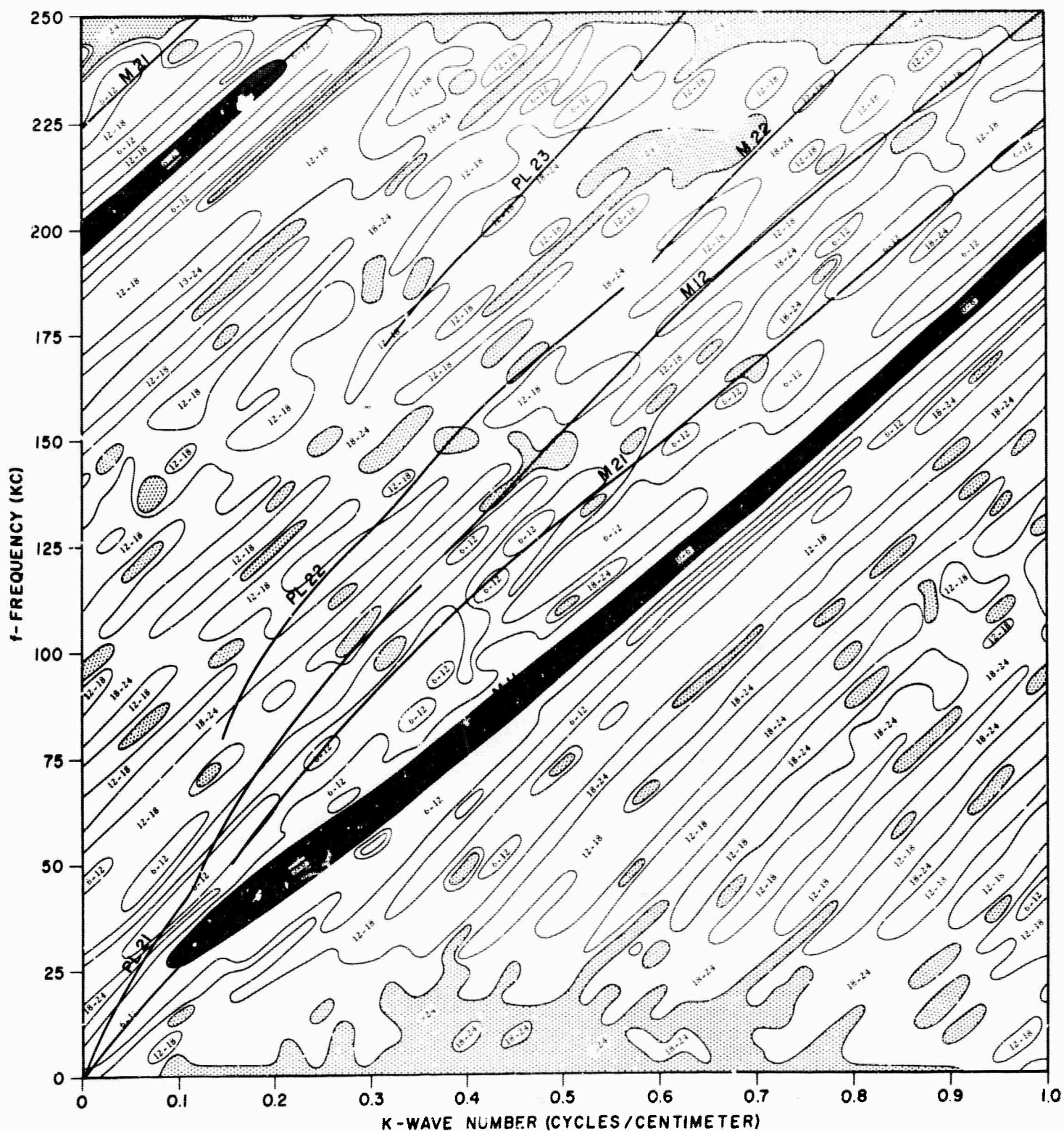
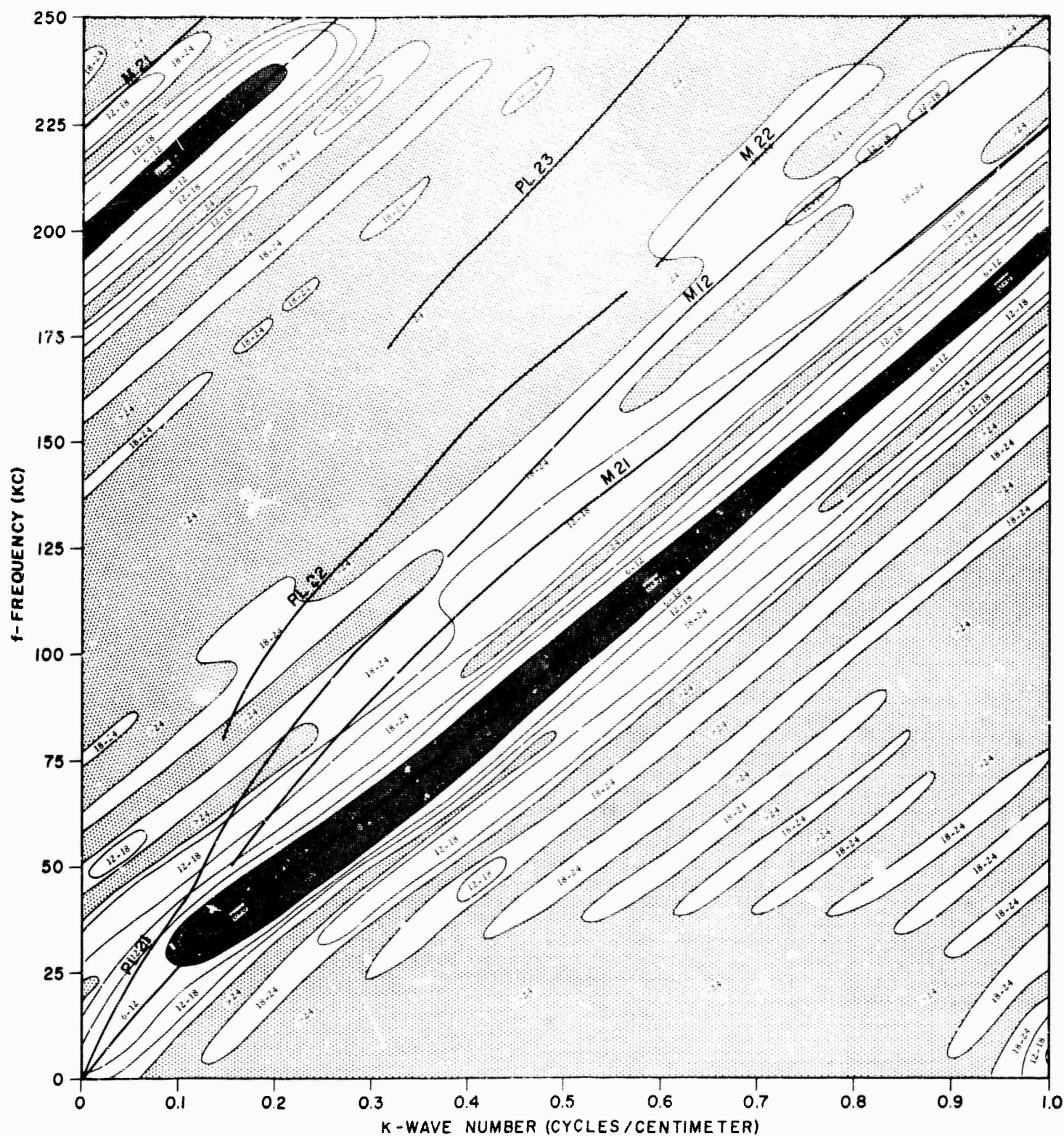


Figure 9. Spectral Estimate of Theoretical Data Using 12-Element Array. The Numbers within the Contours Represent Decibels Down from Maximum Amplitude.



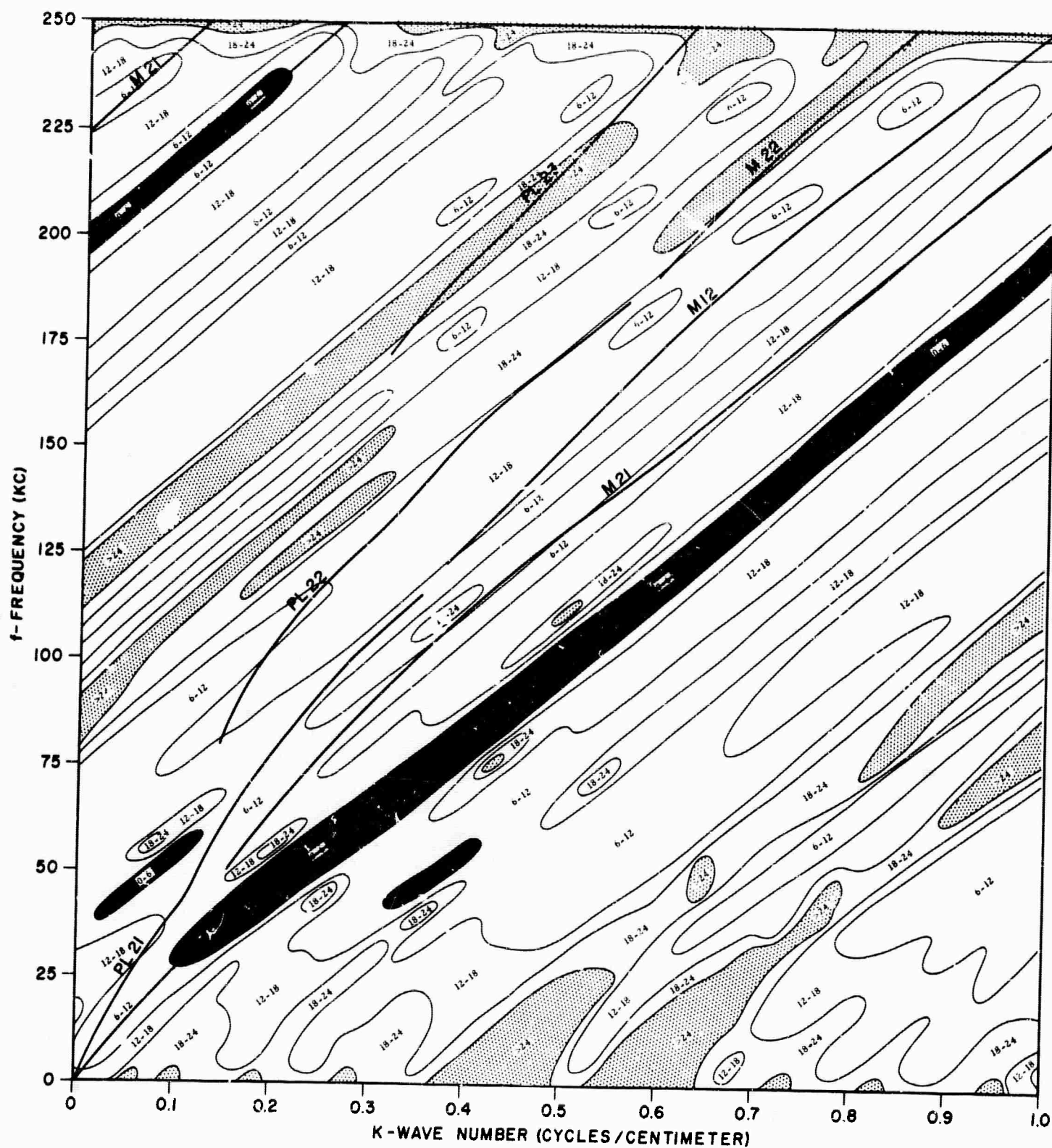


Figure 12. Spectral Estimate of Theoretical Data Using 12-Element Array and Random Receiver Gains (See Table I). The Numbers within the Contours Represent Decibels Down from Maximum Amplitude.

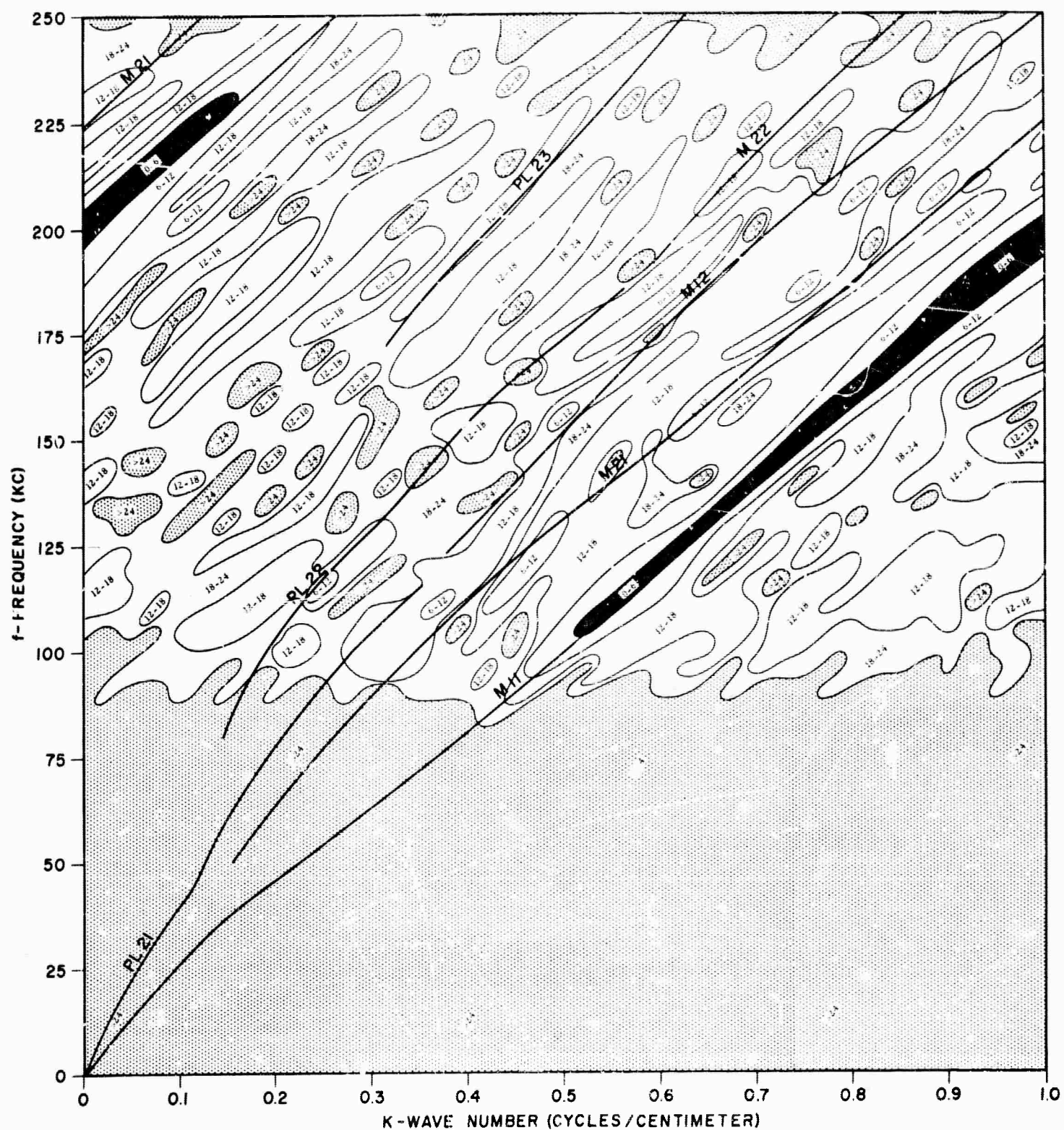


Figure 13. Spectral Estimate of Experimental Data Using 21-Element Array with Equalization Factors. The Numbers within the Contours Represent Decibels Down from Maximum Amplitude.

APPENDIX C

APPLICATION OF MULTICHANNEL FILTERING FOR THE
SEPARATION OF DISPERSIVE MODES OF PROPAGATION

APPLICATION OF MULTICHANNEL FILTERING FOR THE SEPARATION
OF DISPERSIVE MODES OF PROPAGATION*

by Stanley J. Laster⁺ and A. Frank Linville⁺

This paper discusses the results of multichannel mode separation studies using both theoretical and analog model seismograms. Unlike conventional velocity filtering, the mode separation technique makes use of the fact that for dispersive modes the phase velocity is frequency dependent. Other information, such as modal amplitude and the relation between horizontal and vertical components of motion, can be included in the filter design. In the present study two processors are considered. One, having 9 channels, makes use of only the frequency-velocity relationships, while a second (6 channels) also uses two component information. A description of the filter design and the results obtained from applying these filters to the data are given.

*Presented in the Section of Seismology, 46th Annual Meeting of the American Geophysical Union, Washington, D. C.

+Texas Instruments Incorporated, Dallas, Texas.

APPLICATION OF MULTICHANNEL PROCESSING FOR THE SEPARATION OF DISPERSIVE MODES OF PROPAGATION

by Stanley J. Laster and A. Frank Linville

I. Introduction

The use of normal modes to represent the propagation of elastic waves at large horizontal offset is well-known. By addition of the relevant leaking modes, the mode theory has been shown to be useful for representation of the seismograms at shorter range. In any case the method is most applicable when the dominant wavelength of the elastic disturbance is much larger than any physical dimension in the earth model, for then the successive ray arrivals cannot be distinguished and the seismogram has the ringing appearance peculiar to interference phenomena.

A unique characteristic of a "mode" of propagation is the frequency-phase velocity (or frequency-wave number) relationship. The phase velocity, as defined here, is simply the apparent moveout velocity between closely spaced receivers. Another parameter of interest is the group velocity, defined as the average velocity of travel (for each frequency) in the sense of total distance traveled divided by elapsed time. Two or more modes may partially overlap in frequency, phase velocity and group velocity, but no two modes agree completely in the dependence of phase and group velocity on frequency. If all the physical constants of a plane-layered model are known, the frequency-phase velocity relations (dispersion curves) may be computed theoretically. Similarly,

if the dispersion curves for an earth model are known, methods have been developed to approximately recover the elastic parameters of the model (Anderson, 1964).

This paper is concerned with the problem of measuring modal dispersion curves from experimental data. If a single isolated mode could be recorded by a set of seismometers at large horizontal offset from the source, it would be a simple matter to recover the dispersion curve simply by visually correlating "events" (peaks, troughs, or axis crossings) across the array of seismograms. An apparent frequency and phase velocity for each event could be measured directly. At short distances, the dispersion of a single mode is not visually obvious although the dispersion curve may still be recovered by use of Fourier transform methods. However, direct determination of the dispersion curves from the total seismogram is more difficult, so that separation of the modes is usually necessary. The obvious bases for separation are arrival time, frequency content, and phase velocity, although one can also use depth dependence of the various modes and the relation between horizontal and vertical components of motion for each mode. Separation by arrival time (group velocity) has long been used in earthquake seismology, while separation by frequency filtering is common in exploration seismology. Neither method is completely adequate. Except in these two simple cases all the above methods of separation require multichannel recordings of the elastic disturbances.

In the present paper we consider the measurement of dispersion curves from modes separated by using two different array processing schemes.

In the first case a nine element inline array is used to separate the various modes on the basis of known frequency-wavenumber and amplitude relationships. Realizing, however, that this array is not typical of actual arrays now in use, we devised a second scheme by which the inline horizontal and vertical components of motion at three spatial locations were combined, again using known frequency-wavenumber and horizontal-vertical relationships. This six channel process could be implemented using data from standard earthquake stations.

II. Description of Data

The data used in the present study consists of theoretically computed seismograms and analog model seismograms for a simple model consisting of a brass layer over a steel half-space (Laster, Foreman, and Linville, 1965). The dispersion curves for this model are shown in Figure 1. In the frequency band of interest, determined by the source spectrum of the analog model, there are three leaking (PL) modes and four normal (trapped) modes. The various modes are seen to overlap in frequency, phase velocity and group velocity (arrival time).

A complete specification of the elastic disturbance requires a description of the amplitude of the various modes. The relative amplitudes depend on the depth of source and receiver, both of which are assumed to be on the surface (top) of the model. In addition, since the leaking modes radiate energy into the half-space, the relative amplitude depends on the absolute source-receiver distance. The relative power spectra for the seven modes is shown in Figure 2 for the source-receiver distance 50 cm.

The fundamental Rayleigh mode is seen to overwhelm the other modes at all frequencies. In addition, it is seen that the PL modes have very sharply peaked frequency spectra, the peaks of which correspond to minima in the attenuation functions. In Figure 3 are presented the theoretically computed individual modes and their summation (the total seismogram) and, finally, in Figure 4 the experimental analogue model data for the distance range 50-70 cm. The source spectrum of the model embraces only the frequency range 50-250 kc, which explains the difference in appearance between the theoretical and experimental data.

III. Measurement of Dispersion

The description of modal propagation is particularly simple for propagation between two identical receivers on the surface of the model. One may speak of a "transfer function" which operates on a single mode at one distance to change it into the same mode at greater distances. In two dimensions, this transfer function is independent of source-receiver distance and depth of source. The transfer function for the total seismogram, however, is very complicated and changes rapidly with source receiver distance. For normal modes in our two dimensional model the (frequency domain) transfer function is a pure phase distortion which tends to stretch out the seismogram in time. If this function is represented as $e^{i\theta}$, then the phase shift θ is given by

$$\theta(f) = - \frac{2\pi f}{c(f)} \Delta x,$$

where f is the frequency, Δx is the distance between receivers and $c(f)$ is

the frequency dependent phase velocity. For leaking modes the transfer function contains an additional factor e^{-sx} , where $s(f)$ is the frequency dependent attenuation.

Measurement of dispersion is thus seen to require estimation of $\theta(f)$, the phase of the transfer function. For a single, well dispersed mode one might measure this phase shift directly from the seismogram, since the seismic signal approximates a sine wave during each small time interval. This, of course, requires visual trace to trace correlation of peaks and troughs. This method is not so useful at short offset where the dispersion mechanism has not sufficiently separated the various frequency components. Nor is it useful when there is significant noise on the seismogram. Noise may consist either of ambient energy from random sources, or signal scattered by imperfections in the model. Either of these will tend to destroy the visual correlation.

A better method requires the computation of the crosscorrelation function between traces. The cross power spectrum, which is the Fourier transform of the crosscorrelation function, for a single mode recorded at two receivers is just

$$\Phi(f) = |A|^2 e^{-i \frac{2\pi f \Delta x}{c}},$$

where A is the amplitude spectrum (excitation function) of the mode. The phase of the cross power is seen to be the same as the phase of the transfer function. This method has the advantages that the frequencies need not be well dispersed and that random noise tends to be cancelled out in the correlation process. Numerical computations of crosscorrelation functions and Fourier transforms are relatively simple with modern electronic computers.

As an example of the use of the crosscorrelation technique, dispersion curves were computed for the experimental analogue model seismogram of Figure 4. In an attempt to obtain single modes the seismograms were separated on a travel time basis into a leaking mode segment, shear mode segment, and Rayleigh mode segment. The correlations, Fourier transforms and finally phase velocities (shown in Figure 5) were then computed. The

estimate of the Rayleigh mode is excellent over the whole frequency band of the source. The two shear mode curves were adequate over narrow bands, but part of the curves could not be obtained since they overlap the Rayleigh mode in both frequency and group velocity. The PL mode curves are poor. Using different pairs of traces gave somewhat better PL results, but less acceptable shear mode curves.

IV. Mode Separation Filter Design

The equations defining a multichannel processor to separate dispersive modes of propagation may be formulated either in the frequency domain or in the time domain. Each method has its advantages and disadvantages. We have made use primarily of the time domain formulation, but for completeness both methods will be explained and compared.

The frequency domain formulation results when one attempts to find a set of m filters $Y_j(f)$ $j = 1, 2, 3 \dots m$, which may be applied to m seismometer outputs to extract a particular mode with cross-power statistics S_{ij} from the interfering modes whose summed cross-power statistics are represented by $N_{ij}(f)$. The filters are found from the solution of matrix equation (1),

$$\begin{matrix} mxm & mx1 \\ [S_{ij}^*(f) + N_{ij}^*(f)] & [Y_j(f)] = [S_{io}^*(f)], \end{matrix} \quad (1)$$

where the asterisks denote complex conjugation.

This equation, which results from the standard requirement that the mean squared error be minimized, is to be solved for every frequency. However, in practice, it is not possible to treat the frequency as a continuous variable. Instead, the filters $Y_j(f)$ are computed at a finite number of closely spaced frequencies $f = n\Delta f$ where $n = 1, 2, \dots, N$. The corresponding time operators to be convolved with the input channels are then obtained by performing the inverse Fourier transform operation on $[Y_j(f)]$. Solution of equation (1) is not difficult, as it requires only the inversion of an $m \times m$ Hermitian matrix. The use of 30 or more channels is not unreasonable. Also, any number of frequencies can be used, since the solution at any frequency is independent of the solutions at all other frequencies.

Because of the sampling in the frequency domain, the time operators designed by this method are infinitely long, periodic time functions. Use of one period of the operators implies that the filter spectra satisfy the matrix equation exactly at the points $f = n\Delta f$ and have values obtained by use of a particular interpolation formula between these frequencies. This is ordinarily satisfactory in most applications. Unfortunately, it has been found that a single period of one of these mode separation filters does not approximate a transient function. The filters show sizable jumps at the truncation points which lead to larger-than-desired errors in application. Use of more frequencies with closer spacing allows design of longer filters which have smaller truncation errors, but the separation error never quite decreases to the level desired.

A more reasonable approach to the problem is to minimize the mean squared error subject to the constraint that the filter operators vanish outside some time interval, i.e.

$$\int_{-\infty}^{\infty} \left[y_j(f) \right] e^{i2\pi f t} df = 0 \quad \text{for } \begin{cases} t < 0 \\ t > T \end{cases}$$

Obviously, now the solutions at all the frequencies $f = n\Delta f$ cannot be independent. While the problem can be formulated in this manner it is simpler to design the filters directly in the time domain since the constraint is a time domain criterion. In the time domain, the system of m filters, which yield the minimum mean squared error for a fixed filter length r , is given by the solutions $y_j(t)$ of the equation

$$\left[\phi_{ij}(\tau) \right] \left[y_j(\tau) \right] = \phi_{io}(\tau)$$

where $\left[\phi_{ij}(\tau) \right]$ is the $m \times m$ matrix of crosscorrelations of signal plus noise, $\left[y_j(\tau) \right]$ is the $m \times 1$ matrix of filter operator points and $\left[\phi_{io}(\tau) \right]$ is the $m \times 1$ matrix of signal crosscorrelations between the input channels and the output channel. For long filter operators and a large number of channels, this equation is difficult to solve, and high numerical accuracy is required. However, it should be pointed out that the $\left[\phi_{ij}(\tau) \right]$, since it represents a space-time correlation function, will never be singular.

Some special features can be built into the filters to make them more realistic. It is generally observed that a small amount of uncorrelated (random) noise is present in every channel of any real data. Since the power spectrum as a function of frequency for this component usually is not known, it is generally assumed white (a constant). This can be introduced into the frequency domain filter design by adding this constant to the diagonal elements of the cross-spectral matrix. In the time domain design, it is introduced by adding a delta function of the

appropriate height to the zero lag values of the autocorrelation for each channel. In designing the filters, random noise to the extent of about one-tenth percent of the maximum Rayleigh power was added; i.e., the random noise was 60 db down from the peak. A second difficulty occurs in practice because of random differences in receiver gains between channels. This appears as spatially uncorrelated noise, the wavenumber spectrum of which may be assumed constant. Note that the description of random receiver gains includes within its scope the decay of the leaking modes with range. This kind of noise is introduced by scaling up the diagonal elements of the cross-spectral matrix (frequency domain design) or by scaling up the autocorrelations (time domain design.) Addition of noise degrades filter response, but greatly extends the applicability of the processor.

In many cases the initial knowledge about the physical model may be scant, or the model may be known to change within the region of interest. To account for this the mode separation processor may be designed to pass energy lying in a band about the desired mode characteristic. This is achieved by computing the weighted average of the cross-power or correlation statistics in the pass band, the weighting function being just the probability distribution of the possible models.

V. The 9 Channel Mode Separation Processor

A. The Filters

The formulations were used to design the best 9-channel (see Fig. 6) time domain (convolution) operators to pass, in the least mean square sense, one mode and reject the others. Channels to be used were chosen so that no dead traces in the experimental data would be used.

Filters were designed in the frequency domain at 10 kc frequency increments, for the range 0-250 kcps. The auto and cross power spectra were theoretically computed for each mode and then the results for all modes stacked. The spectra were averaged over an ensemble of possible models to allow for errors in an original estimate. Figure 7 shows the the pass and reject bands, depending on which mode is considered to be the signal. The column vector contained only cross power spectra of the signal. The inverse Fourier transform operation was applied to the computed filter spectra obtained by solving the matrix equation, and the time operators thus obtained were $400\mu\text{s}$ long with a time sampling interval of $1\mu\text{s}$.

For the filter formulation directly in the time domain correlation statistics are required. Two correlation matrices are necessary for the design of each set of mode separation filters. The left-hand correlation matrix consists of all possible auto- and crosscorrelations of the signal mode plus interfering modes for channels 1 through 9. The right matrix contains just the desired mode at channels 1 through 9 correlated with itself at the chosen output distance (channel 5 in this case).

It was initially assumed that the signal and noise were space stationary, i.e., that the crosscorrelations depended only on the channel separations but were independent of absolute channel locations. In a 2-dimensional model, this is true for the normal mode taken individually and is approximately true at great distances from the source for the individual leaking modes. In the present case for a space stationary process, the left-hand matrix contains 12 nonredundant correlations.

The Φ_{ij} were computed simply by correlating the seismograms at channels with the appropriate space separation. Realizing that decay of the leaking modes causes some nonstationarity, an attempt was made to use channels distributed approximately uniformly over distances between the two desired output distances. The matrix of correlations is shown in Figure 8. It was found, however, that filters could not be designed using this correlation set, indicating that this estimate of the matrix $[\Phi_{ij}(\tau)]$ was non-positive definite. Since checks showed that the operations had indeed been performed correctly in computing the set of correlations, it was concluded that the correlations chosen to form the nonredundant set did not constitute a consistent space-time correlation function.

The probable reason for this strange behavior was finally inferred from Figure 8. These correlations have considerable amplitude at large lags, a behavior which, in general, tends to cause some difficulty in the matrix inversion. Studies have shown that the auto- and crosscorrelations between channels for any single mode do not show this behavior, so one is led to believe that the difficulty may have been due to large cross-correlation (coupling) between modes. Coupling between modes is a form of nonstationarity (in space) because the crosscorrelation between modes depends strongly on the absolute locations of the channels as well as on their separation. This effect severely restricts filter design if the crosscorrelation between modes is large, and computations have shown in the present model that crosscorrelation between the Rayleigh and any higher mode is an order of magnitude larger than the autocorrelation of that higher mode. The nonstationarity due to decay of the leaking modes

is not believed to have caused a problem. Attention, therefore, was given to eliminating coupling between modes.

Before proceeding to discuss the elimination of crosscoupling, it is worthwhile to point out that there is a technique by which filters could have been designed using the correlations computed from the total seismograms, as was originally attempted. This is achieved by computing all possible correlations for the seismograms from the channels to which the filters are to be applied. None of these correlations can be considered redundant. However, design of filters in this manner would have been rather fruitless because of the strong coupling between modes. The filter design would have made use of the crosscoupling to achieve excellent rejection of the interfering modes when applied to the set of channels from which the correlations had been computed. For another set of identically spaced channels, the coupling between modes is different and the mode separation would have been very poor. Thus, a set of filters would be needed for each output channel.

The coupling between modes can be eliminated by ensemble averaging; i.e., the autocorrelations for all receivers can be averaged, the crosscorrelations for all receiver pairs with unit separation can be averaged, etc. Alternatively, in practice, one can choose fixed pairs of receivers and average the corresponding crosscorrelations for events from a number of sources at various locations. These processes were simulated as follows.

Each individual theoretical mode was correlated at the distances indicated. The individual mode correlations then were summed to produce a left-hand matrix (consisting again of 12 nonredundant correlations) with no correlation coupling. These are shown in Figure 9.

It should be noted that these correlation functions show much more transient behavior than the functions with crosscoupling.

Figure 10 shows the PL_{21} correlations used to form the right-hand matrix for the filter design. The sampling interval of the total seismograms is 1 μ sec; since the seismograms contain no frequencies above 250 kc, the correlations may be resampled at 2 μ sec and the filters designed at 2- μ sec sampling intervals without frequency aliasing. From the left-hand matrix of correlations shown in Figure 9 and the right-hand matrix of correlations shown in Figure 10 a set of 61-point filters (with 2 μ sec sampling interval) was designed to estimate PL_{21} . It should be noted that the left-hand matrix may be used for all sets of mode separation filters and need be computed but once. The desired output mode then is determined by the right-hand matrix.

The fact that the correlations show strongly transient behavior with most of the energy moving across the correlation set with approximately Rayleigh velocity makes it possible to design an even shorter filter operator (31 points) by using only the significant part of the correlations. This is achieved by shifting the original seismograms to a reference velocity to line up the Rayleigh pulse before computing the correlations. The filters designed in this manner must be applied, of course, to the shifted seismograms. (A similar technique was found to reduce the truncation error when applied to the filters designed in the frequency domain.) The short filter operators (31 points) were designed for PL_{21} , PL_{22} , M_{21} , and M_{12} . Figure 11 shows for comparison the 400-point filter operators designed in the frequency domain, the 61-point filters and the 31-point filters designed in the time domain for the mode PL_{21} . Figure 12 shows the 31-point filters designed in the time domain for the modes PL_{22} , M_{21} and M_{12} .

The behavior of the filter operators is obviously non-physical, since the impulse responses yield significant output before time zero (time of input). This is typical for multichannel systems operating on propagating disturbances, but is no limitation since the filters can be realized digitally in the computer or with analogue equipment simply by introducing sufficient delay into the operators. More important is the fact that the filters, particularly those designed in the time domain, show approximately transient behavior. The 31 point operators for PL_{21} closely approximate the significant portions of the corresponding 61 point filters. However, there is seen to be significant difference between the filters designed in the time domain and those designed in the frequency domain. In any case one could not have predicted a priori the shape of the desired filter operators. The various channels are being stacked with frequency dependent weights to "buck out" some modes while passing the signal.

B. Filter Response in Frequency and Wavenumber of the 9 Channel

Mode Separation Filters

The filter response in f (frequency) and k (wavenumber) was computed to determine the rejection capabilities of the multichannel filters designed in the time domain. The responses of the multichannel filters designed to estimate PL_{21} , PL_{22} , M_{21} and M_{12} are shown in Figures 13 through 16, respectively. Each contour represents a range of 6-db rejection and has been normalized to the largest value of power in the f - k response. The filters attempt primarily to reject the Rayleigh mode but, in every case, interfering higher modes are adequately rejected. For PL_{21} , it is seen that the filter system acts as a high-cut frequency filter followed by a system

which rejects only the Rayleigh mode, which agrees with the known requirements of the problem.

In a similar manner the f - k response of the filter set designed in the frequency domain to separate PL_{21} was computed and is shown in Figure 17. The response has been normalized to the largest value of power in the f , k response. Because only a very small amount of random noise has been included (45 db down from the Rayleigh mode) in the signal-noise specification, the set of filters may have very high response in areas not containing coherent modal energy. The zero db reference lies in this area. Thus in order to recover the desired signal with unit gain, the set of filters should be scaled up by an appropriate factor.

In some regions of frequency the signals may be so small that they can never be completely recovered; an example of this is PL_{21} between 50 kc and 110 kc.

A somewhat better picture of the response for one of these processors is shown in Figure 18. Here the response of the filters intended to estimate M_{12} has been plotted versus wave-number at two separate frequencies. For each frequency the wavenumber location of the signal and noise modes has been indicated. Also relative output levels of the signal and noise are shown, based on the processor response and the known input levels. The best indication of the processor performance is the way in which M_{22} and M_{21} are rejected. These modes lie very close to M_{12} in wavenumber, and have about the same power levels. Increased rejection would require a larger array.

A comparison of the rejection capabilities of the short 31-point filters designed in the time domain and the rejection capabilities of the

longer 400-point filters designed in the frequency domain shows that the filters designed in the time domain have equal and in some cases better rejection capabilities than the frequency filters even though they are much shorter. By this means mode separation filters much shorter than originally had been anticipated were used to effect a considerable reduction in computer time cost, both in the filter design and in the multichannel application of the filters to obtain the separated modes.

C. Application of 9 Channel Mode Separation Filters to Theoretical and Experimental Seismograms

Figures 19 through 27 show the results of applying the mode separation filters to the theoretical seismograms. The top trace is the total theoretical seismogram and the bottom trace is the individual theoretical mode which is being estimated. The estimated modes then are shown in the intermediate traces. The low-gain traces give a visual estimate of input signal-to-noise ratio. In Figures 19 through 22, the output location is at 54 cm while, in Figures 23 through 26, the output location is at 62 cm. To determine the dispersion curves, it is necessary to obtain separated modes to at least two output distances.

A comparison of the separated PL_{21} mode using 400-point filters designed in the frequency domain and 31-point filters designed in the time domain is shown in Figure 19. The high-frequency noise seen on the early portion of the mode separated by application of filters designed in the frequency domain is produced in the multichannel convolution process because of the sizable jumps at the truncation points of the filters as discussed in paragraph A. This noise is, to a rough approximation,

just the result of operating on the Rayleigh wave with a step function operator of appropriate height. The separation using the filters designed in the time domain is much better. This is particularly remarkable since the frequency domain filters are almost seven times as long, timewise, as the time domain filters and have 13 times as many points. The time domain filters, with 2 μ sec sampling, are applied to the seismograms, with 1 μ sec sampling, by operating only on alternate points of the seismograms. A comparison of the PL_{21} mode separation results from the theoretical seismograms using the 61-point and the 31-point time domain filters showed no significant differences for the two output distances. It should be noted that none of the filters--long or short time domain, or frequency domain--is able to recover the highly attenuated portion of PL_{21} above 50 kc.

The separation of PL_{21} in the frequency range 0 to 50 kc where the peak power is concentrated may not be considered an adequate test of the mode separation method since only one mode--the Rayleigh mode--is present to be rejected. Separations of other modes are just as successful.

Figures 20 to 22 show similar results for PL_{22} , M_{21} , and M_{12} .

Note that the M_{21} and M_{12} modes overlap the dominant Rayleigh pulse in arrival time and frequency, so the degree of separation is remarkable. The energy following the main PL_{22} wave train is residual Rayleigh energy.

Figures 27 and 28 show the results of applying the mode separation filters to the experimental seismograms obtained from the analog model H-1. The top trace in both figures is the experimental seismogram trace followed by the separated PL_{22} , M_{21} , and M_{12} modes. The output location

in Figure 27 is 54 cm and, in Figure 28, it is 62 cm. Mode separation was performed using the 31-point time domain filters. Note that for M_{21} and M_{12} dispersion is visually apparent. The separation error for all three modes is greater than for the separation using the theoretical seismograms, but this is to be expected because the filters were designed using a theoretical model. The burst of noise following the PL_{22} wave train is relatively large but can be eliminated in the dispersion calculations by simple time truncation. It may be noted that the separation filters have overcome gain differences of up to 20 percent in the experimental seismograms.

VI. The 6 Channel Two Component Processor

A. Design of Filter Operators

A second mode separation processor was designed to use data recorded on two component seismometers located at three sites in an inline array. Only the inline component of horizontal motion is required. In actual practice it may be necessary to rotate the horizontal components to produce an inline and a transverse trace. Another difficulty which may be encountered in practice is that the horizontal and vertical instruments may have different response characteristics. A possible solution to this problem may be the use of a triaxial instrument, in which case rotation must be performed on all three components. No such difficulty is encountered with the analog model data in the present study since the same receiver, a shear mode piezo-electric transducer, was used to measure both components of motion.

The mode separation filters were designed in the time domain using correlation statistics computed in the same manner as for the 9 channel processor discussed above. The matrix of correlations is shown in Figure 29. There is obviously no dispersion between two components at a single spatial location. However, there is a $\pm 90^\circ$ phase shift between these components for the normal modes and a frequency dependent phase shift for the leaking modes. In addition, the excitation functions are different for the horizontal and vertical components. Here it has been assumed that the source and receiver array are both on the surface. However, the excitation functions depend on source depth, so to design filters applicable to sources at depth, one must have at least a rough idea of the correct source depth. No attempt has been made to do this here.

The filters designed for the two component array are shown in Figure 30. Channels 1 to 3 are convolved with the three vertical seismometer outputs, while channels 4 to 6 are convolved with the horizontals. Then the filtered outputs are summed to give an estimate of the desired mode. Again the relative utilization of each channel changes with frequency and the mode being estimated.

The performance of this six channel processor was not expected to equal that of the nine channel processor simply because of the fewer channels used. However, it is difficult to adequately represent the 6 channel response. Because of the use of two components, it is no longer valid to compute simple frequency wavenumber spectra. One might represent the response as a function of frequency and mode number, though

this has not been attempted here. Also the analog of the "unit cell" in frequency and wavenumber is not as well defined here. Certainly the use of two components will help offset the problem of aliasing due to large distances between recording sites, but on the other hand, there will be frequencies at which the relation between the horizontal and vertical component is very similar for two modes (See Figure 31.). This will correspond to an alias in mode number. The representation of the response of multicomponent processors bears additional study.

B. Application of 6 Channel Processor

The 6 channel, two component processor was applied to both the theoretical, and experimental analog model seismograms to separate PL_{22} and M_{21} . The results are shown in Figures 32 and 33. The separations are not so good as those obtained with the 9 channel system, but are still quite adequate for the theoretical data. The present processor is less able to distinguish between M_{11} , M_{12} , and M_{21} . At higher frequencies the horizontal-vertical relations are quite similar for these modes, since the the sign of the 90° phase shift is the same for the Rayleigh mode and the shear modes.

The results obtained by applying the 6 channel filters to the experimental data (Figure 33) are very poor for M_{21} . Since the 9-channel processor is able to extract the correct information from the vertical seismograms, one would surmise that the experimental horizontal data is bad. The probable cause of this has been traced to the finite size of the analogue model receiving transducer (1 mm X 3 mm). When the vertical seismograms are being recorded the amplitude is actually

averaged over the depth range 0 - 3 mm. Fortunately this caused no major problem as can be seen from Figure 34 where this average for M_{21} and M_{11} is plotted, along with the surface amplitude, as a function of frequency. When recording the horizontal component, the amplitude is averaged only over the depth range 0 - 1 mm. However, the horizontal component is much more sensitive to averaging as is seen in Figure 35. The net result is to strongly affect the vertical-horizontal ratio (Figure 36), so that the data does not at all satisfy the model used to design the filter system (compare with Figure 31). The Rayleigh wave ratio in particular, is strongly altered, above 100 kc, and actually crosses the surface M_{21} ratio used in the design of the filters. The ratio for the averaged M_{21} has the same general shape as the surface ratio, but the notch is moved to higher frequency. In addition, this ratio is smaller at high frequencies. Though no curves are shown for PL_{22} , it is known to be less affected by averaging over the receiver depth.*

In recording real data this particular problem does not occur, since the receivers are usually placed on the surface and are very small in size compared to one wavelength. However, if one attempts to design filter systems applicable to events from sources at a range of depths, an analogous problem arises. Averaging over an ensemble of source depths tends to eliminate the correlation between horizontal and

*For any of the modes horizontal averaging (over 1 mm for vertical motion and 3 mm for horizontal motion) corresponds to simple wavenumber filtering. These effects can be readily evaluated and have been shown to offer no problems in the present frequency range.

vertical components of motion. Thus, in practice one would probably have to design several filter systems, each appropriate to a small range of source depths.

C. Dispersion Obtained From the Separated Modes

Figure 37 shows the dispersion obtained from the separated modes using the 9 channel mode separation filters operating on the theoretical seismograms. The dispersion was calculated by taking the crosscorrelation of the separated modes, multiplying by the Hanning time window (See Tukey and Blackman, 1959.) and then taking the Fourier transform of the product. The phase of the transform is used to compute the phase velocity. The agreement with theory is satisfactory, except at very low frequencies. However, one would not expect the results to be completely satisfactory at frequencies whose periods are of the order of magnitude of the length of the filter impulse response, i.e., below 20 kcps. In addition, the results were poor for the leaking modes in the frequency regions where their attenuation is high. The signals were simply too small to be recovered here.

Figure 38 shows the dispersion obtained from the separated modes using the time domain filters and the experimental seismograms. The results are very good and should not agree necessarily with the theoretical curves since it is known that the model material velocities are somewhat different from the velocities used to compute the theoretical curves. Very good dispersion curves have been obtained for the PL_{22} mode and also for the M_{21} and M_{12} modes. It should be noted that the M_{21} mode has been separated effectively from the dominant Rayleigh mode where the two overlap in frequency and arrival time. This result cannot be achieved by any 1-

or 2-channel method. The PL_{22} result is better than any previously obtained for this analog model. It is felt that previous 2-channel estimates failed because there are many small imperfections in the model (such as weak points in the L and) which tend to make the signals at any pair of traces look very noisy relative to those in a perfect model. However, the mode separation filters operating on nine channels are able to extract meaningful information while rejecting this noise. This seems to substantiate the idea that average dispersion characteristics can be recovered from earth models with imperfections.

Similar results were obtained using the 3 channel, 2 component processor. The dispersion results obtained by operating on the theoretical seismograms are shown in Figure 39, while the experimental results are shown in Figure 40. In neither case are the results as good as the 9 channel results. However, the dispersion curves obtained are generally satisfactory except for the experimental M_{21} , which is not shown. The theoretical results show adequate separation between the shear modes and Rayleigh mode except near 160 to 250 kc. As previously mentioned, this area is almost an alias point in mode number for the horizontal-vertical relationship and the only basis for separation is the three channel frequency-wavenumber relationship.

VII. Discussion

The preceding paragraphs have discussed in some detail the design and application of two multichannel processors. The 9 channel system, utilizing only the frequency-wavenumber representation of the dispersive modes, has been shown to be very effective. However, the array used is much larger than most real arrays now in use, scaling to 220 km length

for the real earth. The 6 channel processor, making use of the relations between components of displacement as well as the frequency-wavenumber relation, is not quite so effective, but is more realistic. This array corresponds roughly to three standard earthquake stations, with multi-component sensors, spaced over a total distance of 120 km. In both cases the present study has been aimed at long period data (scaling to the period range 10-20 sec.). Use of higher frequency data is feasible, but more channels and smaller spacing will be required since more modes will be present. At 1 cps on a 40 km crust, one might expect 8 or more normal modes. The smaller spacing is required to overcome the aliasing problem at higher frequencies. All these difficulties should be overcome by installations such as the Large Aperture Seismic Array in Montana.

One problem not touched upon is the question of how one determines the appropriate signal and noise model used to design the multichannel processor. In the present case the correlations and cross power spectra were theoretically computed for a known physical model. This method can be used in practice if a rough approximation to the earth structure is known. Such an approximation can be obtained from refraction seismograms, from approximate dispersion curves obtained in the standard manner, or from direct frequency-wavenumber spectra of signals or ambient noise. In using this method one should allow for error in his model by averaging over an ensemble of possible theoretical models.

On the other hand, the appropriate correlation or cross power statistics can be computed directly from experimental data for a large number of events. Averaging over many events has been shown in the present study to be quite important, since this tends to eliminate spatial non-stationarity due to

intermodal correlation. Averaging over pairs of receivers with the same spacing will also tend to decrease equalization problems. This method yields the total correlation or cross power matrix, but other methods must be used to obtain the signal correlation or cross power between the input channels and the output channels. This can be computed theoretically as above, or one might attempt to find an event at a depth such that a particular desired mode was strongly excited, so that the statistics could be computed directly.

VIII. Acknowledgment

The work described in this paper was supported by the Air Force Office of Scientific Research under contract AF 49(638)-1244. In addition, we wish to acknowledge the helpful discussions with Dr. M. Backus and Dr. W. Schneider during the early phases of this work.

REFERENCES

- Anderson, D., 1964, Universal dispersion tables, I. Love waves across continents and oceans on a spherical earth: Bull. Seism. Soc. Am., v. 54, pp 681-726.
- Laster, S., J. Foreman, and F. Linville, 1965, Theoretical investigation of modal seismograms for a layer over a half-space: Geophysics v. 30, no. 4.
- Tukey, J. and R. Blackman, 1959: The measurement of power spectra from the point of view of communications engineering, Dover, New York, New York.

FIGURE CAPTIONS

Figure	Title
1	Dispersion Curves for the Dominant Leaking Modes and for Normal Modes in Model H-1.
2	Relative Power Spectra of Leaking and Normal Modes at 50 cm Distance from Source.
3	Theoretical Modes and Summations at 54 cm.
4	Experimental Vertical Seismograms Obtained from Analog Model H-1. The Distance Range Is 50 to 70 cm. Small Timing Lines Represent 10 μ Sec.
5	Dispersion Obtained from the Experimental Seismograms by Time Partitioning Traces at 50 and 60 cm. The Theoretical Phase Velocity Curves Are Shown for Reference.
6	A Set of Multichannel Filters Is Designed to Separate One Mode. Each Channel Is Convolved with the Appropriate Seismogram Trace. Each Set of Nine Filtered Outputs Is Summed to Give an Output Trace Which Is the Estimate of the Separated Mode.
7	Location of the Theoretical Modes in Frequency and Wavenumber. The Multichannel Filters Are Designed to Pass or Reject the Band Shown for Each Mode.
8	Correlation Functions of the Total Theoretical Seismogram. A Comparison with Figure 9 Shows the Effect of Cross Coupling Between the Individual Modes and the Dominant Rayleigh Mode.
9	Correlation Functions of the Individual Theoretical Modes Were Computed and Then Stacked to Eliminate the Effect of Cross Coupling.

Figure	Title
10	Correlation Functions of the PL_{21} Mode. This Set of 9 Correlations Is Used to Form the Right-Hand Matrix for Multichannel Filter Design in the Time Domain.
11	PL_{21} Mode Separation Filters. On the Left Are the 400-Point Filters Designed in the Frequency Domain. In the Center Are the 61-Point Filters Designed in the Time Domain. On the Right Are the 31-Point Filters Designed in the Time Domain.
12	The 9-Channel, 31-Point Filters Designed in the Time Domain to Separate the Modes PL_{22} , M_{21} , and M_{12} .
13	fk Response of the 9-Channel Mode Separation Filters, PL_{21} Signal (61-Point Filters Designed in the Time Domain).
14	fk Response of the 9-Channel Mode Separation Filters, PL_{22} Signal (31-Point Filters Designed in the Time Domain).
15	fk Response of the 9-Channel Mode Separation Filters, M_{21} Signal (31-Point Filters Designed in the Time Domain).
16	fk Response of the 9-Channel Mode Separation Filters, M_{12} Signal (31-Point Filters Designed in the Time Domain).
17	fk Response of the 9-Channel Mode Separation Filters, PL_{21} Signal (400-Point Filters Designed in the Frequency Domain).
18	Filter Response and Relative Input and Output Levels of Signal and Noise for M_{12} at Frequencies 133 and 217 kc.
19	PL_{21} Mode Separation Results from the Theoretical Seismograms. The Output Location Is at 54 cm. Time in μ Sec.
20	PL_{22} Mode Separation Results from the Theoretical Seismograms. The Output Location Is at 54 cm. Time in μ Sec.

Figure	Title
21	M_{21} Mode Separation Results from the Theoretical Seismograms. The Output Location Is at 54 cm. Time in μ Sec.
22	M_{12} Mode Separation Results from the Theoretical Seismograms. The Output Location Is at 54 cm. Time in μ Sec.
23	PL_{21} Mode Separation Results from the Theoretical Seismograms. The Output Location Is at 62 cm. Time in μ Sec.
24	PL_{22} Mode Separation Results from the Theoretical Seismograms. The Output Location Is at 62 cm. Time in μ Sec.
25	M_{21} Mode Separation Results from the Theoretical Seismograms. The Output Location Is at 62 cm. Time in μ Sec.
26	M_{12} Mode Separation Results from the Theoretical Seismograms. The Output Location Is at 62 cm. Time in μ Sec.
27	PL_{22} , M_{21} and M_{12} Mode Separation Results from the Experimental Seismograms Using the 31-Point Filters Designed in the Time Domain. The Output Location Is at 54 cm. Time in μ Sec.
28	PL_{22} , M_{21} and M_{12} Mode Separation Results from the Experimental Seismograms Using the 31-Point Filters Designed in the Time Domain. The Output Location Is at 62 cm. Time in μ Sec.
29	Correlation Functions to Form the Signal Plus Noise Matrix for Multichannel Filter Design in the Time Domain. The 6 Channels Are the Verticals and Horizontals at Three Spatial Locations.
30	The 6-Channel, 31-Point Filters Designed in the Time Domain to Separate the PL_{22} and M_{21} Modes.
31	Horizontal/Vertical Amplitude Ratios of the Normal Modes.

Figure

- 39 Dispersion Obtained from the Modes PL_{22} and M_{21} Separated by Applying the 6-Channel Multichannel Filters to the Theoretical Seismograms. The Theoretical Phase Velocity Curves Are Shown for Reference.
- 40 Dispersion Obtained from the PL_{22} Mode Separated by Applying the 6-Channel Multichannel Filters to the Experimental Seismograms. The Theoretical Phase Velocity Curves Are Shown for Reference. The M_{21} Results (Not Shown) Were Questionable.

Figure

- 32 PL_{22} and M_{21} Mode Separation Results from the Theoretical Seismograms Using the 6-Channel, 31-Point Filters.
- 33 PL_{22} and M_{21} Mode Separation Results from the Experimental Seismograms Using the 6-Channel, 31-Point Filters.
- 34 Theoretical Frequency Dependence of Vertical Amplitude as It Would Be Observed at the Surface (Solid Curves) and as It Would Be Observed by Averaging Over the Receiver Depth Range 0 - 3 mm (Open Circles).
- 35 Theoretical Frequency Dependence of Horizontal Amplitude as It Would Be Observed at the Surface (Solid Curves) and as It Would Be Observed by Averaging Over the Receiver Depth Range 0 - 1 mm (Open Circles).
- 36 Theoretical Frequency Dependence of Ratio of Average Horizontal Displacement (0 - 1 mm) to Average Vertical Displacement (0 - 3 mm). Compare With Figure 31.
- 37 Dispersion Obtained from the Modes PL_{21} , PL_{22} , M_{21} and M_{12} Separated by Applying the 9-Channel, 31-Point Multichannel Filters Designed in the Time Domain to the Theoretical Seismograms. The Theoretical Phase Velocity Curves Are Shown For Reference.
- 38 Dispersion Obtained from the Modes PL_{22} , M_{21} , and M_{12} Separated by Applying the 9-Channel, 31-Point Multichannel Filters Designed in the Time Domain to the Experimental Seismograms. The Theoretical Phase Velocity Curves Are Shown for Reference.

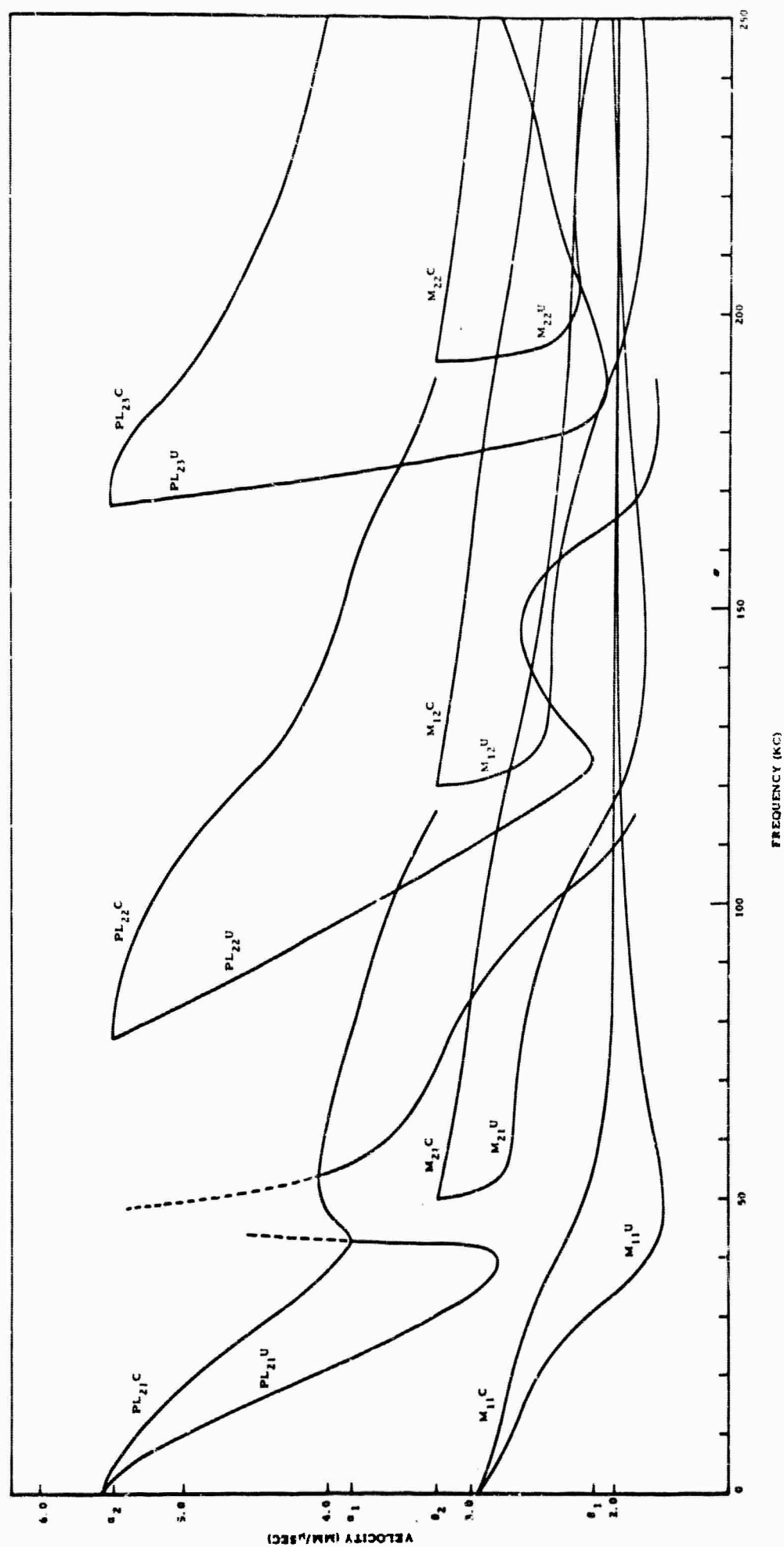


Figure 1 Dispersion Curves for the Dominant Leaking Modes and for Normal Modes in Model H-1.

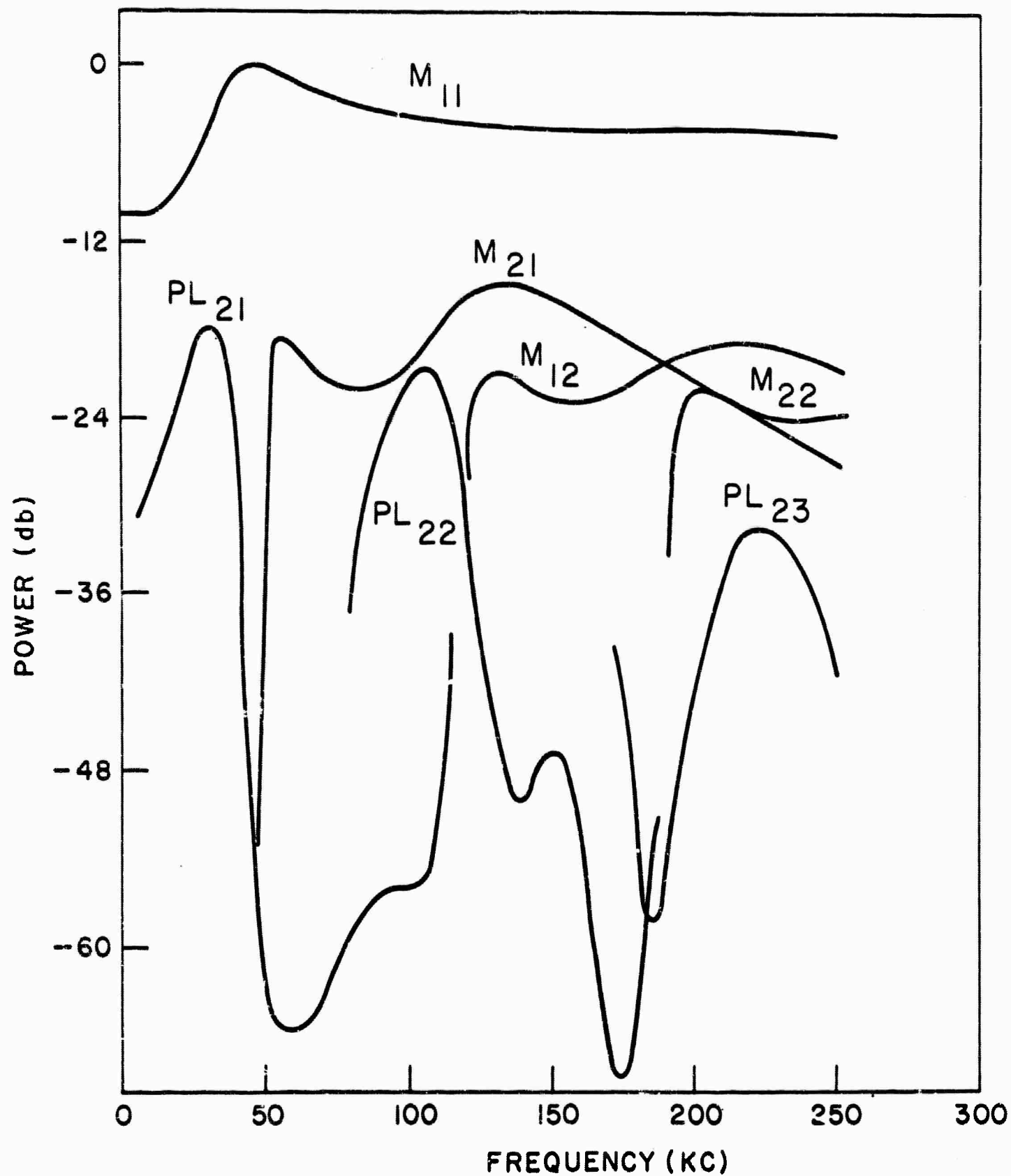


Figure 2 Relative Power Spectra of Leaking and Normal Modes at 50 cm Distance from Source.

MODEL H-I THEORETICAL SEISMOGRAM

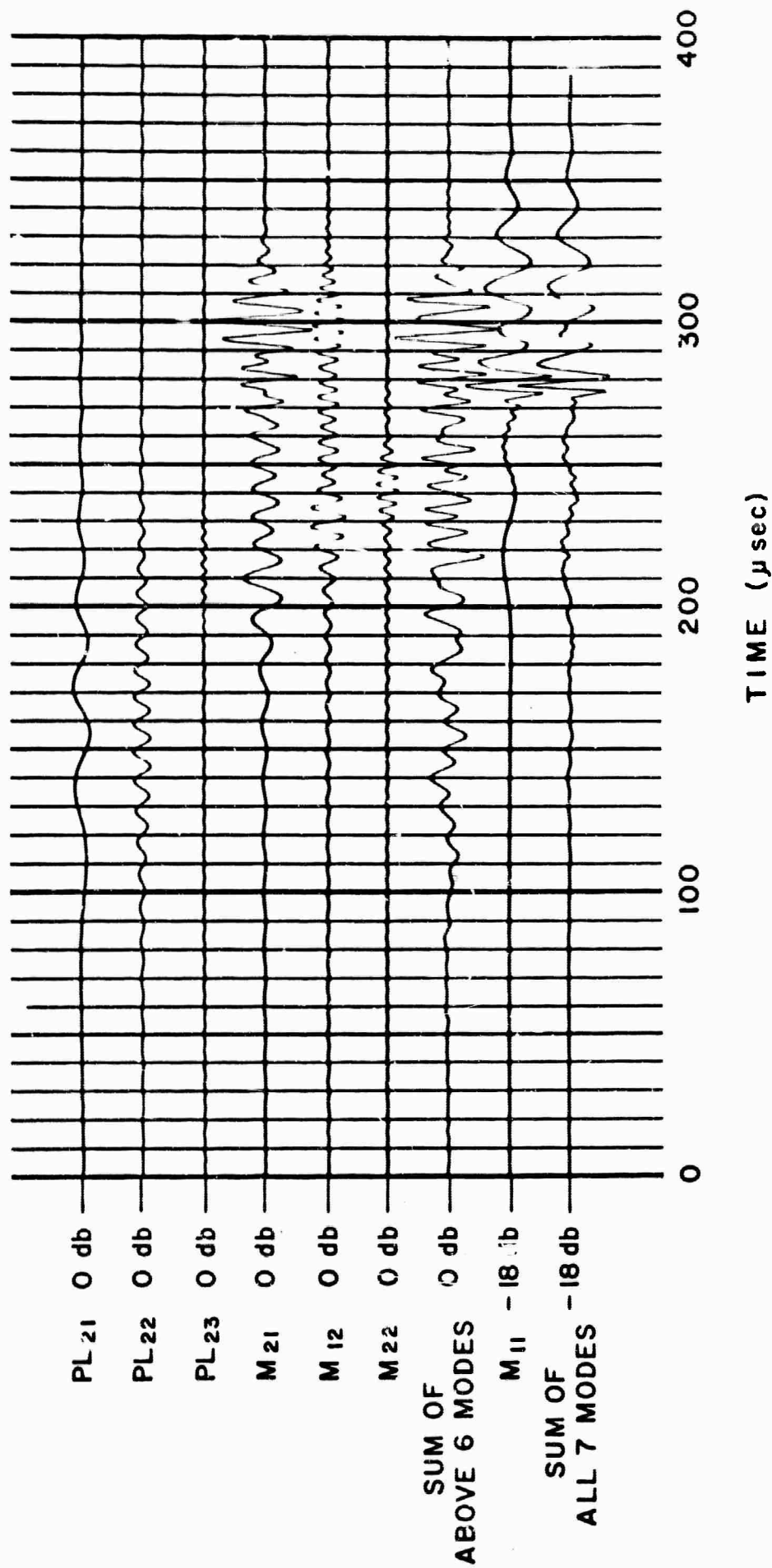
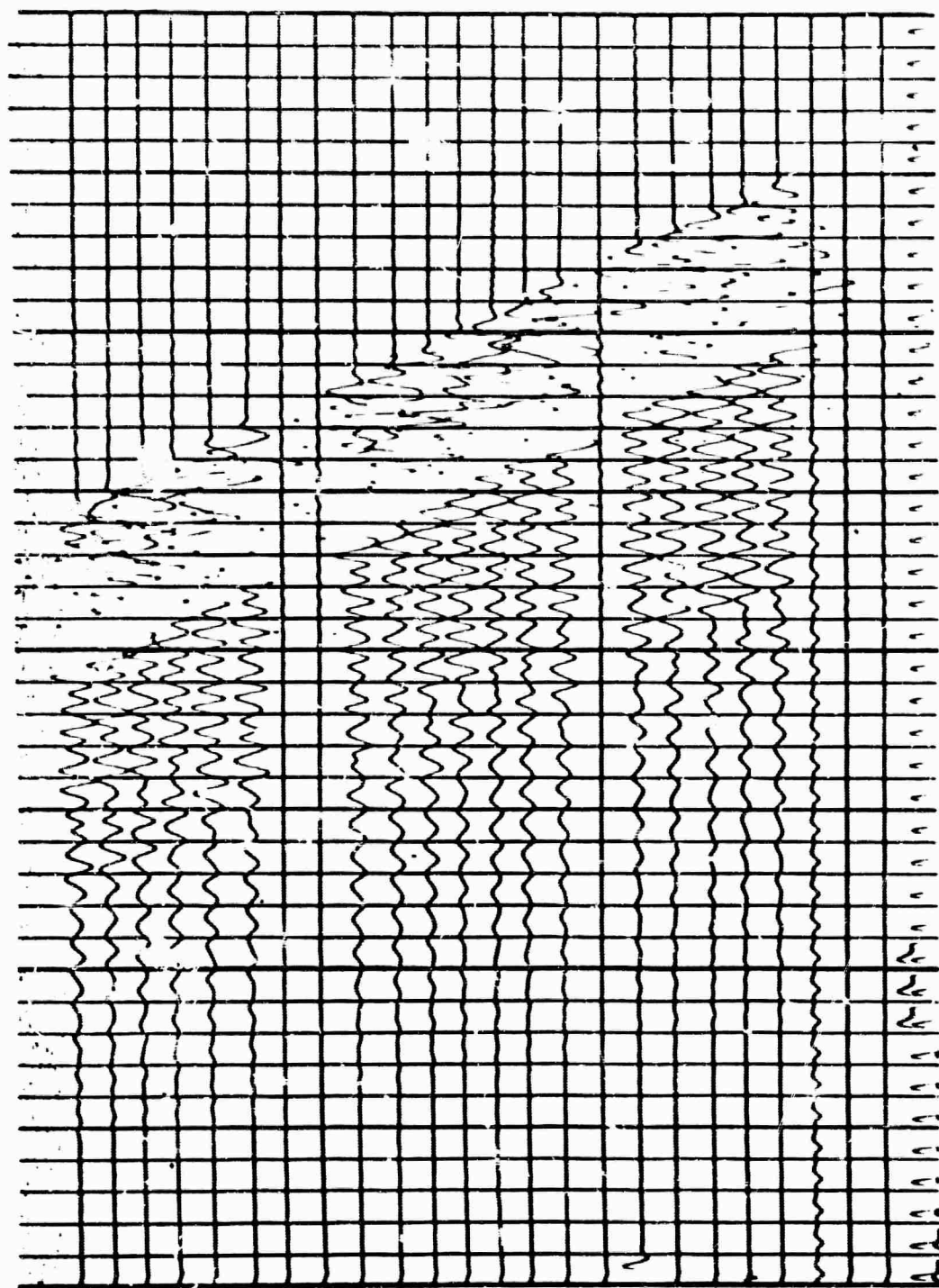


Figure 3 Theoretical Modes and Summations at 54 cm.



R : 50 - 70 cm
Filter : H Out L Out
Delay Time : 60 ms

Figure 4 Experimental Vertical Seismograms Obtained from Analog Model
H-1. The Distance Range Is 50 to 70 cm. Small Timing Lines
Represent 10 μ Sec.

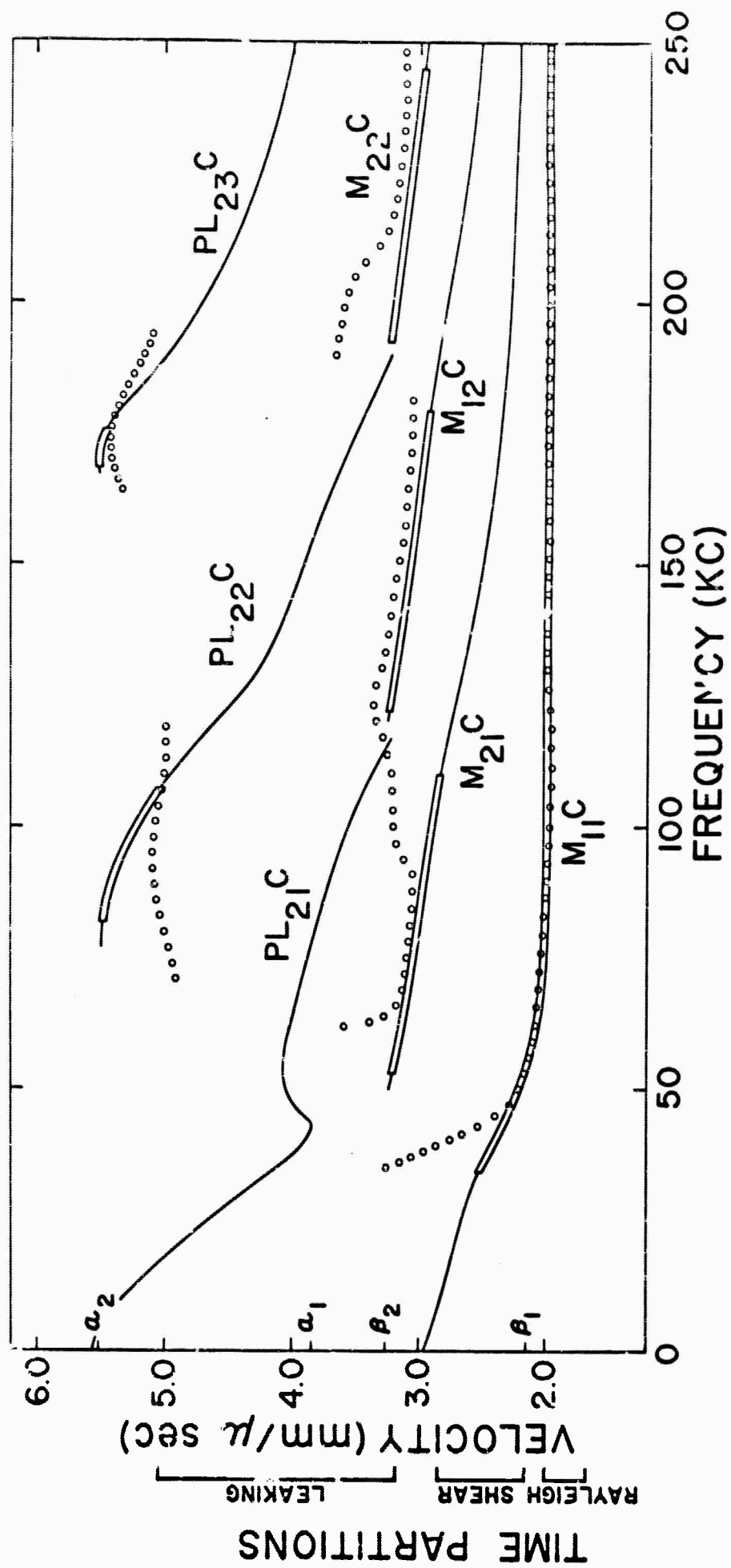


Figure 5 Dispersion Obtained from the Experimental Seismograms by Time Partitioning Traces at 50 and 60 cm. The Theoretical Phase Velocity Curves Are Shown for Reference.

Diagram illustrating the components and dimensions of a harness system, likely for a horse or similar animal, showing the arrangement of straps and buckles.

The diagram shows a side view of a harness with multiple straps and buckles. The dimensions and components are labeled as follows:

- 50 cm.**: Dimension for the top horizontal strap.
- 55 cm.**: Dimension for the middle horizontal strap.
- 60 cm.**: Dimension for the bottom horizontal strap.
- 65 cm.**: Dimension for the vertical strap on the right side.
- 70 cm.**: Dimension for the vertical strap on the left side.
- 2 cm.**: Dimension for the small vertical strap on the right side.
- BRASS**: Material type for the buckles.
- STEEL**: Material type for the straps.

Figure 6 A Set of Multichannel Filters Is Designed to Separate One Mode. Each Channel Is Convolved with the Appropriate Seismogram Trace. Each Set of Nine Filtered Outputs Is Summed to Give an Output Trace Which Is the Estimate of the Separated Mode.

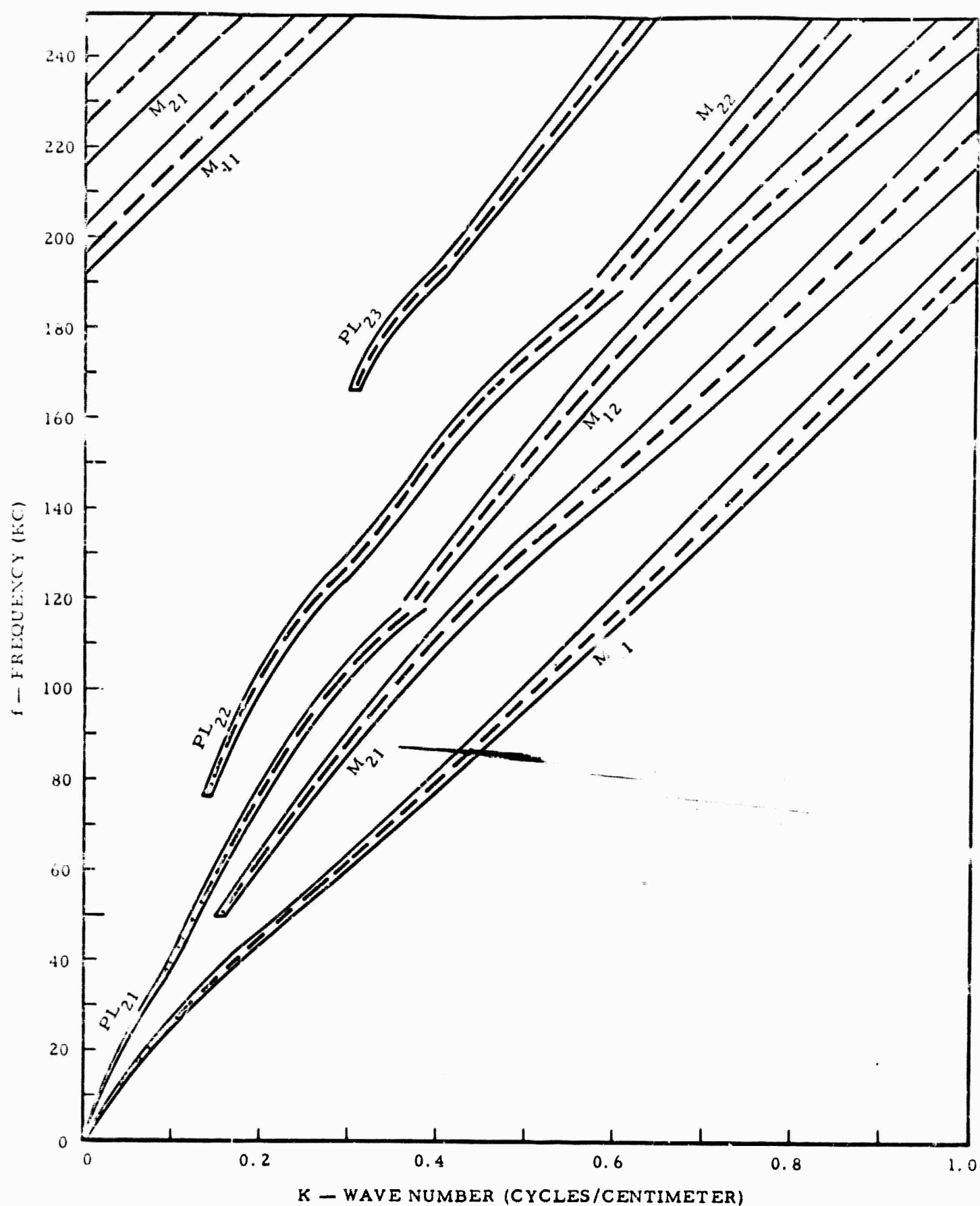


Figure 7 Location of the Theoretical Modes in Frequency and Wave number. The Multichannel Filters Are Designed to Pass or Reject the Band Shown for Each Mode.

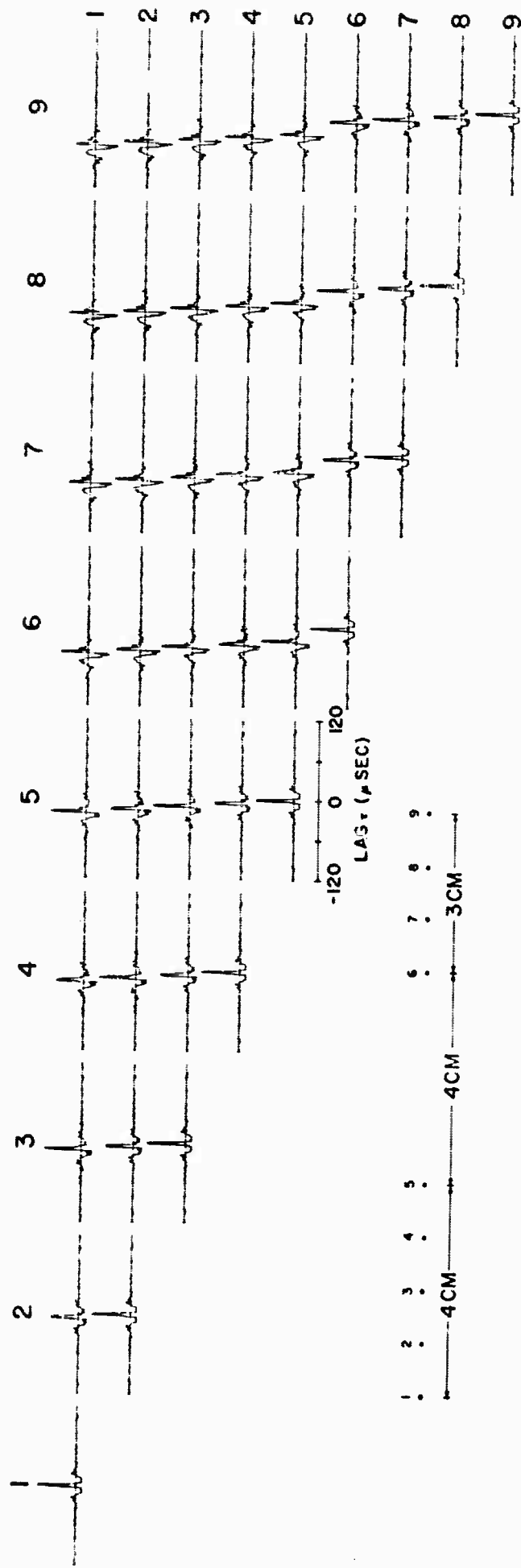


Figure 8 Correlation Functions of the Total Theoretical Seismogram. A Comparison with Figure 9 Shows the Effect of Cross Coupling Between the Individual Modes and the Dominant Rayleigh Mode.

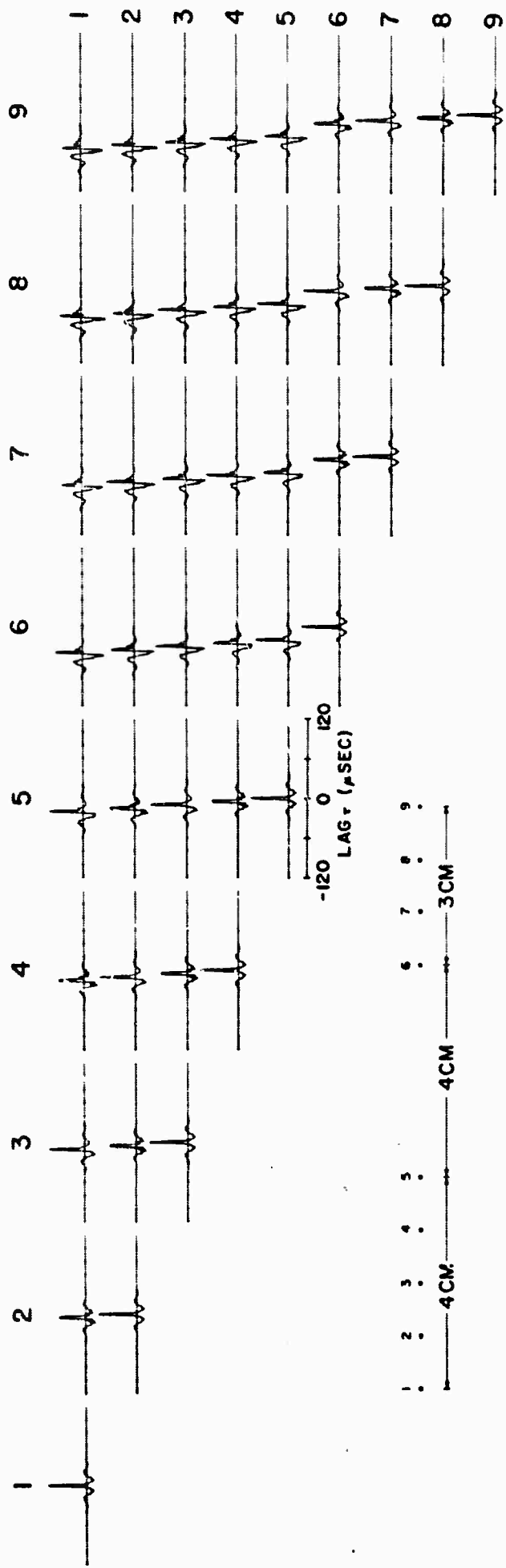


Figure 9 Correlation Functions of the Individual Theoretical Modes Were
Computed and Then Stacked to Eliminate the Effect of Cross Coupling.

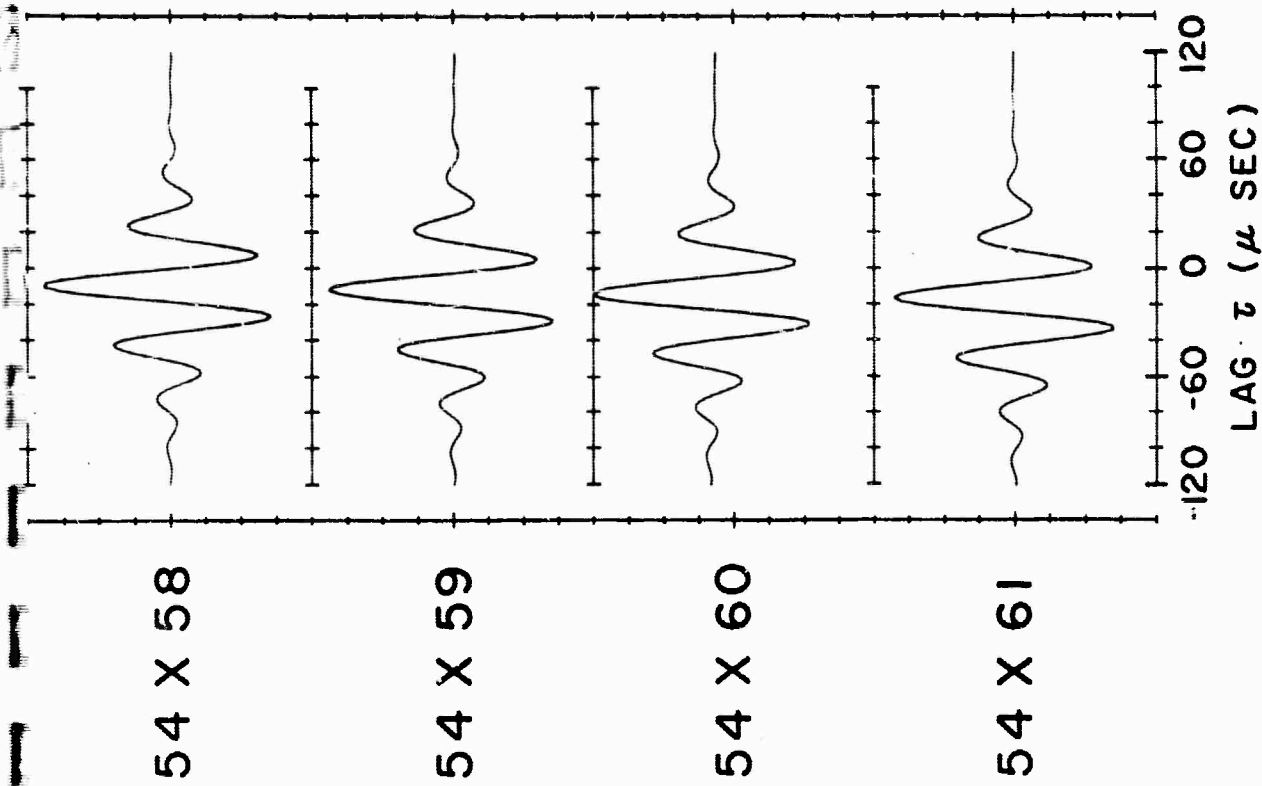
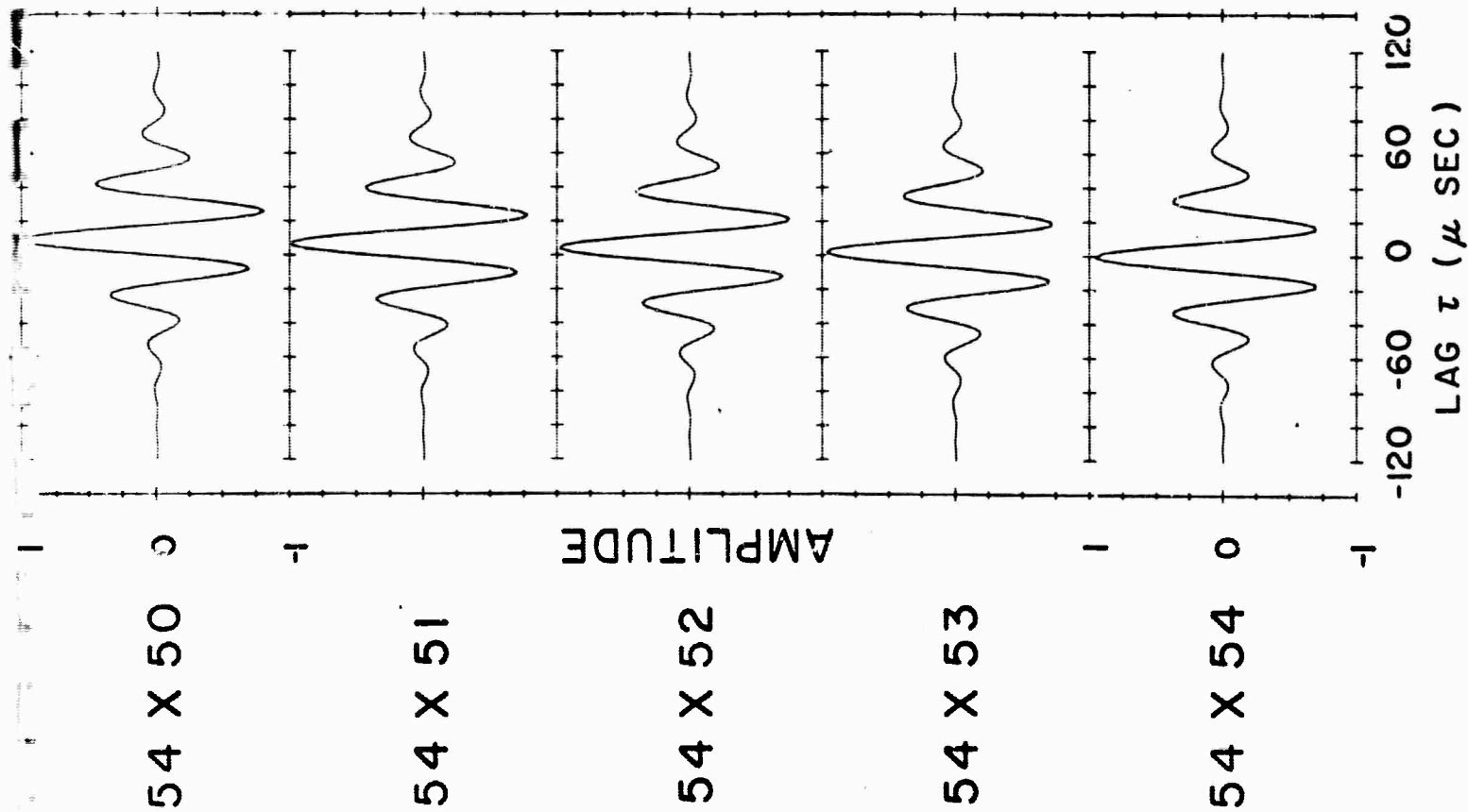


Figure 10

Correlation Functions of the PL₂₁

Mode. This Set of 9 Correlations

Is Used to Form the Right-Hand

Matrix for Multichannel Filter

Design in the Time Domain.

ANNEL

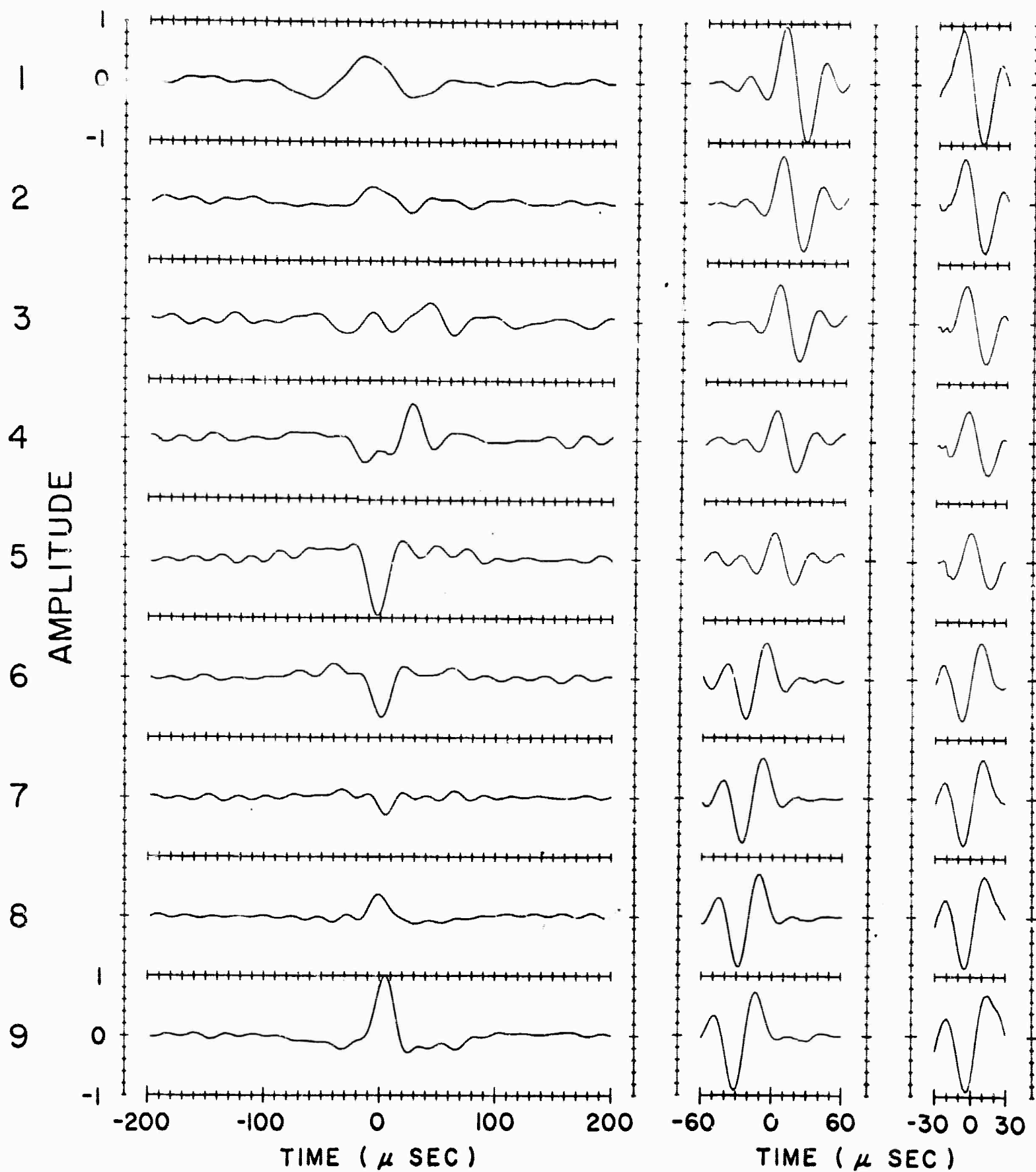


Figure 11 PL_{21} Mode Separation Filters. On the Left Are the 400-Point Filters Designed in the Frequency Domain. In the Center Are the 61-Point Filters Designed in the Time Domain. On the Right Are

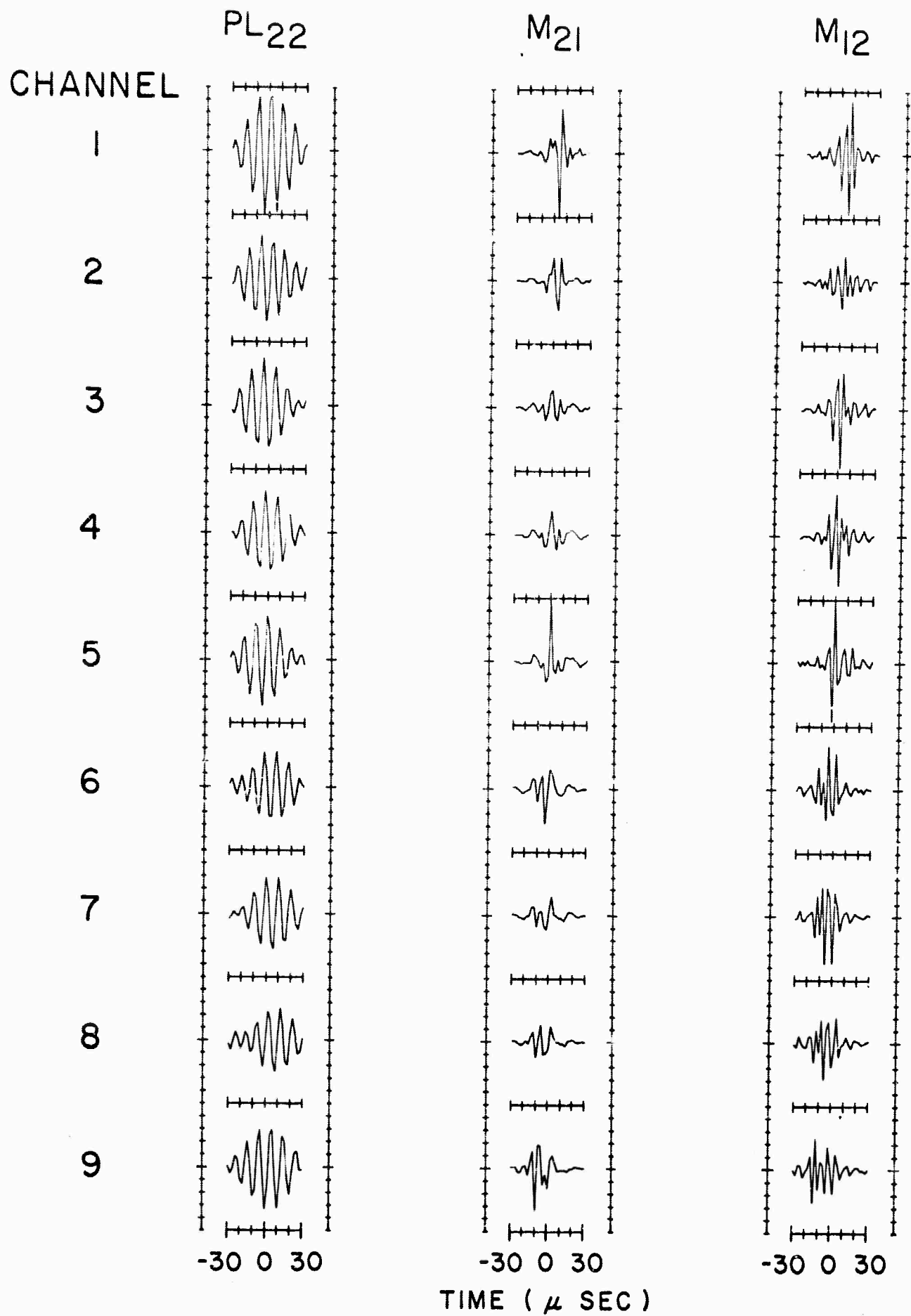


Figure 12 The 9-Channel, 31-Point Filters Designed in the Time Domain to Separate the Modes PL_{22} , M_{21} , and M_{12} .

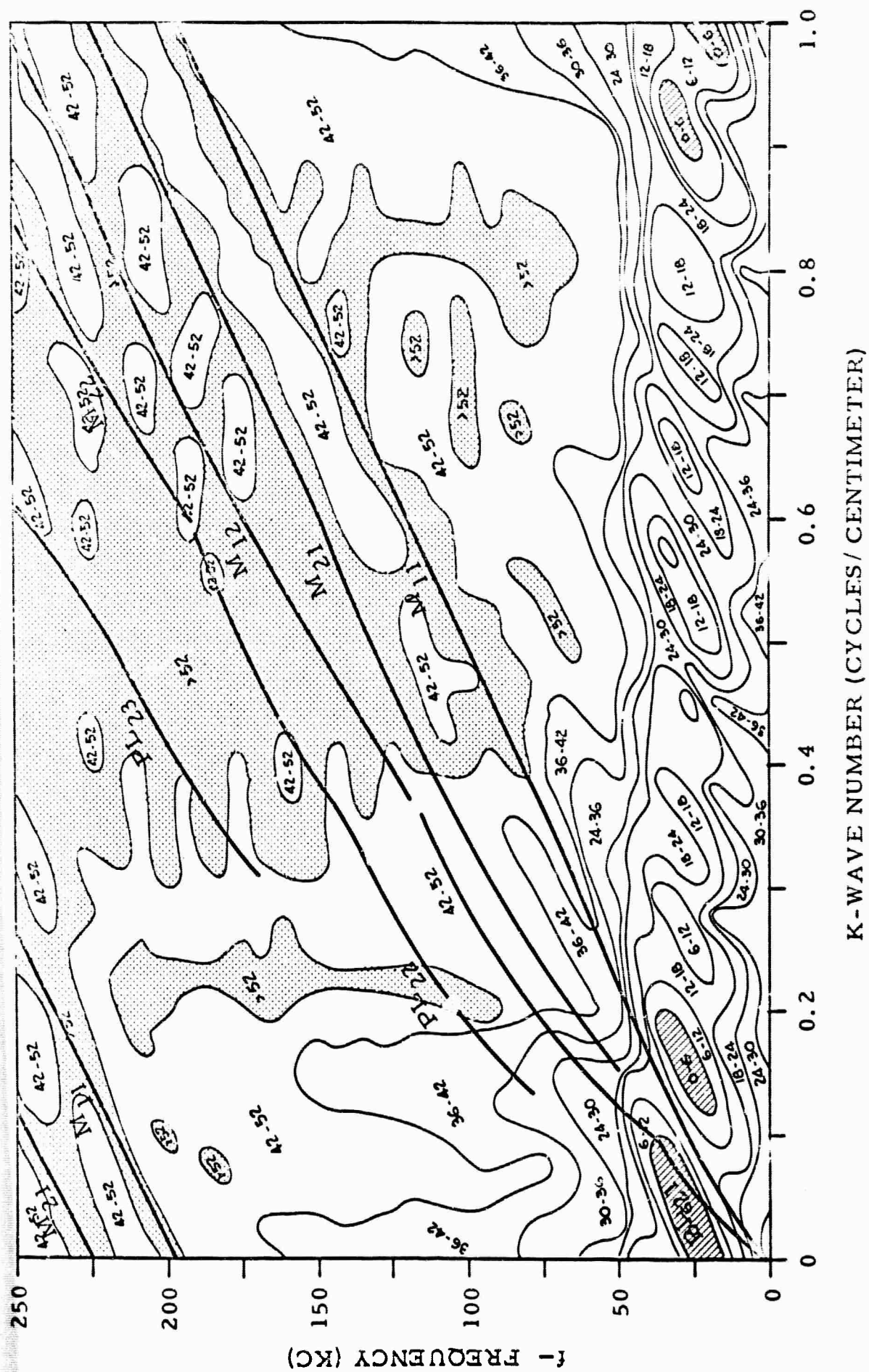


Figure 13 f_k Response of the 9-Channel Mode Separation Filters, PL₂₁
Signal (61-Point Filters Designed in the Time Domain).

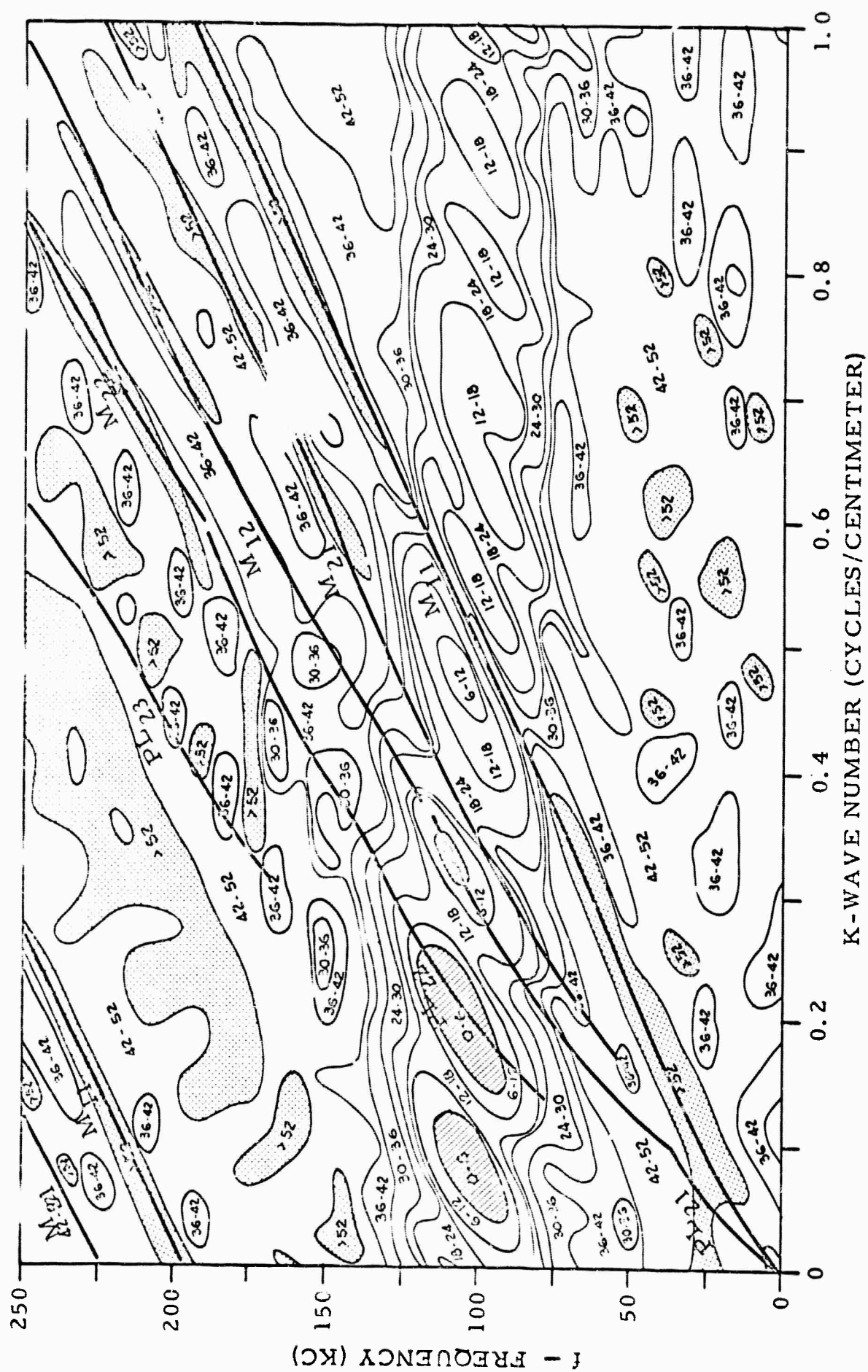


Figure 14 f_k Response of the 9-Channel Mode Separation Filters, PL₂₂
Signal (31-Point Filters Designed in the Time Domain).

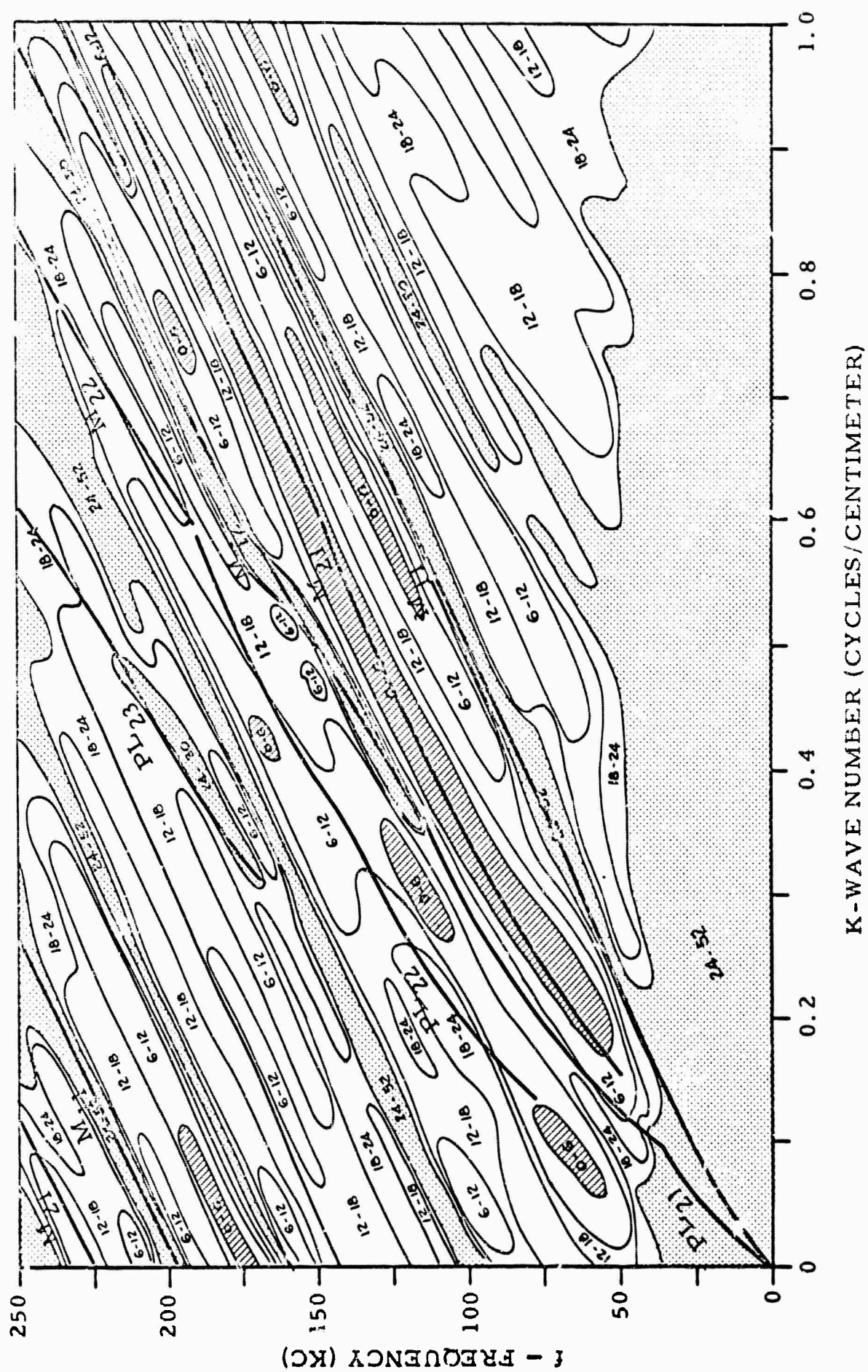
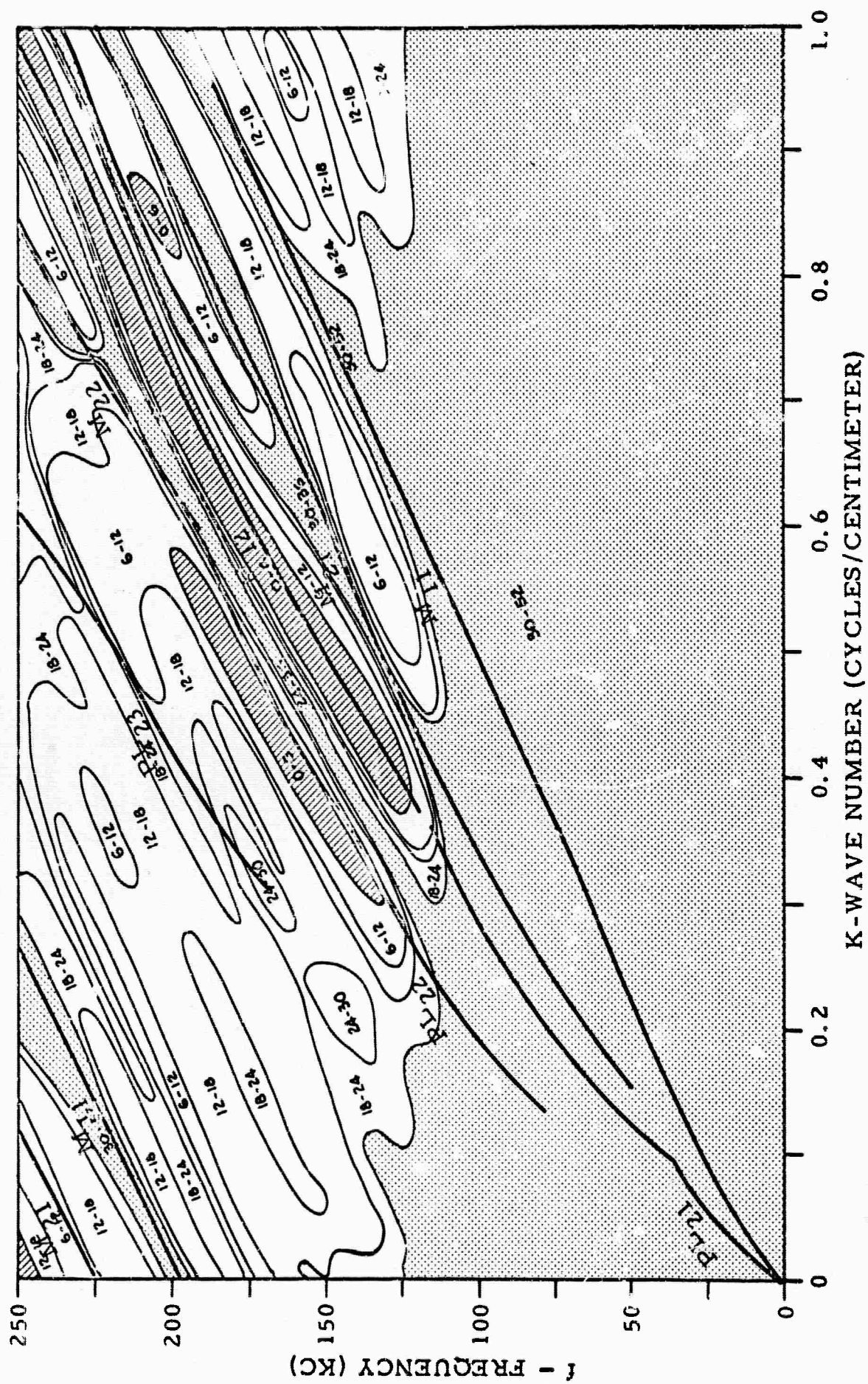
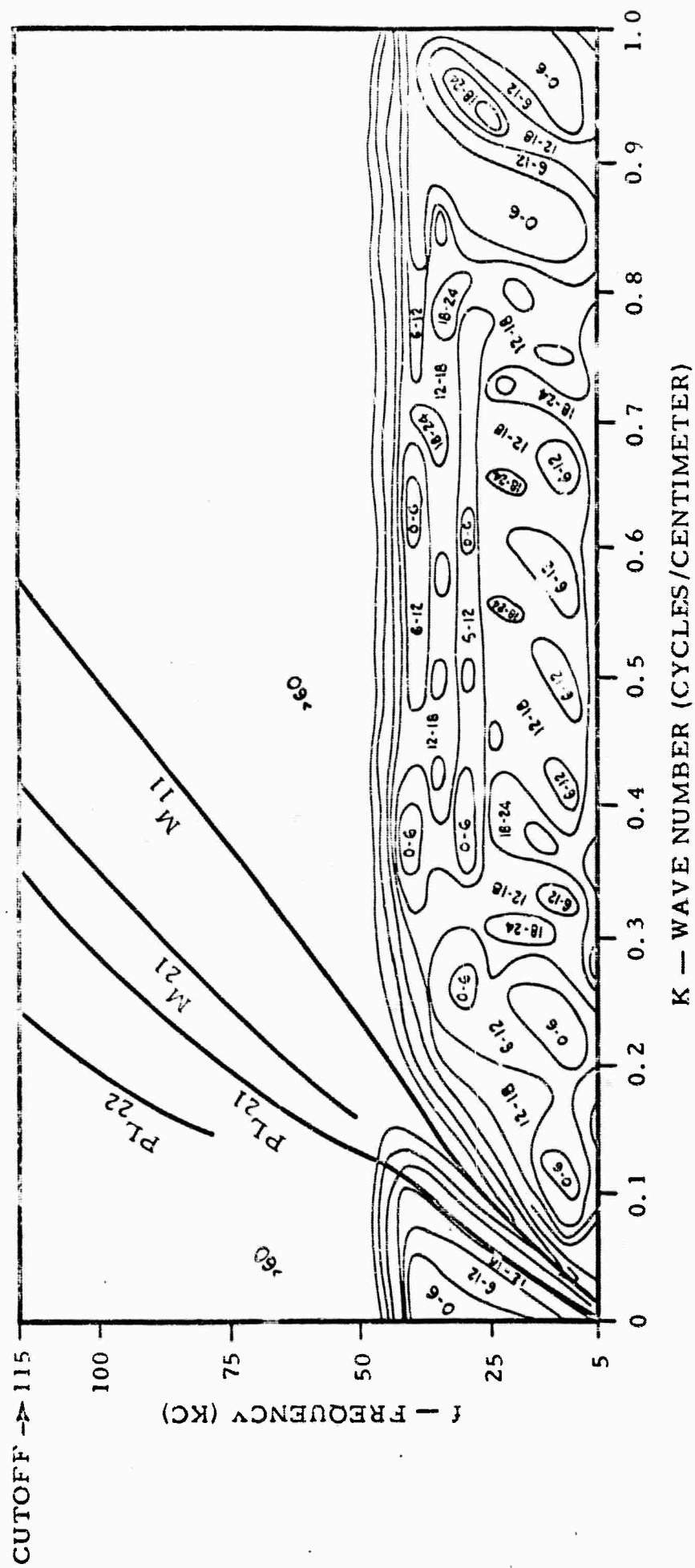


Figure 15 f_k Response of the 9-Channel Mode Separation Filters, M_{21}
Signal (31-Point Filters Designed in the Time Domain).





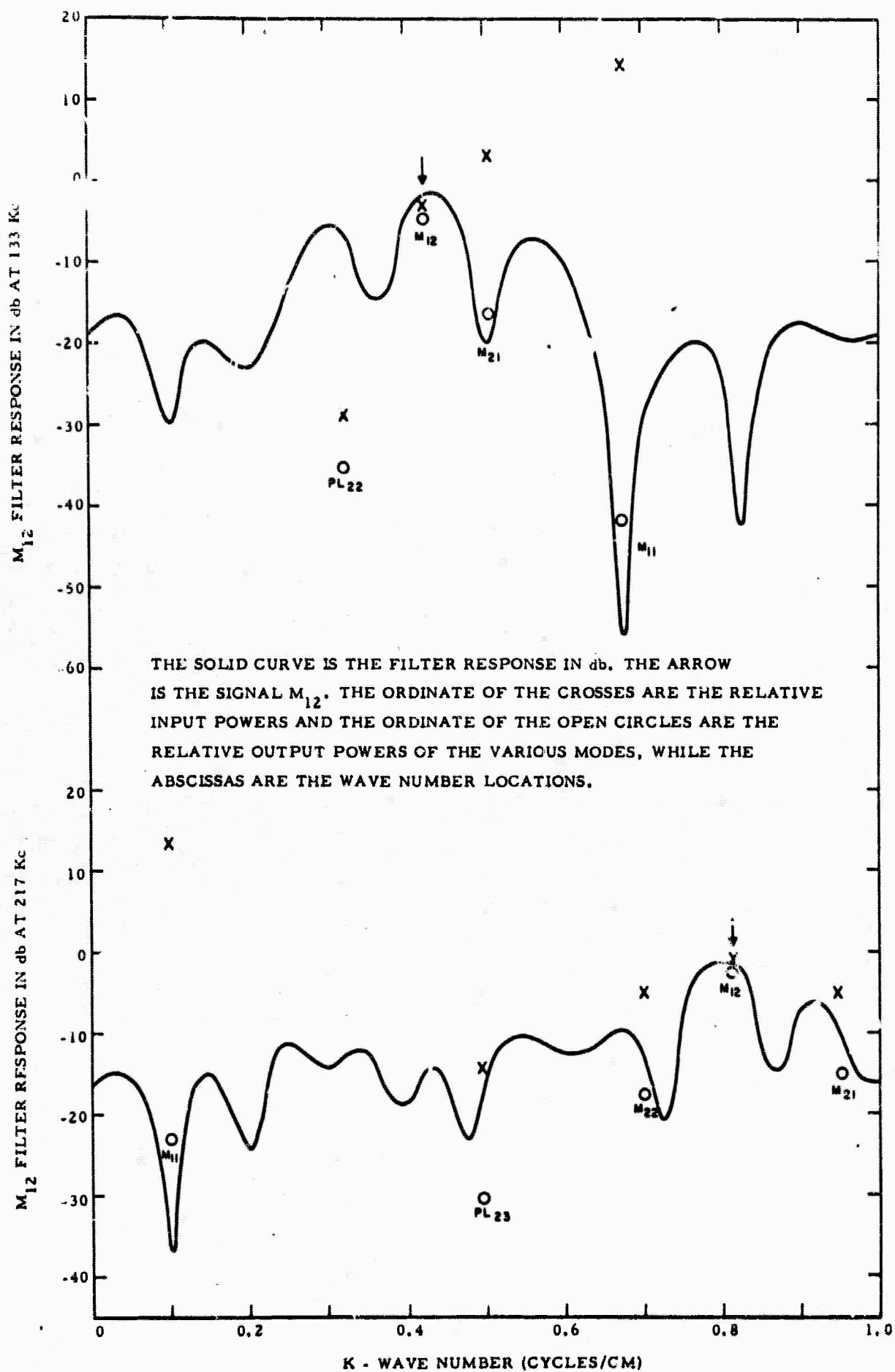


Figure 18 Filter Response and Relative Input and Output Levels of Signal and Noise for M_{12} at Frequencies 133 and 217 kc.

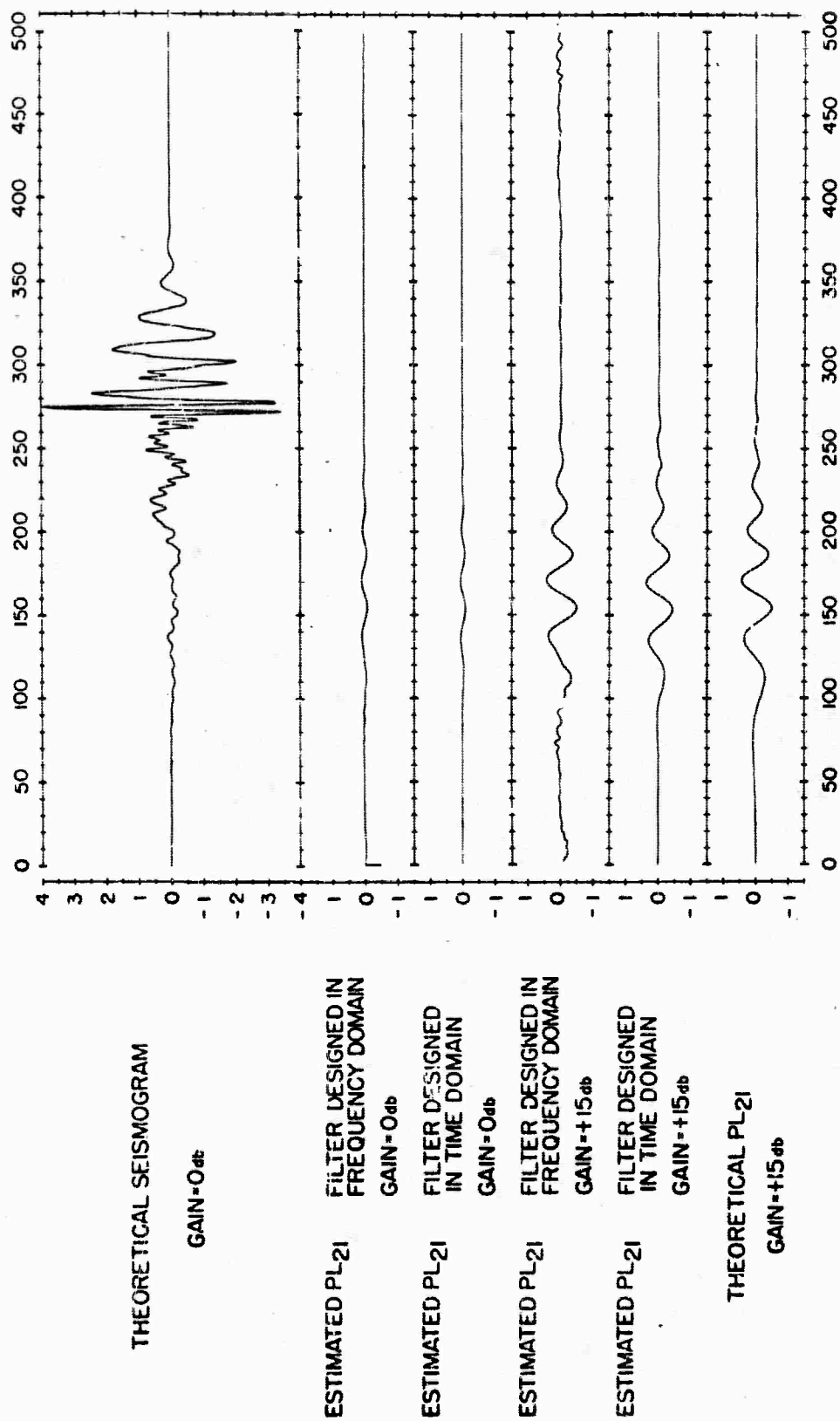


Figure 19 PL₂₁ Mode Separation Results from the Theoretical Seismograms.

• The Output Location Is at 54 cm. Time in μ Sec.

THEORETICAL SEISMOGRAM

GAIN=0db

ESTIMATED PL₂₂ FILTER DESIGNED
IN TIME DOMAIN

GAIN=0db

ESTIMATED PL₂₂ FILTER DESIGNED
IN TIME DOMAIN

GAIN=+15db

THEORETICAL PL₂₂

GAIN=+15db

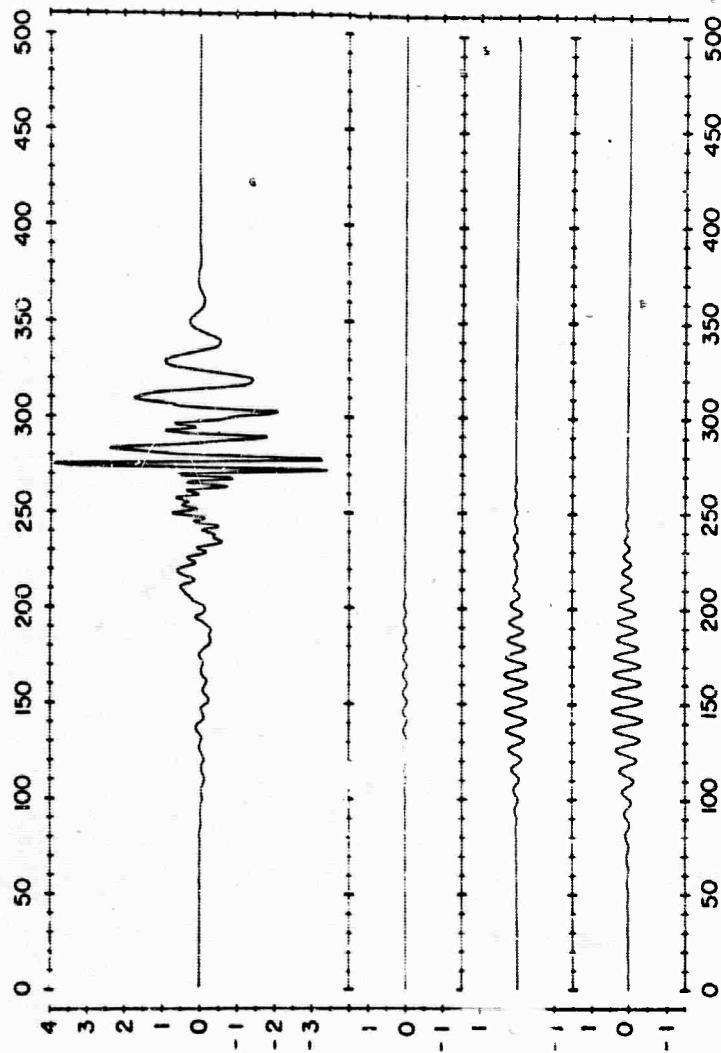


Figure 20 PL₂₂ Mode Separation Results from the Theoretical Seismograms.

The Output Location Is at 54 cm. Time in μ Sec.

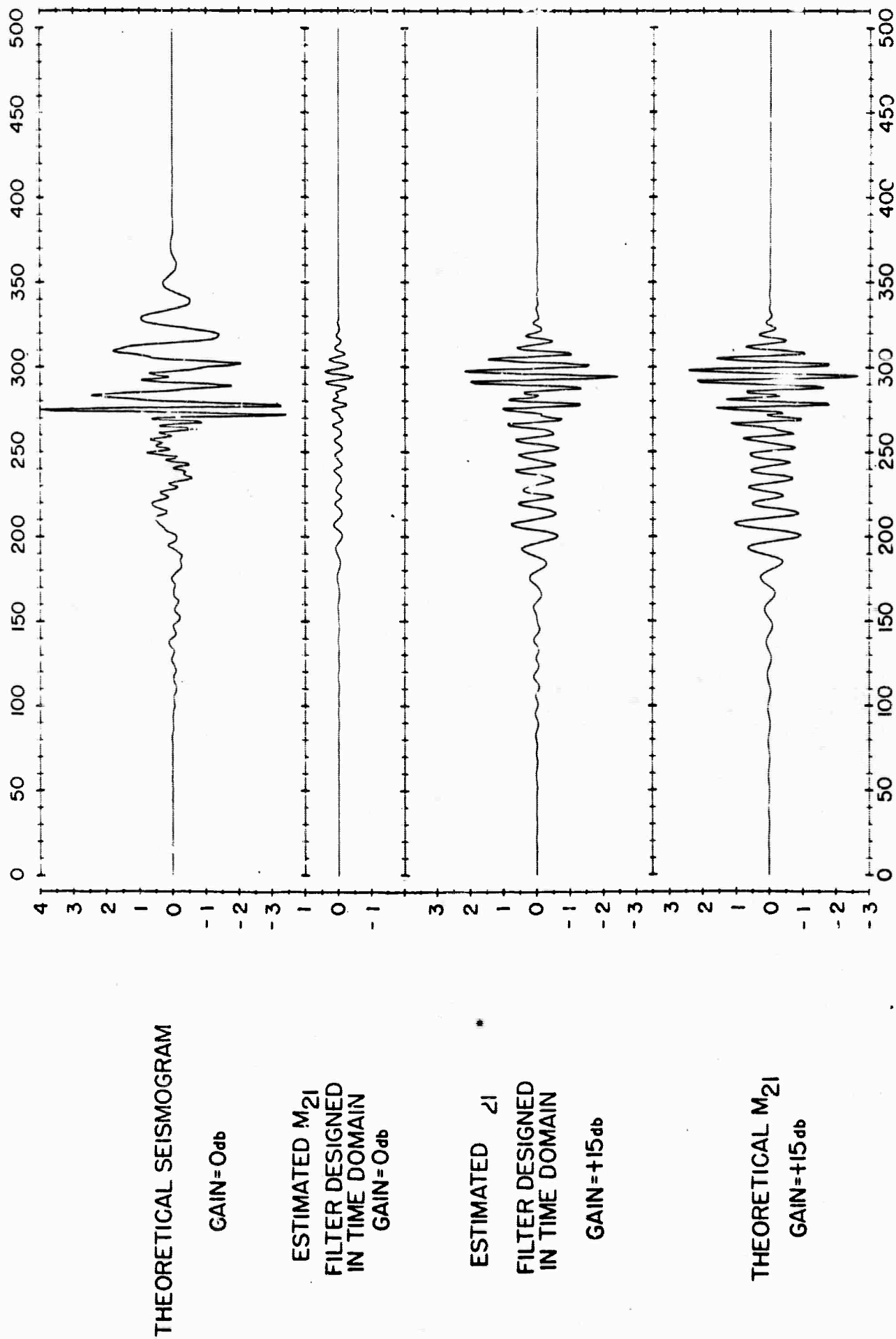


Figure 21 M_{21} Mode Separation Results from the Theoretical Seismograms. The
Output Location Is at 54 cm. Time in μ Sec.

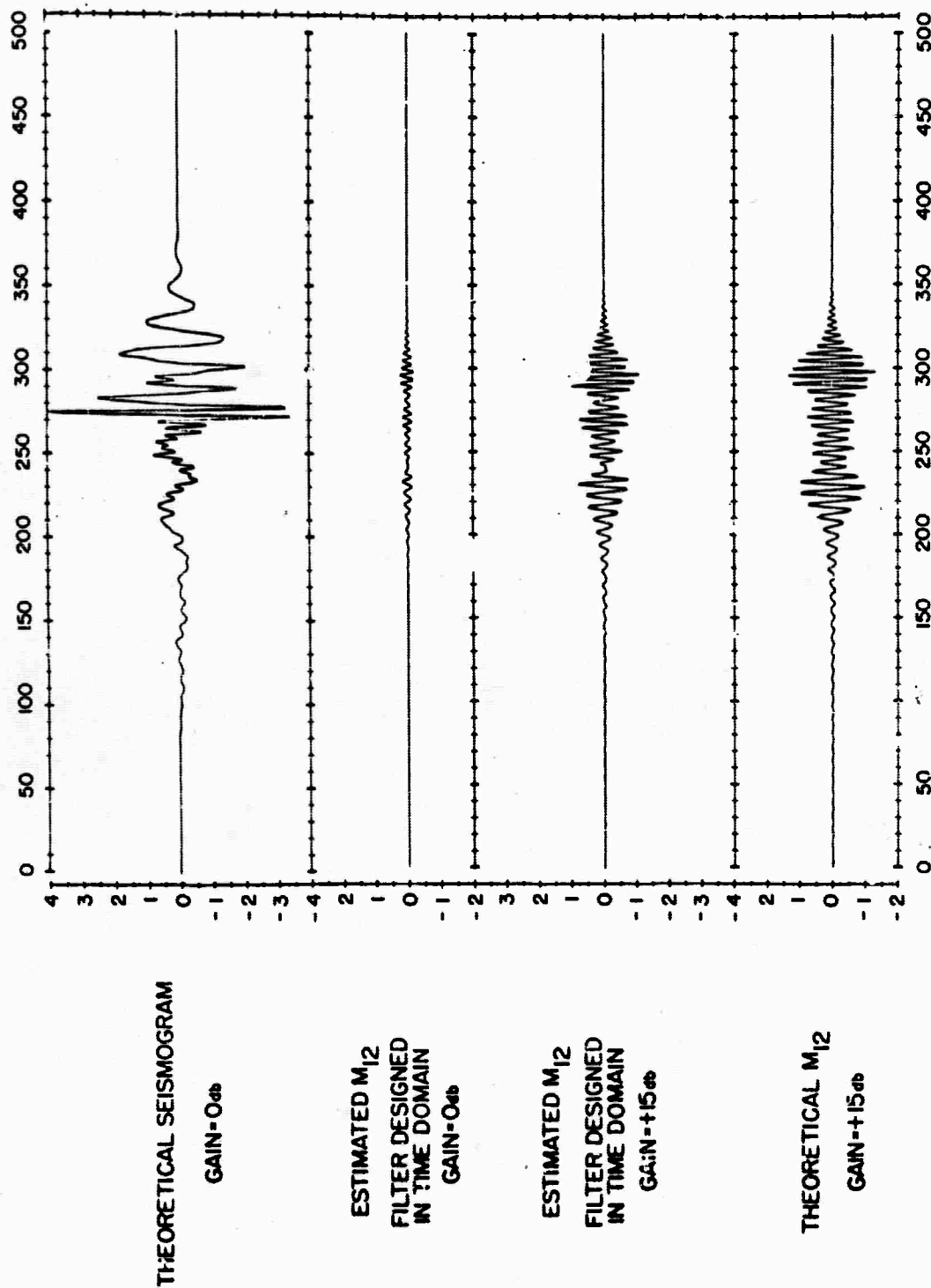


Figure 22 M_{12} Mode Separation Results for the Theoretical Seismograms.
The Output Location Is at 54 cm. Time in μ Sec.

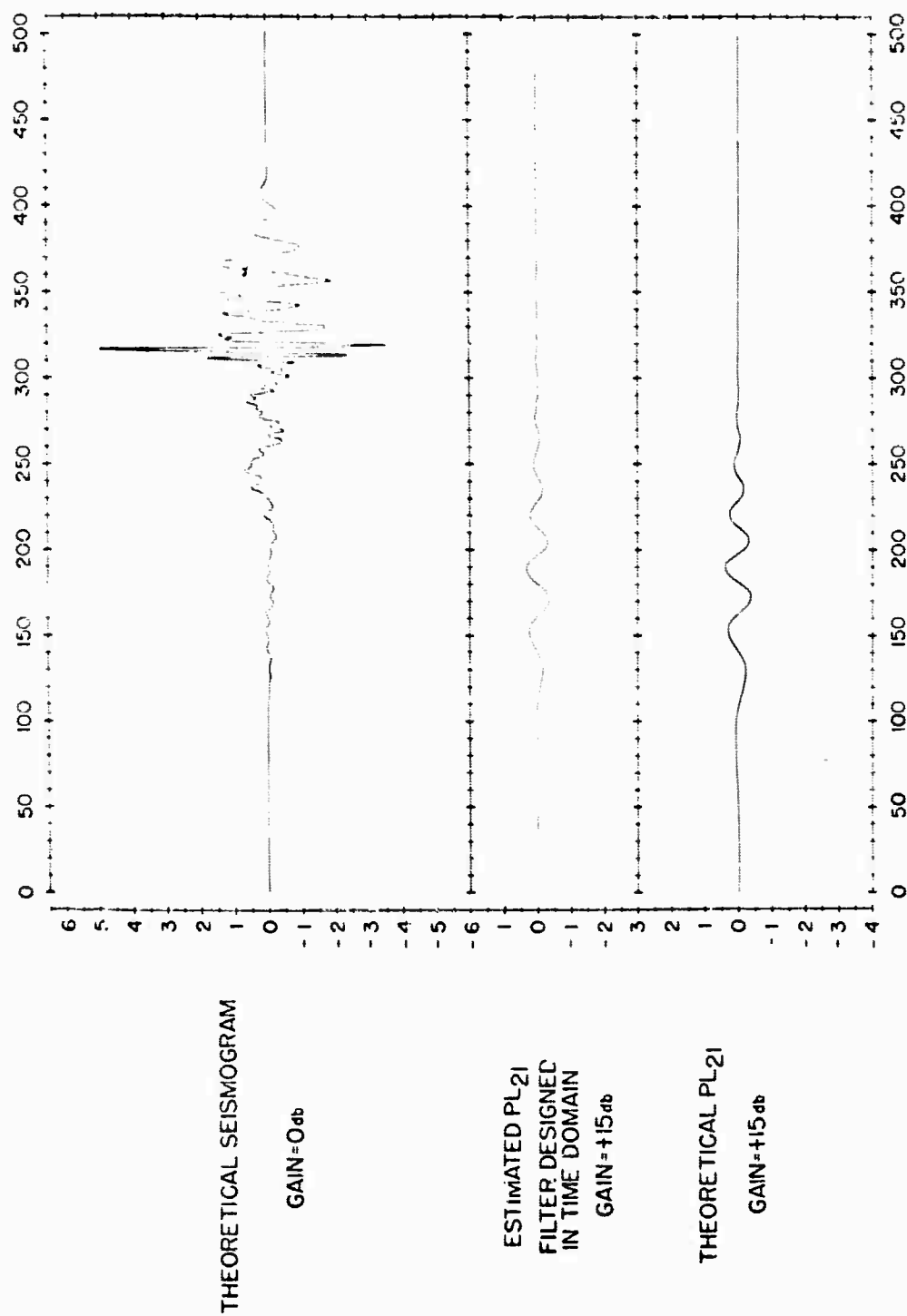


Figure 23 PL₂₁ Mode Separation Results from the Theoretical Seismograms.
The Output Location Is at 62 cm. Time in μ Sec.

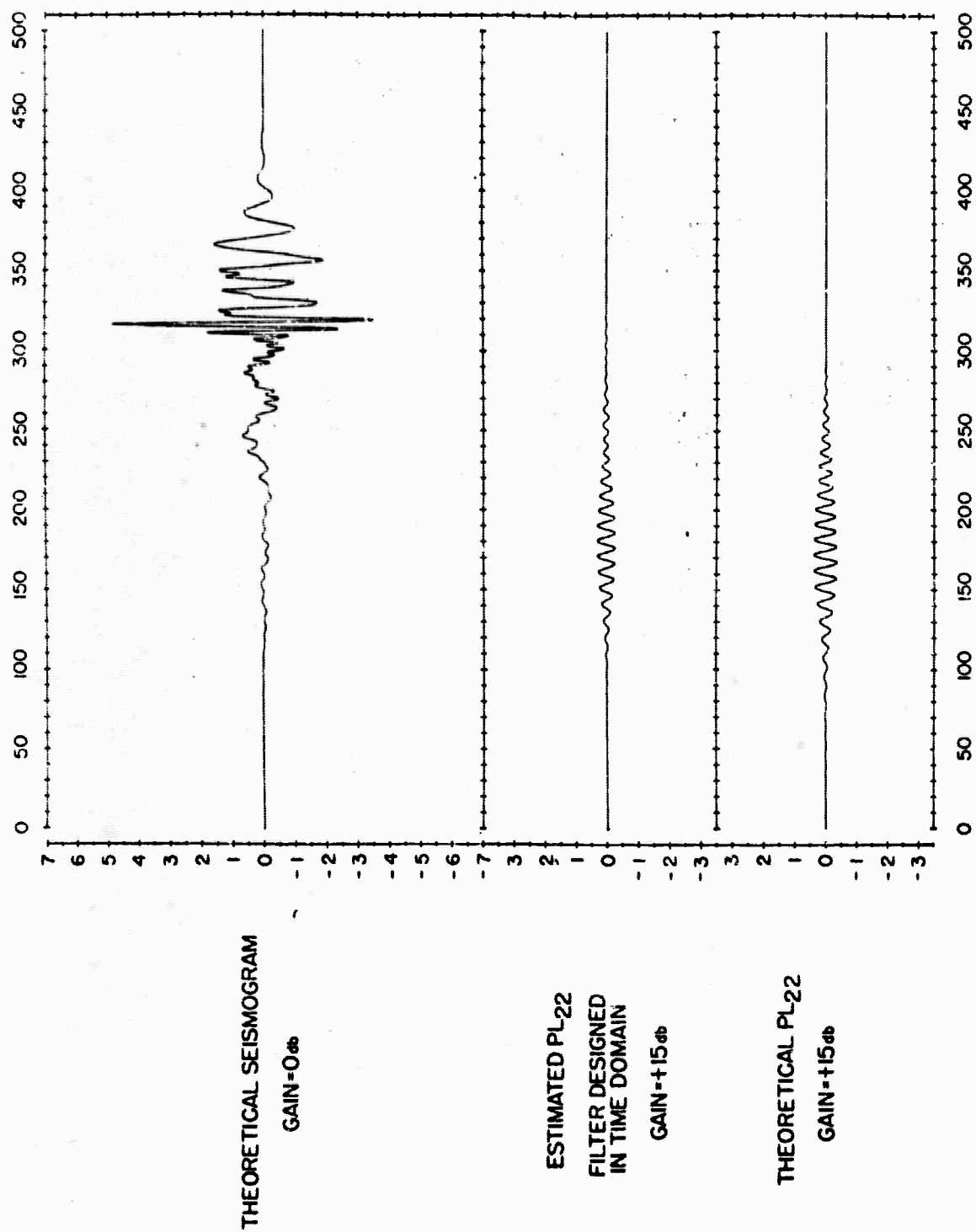


Figure 24 PL₂₂ Mode Separation Results from the Theoretical Seismograms.
The Output Location Is at 62 cm. Time in μ Sec.

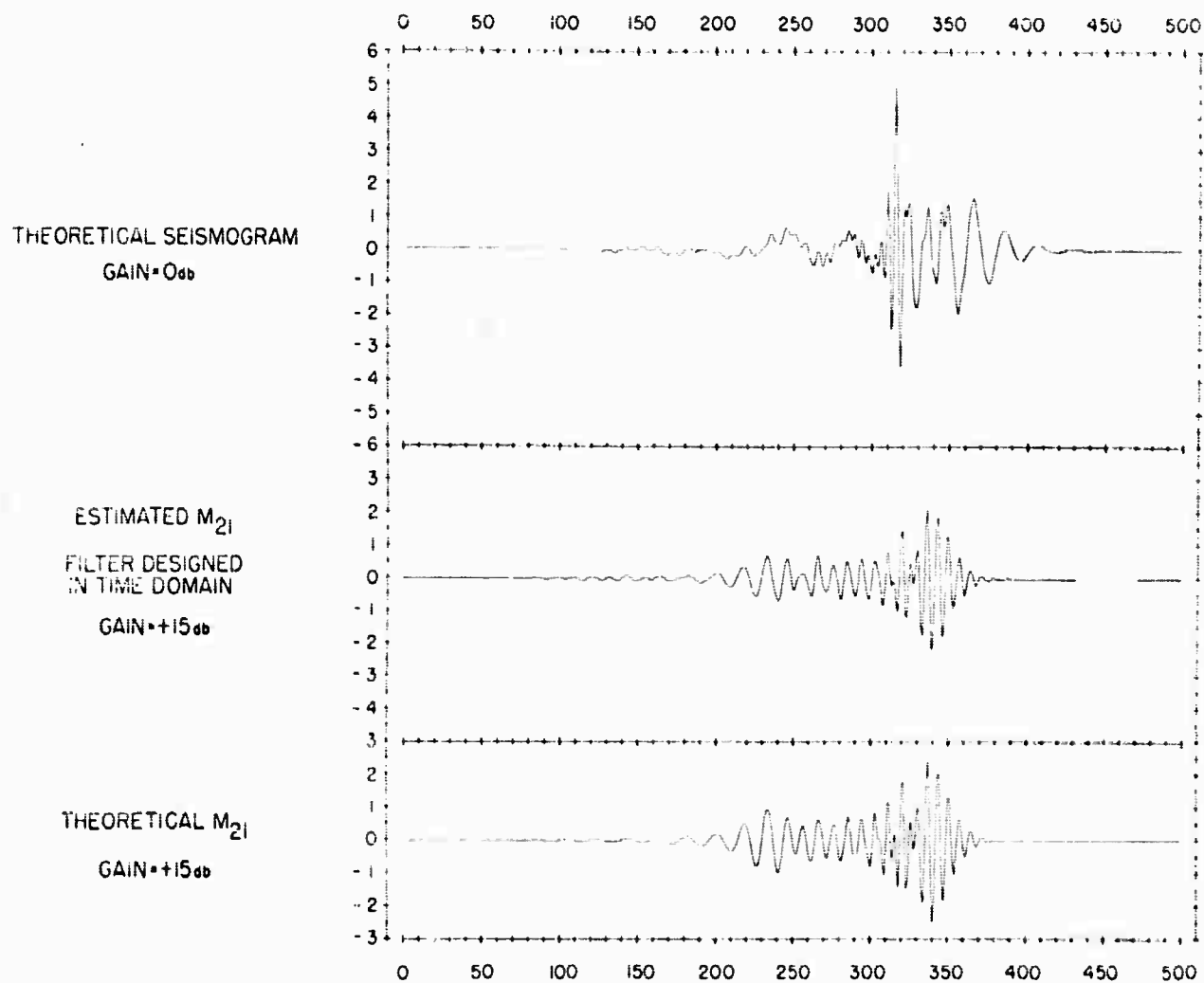


Figure 25 M_{21} Mode Separation Results from the Theoretical Seismograms.
The Output Location Is at 62 cm. Time in μ Sec.

THEORETICAL SEISMOGRAM

GAIN=0db

ESTIMATED M_{12}
FILTER DESIGNED
IN TIME DOMAIN

GAIN=+15db

THEORETICAL M_{12}

GAIN=+15db

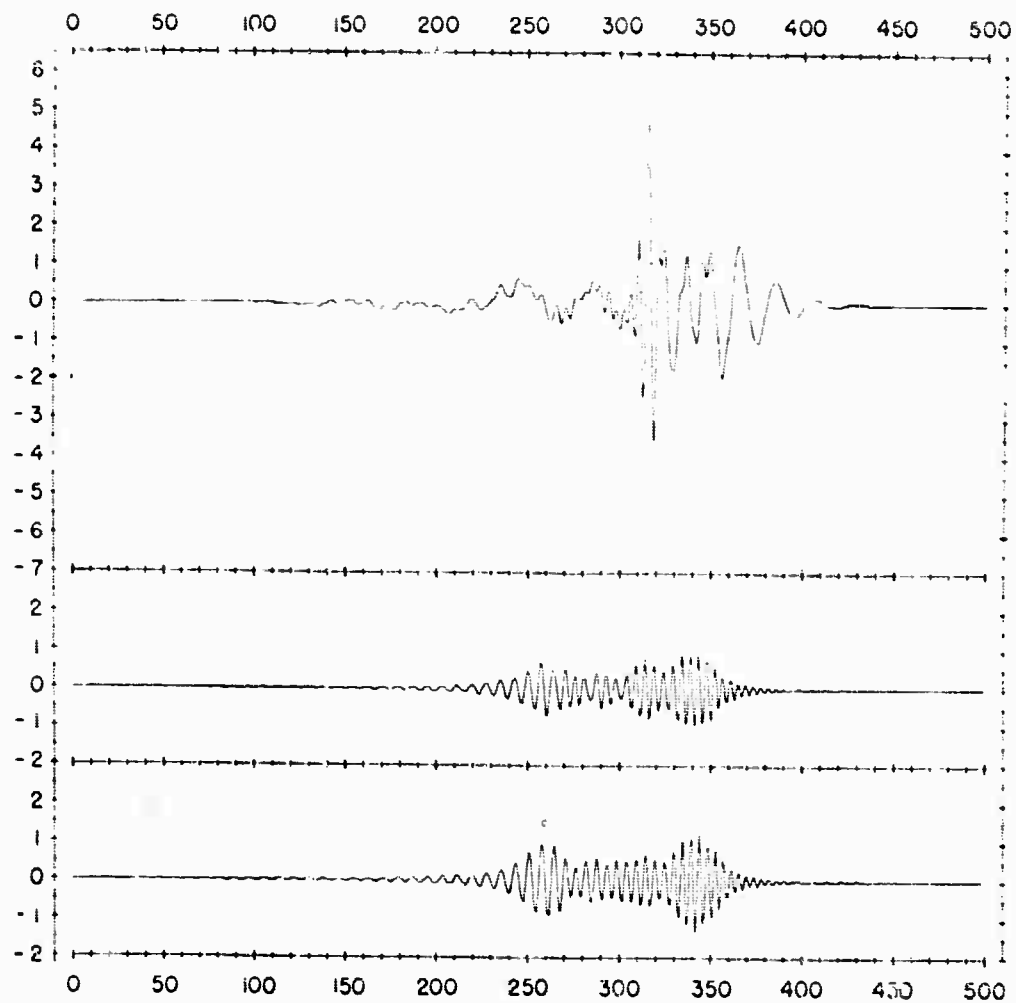


Figure 26

M_{12} Mode Separation Results from the Theoretical Seismograms.
The Output Location Is at 62 cm. Time in μ Sec.

EXPERIMENTAL SEISMOGRAM

GAIN = 0db

ESTIMATED PL_{22}

GAIN = +12db

ESTIMATED M_{21}

GAIN = +12db

ESTIMATED M_{12}

GAIN = +12db

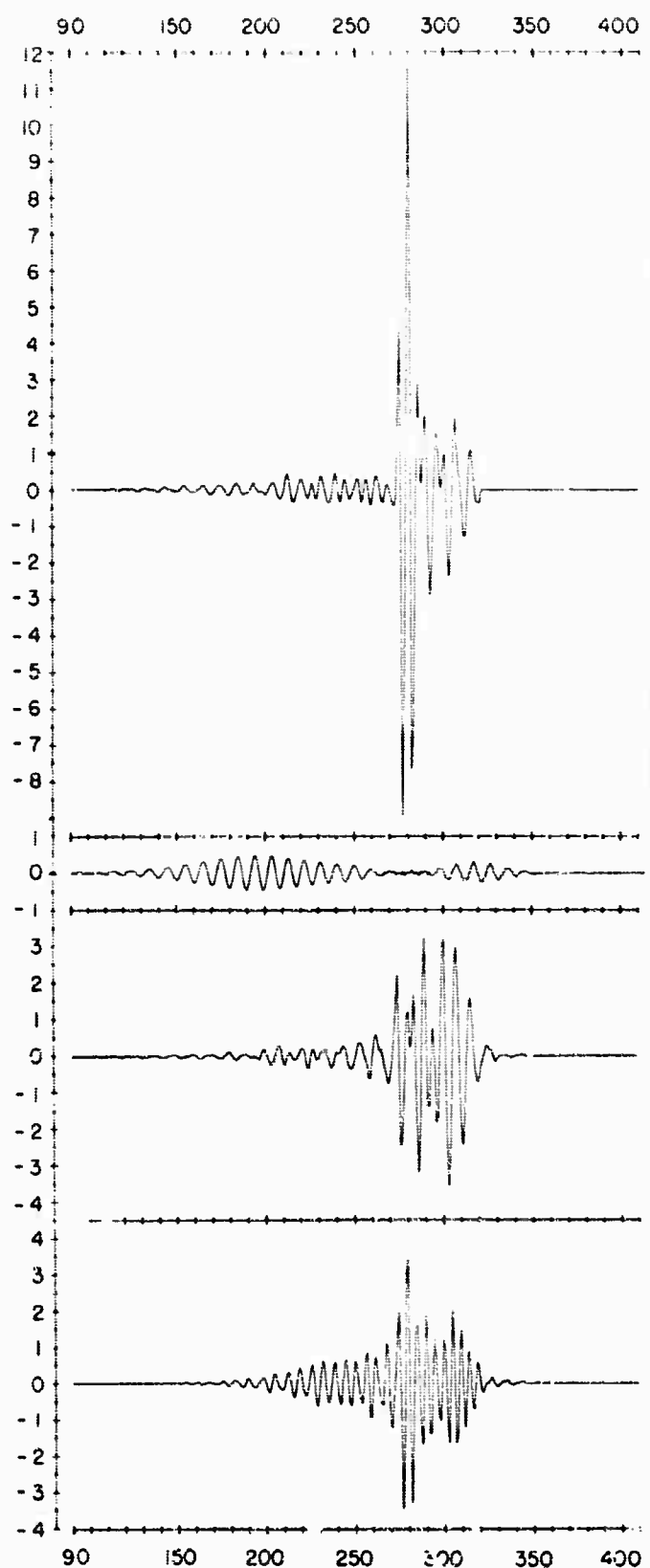


Figure 27 PL_{22} , M_{21} and M_{12} Mode Separation Results from the Experimental Seismograms Using the 31-Point Filters Designed in the Time Domain. The Output Location Is at 54 cm. Time in μ Sec.

EXPERIMENTAL SEISMOGRAM

GAIN = 0db

ESTIMATED PL_{22}

GAIN = +12db

ESTIMATED M_{21}

GAIN = +12db

ESTIMATED M_{12}

GAIN = +12db

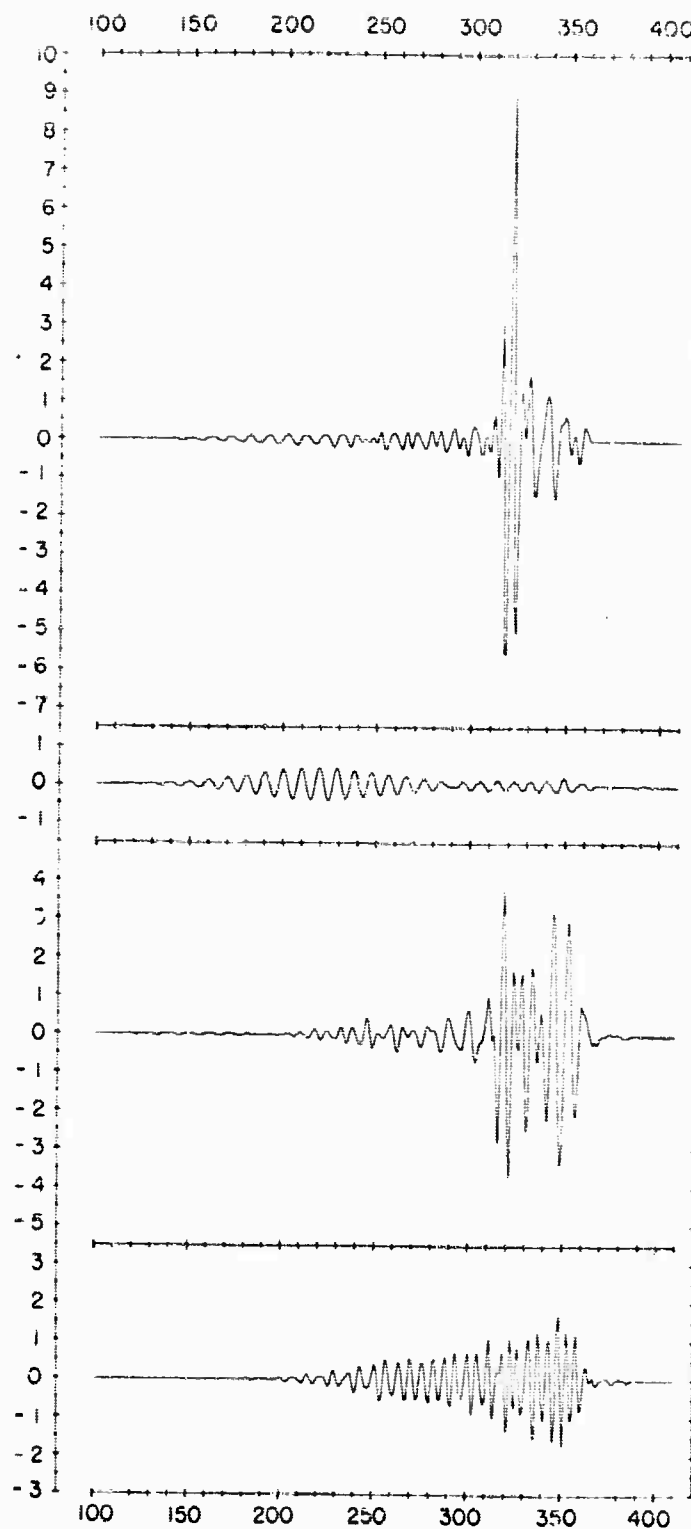


Figure 28

PL_{22} , M_{21} and M_{12} Mode Separation Results from the Experimental Seismograms Using the 31-Point Filters Designed in the Time Domain. The Output Location Is at 62 cm. Time in μ Sec.

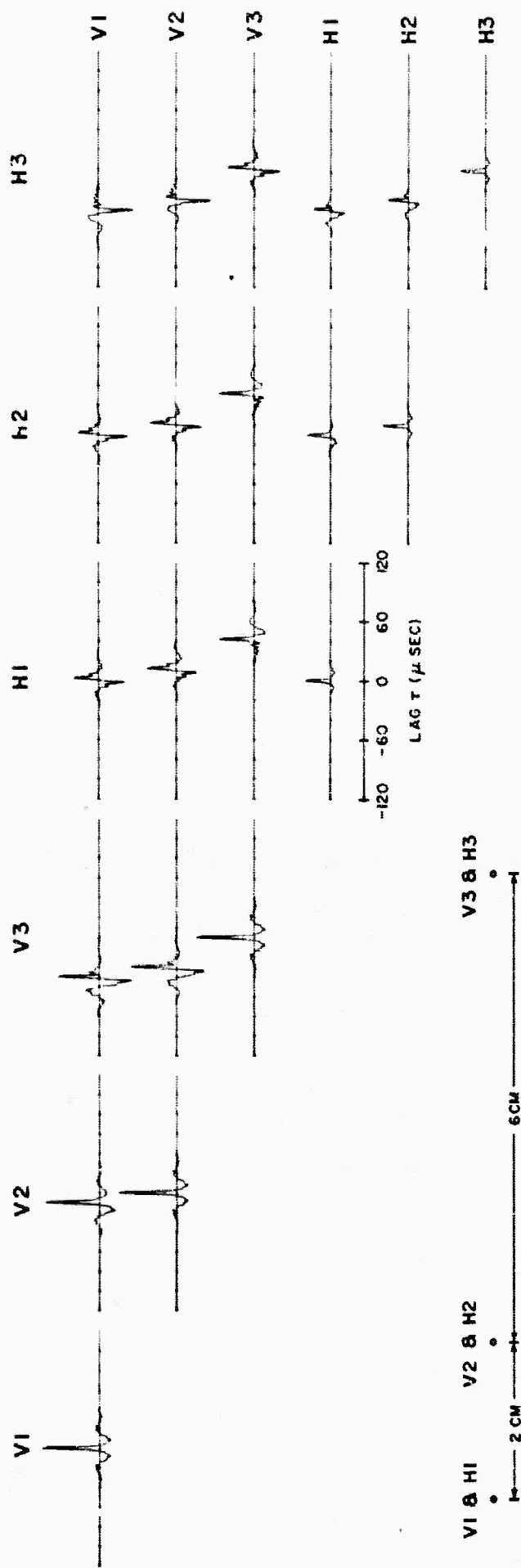


Figure 29 Correlation Functions to Form the Signal Plus Noise Matrix for Multichannel Filter Design in the Time Domain. The 6 Channels Are the Verticals and Horizontals at Three Spatial Locations.

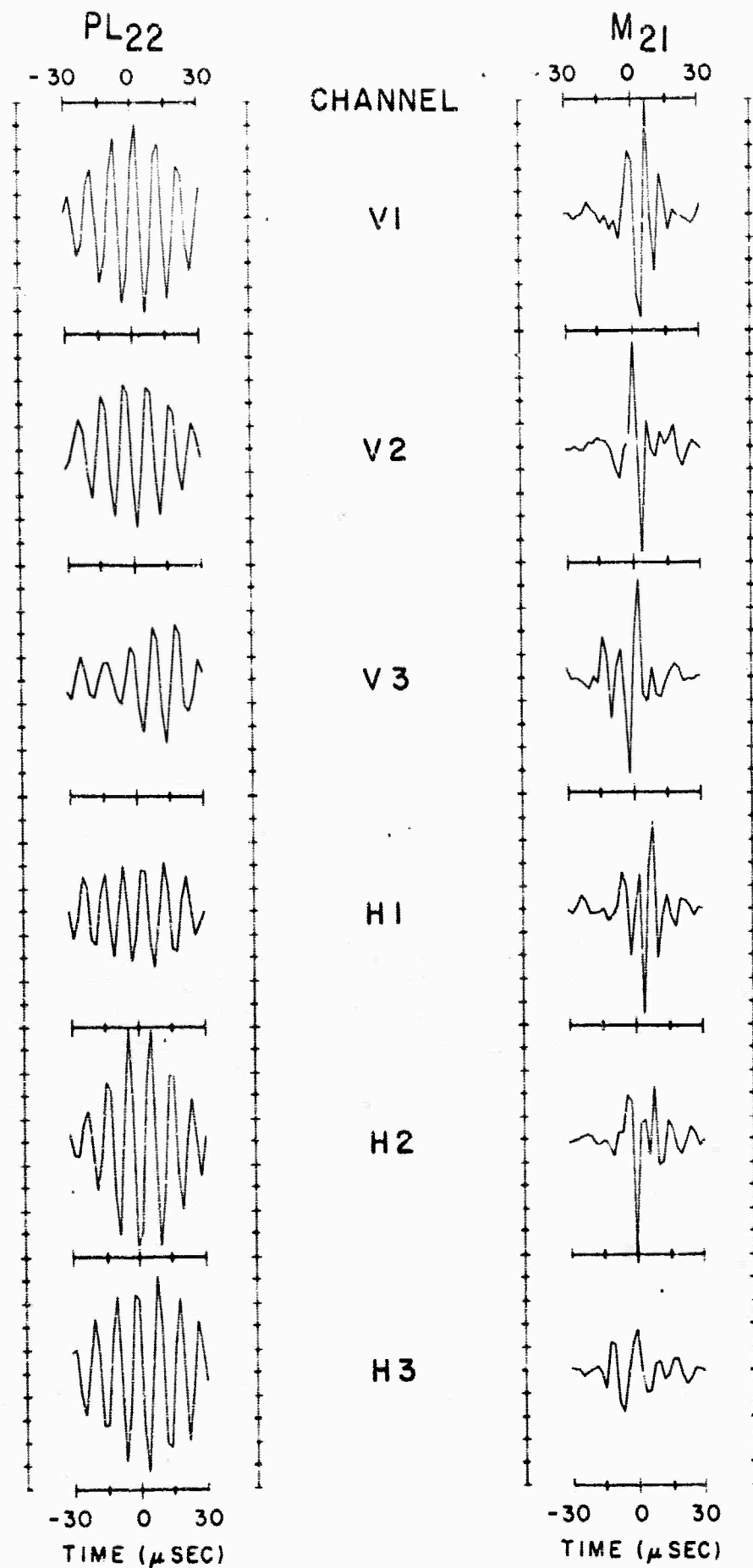


Figure 30 The 6-Channel, 31-Point Filters Designed in the Time Domain to Separate the PL_{22} and M_{21} Modes.

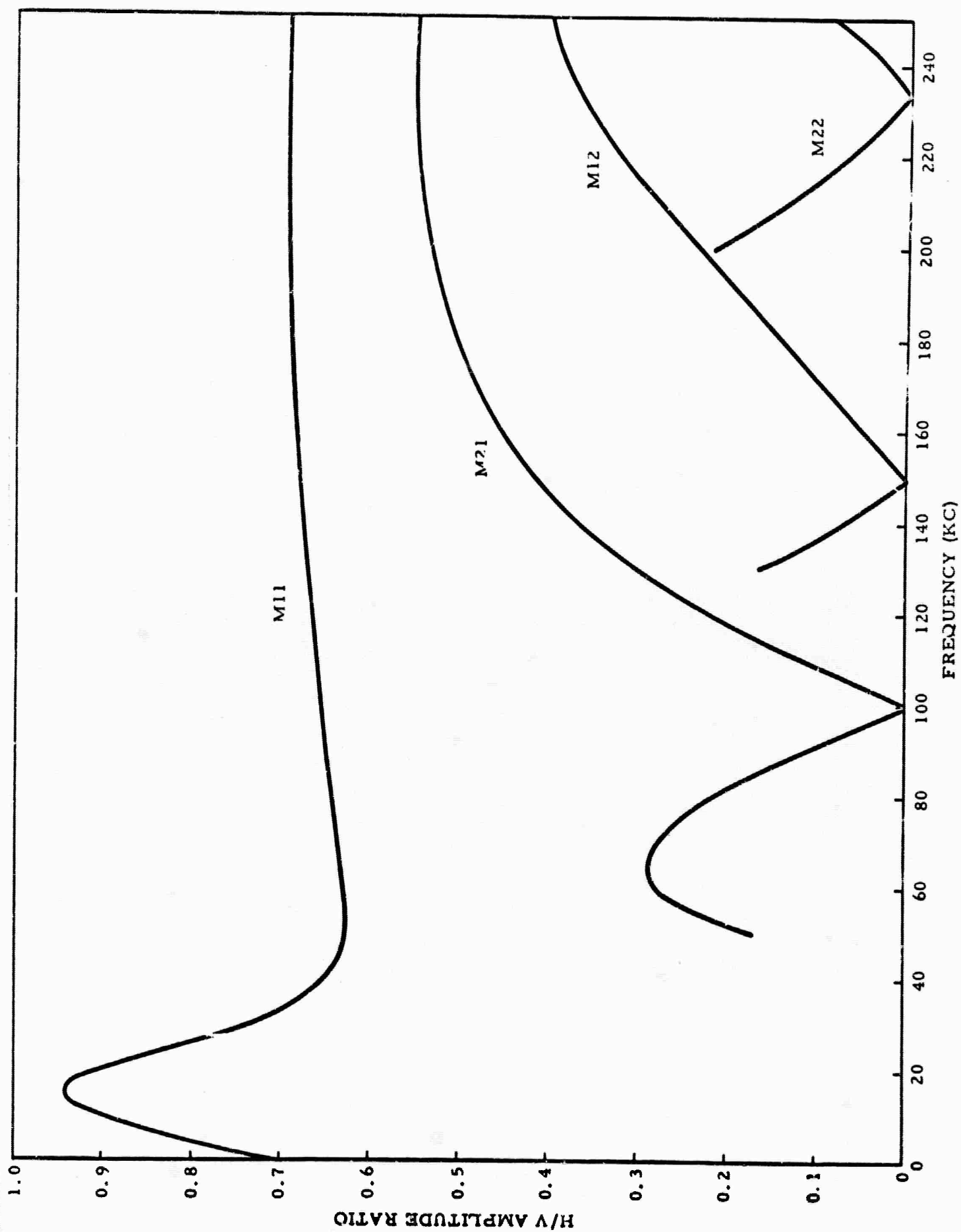


Figure 31 Horizontal/Vertical Amplitude Ratios of the Normal Modes.

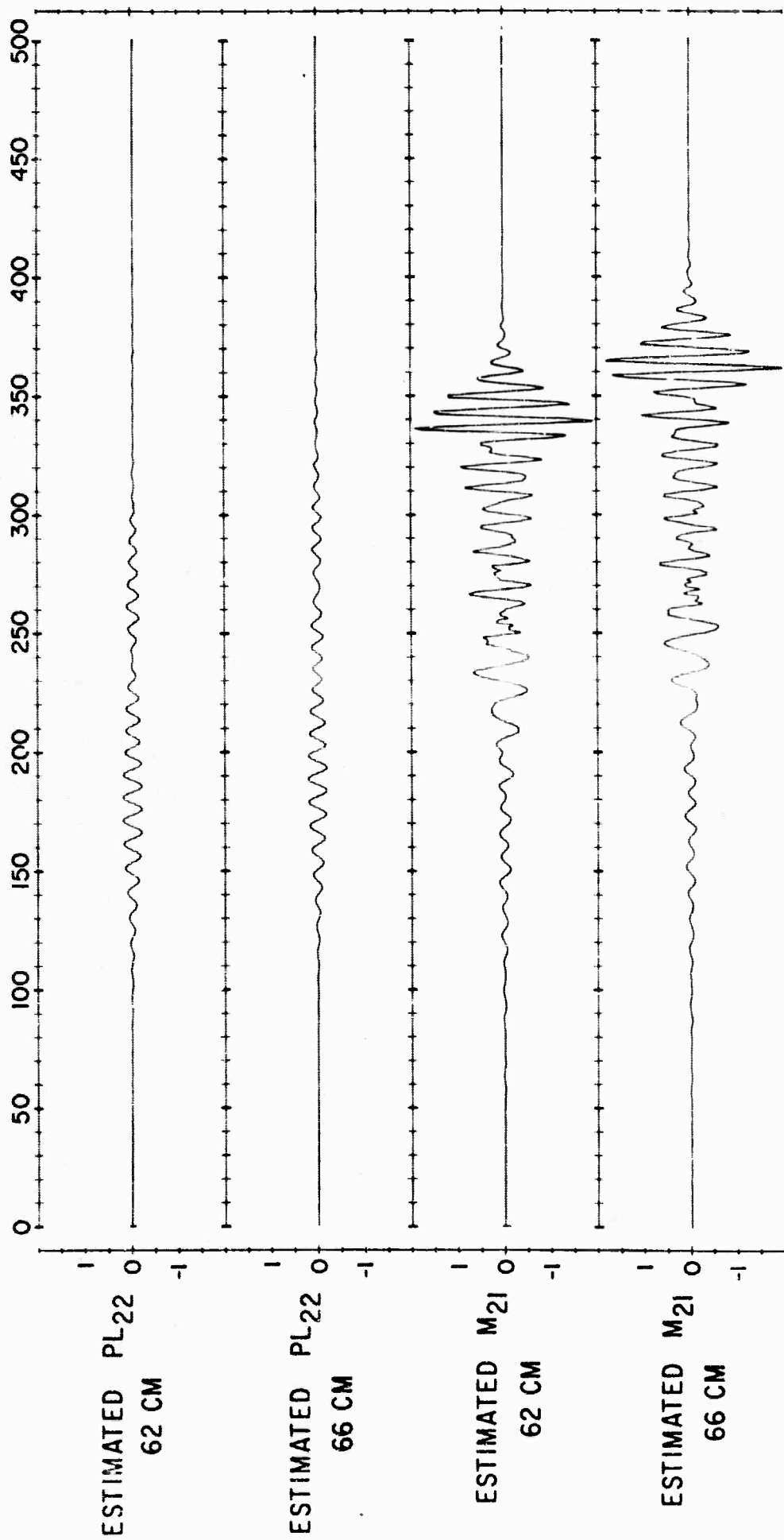


Figure 32 PL₂₂ and M₂₁ Mode Separation Results from the Theoretical Seismograms Using the 6-Channel, 31-Point Filters.

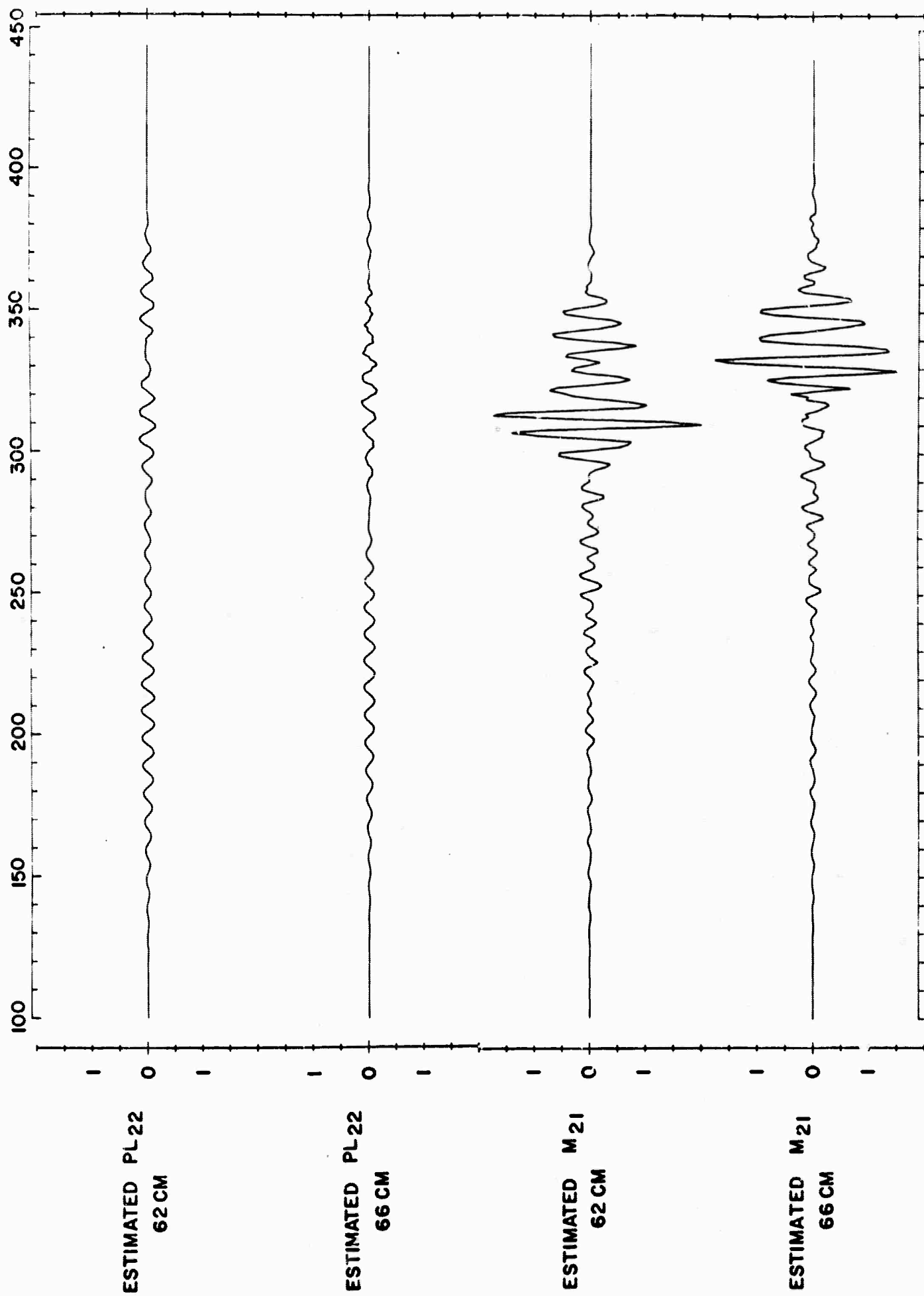


Figure 33 PL_{22} and M_{21} Mode Separation Results from the Experimental Seismograms Using the 6-Channel, 31-Point Filters.

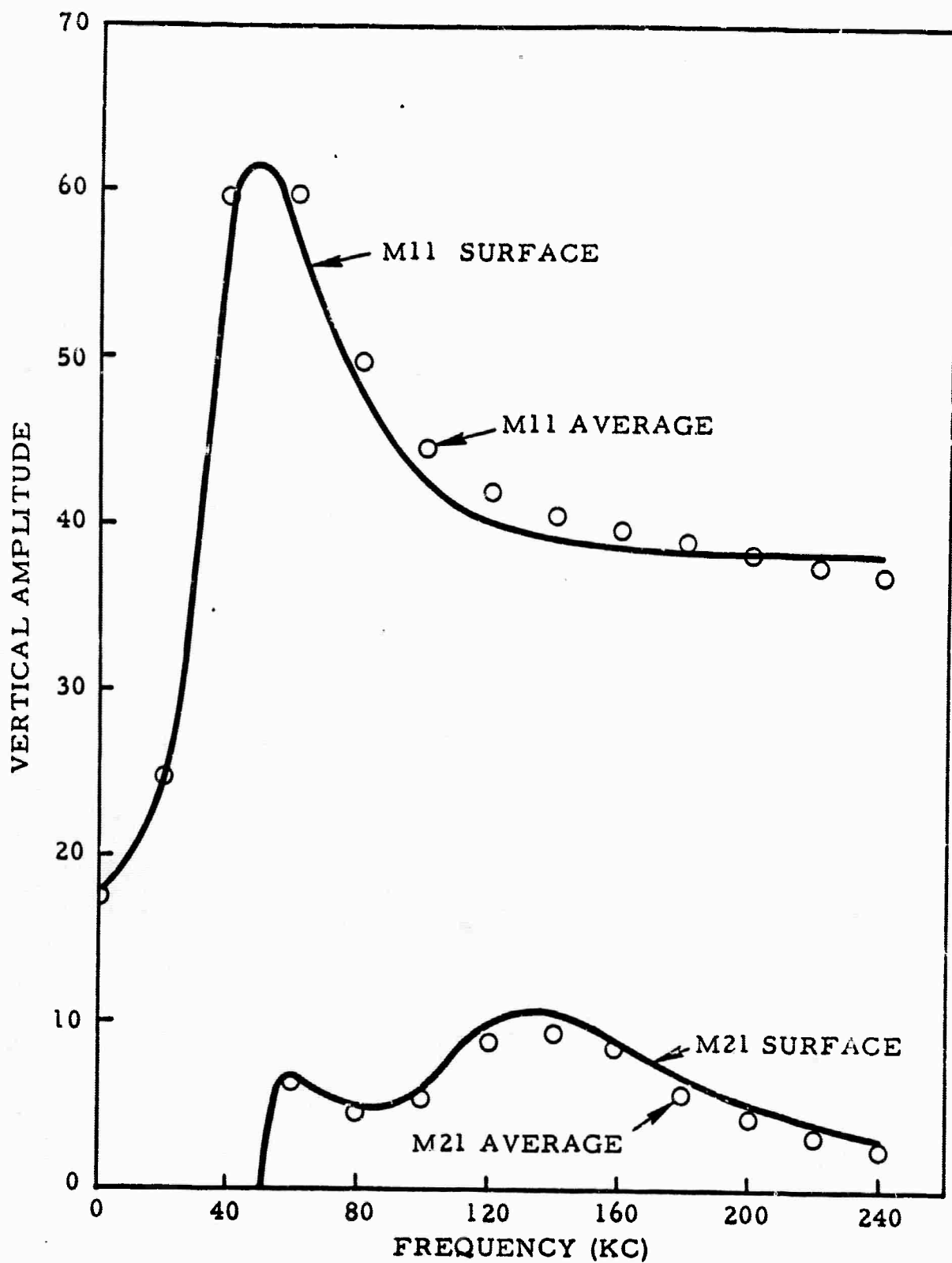


Figure 34

Theoretical Frequency Dependence of Vertical Amplitude as It Would Be Observed at the Surface (Solid Curves) and as It Would Be Observed by Averaging Over the Receiver Depth Range 0 - 3 mm (Open Circles).

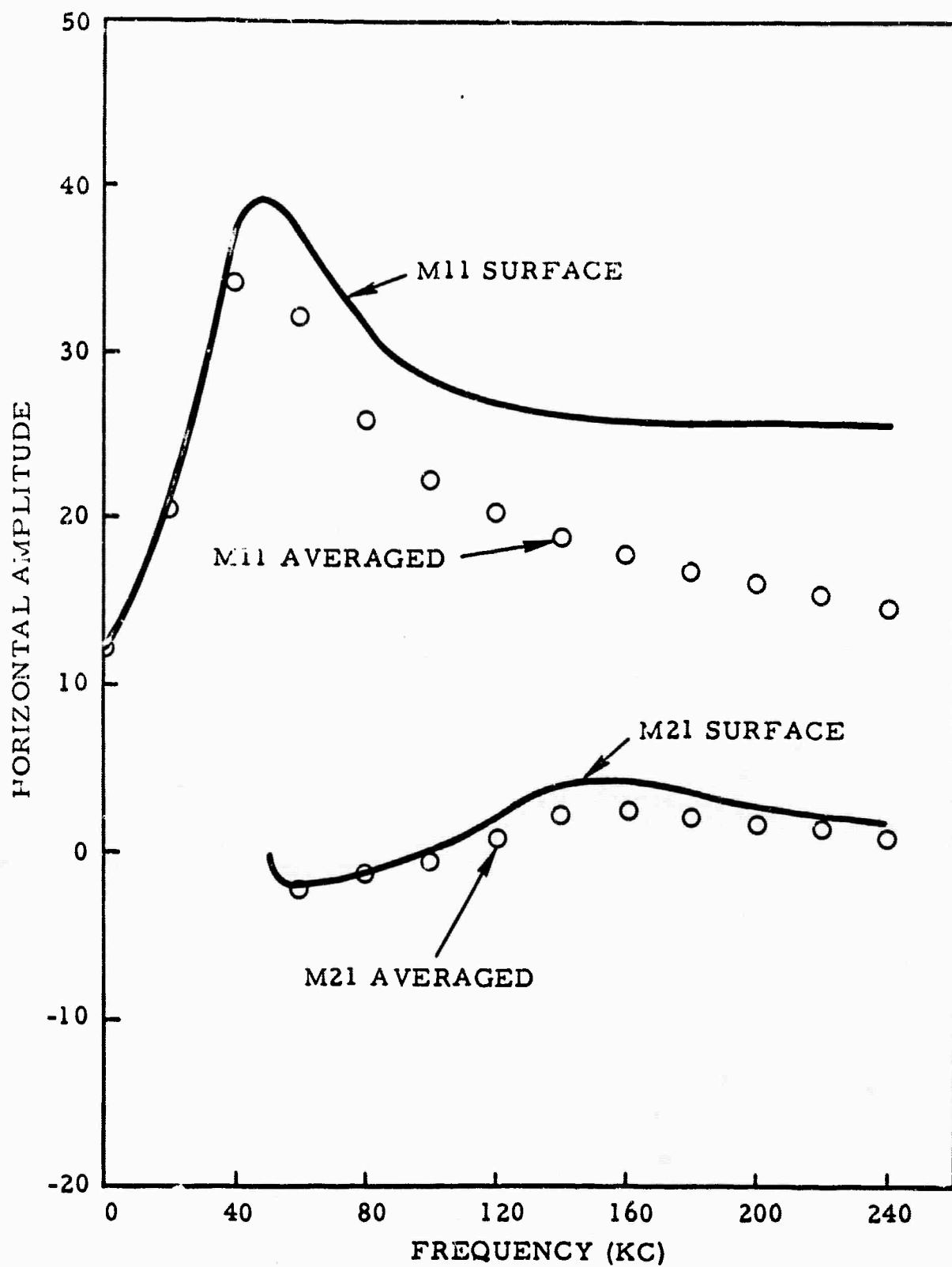


Figure 35 Theoretical Frequency Dependence of Horizontal Amplitude
as It Would Be Observed at the Surface (Solid Curves) and
as It Would Be Observed by Averaging Over the Receiver
Depth Range 0 - 1 mm (Open Circles).

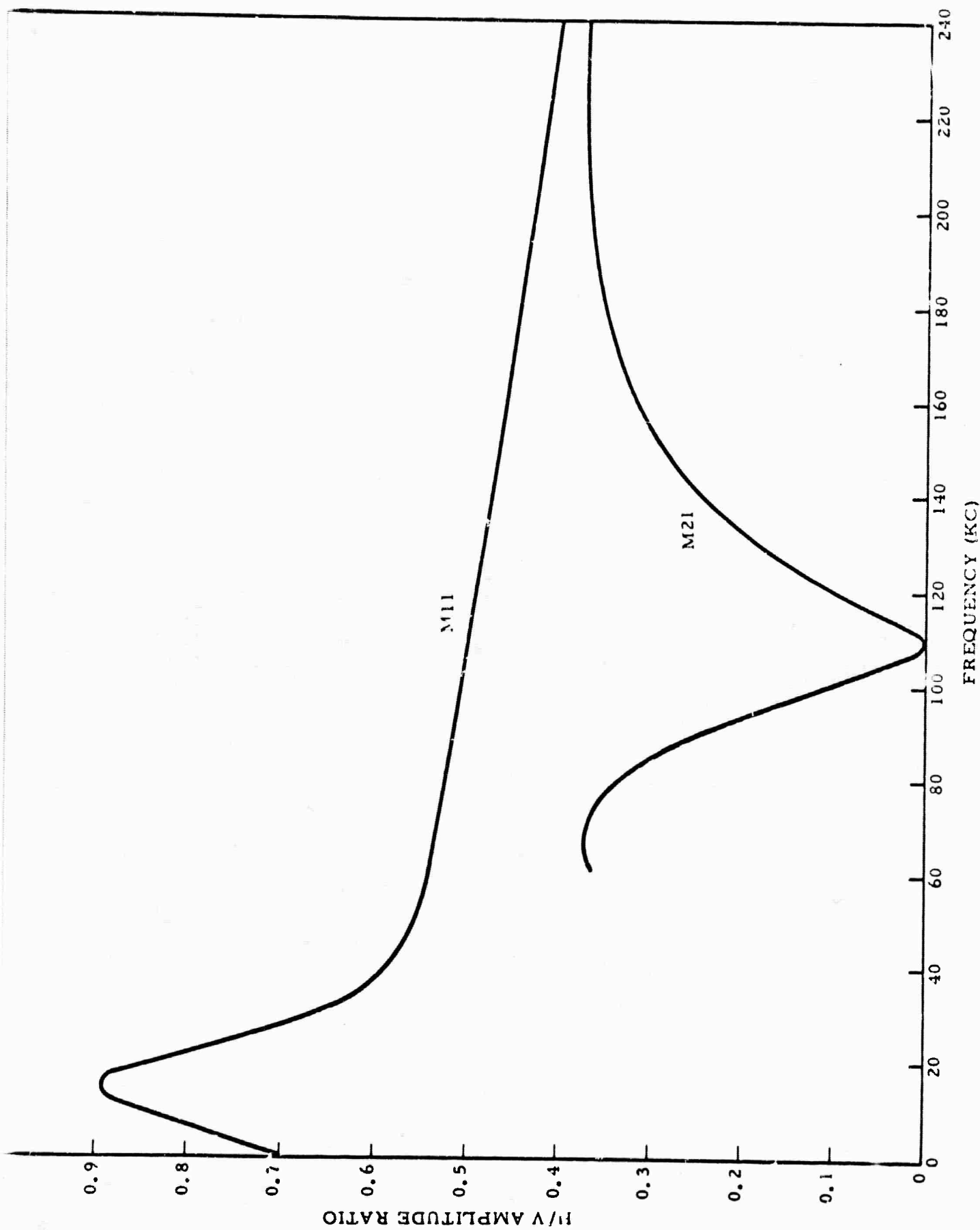


Figure 36 Theoretical Frequency Dependence of Ratio of Average Horizontal Displacement (0 - 1 mm) to Average Vertical Displacement (0 - 3 mm). Compare With Figure 31.

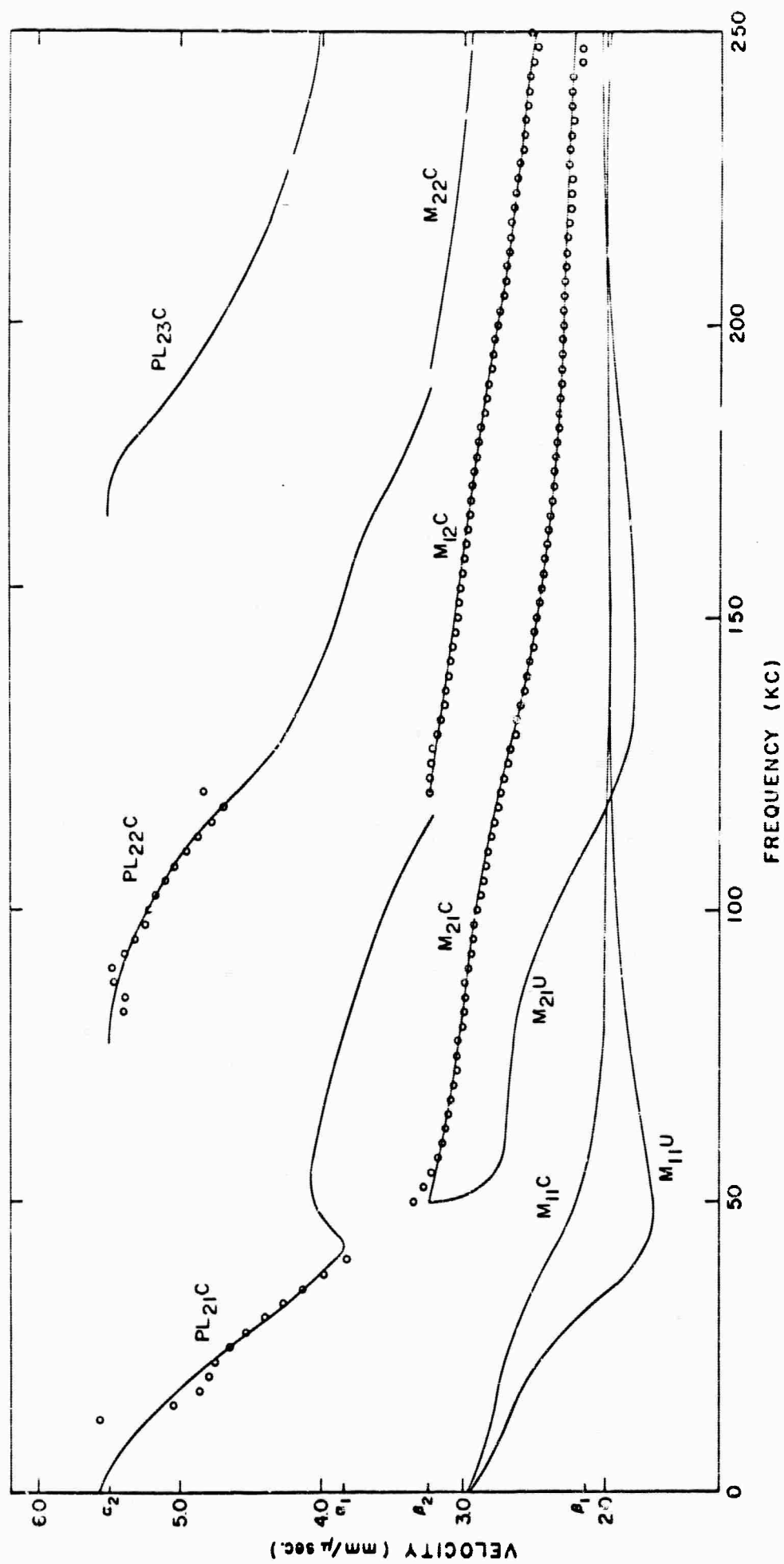


Figure 37 Dispersion Obtained from the Modes PL_{21} , PL_{22} , M_{21} and M_{12} Separated by Applying the 9-Channel, 31-Point Multichannel Filters Designed in the Time Domain to the Theoretical Seismograms. The Theoretical Phase Velocity Curves Are Shown For Reference.

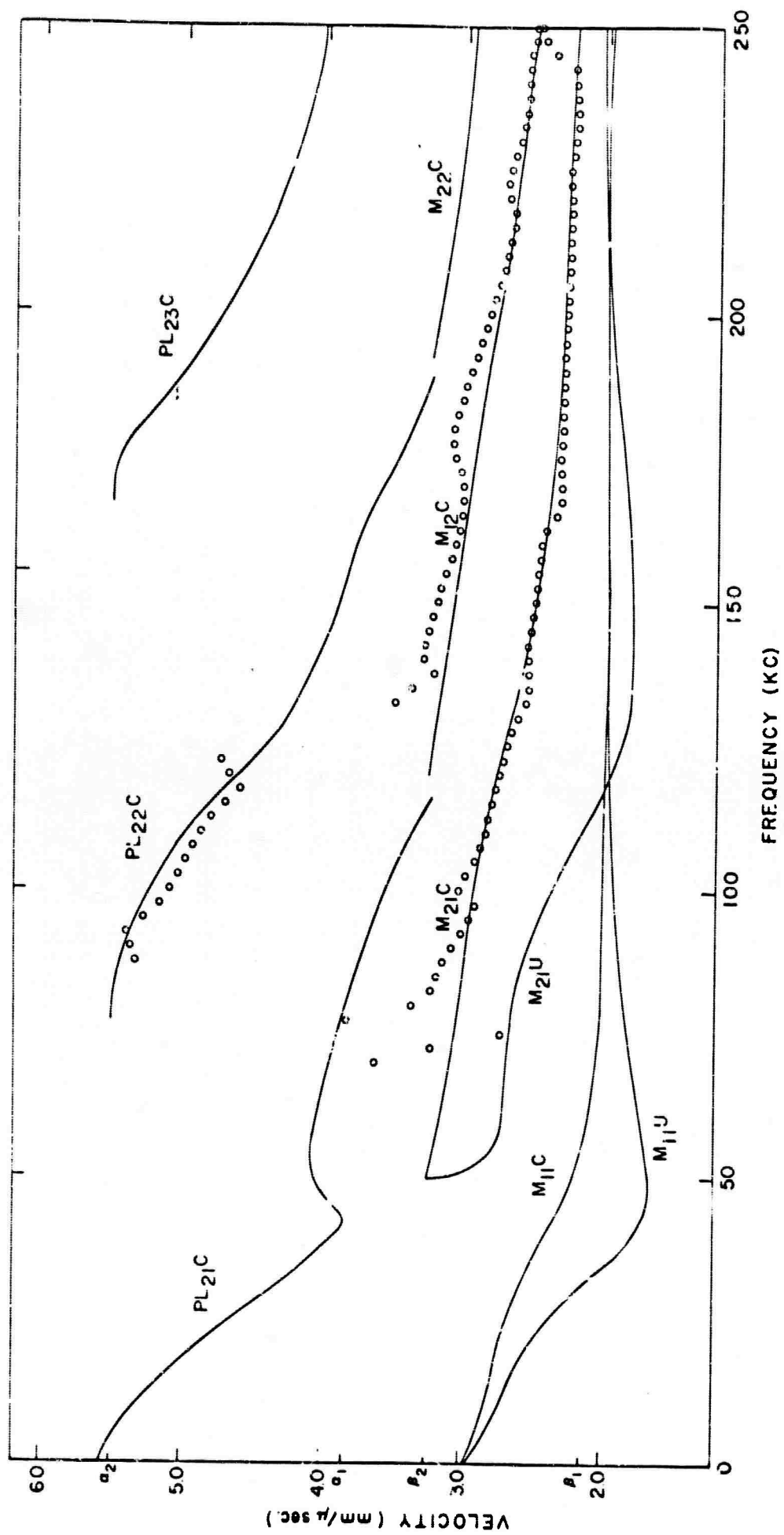


Figure 38 Dispersion Obtained from the Modes PL₂₂, M₂₁, and M₁₂ Separated by Applying the 9-Channel, 31-Point Multichannel Filters Designed in the Time Domain to the Experimental Seismograms. The Theoretical Phase Velocity Curves Are Shown for Reference.

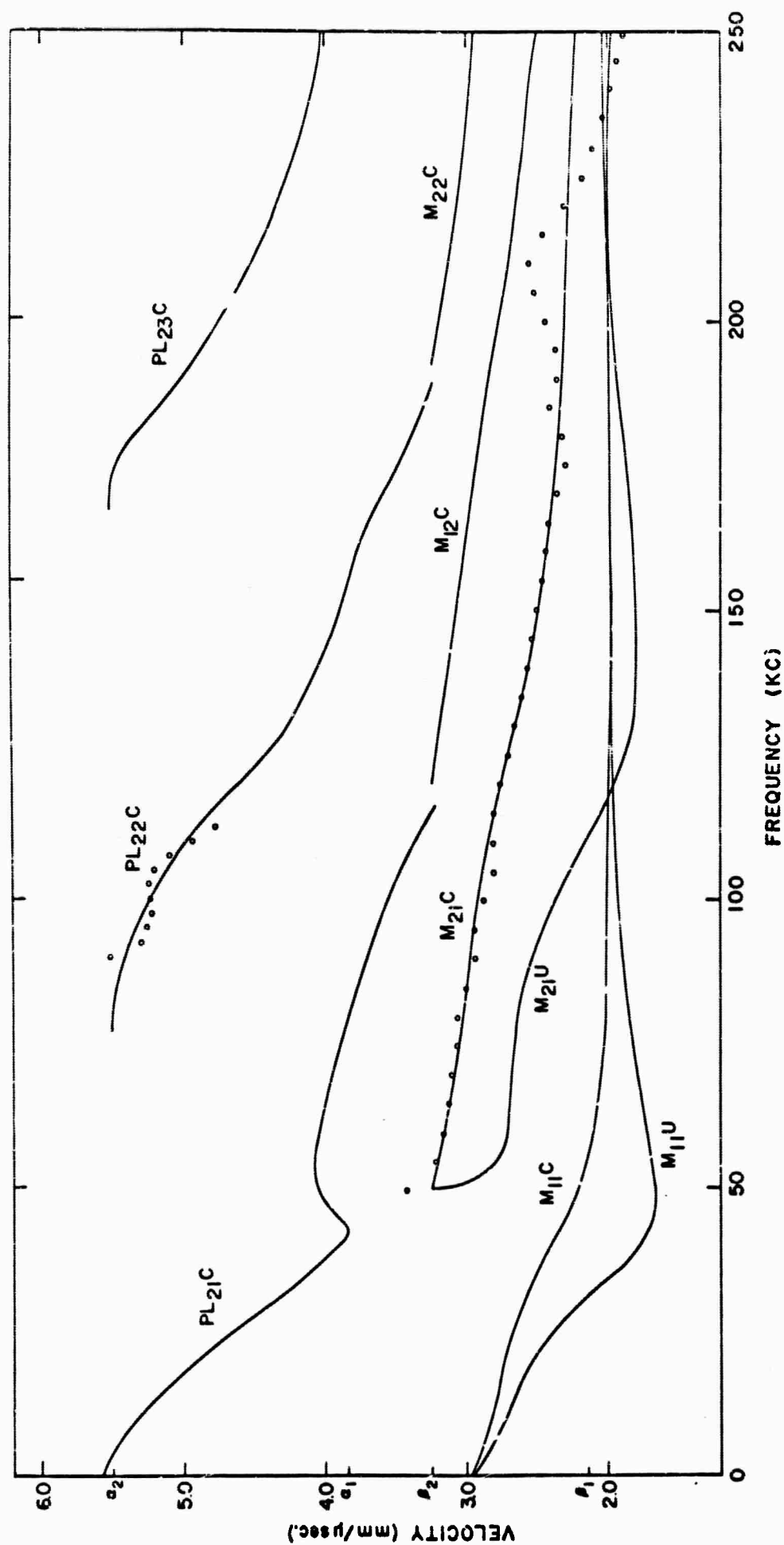


Figure 39 Dispersion Obtained from the Modes PL_{22} and M_{21} Separated by Applying the 6-Channel Multichannel Filters to the Theoretical Seismograms. The Theoretical Phase Velocity Curves Are Shown for Reference.

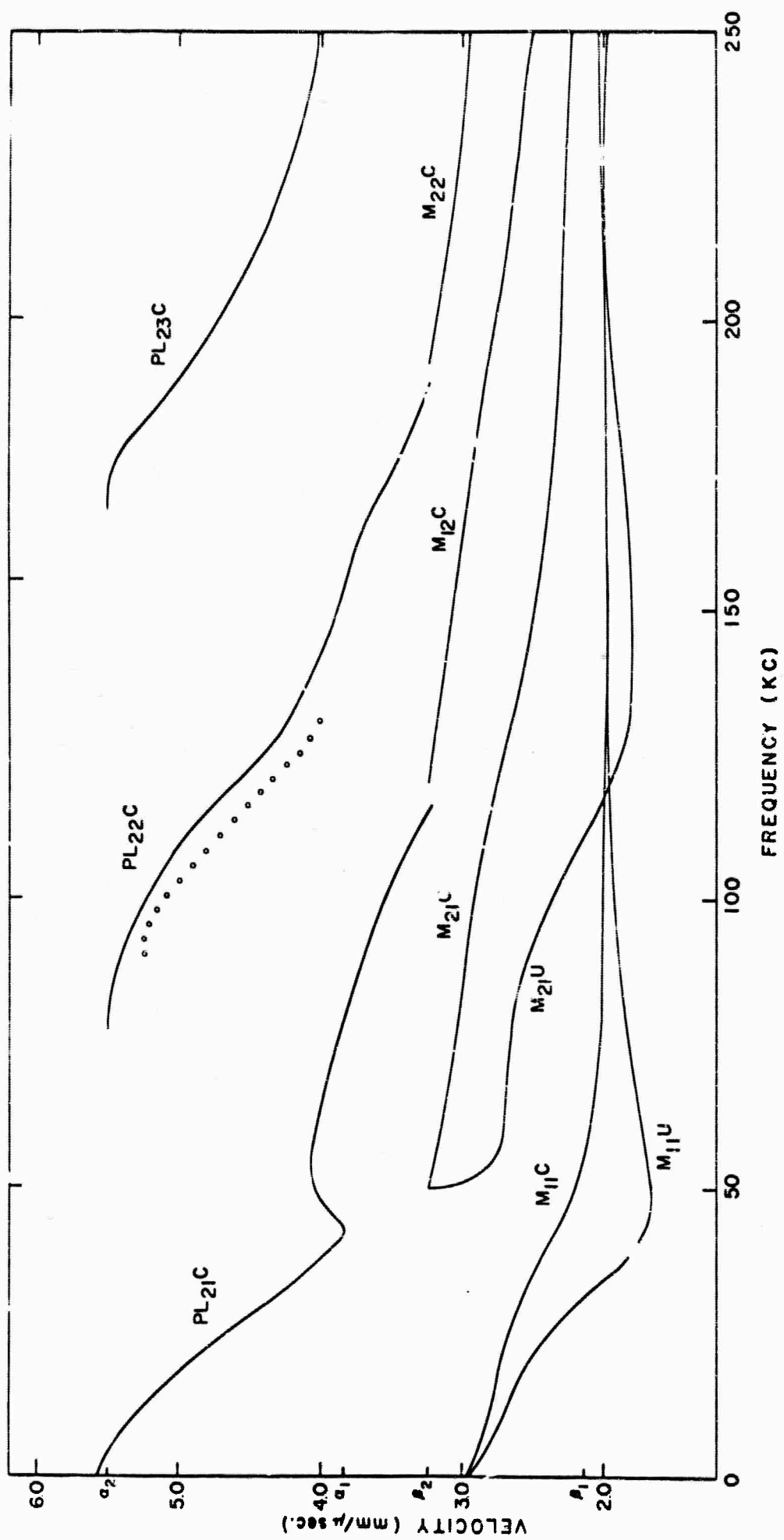


Figure 40 Dispersion Obtained from the PL₂₂ Mode Separated by Applying the 6-Channel Multichannel Filters to the Experimental Seismograms. The Theoretical Phase Velocity Curves Are Shown for Reference. The M₂₁ Results (Not Shown) Were Questionable.

APPENDIX D

WAVE PROPAGATION IN A 2-LAYERED MODEL OF THE EARTH'S CRUST

ABSTRACT

A number of theoretical seismograms have been synthesized from their constituent modal seismograms which have been obtained by numerical integration using amplitude spectra and dispersion curves derived from the classical theory of seismic wave propagation. A laboratory model corresponding to the theoretical model provides a comparative set of experimental seismograms and, after suitable processing, a comparative set of dispersion curves. While qualitative agreement is achievable, a completely satisfactory quantitative match between the theoretical and experimental results has not been accomplished yet. A study of the theoretical excitation functions, dispersion curves and attenuation functions of the early-arriving PL (leaky) modes furnished important insight into the characteristics of seismic energy propagating through the crust.

BLANK PAGE

APPENDIX D

WAVE PROPAGATION IN A 2-LAYERED MODEL OF THE EARTH'S CRUST

by

Hugh K. Harris and Joe G. Foreman

I. INTRODUCTION

When a layered elastic medium is excited, the resultant ground motion at any point may be represented by a superposition of a possibly infinite set of plane waves. A fundamental consequence of such a vibrating system is existence of a period equation expressing the condition of constructive interference between these plane waves which are undergoing multiple reflections in the various layers. Each distinct condition of constructive interference yields a period of "natural vibration" or a "normal mode." Thus, normal modes are interference phenomena—each successively higher mode representing a higher order of interference—and the disturbance at a distant point may be approximately obtained by the superposition of waves arriving at that point along the oblique rays for which constructive interference occurs.

Higher-order normal (trapped) modes contribute heavily to the information contained in earthquake records in the later (shear) arrivals. Much of the noise which masks refraction and reflection arrivals is probably higher-mode energy in near-surface layers. Characteristics of the higher modes are sensitive to changes in velocity, density and layer thickness. Thus, higher modes may represent a useful tool for probing the earth's crust.

For the case of leakage of energy from the deepest crustal layer into the semi-infinite half-space below (i.e., the mantle), the corresponding mode is termed "leaky". Observed spectral components of leaky or PL modes always include much long-period energy. Earthquake-generated PL waves frequently include periods greater than 10 sec at

distances less than about 30° . The PL phase characteristically has the form of an oscillatory wavetrain which arrives during the interval between the initial P-wave and the S-wave. The mathematical representation of a mode of propagation is expressed by

$$u(t, x, z) = \frac{1}{2\pi} \int_{-\infty}^{\infty} H(\omega) e^{i(\omega t - k_r x)} d\omega$$

where $H(\omega)$ is the complex frequency spectrum of the given mode at the source. A derivation of this formula and a discussion of its integration are given by Laster et al (1965).

For the normal modes, the excitation function $H(\omega)$ represents the amplitude spectrum of the associated modal seismogram. In the case of the leaky modes, this amplitude spectrum is weighted by an attenuation function. Associated with each amplitude spectrum of a normal or leaky mode is a period equation which yields the modal dispersion curves displayed in this appendix, Figures 1 through 7, as graphs of phase and group velocity vs frequency. A knowledge of the dispersion curves is not sufficient to define the model uniquely; however, in principle, the shear and compressional velocities in the various layers (β_i and α_i), the ratios of layer densities (ρ_i/ρ_j), and the layer thicknesses (d_i) may be inferred from such data.

Theoretical solutions for a simple crustal model (H1) consisting of a single layer overlying an infinitely deep half-space have been presented and discussed in Semiannual Technical Reports No. 1 (30 March 1964), No. 2 (29 September 1964), and No. 3 (1 April 1965). Table 1 gives the elastic parameters of this model.

Table 1

ELASTIC PARAMETERS OF MODEL H1

Material	P-Velocity (mm/ μ sec)	S-Velocity (mm/ μ sec)	Density Ratio	Layer Thickness (mm)
Half-Hard Brass	3.83	2.14	1.0	20
Cold-Rolled Steel	5.49	3.24	1.0	∞

The leaky modes of model H1 proved to be important in representing short-range seismograms even though individual modes did not approximate transients with definite arrival times. Effective determination of dispersion curves from the theoretically computed seismograms required the application of mode-separation techniques.

II. ANALOG MODEL STUDIES OF THE 3-LAYER MODEL

A. DESCRIPTION OF MODEL

A 2-dimensional laboratory earth model having two layers over a half-space and referred to as model H2 has been constructed and experimental seismograms obtained for comparison purposes. Laboratory model H2 consists of a 10-mm layer of half-hard brass over a 10-mm layer of monel over a 914.4-mm half-space of cold-rolled steel. The length of the model is 121.92 cm. The 1.57-mm thick plates are bonded with epoxy resin. Compressional (α) and shear (β) velocities have been determined by direct measurement of first arrivals and by theoretical calculations using the typical elastic constants of the materials. The theoretical shear velocities are in close agreement with the experimental shear velocities, verifying the accuracy of the laboratory measurements. Table 2 gives the two sets of shear velocities.

The theoretical compressional velocities differ from the experimental compressional velocities by as much as 10 percent. This is to

Table 2

THEORETICAL AND EXPERIMENTAL SHEAR VELOCITIES FOR MODEL H2

	<u>Theoretical</u> <u>(mm/μsec)</u>	<u>Experimental</u> <u>(mm/μsec)</u>
β_1	2.2	2.20
β_2	2.7	2.77
β_3	3.2	3.25

be expected, however, as the 2-dimensional compressional velocity is not the same as the 3-dimensional compressional velocity (Oliver et al, 1954). Judging from the good agreement obtained for the shear velocities, the maximum error in the model velocity measurements should not exceed 5 percent.

The elastic parameters of laboratory model H2, which are also used in the theoretical calculations, are given in Table 3.

Table 3

ELASTIC PARAMETERS FOR MODEL H2

α	β	Layer Thickness	Density Ratio
<u>(mm/μsec)</u>	<u>(mm/μsec)</u>	<u>(mm)</u>	
3.85	2.20	10.0	
4.78	2.77	10.0	1.0
5.46	3.25	∞	

The laboratory results are dependent on the source and receiver parameters. A barium titanate block serves as a source transducer. The receiving transducer is also a barium titanate crystal. Orientation of the transmitter is such that it operates in a compressional mode, while the receiver responds in a transverse mode.

A square pulse of about 3- μ sec duration and 1000-v amplitude is delivered to the source crystal.

The model output seismogram is bandpass-filtered over the frequency range of 0.5 kc to 330 kc. The frequency spectrum of the crystal's driving pulse is such that most of the energy falls between 70 kc and 250 kc. The piezoelectric source crystal was mounted 200 mm from the end of the model. A profile was obtained by moving the receiving crystal away from the source in 10-mm steps beginning at a separation of 50 mm and continuing to 900 mm. Figures 3 through 10 show segments of these profiles around 300 mm, 500 mm and 700 mm. The data were digitized automatically with a sample interval of 1 μ sec. Figures 3, 4 and 5 are low-gain vertical seismograms showing primarily the large-amplitude Rayleigh waves. Figures 6 through 10 are high-gain vertical and horizontal recordings which allow inspection of the leaky and normal modes preceding the Rayleigh arrival. In these high-gain records, the Rayleigh wave is clipped.

B. MODEL-TO-EARTH SCALING

The H2 theoretical/experimental model has been shown to scale to a reasonable earth model (Semiannual Technical Report No. 3). Let the distance and time transformations be given by the two equations

$$\bar{x}_e = a \bar{x}_m$$

$$t_e = b t_m$$

where a and b are the scale factors relating earth distance (\bar{x}_e) to model distance (\bar{x}_m) and earth time (t_e) to model time (t_m), respectively. The following two equations must be satisfied if the wave equation is to remain invariant in going from the earth to the laboratory model of the earth:

$$\alpha_e = \frac{a}{b} \alpha_m$$

$$\beta_e = \frac{a}{b} \beta_m$$

Here, β denotes the shear velocity and α the compressional velocity. For $a = 2 \times 10^6$ and $\alpha_e = 8.1$ km/sec, b must be 1.35×10^6 . This set of scale factors for model H2 corresponds to a 40-km earth crust having the following velocity characteristics:

$\alpha_1 = 5.71$ km/sec	$\beta_1 = 3.26$ km/sec
$\alpha_2 = 7.09$ km/sec	$\beta_2 = 4.11$ km/sec
$\alpha_3 = 8.1$ km/sec	$\beta_3 = 2.82$ km/sec

One microsecond in model H2 scales to 1.35 sec in the earth model, and 1 cycle / μ sec scales to 0.742 cps.

Because unscaled frequencies extending at least to 0.742 cps were of interest, theoretical calculations were predicated on a 1-cycle/ μ sec folding frequency or a 0.5- μ sec sample rate. It follows that unfiltered theoretical seismograms contain frequency components well beyond the 250-kc cutoff imposed on the laboratory model by the nature of the source spectrum. Furthermore, actual short-period seismograms are typically most useful at frequencies above 0.4 cps, which corresponds to a scaled frequency of about 539 kc. Therefore, in comparing the theoretical seismograms with laboratory and field records, account must be taken of their different frequency spectra. In general, the higher frequencies are associated with the higher modes and the inclusion of high-order modes will result in more pulse-like theoretical seismograms. This provides some basis for comparison with crustal refraction records.

III. THEORETICAL INVESTIGATION OF 3-LAYER MODEL

There are 10 normal modes and 7 leaky modes below the 1-cycle/ μ sec folding frequency of model H2. For these modes, the theoretical part of the crustal studies program required computation of dispersion curves and excitation functions, attenuation functions for the seven leaky modes, and modal seismograms of horizontal and vertical motion. Three pairs of composite seismograms were constructed by summing all 17 modal seismograms at the source-to-receiver distances of 300 mm, 500 mm and 700 mm (Figure 11). In this figure each pair of summed seismograms consists of a horizontal and a vertical trace.

Figures 12 through 15 give the attenuation per 100 mm for the various leaky modes. Figure 16 presents the attenuation per microsecond. A rate of 1 db/mm or μ sec means a decay to 10 percent of original amplitude in traveling 20 mm or 20 μ sec, respectively. Note that each attenuation curve begins at a low level and increases rapidly. Even though the excitation functions (Figures 17 through 20) tend to increase with increasing attenuation, the net effect is one of rapid decay in both space and time, except where there are attenuation minima. For both sets of curves, these minima occur roughly at the same frequencies. Since each mode's spatial attenuation rate typically increases with frequency, the frequency components above the modal cutoff frequency rapidly decay with increasing source-to-receiver distance. At any one distance, each mode's time attenuation rate also increases with frequency and, after a sufficiently long time, only frequencies around the modal cutoff frequency will be present. These attenuation properties tend to accentuate the high-velocity (group and phase) leaky-mode energy, as can be seen from the dispersion curves. Because of the severe attenuation with frequency, the leaky-mode experimental dispersion curves ordinarily exhibit only normal dispersion; i.e., phase velocity always decreases with decreasing period. For the PL modes, a quantity Q was defined as

$$Q = 2 \pi \frac{\text{Maximum Energy Stored}}{\text{Energy Loss in One Period}} = \frac{\pi}{\delta U T}$$

where δ is attenuation per unit distance, U is group velocity and T is period. Curves of Q vs frequency are shown in Figures 21 through 24. While the very sharp peaks in Q indicate that the largest part of the modal power is concentrated in a band of frequencies near cutoff frequency, important subsidiary peaks in power are present for each mode for frequencies other than at cutoff.

It can be seen from Figure 2 that leaky-mode phase and group-velocity curves cut off at a low-frequency limit where $C = U = \alpha_3$ (U = group velocity and α_3 = compressional velocity in the steel half-space). Another feature is the occurrence of at least one minimum and maximum on each group-velocity curve. Beginning with PL_{24} , the phase-velocity curves flatten out over a very broad band of frequencies above the modal cutoff frequency with a velocity approximately equal to the compressional velocity of the monel (4.78 mm/ μ sec). Undoubtedly, it is the presence of the intermediate monel layer which causes this flattening out in the phase-velocity curves. The physical implication is that energy is refracted along the brass-monel interface. This indicates that the influence of the intermediate layer is most potent at the higher frequencies (higher-order modes). At the low frequencies, the wavelengths are too long compared to the layer thickness for any effective physical discrimination; i.e., the monel and brass cannot be "seen" as individual layers by the longer wavelengths. From the strong attenuation and steep group-velocity curves for the leaky modes (Figure 2), it is expected that the early-arriving PL phase will possess an almost sinusoidal appearance. Such behavior is observable both in the laboratory model and the mathematical model, particularly in the latter.

Figures 25 through 30 show seven theoretical leaky-mode seismograms for source-to-receiver distances of 300 mm, 500 mm and

700 mm. The corresponding composite (sum) seismogram for all of these modes is given in Figure 31. Figures 34 through 37 are especially good examples of the final sum seismograms which show the ringing PL modes. The traces in Figures 32, 33 and 34 contain much more high-frequency information than previous computations. Both the PL_{21} and PL_{22} modes are present in Figure 35; chiefly, PL_{22} in Figure 36 and PL_{22} and PL_{23} in Figure 37.

Horizontal and vertical excitation amplitudes for the PL modes have been computed for a receiver and vertical-force source, both located at the free surface of the brass layer (Figures 17 through 20). Unlike the normal-mode excitation functions (Figures 38 through 47) which have a $\pi/2$ phase difference between horizontal and vertical displacement at every frequency, the PL excitation functions are complex. Therefore, the phase difference between horizontal and vertical displacements is different at each frequency. The low-frequency end of each mode begins with low amplitude and builds up with increasing frequency, giving a series of maxima and minima. The frequencies at which the excitation minima occur coincide roughly with the frequencies of group-velocity maxima and attenuation minima; i. e., frequency bands having low-excitation amplitude propagate with high velocity and decay slowly with distance. The converse is true for excitation maxima.

Except for the M_{11} mode, the normal-mode solutions vanish at $C = U = \beta_3$ and thus, significant normal-mode contributions first begin to arrive with the cutoff frequency after the time X/β_3 (X =source-to-receiver distance). In general, corresponding to a given phase or group velocity, the periods of higher modes become progressively shorter. At high frequencies, the normal-mode phase and group-velocity curves approach the velocity of shear-wave propagation in the top layer (β_1). An important feature of several of the normal-mode dispersion curves is the strong tendency for the group-velocity curve to have a maximum value that approaches the accompanying phase-velocity

curve. This occurs in modes M_{13} , M_{14} , M_{15} , M_{23} , and M_{24} at frequencies well above cutoff. The explanation for this phenomenon is that energy is refracted as shear waves along the brass-monel interface beginning with wavelengths which are sufficiently short for the two layers to be discriminated. Such a refraction results in a simple and direct path length which requires that the phase velocity approach the group velocity in magnitude.

Haskell (1953) pointed out that one of the general properties of the solution to the multilayer dispersion problem was the equivalency of models having the same fd product (f is frequency and d is the single-layer crustal thickness). This means that a doubling of crustal thickness with no other model change will result in the same set of dispersion curves on a frequency axis scaled by one-half. An increase of roughly 40 percent in the frequency scale of the dispersion curves of H2 relative to H1 has been found. This shift in frequency scale between the dispersion curves of the two models would be theoretically predicted if the only difference between them was a 30 percent reduction in crustal thickness in going from model H1 to model H2. Since the average single-layer velocities for model H2 are greater than the velocities used for model H1, it is reasonable to expect the effective single-layer crustal thickness for H2 to be less than the crustal thickness for H1.

IV. COMPARISON OF ANALOG AND THEORETICAL RESULTS

A. SEISMOGRAMS

For comparison with the analog model results, 3 bandpass filters were designed and their corresponding time-domain operators convolved with the theoretical seismograms (Figures 48 through 53). The filter spectra were to approximate the frequency characteristics of the laboratory source function. Table 4 gives the three filters' cutoff frequencies (6 db below 0 attenuation). Response was essentially flat within the chosen passbands.

Table 4

FILTER CUTOFF FREQUENCIES

Filter	Cutoff Frequencies (kc)	
1	45	450
2	90	450
3	45	360

Figures 3, 4 and 5 exhibit the experimental seismograms obtained with a low-receiver gain. The Rayleigh phase dominates the records. The detailed structure of low-amplitude arrivals preceding the Rayleigh wave is not readily discernible at the gain of these recordings. The unfiltered theoretical seismograms (Figure 11) are also dominated by the Rayleigh wave which is isolated (Figure 60) for mode M_{11} . The filtered theoretical traces (Figures 48 through 53) do not resemble the experimental traces any more closely than do the unfiltered theoretical traces because most of the excitation energy falls within the band of frequencies ranging from 70 kc to 250 kc (Figures 38 and 45). There is a significant amount of energy arriving after the initial large-amplitude Rayleigh wave in the experimental records. At 500 mm, energy is still clearly arriving at 320 μ sec. This energy may originate in lateral flexural waves and reflections from the boundaries of the laboratory model. The overpowering effect of the Rayleigh mode is clearly seen upon comparing the sum of all of the normal modes (Figure 58) with the sum of all of the normal modes except M_{11} (Figure 59). Each normal mode is displayed separately in Figures 60 through 65. The clipped, high-gain, experimental seismograms (horizontal and vertical) displayed in Figures 6 through 10 compare favorably with the corresponding theoretical seismograms; however, first-arrival events due to the PL modes are comparatively quite weak in the experimental seismograms. One reason for such relatively low amplitudes is that the dynamic range of the laboratory

recording equipment was insufficient for processing with an absolute gain as great as that utilized in the theoretical calculations. In fact, the early arrivals are at the limit of detectability in the 700-mm recording. The strongest leaky mode present is PL_{22} which can be faintly detected at 700 mm. Although the arrival time of the PL_{22} energy is satisfactory, the frequency associated with this modal event is not as high as the theoretical dispersion curves require. This discrepancy is believed to be due to a fundamental difference in the laboratory and mathematical models, the nature of which is currently undetermined. A very low-amplitude horizontal wave occurs at $\sim 150 \mu\text{sec}$ at 700 mm. This wave is the first visible arrival on the original experimental recording and cannot be easily detected in Figure 8 after photographic reduction. It does not arrive as early as theoretically predicted; this can be seen from Table 5 which gives the minimum PL- and normal-mode arrival times for the three source-to-receiver distances of 300 mm, 500 mm and 700 mm.

Table 5

MINIMUM PL AND NORMAL MODE ARRIVAL TIMES

Source-to- Receiver Distances (mm)	PL Arrival Time (μsec)	Shear Arrival Time (μsec)
300	~ 61	~ 103
500	~ 97	~ 164
700	~ 134	~ 226

Similarly, the first arrival at 500 mm is a very low-amplitude wave at $\sim 112 \mu\text{sec}$. The first arrival at 300 mm occurs at $\sim 74 \mu\text{sec}$. These first arrivals have very high phase velocities, typically around $5 \frac{\text{mm}}{\mu\text{sec}}$. Such high phase velocities agree well with the theoretical dispersion and attenuation curves for the PL modes. At phase velocities much lower than $4.5 \text{ mm}/\mu\text{sec}$, the attenuation becomes so severe that relatively little leaky-mode energy is propagated. Consider the theoretical power spectra

displayed in Figure 54 for a source-to-receiver distance of 500 mm. The power spectrum of any leaky mode is sharply peaked in a frequency band near the cutoff frequency for that particular mode. Since the cutoff frequencies correspond to very high phase velocities, the power in the PL modes will be associated with very high phase velocities. Note that the relative power of leaky and normal modes within appropriate narrow frequency bands is comparable.

The PL_{21} mode perhaps manifests itself in the 300-mm records where the attenuation is least. At $\sim 100 \mu\text{sec}$, a low-frequency event which corresponds in shape and arrival time to the theoretical PL_{21} mode can be seen. However, shear-mode energy also can be present beginning at about $103 \mu\text{sec}$.

There is little visible evidence of the presence of the PL_{23} mode. The source spectrum embraces only very small portions of the spectra of the PL_{21} and PL_{23} modes, and their relative weakness is not surprising. (The theoretical source spectrum is such that PL_{23} may be detected.) Dispersion curves obtained from the experimental data indicate significant energy at $\sim 94 \text{ kc}$ and $\sim 210 \text{ kc}$. This result is compatible with the presence of the PL_{22} and PL_{23} modes, respectively. The theoretical arrival time for the normal-mode energy is consistent with the laboratory observations as can be seen from Table 5 and a comparison of the measured and computed time traces.

B. DISPERSION FROM THE EXPERIMENTAL SEISMOGRAMS BY TIME PARTITIONING

Several experimental seismograms were time-partitioned (on the basis of the phase velocity of arrivals across the array) into leaking-mode, shear-mode and Rayleigh-mode segments. Linear time-domain filters, which best changed the time segment at one distance to the same segment at a longer distance, were computed. The phase spectra of these filters gave an estimate of the dispersion.

If there is more than one mode in the time segment, the obtained dispersion estimates will be inaccurate unless

- The modes are separated in frequency. (In this case, an estimate of the dispersion of each mode can be obtained.)
- One mode has much more power than the other modes. (In this case, an estimate of the dispersion of the "strong" mode can be obtained.)

For the distances used in this analysis, both the leaking and shear modes were reasonably well-separated in frequency and the Rayleigh mode had much more power than the others. Consequently, reasonably good estimates of all the modes might be expected, except where the leaky modes overlap the normal modes and the normal modes overlap the Rayleigh mode in arrival time.

Figure 55 shows dispersion estimates for the two significant leaking modes in the leaking-mode time segment. The estimates are consistent among themselves but differ from the theoretically computed curves. They fall below the theoretical curves and are shifted to lower frequencies, which suggests a fundamental difference between the theoretical and experimental models. A possible explanation is that the low-velocity bonding material (which has a small but finite thickness) acts to effectively thicken the second layer, which would displace the curves to the left. A second possible explanation is that there is poor bonding somewhere in the section. The theoretical curves were not significantly affected by slight errors (2 percent) in velocities and densities, which rules out explanations on these grounds.

Figure 56 shows dispersion estimates for the three significant shear modes in the shear-mode time segment. Again, the results are consistent among themselves. As was seen for the leaking modes, the shear estimates are below the theoretical curves (to the left of them for M_{21}), although the differences are somewhat smaller.

Figure 57 shows the dispersion estimate for the Rayleigh mode. Agreement with the theoretical curve is excellent except at low

frequencies (70 to 120 kc) where the estimate is slightly low. This is consistent with the low-power density of the source at these frequencies.

In summary, fairly good dispersion estimates over a narrow frequency band near cutoff were obtained by time-partitioning the records for all the significant modes in the seismogram. Velocity estimates for leaking and shear modes were slightly lower than the theoretical curves but consistent among themselves. Impreciseness in the experimentally determined dispersion curves may explain some of the discrepancy. However, the results do imply that there may be some important model differences between the mathematical and laboratory simulations.

V. SUMMARY

A consistent set of experimental dispersion curves can be determined under suitable conditions but their employment as an absolute measurement technique for crustal structure has not been completely satisfying in all cases. The transfer function representation of dispersion should be most useful in comparative or relative measurements of the properties of the crust where one region may be weighed against another with regard to average velocities of propagation, average crustal thickness and layering multiplicity. In this study, for example, the presence of a second intermediate crustal layer (Model H2) has been revealed by a significant change in the shape of leaky- and normal-mode dispersion curves for a single crustal layer (Model H1), particularly at the higher frequencies (higher-order modes). A relative shift in frequency of two sets of experimentally determined dispersion curves indicates important differences in average crustal velocities or thickness. Agreement between the mathematical- and laboratory-model seismograms was qualitatively good in the sense that PL and normal modes were evident in both cases with generally satisfactory amplitudes and arrival times. However, exact quantitative agreement, especially with regard to leaky-mode dominant frequencies, has not been achieved. Both sets of records

(calculated and observed) show the PL_{22} mode to be the primary early arrival with a very complicated shear-mode zone.

VI REFERENCES

Haskell, N.A., 1953: The dispersion of surface waves on multilayered media, Bull. Seis. Soc. of Am. 43(1), 17-34.

Laster, Stanley J., Joe G. Foreman and A. Frank Linville, 1965: Theoretical investigation of modal seismograms for a layer over a half-space, Geophysics, 30(4), 571-596.

Oliver, Jack, Frank Press and Maurice Ewing, 1954: Two-dimensional model seismology, Geophysics, 19(2), 202-219.

LIST OF ILLUSTRATIONS

- Figure 1. Normal Mode Dispersion Curves for M_{11} through M_{15} and M_{21} through M_{25}
- Figure 2. Leaky Mode Dispersion Curves for PL_{21} Through PL_{27}
- Figure 3. Low-Gain Experimental Vertical Seismogram at 290-310 mm Showing the Dominant Rayleigh Mode M_{11}
- Figure 4. Low-Gain Experimental Vertical Seismogram at 490-510 mm Showing the Dominant Rayleigh Mode M_{11}
- Figure 5. Low-Gain Experimental Vertical Seismogram at 690-710 mm Showing the Dominant Rayleigh Mode M_{11}
- Figure 6. High-Gain Experimental Horizontal Seismogram at 300-330 mm Showing Early Arriving Leaky and Normal Mode Energy
- Figure 7. High-Gain Experimental Horizontal Seismogram at 470-520 mm Showing Early Arriving Leaky and Normal Mode Energy
- Figure 8. High-Gain Experimental Horizontal Seismogram at 690-750 mm Showing Early Arriving Leaky and Normal Mode Energy
- Figure 9. High-Gain Experimental Vertical Seismogram at 300-320 mm Showing Early Arriving Leaky and Normal Mode Energy
- Figure 10. High-Gain Experimental Vertical Seismogram at 490-510 mm Showing Early Arriving Leaky and Normal Mode Energy
- Figure 11. Horizontal and Vertical Theoretical Seismograms — Distance Range 300-700 mm (unfiltered)
- Figure 12. Spatial Attenuation Rate for Leaky Modes PL_{21} and PL_{23} as a Function of Frequency
- Figure 13. Spatial Attenuation Rate for Leaky Modes PL_{22} as a Function of Frequency
- Figure 14. Spatial Attenuation Rate for Leaky Modes PL_{24} and PL_{25} as a Function of Frequency
- Figure 15. Spatial Attenuation Rate for Leaky Modes PL_{26} and PL_{27} as a Function of Frequency
- Figure 16. Time Attenuation Rate for Leaky Modes PL_{21} Through PL_{27} as a Function of Frequency

LIST OF ILLUSTRATIONS (CONTD)

- Figure 17. Horizontal Leaky Mode Excitation Functions (PL_{23} and PL_{24})
- Figure 18. Horizontal Leaky Mode Excitation Functions (PL_{25} and PL_{26})
- Figure 19. Horizontal Leaky Mode Excitation Functions (PL_{21} , PL_{22} and PL_{27})
- Figure 20. Vertical Leaky Mode Excitation Function (PL_{22})
- Figure 21. 2Q for Leaky Mode PL_{22}
- Figure 22. 2Q for Leaky Modes PL_{23} , PL_{25} and PL_{27}
- Figure 23. 2Q for Leaky Mode PL_{24}
- Figure 24. 2Q for Leaky Mode PL_{26}
- Figure 25. Horizontal Modal Seismograms for Leaky Modes PL_{21} Through PL_{27} at 300 mm
- Figure 26. Horizontal Modal Seismograms for Leaky Modes PL_{21} Through PL_{27} at 500 mm
- Figure 27. Horizontal Modal Seismograms for Leaky Modes PL_{21} Through PL_{27} at 700 mm
- Figure 28. Vertical Modal Seismograms for Leaky Modes PL_{21} Through PL_{27} at 300 mm
- Figure 29. Vertical Modal Seismograms for Leaky Modes PL_{21} Through PL_{27} at 500 mm
- Figure 30. Vertical Modal Seismograms for Leaky Modes PL_{21} Through PL_{27} at 700 mm
- Figure 31. Horizontal and Vertical Leaky Mode Seismograms in the Distance Range 300-700 mm, Constructed by Summing All Seven PL Modes
- Figure 32. Sum of Leaky Modes, Normal Modes, and Leaky and Normal Modes in the Distance Range 300-700 mm (Unfiltered)
- Figure 33. Sum of Leaky Modes, Normal Modes, and Leaky and Normal Modes in the Distance Range 300-700 mm (Primarily Composed of Higher-Order Modes Due to Filtering)

LIST OF ILLUSTRATIONS (CONTD)

- Figure 34. Sum of Leaky Modes and Leaky and Normal Modes in the Distance Range 300-700 mm. This suite of records exhibits the initial sinusoidal appearance of the seismogram due to the leaky modes
- Figure 35. Sum of Leaky Modes, Normal Modes, and Leaky and Normal Modes in the Distance Range 300-700 mm. Most leaky-mode energy is contributed by the PL_{21} and PL_{22} modes
- Figure 36. Sum of Leaky Modes, Normal Modes, and Leaky and Normal Modes in the Distance Range 300-700 mm. Most of the leaky-mode energy is due to the PL_{22} mode
- Figure 37. Sum of Leaky Modes, Normal Modes, and Leaky and Normal Modes in the Distance Range 300-700 mm. Most leaky-mode energy is contributed by PL_{22} and PL_{23}
- Figure 38. Horizontal Normal Mode Excitation Function for M_{11}
- Figure 39. Horizontal Normal Mode Excitation Functions for M_{12} and M_{14}
- Figure 40. Horizontal Normal Mode Excitation Functions for M_{13} and M_{15}
- Figure 41. Horizontal Normal Mode Excitation Function for M_{21}
- Figure 42. Horizontal Normal Mode Excitation Function for M_{22} , M_{23} , M_{24} , and M_{25}
- Figure 43. Vertical Normal Mode Excitation Functions for M_{23} and M_{24}
- Figure 44. Vertical Normal Mode Excitation Functions for M_{21} , M_{22} and M_{25}
- Figure 45. Vertical Normal Mode Excitation Function for M_{11}
- Figure 46. Vertical Normal Mode Excitation Functions for M_{12} and M_{14}
- Figure 47. Vertical Normal Mode Excitation Functions for M_{13} and M_{15}
- Figure 48. Filtered Theoretical Horizontal and Vertical Seismograms in the Distance Range 300-700 mm at Low Gain (Filter 1)
- Figure 49. Filtered Theoretical Horizontal and Vertical Seismograms in the Distance Range 300-700 mm at Low Gain (Filter 2)
- Figure 50. Filtered Theoretical Horizontal and Vertical Seismograms in the Distance Range 300-700 mm at Low Gain (Filter 3)

LIST OF ILLUSTRATIONS (CONTD)

- Figure 51. Filtered Theoretical Horizontal and Vertical Seismograms in the Distance Range 300-700 mm at High Gain (Filter 1)
- Figure 52. Filtered Theoretical Horizontal and Vertical Seismograms in the Distance Range 300-700 mm at High Gain (Filter 2)
- Figure 53. Filtered Theoretical Horizontal and Vertical Seismograms in the Distance Range 300-700 mm at High Gain (Filter 3)
- Figure 54. Theoretical Power Density Spectra at Source-to-Receiver Distance of 500 mm for Modes PL_{21} , PL_{22} , PL_{23} , M_{11} , M_{12} , and M_{21}
- Figure 55. Comparison of Phase-Velocity Estimates for PL_{22} and PL_{23} Modes (from Time-Partitioning) with the Theoretical Curves
- Figure 56. Comparison of Phase-Velocity Estimates for M_{21} , M_{22} and M_{12} Shear Modes (from Time-Partitioning) with the Theoretical Curves
- Figure 57. Comparison of Phase-Velocity Estimates for the Rayleigh Mode M_{11} (from Time-Partitioning) with the Theoretical Curves
- Figure 58. Sum of all Normal Modes (M_{11} , M_{21} , M_{12} , M_{13} , M_{23} , M_{14} , M_{24} , M_{15} , M_{25} , and M_{22})
- Figure 59. Sum of all Normal Modes Except the Rayleigh Mode M_{11}
- Figure 60. Horizontal and Vertical Modal Seismograms for Modes M_{11} and M_{13} - Distance Range 300-700 mm
- Figure 61. Horizontal and Vertical Modal Seismograms for Modes M_{13} and M_{14} - Distance Range 300-700 mm
- Figure 62. Horizontal and Vertical Modal Seismograms for Mode M_{15} - Distance Range 300-700 mm
- Figure 63. Horizontal and Vertical Modal Seismograms for Modes M_{21} and M_{22} - Distance Range 300-700 mm
- Figure 64. Horizontal and Vertical Modal Seismograms for Modes M_{23} and M_{24} - Distance Range 300-700 mm
- Figure 65. Horizontal and Vertical Modal Seismograms for Modes M_{25} - Distance Range 300-700 mm

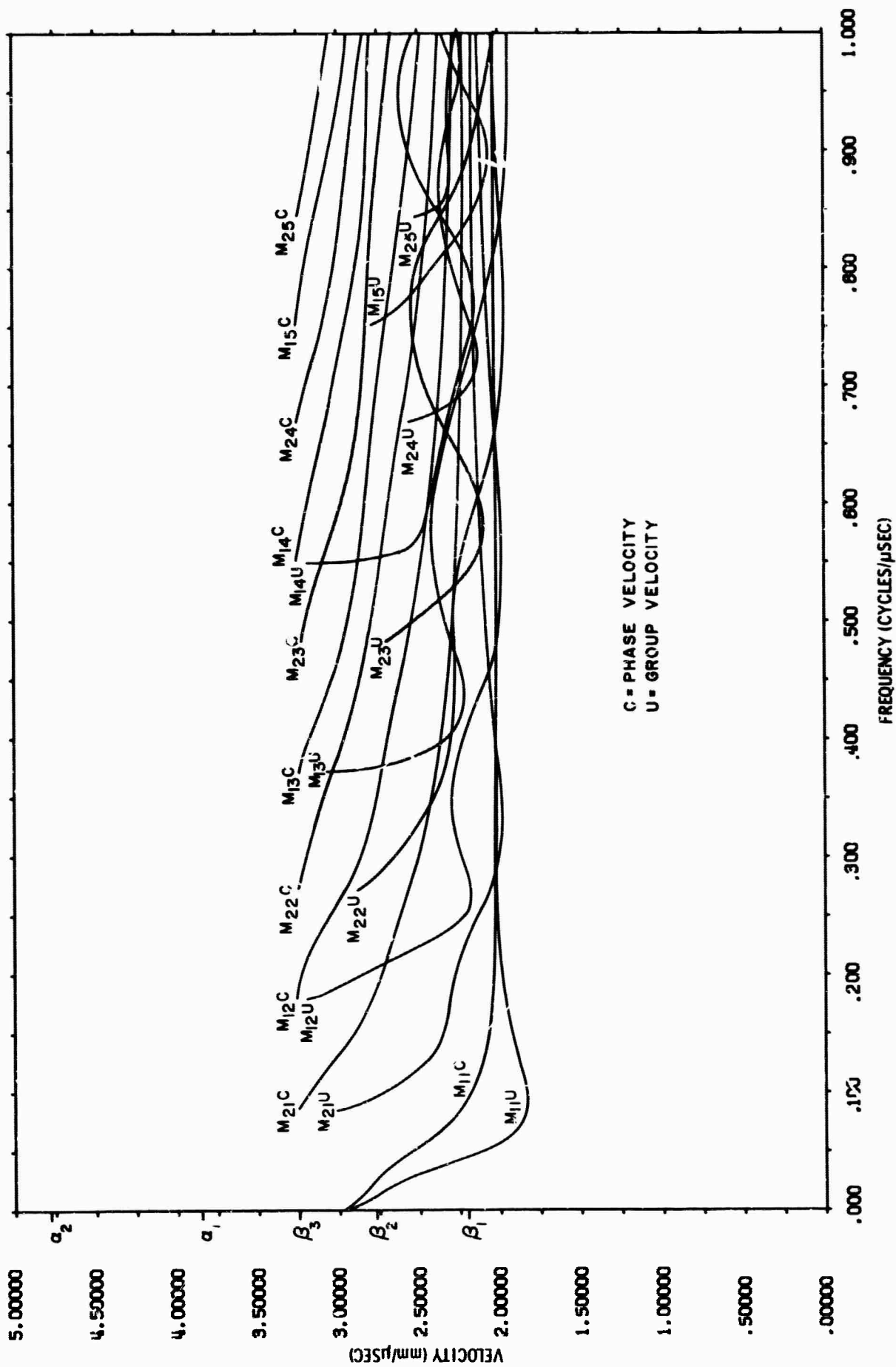


Figure 1. Normal Mode Dispersion Curves for M_{11} through M_{15} and M_{21} through M_{25}

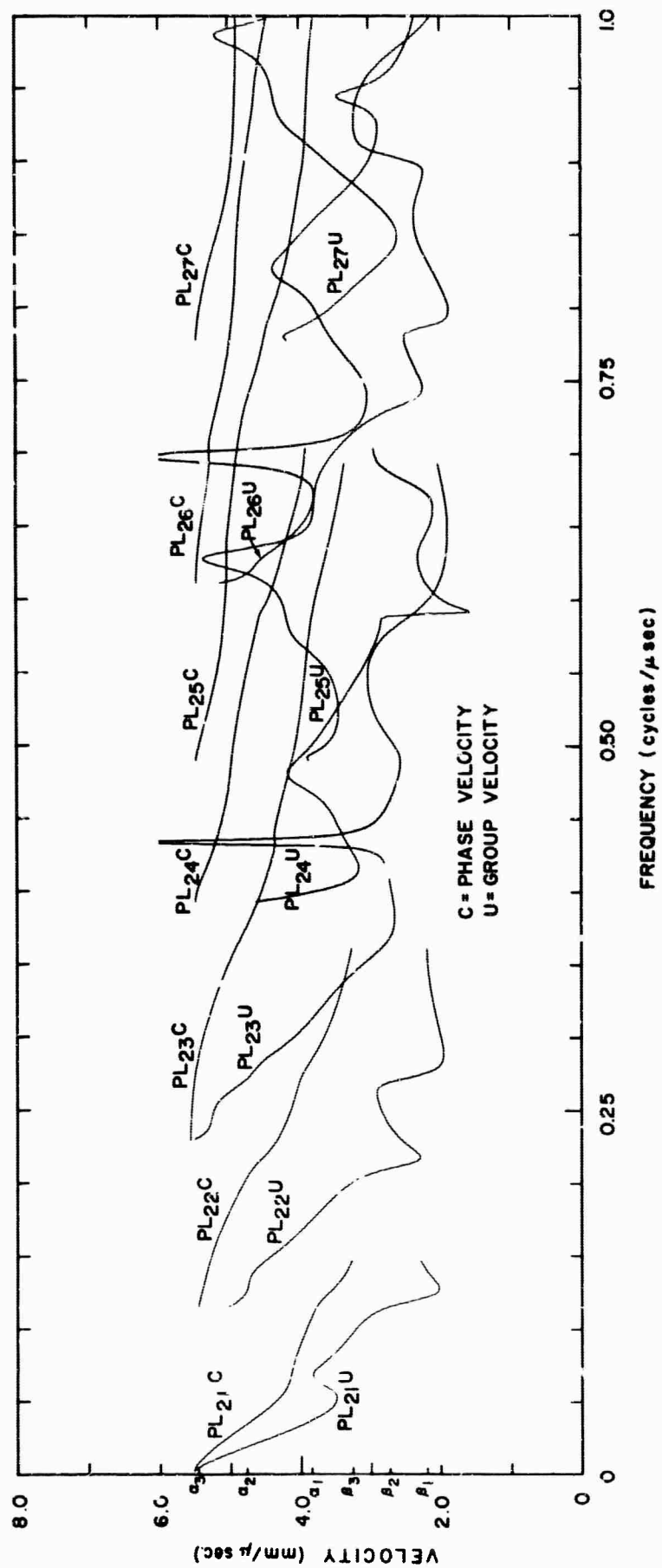


Figure 2. Leaky Mode Dispersion Curves for PL₂₁ Through PL₂₇

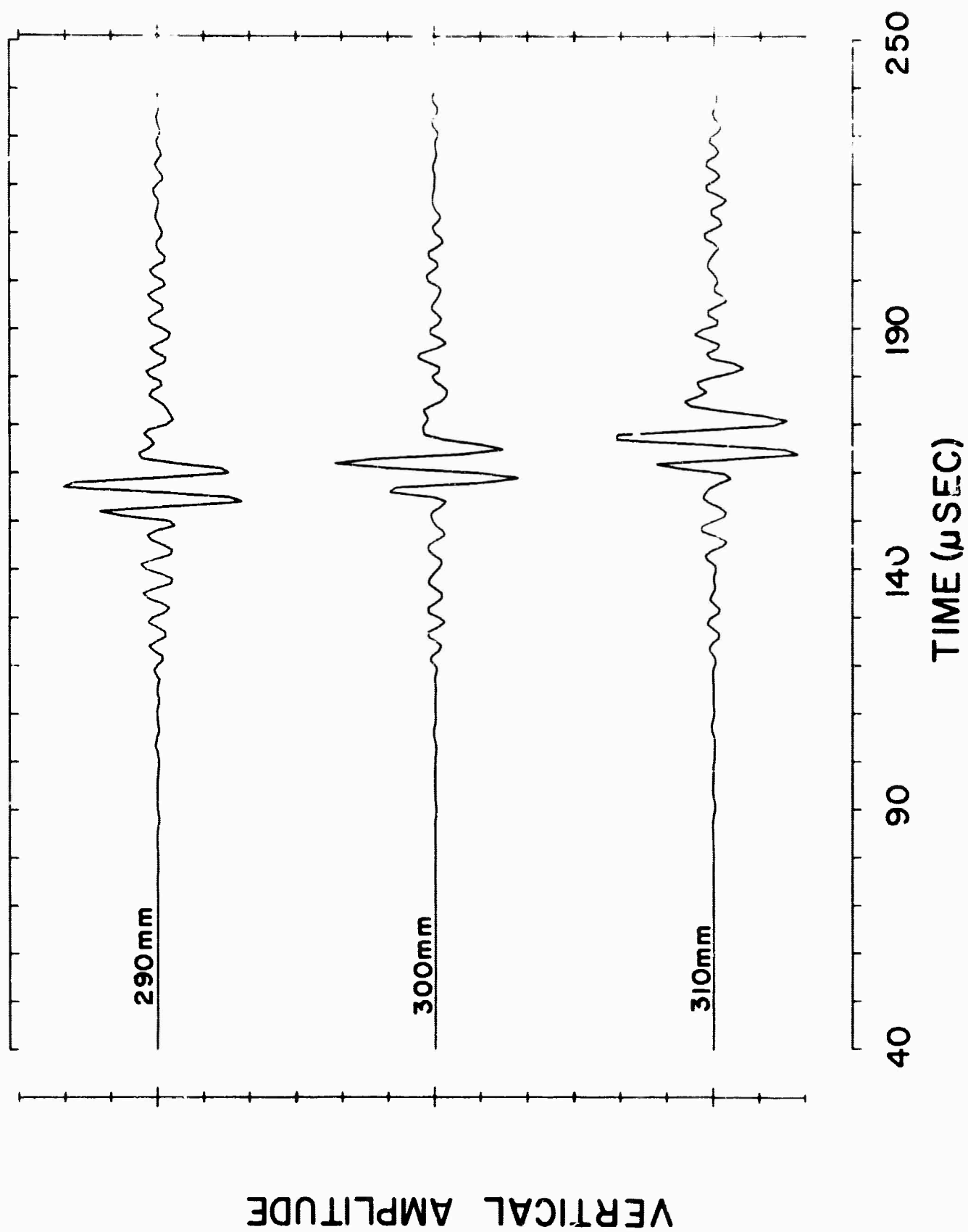


Figure 3. Low-Gain Experimental Vertical Seismogram at 290-310 mm Showing the Dominant Rayleigh Mode M_{11}

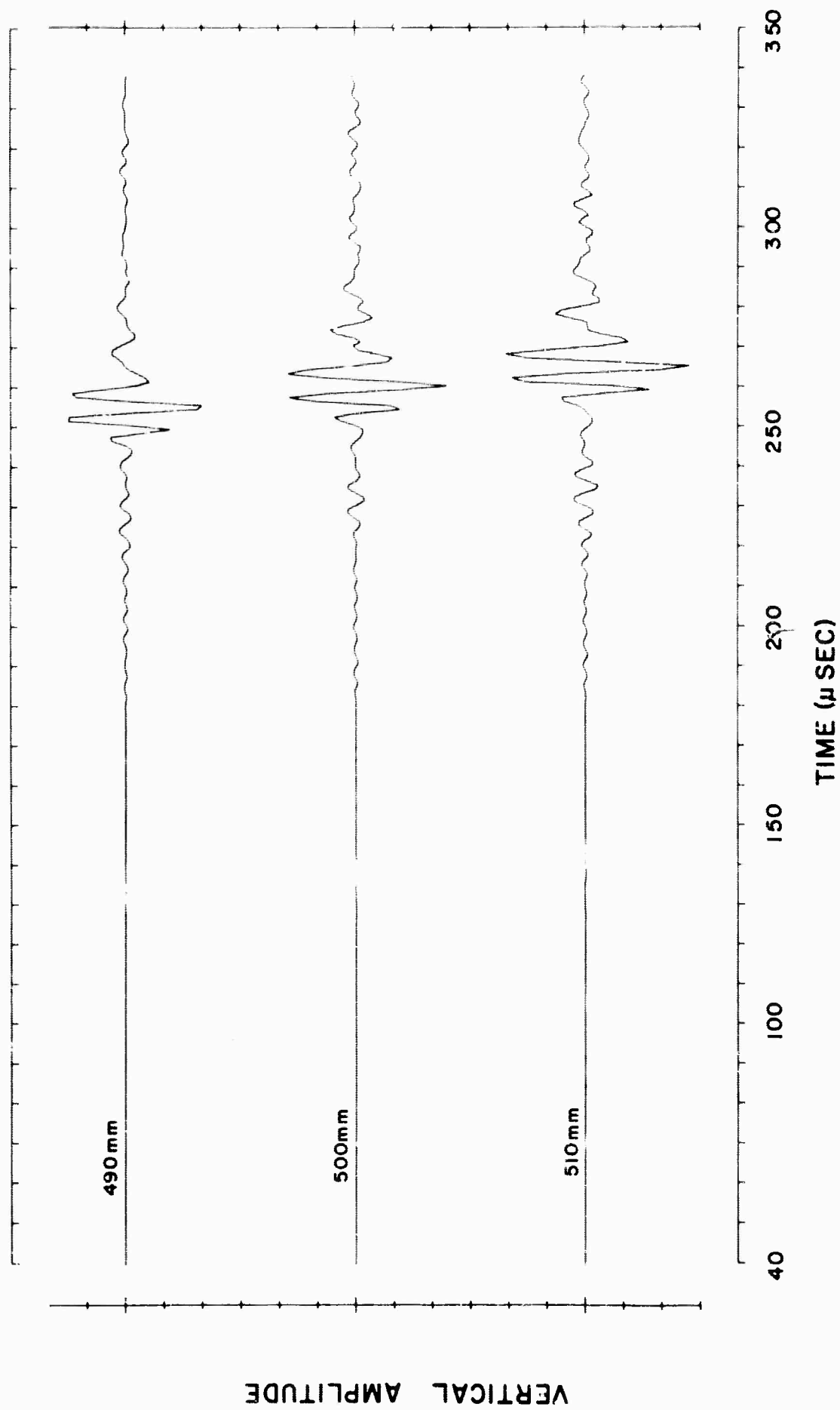


Figure 4. Low-Gain Experimental Vertical Seismogram at 490-510 mm Showing the Dominant Rayleigh Mode M_{11}

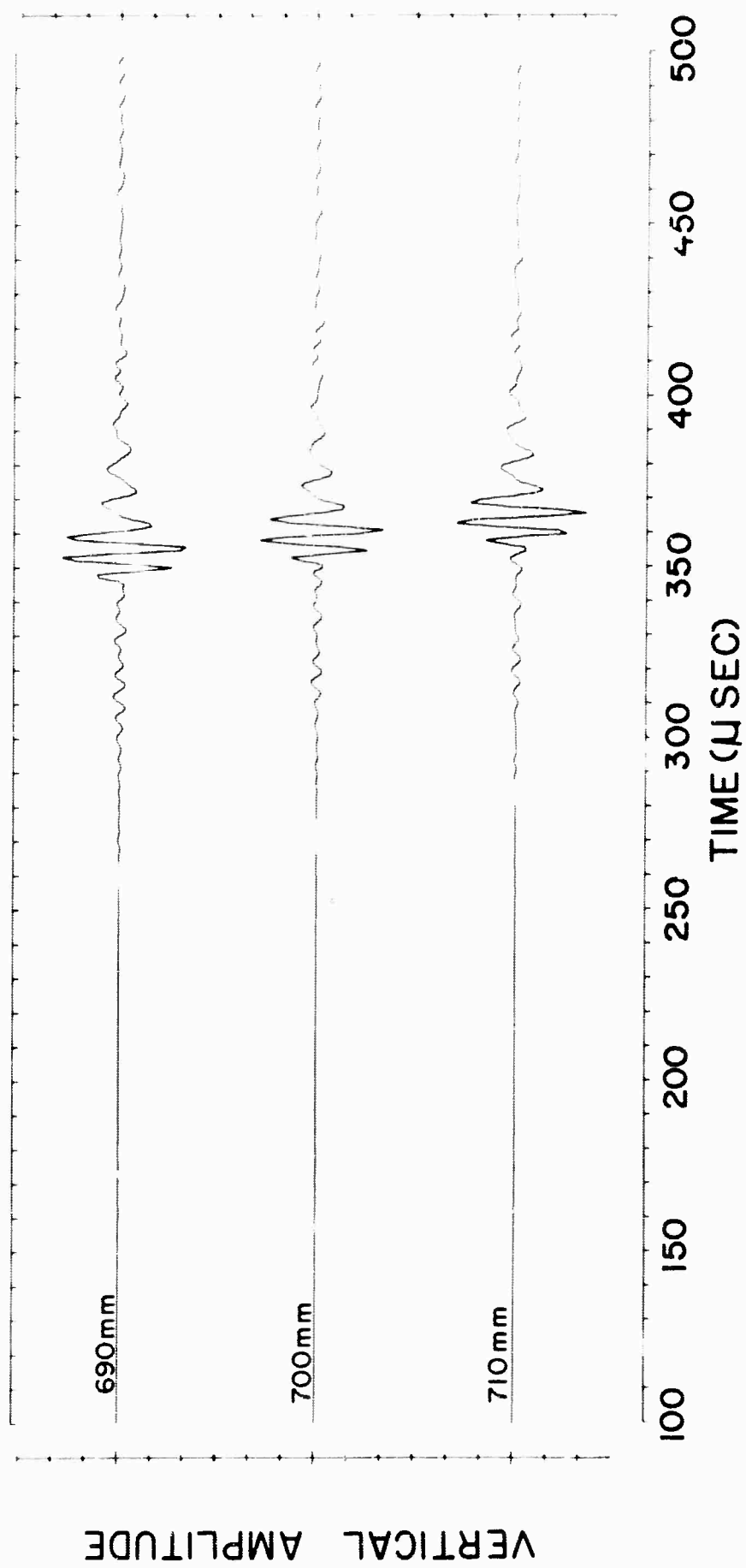


Figure 5. Low-Gain Experimental Vertical Seismogram at 690-710 mm Showing the Dominant Rayleigh Mode M_{11}

HORIZONTAL AMPLITUDE

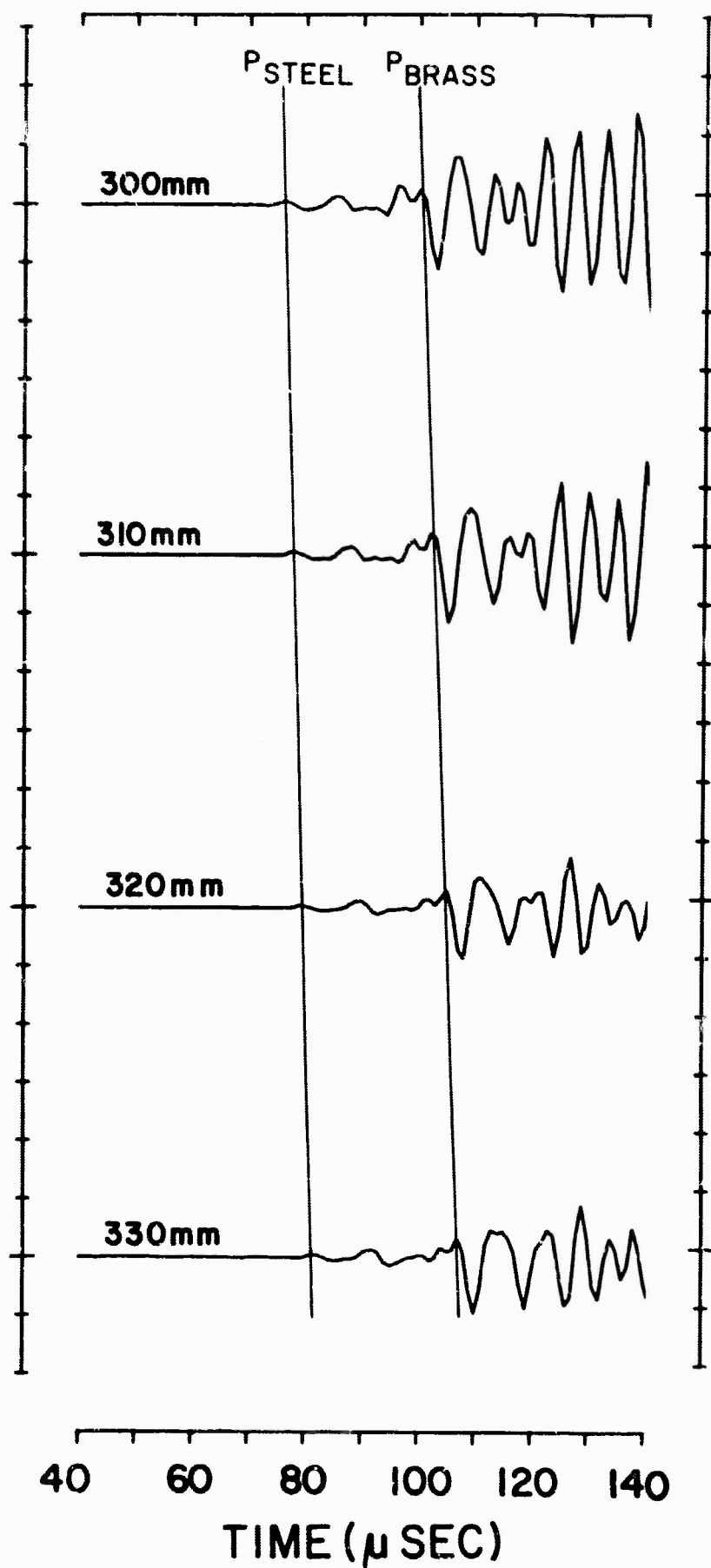


Figure 6. High-Gain Experimental Horizontal Seismogram at 300-330 mm Showing Early Arriving Leaky and Normal Mode Energy

HORIZONTAL AMPLITUDE

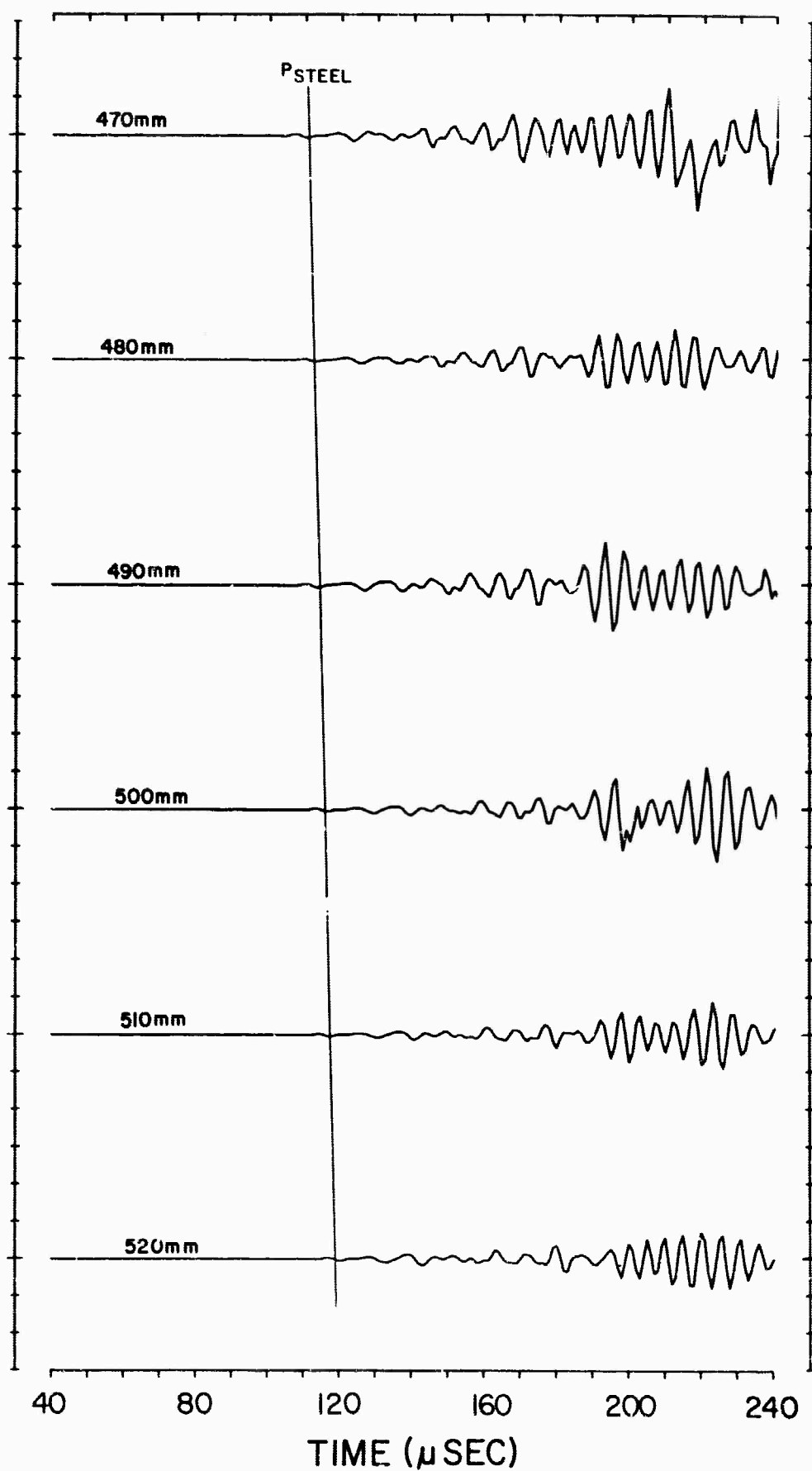


Figure 7. High-Gain Experimental Horizontal Seismogram at 470-520 mm Showing Early Arriving Leaky and Normal Mode Energy

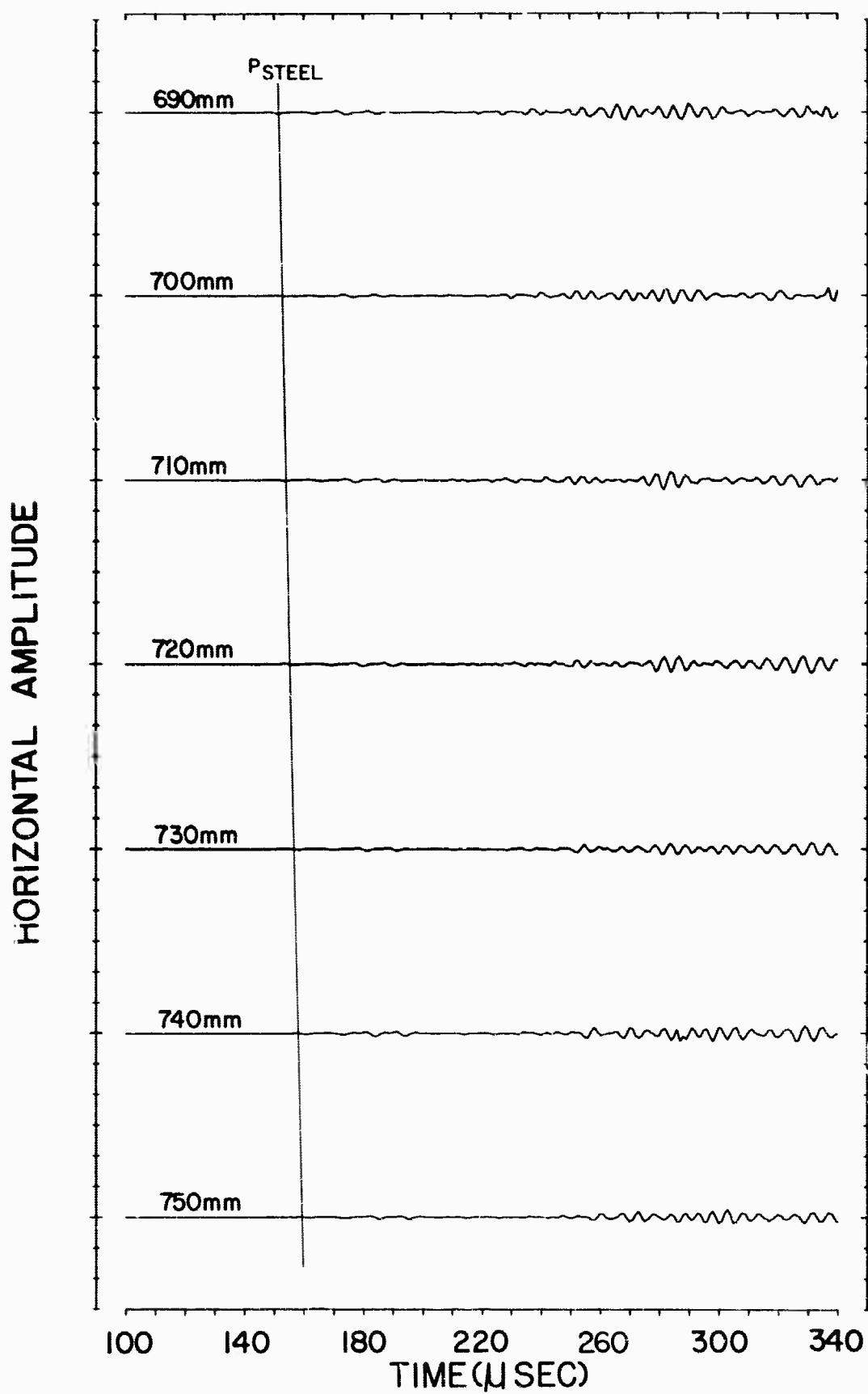


Figure 8. High-Gain Experimental Horizontal Seismogram at 690-750 mm Showing Early Arriving Leaky and Normal Mode Energy

VERTICAL AMPLITUDE

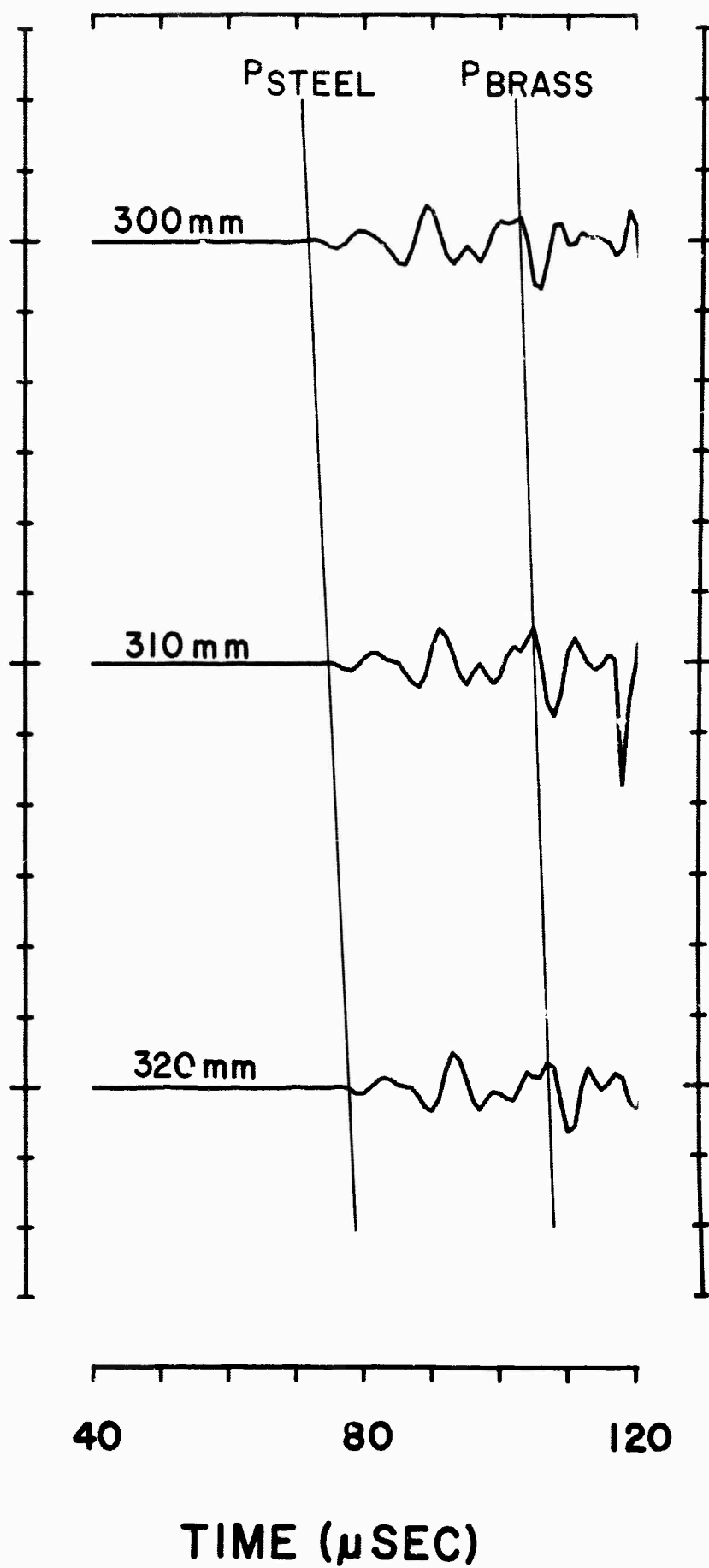


Figure 9. High-Gain Experimental Vertical Seismogram at 300-320 mm Showing Early Arriving Leaky and Normal Mode Energy

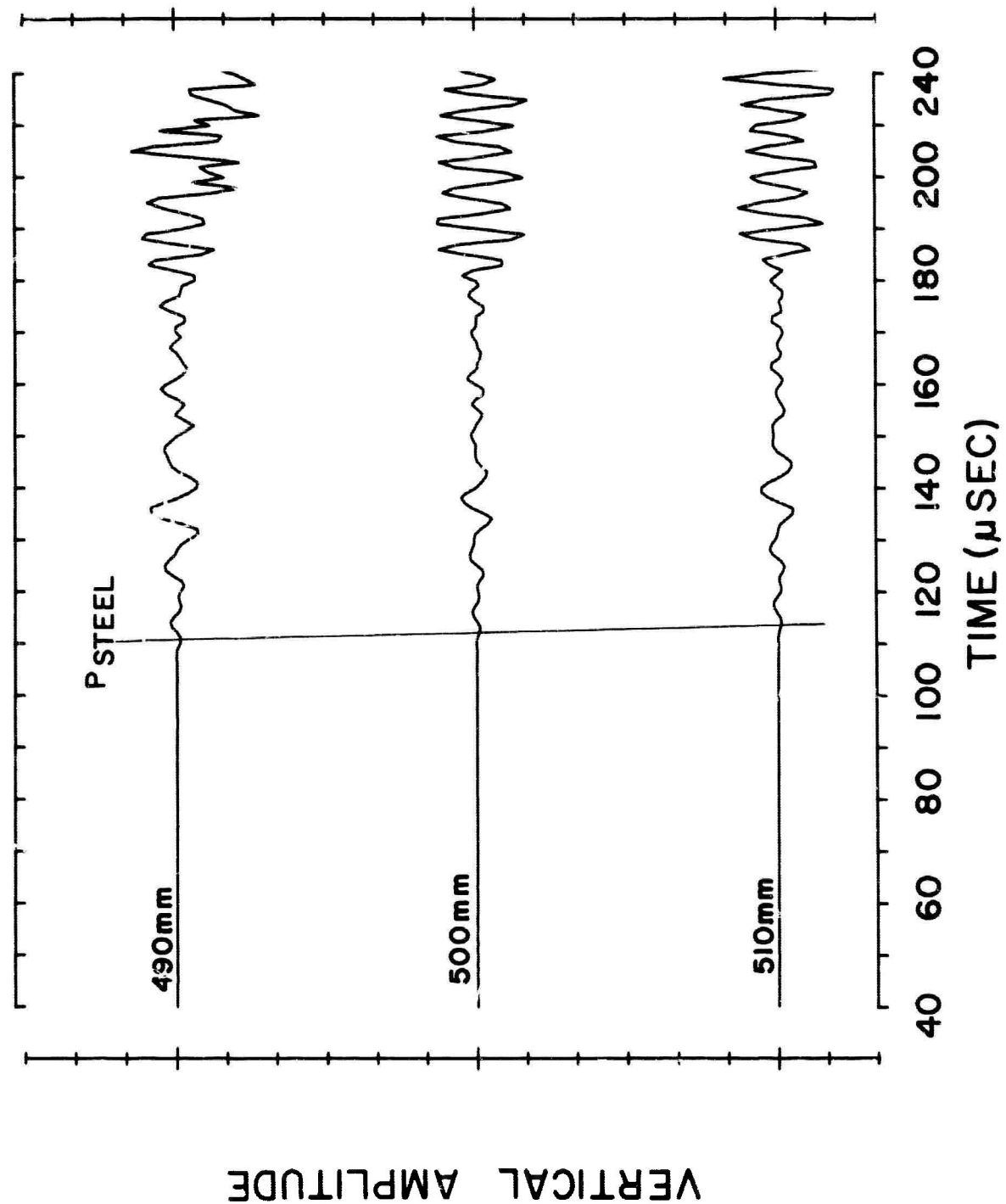


Figure 10. High-Gain Experimental Vertical Seismogram at 490-510 mm Showing Early Arriving Leaky and Normal Mode Energy

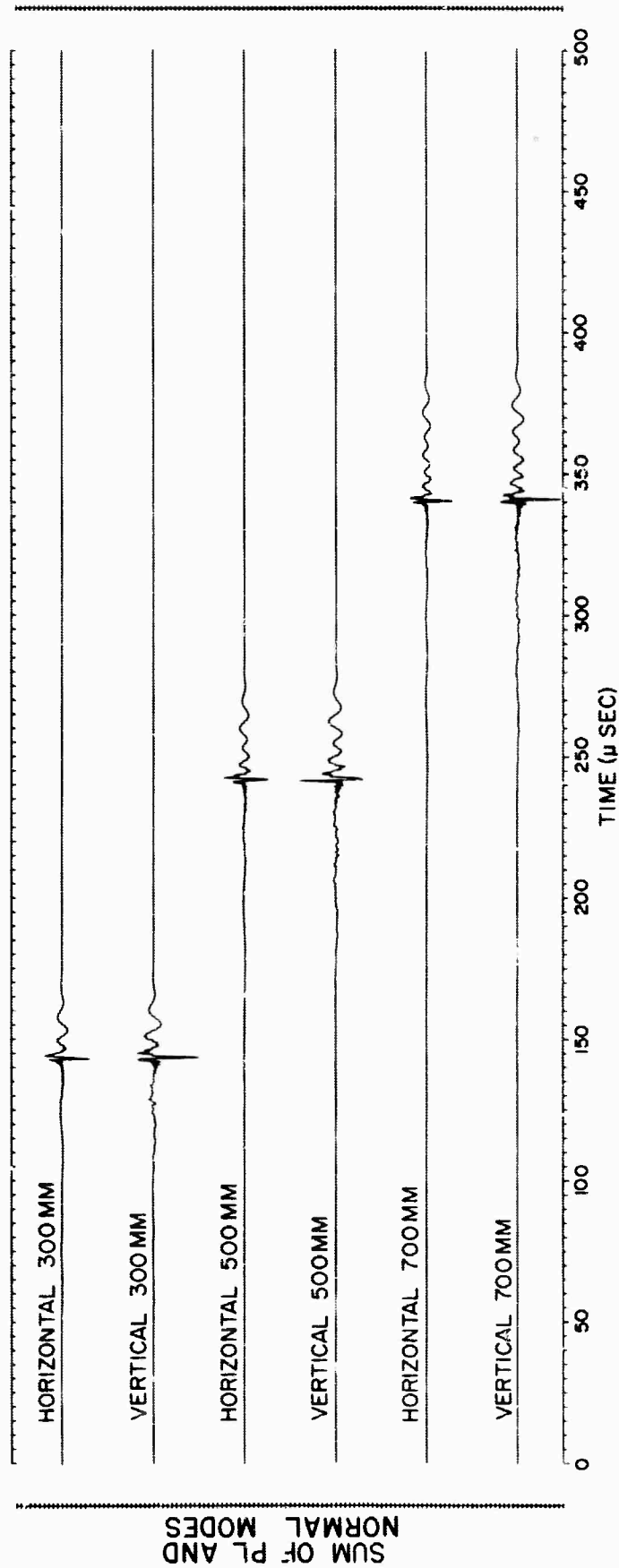


Figure 11. Horizontal and Vertical Theoretical Seismograms --Distance Range 300-700 mm (unfiltered)

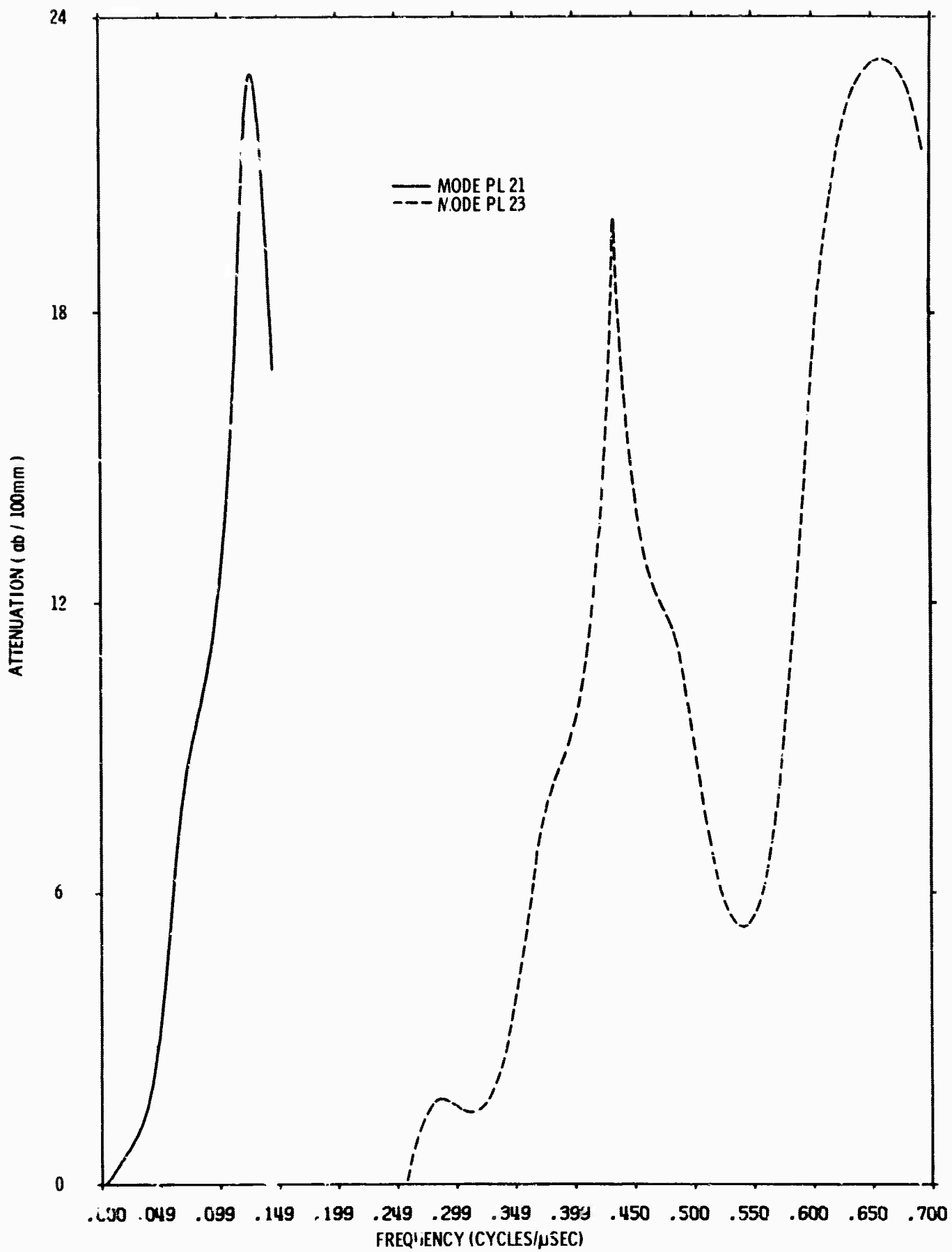


Figure 12. Spatial Attenuation Rate for Leaky Modes PL_{21} and PL_{23} as a Function of Frequency

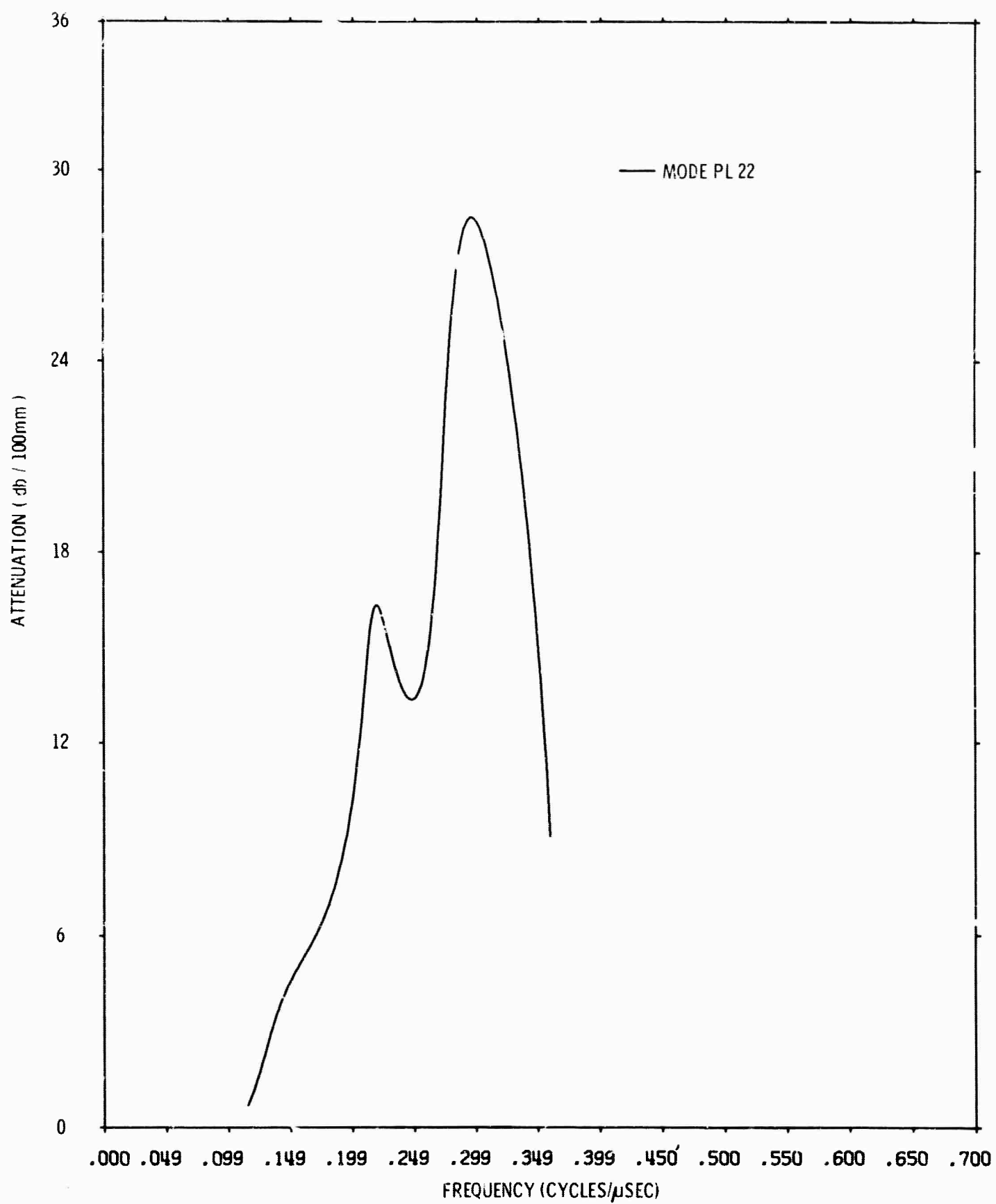


Figure 13. Spatial Attenuation Rate for Leaky Modes PL₂₂ as a Function of Frequency

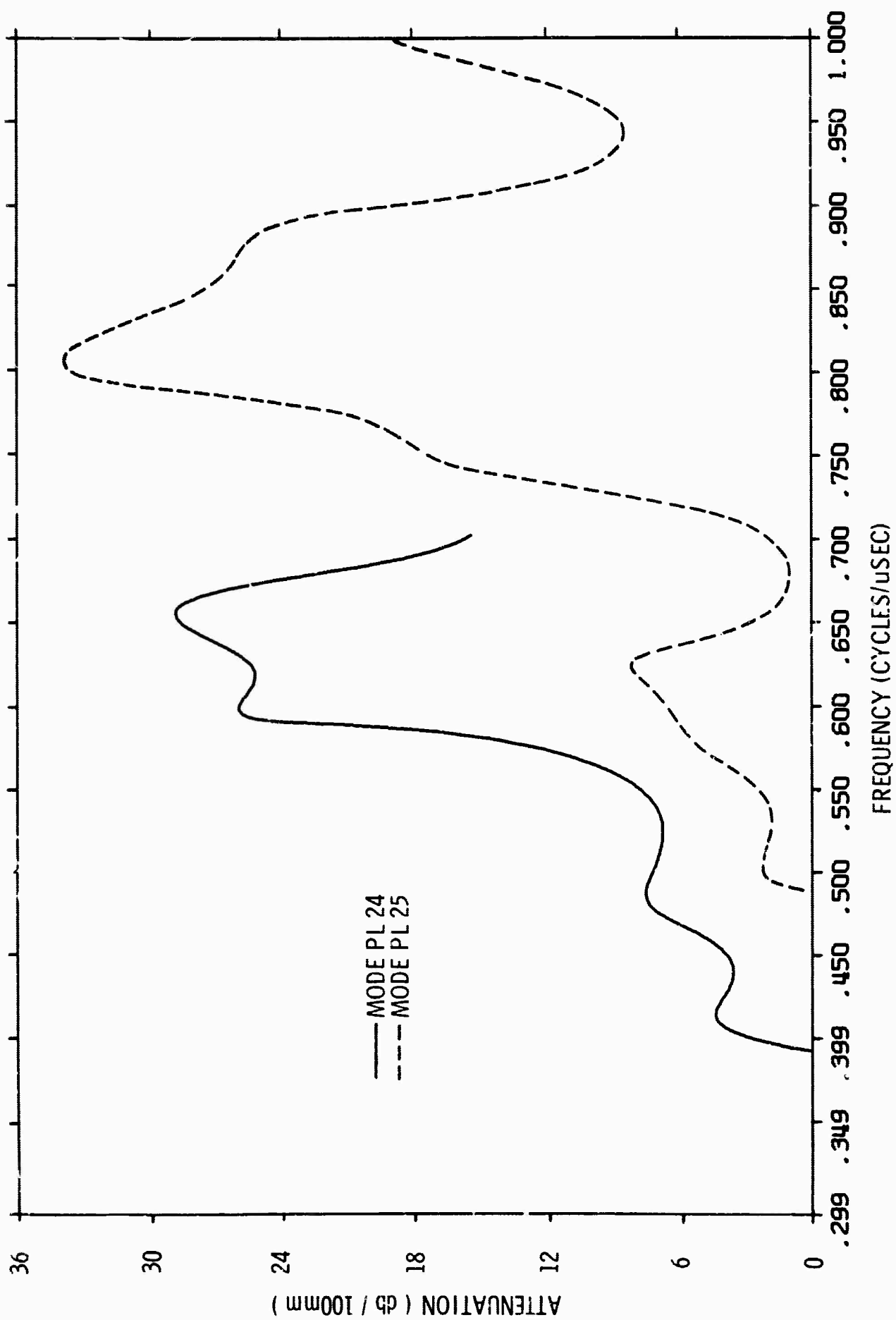


Figure 14. Spatial Attenuation Rate for Leaky Modes PL₂₄ and PL₂₅ as a Function of Frequency

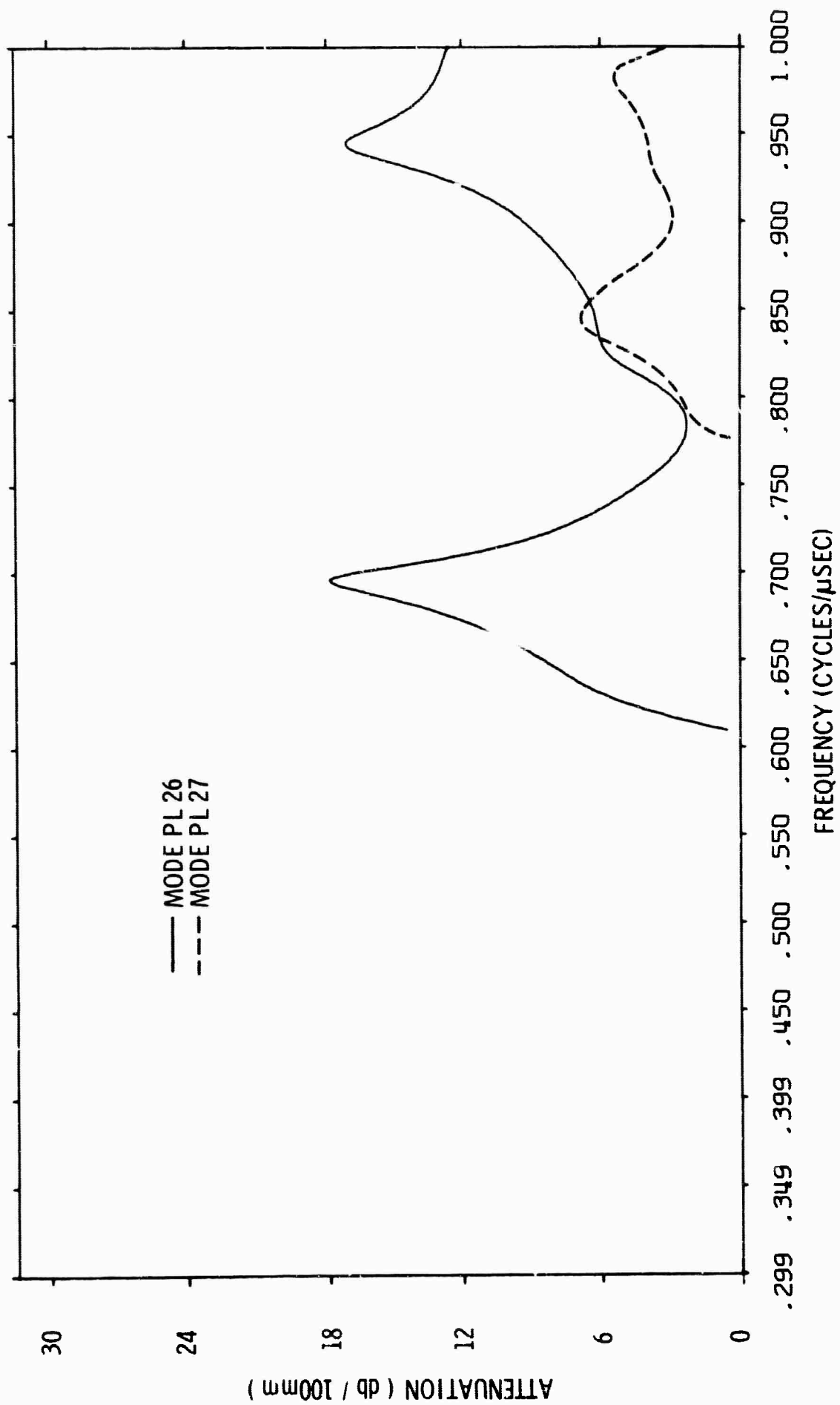


Figure 15. Spatial Attenuation Rate for Leaky Modes PL₂₆ and PL₂₇ as a Function of Frequency

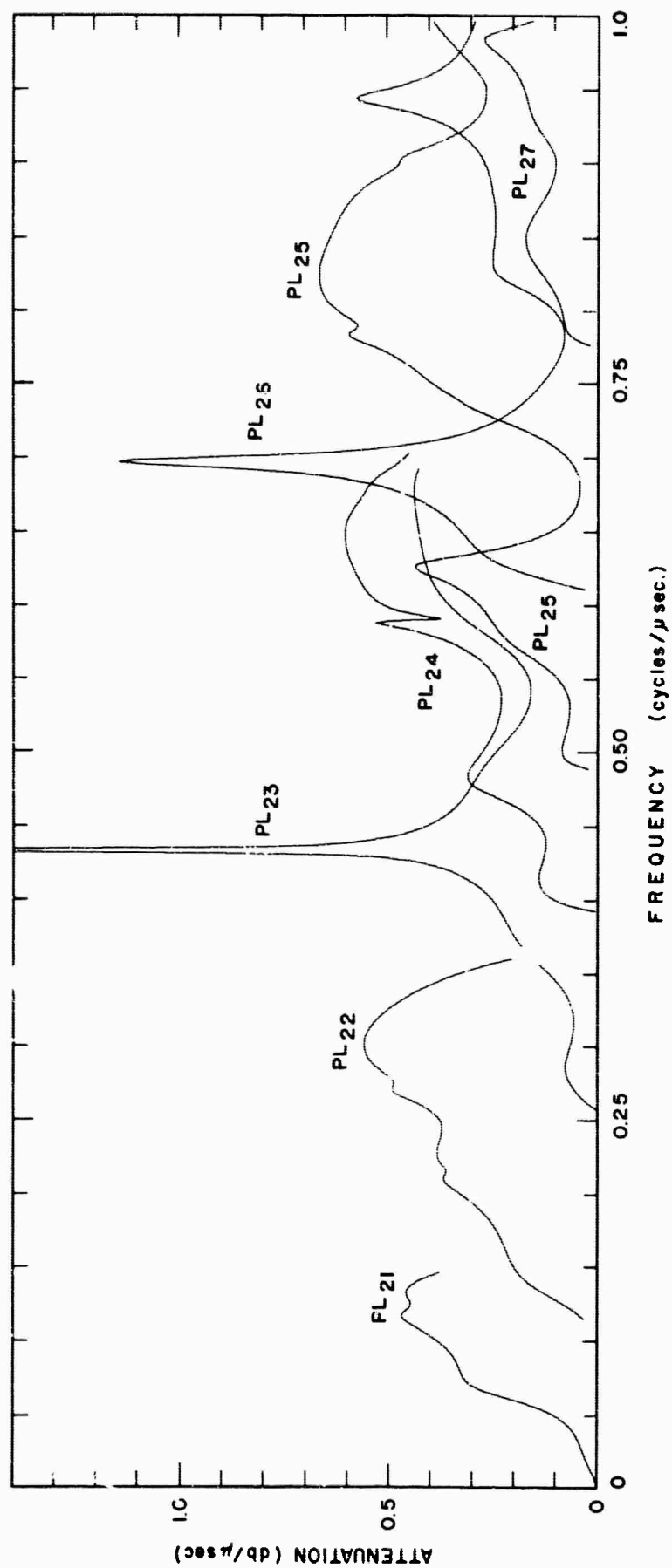


Figure 16. Time Attenuation Rate for Leaky Modes PL_{21} Through PL_{27} as a Function of Frequency

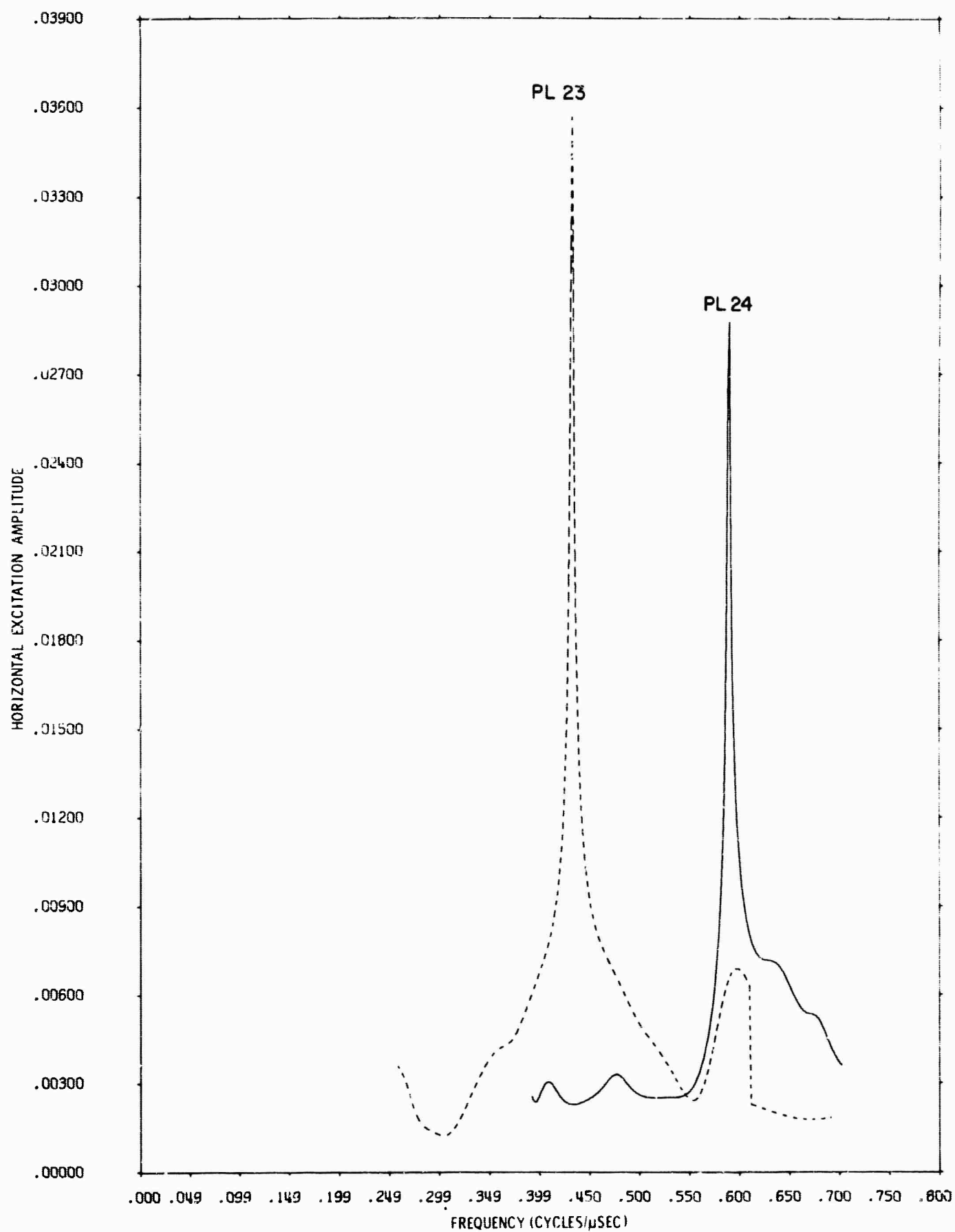


Figure 17. Horizontal Leaky Mode Excitation Functions (PL_{23} and PL_{24})

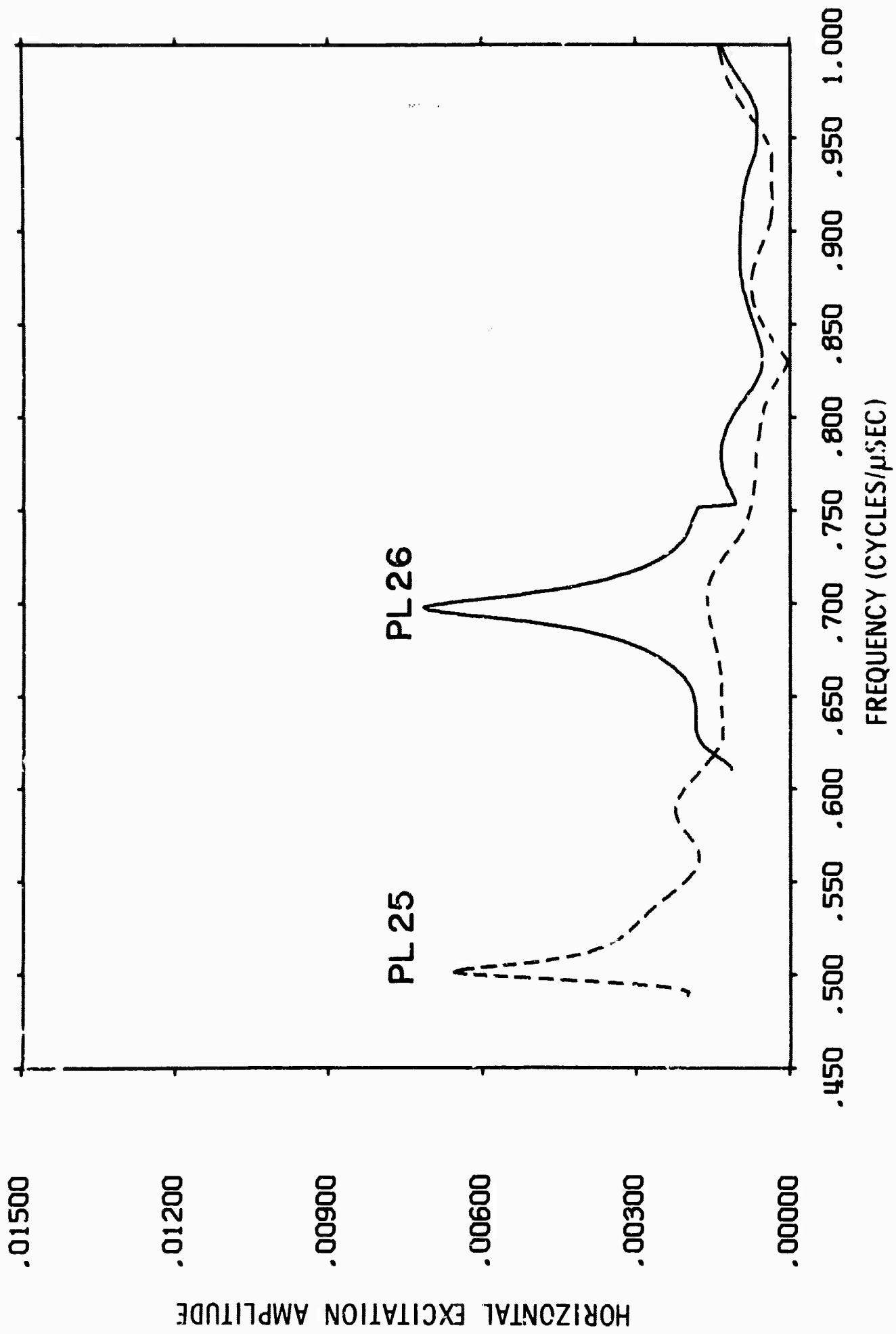


Figure 18. Horizontal Leaky Mode Excitation Functions (PL_{25} and PL_{26})

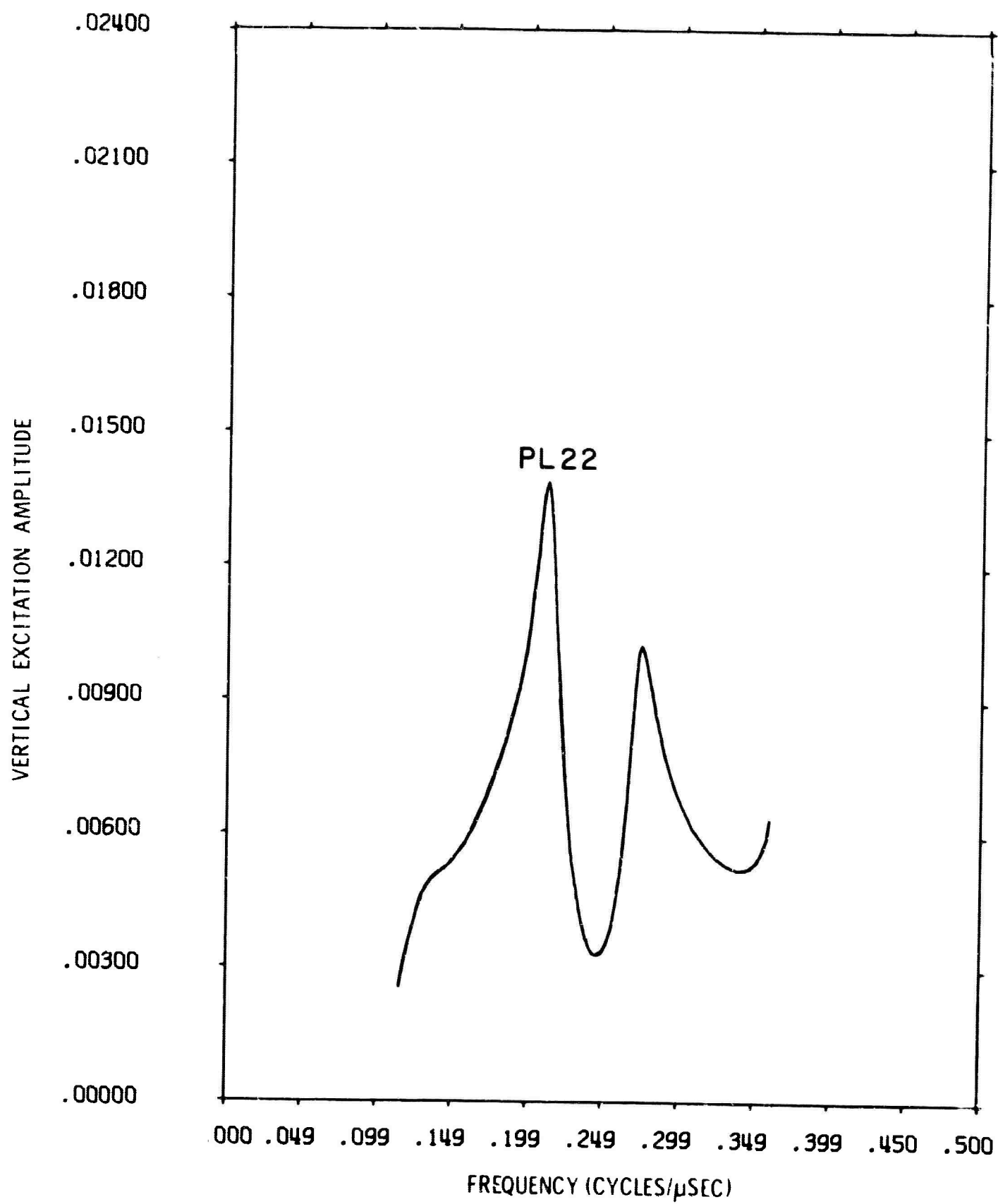


Figure 20. Vertical Leaky Mode Excitation Functions (PL₂₂)

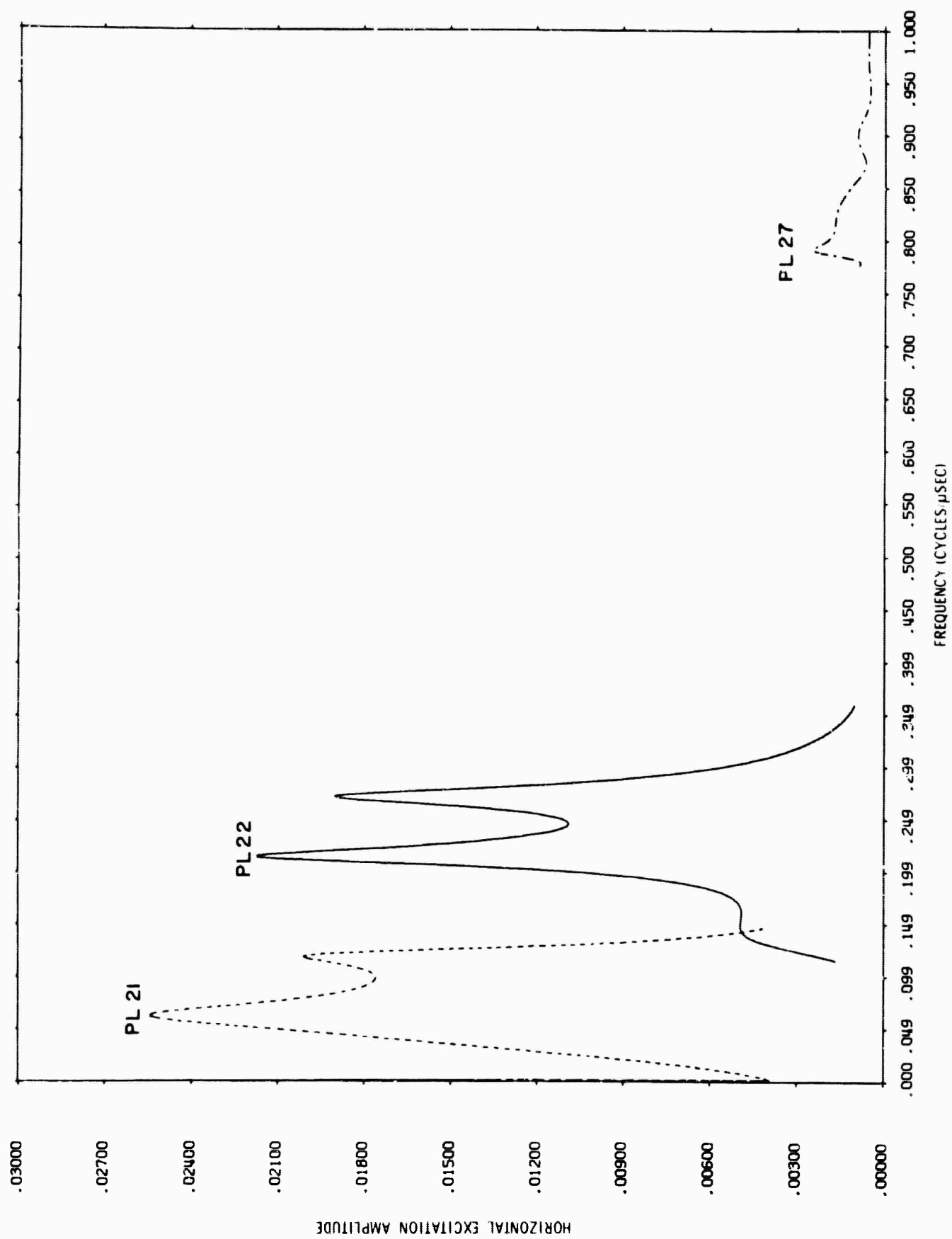


Figure i9. Horizontal Leaky Mode Excitation Function (PL_{21} , PL_{22} and PL_{27})

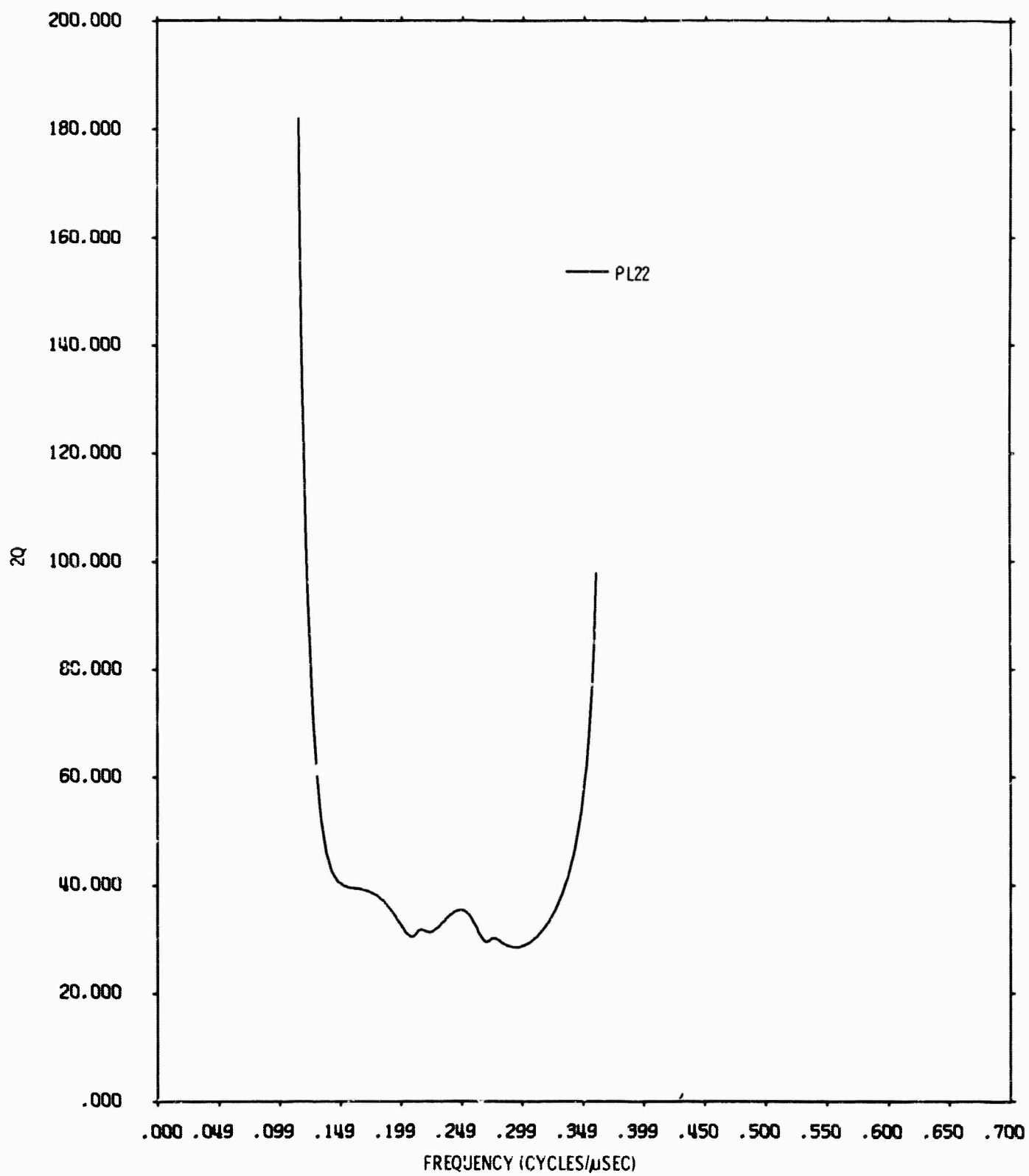


Figure 21. $2Q$ for Leaky Mode PL_{22}

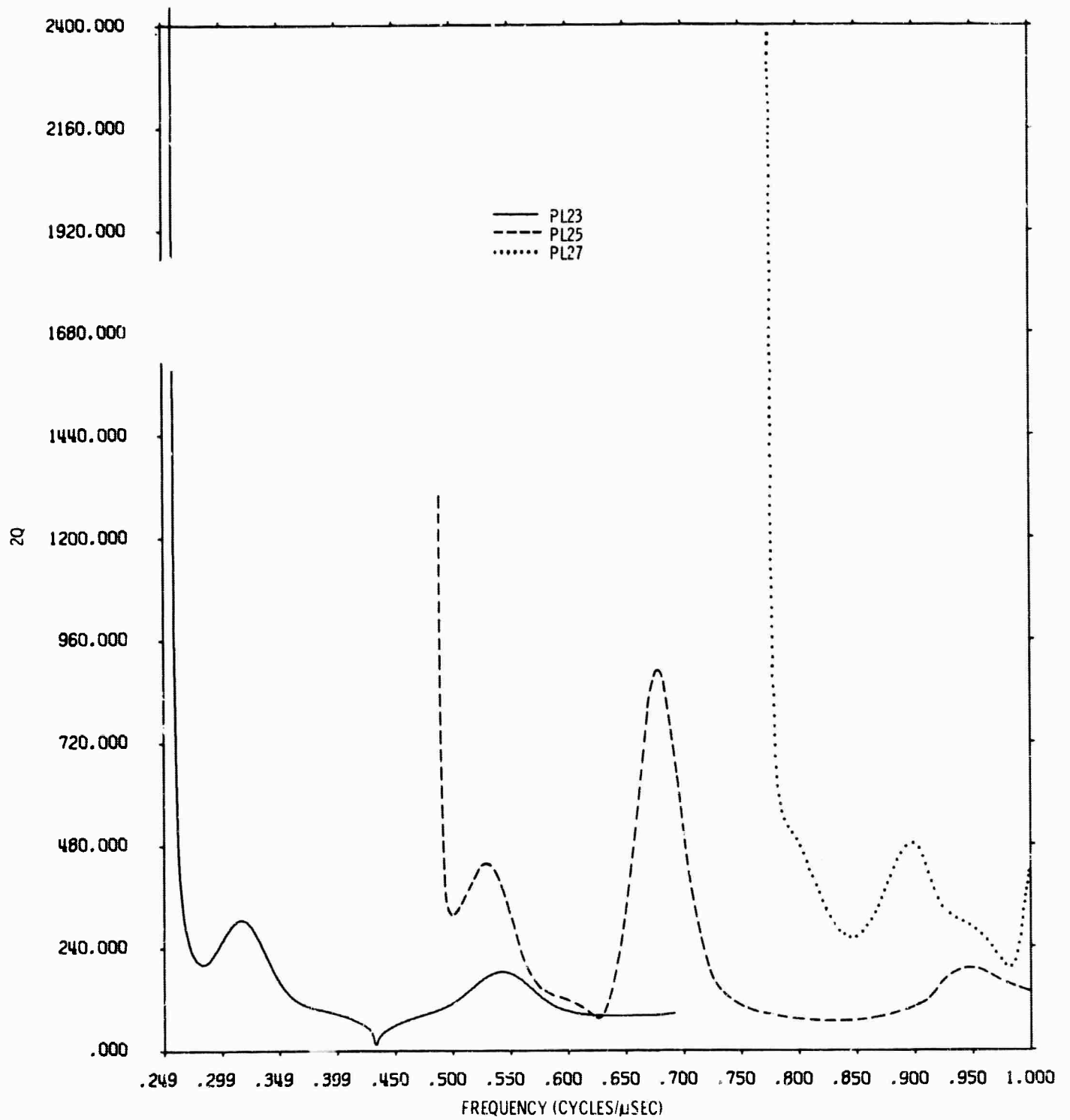


Figure 22. 2Q for Leaky Modes PL_{23} , PL_{25} and PL_{27}

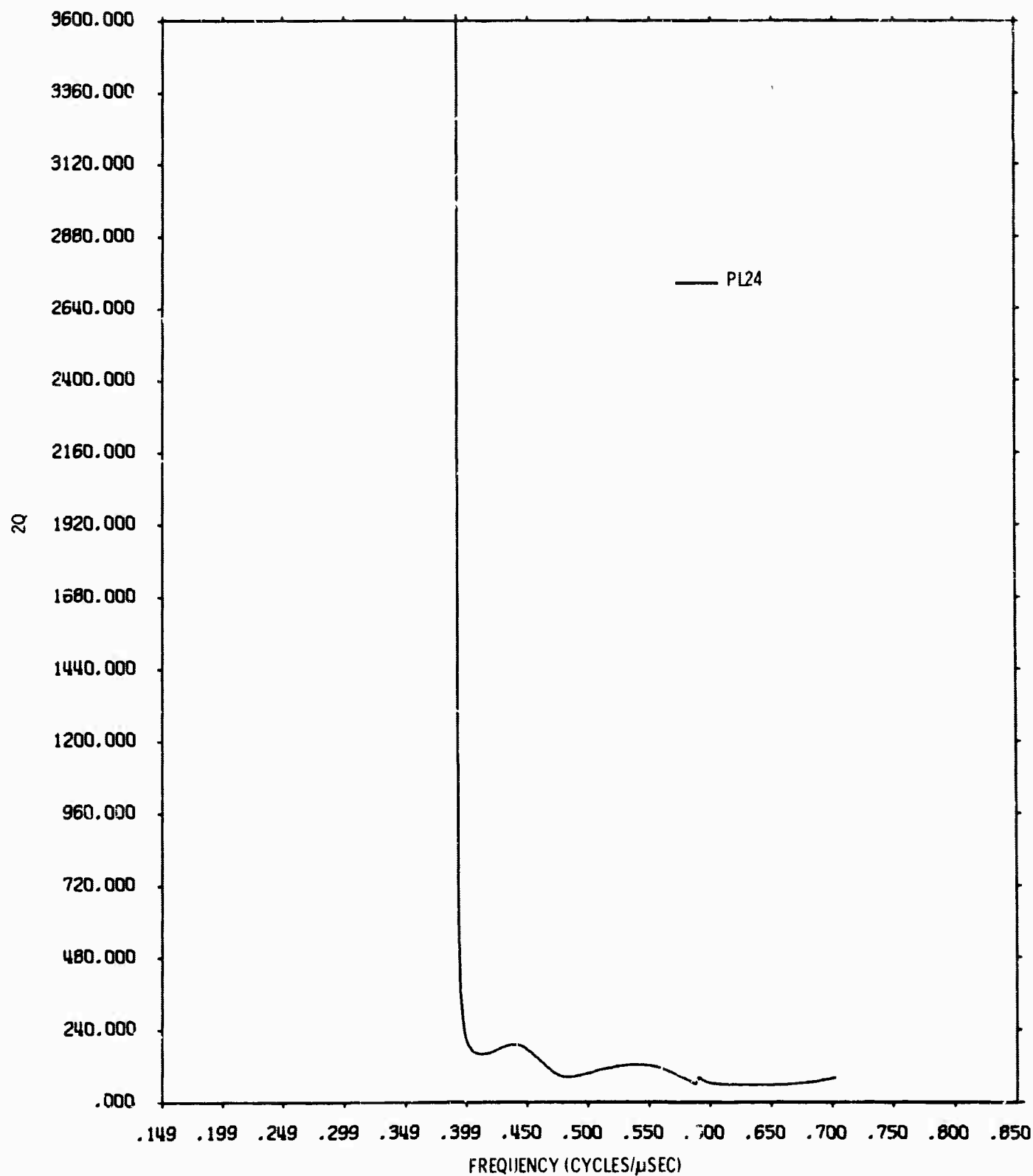


Figure 23. 2Q for Leaky Mode PL₂₄

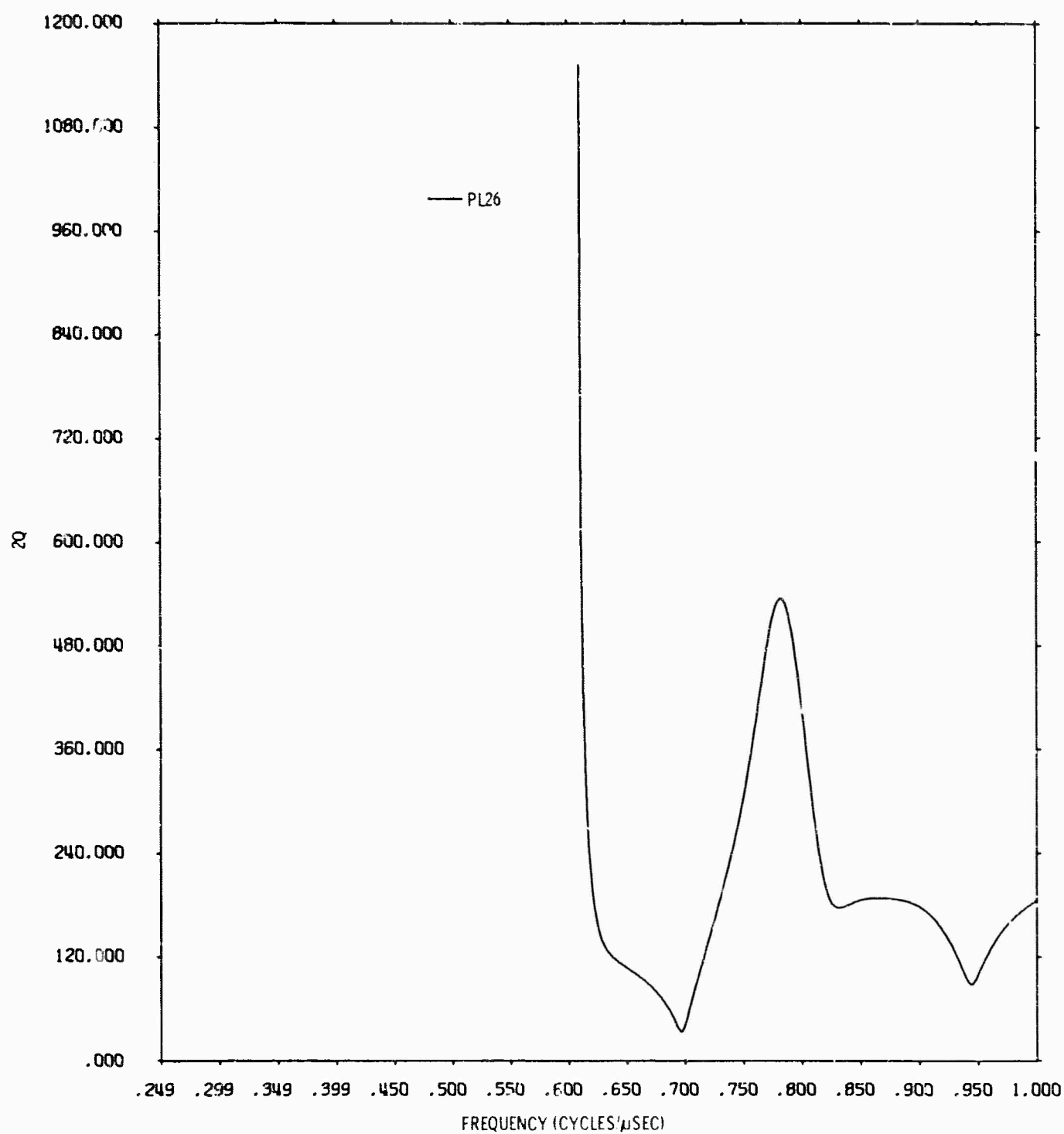


Figure 24. 2Q for Leaky Mode PL₂₆



Figure 25. Horizontal Modal Seismograms for Leaky Modes
PL₂₁ Through PL₂₇ at 300 mm

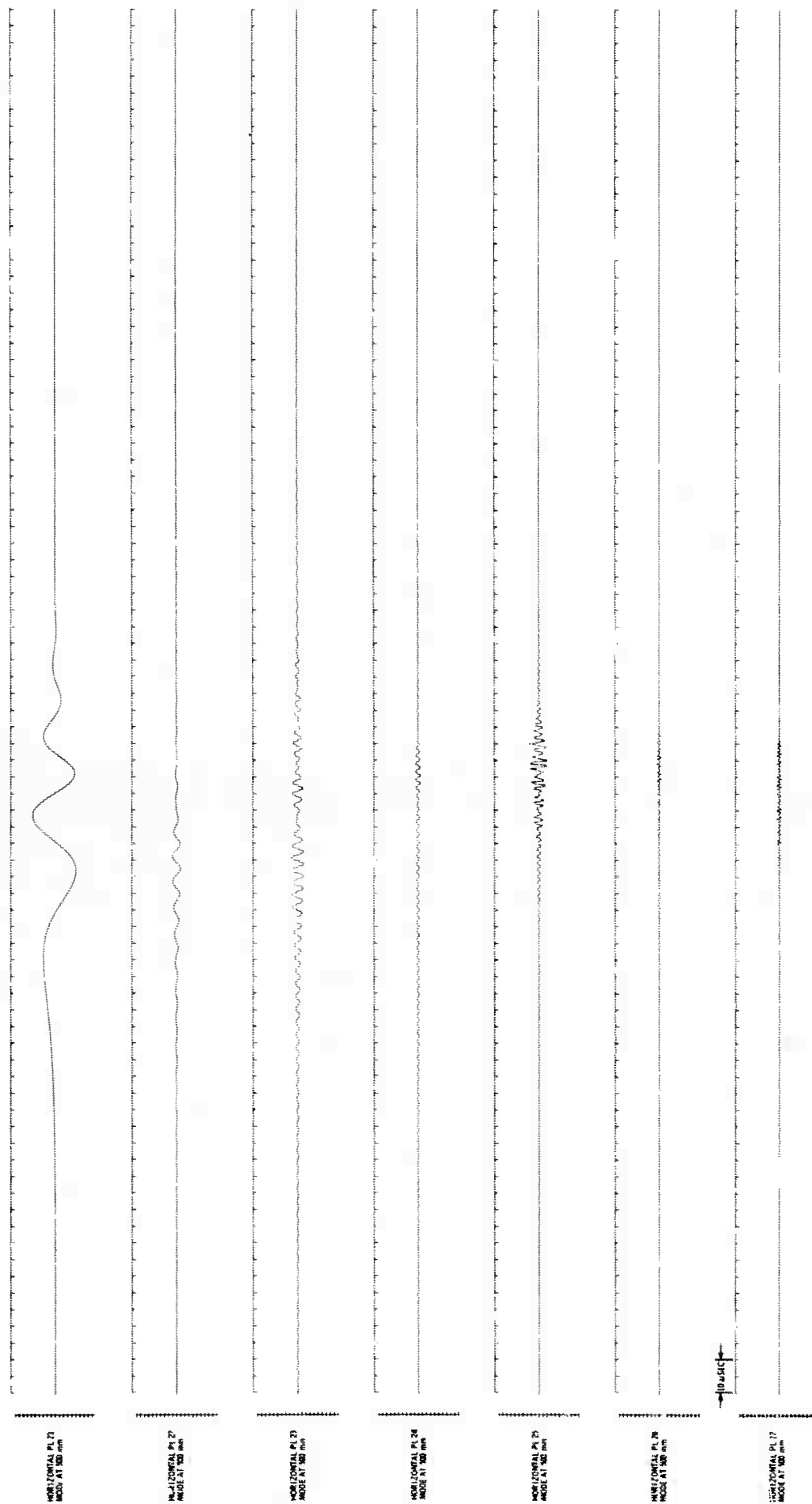


Figure 26. Horizontal Modal Seismograms for Leaky Modes
 PL₂₁ Through PL₂₇ at 500 mm

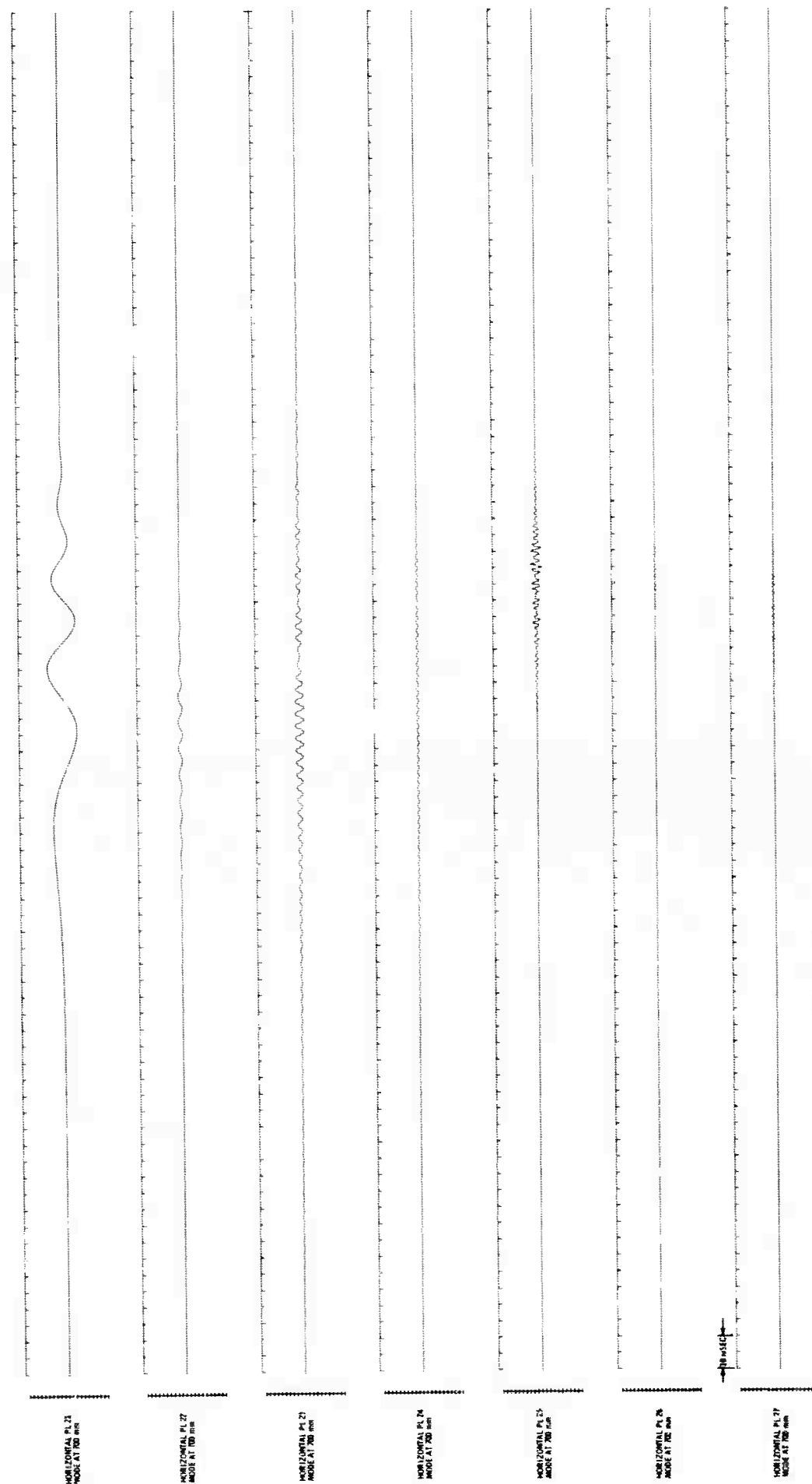


Figure 27. Horizontal Modal Seismograms for Leaky Modes
PL₂₁ Through PL₂₇ at 700 mm

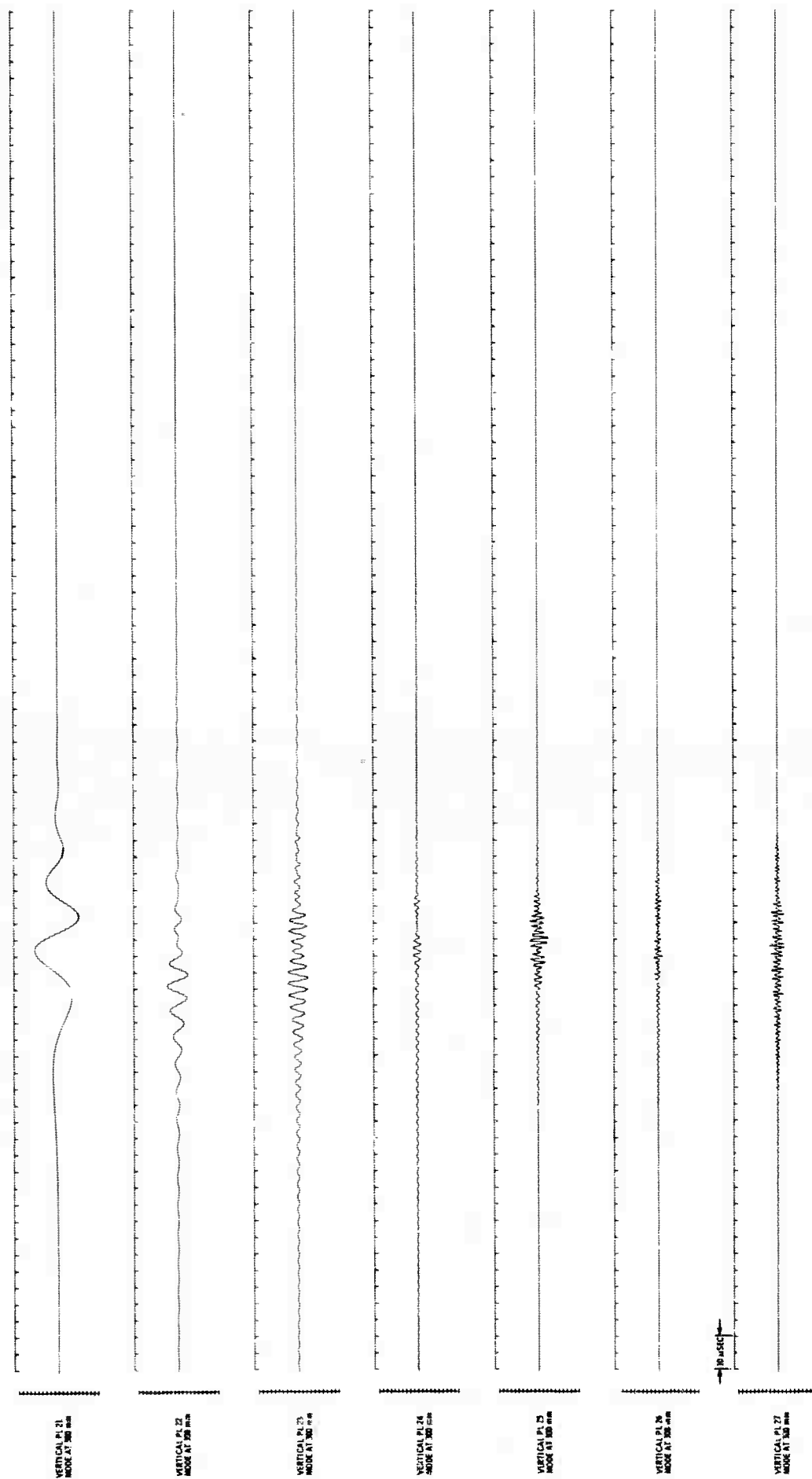


Figure 28. Vertical Modal Seismograms for Leaky Modes PL₂₁ Through PL₂₇ at 300 mm

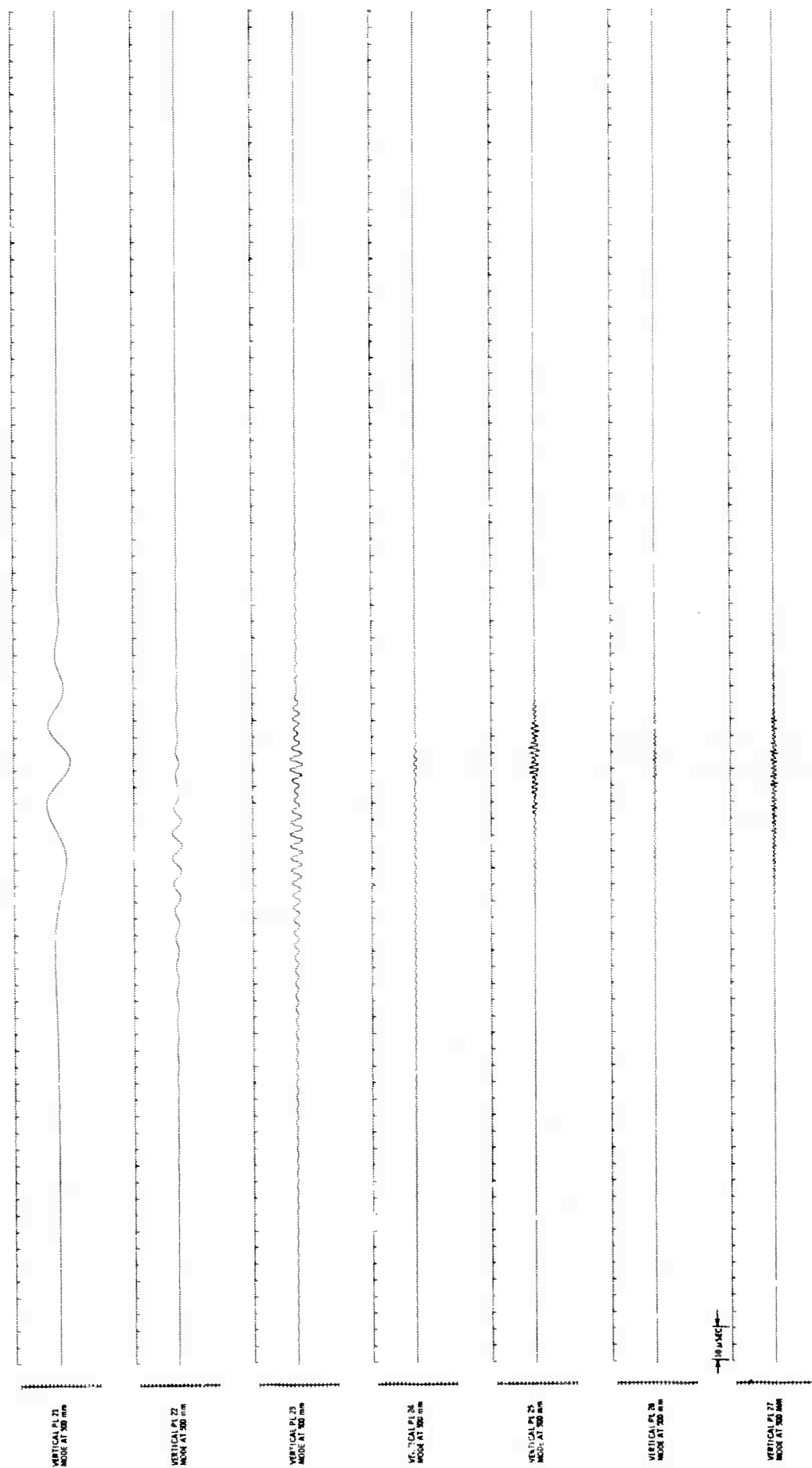


Figure 29. Vertical Modal Seismograms for Leaky Modes PL₂₁ Through PL₂₇ at 500 mm

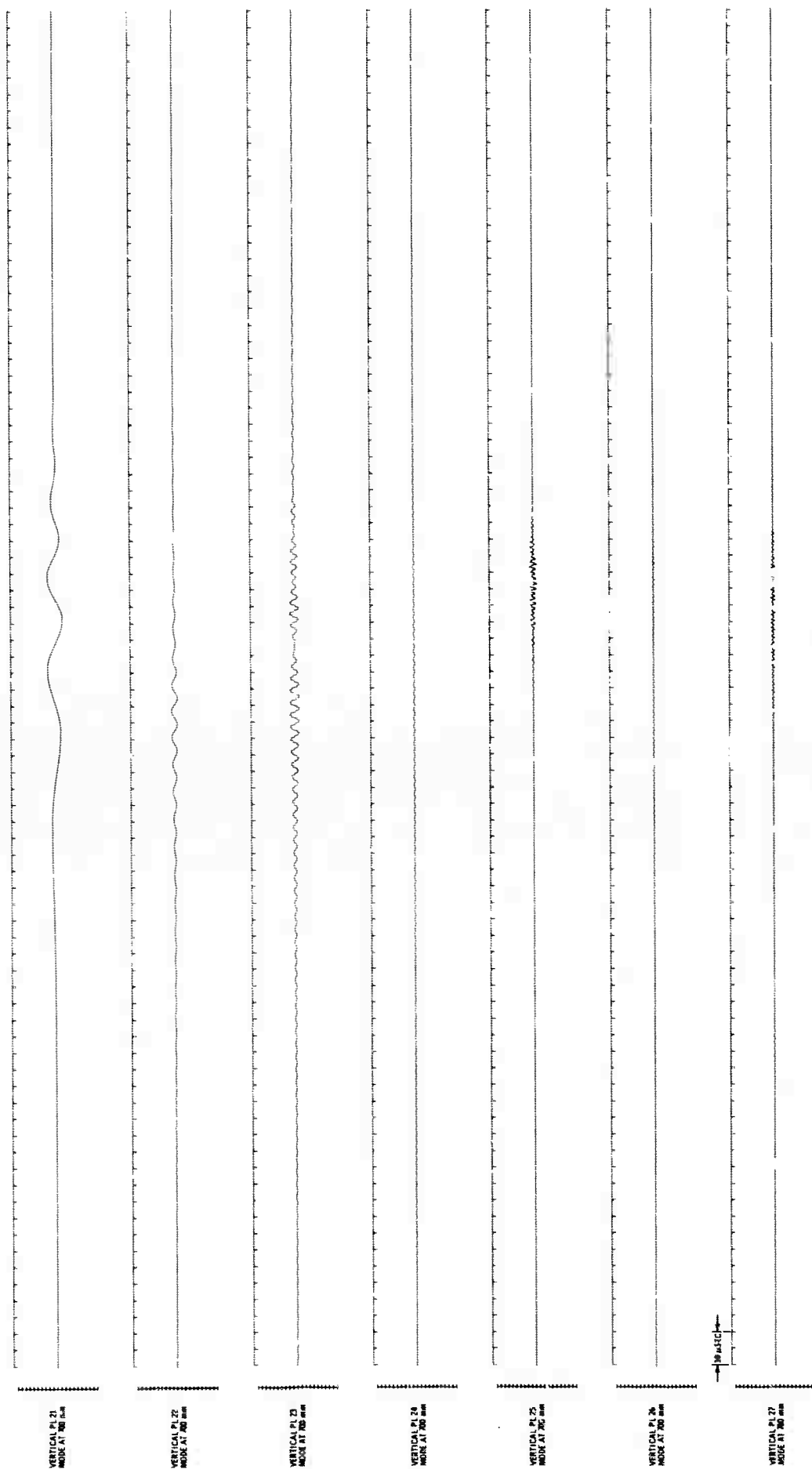


Figure 30. Vertical Modal Seismograms for Leaky Modes PL_{21} Through PL_{27} at 700 nm

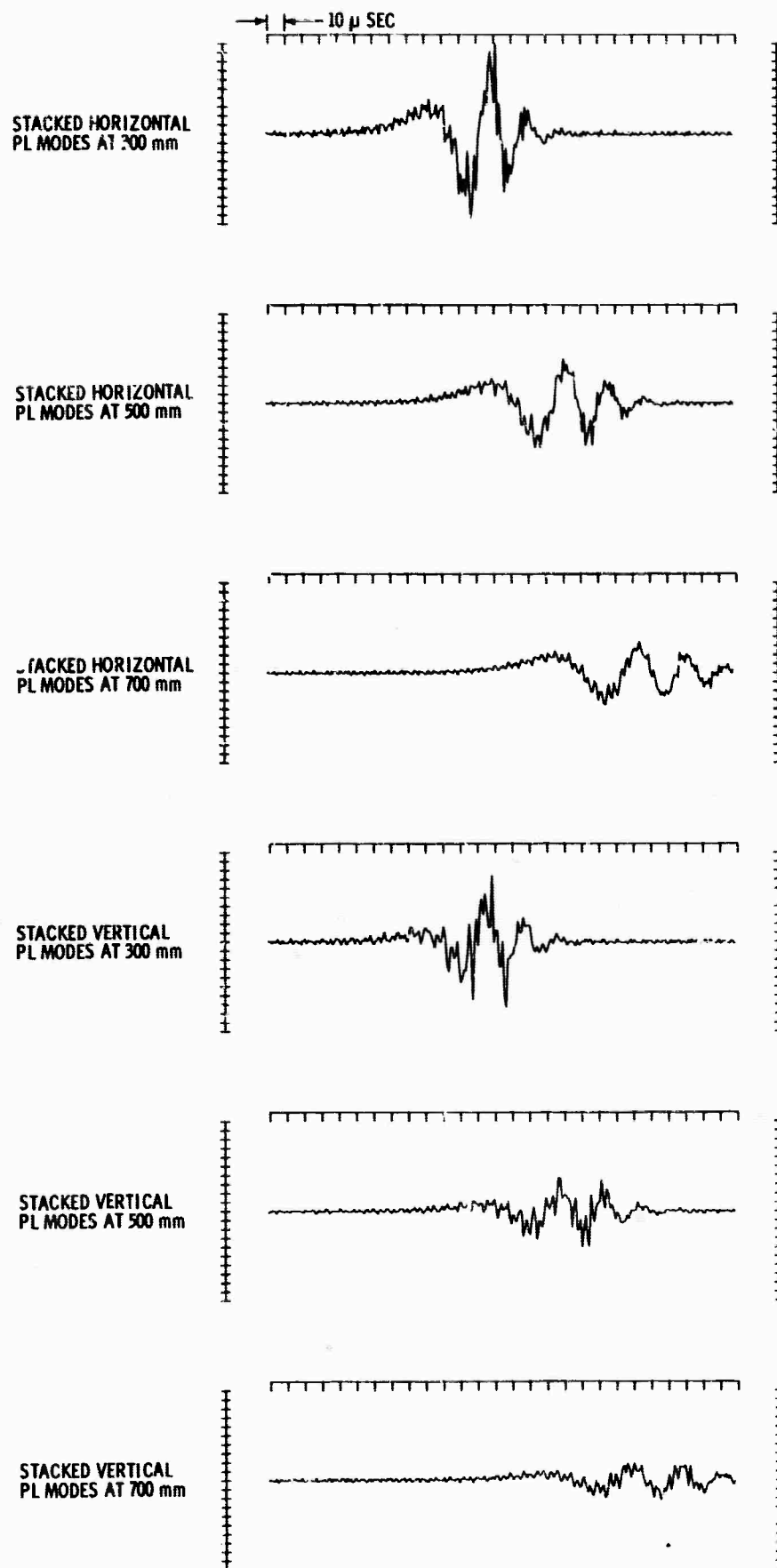


Figure 31. Horizontal and Vertical Leaky Mode Seismograms in the Distance Range 300-700 mm, Constructed by Summing All Seven PL Modes

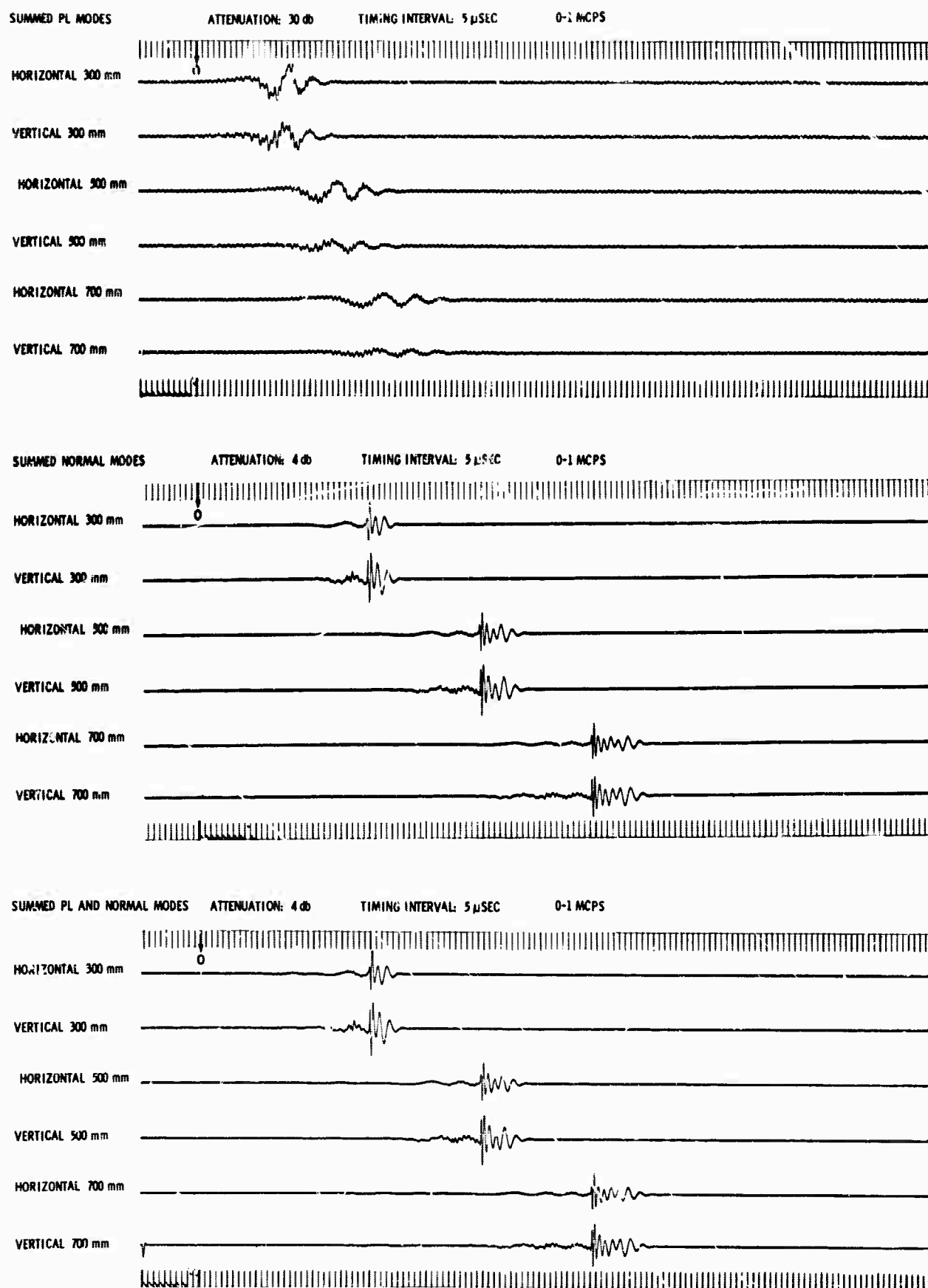


Figure 32. Sum of Leaky Modes, Normal Modes, and Leaky and Normal Modes in the Distance Range 300-700 mm (Unfiltered)

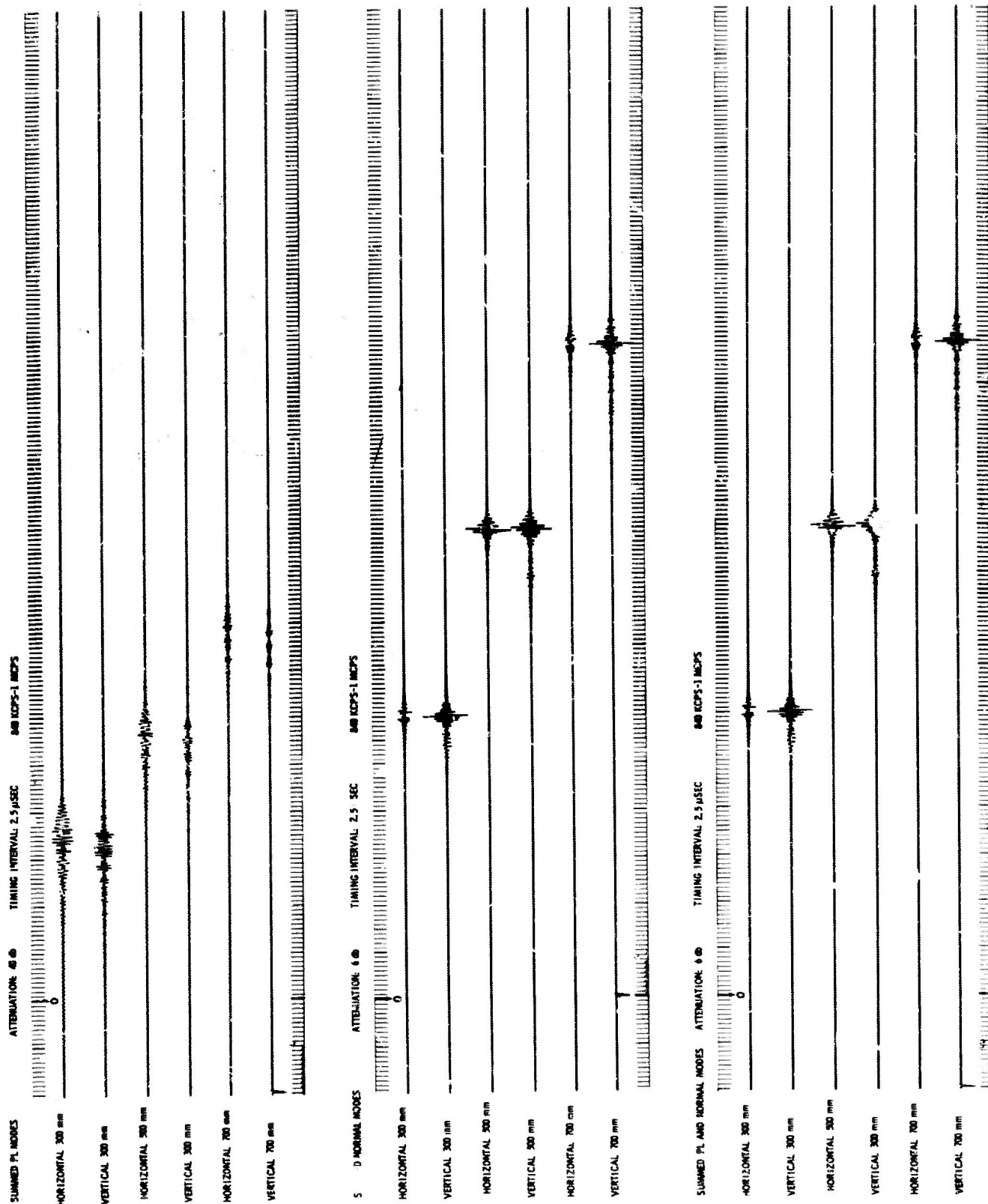


Figure 33. Sum of Leaky Modes, Normal Modes, and Leaky and Normal Modes in the Distance Range 300-700 mm (Primarily Composed of Higher-Order Modes Due to Filtering)

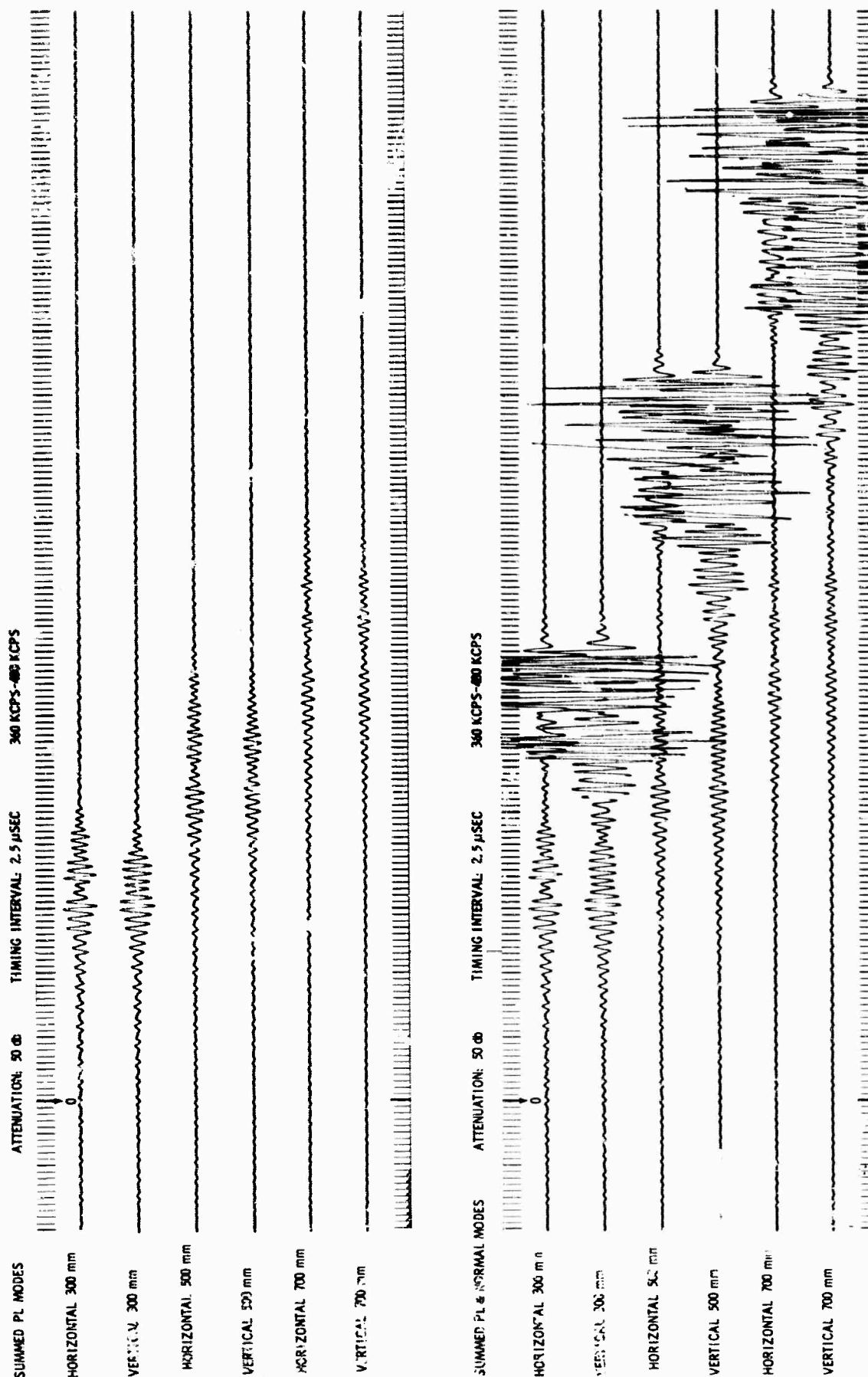


Figure 34. Sum of Leaky Modes and Normal Modes in the Distance Range 300-700 mm. This suite of records exhibits the initial sinusoidal appearance of the seismogram due to the leaky modes

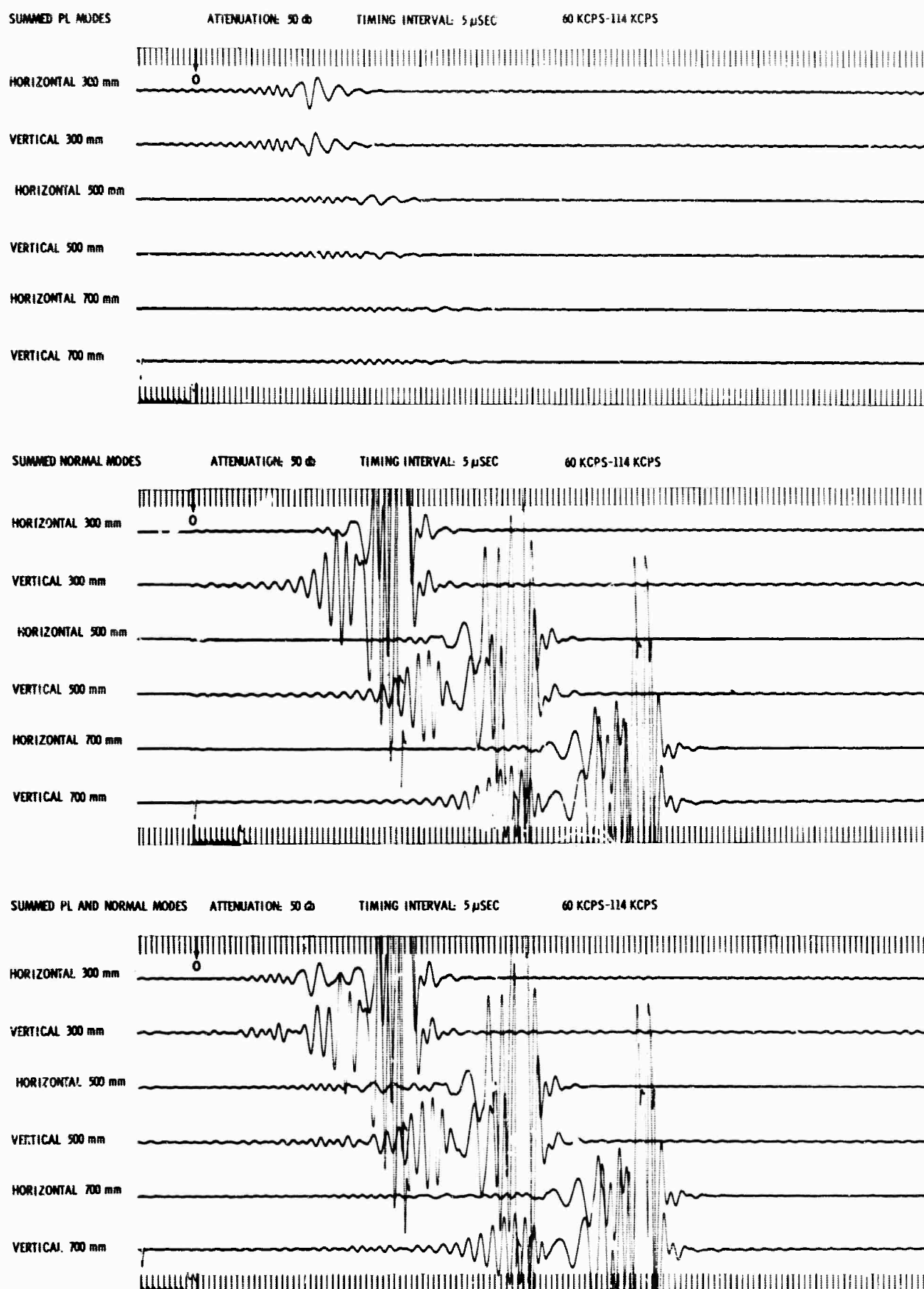


Figure 35. Sum of Leaky Modes, Normal Modes, and Leaky and Normal Modes in the Distance Range 300-700 mm. Most leaky-mode energy is contributed by the PL_{21} and PL_{22} modes

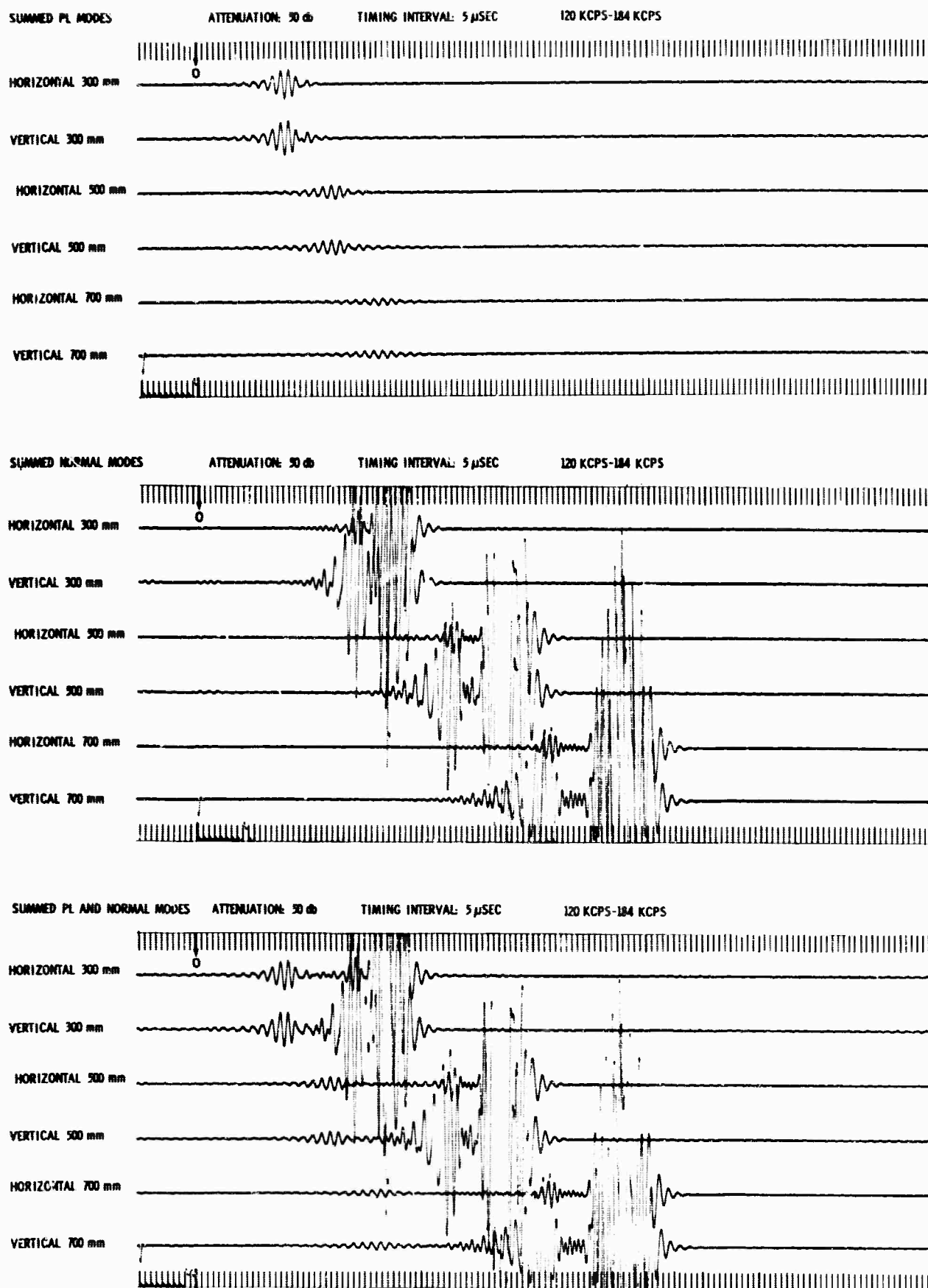


Figure 36. Sum of Leaky Modes, Normal Modes, and Leaky and Normal Modes in the Distance Range 300-700 mm. Most of the leaky-mode energy is due to the PL_{22} mode

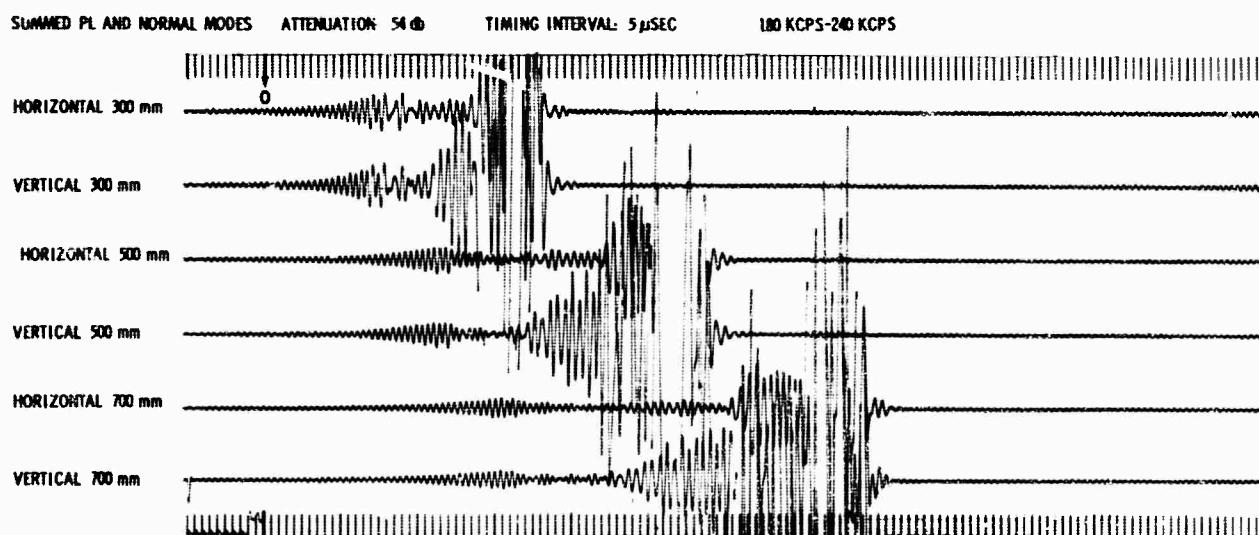
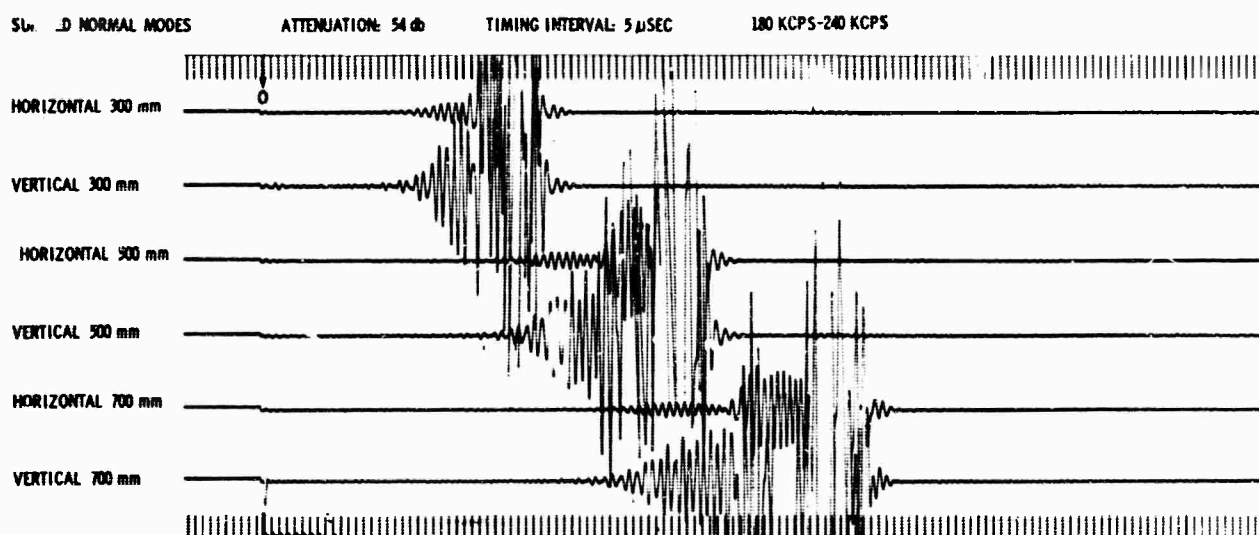
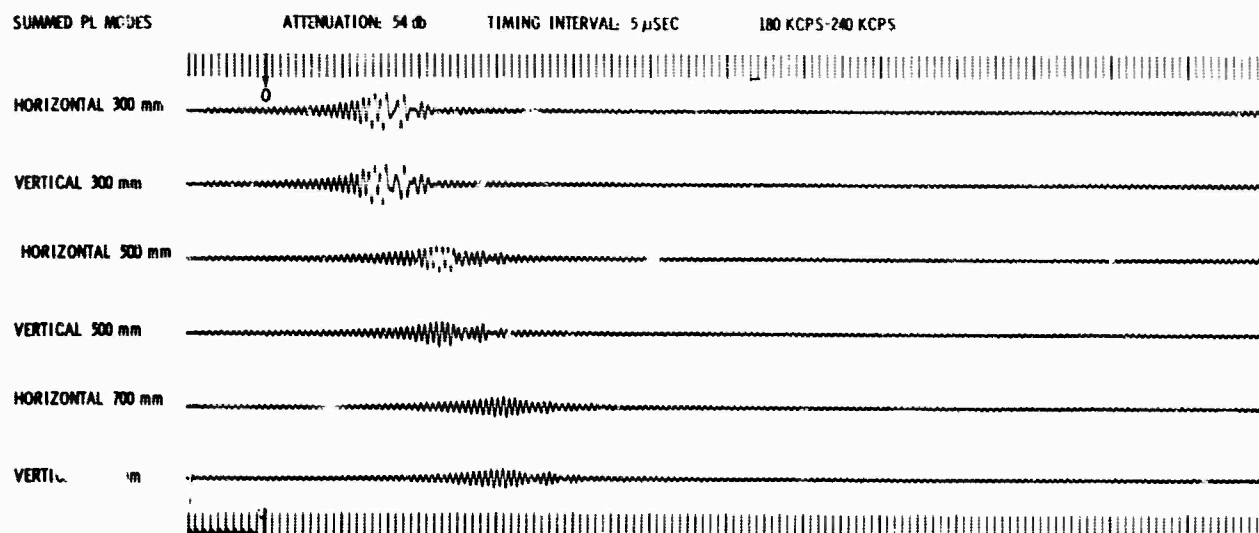


Figure 37. Sum of Leaky Modes, Normal Modes, and Leaky and Normal Modes in the Distance Range 300-700 mm. Most leaky-mode energy is contributed by PL_{22} and PL_{23}

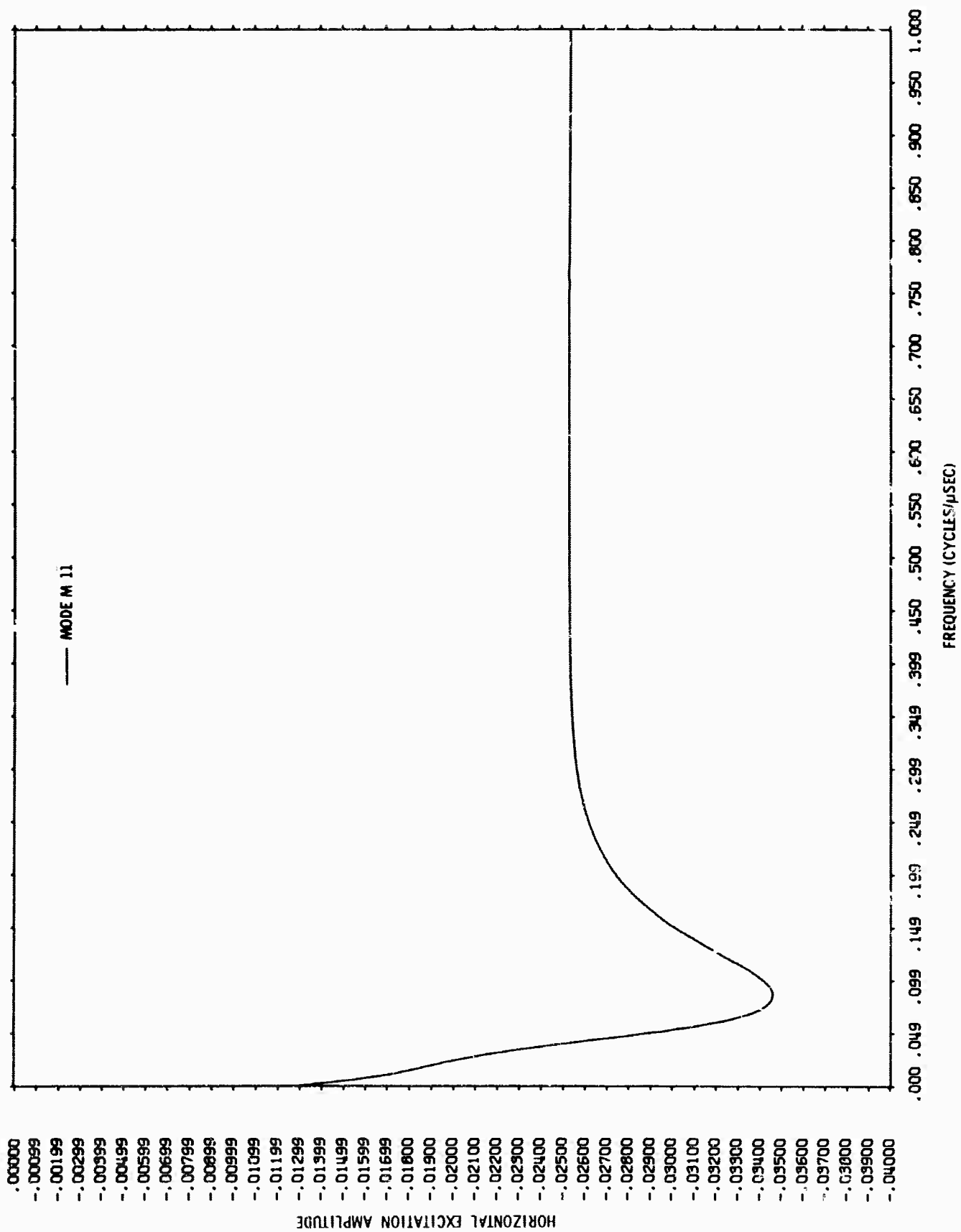


Figure 38. Horizontal Normal Mode Excitation Function for M_{11}

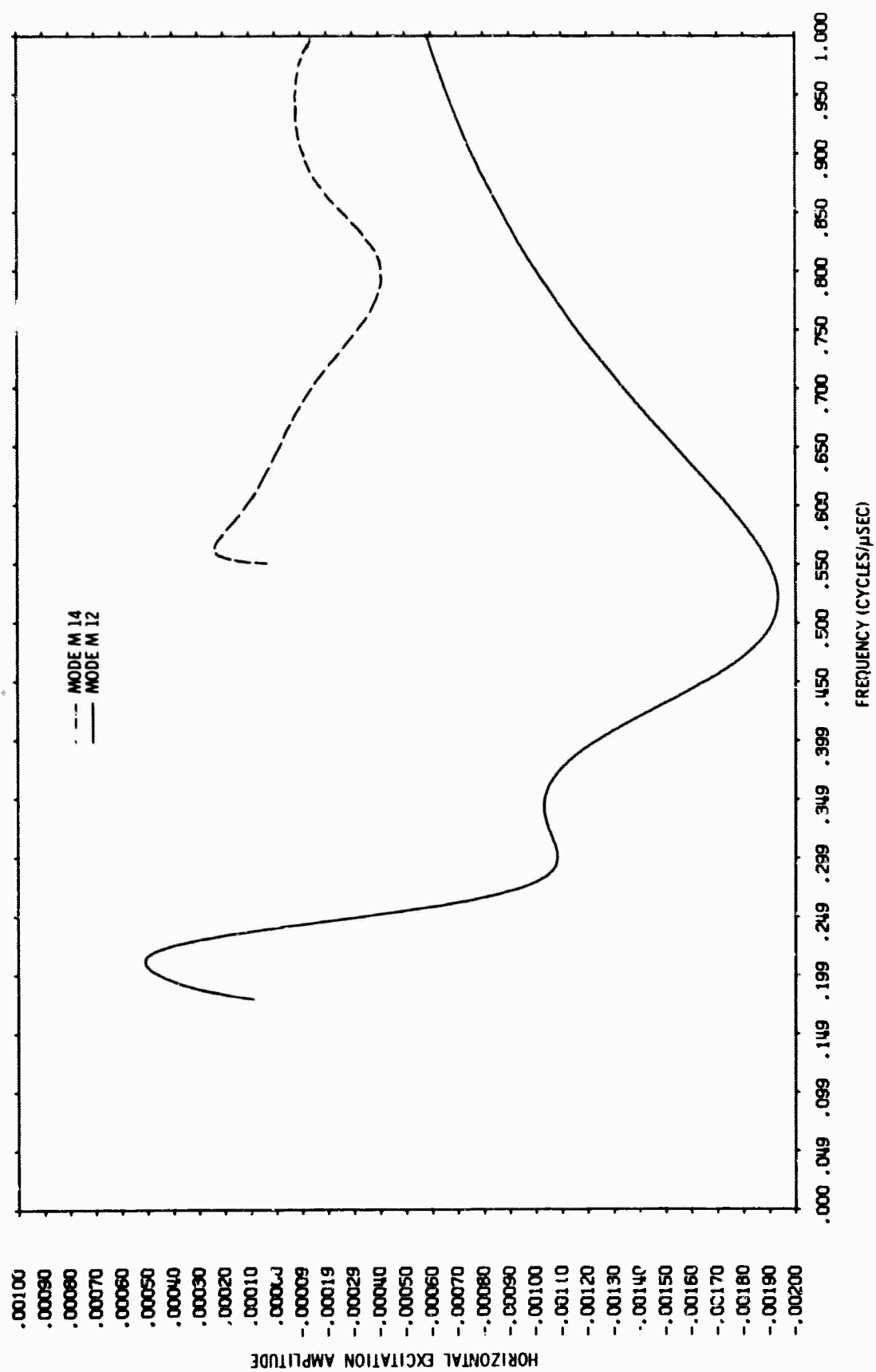


Figure 39. Horizontal Normal Mode Excitation Functions for M_{12} and M_{14}

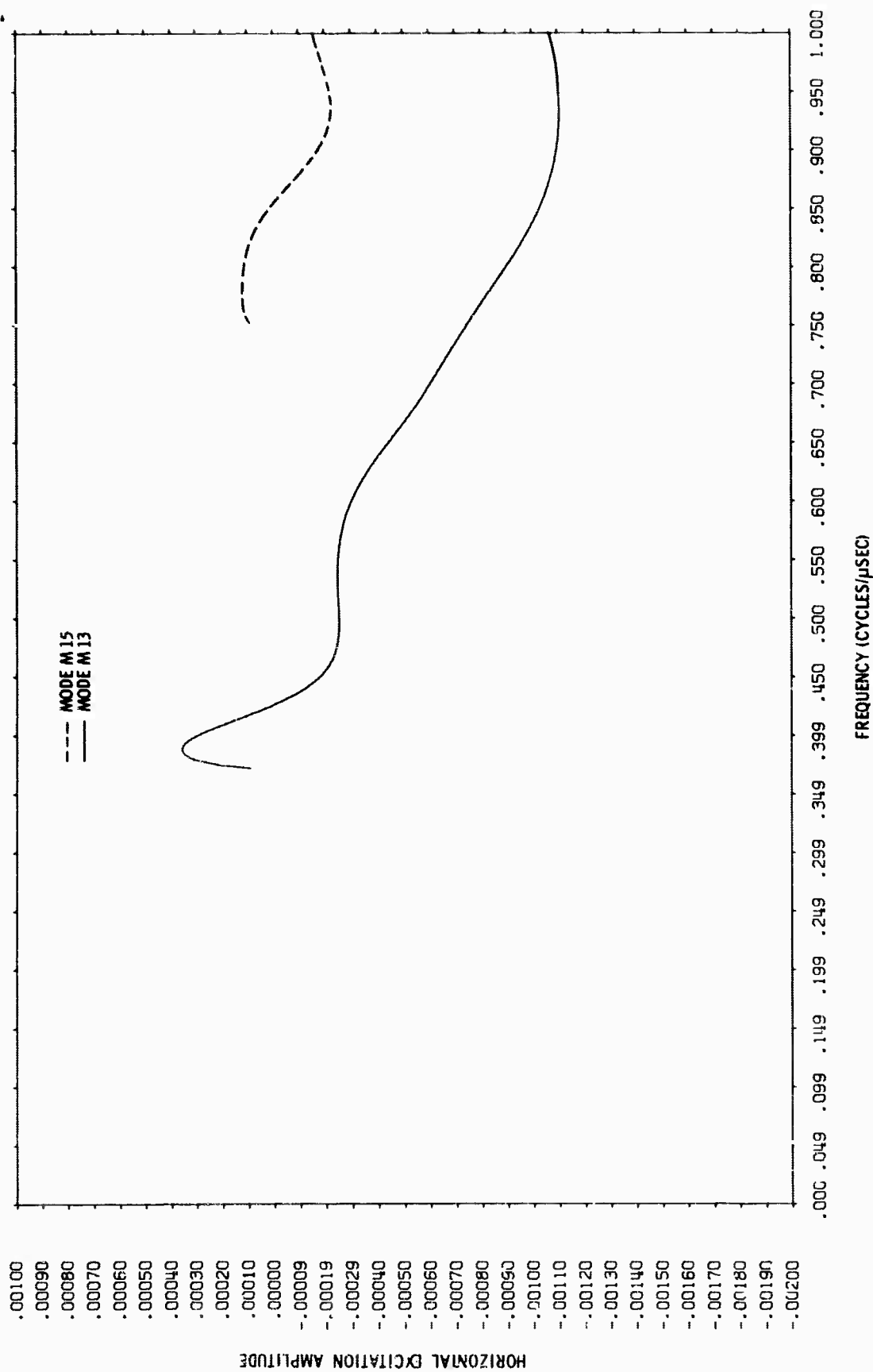


Figure 40. Horizontal Normal Mode Excitation Functions for M_{13} and M_{15}

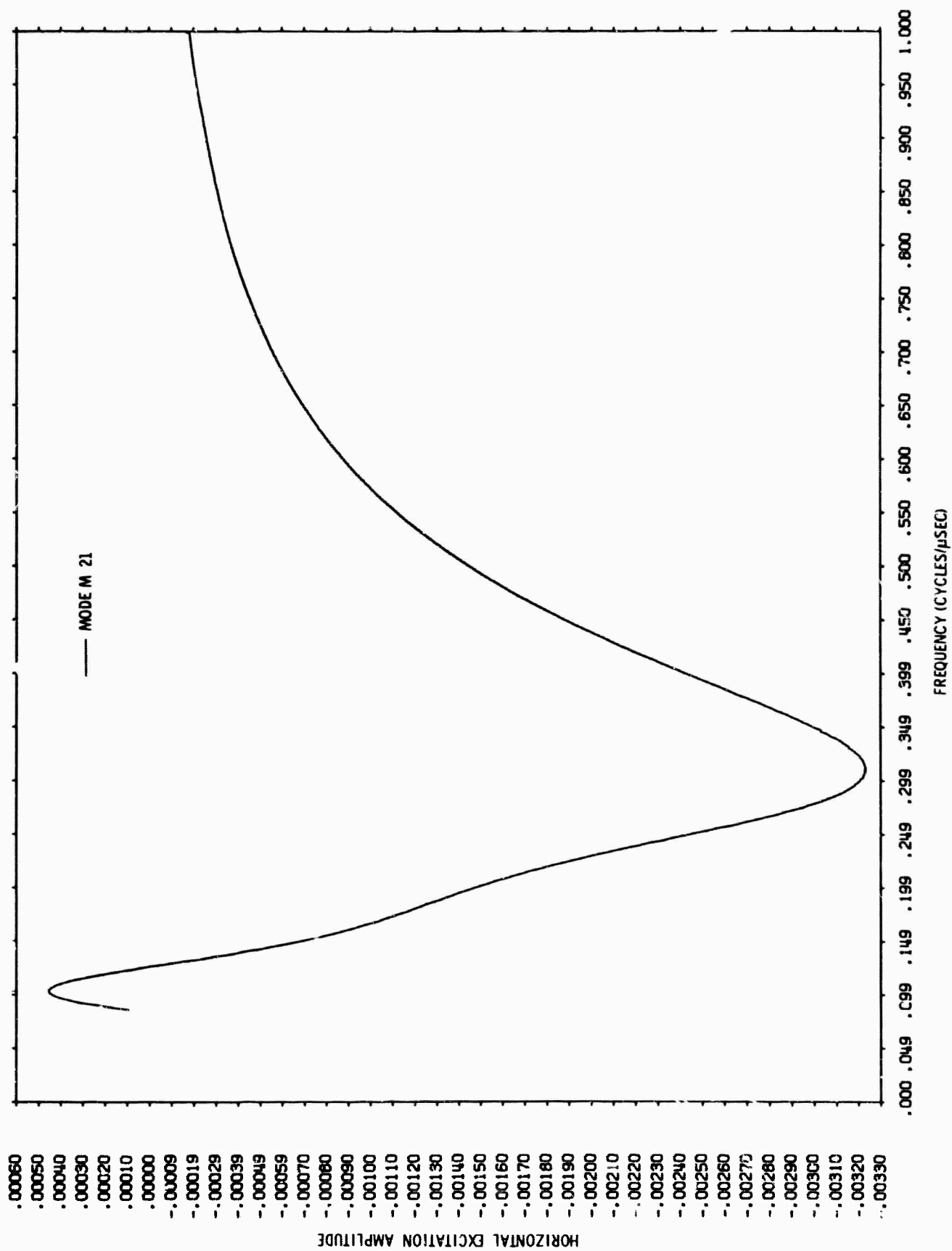


Figure 41. Horizontal Normal Mode Excitation Function for M_{21}

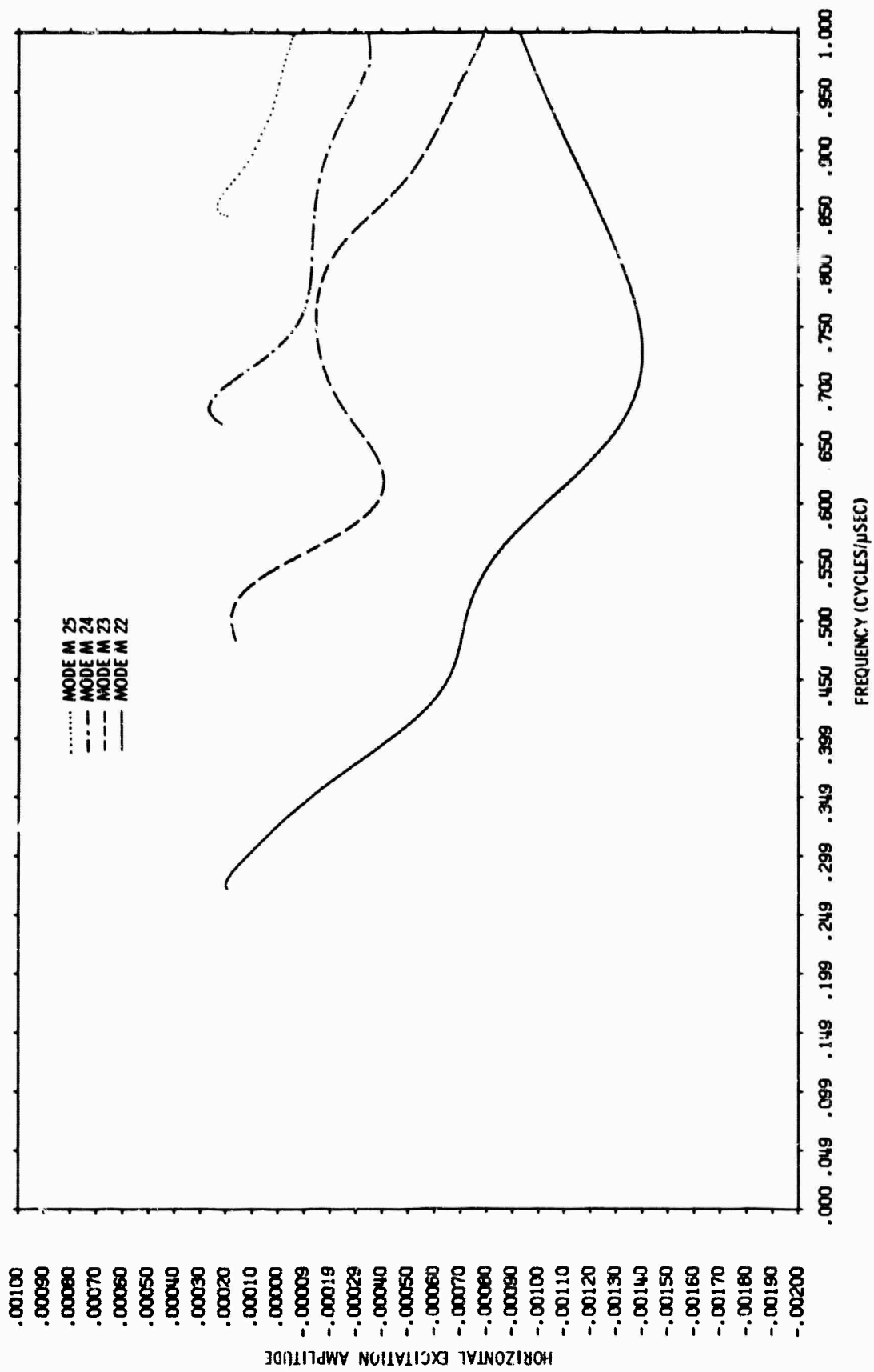


Figure 42. Horizontal Normal Mode Excitation Function for M_{22} , M_{23} , M_{24} , and M_{25}

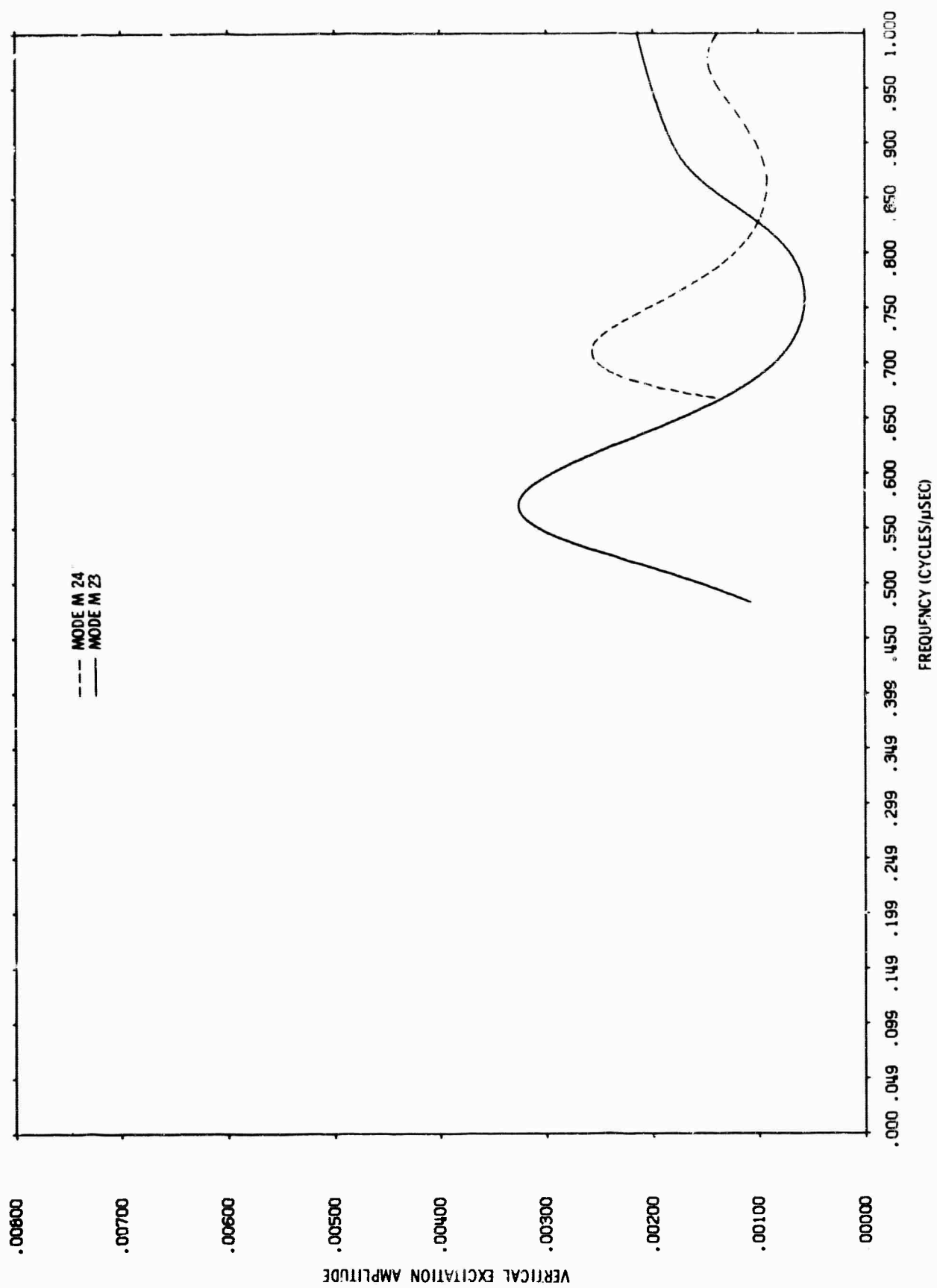
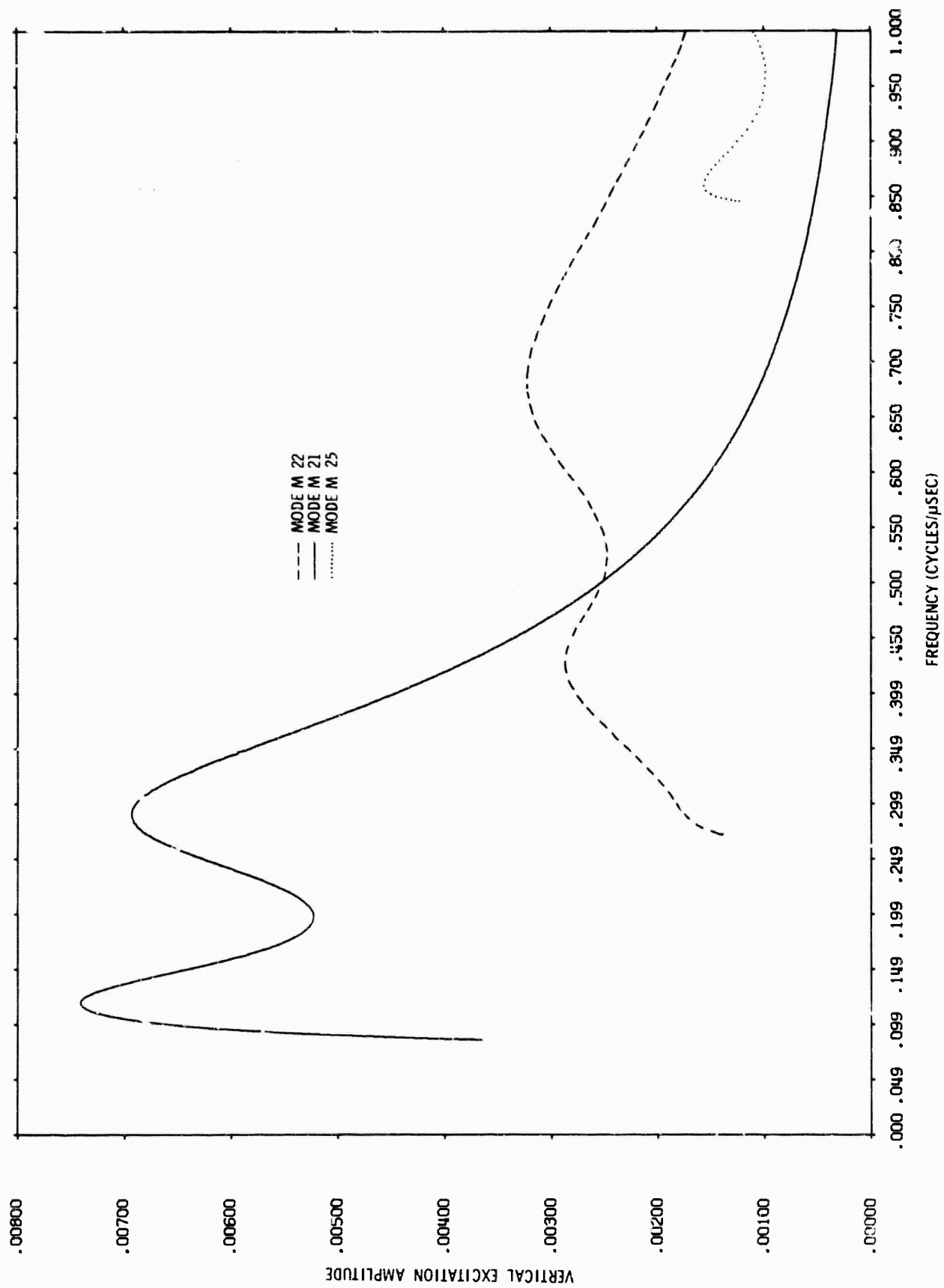


Figure 43. Vertical Normal Mode Excitation Functions for M_{23} and M_{24}

Figure 44. Vertical Normal Mode Excitation Functions for M_{21} , M_{22} , and M_{25}

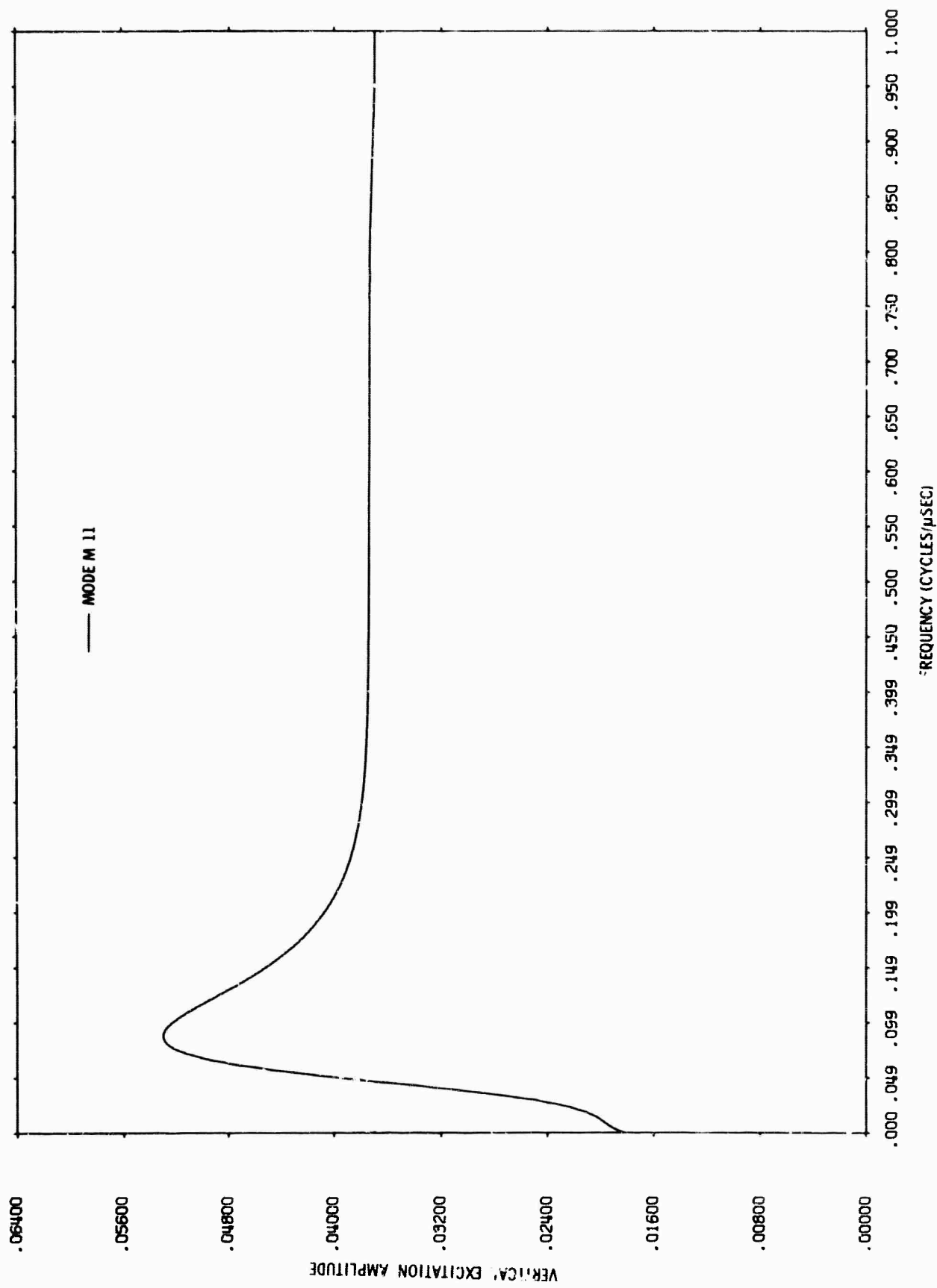


Figure 45. Vertical Normal Mode Excitation Function for M_{11}

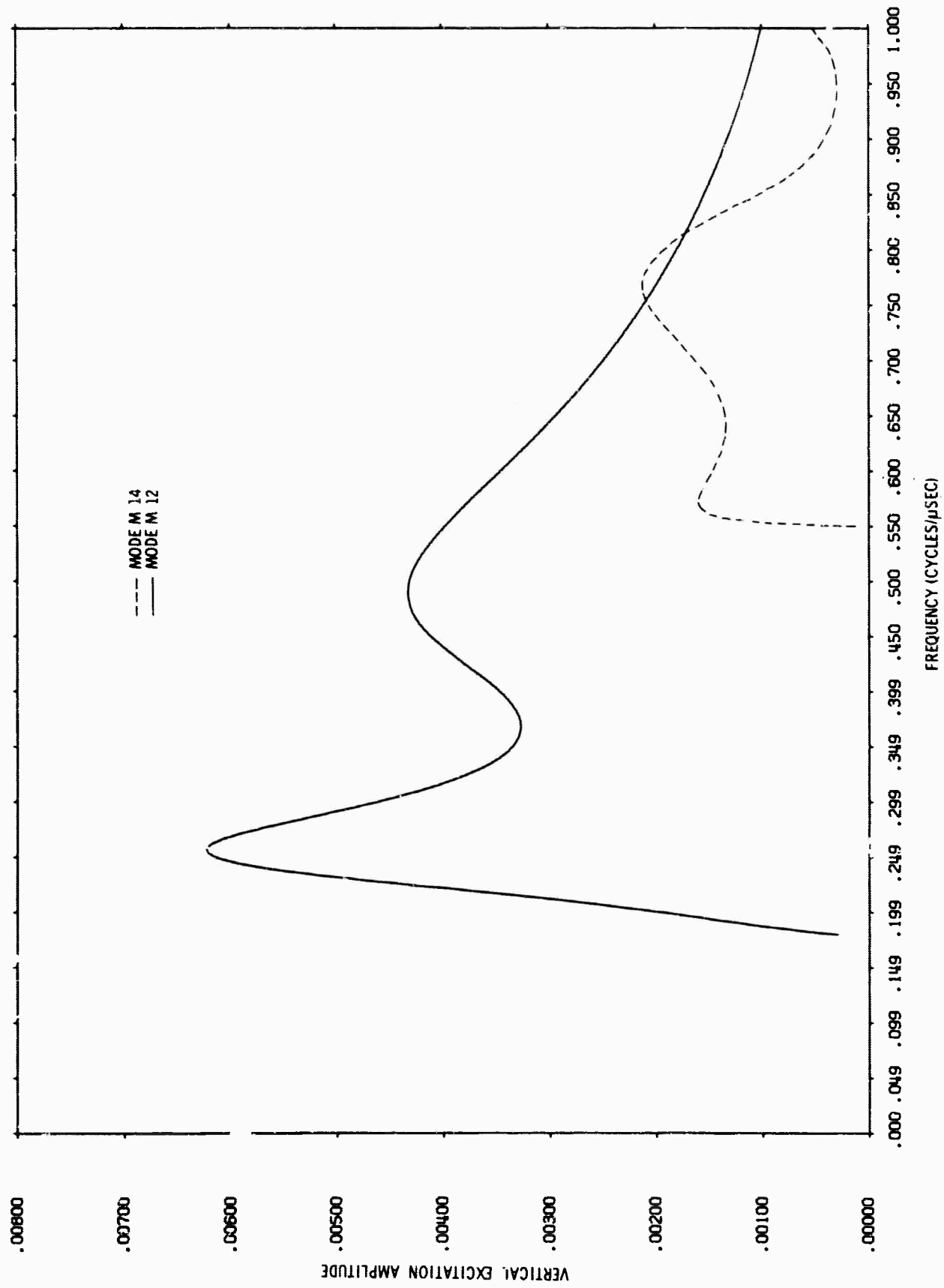


Figure 46. Vertical Normal Mode Excitation Functions for M_{12} and M_{14}

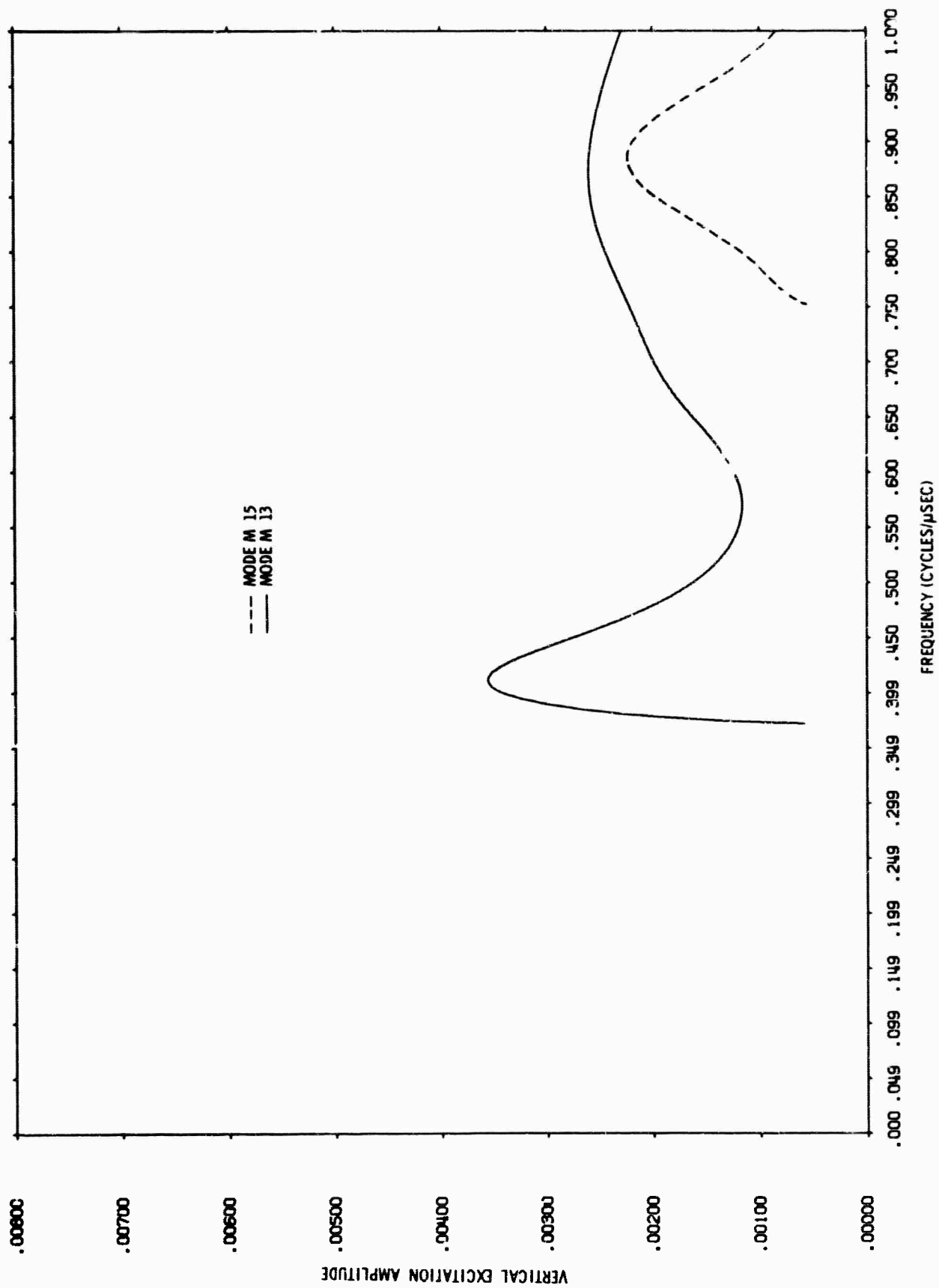


Figure 47. Vertical Normal Mode Excitation Functions for M_{13} and M_{15}

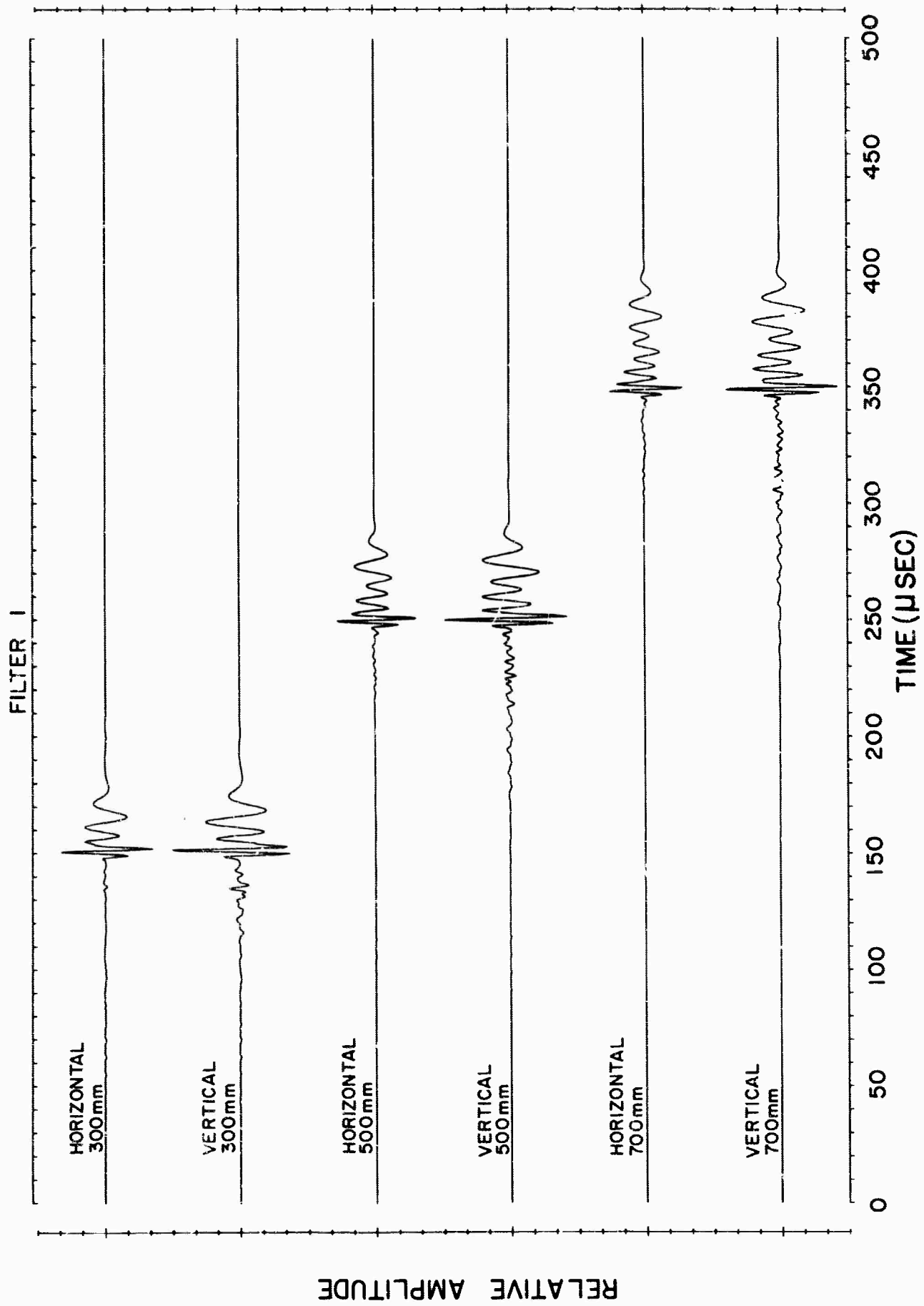


Figure 48. Filtered Theoretical Horizontal and Vertical Seismograms in the Distance Range 300-700 mm at Low Gain (Filter 1)

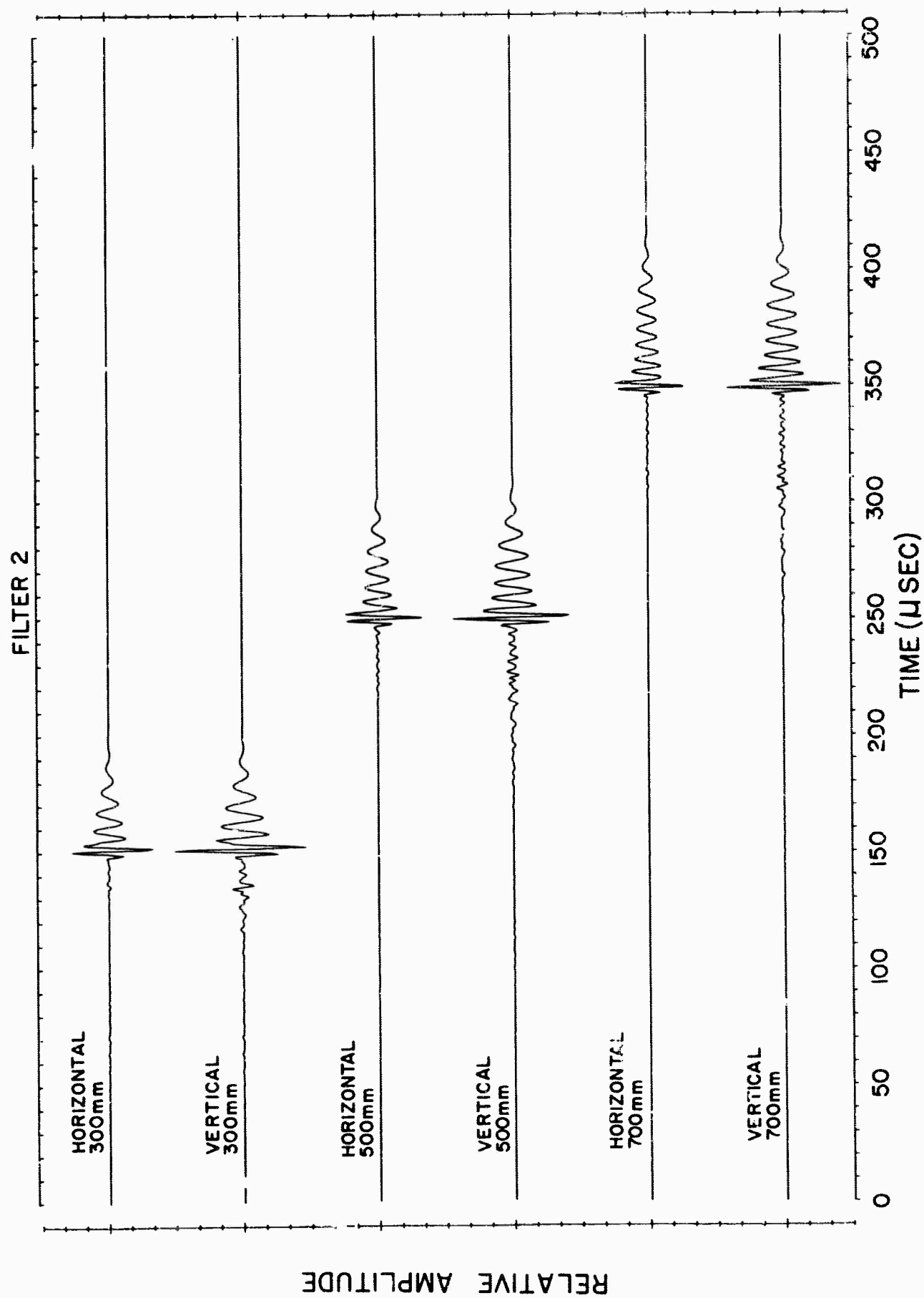


Figure 49. Filtered Theoretical Horizontal and Vertical Seismograms in the Distance Range 300-700 mm at Low Gain (Filter 2)

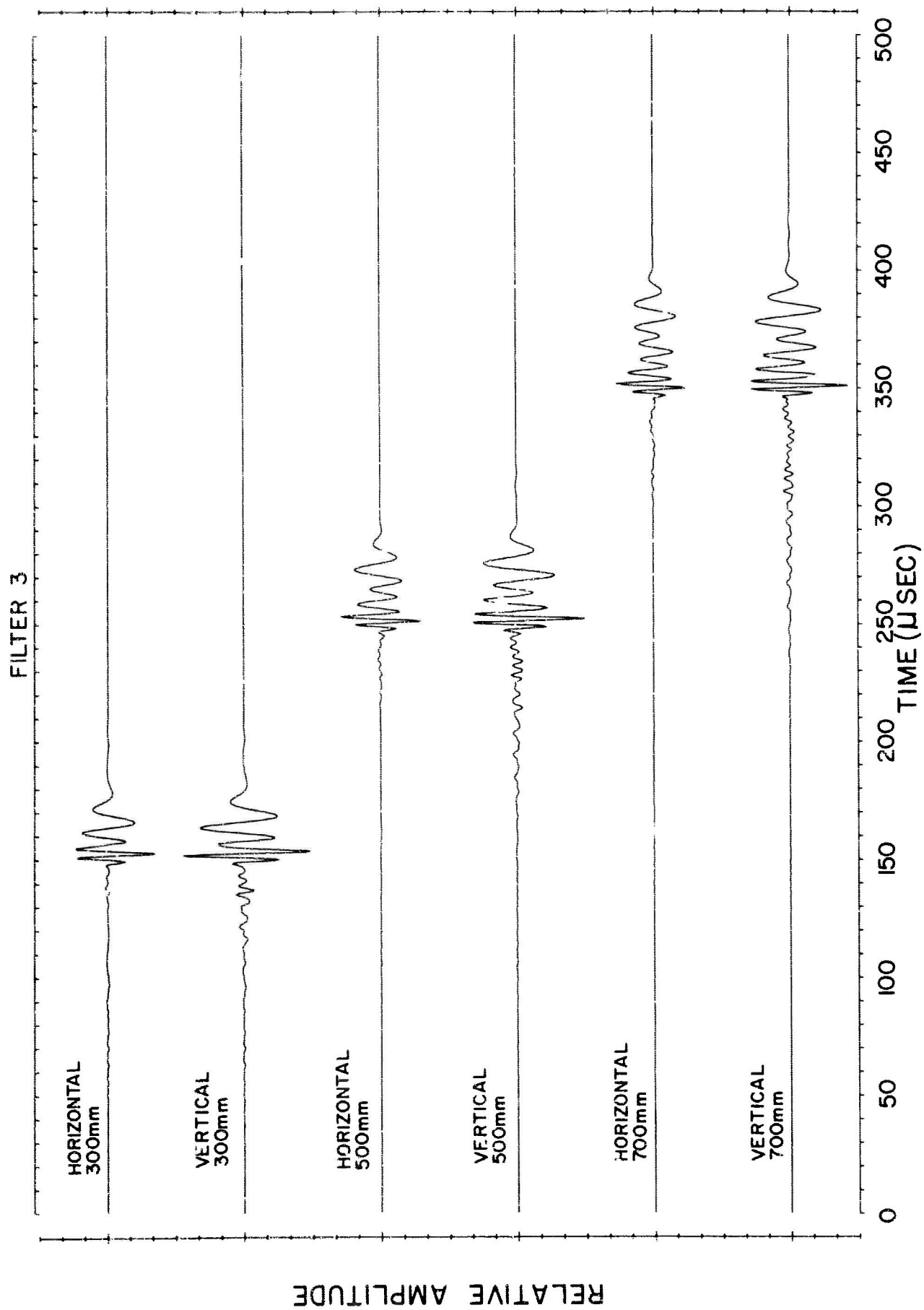


Figure 50. Filtered Theoretical Horizontal and Vertical Seismograms in the Distance Range 300-700 mm at Low Gain (Filter 3)

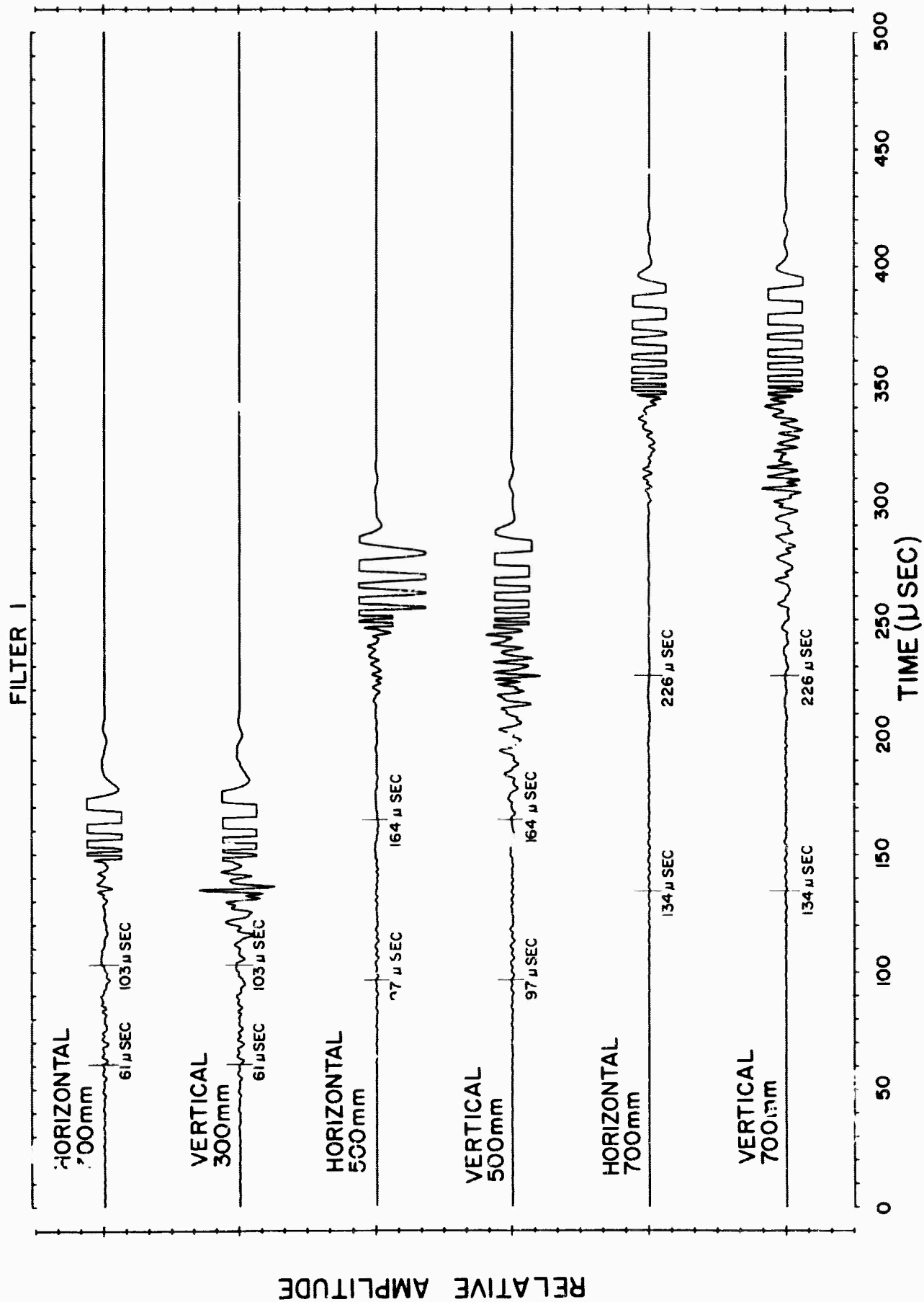


Figure 51. Filtered Theoretical Horizontal and Vertical Seismograms in the Distance Range 300-700 mm at High Gain (Filter 1)

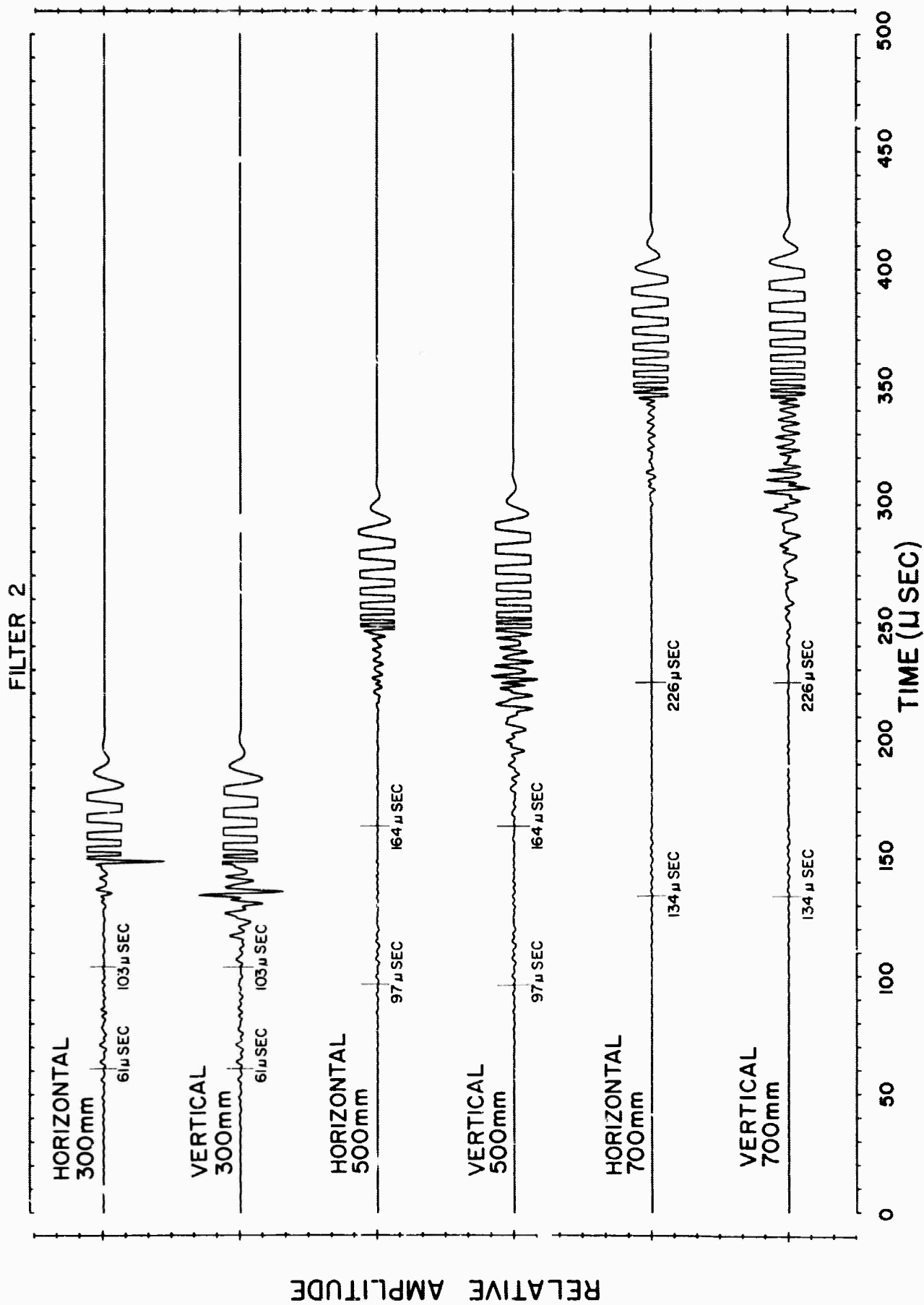


Figure 52. Filtered Theoretical Horizontal and Vertical Seismograms in the Distance Range 300-700 mm at High Gain (Filter 2)

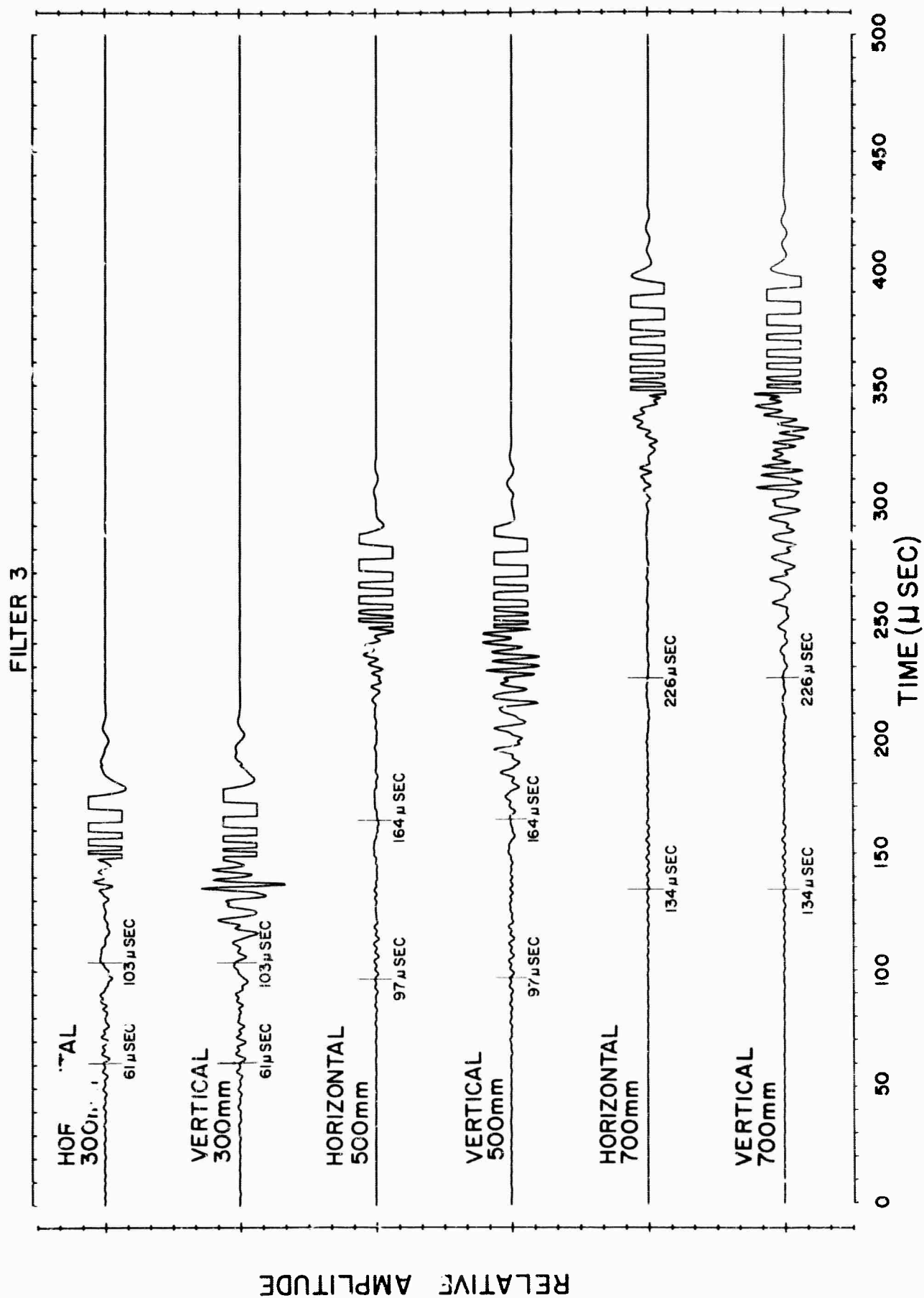


Figure 53. Filtered Theoretical Horizontal and Vertical Seismograms in the Distance Range 300-700 mm at High Gain (Filter 3)

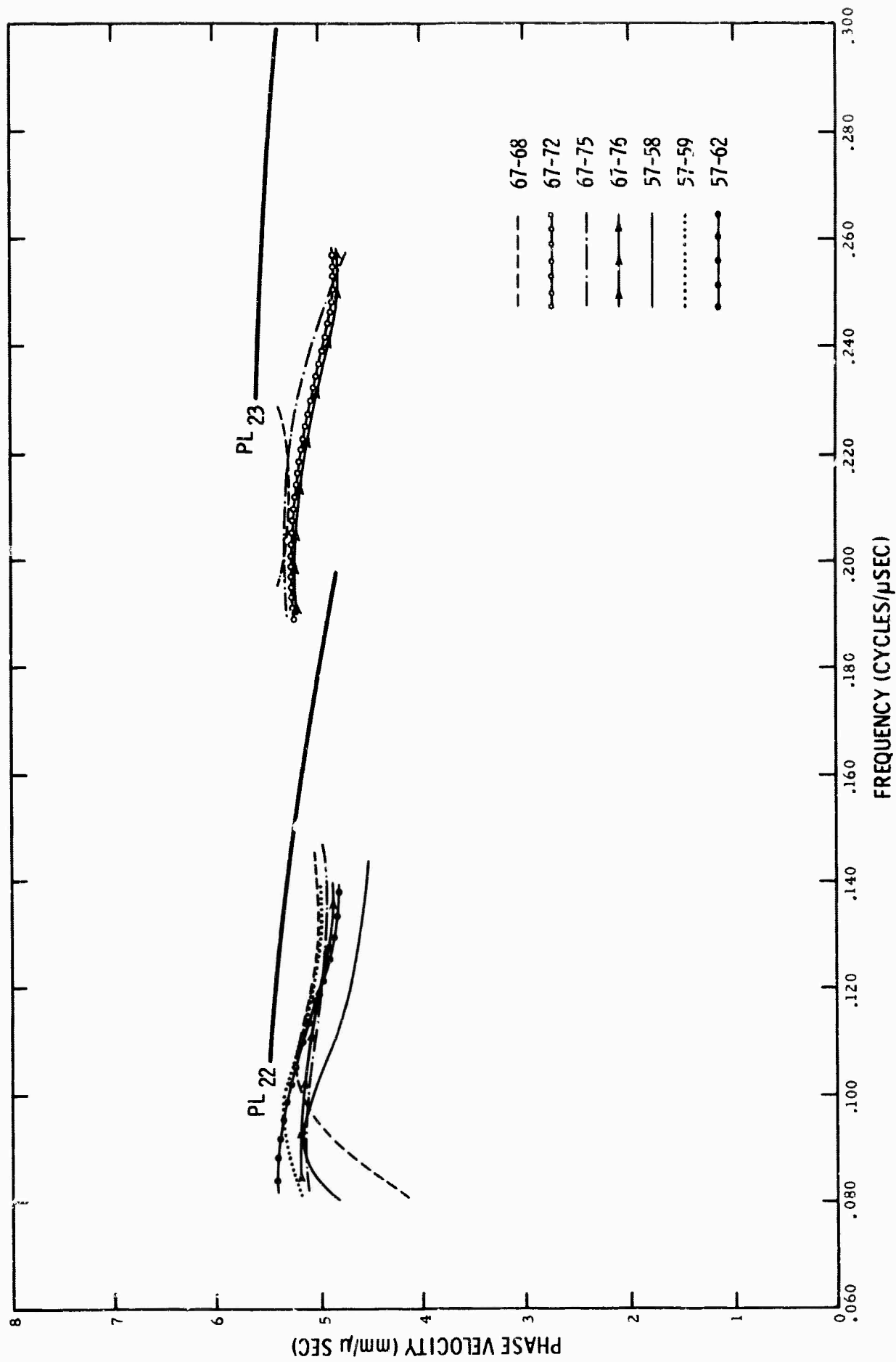


Figure 55. Comparison of Phase-Velocity Estimates for PL₂₂ and PL₂₃ Modes
(from Time-Partitioning) with the Theoretical Curves

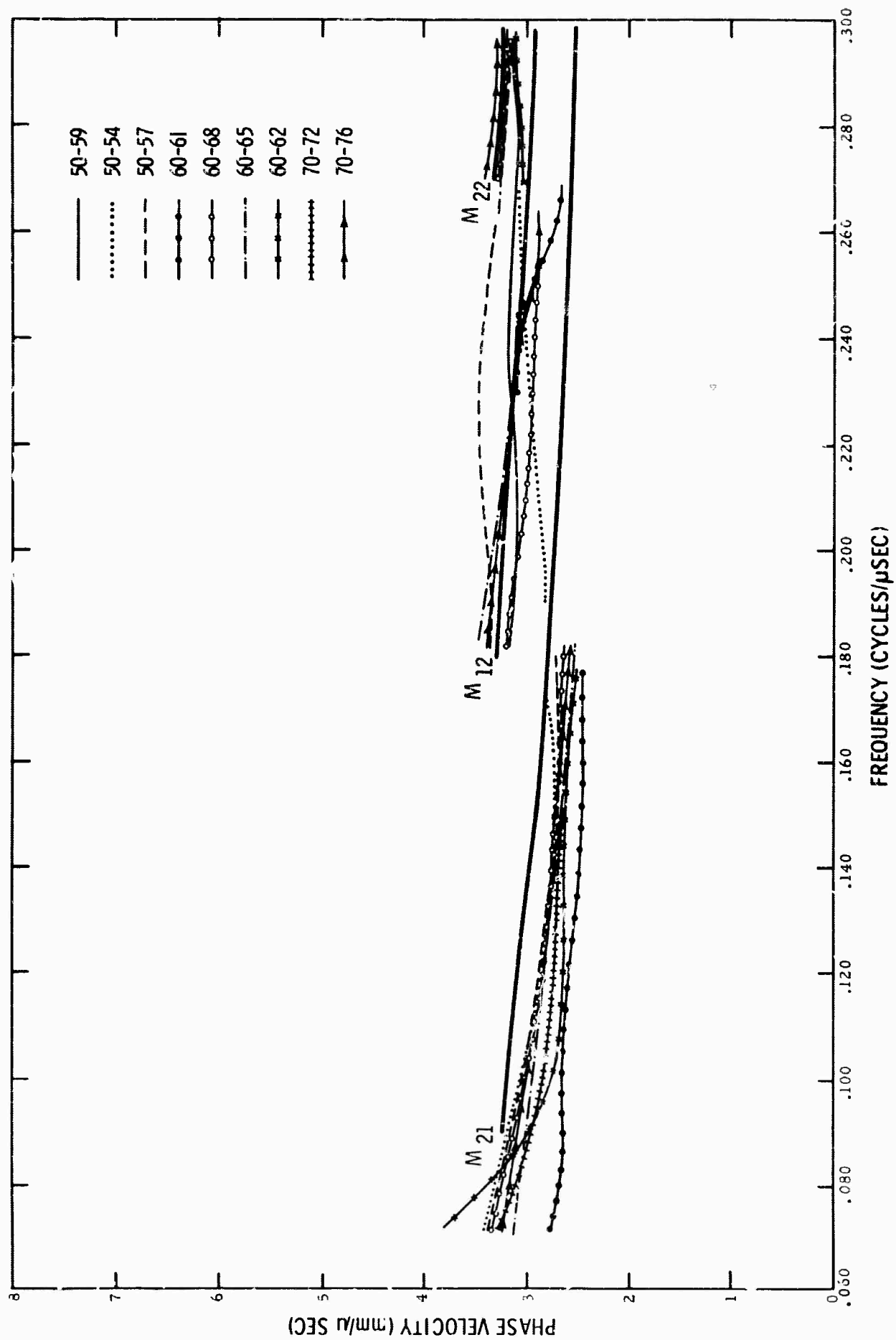


Figure 56. Comparison of Phase-Velocity Estimates for M₂₁, M₂₂ and M₁₂ Shear Modes (from Time-Partitioning) with the Theoretical Curves

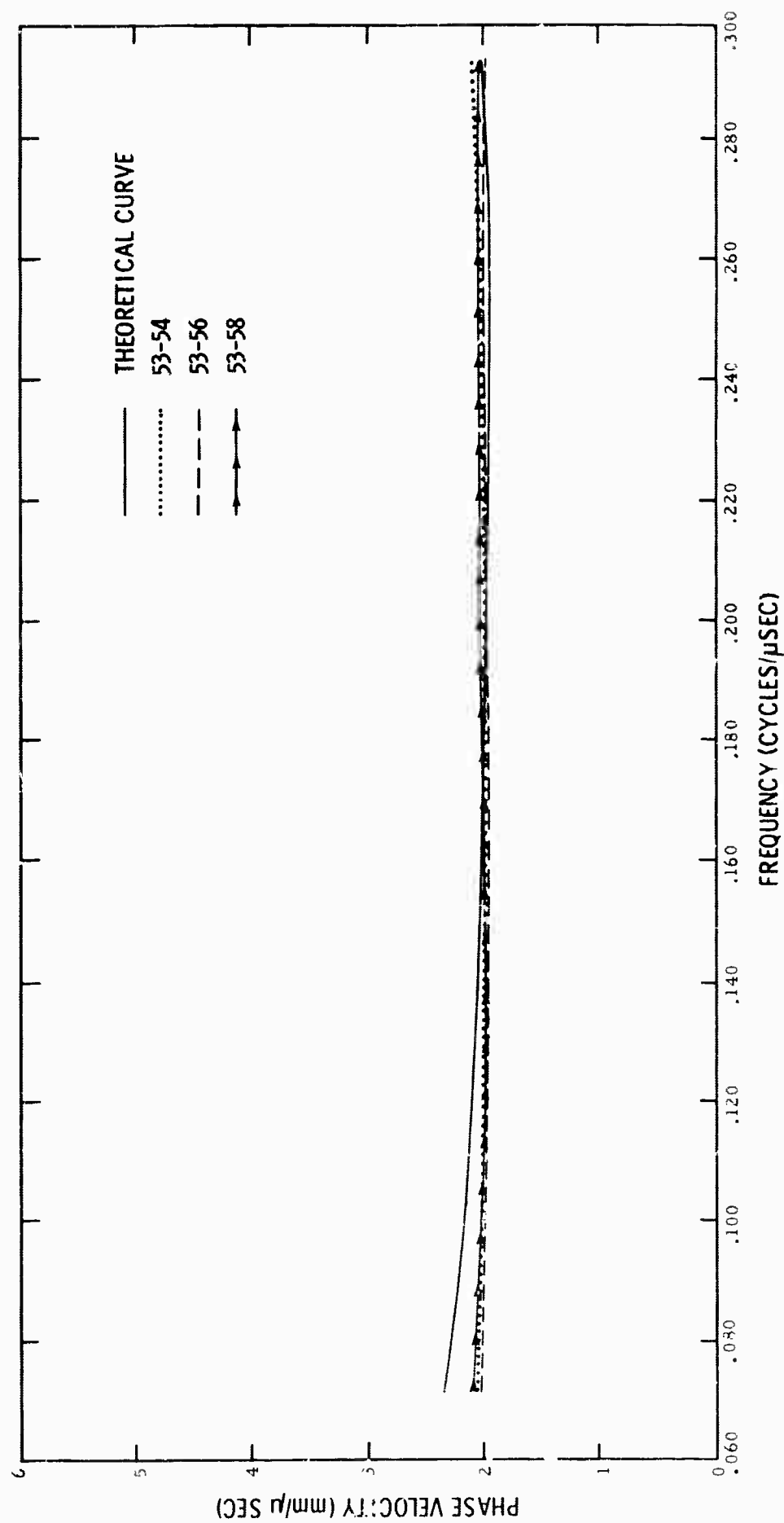


Figure 57. Comparison of Phase-Velocity Estimates for the Rayleigh Mode M11
(from Time-Partitioning) with the Theoretical Curves

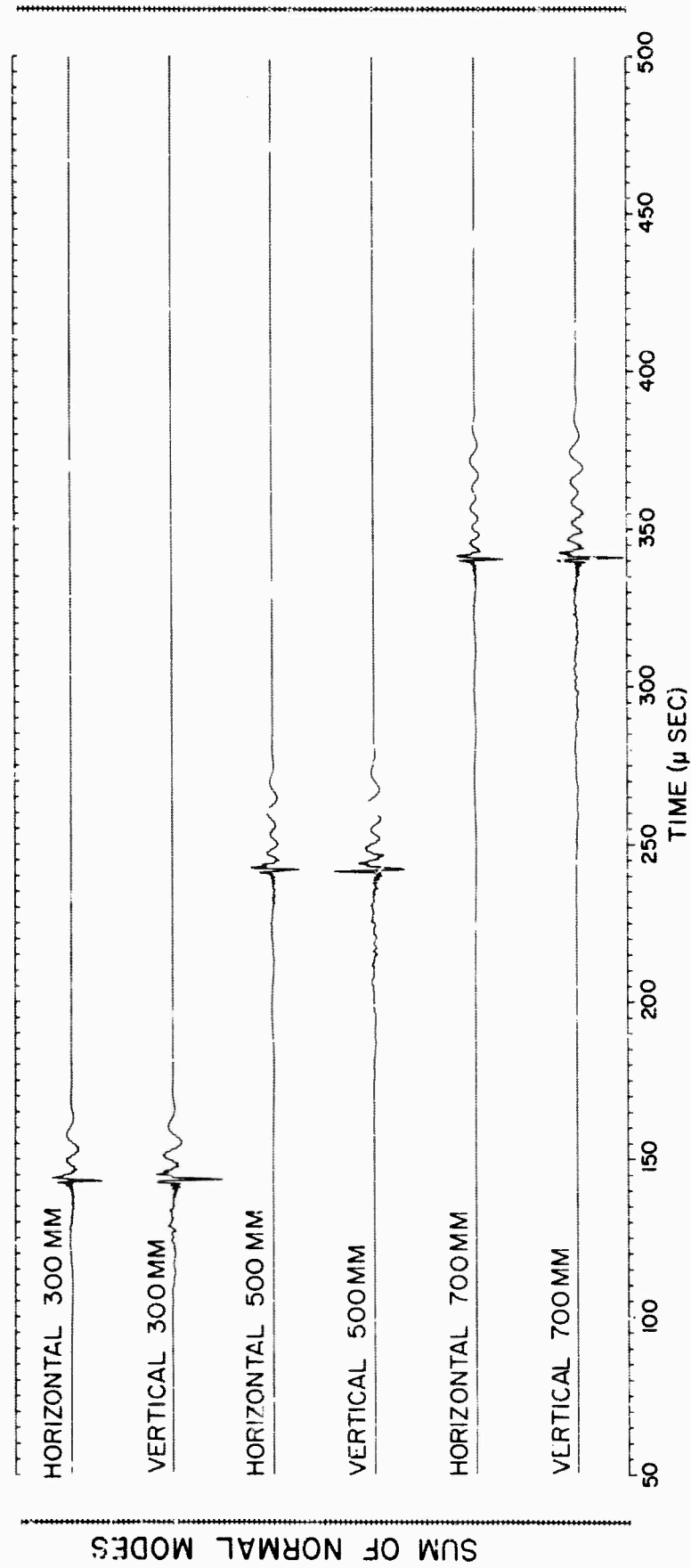


Figure 58. Sum of all Normal Modes (M_{11} , M_{21} , M_{12} , M_{22} , M_{13} , M_{23} , M_{14} , M_{24} , M_{15} , and M_{25})

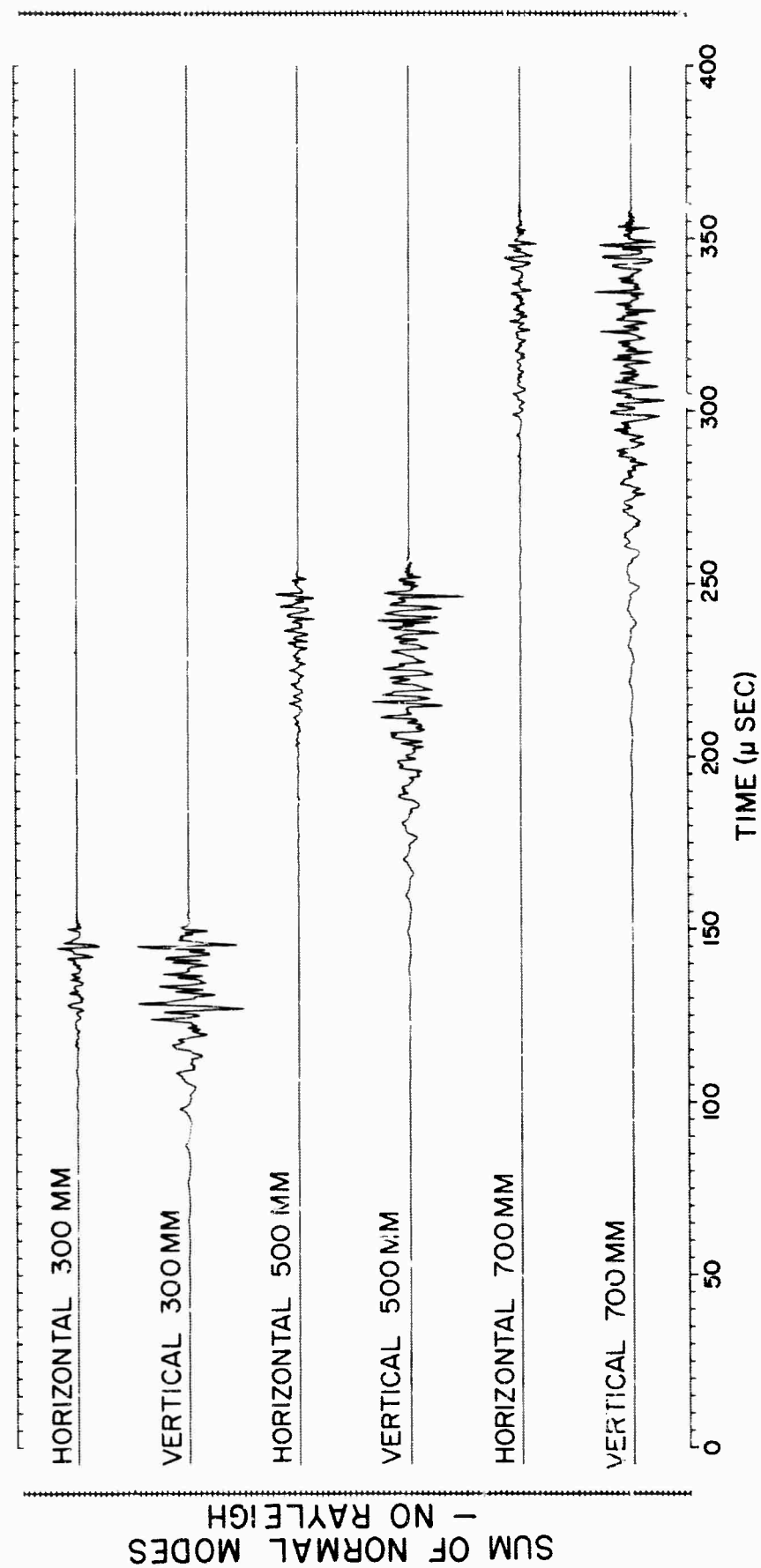


Figure 59. Sum of all Normal Modes Except the Rayleigh Mode M_{11}

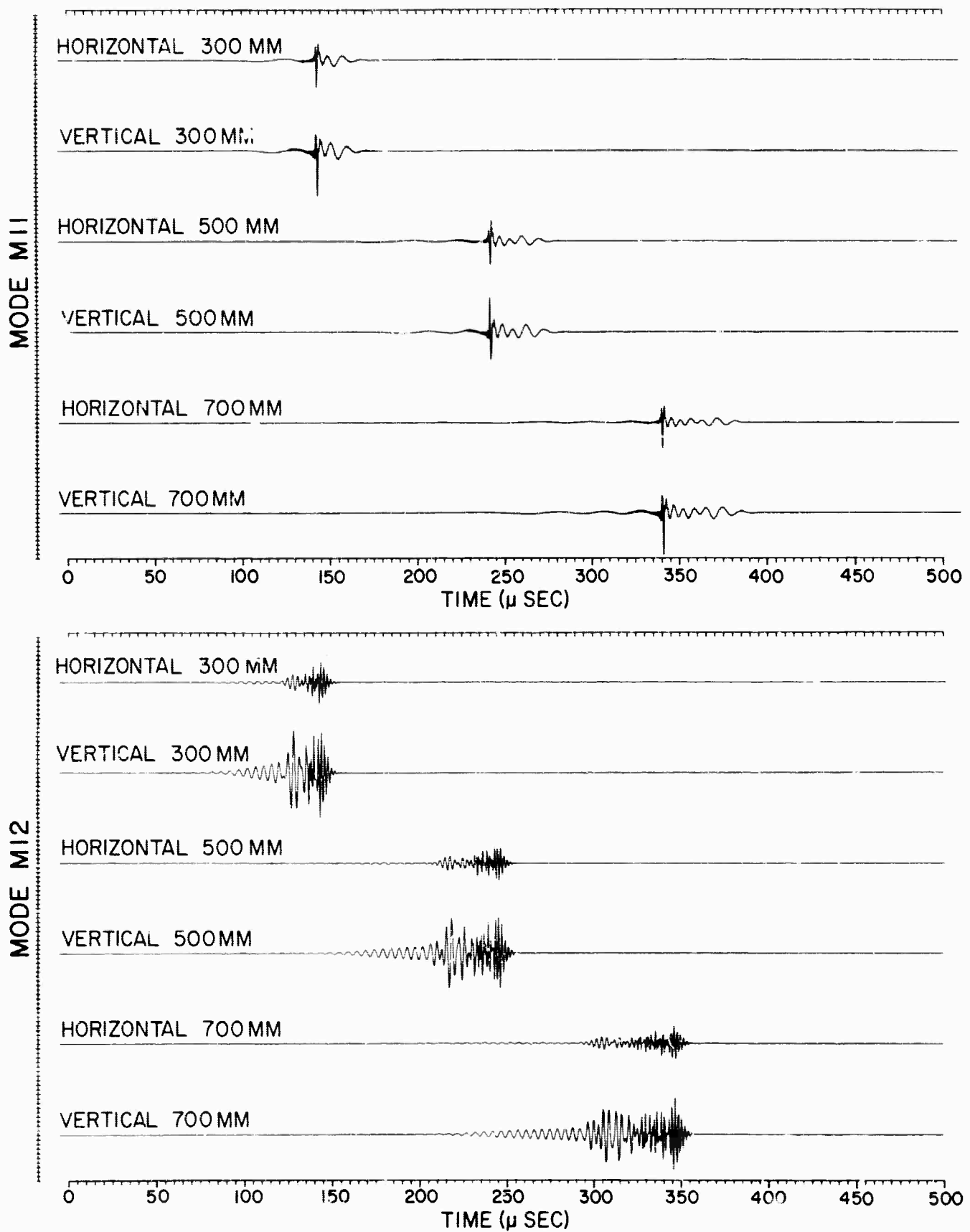


Figure 60. Horizontal and Vertical Modal Seismograms for Modes M_{11} and M_{12} - Distance Range 300-700 mm

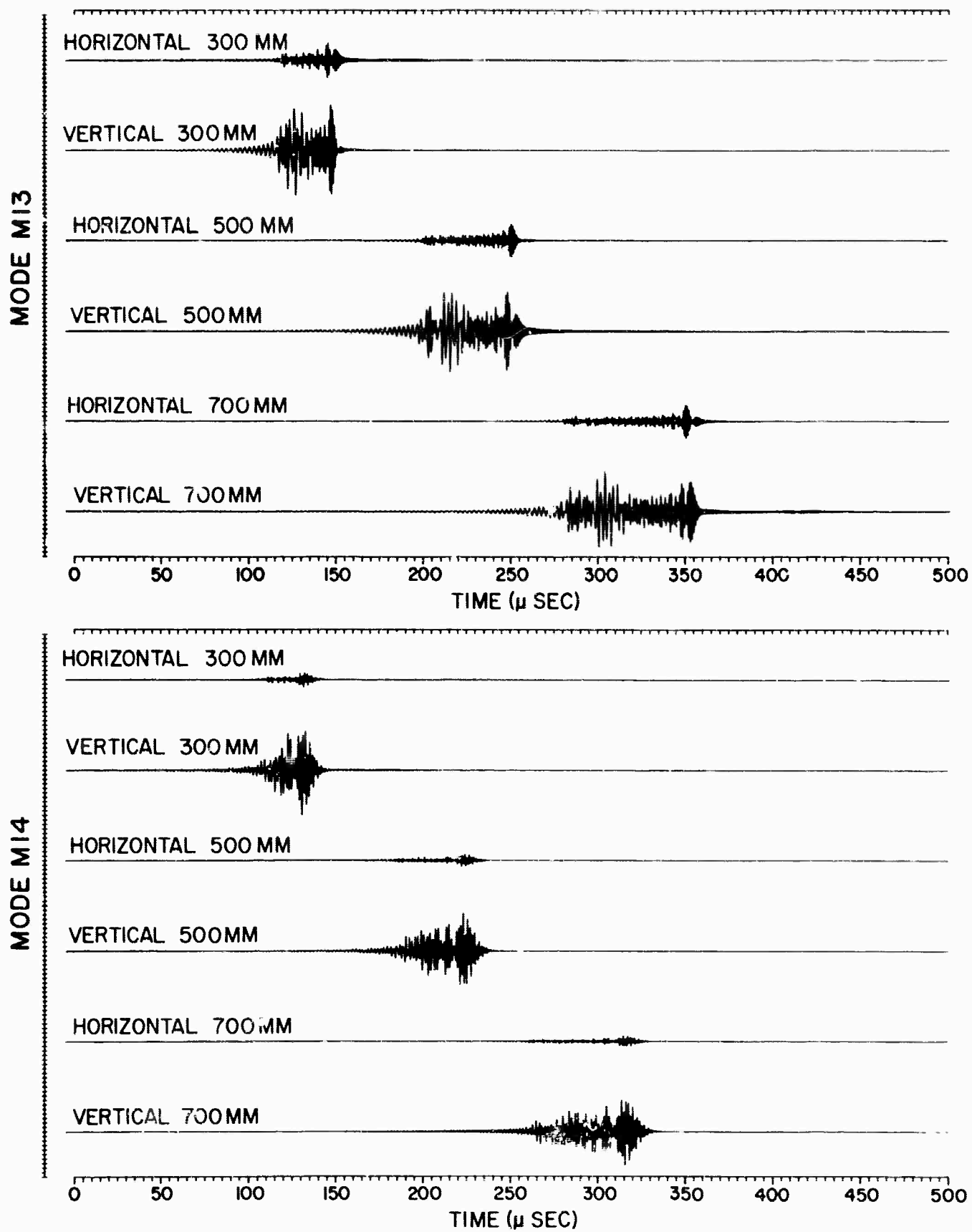


Figure 61. Horizontal and Vertical Modal Seismograms for Modes M₁₃ and M₁₄ - Distance Range 300-700 mm

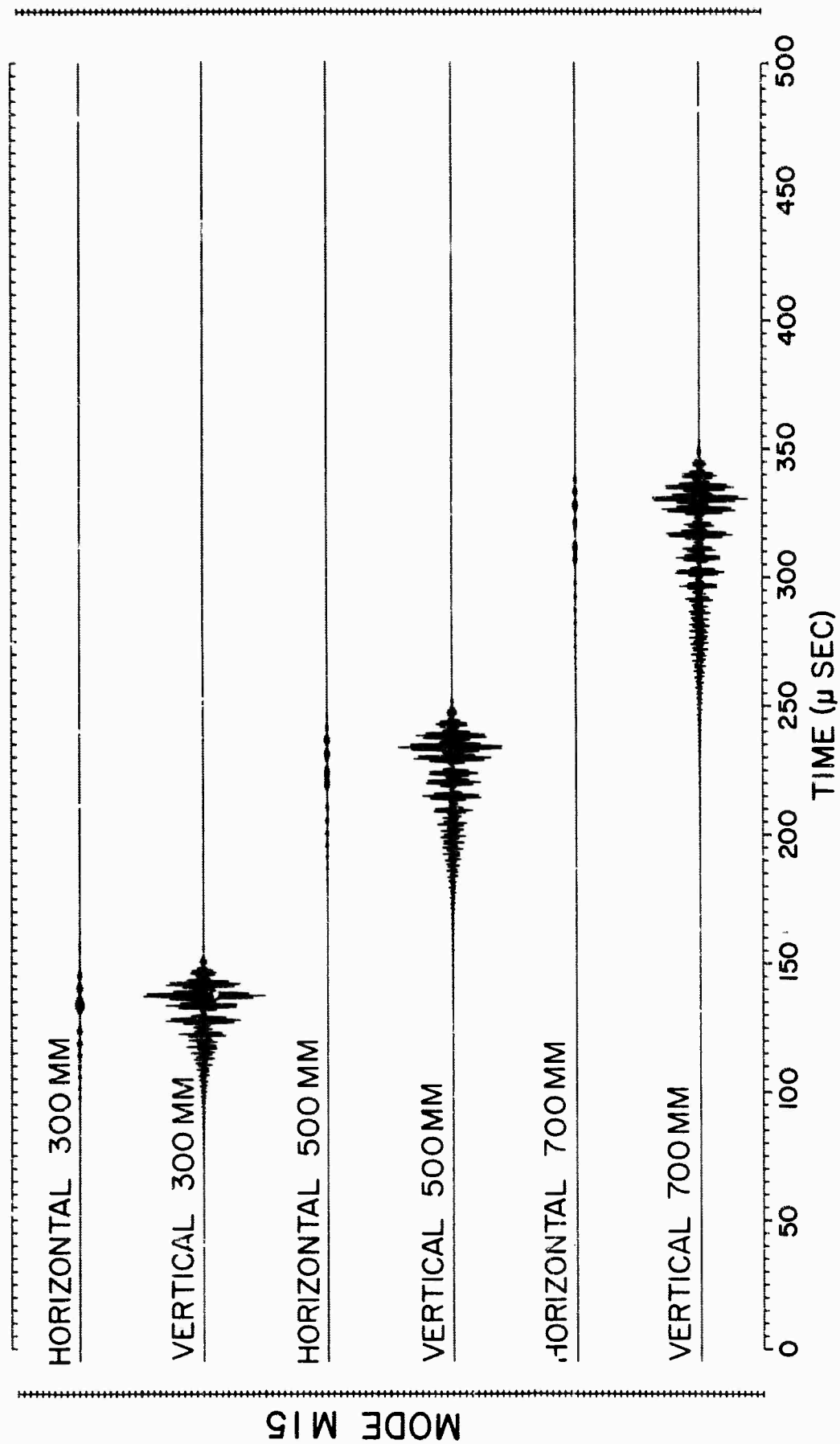


Figure 62. Horizontal and Vertical Modal Seismograms for Mode M₁₅ - Distance Range 300-700 mm

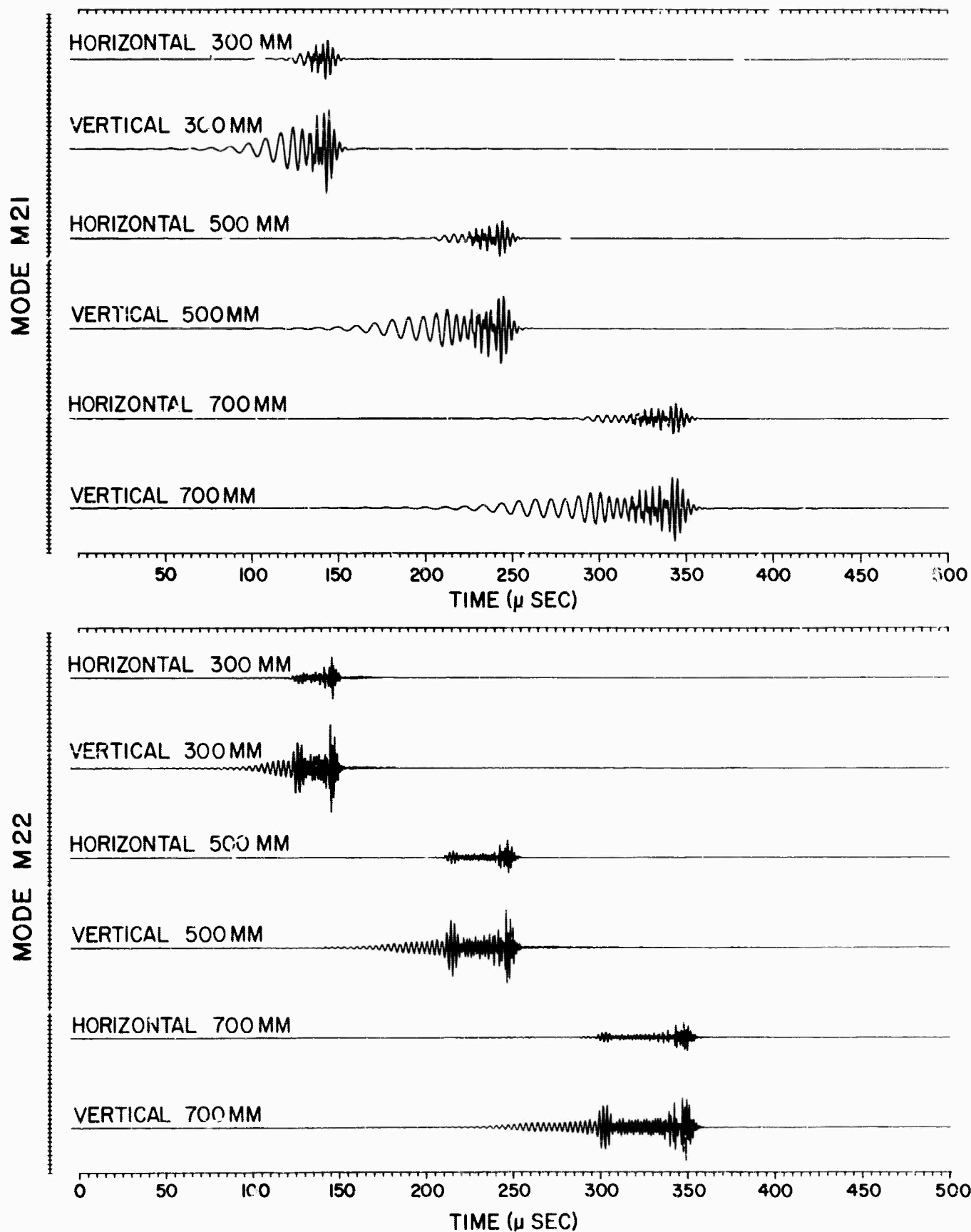


Figure 63. Horizontal and Vertical Modal Seismograms for Modes M_{21} and M_{22} - Distance Range 300-700 mm

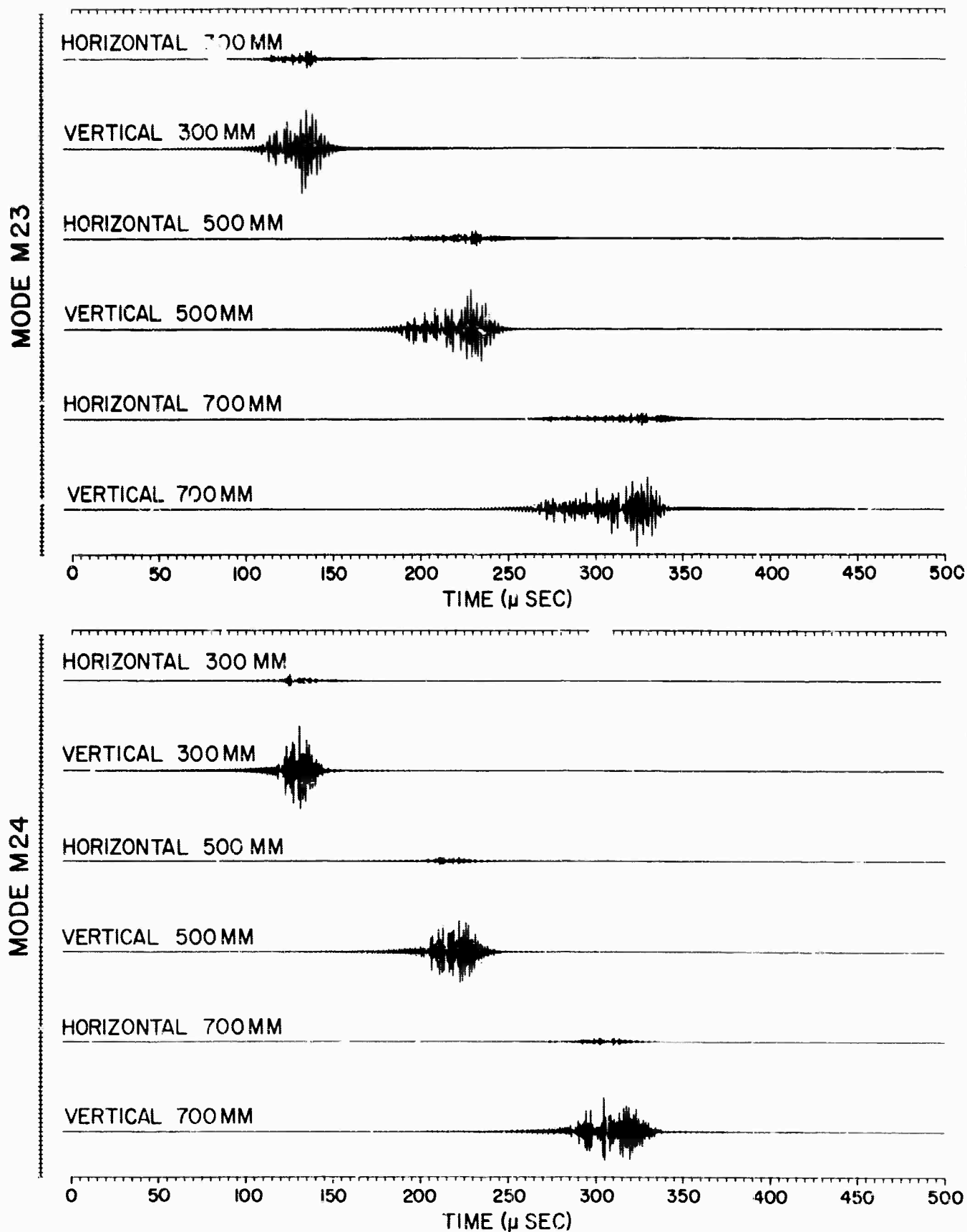


Figure 64. Horizontal and Vertical Modal Seismograms for Modes M₂₃ and M₂₄ - Distance Range 300-700 mm.

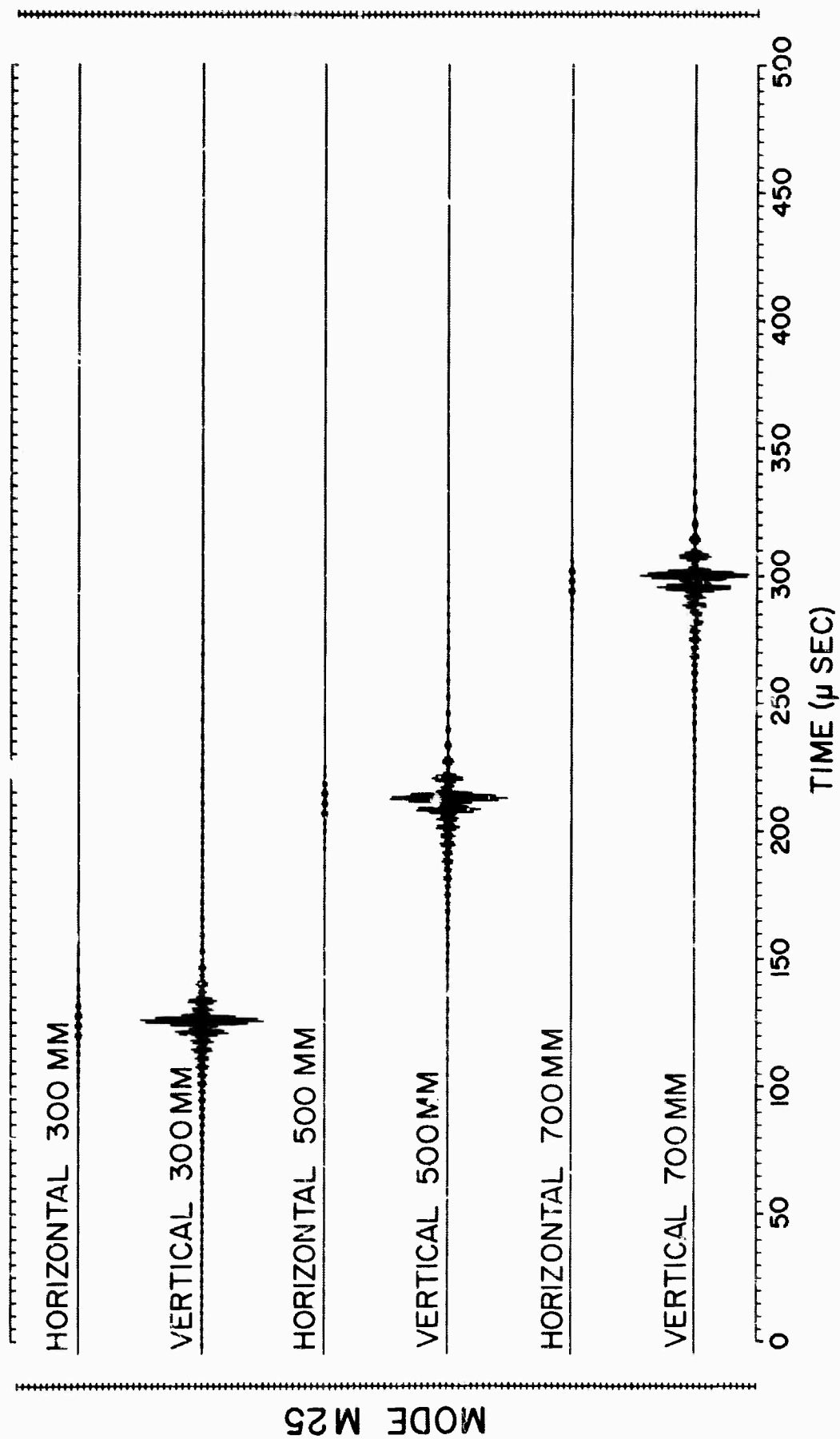


Figure 65. Horizontal and Vertical Modal Seismograms for Modes M_{25} - Distance Range 300-700 mm

APPENDIX E

ANALOG MODEL STUDIES OF WAVE PROPAGATION IN A CRUST WITH A DIPPING INTERFACE

by

Stanley J. Laster* and A. Frank Linville*

ABSTRACT

Analogue model studies of a single layer with dipping interface upon a half-space show that the most striking prediction of ray theory is the production of a multiplicity of phase velocities for compressional refracted events, as opposed to the single phase velocity found in parallel layered models. An attempt is made to determine the true refractor velocity and dip from measured velocities associated with particular ray paths. For low frequencies the chief prediction of mode theory is a dependence of the dispersion curves on horizontal distance, as a result of their dependence on layer thickness. An attempt is made to measure the leaking mode dispersion curves for comparison with theory.

*Texas Instruments Incorporated, Dallas, Texas

APPENDIX E

ANALOG MODEL STUDIES OF WAVE PROPAGATION IN A CRUST WITH A DIPPING INTERFACE

by

Stanley J. Lastner and A. Frank Linville

I. INTRODUCTION

The problem of wave propagation in plane-parallel stratified media has been studied in great detail in recent years. These studies are of direct significance in seismology because many parts of the earth's crust and upper mantle can be approximated by plane-parallel layered models. The studies also have secondary significance because the perturbation solutions for nonplanar or nonparallel layering are often derived from the plane-parallel solutions. A property of great importance possessed by plane-parallel layered models is that exact formal solutions can be obtained in terms of integrals of known functions. The only approximation occurs in evaluating these integrals and, if one is prepared to use Cagniard's method, even this can be effected in closed form for any finite time span.

However, the next stage of difficulty — models with plane-dipping boundaries — also has significant intrinsic interest. In particular for these models, the exact Cagniard solution can be found for a given time span, i. e., the least time required for energy to travel from the source to a corner (pinchout) and then to the receiver. Approximation of this solution for high frequencies yields the familiar geometrical ray solution. If the radiation from the source contains much low-frequency (large-wavelength) energy, the geometrical ray solution is not useful. However, the term "low frequency" is not well-defined for a model with dipping boundaries because there is no characteristic dimension associated with the model. Two approaches can be used. First, it is obvious that diffracted events from a corner cannot be ignored in favor of the geometrical ray terms if the source or receiver is located only a few wavelengths from the corner. In this case, the problem (the classical "wedge" problem) is very difficult and no satisfactory solution has been found yet. A second definition of "low frequency" is possible for very small wedge angles, and these are most frequently encountered in practice. In this case, the source and receiver may be located many wavelengths from the corner but the average layer thickness in the neighborhood of the source or receiver may be much less than a wavelength. A modal solution analogous to that for plane-parallel layers is suggested. In fact, approximate theoretical solution for this problem based on a sequence (in space) of plane layered models can be found in the literature.

The present paper deals with analog model studies of a single layer with dipping interface upon a half-space. Only two aspects of the problem are considered in any detail. First, we have studied propagation in a

portion of the model amenable to ray theory (high frequency). Here, the most striking prediction of the theory is the production of a multiplicity of phase velocities for compressional refracted events, as opposed to the single-phase velocity found in parallel layered models. An attempt is made to measure the various velocities, identify them with ray paths and use them for determination of the true refractor velocity and dip. Second, for a part of the model appropriate to mode theory (low frequency), we have attempted to measure dispersion curves of the leaking modes. The chief prediction of the theory is a dependence of these dispersion curves on horizontal distances, as a result of their dependence on layer thickness. Attempts to measure these curves and a comparison with theory are covered in later paragraphs of this appendix.

II REFRACTION ARRIVALS ALONG A PLANE-DIPPING INTERFACE

Critically refracted signals in media consisting of plane-parallel layers have many simple properties. A series of pulse events is found to be associated with each interface. These consist of the primary refracted event and its multiples, many of which have shear legs. These events travel with a constant phase velocity characteristic of the refracting medium and, as a result, the time interval between two given events is independent of distance traveled. Of course, this time interval can be different for different pairs of successive events. An interesting property of the multiply-reflected refractions is the degeneracy in travel time. For example, the refracted reflection and reflected refraction (Figure 1) are physically different events but have the same travel time.

One also might draw ray paths of the third kind shown in Figure 1 (having the same travel time as the previous events), but there are theoretical reasons for the nonexistence of such events. The critically refracted arrival at C is a plane wave (in three dimensions, a conical wave) and remains a plane wave after reflection from the free surface. Therefore, when the reflection from the free surface touches the interface at point D, no energy will be propagated along the D-to-E path since it is well-known that a plane wave generates a critically refracted wave of zero amplitude. The critically refracted arrivals are diffraction effects and, in general, no energy will be propagated as a diffraction if the incident wave and reflecting surface have the same shape. (Note that, if any event of this type did exist, there would be a continuum of such events because the point of reflection at the surface (C) could be moved continuously from point A to point B.)

With the introduction of dipping interfaces, the behavior of the critically refracted events becomes more complicated. In the first place, the velocity of the events now depends not only on the velocity of the refracting medium but on the dip and on the velocities of layers above the interface. As a result, the phase velocity of the first refracted arrival is found to be

less for an event traveling downdip than for an event traveling updip. The expression for the downdip phase velocity in a single-layer crust (Figure 2) is

$$C = \frac{1}{\frac{\cos \gamma}{\alpha_2} + \frac{\cos \theta \sin \gamma}{\alpha_1}}$$

where γ is the dip of the interface, α_1 and α_2 are the velocities in the upper and lower materials respectively, and θ is given by $\sin \theta = \alpha_1/\alpha_2$. The dip γ is taken positive if the interface is deeper beneath the receiver than at the source. Obviously, as γ approaches 0, C approaches α_2 . It is also seen that the second term in the denominator contains the only information about the upper-layer materials. For very small dip, we can approximate C by

$$C = \alpha_2 (1 - \gamma \cot \theta)$$

In general, the measurement of a refracting interface dip requires experimental data recorded both updip and downdip from the source, since α_1 (or θ) also appears as an unknown parameter.

A second complication introduced by dipping interfaces is the "splitting" of events which are degenerate in travel time. (One might compare this to the splitting of spectral lines by a magnetic field in the Zeeman effect.) For instance, the two events shown at the top of Figure 1 have different velocities in the model with dip. At any distance greater than the critical distance, they have different arrival times — and the difference in arrival times increases with distance. It is worthwhile also to consider the event shown at the bottom of Figure 1. In the case of a dipping interface, it is obvious that this event cannot exist since the ray returning from the point of surface reflection will never strike the interface at the critical angle of incidence (Figure 3) for any dip angle other than 0. For this reason, we conclude that the degenerate refracted event with four P-legs will be split into two well-defined pulses traveling with slightly different phase velocities. One of these, the refracted reflection, will have the same phase velocity as the primary refracted event. The phase velocity for the two events will be (for small dips)

$$C = \alpha_2 (1 - \gamma \cot \theta) \quad (\text{refracted reflection})$$

$$C = \alpha_2 (1 - 3\gamma \cot \theta) \quad (\text{reflected refraction})$$

These expressions offer the possibility of determining the true velocity of the refractor from measurements made in a single direction (updip or downdip). This requires, however, that the reflected refraction and refracted reflection (or possibly other multiple events) be identified in the experimental data and that the phase velocity of these two events be measurable with sufficient precision. If these requirements are met, the required velocity is given by

$$\alpha_2 = \frac{3C_1 - C_2}{2}$$

where C_1 and C_2 are the phase velocities of the refracted reflection and the reflected refraction, respectively. The quantity $\gamma \cot \theta$ also can be found, but it is not possible to separate the γ and α_1 (or θ) variables without additional measurements. Similar arguments can be given for multiple events with more legs.

III. DESCRIPTION OF MODEL AND DATA

The analog model used in the present study (designated H4) consists of a single brass layer overlying a stainless steel half-space (Figure 4). Table 1 gives the elastic parameters of these materials. The thickness of the brass layer varied uniformly from 3 cm at one end of the model to 6 cm at the other over a total length of 244.4 cm. This corresponds to a dip of 0.715° . Bonding is achieved with a commercial epoxy resin compound. The source was a 1-mm square piezoelectric crystal (1-Mc resonant frequency) mounted on the top of the model, 55 cm from the thin end. Signals were received using a shear-mode transducer mounted on the side of the model.

Table 1

ELASTIC PARAMETERS OF BRASS AND STAINLESS STEEL

	P-Velocity (mm/ μ sec)	S-Velocity (mm/ μ sec)	Thickness at Source (mm)	Dip
Brass	3.91	2.69	36.86	0.715°
Stainless Steel	5.29	3.07	908.14	0.0

The electrical output of the transducer was automatically digitized and punched on paper tape for input to various electronic computer systems.

Exploratory measurements on this model showed the signals to have a very large dynamic range. At 80 cm, the first arrival had an amplitude of 1.8 mv, while the Rayleigh wave had an amplitude of 7 v. To make use of all the information available, the data were recorded at high as well as at low gain. Typical low-gain data are shown in Figures 5, 6 and 7. On this scale, the Rayleigh wave is well-defined but the refracted events are very small. The small events preceding the Rayleigh wave contain the events refracted as P-waves along the top of the stainless steel half-space and a number of events reflected at greater than critical angle from the brass-steel interface. All these latter events are better observed on the high-gain recordings discussed in a later paragraph. No good evidence is found for refracted shear waves. The large low-frequency events following the Rayleigh pulse are probably flexural waves.

In Figure 5, the signal is traveling updip from the source into the thin end of the crustal layer. The first trace is farthest from the source. In Figures 6 and 7, the signal is traveling downdip into the thick end of the crustal layer. It is seen that the Rayleigh wave pulse shape is insensitive to the direction of travel (updip or downdip) although the pulse shape changes somewhat from trace to trace. Its velocity is found to be 2 mm/ μ sec and is also insensitive to direction of travel. This is not surprising with a crustal layer of this thickness. Previous studies have shown the Rayleigh dispersion curve in the frequency range used here (70 to 250 kc/s) to be essentially constant at the velocity of Rayleigh waves on brass. This Rayleigh wave energy is concentrated very near the surface and does not "see" the stainless steel half-space. Thus, for this model, one must conclude that little usable information about the model structure at depth can be gained from the Rayleigh wave. However, with a lower frequency source or a thinner crustal layer, dispersion studies of the Rayleigh mode will yield such information (Kuo and Thompson, 1963).

Typical high-gain recordings are shown in Figures 8 through 11. At this level of amplification, the Rayleigh wave overdrives the system (is "clipped"), but care has been taken to prevent this from affecting the refraction arrivals. As expected, this first-arriving pulse is the event refracted along the top of the steel. Its apparent velocity is about 5.2 mm/ μ sec (measured downdip from the source). At distances greater than 85 cm, a large event with velocity greater than 5.3 mm/ μ sec emerges from the Rayleigh wavetrain. This has been found to be a reflection from the bottom of the stainless steel plate. Such an event violates the similitude between the analog model and the earth but causes no actual difficulty in the present study since it can be easily identified. In fact, this bottom reflected pulse can be used to obtain a better estimate of the P-wave velocity in the half-space.

Obviously, the refracted events can be used for studies of the dipping interface since they represent events traveling along that interface. For that reason, the remainder of this appendix will deal with the early-arriving portion of the recordings.

IV. TRAVEL TIME AND VELOCITY MEASUREMENTS OF RAY EVENTS

The theoretical downdip travel times and phase velocities for a number of expected ray events were computed for model H4. These are shown in Figure 12. The ray paths associated with the travel-time curves identified by numbers are shown in Table 2. It is seen that a range of phase velocities are to be expected for the refracted events, beginning with 5.23 mm/ μ sec and decreasing. Second, it is seen that, except for the first refracted arrival, the refracted events occur for a given offset in "packets" of several events with slightly different phase velocities and slightly different arrival times. An example of such a packet would be all the events with four compressional (P) legs in the brass layer. In the absence of dip, these would coalesce into a single event. As offset is increased, the wave packet is spread out in time due to the slight differences in velocity. In this particular model, the travel time along an S-leg in the brass layer is about equal to the travel time along three P-legs, so events with N P-legs and 1 S-leg in the brass layer occur in the same packet of arrivals as events with (N+3) P-legs. These events, however, do not coalesce when the dip vanishes.

A number of coherent events were picked on the high-gain downdip recordings. These are labeled A, B, C, etc., in Figures 9 through 11. The travel times for these events were measured and the results plotted in Figure 13. The measured phase velocities of these events are shown in Table 3. Some ambiguity occurs in trying to identify these with the theoretical curves. In the first place, the theoretical curves apply to first motion, while we are obliged to pick measurable peaks or troughs in the experimental data. A correction for this requires the addition of about 10 μ sec to the theoretical times. Second, because surface reflection will cause some events to be reversed, some of the theoretical curves correlate with peaks while others correlate with troughs. Since the events arrive in groups, it is difficult to overcome this ambiguity completely. However, it appears possible to correlate event A with event 1, the first refracted event, and event D with event 4, the first wide-angle reflection. The first large events following the first arrival (B) seem to correlate with the packet containing events with 6 P-legs and also with 3 P-legs and 1 S-leg. The packet following A by 10 to 15 μ sec, containing the events with 4 P-legs and with 1 P-leg and 1 S-leg, is very small and was overlooked at first. The small amplitude of these events relative to the first and third refracted arrivals is not understood but probably depends on a condition of destructive interference.

Table 2

IDENTIFICATION OF RAY PATHS ASSOCIATED WITH THEORETICAL
TRAVEL-TIME CURVES

(Shown in Figures 12 and 14) (R Stands for a P-Refracted Leg)

No.	Path	Phase Velocity (mm/ μ sec)	
		Downdip	Updip
1	PRP	5.23	5.35
2	PRS	5.14	—
3	SRP	5.23	—
4	PP	~3.91 @ 145 cm	~4.00 @ 35 cm
5	PS	~3.83 @ 145 cm	—
6	SP	~3.91 @ 145 cm	—
7	PPPRP	5.23	5.35
8	PRPPP	5.12	5.48
9	PPPRS	5.14	—
10	PRPPS	5.03	—
11	PPPP	~3.93 @ 145 cm	~4.25 @ 35 cm
12	PPPS	~3.85 @ 145 cm	—
13	PRPPPPP	5.02	—
14	PPPRPPP	5.12	—
15	PPPPRP	5.23	—
16	PPPPPP	~3.94 @ 145 cm	~4.66 @ 35 cm
17	PPPPPPP	~3.97 @ 145 cm	—
18	PRPPPPPP	4.92	—
19	PPPPPPRP	5.23	—

Table 3

EXPERIMENTAL DOWNDIP PHASE VELOCITIES
(for Events Shown in Figure 13)

Event	Velocity (mm/ μ sec)
A	5.20
B	5.10
C	4.95
D	4.00
E	4.00
F	4.00
G	4.05
H	3.90

Similarly, the fifth refracted arrival seems to be observable, but not the fourth. Additional reflected events which can be identified are F, which correlates with either 6 or 17, and E, which correlates with 16.

Although several events are expected in the second observable refracted packet (B), only two — presumably, the first and last — are consistently observable. To show that these do indeed have different phase velocities, we have measured the time interval between the peak preceding B (B-) and the peak following B (B+) at two distances from the source. This is found to be 7.5 μ sec at 127 cm and 9.5 μ sec at 145 cm. Also, we find a phase velocity of 5.14 mm/ μ sec for B- and 4.86 mm/ μ sec for B+. If the maximum error in time measurements is ± 0.5 μ sec, the phase velocity of B- could be as high as 5.21 mm/ μ sec or as low as 5.06 mm/ μ sec. Similarly, the phase velocity of B+ could be between 4.93 and 4.80 mm/ μ sec. The formula obtained in a previous section of this appendix yields a "true" velocity of 5.28 mm/ μ sec for the stainless steel. This compares well with the value of 5.29 mm/ μ sec obtained from direct measurements in the steel. However, using the extreme values for the phase velocities of B- and B+, we see that the stainless steel velocity could be between 5.41 and 5.13 mm/ μ sec. As a check on the validity of our identifications, we find the A to B- time interval to be 25 μ sec at 127 cm and not more than 25.5 μ sec at 145 cm, as would be expected.

Measurement of the dip angle requires a knowledge of the brass-layer velocity. This can be obtained from the wide-angle reflections, but there is considerable scatter in the measured phase velocity of these events. This is not surprising because the phase velocity is not really constant but decreases slowly with distance and because adequate measurement of the phase velocity requires measurement of the travel-time difference for the reflected pulse recorded on two receivers with large space separation. However, it is known that the actual velocity of the material cannot exceed the phase velocity of the first wide-angle reflections and that the latter approaches the former asymptotically with distance. For experimental purposes, we will take the two to be equal. This value yields a dip angle of 1.01° , not greatly in error from the correct value of 0.715° .

A second method of measuring the true velocity of the stainless steel requires the differences in phase velocity between the first refracted arrival traveling updip and the same event traveling downdip. This method is more convenient than that used previously because it is easier to identify the first arrival than secondary events. In order to make use of this method, updip travel times were computed. These are shown in Figure 14, while the events are identified and the phase velocities given as before in Table 2. Events were picked from Figures 5 and 8 and travel times plotted in Figure 15. Measured phase velocities are given in Table 4. Using the expression for the phase velocity given in a previous section one estimates — by averaging updip and downdip phase velocities for the first arrival — that the true velocity in the stainless steel is $5.25 \text{ mm}/\mu\text{sec}$. This is somewhat further from the correct value than the previous result; however, the updip velocity measurements were not as reliable as the downdip. Again, measurement of the dip angle requires some knowledge of the velocity in the brass layer.

Table 4

EXPERIMENTAL UPDIP PHASE VELOCITIES
(for Events Shown in Figure 15)

Event	Velocity (mm/ μsec)
A	(5.30)
B	3.90
C	4.15
D	4.95
E	4.35

V. AMPLITUDE MEASUREMENTS

It is also well-known that, for high enough frequencies and large enough source-receiver distances, the refracted events decay as $L^{-3/2}$ (for plane-parallel layers) where L is the distance traveled in the refracting medium. At a given source-receiver distance, L will differ for the various multiples, so each event with distinct travel time will have a separate decay law. This law fails completely near the critical distance since it predicts an infinite amplitude for the refracted event.

The amplitude relations for refractions are not greatly altered by dipping interfaces if the dip is small. In fact, for times prior to the arrival of the first event from a corner (or pinchout), the exact solution can be found by the Cagniard method. Approximation of the exact solution for high frequencies and long distances gives the familiar $L^{-3/2}$ law times an additional spreading factor due to the increasing (or decreasing for updip propagation) length of the ray path reaching the receiver. L is now the slanted distance along the refracting interface. At large distances for downdip propagation, the extra factor approaches 1 and can be ignored.

Measurements of the amplitude of the first arrival showed quite large trace-to-trace variations — probably because of variability in the coupling of the receiver transducer to the model. The measured results are shown in Figure 16. Despite the large amount of scatter, the results are in reasonable agreement with the $L^{-3/2}$ law. (Note that, in practice, L will not be known since it depends both on dip and velocities and thickness of the layers above the refractor.)

VI. LEAKING-MODE DISPERSION STUDIES

At one end of the model, the crustal layer thickness is small enough to allow an interpretation in terms of normal and leaking modes. On the basis of previous studies it is expected that four leaking modes and six normal modes might be excited. While it is obvious that the term "mode" will not have the well-defined meaning in the presence of a dipping interface that it does in a parallel layered model, the work of Kuo and Thompson (1963) indicates that an adequate representation can be found in terms of a sequence of parallel layered models — each valid over a small distance range in the model. This is, of course, just the solution provided by Hamilton's eikonal method (Backus, 1962). For each mode, one may define a dispersion curve which varies slowly with distance.

In this study, there was an attempt to measure the leaking-mode dispersion curves over two distance ranges. Two problems occurred. First, the leaking modes are the smallest energy on the seismograms and

are completely overwhelmed by the Rayleigh mode and other possible events. Second, it was known that the data contained some noise in the form of large random spikes. To reduce the Rayleigh wave, new data were recorded with a receiver depth of 5 cm. Figure 17 shows an example of these data. Next, these data were divided into four groups of 12 traces each — two groups updip and two downdip from the source. A 12-channel Pie Slice* process designed to pass energy between 3.3 and 10 mm/μsec was applied to each set of 12 traces. This reduced the Rayleigh wave energy by 20 db and the random noise by about 10 db ($\sqrt{12}$). Then, dispersion was measured between the two output traces updip from the source and the two downdip from the source. The first step in this procedure requires computation of the cross-power spectrum between the two traces. Phase angle θ of the crosspower is related to phase velocity C and frequency f by the relation

$$\theta(f) = - \frac{2\pi f \Delta x}{C(f)}$$

where Δx is the separation in distance between the two traces. (Note that there is some ambiguity in this expression since $\theta(f)$ can be increased by any multiple of 2π . This means that several phase velocity curves can be drawn for a given phase spectrum, each corresponding to a different multiple of 2π .) Phase velocity curves determined by this method are shown as crosses in Figures 18 and 19. The results in Figure 18 were determined by using Pie Slice output traces corresponding to 83.5 and 95.5 cm. The dispersion thus measured should be valid for a portion of the model centered at 89.5 cm. At this point, the layer thickness is 4.15 cm. Theoretical curves for a plane-layered model with the layer thickness are shown as solid lines in Figure 18. For this model, the attenuation with distance of the PL_{24} mode is significantly less than the attenuation of the PL_{23} mode. Thus, of the three possible curves, probably only the uppermost is valid. Figure 19 shows the dispersion measured for a distance range centered at 20.5 cm where the layer thickness is 3.32 cm. Again, only the upper curve seems to be valid. (Note that the cutoff for PL_{24} is about 145 kc for the 20.5-cm range but is 120 kc for the 89.5-cm range. The agreement between theory and experiment is quite good in both cases.)

In an attempt to evaluate the effects of recording at depth and using Pie Slice, a similar experiment was performed using low-gain data recorded at 27 to 30 cm and at 19 to 23 cm on the top of the model. The time traces were truncated at the onset of the Rayleigh wave. Figure 20 shows that the results are much less satisfactory. It seems likely that the use of Pie Slice was very significant through its tendency to average out inhomogeneities in the data due to nonreproducibility of recording.

*GSI Service Mark

VII. CONCLUSION

The studies described in this appendix may be regarded as generally successful. The velocities (in the downdip direction) of a series of refracted events were measured, the events identified with ray paths and the velocity in the half-space computed. Agreement with the known velocity was reasonably good. Similar results were obtained using a single event (the first arrival) with velocities measured both updip and downdip. Experimental results were also in reasonable agreement with the predicted amplitude decay law, although the scatter was so great that this could not be considered significant. Certain difficulties do arise. Because of the very small differences in velocity between refracted events, it is necessary to measure travel times over a large horizontal range. In practice, it would probably be found that the dip varied significantly over such ranges. Probably, the most significant indicator of structure is the arrival-time difference between two pulses, though this depends both on structure in the layer and structure on the interface. Another problem not completely understood is the small amplitude of certain refracted events such as those with four P-legs in the layer. Computation of amplitude is necessary to explain this, and this has not been attempted here.

Measurement of leaking-mode dispersion curves was relatively successful — perhaps because only a single mode was strongly excited. However, averaging to remove noise — effected here by use of the Pie Slice velocity filter — was very necessary as was seen from the poor results obtained without averaging. Again, for the dispersion computations, measurements over a large range of distances are required. This results both because of the averaging process, which requires a number of measurements, and because of the separation required between averaged outputs.

A comparison of ray interpretation and mode interpretation shows a striking difference. Phase velocities for the refracted rays depend directly on both the angle of dip and the average parameters of the layer. However, dispersion curves for the leaking modes — to the degree of approximation contemplated here — do not depend directly on the angle of dip. The germane parameters are the average layer velocities and the average layer thickness (assumed to vary slowly with distance). Average dip angle is obtained indirectly from layer thickness. Because of the large range of distances required to make precise measurements using either method, the modal approach would appear to be more generally useful because of its averaging properties. However, one must bear in mind that the problem becomes considerably more complicated if more than two or three modes of propagation are excited.

VIII. ACKNOWLEDGMENTS

The authors wish to thank Bobby Warren, who operated the seismic analog model; and Leon Horowicz, a summer employee from MIT, who processed the data to obtain leaking-mode dispersion curves. This work was supported by the Air Force Office of Scientific Research under Contract AF 49(638)-1244.

IX. REFERENCES

- Kuo, J. and G. Thompson, 1963, Model studies on the effect of a sloping interface on Rayleigh waves: J. Geophys. Res., v. 68, p. 6187.
- Backus, G., 1962, Propagation of short elastic surface waves on a slowly rotating earth: Bull. Seis. Soc. of Am., v. 52, n. 4, p. 823.

FIGURE CAPTIONS

- Figure 1. Ray Paths Showing Refracted Reflection, Reflected Refraction and Virtual Multiple Event
- Figure 2. Refracted Ray Path for Dipping Interface
- Figure 3. Mechanisms for Multiple Generation on a Dipping Interface. The angle of incidence θ' at A is greater than the critical angle of incidence θ . If the ray is traveling updip, θ' will be less than θ
- Figure 4. Schematic Diagram of Model H4
- Figure 5. Low-Gain Vertical Seismograms for Model H4, Measured in an Updip Direction. Distance range, 23 to 30 cm
- Figure 6. Low-Gain Vertical Seismograms for Model H4, Measured in a Downdip Direction. Distance range, 30 to 50 cm
- Figure 7. Low-Gain Vertical Seismograms for Model H4, Measured in a Downdip Direction. Distance range, 55 to 70 cm
- Figure 8. High-Gain Vertical Seismograms for Model H4, Measured in an Updip Direction. Distance range, 17-24 cm
- Figure 9. High-Gain Vertical Seismograms for Model H4, Measured in a Downdip Direction. Distance range, 65 to 85 cm
- Figure 10. High-Gain Vertical Seismograms for Model H4, Measured in a Downdip Direction. Distance range, 125 to 134 cm
- Figure 11. High-Gain Vertical Seismograms for Model H4, Measured in a Downdip Direction. Distance range, 136 to 145 cm
- Figure 12. Theoretical Downdip Travel-Time Curves for Model H4. Ray paths associated with the numbers are given in Table 2
- Figure 13. Experimental Downdip Travel Times for Events Shown in Figures 9 through 11. Measured phase velocities are given in Table 3
- Figure 14. Theoretical Updip Travel-Time Curves for Model H4. Ray paths associated with the numbers are given in Table 2

FIGURE CAPTIONS (CONTD)

- Figure 15. Experimental Updip Travel-Time Curves for Events Shown in Figure 8. Measured phase velocities are given in Table 4
- Figure 16. Amplitude of First Refracted Arrival vs Distance Traveled in the Refractor
- Figure 17. Experimental Data Recorded by a Receiver at 5-cm Depth. Distances range 21 to 32 cm from source
- Figure 18. Leaking-Mode Dispersion Curves for a Distance Range Centered at 89.5 cm. Crosses are experimental points; solid lines, theoretical. Source located at 55 cm; Pie Slice applied to data
- Figure 19. Leaking-Mode Dispersion Curves for a Distance Range Centered at 20.5 cm. Crosses are experimental points; solid lines, theoretical. Source located at 55 cm; Pie Slice applied to data
- Figure 20. Leaking-Mode Dispersion Curves for a Distance Range Centered at 28.5 and 21 cm. Source located on top of model; Pie Slice not used

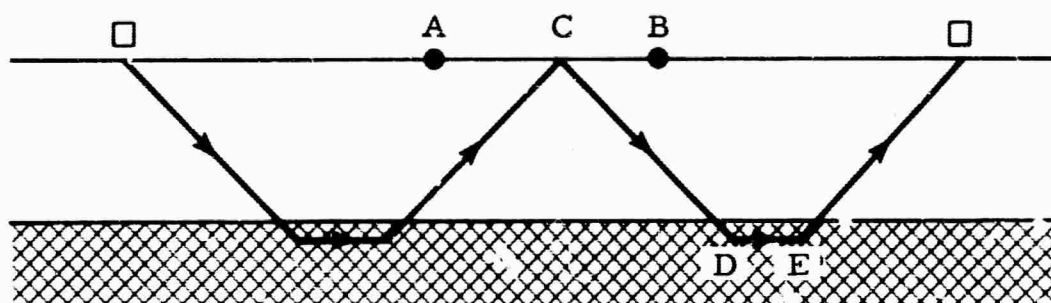
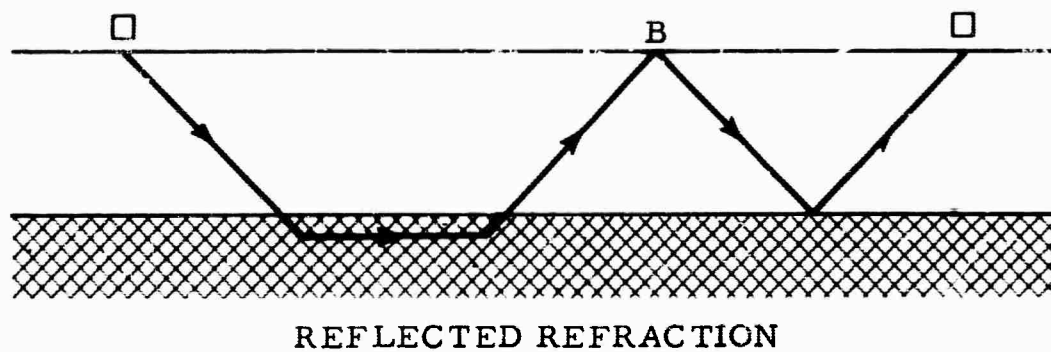
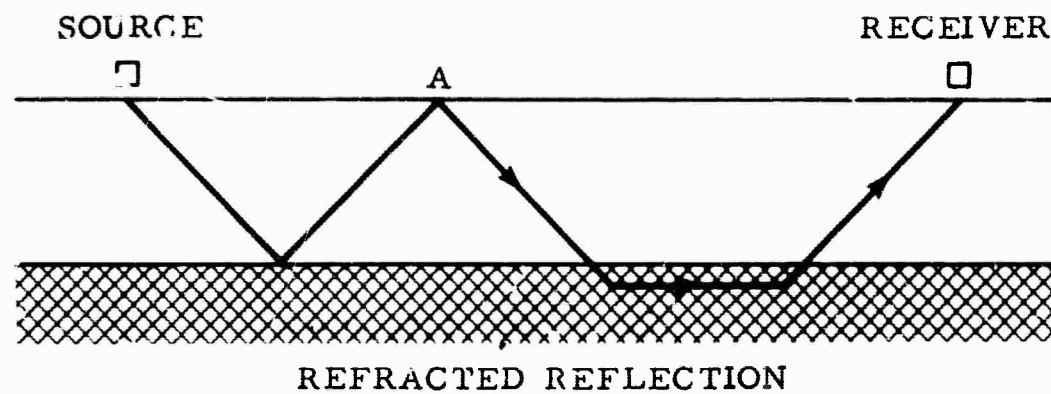


Figure 1. Ray Paths Showing Refracted Reflection, Reflected Refraction and Virtual Multiple Event

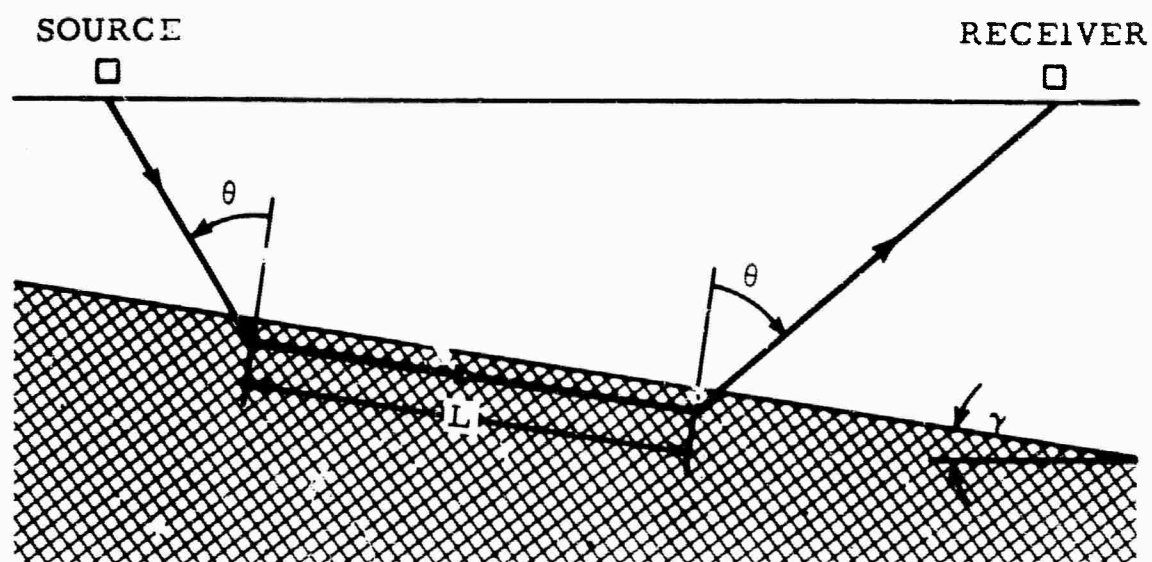


Figure 2. Refracted Ray Path for Dipping Interface

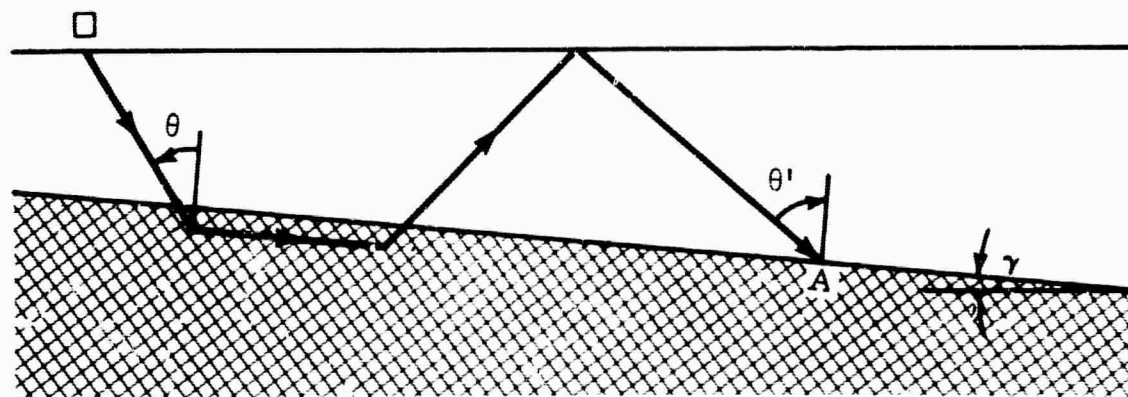


Figure 3. Mechanisms for Multiple Generation on a Dipping Interface. The angle of incidence θ' at A is greater than the critical angle of incidence θ . If the ray is traveling updip, θ' will be less than θ

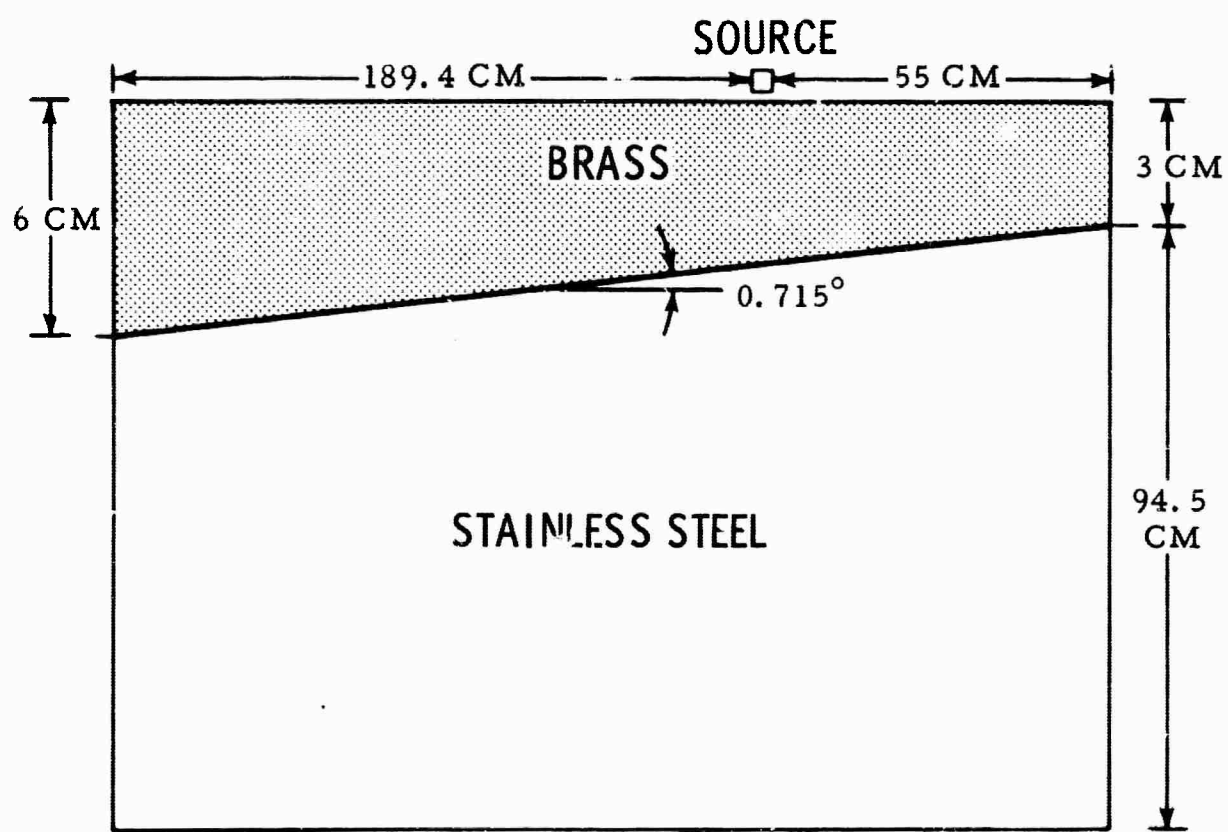


Figure 4. Schematic Diagram of Model H4

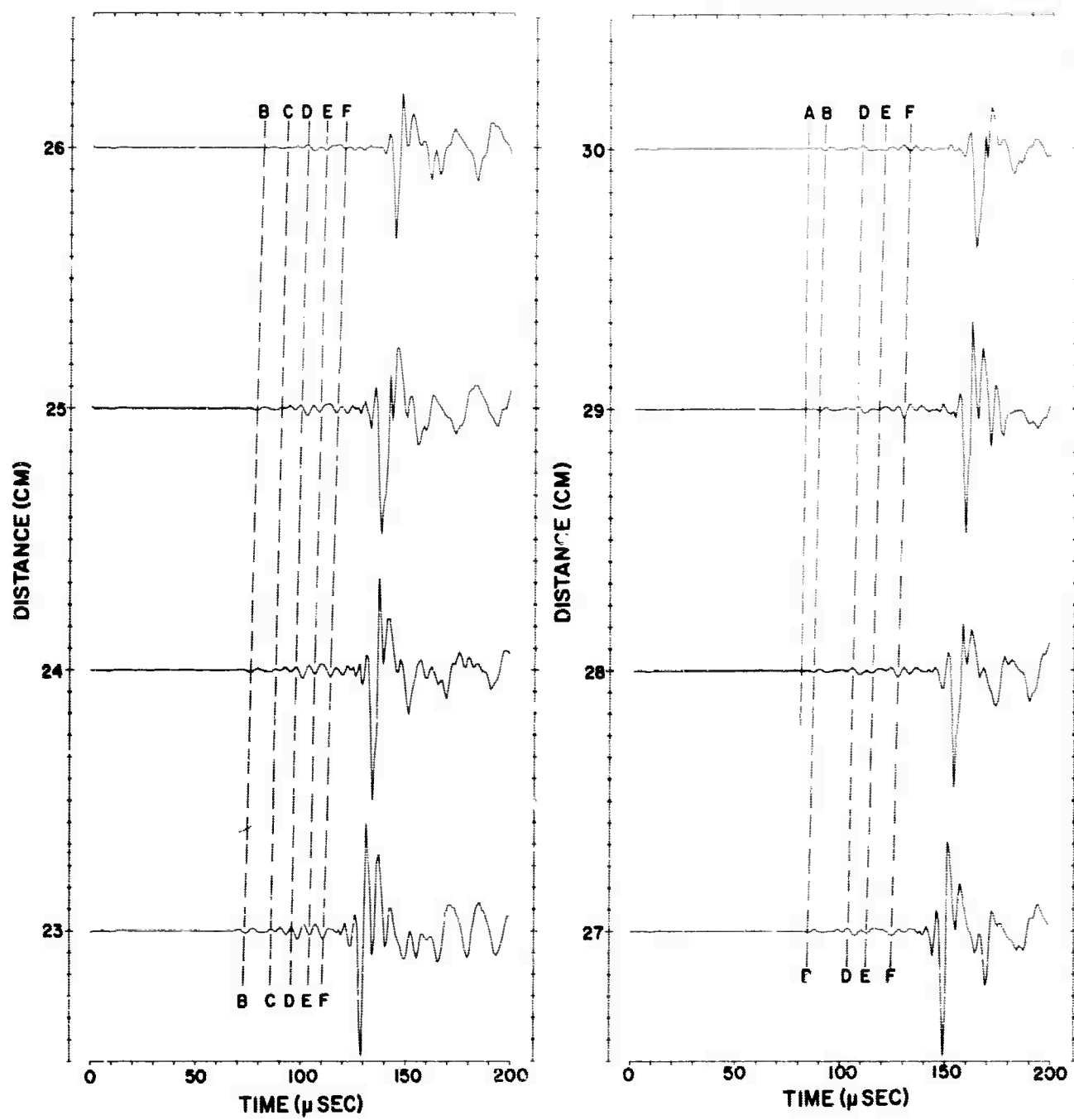


Figure 5. Low-Gain Vertical Seismograms for Model H4, Measured in an Updip Direction. Distance range, 23 to 30 cm

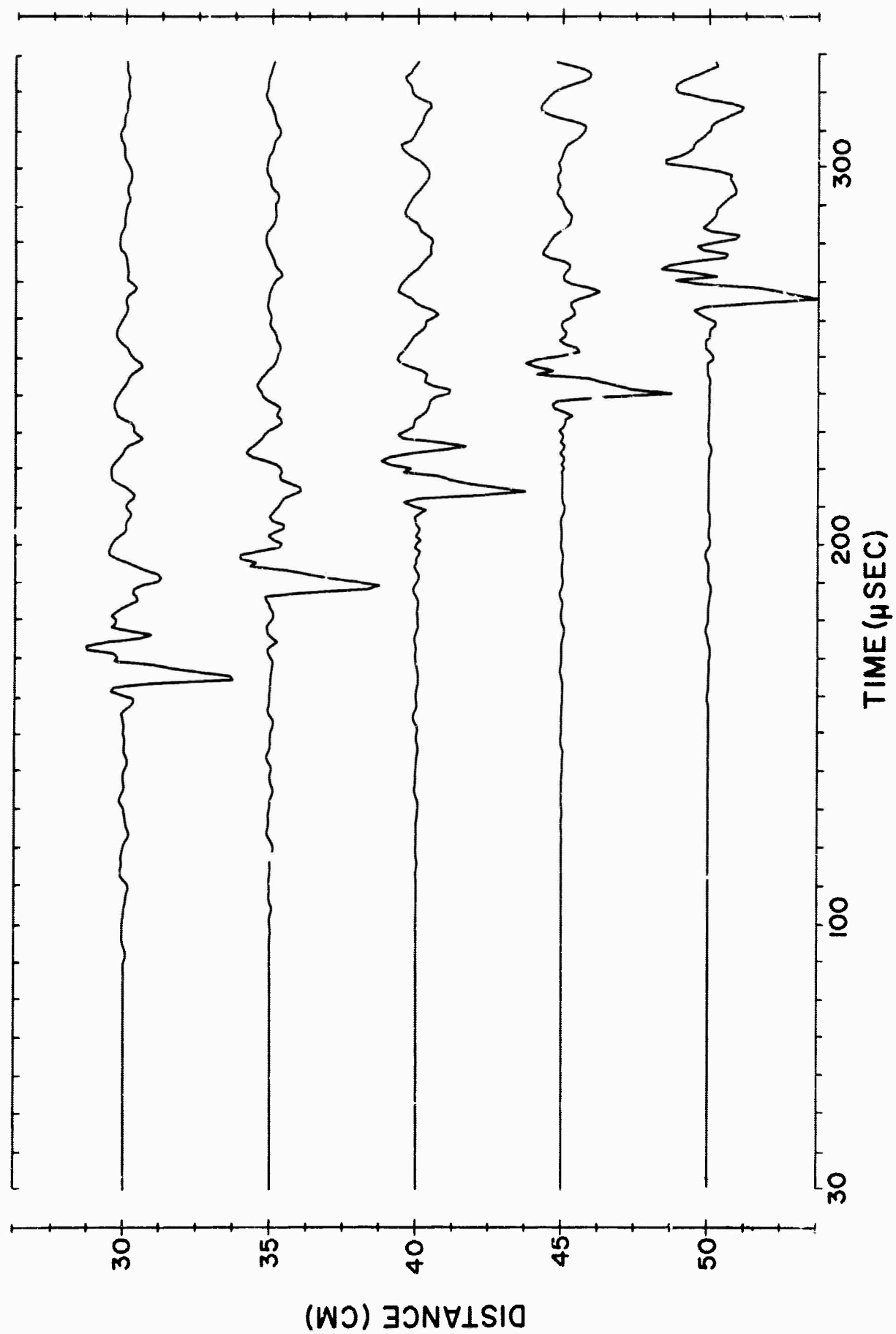


Figure 6. Low-Gain Vertical Seismograms for Model H4, Measured in a Downdip Direction. Distance range, 20 to 50 cm

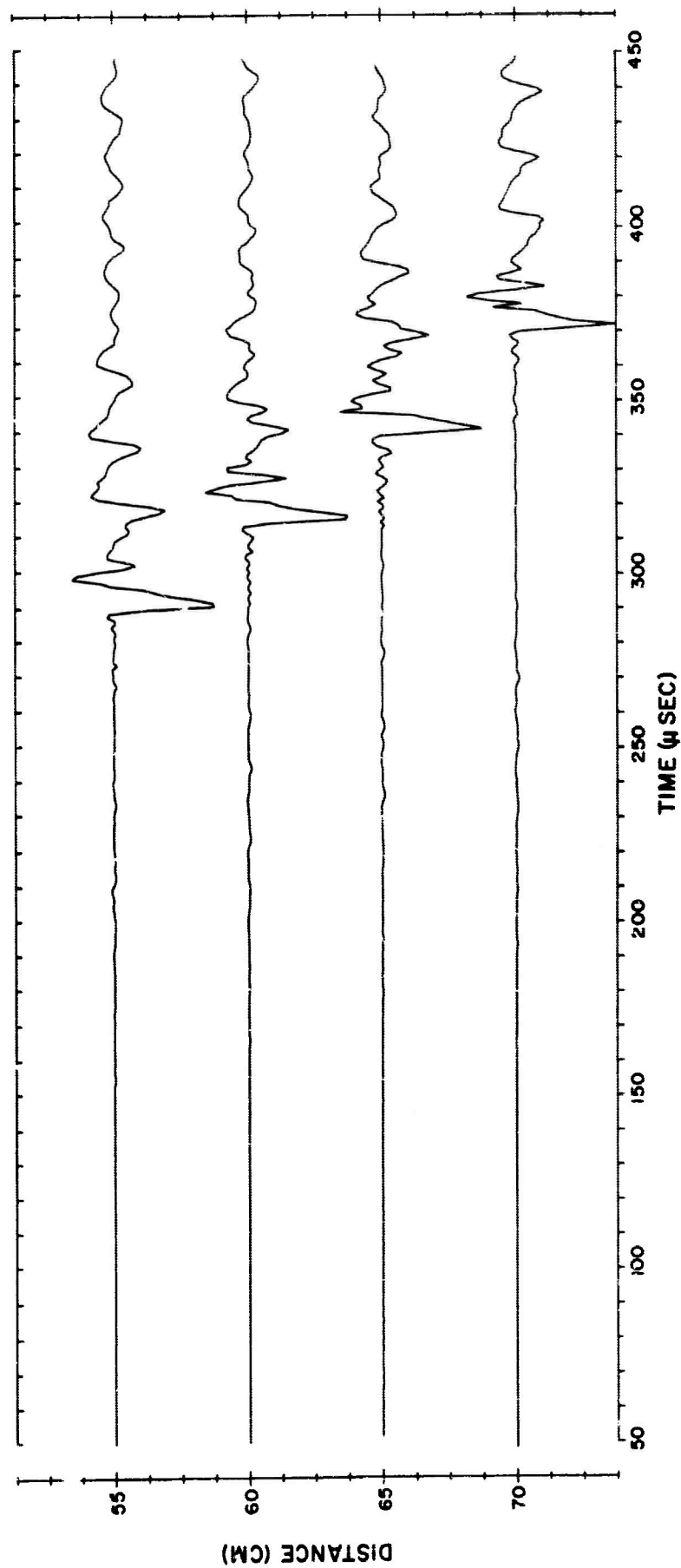


Figure 7. Low-Gain Vertical Seismograms for Model H4, Measured in a Downdip Direction. Distance range, 55 to 70 cm

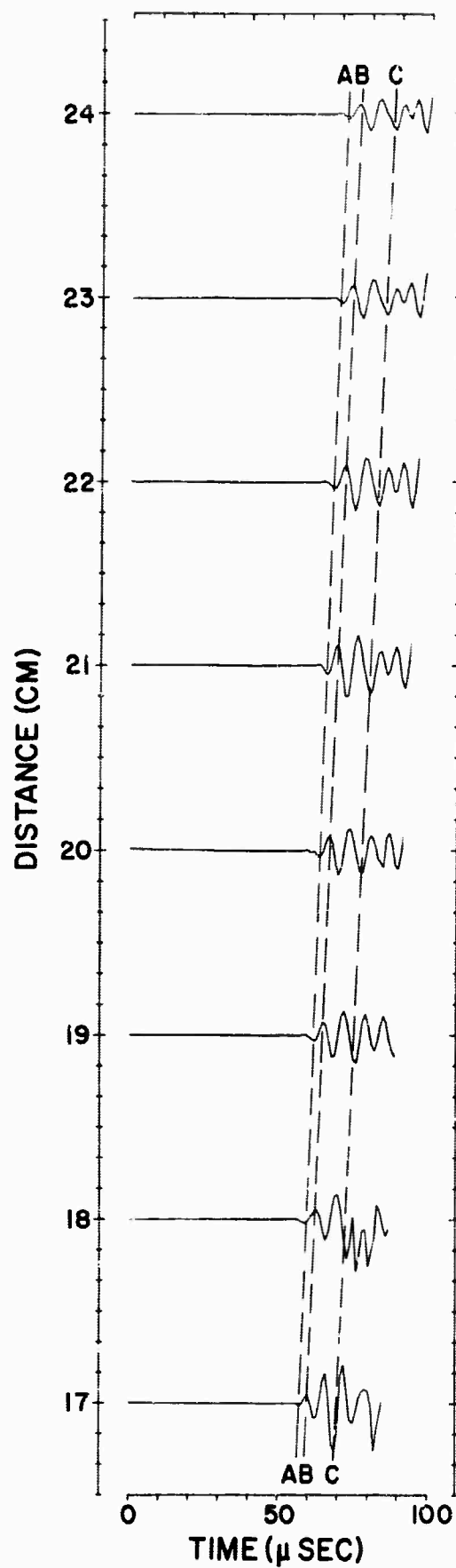


Figure 8. High-Gain Vertical Seismograms for Model H4, Measured in an Updip Direction. Distance range, 17-24 cm

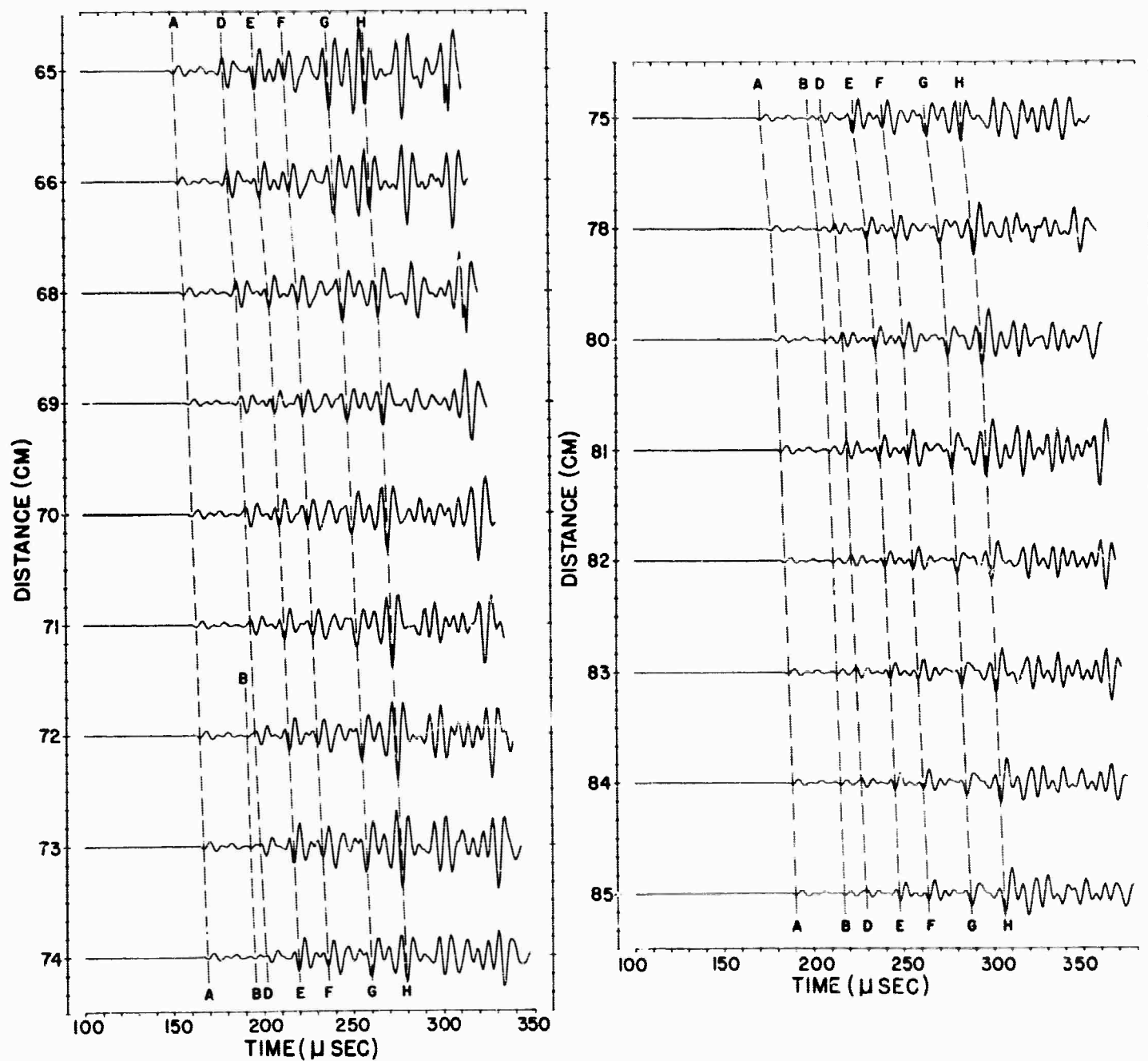


Figure 9. High-Gain Vertical Seismograms for Model H4, Measured in a Downdip Direction. Distance range, 65 to 85 cm

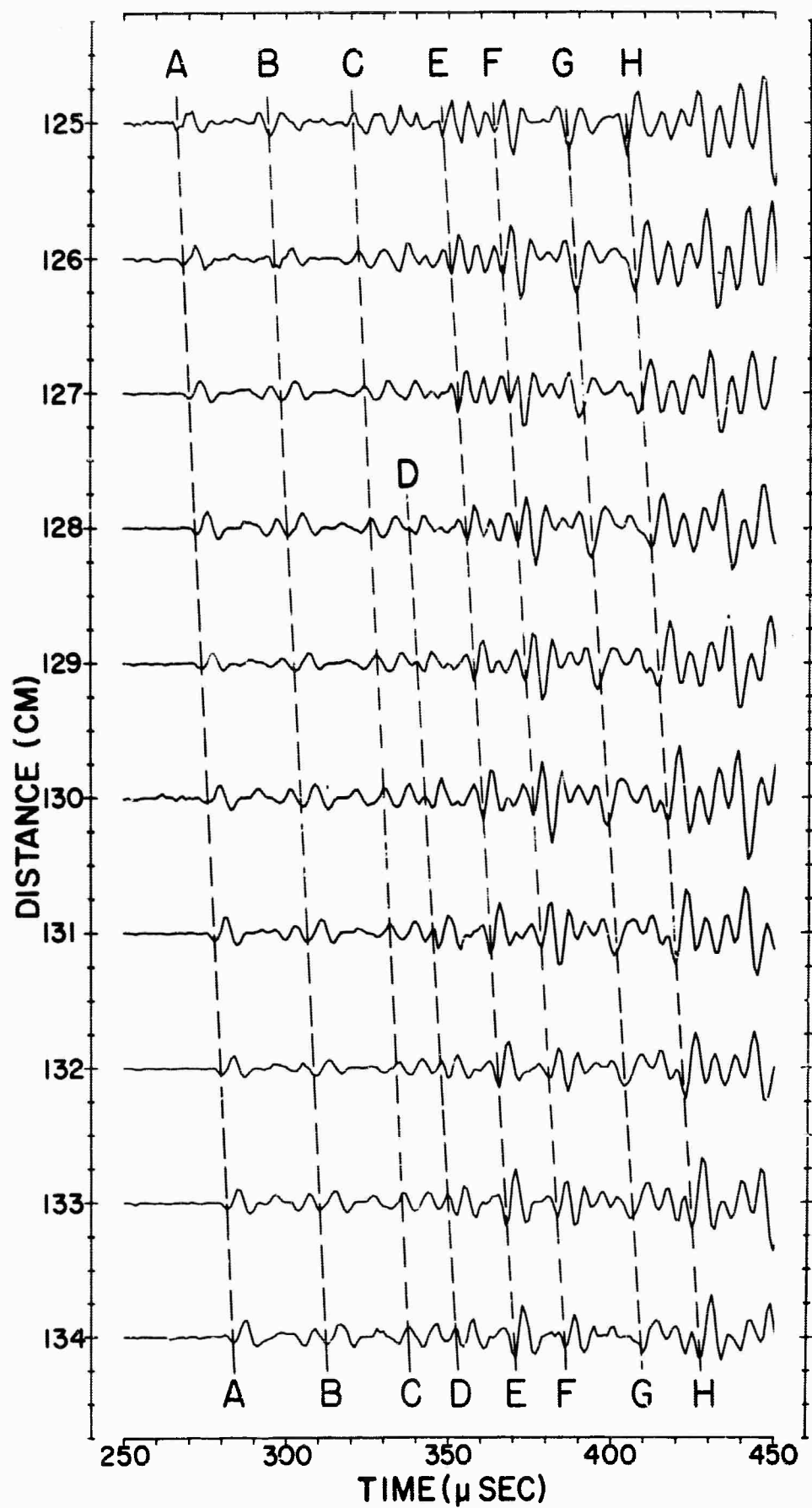


Figure 10. High-Gain Vertical Seismograms for Model H4, Measured in a DOWNDIP Direction. Distance range, 125 to 134 cm

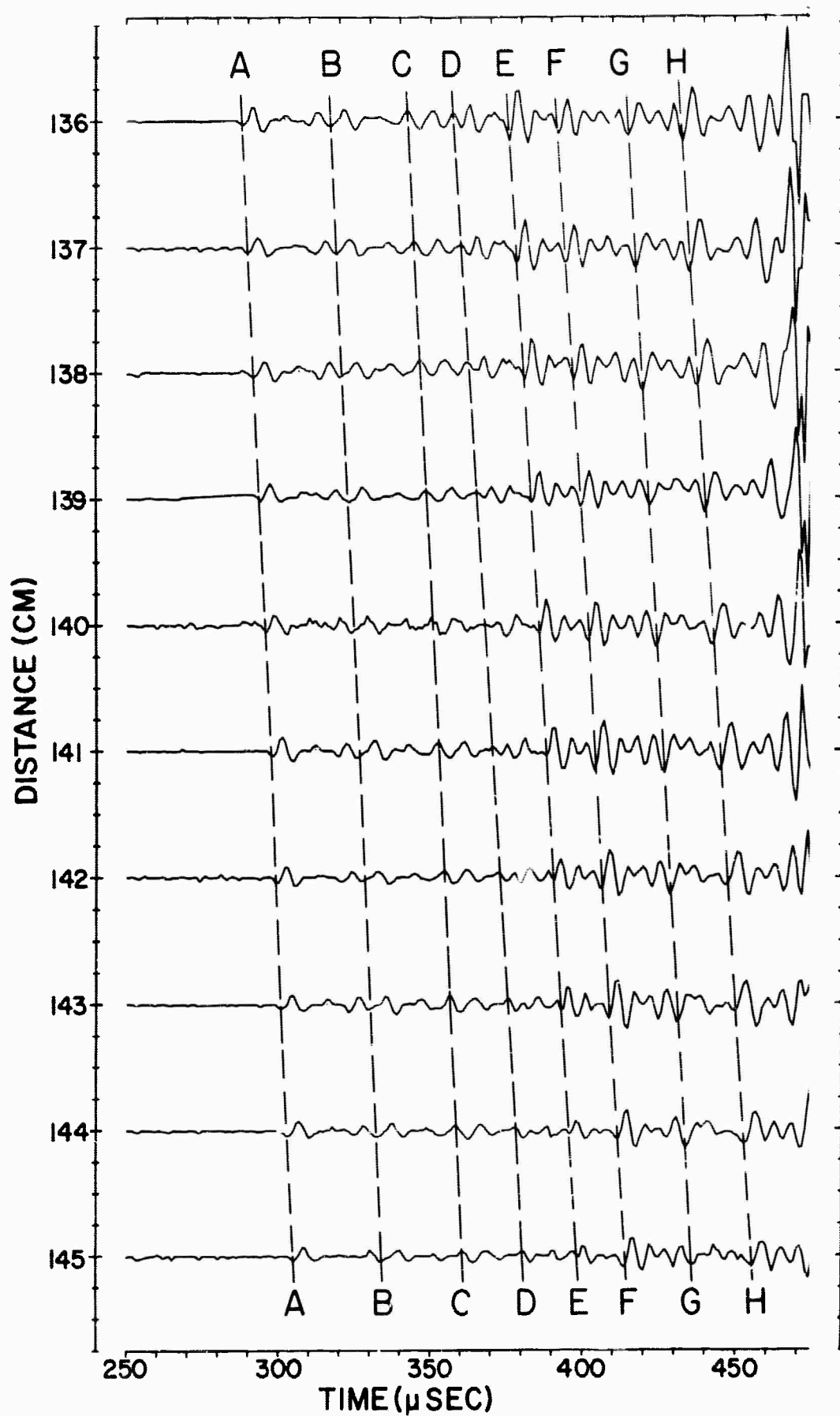
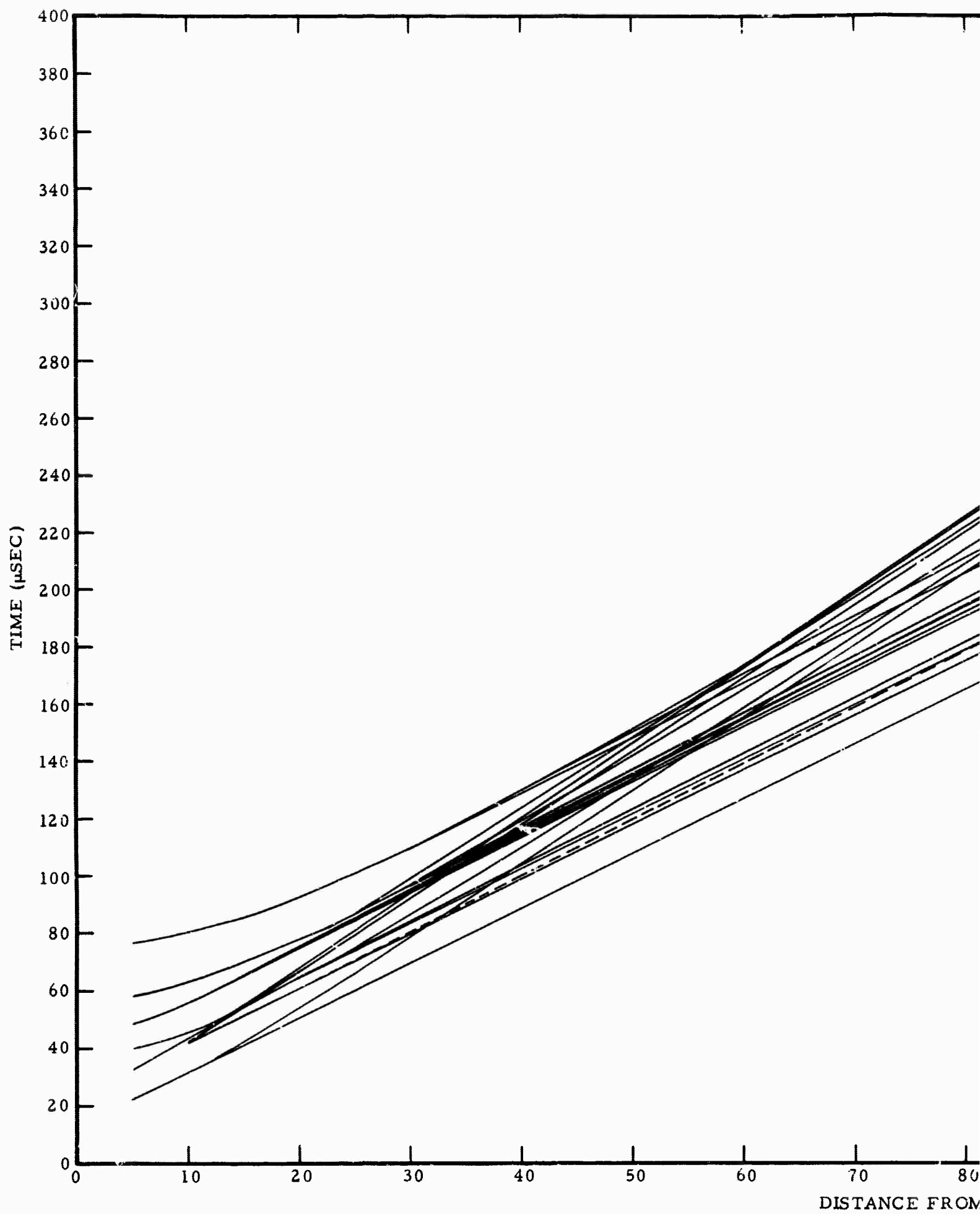


Figure 11. High-Gain Vertical Seismograms for Model H4, Measured in a Downdip Direction. Distance range, 136 to 145 cm



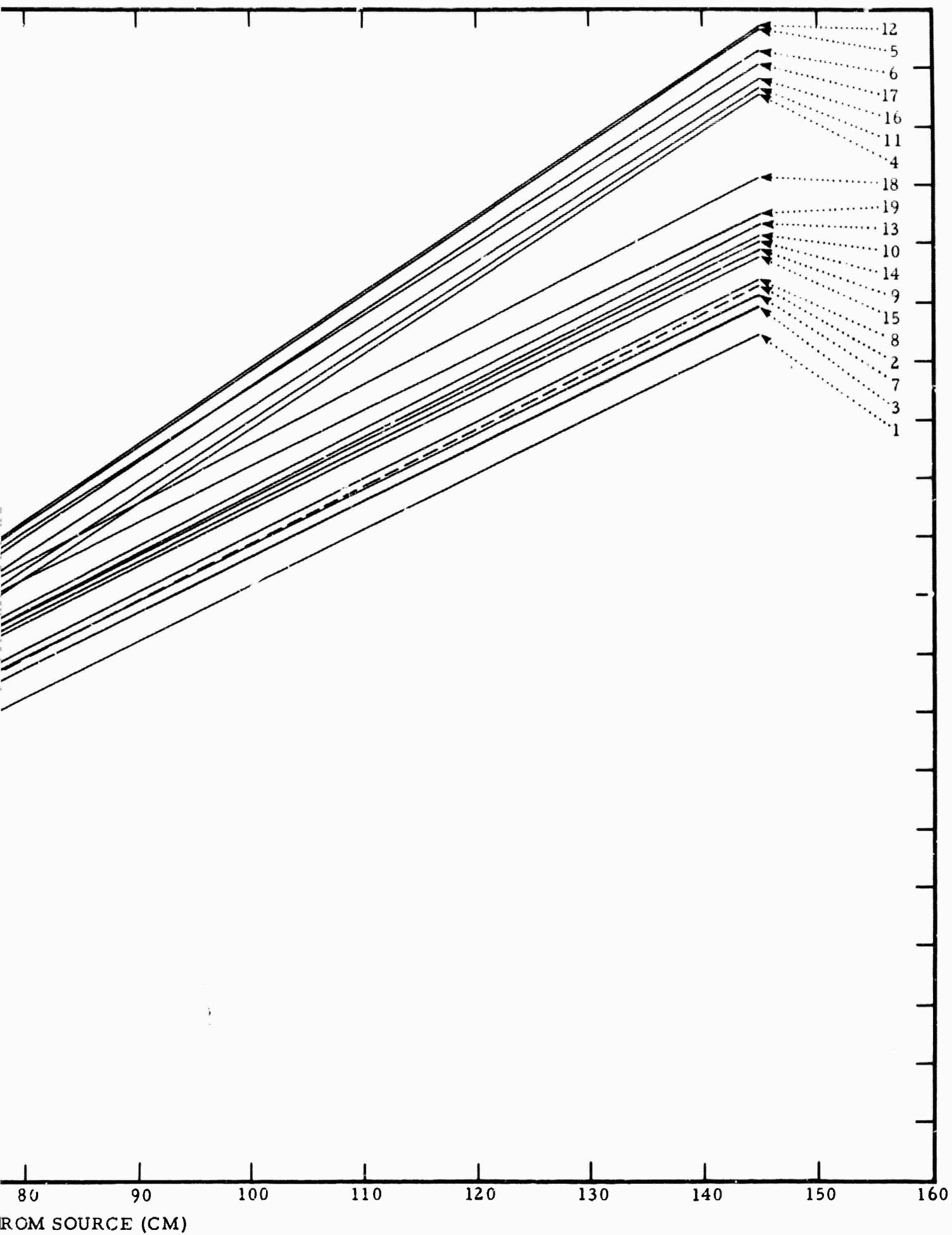


Figure 12. Theoretical Downdip Travel-Time Curves for Model H4. Ray paths associated with the numbers are given in Table 2

BLANK PAGE

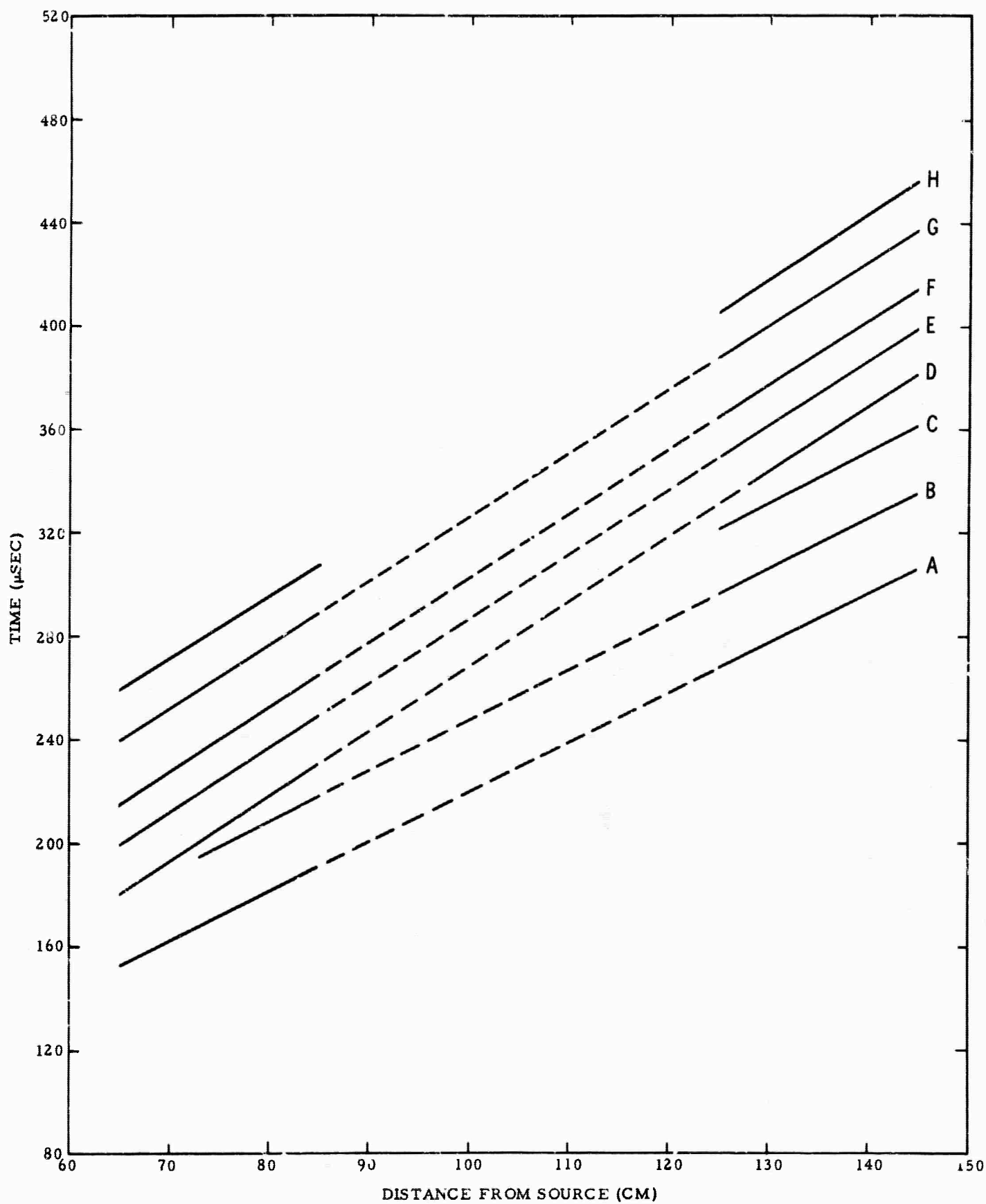


Figure 13. Experimental Downdip Travel Times for Events Shown in Figures 9 through 11. Measured phase velocities are given in Table 3

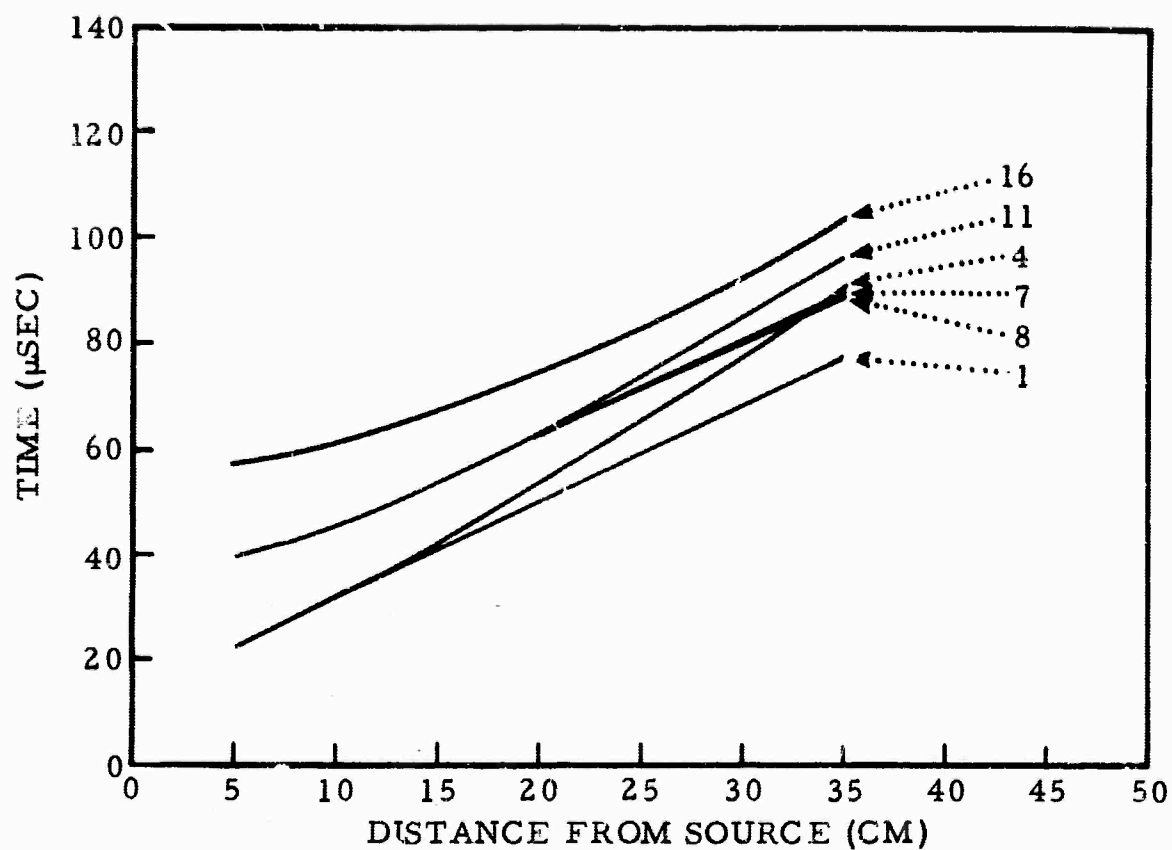


Figure 14. Theoretical Updip Travel-Time Curves for Model H4. Ray paths associated with the numbers are given in Table 2

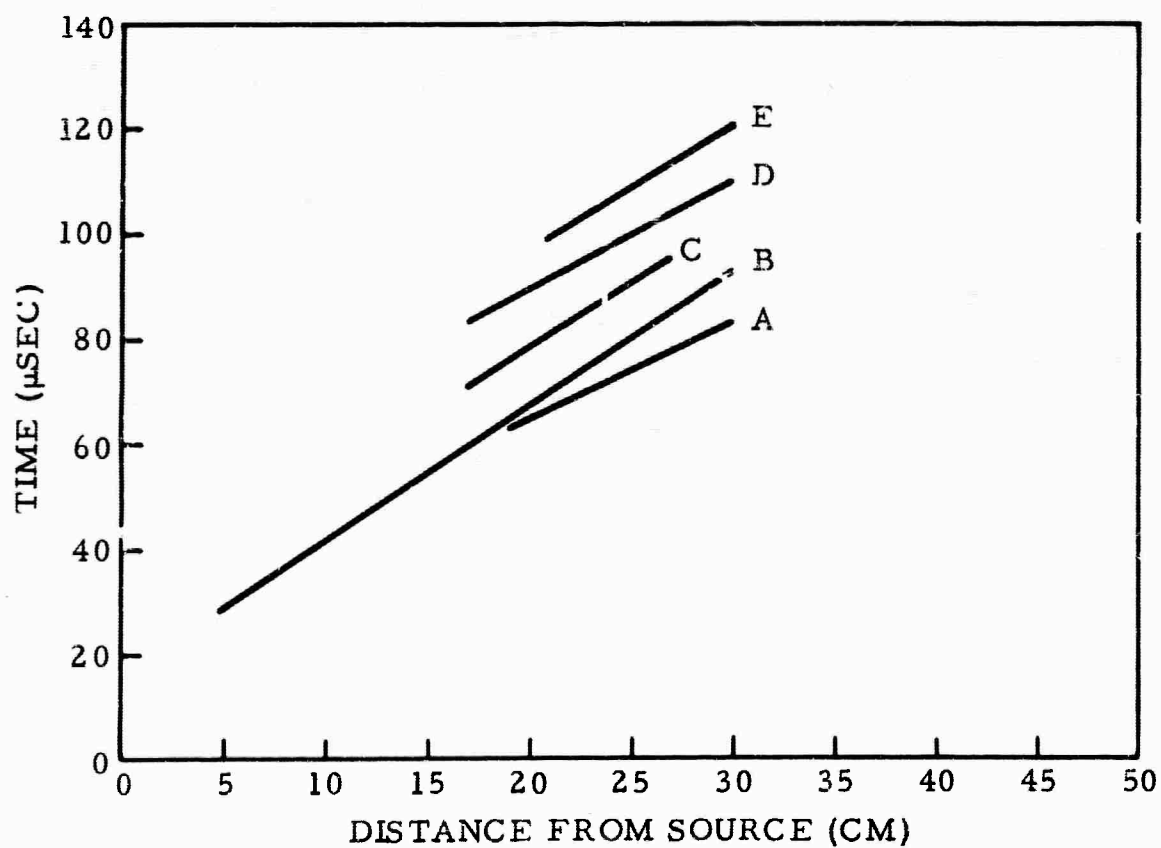


Figure 15. Experimental Updip Travel-Time Curves for Events Shown in Figure 8. Measured phase velocities are given in Table 4

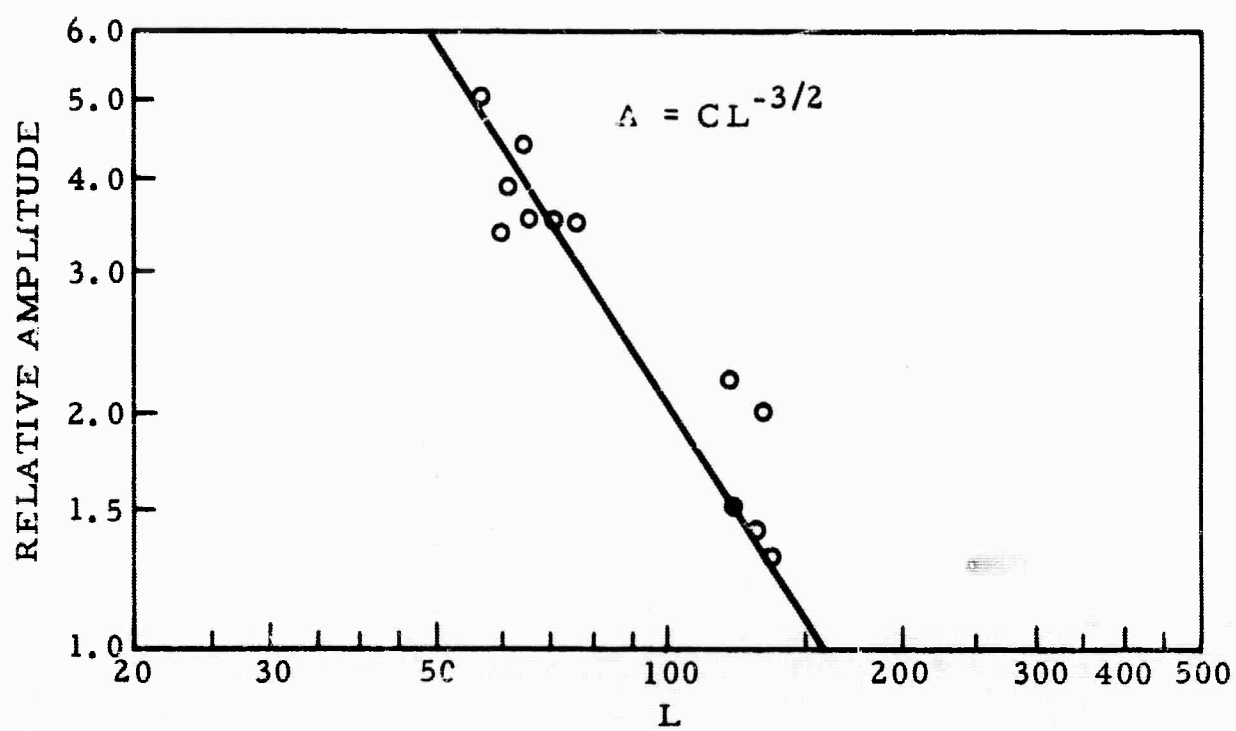


Figure 16. Amplitude of First Refracted Arrival vs Distance Traveled in the Refractor

EXPERIMENTAL SEISMOGRAMS

SOURCE POSITION 55 CMS FILTER 90 KC - OUT

Position
in cms

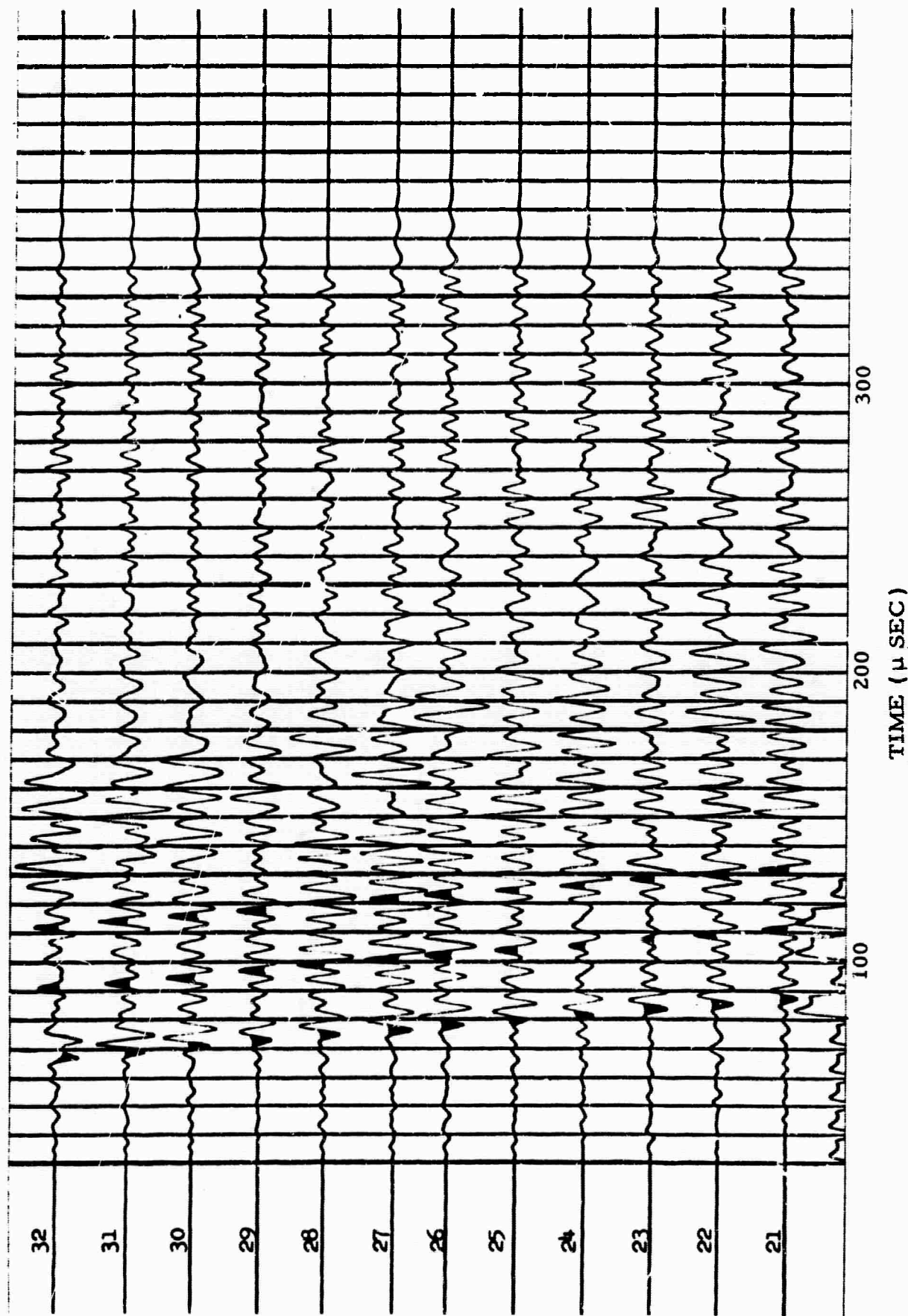


Figure 17. Experimental Data Recorded by a Receiver at 5-cm Depth.
Distances range 21 to 32 cm from source

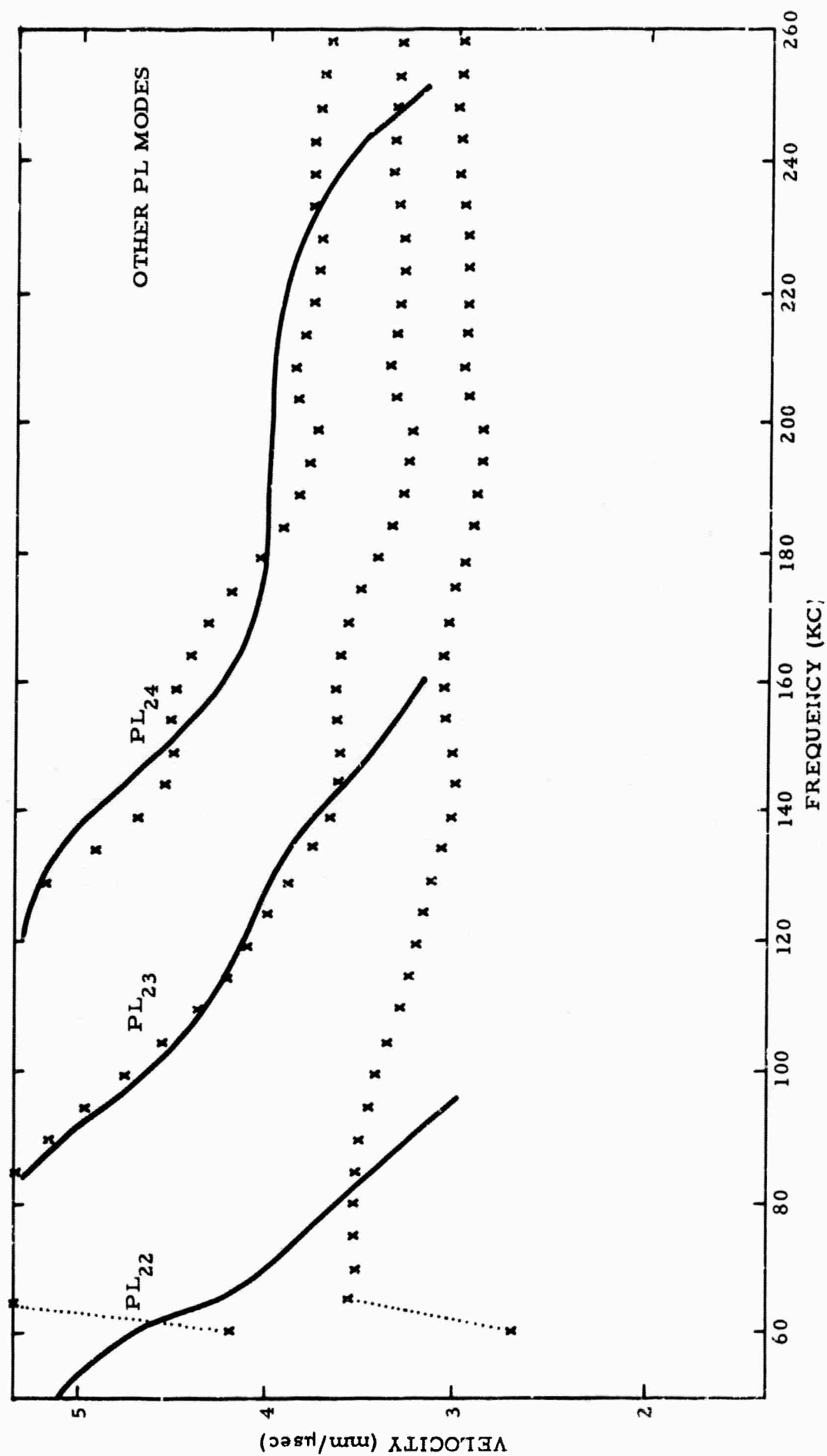


Figure 18. Leaking-Mode Dispersion Curves for a Distance Range Centered at 89.5 cm. Crosses are experimental points; solid lines, theoretical. Source located at 55 cm; Pie Slice applied to data

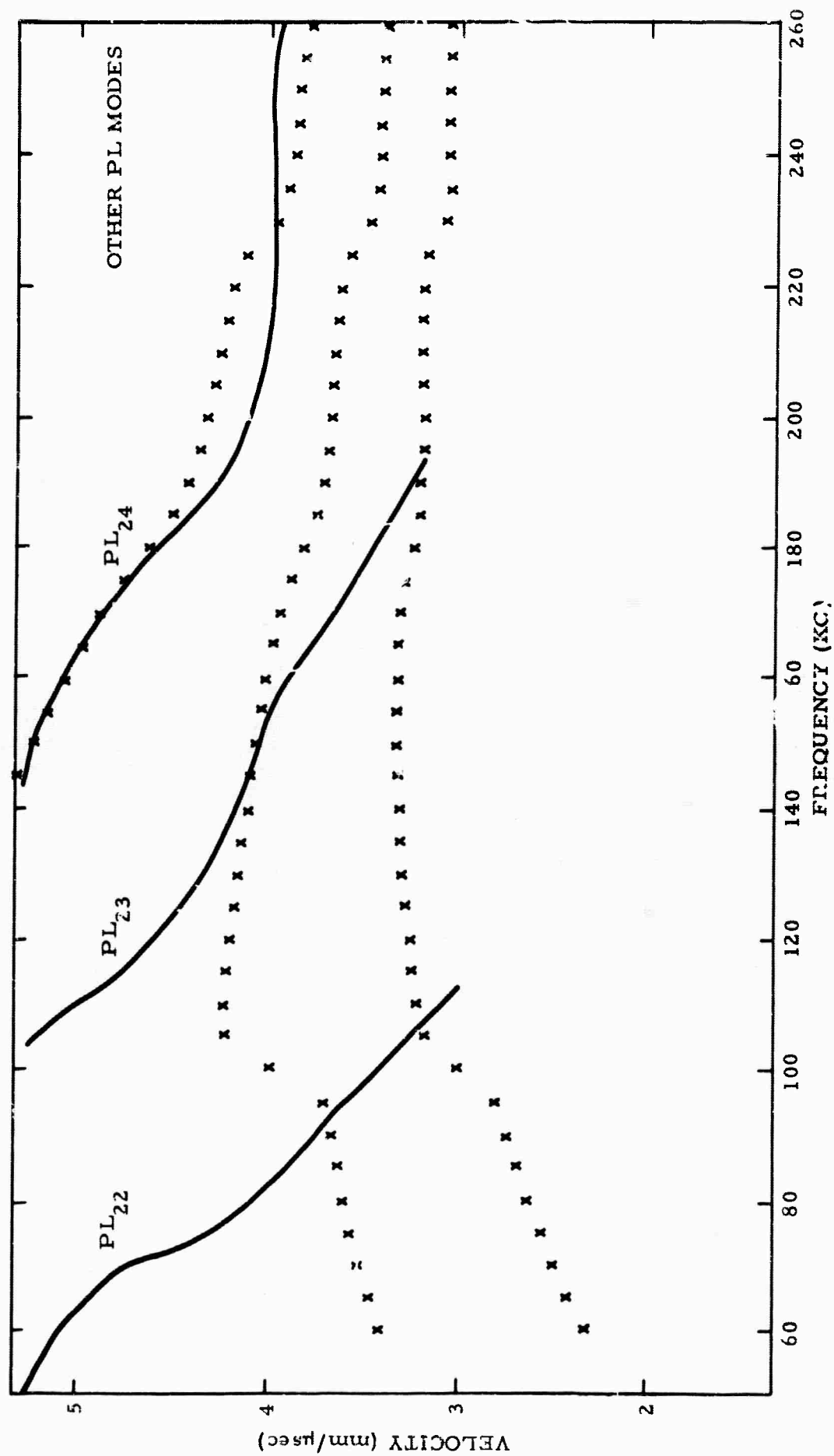


Figure 19. Leaking-Mode Dispersion Curves for a Distance Range Centered at 20.5 cm. Crosses are experimental points; solid line theoretical. Source located at 55 cm; Pie Slice applied to data

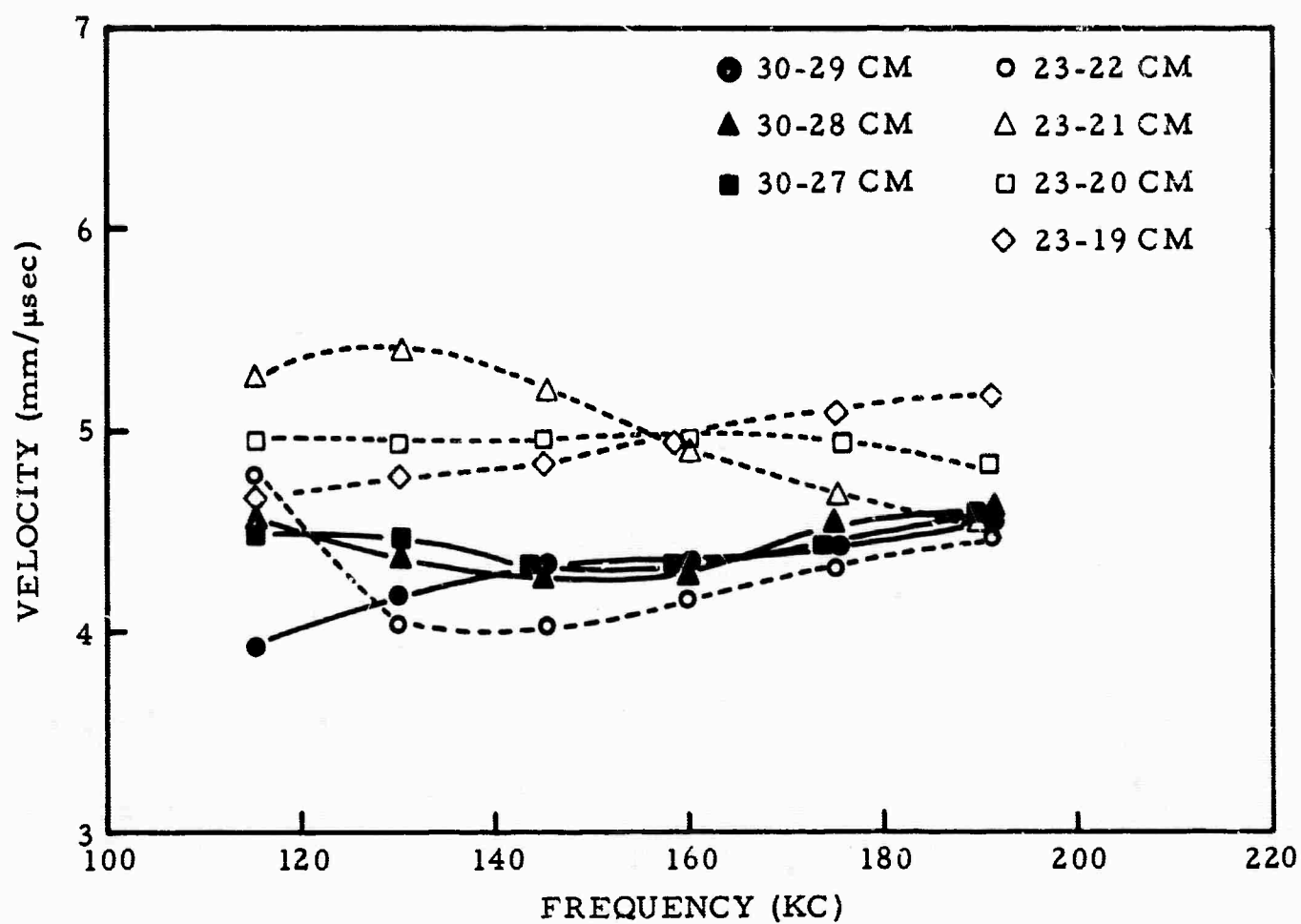


Figure 20. Leaking-Mode Dispersion Curves for a Distance Range Centered at 28.5 and 21 cm. Source located on top of model; Pie Slice not used

APPENDIX F

MULTICHANNEL PROCESSING APPLIED TO THE ANALYSIS OF REFRACTION SEISMOGRAMS RECORDED AT TONTO FOREST SEISMOLOGICAL OBSERVATORY

by Terence W. Harley, Renner B. Hofmann,
and Stanley J. Laster

Abstract

A group of experimental crustal seismograms from the Tonto Forest Seismological Observatory have been selected which show a large number of coherent, pulse-like events. These include both recordings of nuclear devices detonated in Nevada and shots recorded during the 1964 USGS calibration program. The nuclear records have been subjected to wideband velocity filtering and the results clearly illustrate the P_n and P_g arrivals, with little indication of P^* . Following the first arrival of each of these events is a series of pulses with the same or approximately the same characteristic velocity, persisting throughout the seismogram and indicating many multiples of the simple crustal phases. The similarity in velocity between P_n and the P_n multiples suggests that dip of the M discontinuity under Tonto Forest is very small or absent.

The USGS shots indicate a significant difference between the crust to the north of the array as compared to the crust south of the array. P_g is observed on all records, but P_n is observed only from shots in the north, while a lower velocity event, perhaps P^* , is seen from shots in the south. Well-developed surface waves are also more

common from shots in the north, presumably due to greater thickness of sedimentary cover.

The application of data-dependent prewhitening, or deconvolution, to one reverberatory event enhanced several weak arrivals which were not evident on the raw record, and allowed a more detailed interpretation of the event.

Finally, the seismometer to seismometer predictability of a shot from the Bylas shotpoint and of a quarry blast from near the Clarkdale shotpoint are investigated. Significant pulse-shape changes across the array are observed in the raw data, and it is found that only about 50 percent of the energy is predictable from one seismometer to the next. Use of additional channels in the prediction process offers only slight improvement in predictability, indicating that the remaining energy is almost random in space. The probable cause of this is the presence of a large number of scattering centers in the vicinity of the array.

BLANK PAGE

APPENDIX F

MULTICHANNEL PROCESSING APPLIED TO THE ANALYSIS OF REFRACTION SEISMOGRAMS RECORDED AT TONTO FOREST SEISMOLOGICAL OBSERVATORY

by Terence W. Harley, Renner B. Hofmann,
and Stanley J. Laster

I. Introduction

The present paper describes attempts to apply some recently developed data processing techniques to aid in the interpretation of crustal seismic refraction records. These new techniques have come about as a result of the VELA UNIFORM program and as a result of the impact of computer technology on the seismic exploration industry. The technique most immediately applicable is velocity filtering, which makes use of filtering operations in both space and time. However, other techniques, such as data-dependent prewhitening, and multichannel processing based on correlation statistics of the data may also be useful.

The seismograms discussed in this paper are recordings obtained from the large-cross array at Tonto Forest Observatory, Arizona (Figure 1). This facility has been described elsewhere (Linville and Laster, 1965) so it will only be briefly summarized here.

A plan view of the cross array is shown in Figure 2. Each of the two 10-km linear spreads consists of 11 seismometers which are short-period Johnson-Matheson instruments whose passband is about 0.5 to 5 cps. The two arms share the center seismometer. The seismograms were recorded digitally on magnetic tape with a sample period of 24 msec.

TFO is just south of the Colorado Plateau boundary and is considered in the basin and range province, although from the standpoint of elevation, typical basin and range topography does not occur until some distance to the south (see Figure 10). It is fairly certain that TFO is near a zone of change in crustal structure but the actual boundary has not been fixed yet.

A rough idea of the configuration of the sedimentary cover is essential to interpret crustal structure from seismograms. Although sediments are thick in parts of the Basin and Range province, geologic maps show frequent exposures of Pre-Cambrian rocks, suggesting a complex and heterogeneous cover. In general, waves of longer wavelength should be less perturbed by the heterogeneity than by the average thickness. Most of the Tonto Forest array is located on a granite outcrop with the maximum elevation difference between seismometers being about 150 meters. Significant sedimentary cover begins 10 km north of TFO near the Mogollon Rim, a steep ridge 350 meters high. This ridge has significant effects upon seismic waves through the mechanism of scattering. It is hypothesized that compressional waves striking this ridge generate low-velocity surface waves which propagate across the array to corrupt later arrivals.

It is worthwhile to point out here that the purpose of this paper is to evaluate interpretation aids, as opposed to developing a detailed model of the Tonto Forest subsurface environment. In any event, considerably more data than is used here would be required to obtain a complete solution.

II. The Data

All the seismic events considered in this paper were recorded digitally using the large cross array. Two categories of data were used. The first set consists of recordings of two nuclear devices detonated in Nevada. The second set consists of recordings of the 1964 U. S. Geological Survey calibration shots at Tonto Forest. The two sets of data are considered separately.

A. The Nuclear Events

The two nuclear events were detonated in Nevada at the locations given in Table I and shown on the map in Figure 3. As is noted from the table, the travel path of the Greys shot is almost inline with the northwest-southeast arm of the cross, while the Fallon travel path is oriented somewhat more to the north. The result of this is to reduce the effective inline spacing for the Fallon shot.

TABLE I

LOCATION OF GREYS AND FALLON SHOT WITH RESPECT TO TFO
(Center Seismometer Z-21)

	<u>Greys</u>	<u>Fallon</u>
Azimuth	N 54° W	N 47.3° W
Distance	569 km	837 km

Selected traces of the seismograms which were edited from the field reels of magnetic tape are shown in Figure 4 and 5. Traces 12 to 22 in each case make up the northwest-southeast (inline) spread while traces 1 to 11 make up the perpendicular spread. No corrections were applied to these records. It was originally intended to apply

approximate static corrections for elevation differences, but the corrections all turned out to be less than one time sample interval.

The records contain two significant bands of arrivals. The first of these begins with P_n and is of low amplitude, though still well-defined. The second band of arrivals begins with the P_g event, although the exact onset time is difficult to determine. A number of other large events occur following P_g on both records. At the very end of the Greys record a low-velocity event is seen which was later determined to be S_g . On neither record is there seen to be a well-defined P^* arrival. From these two records the velocities of P_n , P_g , and S_g are found to be 7.6, 6.05, and 3.4 km/sec, respectively.

Power spectra (Figure 6.1) were computed for various time segments of the Fallon record shown in Figure 6.2. The noise spectrum was computed for the 2.5 sec interval immediately preceding the first arrivals. This spectrum is quite different from those of P_n , P_g and the Coda, but the time window used is so short that this may not be significant. No really important differences exist in the overall shapes of the other spectra. This overall shape is determined by the source spectrum, the receiver response and the inelastic attenuation properties of the earth. The particular peaks in the spectra are probably due to multiple arrivals and reverberations. It is well-known that pulse-like arrivals with large time separation give rise to closely spaced peaks in the spectrum. Reverberations, i.e., multiply reflected events with short-time spacing, generate rather well-defined spectral peaks with somewhat larger spacing. If the various multiples or reverberations do not have exactly the same period, the spectral peaks will

tend to be smeared over a wider frequency band. This appears to be the case here and is probably due to slight lateral variations of velocity or layer thickness within the crust.

Since the overall spectral shapes of the various events are so similar, there is little hope of separating interfering events by frequency filtering.

B. USGS Shots

1. General Description

The USGS detonated a series of shots during April and May, 1964 in the vicinity of TFO which were digitally recorded on the 21-element cross array, the 3-component at Z-1 and the ring summations of the 31-element array. The shots are described in Table II, their locations are shown in Figure 7.

Paper playbacks of the shots were examined and all evident arrivals were picked; analysis of the paper records is discussed below. Additional digital processing was performed on the Bylas and Clarkdale shots and on a Clarkdale quarry blast; results of the analysis are given in Section IV.

2. Paper Record Analysis

Figures 8 to 15 show the best (i.e., highest signal-to-noise ratio) event of the 8-shot locations. Obvious arrivals are identified and their travel times (to Z-21) and phase velocities across the array are given in Table III.

Table III shows that the arrival P_g with velocity $6.1 (\pm .1)$ km/sec can be identified for all events. Thus, it appears that

TABLE II
USC&GS Shot Information

Shot Name	Distance from TFO Seis. 2-21 (km)	Azimuth (degrees)	Date of Detonation	Origin Time	Size of Recorded Signal Rel. to Ambient Noise
Sunrise #1	190	43	4/30/64	13:49:59.91	Medium
#2	"	"	5/4/64	12:59:59.97	Large
Winslow #1	100	35	4/24/64	13:30:00.12	Medium
#2	"	"	5/1/64	14:00:00.0*	Low
#3	"	"	5/4/64	13:29:59.97	Medium
Ft. McDowell #1	74	203	4/24/64	14:00:00.7	Low-Medium
#2	"	"	5/1/64	13:30:00.23	Medium
#3	"	"	5/2/64	13:00:00.40	Medium
#4	"	"	5/3/64	13:30:00.38	Low
Gila Bend #1	193	224	4/30/64	14:40:00.23	Low-Medium
#2	"	"	5/6/64	13:00:00.69	Low-Medium
Blue Mt. #1	235	307	4/16/64	13:30:00.0*	Medium
Clarkdale #1	94	307	4/20/64	15:00:00.20	Medium
Carrizo #1	95	107	4/18/64	14:00:00.0*	Low-Medium
#2	"	"	4/20/64	13:29:59.97	Medium
Bylas #1	162	139	4/16/64	14:30:00.0*	Large
#2	"	"	4/21/64	13:29:59.95	Large

*Assumed origin time.

TABLE III

PHASE VELOCITIES AND TRAVEL TIMES OF OBVIOUS ARRIVALS FROM TFO SHOTS

Shot	Distance from Z-21 (km)	Azimuth (degrees)	Vel. Across Array (km/sec)	Travel Time to Z-21 (sec)	Phase
Sunrise	190	43	6.2	32.4	P_g (P_n) Surface
			7.4	33.6	
			3.9	58.3	
Winslow	100	35	6.1	17.1	P_g (P_r) Surface
			7.5	20.2	
			3.7	29.5	
Ft. McDowell	74	203	6.2	12.8	P_g P_2 Surface
			6.9	14.9	
			3.6	21.9	
Gila Bend	193	224	6.9	30.5	P_2 P_g Surface
			6.2	32.7	
			3.7	56.0	
Blue Mt.	235	307	7.3	38.1	(P_n) P_g Surface
			6.0	40.8	
			3.5	69.5	
Clarkdale	94	307	6.0	16.4	P_g (P_n) Surface
			7.8	20.2	
			3.5	29.4	

Cont.

TABLE III CONT.

Shot	Distance from Z-21 (km)	Azimuth (degrees)	Vel. Across Array (km/sec)	Travel Time to Z-21 (sec)	Phase
Carrizo*	95	107	7.0	16.1	P ₂
Bylas*	162	139	6.2	27.7	P _g
			7.0	28.4	P ₂

*Surface waves very poorly developed.

there is a 6.1-km/sec layer which exists over the whole region encompassed by the shots. Assuming P_g is a refraction, the two-way travel time for P_g in the sediments above the 6.1-km/sec layer is about 1 sec on the average. Thus, the depth to the 6.1-km/sec layer is about 2 km. From topographic information and from the observation that the short period surface waves are much better developed to the north, it is evident that the sedimentary cover thickens to the north.

The depth of the 6.1-km/sec layer cannot be estimated because of the apparently complicated structure beneath it.

From Table III and Figures 8 through 15, several differences between the arrivals from shots south of the array and those from shots north of the array can be noted:

- (1) A 6.9 (± 0.1) km/sec arrival is well defined for the south shots, but does not appear for the north shots.
- (2) All north shots except Winslow have an arrival with velocity 7.6 (± 0.2) km/sec (which is close to the P_n velocity), but no south shots show this arrival.

It appears that below the top of the 6.1-km/sec layer there are definite differences in the section north and south of the array. This observation agrees with geological information in the TFO area which shows that geologic boundaries exist near the station (Figure 16). An explicit description of the differences is not possible from the raw data.

The shots shown in Figures 8 through 15 do not have many obvious arrivals. Most records have just 2 "P" arrivals and a surface arrival; a few have indications of additional "P"

arrivals and perhaps a weak "S" arrival. The relatively simple seismograms can be explained in terms of:

- (1) Scattered energy (generated by reflections of the strong arrivals off topographic discontinuities in the area) masking the weaker direct arrivals. Signal-generated scattered energy has been observed previously at TF0 (Figures 57 through 60, Semiannual Technical Report 1). In Section IV its effect on the additional digital processing will be discussed.
- (2) The charge sizes used may not have been sufficient to generate the amount of energy necessary to excite deep reflections and arrivals with more complicated paths such as multiples. (For several events, e.g., Figures 10 and 14, the signal-to-ambient-noise level is quite small.)

Finally, Figures 8 through 15 show that even the strong arrivals generally have a considerable change in waveform across the array (for example, the first arrival of the Bylas event, Figure 15).

The changes are probably due to a combination of:

- (1) interference of the scattered energy with the signal arrival (especially for events after the first arrival)
- (2) differences in propagation paths for shots not directly inline
- (3) differences in geology in the immediate area of the seismometers (e.g., Z-74 and Z-73 are located in the Little Diamond Rim and are at least 120 meters and 80 meters higher than the other seismometers)

III. Velocity Filtering of Nuclear Events

The spectra of the P_n , P_g , and S (or Surface) pulse trains has been seen to be very similar for the two nuclear events. This suggests that something other than frequency filtering must be used for detailed analysis of the arrivals. A second, more useful means of separating the various events is based on apparent horizontal velocity. The seismogram may be considered a function of space as well as a function of time. Each trace represents one sample in space. The wavenumber spectrum of the seismogram can be multiplied by a filter response as a result of weighting each trace appropriately and summing. In combined frequency-wavenumber filtering, each trace is separately filtered (timewise) and the outputs summed to give a single trace. This combined filtering is most appropriate for the present application since a single discrete velocity is represented by energy concentrated along a straight line through the origin in the frequency-wavenumber plane. In the present paper, we have used the Pie Slice* process which rejects energy traveling at all velocities outside a narrow band (Embree, Backus, and Burg, 1963). Both the center velocity and the width of the band are variable. The degree of rejection achieved depends on the length of the receiver array and the number of traces used, while the alias point in frequency and wavenumber is determined by the sampling intervals. The response for a 12-channel Pie Slice is shown in Figure 17 for an infinite center velocity. All other cases can be reduced to this by time shifting the traces so that events traveling at the center velocity line up across the record. The Pie Slice process rejects

*A registered Texas Instruments Incorporated trademark.

random noise according to the well known \sqrt{N} law; for the present example the random noise is down by 10 db in the output.

The Pie Slice process was applied to the inline (northwest-southeast) spread for both the Greys shot and the Failon shot, and to the perpendicular (southwest-northeast) spread for the Greys shot. The output records are shown in Figures 18 and 19. In each case, one output trace is produced for each of a series of center velocities. Pulses traveling at exactly a given center velocity would be down by 6 db on the two adjoining traces. For the two inline seismograms, the velocities decrease from top to bottom. No significant backscatter was expected. For the cross spread, the highest velocity trace is in the center and the velocity decreases in both directions away from the center. The original, unprocessed inline seismograms are also shown at the top of each figure, along with the 3-component traces. The polarity of the N-S horizontal trace has been reversed. Because the paths of these two events come close to bisecting the angle between the N-S and E-W instruments, all P arrivals should be in-phase. SV arrivals should be in-phase on the east and south traces but out of phase on the vertical trace. SH will be out of phase on the east and south traces and of very low amplitude on the vertical trace. Phasing will not be as simple for S arrivals polarized at other angles, or for mixed arrivals and some surface modes.

The original record is well-recorded and, at first glance, the new data supplied by the pie sliced record may not be readily discerned. Three dominant arrivals are identified tentatively on the original record. Velocities can be accurately obtained from a high-speed playback of the unprocessed record. However, many other arrivals are also

apparent. Some appear to have velocities identical to the dominant arrivals; others are obscure. The pie slice display delineates these and reveals velocities and arrival times scarcely apparent on the original seismogram.

A study of the pie sliced record for the inline spread on both events shows that P_n , the first arrival, has a velocity between 7.4 and 8.8 km/sec, being much closer to the lower value. On the other hand P_g has a velocity close to 6.3 km/sec. These two results are not unexpected and are not as precise as the results obtained from the raw records. However, this points out the fact that the purpose of multichannel processes such as Pie Slice is not to measure velocities, but rather to separate and clarify events. It happens in almost every case that the velocities of some events can be measured after processing, but not before, simply because the event was obscured by a much stronger event of different velocity. A striking example of this on both events is the energy packet, identified as scattered Rayleigh waves (probably scattered from the Mogollon Rim). This event has considerable energy, but is not at all obvious on the raw seismogram. If the original energy is assumed to have come from the onset of P_g and using a Rayleigh velocity based on S_g , the scattering center is found to be about 20 km away. This is roughly the distance to the rim. Further evidence that this is Rayleigh energy is obtained from the 3-component traces. For all events arriving as P , the three traces are in phase. For the event in question, the phase relationship is quite complicated, but is definitely not in phase.

There is no evidence on the Greys shot for events with velocities between 6.1 and 7.6 km/sec, which would correspond to the classical P^* event. On the Fallon shot, there is one obscure event which could be interpreted in this manner, but the evidence is weak. This event is best seen on the Pie Slice of the inline array, where it arrives at about 2 min 6 sec after the shot instant. It has almost exactly the same amplitude on the 7.2- and 6.2-km/sec traces and on the 8.6- and 5.4-km/sec traces. This would suggest a velocity of 6.7 km/sec, but this apparent velocity could also be produced by other means, so the interpretation is not unique.

P_n multiples are seen on seismograms from both shots, but are better developed on the Fallon seismogram. Since the two events share a common subsurface path near the receiver array, it is reasonable to assume that the major differences in the P_n multiple time span are due to differences in crustal structure near the source. The P_n first arrival and the complex of events in the 3 sec immediately following are similar, though not identical for the two shots, so this may contain some information about the near surface under the receiver array. The large complex of pulses seen on the Fallon record following the first arrival by about 9 sec are not nearly so apparent on the Greys shot. This is probably the first multiple of P_n , reflected between the Mohorovicic discontinuity and the free surface before being critically refracted. Assuming an average crustal velocity of 6.5 km/sec suggests that the crustal thickness near the Fallon shot point is about 25 km, a reasonable value.

Most of the other intervals between arrivals in both the P_n and P_g section of the two seismograms are so short as to prohibit their being

reflected between the Mohorovicic discontinuity and the free surface. Their existence would require other interfaces, or zones of rapid velocity change within the crust. This is the best evidence we have from these two records for intermediate layers.

It has been suggested that the 7.6-km/sec velocity found for P_n is too low for a sub-Mohorovicic velocity. The alternatives are that either we are seeing an intermediate velocity, and the Mohorovicic discontinuity is much deeper, or else the discontinuity is dipping downward toward Tonto Forest from the northwest. We cannot evaluate the former suggestion here, but limitations can be placed on the latter hypothesis. Suppose the true velocity to be 8.0 km/sec. Then a dip of about 4 degrees would be required to bring the apparent velocity down to 7.6 km/sec. Such a dip is unlikely, but not impossible. However, if such a dip did occur, the P_n multiple events reflected near the receiving array would have significantly different velocities from the first arrival (i.e., about 6.8 km/sec for the first multiple). These events have not been identified, but it is obvious from the seismograms and the velocity filtered sections that no such velocities occur. Thus, it seems likely that 7.6 km/sec is nearly the correct velocity below the refracting interface, no matter which interface is involved.

For the Greys event, S_g arrives with a large proportion of SH motion at a source-to-receiver velocity of about 3.0 km/sec. This implies that considerable SH is generated by or near the source. The cross-spread S_g is 3.4 km/sec. The S_g Love-wave energy is identified on the 3-component instruments by being out of phase on the two horizontal

instruments and small on the vertical component. Some SV energy arrives at the same time, so the vertical instrument still has some output.

The cross-spread Pie Slice gives some indication of the direction of arrival of the various events. A pulse traveling directly down the inline array would appear to have infinite velocity on the broad-side array and would have highest amplitude on the center trace of the Pie Slice output. Events from the north of the inline array are larger on the upper traces, while those west of the inline array are larger on the lower traces. It is seen at once that the P_n event and all of its multiples are strongest on the infinite velocity trace, meaning they propagate almost inline with the northwest-southeast array. This suggests that the depth of the Mohorovicic discontinuity has no significant variation in a direction perpendicular to that array in the immediate vicinity of Tonto Forest. However, a number of events traveling with P_g velocity are strongest on the -44.4 km/sec trace, indicating lateral refraction to the south of the inline array. This could be caused by thinning to the south of the low velocity near surface materials overlying the competent granite. It is, in fact, known that the sedimentary cover is thicker to the north of Tonto Forest than to the south.

IV. Processing USGS Shots

A. Deconvolution of Clarkdale Shot

Figure 20 shows the portion of the USGS Clarkdale shot between the first arrival and the surface-wave arrival. Two distinct arrivals are evident; both the first arrival (P_g) and the larger arrival about 4.3 sec later (P_n) have a reverberatory character. A poorly-defined arrival about 2.5 sec. after P_n (P_n^2) can also be seen.

Because of the reverberatory nature of the record, deconvolution filters 1.32 sec long were designed for each trace using the entire P gate (12 sec). (See Backus, 1965, for a description of the deconvolution process.) Figure 21 shows the deconvolved outputs and Figure 22 shows the Pie Slices (Embree et al, 1963) of these outputs at several velocities.

It is possible to identify several additional arrivals on the deconvolved outputs. (All arrivals except P_2 were identified from the deconvolved outputs first and then, checked on the pie-sliced outputs.) The arrival P_2 has a slightly higher velocity than P_g and may be either a refraction from an intermediate layer or some P_g reflection. The arrivals following P_n (P_n^1 , P_n^2 , P_n^3) appear to be multiples of P_n . (Note the poorly-defined arrival on the original record (P_n^2) is quite distinct on the deconvolved outputs.) The multiples are not sufficiently delayed in time to be the surface-to-Moho type, which suggests that there is structure (i.e., velocity contrasts) at depth.

Figure 23 shows the same portion of the recording of a large quarry blast which was detonated within 5 km of the USGS shot location. The signal-to-ambient-noise ratio is much larger for this event and it is possible to identify on the unprocessed record arrivals which were brought out by deconvolution on the USGS shot. The time tie between arrivals for the two events is quite good (within 1/2 sec).

The arrival P_3 (which cannot be identified on the shot record) has about the same velocity as P_n and may actually be the first P_n arrival. (Note even if this arrival is taken as P_n , the multiples are still not the surface-to-Moho type.)

Figure 24 shows pie slices of the quarry blast at several velocities. Velocities of the identified arrivals agree with those obtained for the USGS shot. Thus, it can be concluded that deconvolution enhanced valid arrivals and appears to be a useful method for improving interpretation of reverberatory refraction records.

B. Notch Velocity Filtering of the Bylas Shot

As discussed in Section II(B), records from shots south of the array did not have an identifiable P_n arrival. It was, therefore, decided to attempt to extract P_n by means of notch velocity filtering. Notch velocity filtering is different from the Pie Slice process. Pie slicing passes a range of velocities and uniformly rejects all other velocities; notch velocity filtering passes a specific velocity (or velocities) and rejects other specific velocities. (For velocities other than those specified, the frequency-wavenumber response is not restricted, and so could have areas of high response.)

Figure 25 shows the f - k response of the notch velocity filter designed to pass 6.2-km/sec arrivals and reject 7.0- and 8.0-km/sec arrivals (these velocities were referenced to 5.375 km/sec so that short filters could be used, therefore, the vertical line represents 5.375 km/sec and not infinite velocity as is usually the case).

The filter was designed using the following assumptions:

- (1) the only 3 velocities present in the P gate are 6.2, 7.0 and 8.0 km/sec
- (2) all arrivals have equal amplitudes
- (3) all arrivals have a flat power spectrum between 0 and 10 cps

Similar filters were designed to pass the 7.0- and 8.0-km/sec arrivals, respectively.

Application of the 8.0 km/sec pass filter to the Bylas event did not succeed in extracting the P_n arrival, because:

- (1) The P_n velocity in the area appears to be slightly lower than 8.0 km/sec (about 7.6 km/sec). A 7.6 km/sec velocity would be significantly attenuated by the filter (about 6 db relative to 8.0 km/sec)
- (2) Any scattered energy, which had apparent velocities corresponding to highs in the f-k response, would mask the P_n arrival
- (3) Changes in waveform of the arrivals across the array (as discussed in Section II(B)) would reduce the effectiveness of the filter. That is, the assumption of space stationarity would not be completely valid
- (4) The relative amplitude of the three arrivals are actually different; building the differences into the model may improve results

Time was not sufficient to permit further investigation of the notch velocity filter technique. It is possible that it would have been successful if the above factors had been accounted for.

C. Prediction Filtering

1.. Single Channel Prediction

In single-channel prediction, one channel is used to predict the adjacent channel. To design the best linear filter (in the least-mean-square-error sense) one needs the autocorrelation of the channel to be transformed and the crosscorrelation between the channel to be predicted and the channel to be transformed.

That is, it is necessary to solve the time domain formulation of the Weiner equation:

$$\begin{Bmatrix} \varpi_{ii}(0) & \varpi_{ii}(1) & \dots & \varpi_{ii}(n-1) \\ \varpi_{ii}(1) & \varpi_{ii}(0) & \dots & \varpi_{ii}(n-2) \\ \vdots & & & \\ \varpi_{ii}(n-2) & \varpi_{ii}(n-3) & \dots & \varpi_{ii}(1) \\ \varpi_{ii}(n-1) & \varpi_{ii}(n-2) & \dots & \varpi_{ii}(0) \end{Bmatrix} \begin{Bmatrix} a_0 \\ a_1 \\ \vdots \\ a_{n-2} \\ a_{n-1} \end{Bmatrix} = \begin{Bmatrix} \varpi_{oi}(\frac{n-1}{2}) \\ \varpi_{oi}(\frac{n-3}{2}) \\ \vdots \\ \varpi_{oi}(\frac{-n+3}{2}) \\ \varpi_{oi}(\frac{-n+1}{2}) \end{Bmatrix} \quad (1)$$

where: $\varpi_{ii}(k)$ are the 0 to $(n-1)$ lags of the autocorrelation of the channel to be transformed.

$\varpi_{oi}(k)$ are the $\frac{-n+1}{2}$ to $(\frac{n-1}{2})$ lags of the crosscorrelation between the channel to be predicted and the channel to be transformed.

a_k are the filter point weights.

n is the number of filter points (n is odd) and the output is at the center of the filter.

Also, the ratio of the mean-square-error (MSE) in the prediction filter design to the total power in the trace to be predicted gives the proportion of the total power which is predictable according to

$$\text{Percent of total predictable power} = 100(1 - \frac{\text{mean-square-error}}{\text{total power}})$$

Thus, if the mean-square-error goes to zero, there is total predictability; if the mean-square-error does not decrease, there is no predictability.

The Bylas shot and the Clarkdale quarry blast were chosen for the prediction analysis because of the large signal-to-ambient-noise ratio. Figures 26 and 27 show the two events.

For the Bylas event the "P" portion of Z-66 was predicted from that of Z-67 using a 31 point (0.72 sec) filter designed from the entire "P" gate (14.4 sec). The MSE indicated that 43 percent of the total power was predictable. Figure 28 shows the original, predicted and error (original minus predicted) traces for Z-66 (note the relative scale factor of the traces). It can be seen that there is little similarity between the original and predicted traces except in the region shown by arrows. The prediction is especially poor following the main (P_2) arrival. The low predictability was probably due to the large amount of scattered energy present (especially after the P_2 arrival), which is essentially unpredictable.

A filter was then computed from averaged correlations using all 11 channels to compute 11 autocorrelations and 10 one-space lag crosscorrelations. However, in this case the MSE indicated only 32 percent of the power was predictable between adjacent channels. The predictability was poorer because:

- (1) as discussed in Section IV(B) the signal was not truly space stationary and energy which was coherent across a pair of seismometers but not across the entire array, appeared to be random after averaging.
- (2) the seismometers are not exactly equally spaced,

so crosscorrelations would not be peaked at exactly the same lag.

For the Clarkdale quarry blast, the "P" portions of Z-66 and Z-64 were predicted from those of Z-67 and Z-65 respectively, using 31 point (0.72 sec) filters designed from the entire "P" gate (12 sec). The MSE indicated that 50 percent of the power in Z-66 was predictable from Z-67 and 46 percent of the power in Z-64 was predictable from Z-65. These numbers are essentially the same as those for the Bylas event.

Thus, it appears that at TF0 due to the large amount of scattered energy present in the "P" gate, only 50 percent of the energy is predictable between adjacent traces. This is a severe limitation which reduces the effectiveness of multichannel processing. The effect of scattered energy is probably more serious at TF0 than at most stations, because of the rough topography in the TF0 area.

2. Multichannel Prediction

In multichannel prediction, several channels are used to predict another channel. The formulation is the same as for the single-channel case, except each element of the square matrix (Equation 1) becomes a square matrix and each element of the column vectors becomes a column vector. The MSE in the filter design is again a measure of the predictability. The Bylas shot and the Clarkdale quarry blast were used for the multichannel analysis also. Several filters were designed for each event.

a. Bylas Filters

The first filter designed used seismometers Z-67 to Z-13 to predict Z-17. The filter was 31 points (0.72 sec) long and the entire "P" gate (14.4 sec) was used in computing the correlations. The MSE indicated that about 53 percent of the total power in Z-17 was predictable (compared to 48 percent in the prediction of Z-66 from Z-67). Thus, little was gained in the prediction by adding channels, which is further proof that the low predictability can be attributed to the scattered energy.

Two 21-point (0.48 sec) filters were then designed using a 3.6-sec gate which included the strongest signal arrival only (Figure 26). The first filter used five seismometers, Z-67 to Z-13, to predict Z-17; the second filter used four seismometers, Z-65 to Z-17 to predict Z-21. Before the second filter was designed, the traces were equalized on average absolute amplitude basis over the gate. The MSE indicated that 78 percent of the power in Z-17 and 35 percent of the power in Z-21 was predictable. The high predictability indicates that the gate chosen omitted most of the scattered energy. Thus, most scattered energy arrives later than the strongest signal arrival and is probably generated mainly by reflections of the strongest arrival off topographic discontinuities in the vicinity of TF0.

The difference in the predictability of Z-17 and Z-21 is probably due to the arrival having better space stationarity over seismometers Z-65 to Z-21.

b. Clarkdale Filters

Two 4-channel filters were computed for the Clarkdale event using 31 point (0.72 sec) filters designed from the entire "P" gate (12 sec); the first used seismometers Z-67 to Z-64 to predict Z-13, the second used Z-21 to Z-69 to predict Z-70. Both sets of traces were equalized on an average absolute amplitude basis before filter design. The MSE indicated 56 percent of the power in Z-13 and 65 percent of the power in Z-70 was predictable. The two numbers are both somewhat higher than the 46 percent and 50 percent obtained in the single-channel case. One would expect better prediction in the multichannel case, for this event, because there is more than one strong arrival in the "P" gate; whereas for Bylas, one arrival predominated. The scattered energy is still important, because the improvement is not large (3 db at most). Again, the better predictability of Z-70 probably results from better space stationarity of the signal over seismometers Z-21 to Z-70.

Finally, a short gate (3.6 sec) over the strongest arrival (Figure 27) was used to compute a 21-point (0.48 sec) filter to predict Z-13 from Z-67 to Z-64. The traces were again equalized on an average absolute amplitude basis over the

gate, prior to filter design. The MSE indicated 64 percent of the power in Z-13 was predictable (compared with 56 percent when the entire gate was used), which indicates that there is a significant amount of scattered energy in the gate.

V. Conclusions

The velocity-filtering studies of the nuclear events have shown the usefulness of this process for separating and enhancing refracted arrivals. From these results, we are able to conclude that the P_n multiples have nearly the same velocity as the first P_n arrival and as a result, the dip of the Mohorovicic discontinuity under Tonto Forest must be very small. A second result of this is that 7.6 km/sec must be the true velocity just below this discontinuity. Little, if any, indication of P^* is seen on the nuclear events. The velocity filtering does bring out certain low-velocity events which, on account of their arrival time, must be generated by P_g striking local discontinuities. One likely scattering center is the Mogollon Rim to the north of Tonto Forest.

A careful study of the USGS shots shows significant differences in the crust to the north and south of Tonto Forest. To the north, P_n with a velocity of 7.6 km/sec and P_g with a velocity of 6.1 km/sec are readily observed. Also for these paths surface waves are well developed probably because of the greater thickness of sedimentary cover. To the south, P_g (6.1 km/sec) and P_2 (6.9 km/sec) are observed, but not P_n . Surface wavetrains are absent or not well-organized. P_2 may perhaps be identified with

the classical P*. The results suggest a significant change in crustal structure somewhere in the neighborhood of Tonto Forest.

On many of the USGS shots, no well-defined secondary events are seen. The use of the Pie Slice velocity filter process on a record from Clarkdale shotpoint allows some previously obscure secondary events to be picked. Data-dependent prewhitening or "deconvolution", prior to applying the Pie Slice, also contributed significant improvement. The validity of these low-level secondary events is demonstrated by their presence on a quarry-blast recording from the same area. The considerably larger charge size of the quarry blast makes the events visible on the raw record in the latter case. It is found that the time intervals between secondary events for both the USGS shots and the nuclear events are too small to be explained by reflection between the M discontinuity and free surface. This suggests other interfaces or zones of rapid velocity change within the crust and is perhaps our most direct evidence of such structure.

Prediction studies carried out for the Bylas shot and a Clarkdale quarry blast show that only about 50 percent of the energy present is predictable from one seismometer to the next. This could be explained either by a large amount of energy which has random spatial characteristics or by a multiplicity of coherent events traveling across the array with different velocities or from different source points. Use of additional channels in the prediction process improved the predictability only slightly, so we must conclude that the remaining energy is random in space. However, it must be pointed out that the two interpretations are not really

different, as energy from a number of independent sources begins to approach random spatial characteristics as the number of sources becomes very large. The source of the random energy in this case is probably the coherent energy from the source impinging upon a large number of scattering centers around and within the receiving array.

VI. Acknowledgment

The authors wish to thank the U. S. Geological Survey for its cooperation during the 1964 series of calibration shots. This work was supported by the Air Force Office of Scientific Research under contract AF 49(638)-1244.

REFERENCES

- Backus, Milo M., 1965, Teleseismic Signal Extraction: Royal Society of London, presented Jan. 28 and 29, In Press.
- Embree, P., J. P. Burg and M. M. Backus, 1963, Wide-Band Velocity Filtering--The Pie-Slice Process: Geophysics, Vol. 28, pp. 943-974.
- Linville, A. F., and S. J. Laster, 1965, Near Surface Dispersion Studies at the Tonto Forest Seismic Observatory: Final Report, Basic Research in Crustal Studies, Contract AF 49(638)-1244, Appendix G.

FIGURE CAPTIONS

<u>Figure</u>	<u>Title</u>
1	General Location of Tonto Forest Seismological Observatory.
2	Plan View of Large Cross Array at Tonto Forest Observatory.
3	Location of Nuclear Detonation Relative to Tonto Forest Observatory.
4	Seismogram Recorded from Greys Shotpoint. Distance from array 569 km. Traces 1-11 make up the southwest-northeast (broad-side) arm of the array. Traces 12-22 are the northwest-southeast (inline) arm.
5	Seismogram Recorded from Fallon Shotpoint. Distance from array 837 km. Traces 1-11 make up the southwest-northeast (broad-side) arm of the array. Traces 12-22 are the northwest-southeast (inline) arm.
6.1	Power Spectra for Various Time Partitions of the Fallon Seismogram (as shown in Figure 6.2).
6.2	Time Partitions of Fallon Seismogram Used for Computing Power Spectra.
7	Location of USGS Shots.
8	USGS Shot "Sunrise."
9	USGS Shot "Winslow."
10	USGS Shot "Ft. McDowell."
11	USGS Shot "Gila Bend."
12	USGS Shot "Blue Mt."
13	USGS Shot "Clarkdale."

<u>Figure</u>	<u>Title</u>
14	USGS Shot "Carrizo."
15	USGS Shot "Bylas."
16	Summary of Colorado Plateau Geological Boundaries in the TFO Area.
17	Frequency-Wavenumber Response of 12-Channel Pie Slice Process.
18	Pie Sliced Seismograms from Greys Shot. Upper record is unprocessed data recorded on northwest-southeast (inline) arm of array. Middle record is Pie Sliced output for northeast-southwest (broad-side) arm of array. Lower record is Pie Sliced output for inline arm of array. Major timing lines are 2.5 sec apart.
19	Pie Sliced Seismograms from Fallon Shot. Upper record is unprocessed data from inline arm of array. Lower record is Pie Sliced output of upper record.
20	Original USGS Clarkdale Shot.
21	Deconvolved USGS Clarkdale Shot.
22	Pie Sliced USGS Clarkdale Shot.
23	Original Clarkdale Quarry Blast.
24	Pie Sliced Clarkdale Quarry Blast.
25	Frequency-Wavenumber Response of Notch Velocity Filter Designed to Pass 6.2 km/sec and Reject 7.0 and 8.0 km/sec.
26	USGS Bylas Shot.
27	Clarkdale Quarry Blast.
28	Original and Predicted Z-66 Output (for "P" gate) and Error Trace.

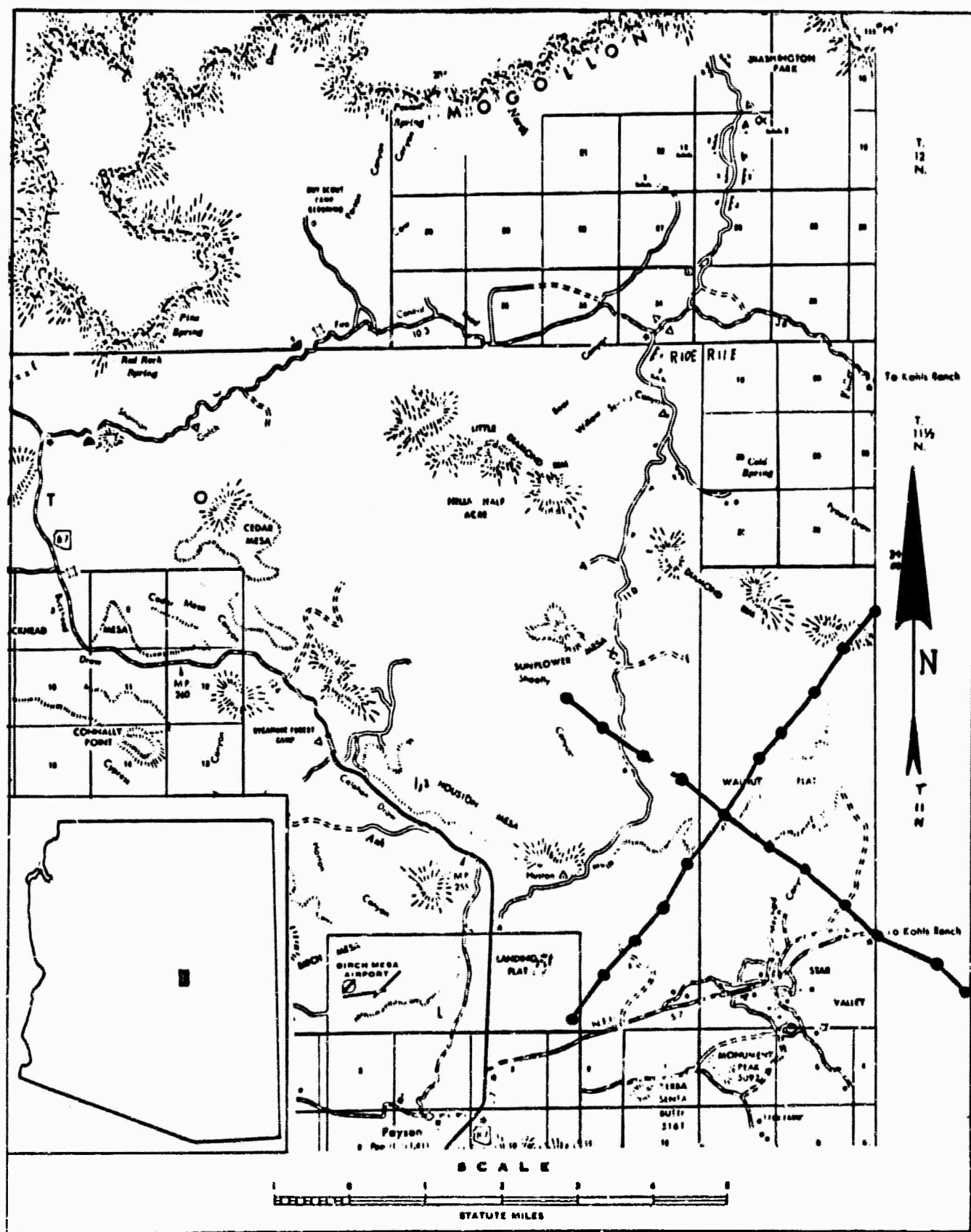
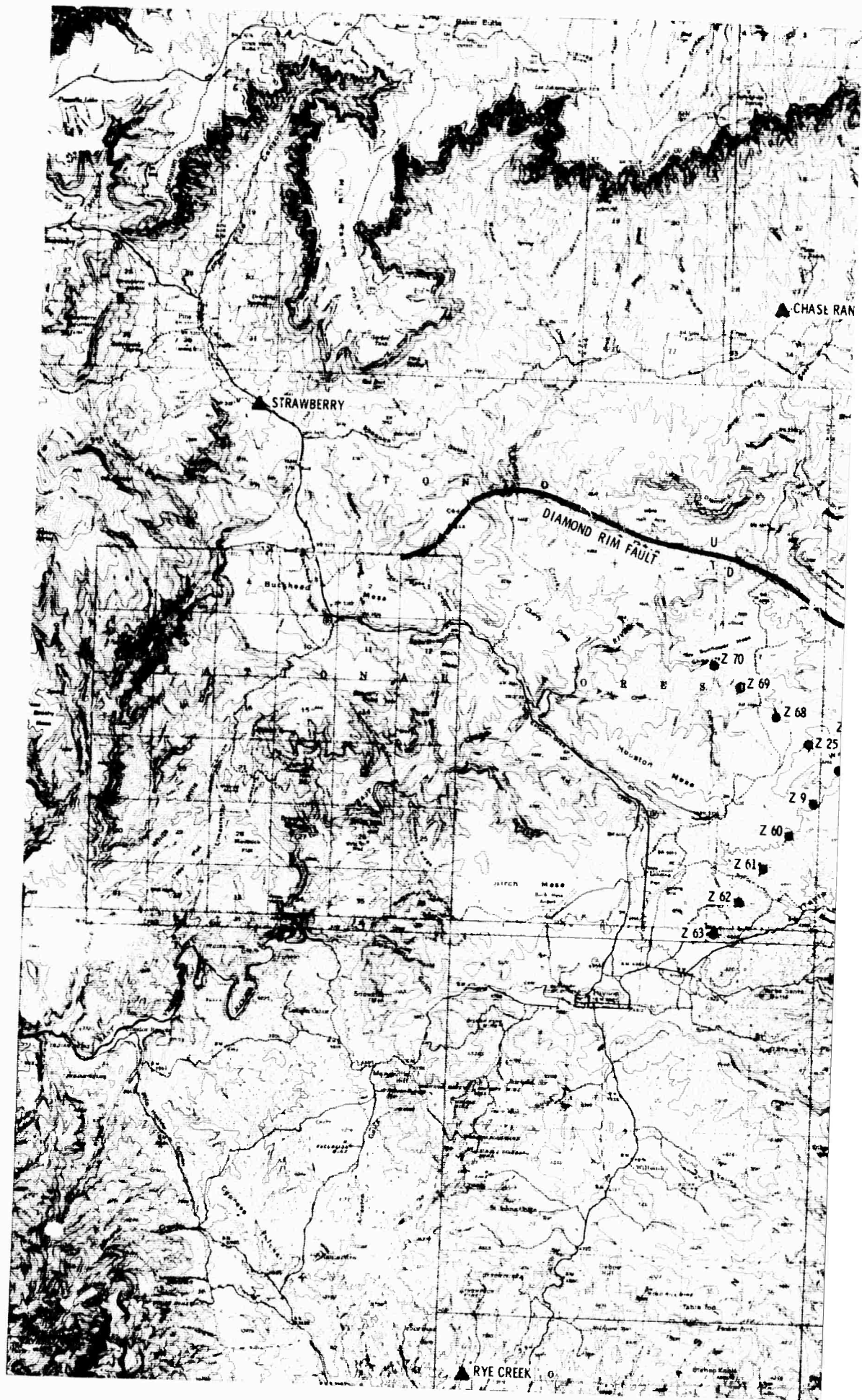


Figure 1. General Location of Tonto Forest Seismological Observatory



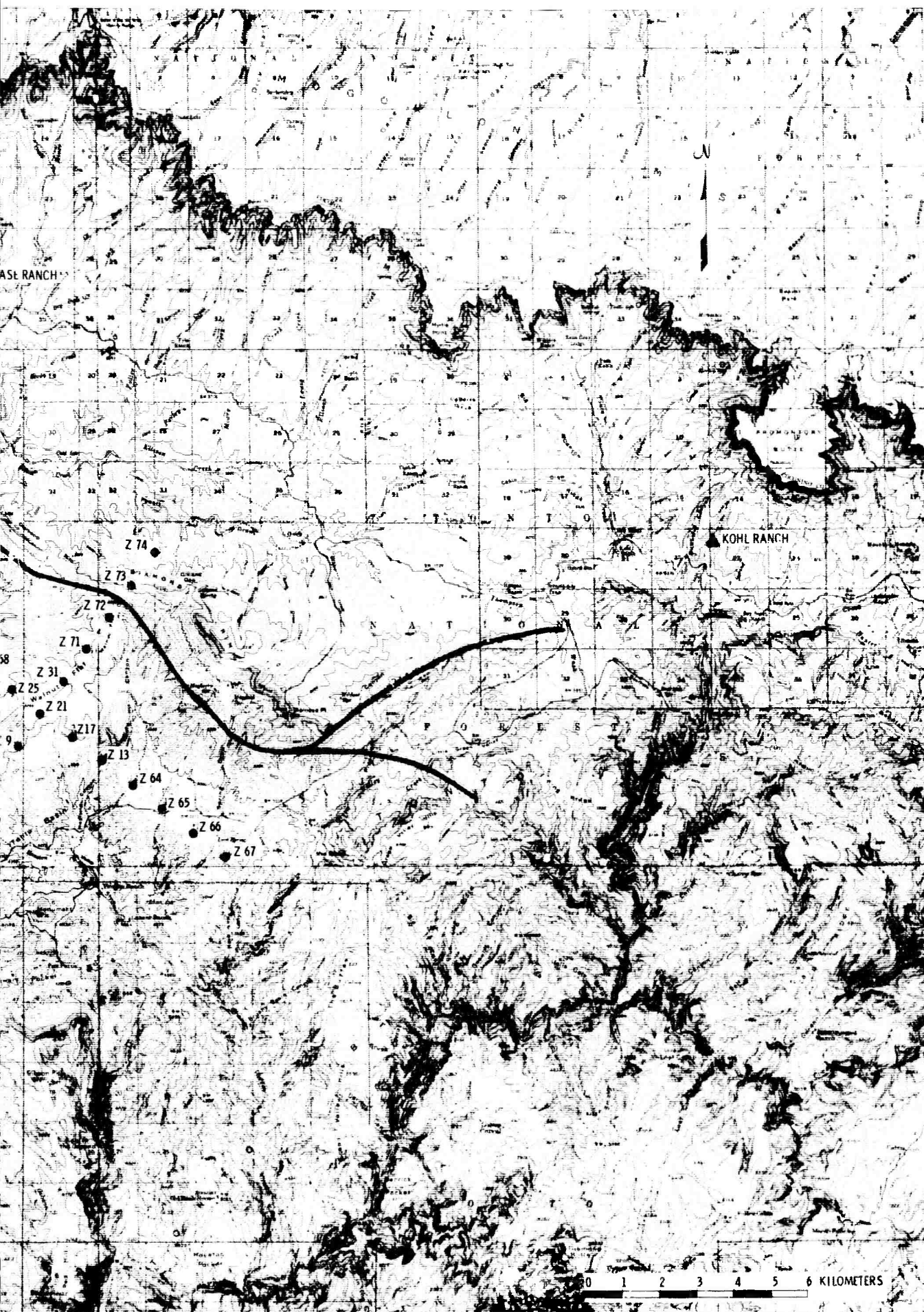


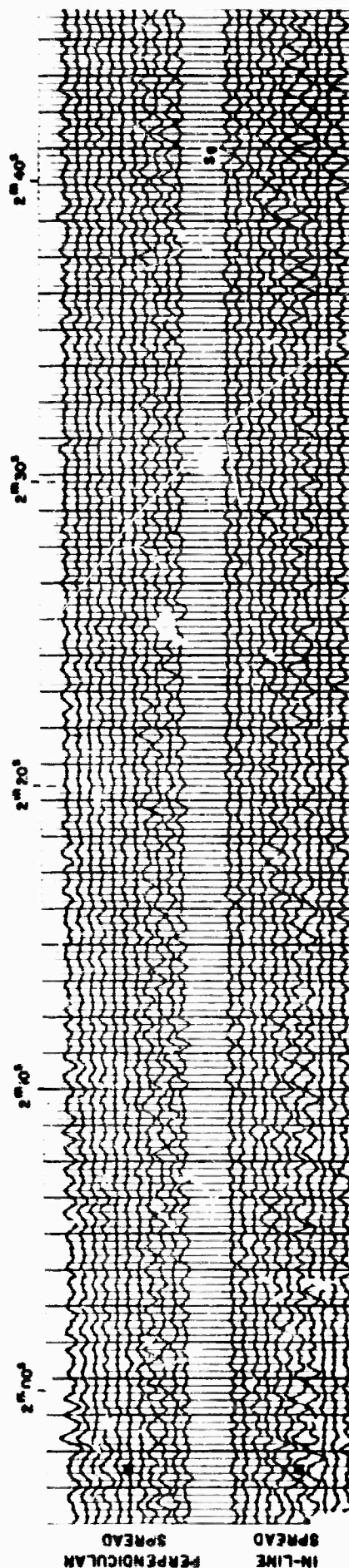
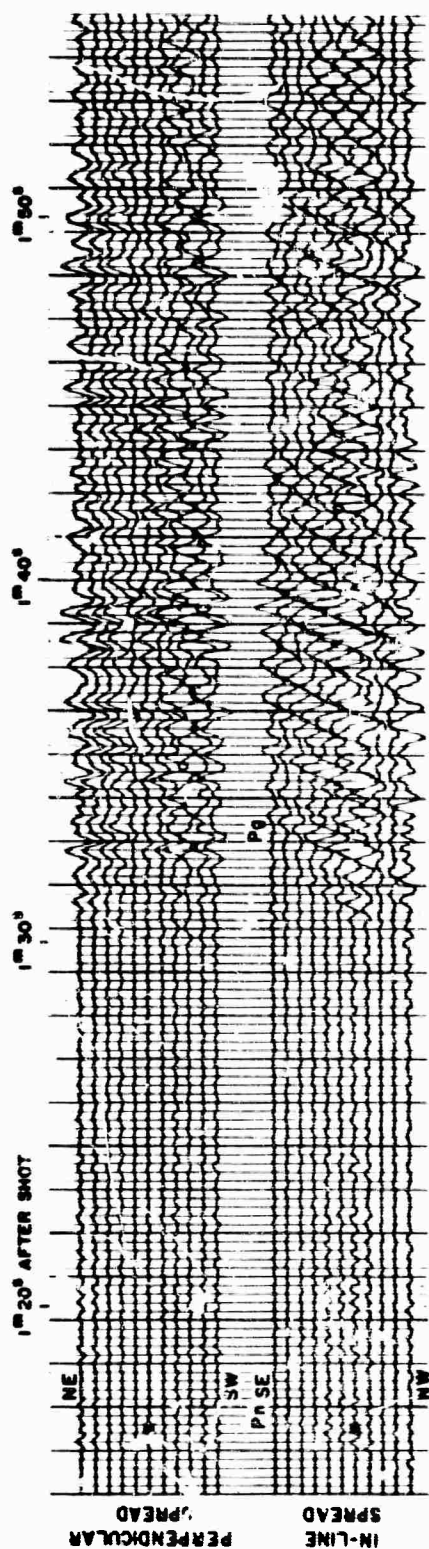
Figure 2. Plan View of Large Cross Array at Tonto Forest Observatory

BLANK PAGE



Figure 3. Location of Nuclear Detonation Relative to Tonto Forest Observatory

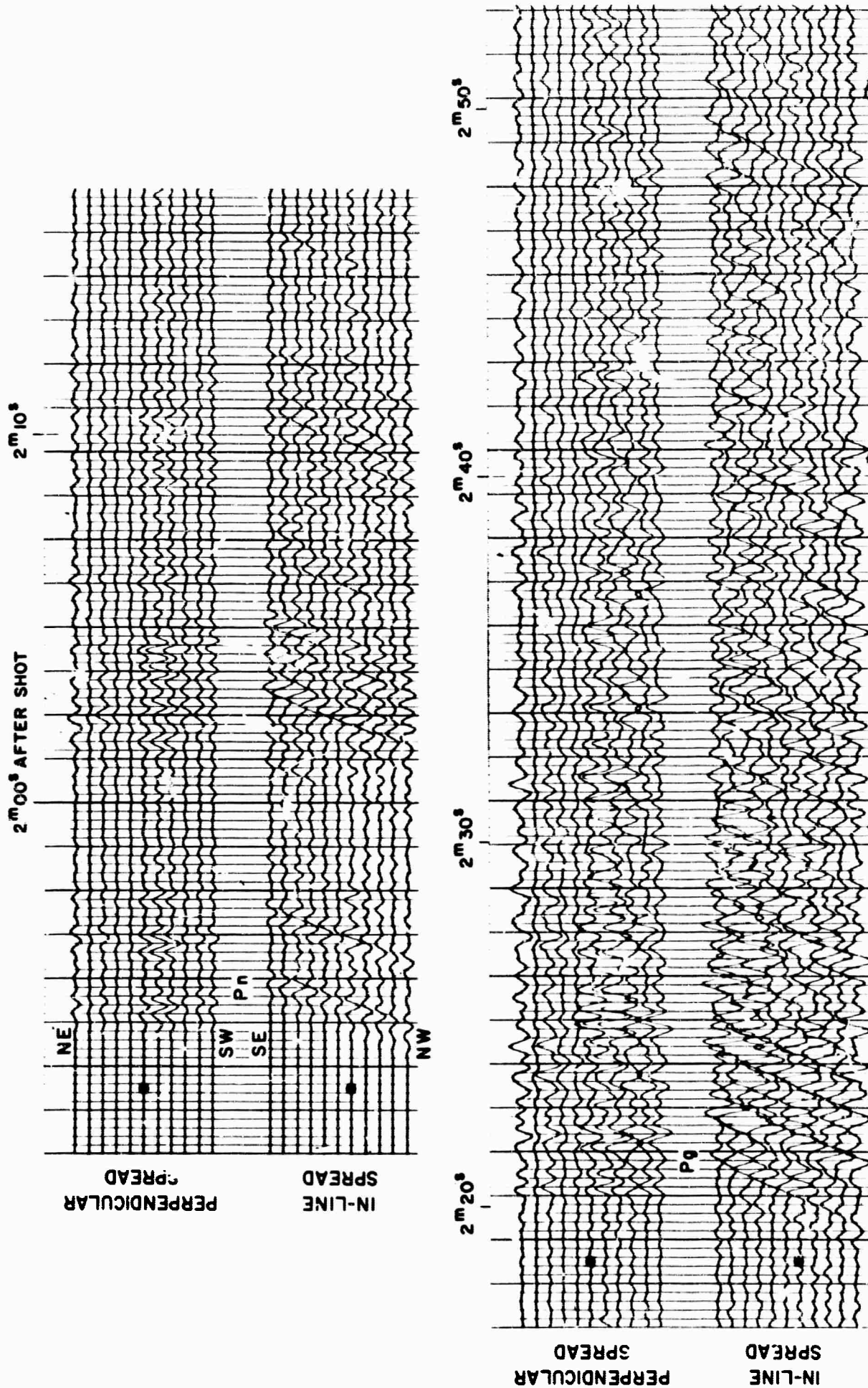
FREQUENCY FILTER: H 38, L 0.8



Distance from array — 569 km. Traces 1-11 make up the southwest-northeast (broad-side) arm of the array. Traces 12-22 are the northwest-southeast (inline) arm.

Figure 4. Seismogram Recorded from Grey's Shotpoint.

FREQUENCY FILTER: H 3.8, L 0.8



Distance from array — 837 km. Traces 1-11 make up the southwest-northeast (broad-side arm of the array. Traces 12-22 are the northwest-southeast (inline) arm.

Figure 5. Seismogram Recorded from Fallon Shotpoint

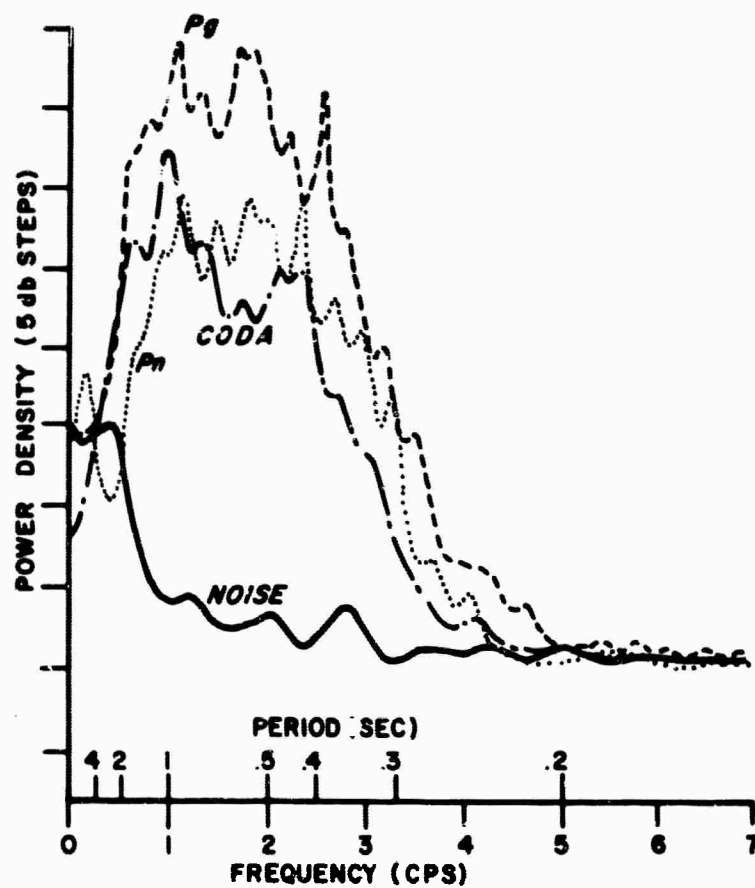


Figure 6.1. Power Spectra for Various Time Partitions of the Fallon Seismogram) (as shown in Figure 6.2)

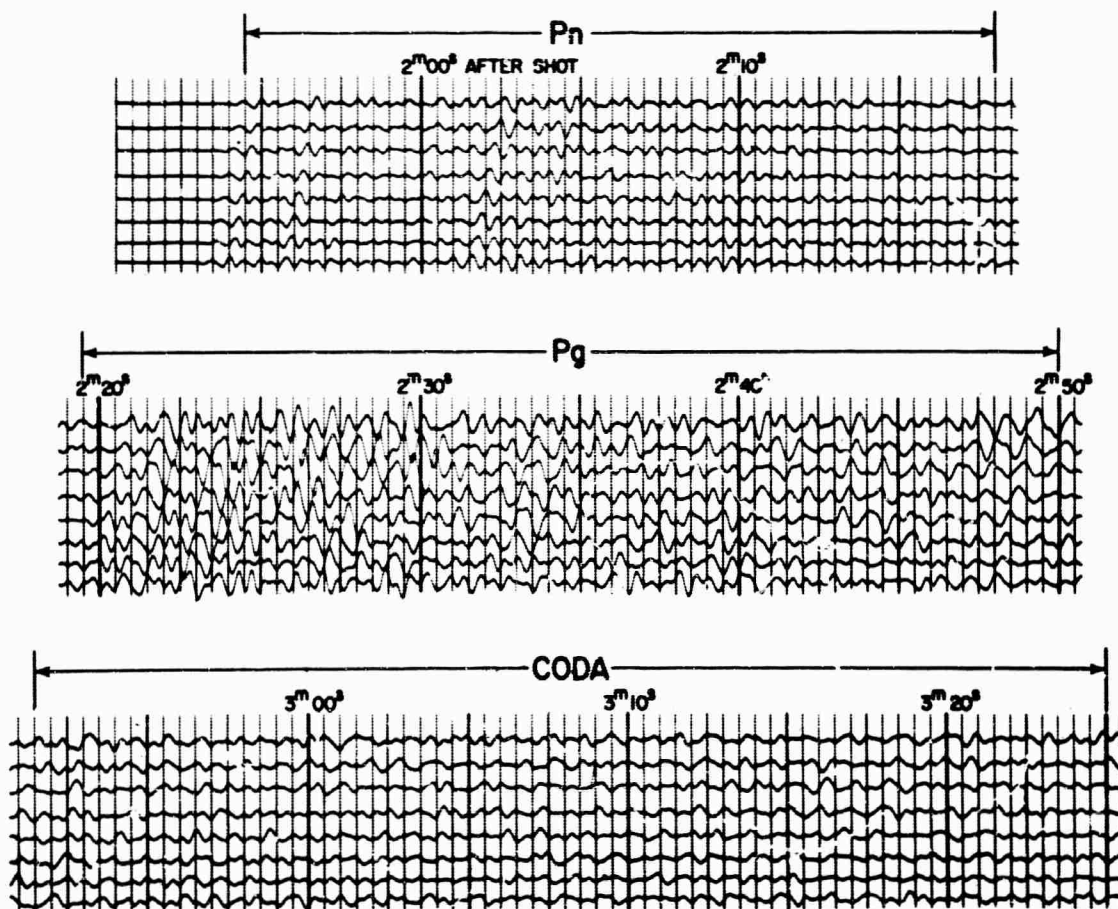


Figure 6.2. Time Partitions of Fallon Seismogram Used for Computing Power Spectra

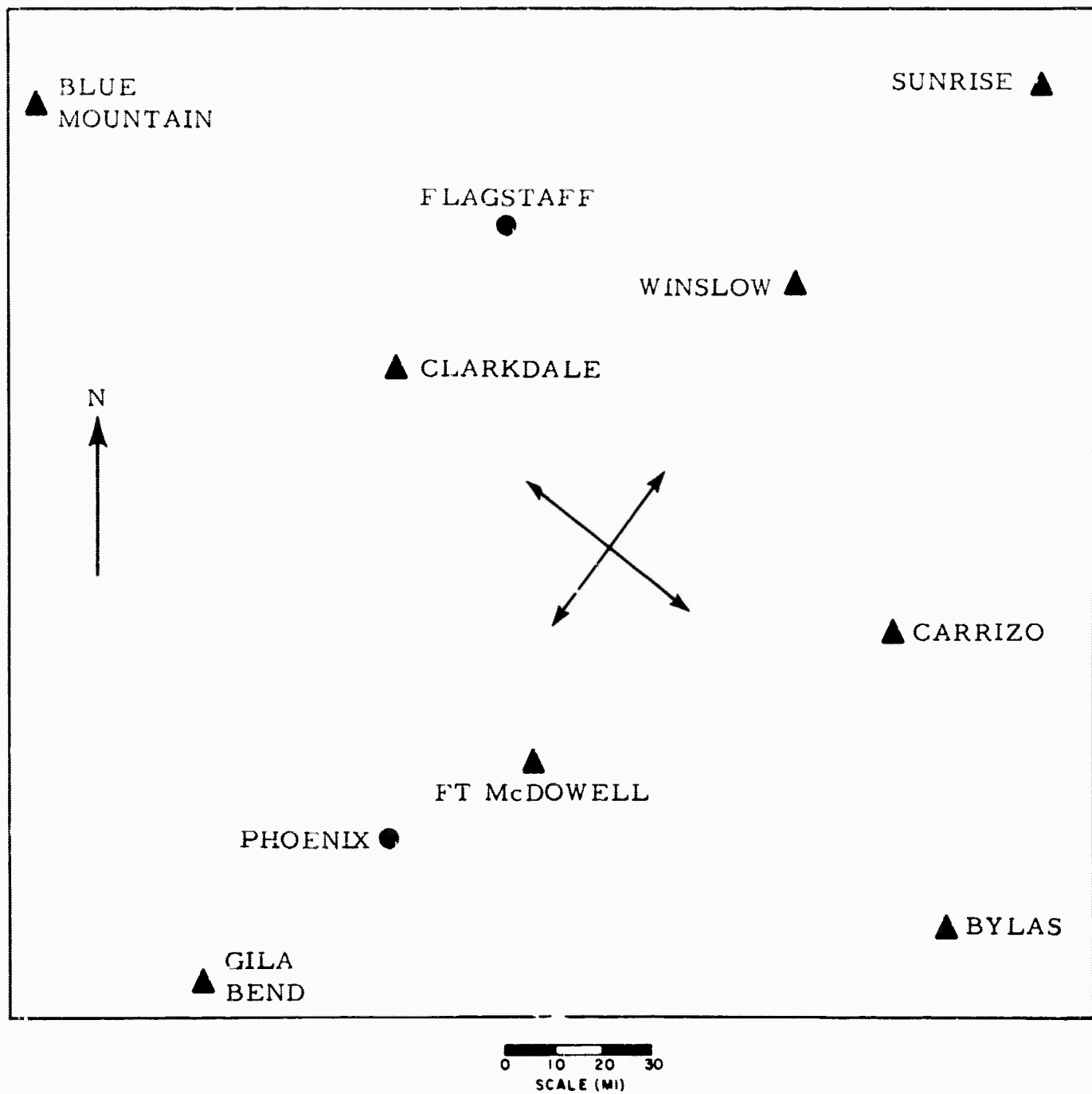


Figure 7. Location of USGS Shots

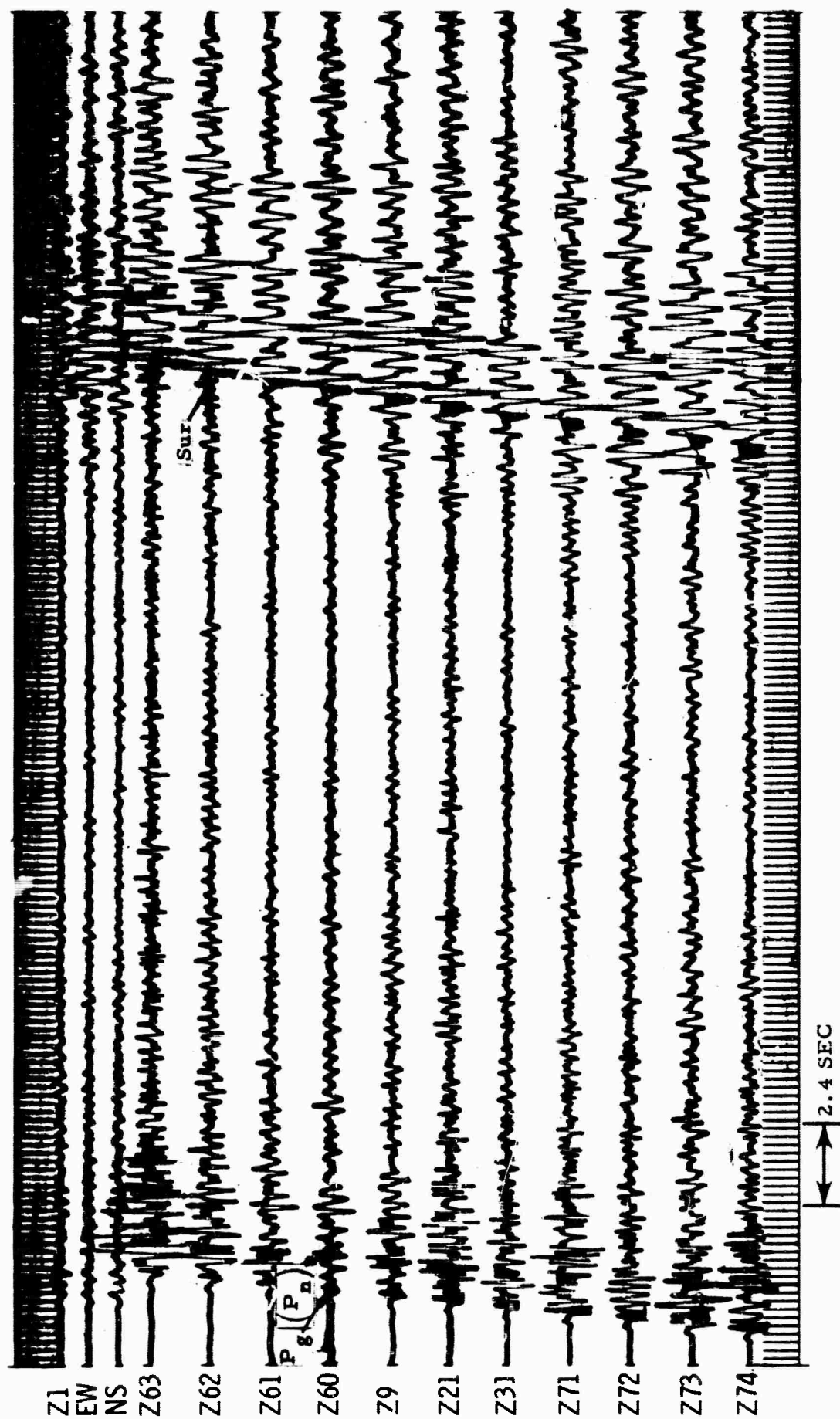


Figure 8. USGS Shot "Sunrise"

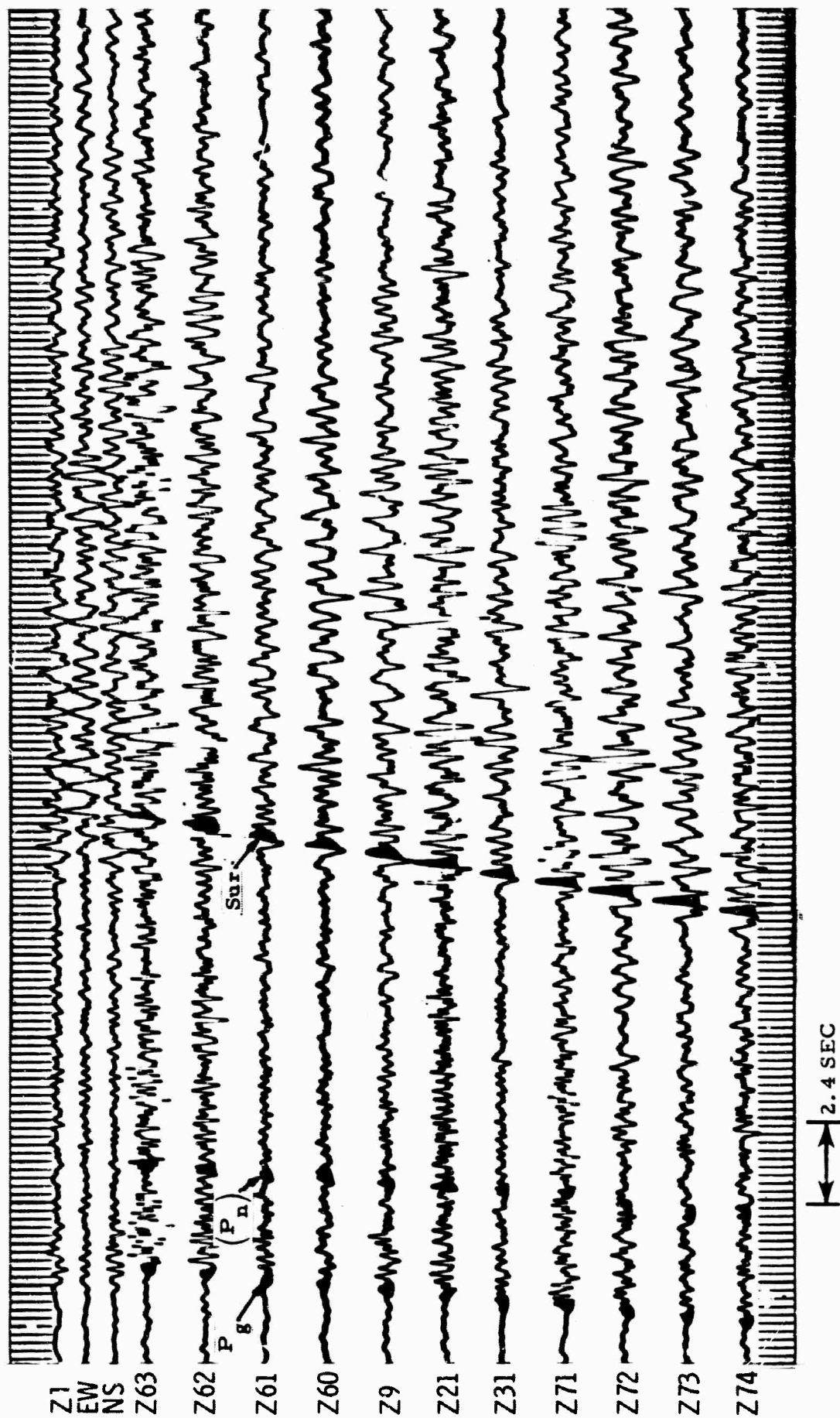


Figure 9. USGS Shot "Winslow"

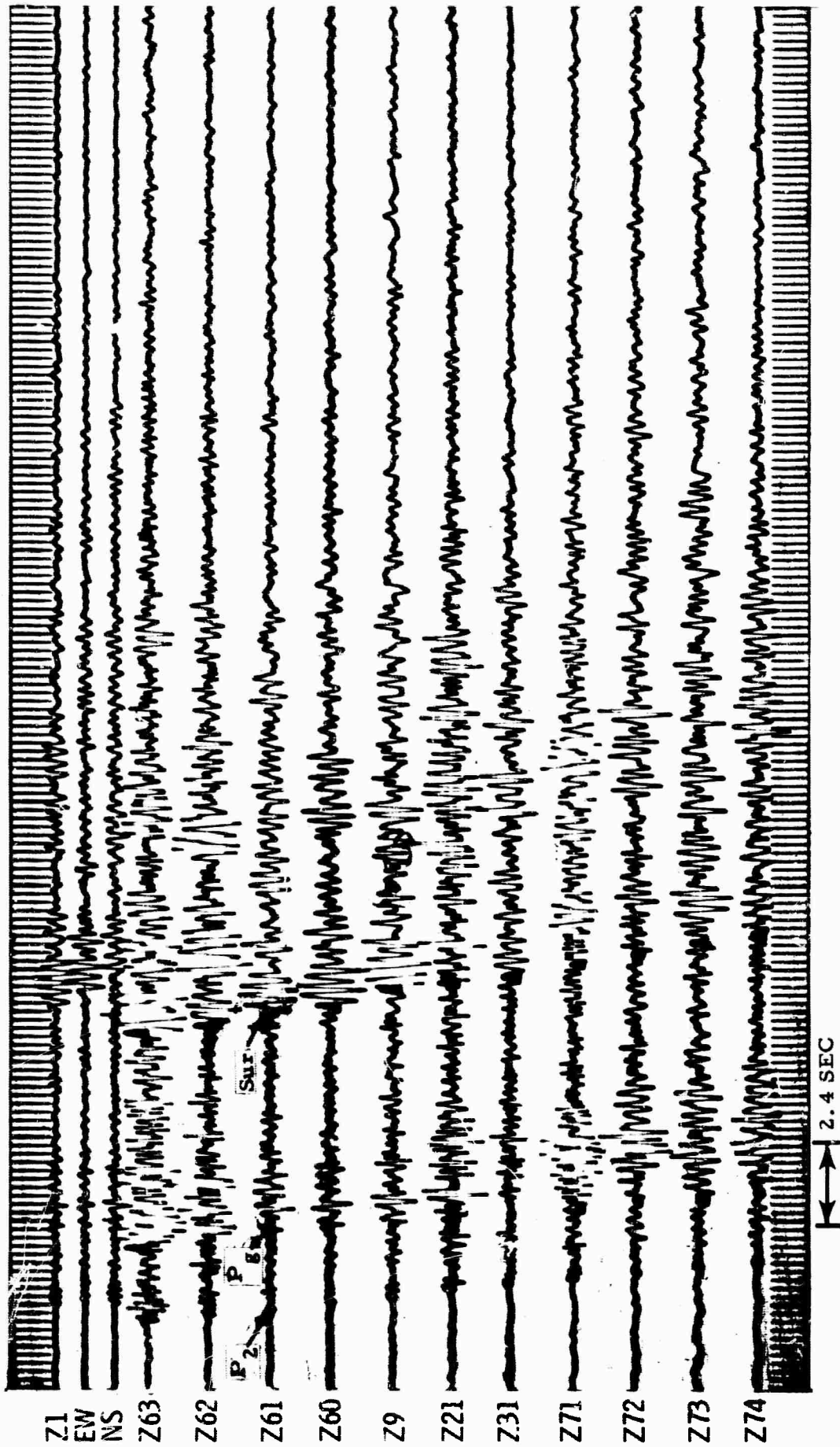


Figure 10. USGS Shot "Ft. McDowell"

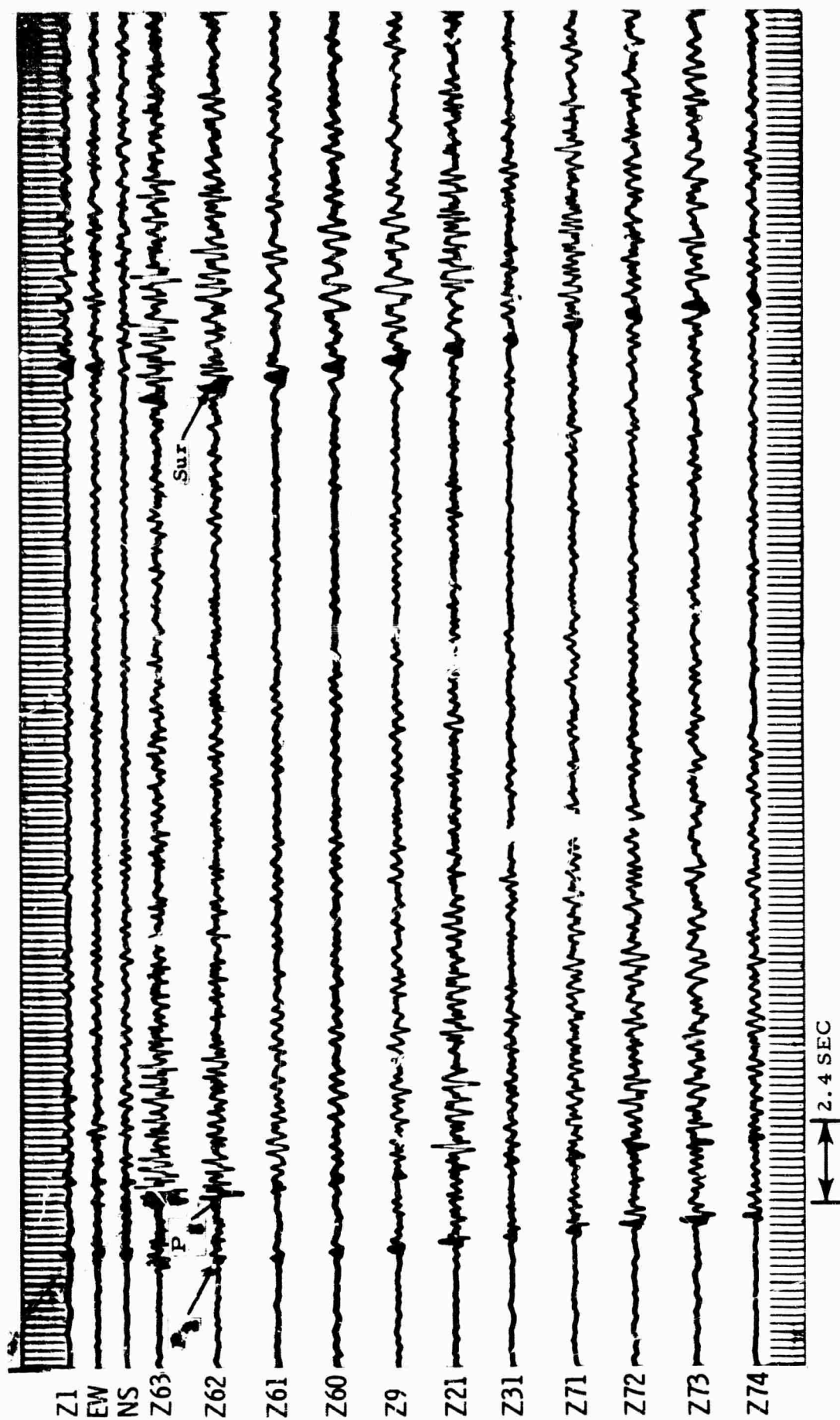


Figure 11. USGS Shot "Gila Bend"

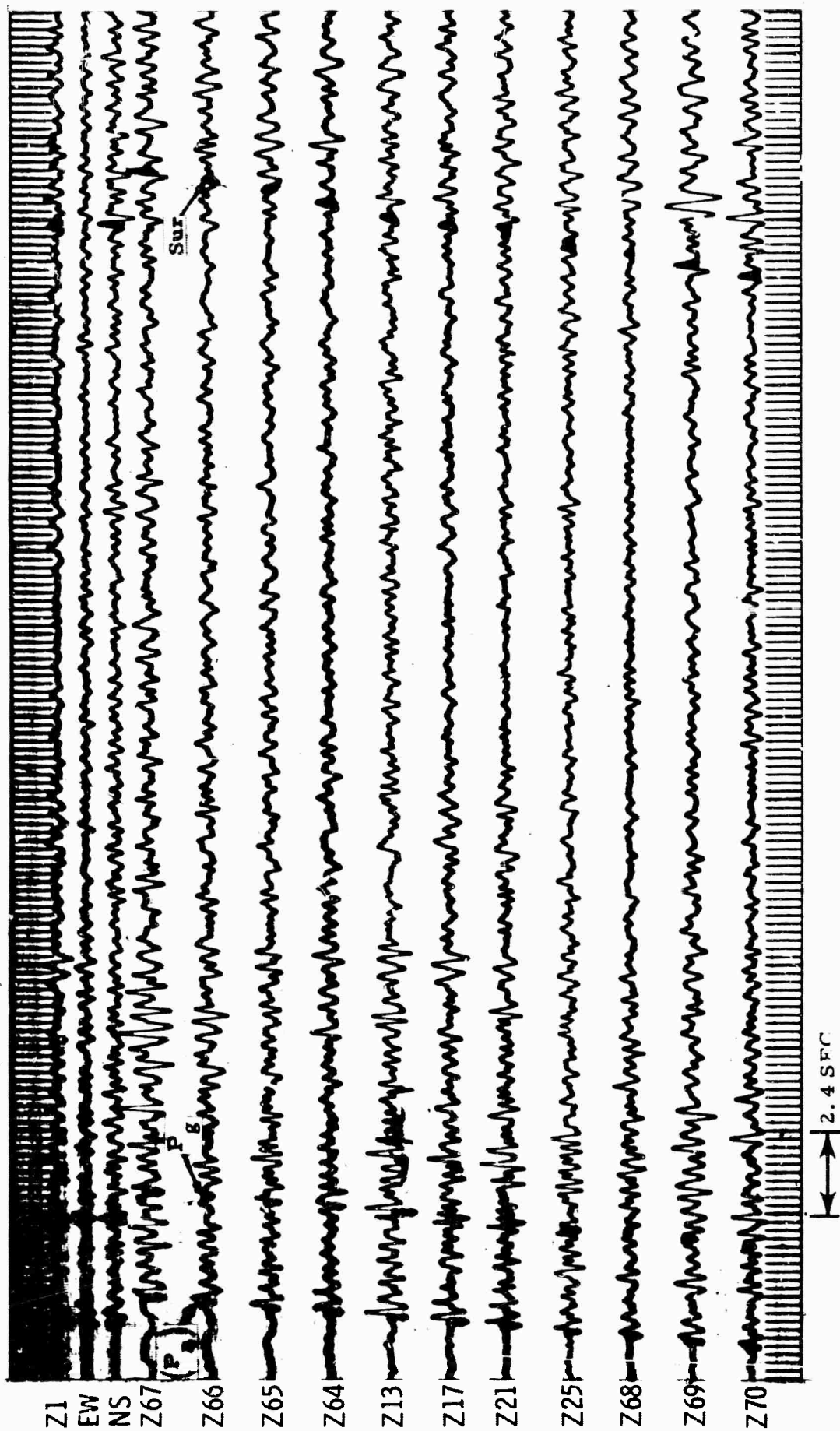


Figure 12. USGS Shot "Blue Mt."

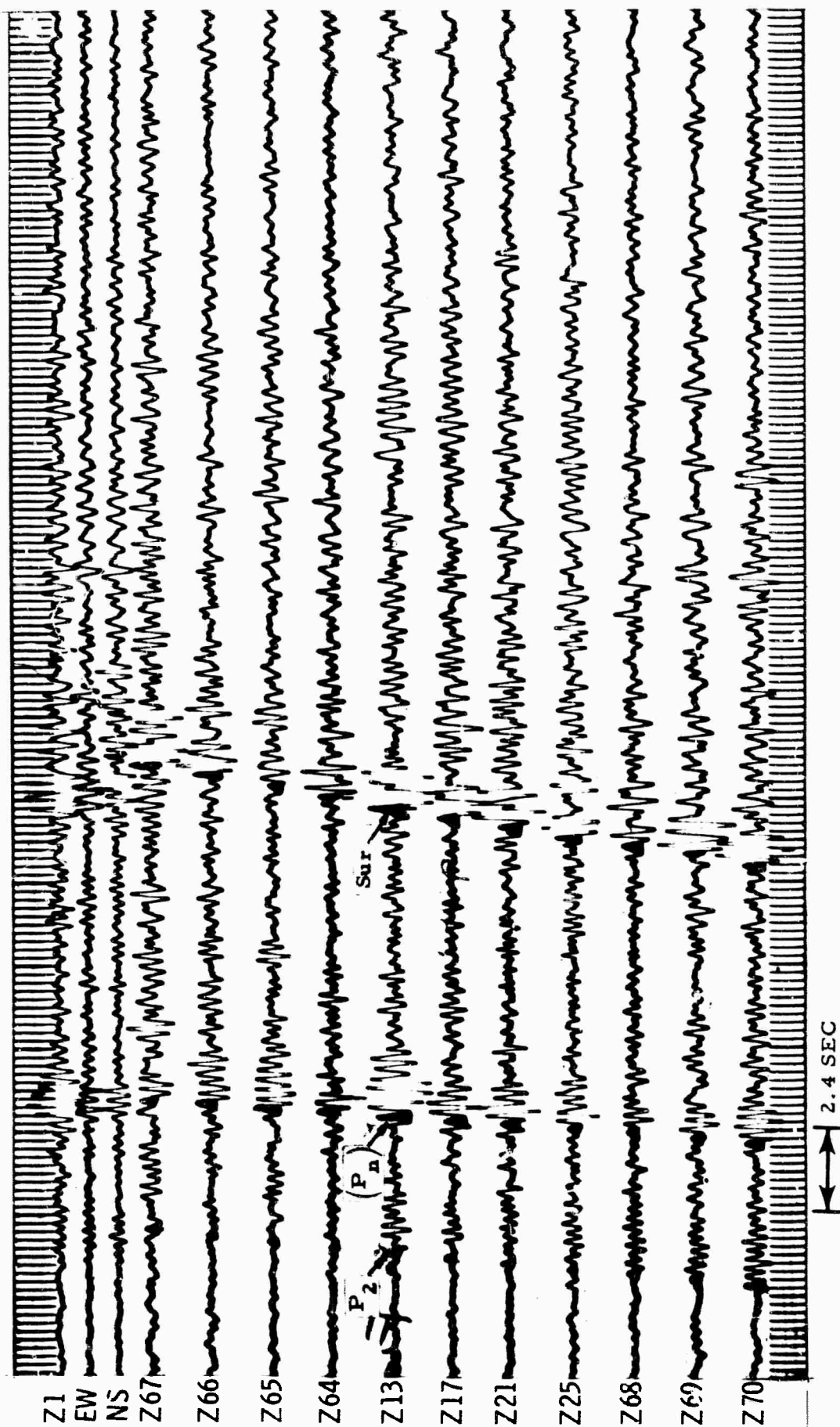


Figure 13. USGS Shot "Clarkdale"

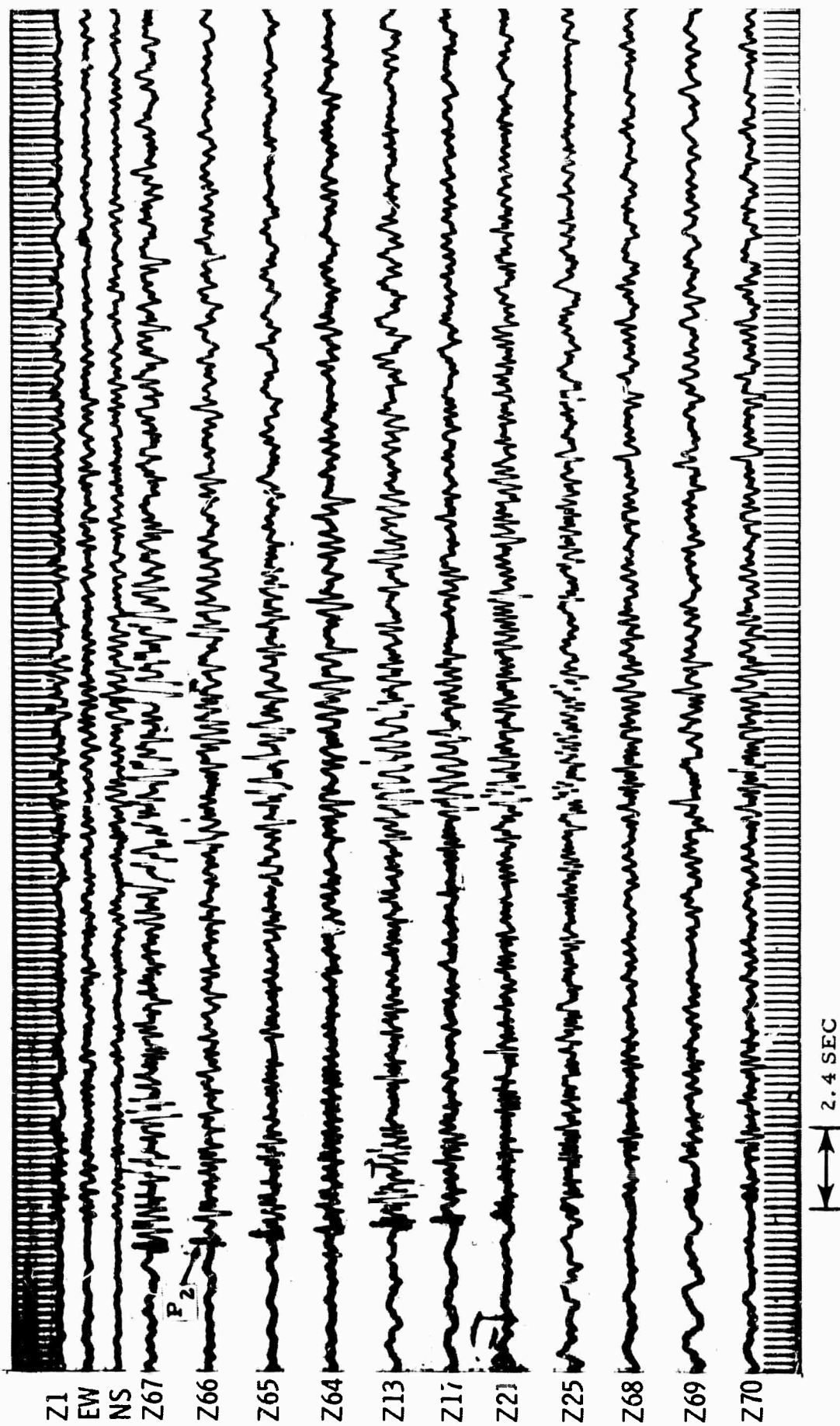


Figure 14. USGS Shot "Carrizo"

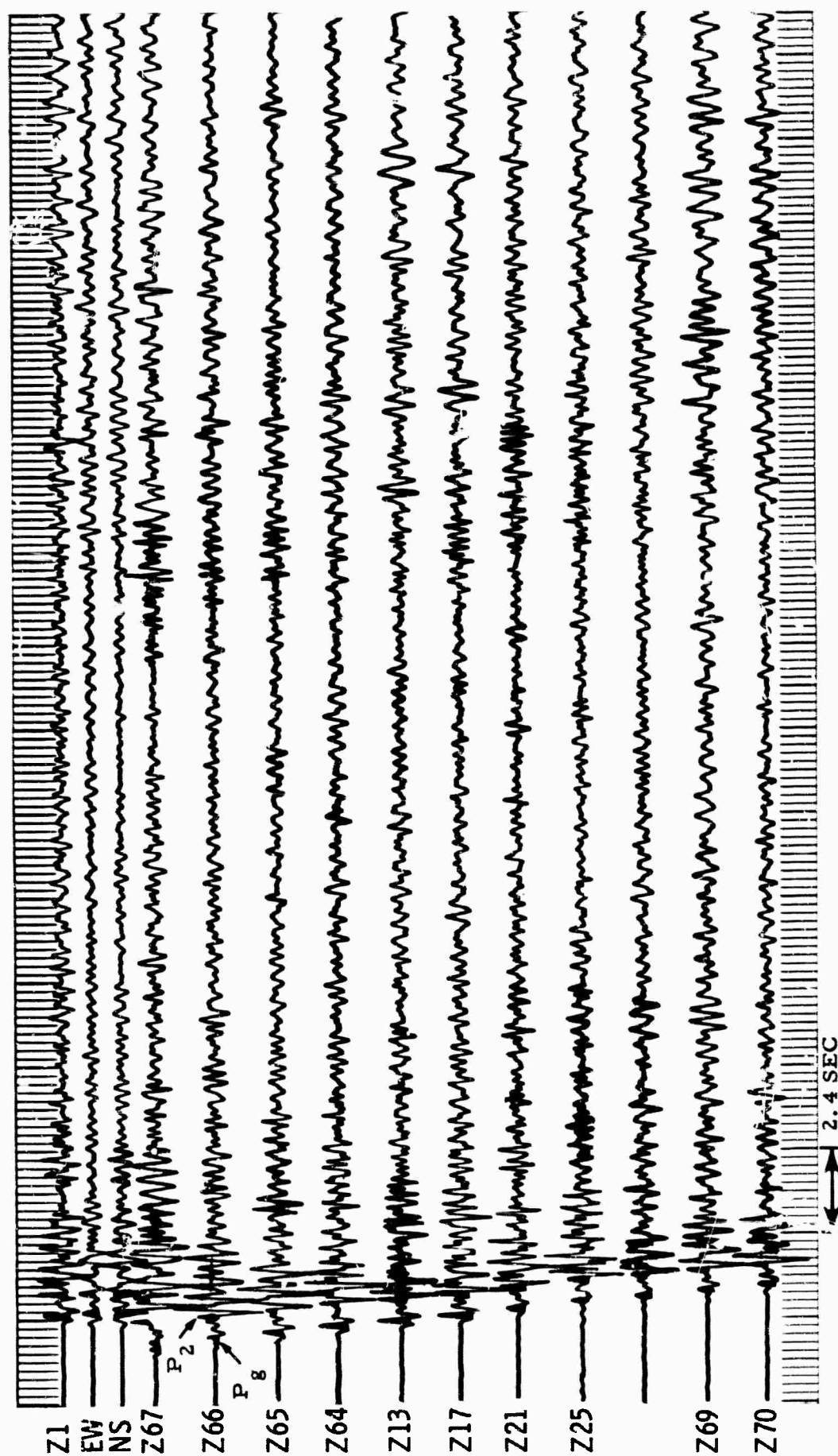


Figure 15. USGS Shot "Bylas"



Figure 16. Summary of Colorado Plateau Geological Boundaries in the TFO Area

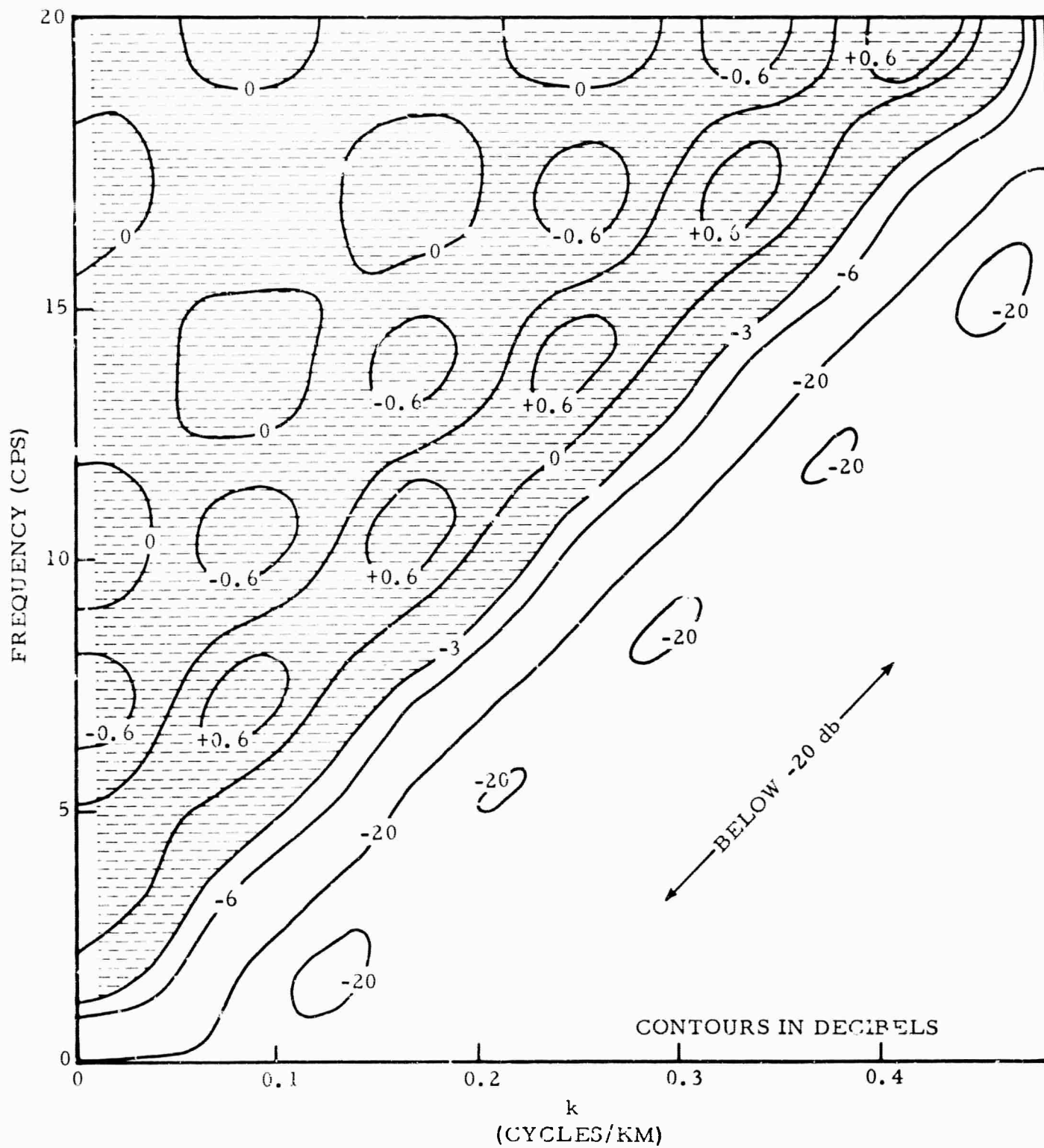
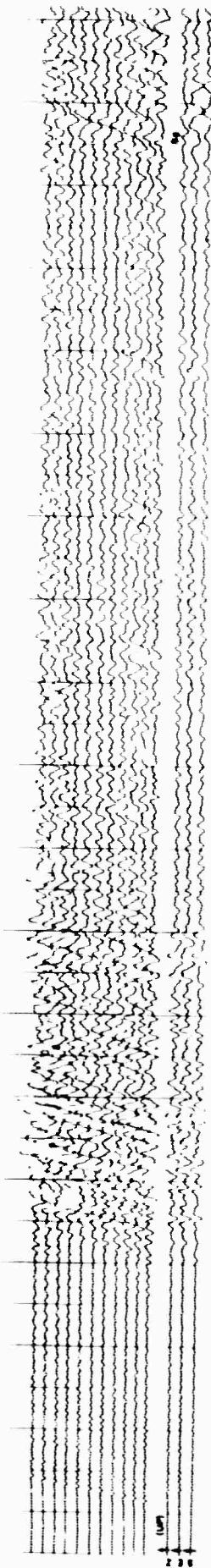
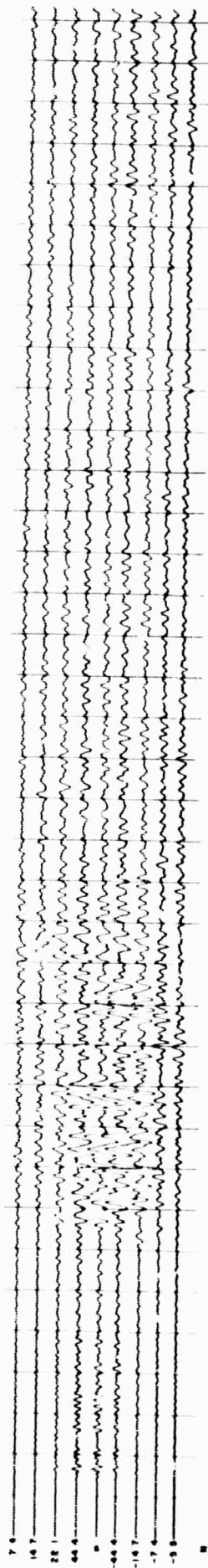


Figure 17. Frequency-Wavenumber Response of 12-Channel Pie Slice Process

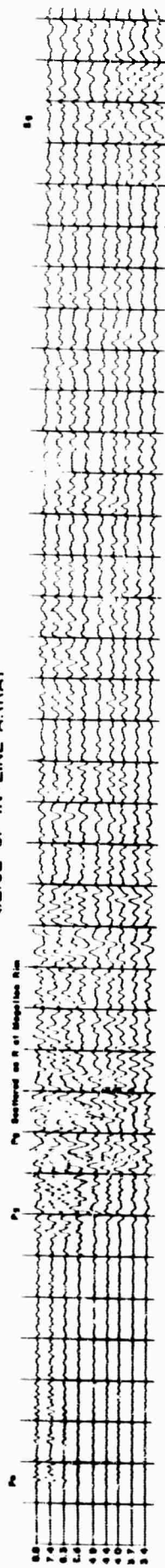
ORIGINAL RECORD



SLICE OF CROSS ARRAY



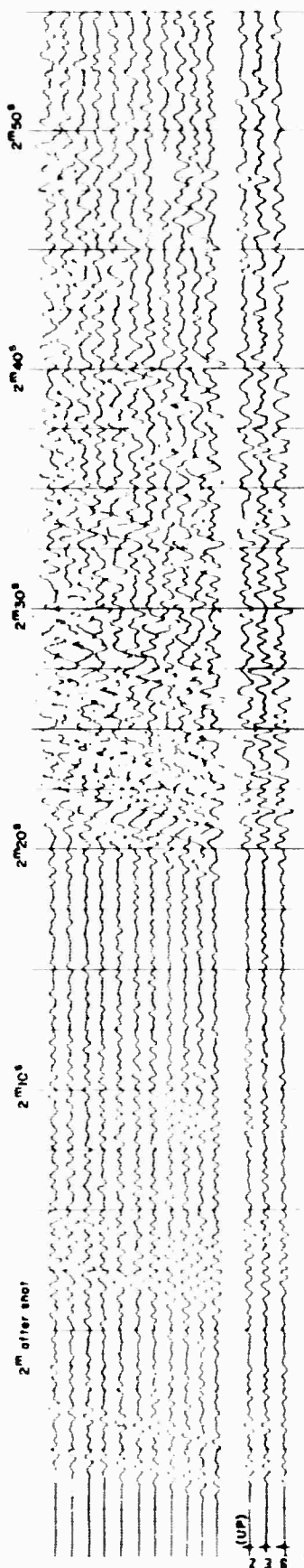
SLICE OF IN-LINE ARRAY



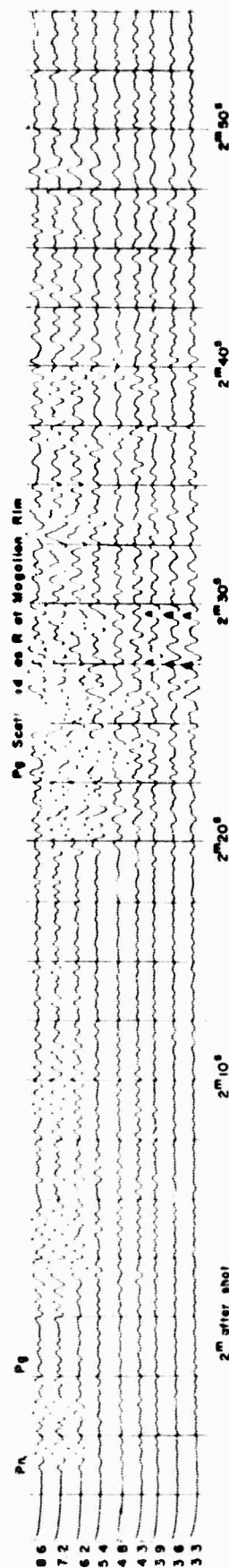
Upper record is unprocessed data recorded on northwest-southeast (inline) arm of array. Middle record is Pie-Sliced output for northeast-southwest (broadside) arm of array. Lower record is Pie-Sliced output for inline arm of array. Major timing lines are 2.5 sec apart.

Figure 18. Pie-Sliced Seismograms from Grey's Shot

ORIGINAL RECORD



SLICE OF IN-LINE ARRAY



Upper record is unprocessed data from inline arm of array. Lower record is Pie-Sliced output of upper record.

Figure 19. Pie-Sliced Seismograms from Fallon Shot

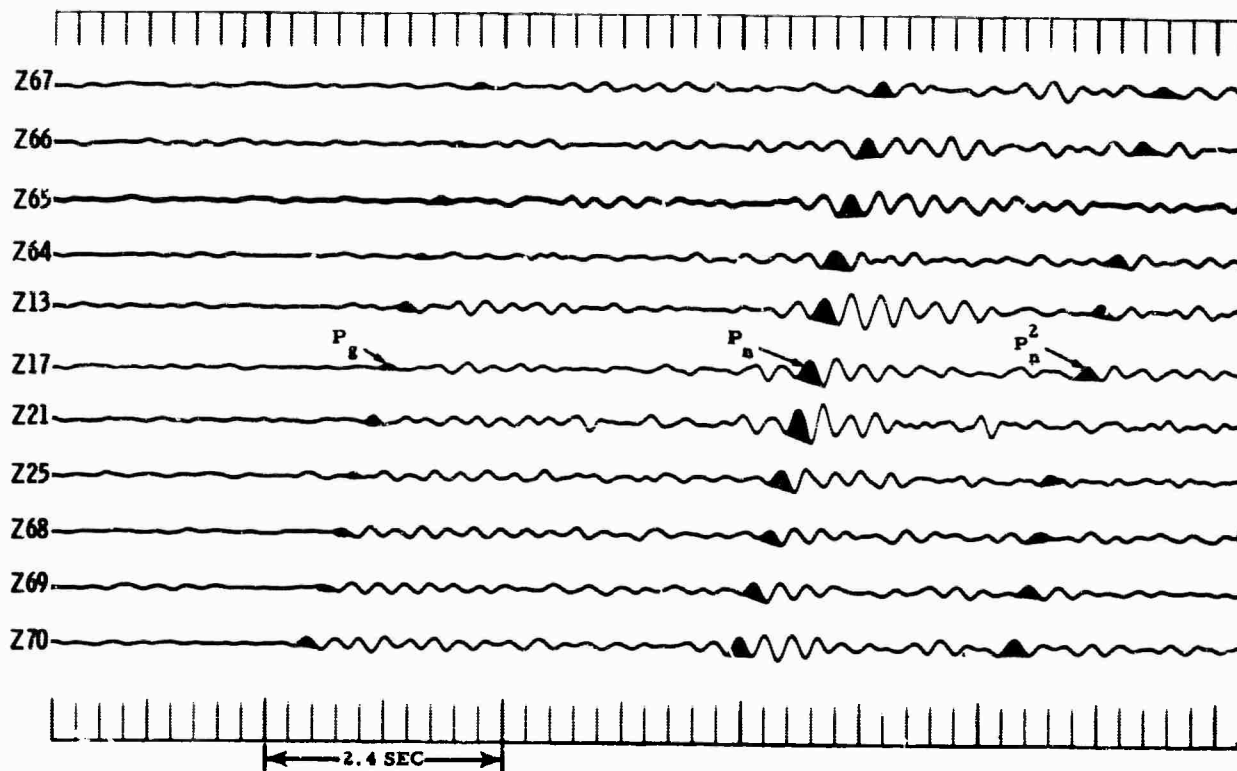


Figure 20. Original USGS Clarkdale Shot

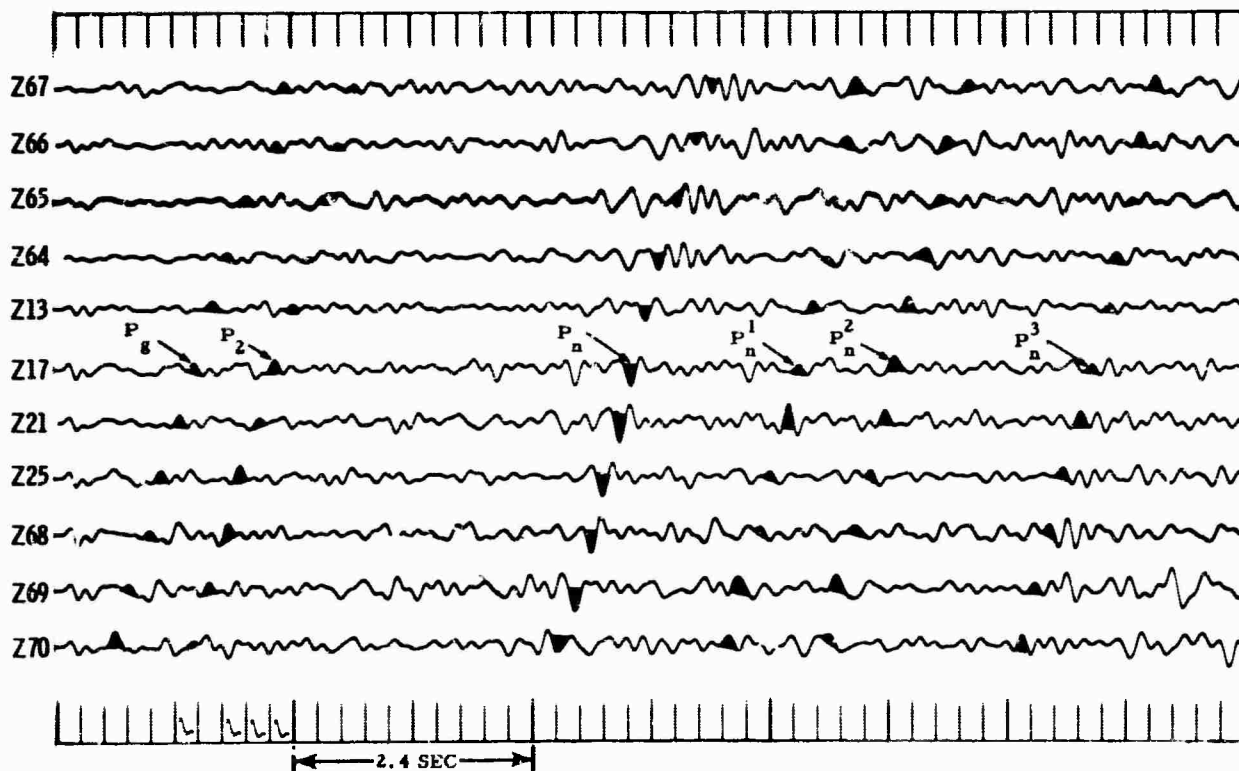


Figure 21. Deconvolved USGS Clarkdale Shot

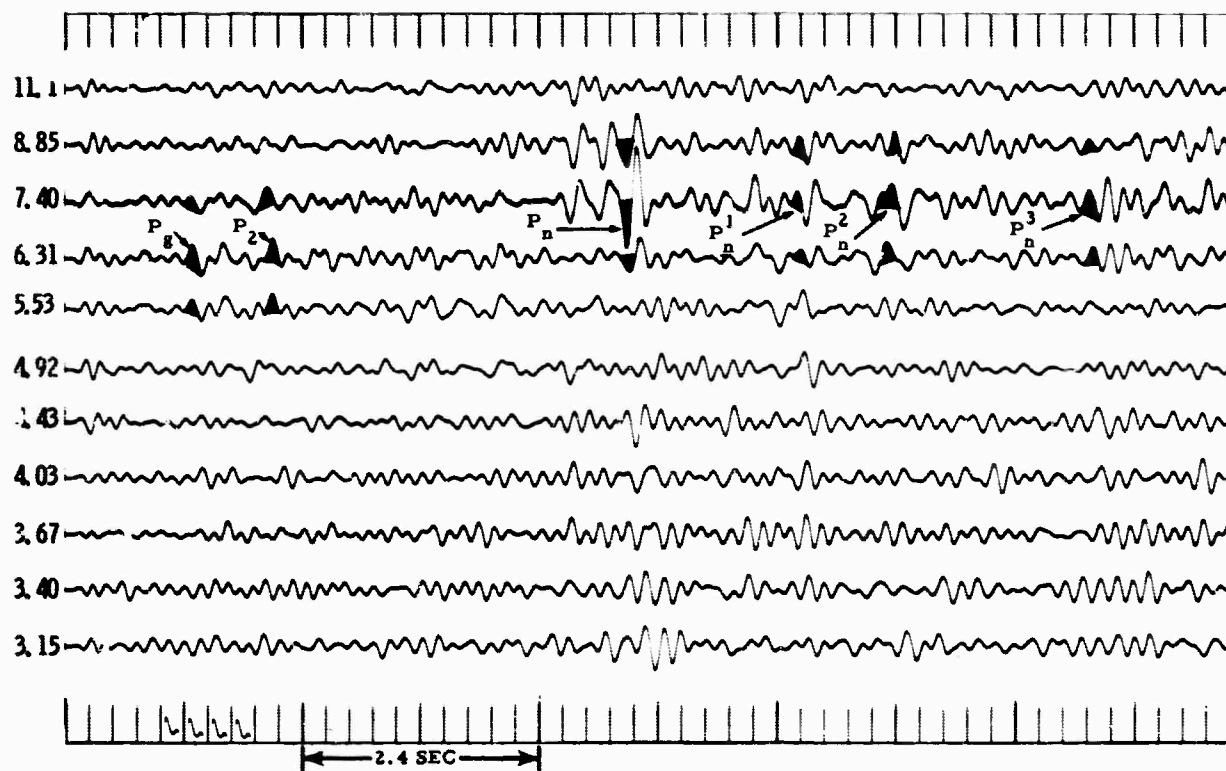


Figure 22. Pie-Sliced USGS Clarkdale Shot



Figure 23. Original Clarkdale Quarry Blast

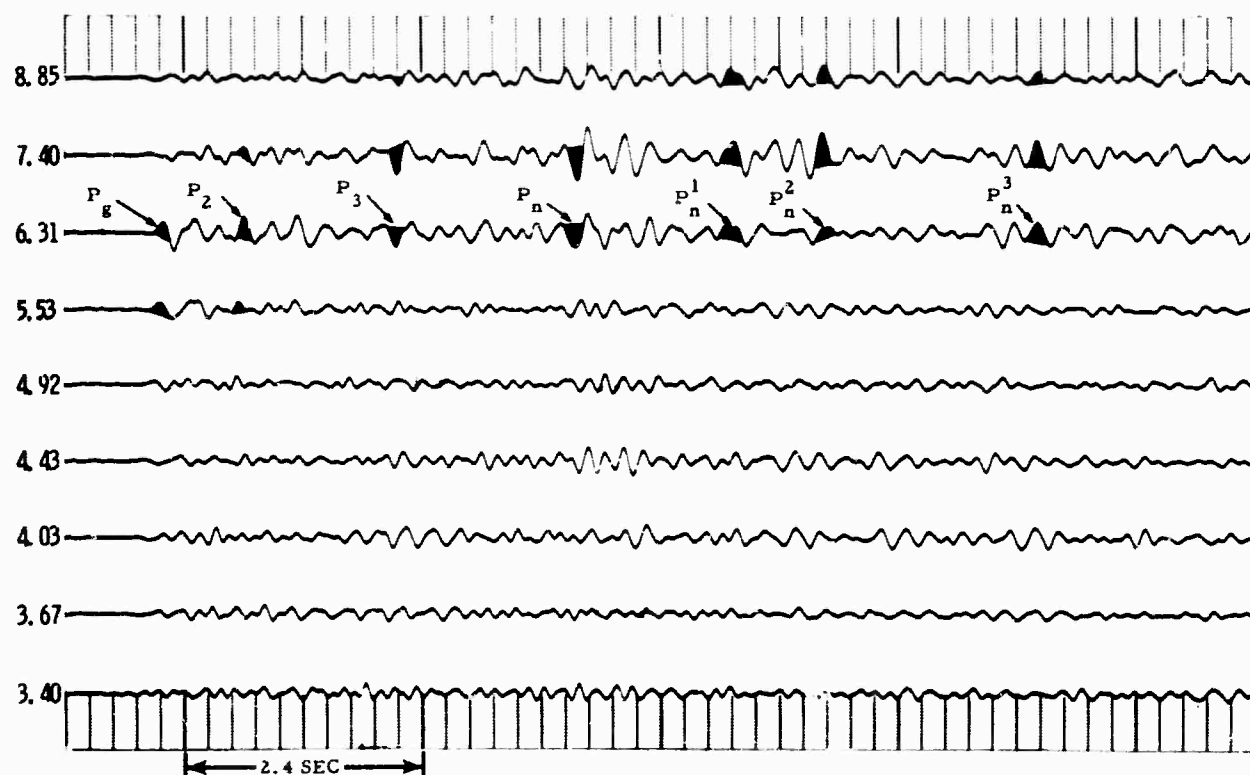


Figure 24. Pie-Sliced Clarkdale Blast

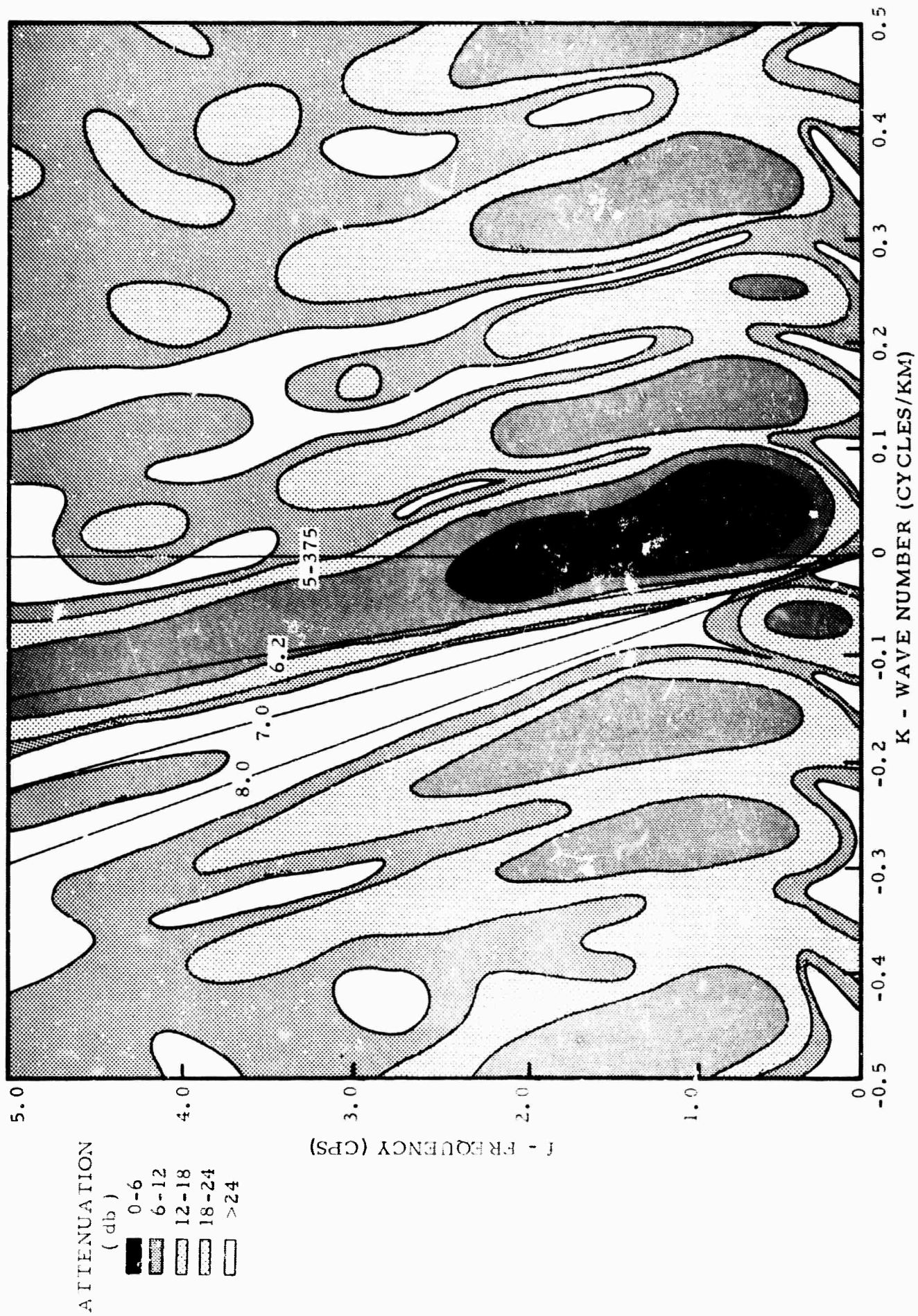


Figure 25. Frequency-Wavenumber Response of Notch Velocity Filter Designed to Pass 6.2 km/sec and Reject 7.0 and 8.0 km/sec

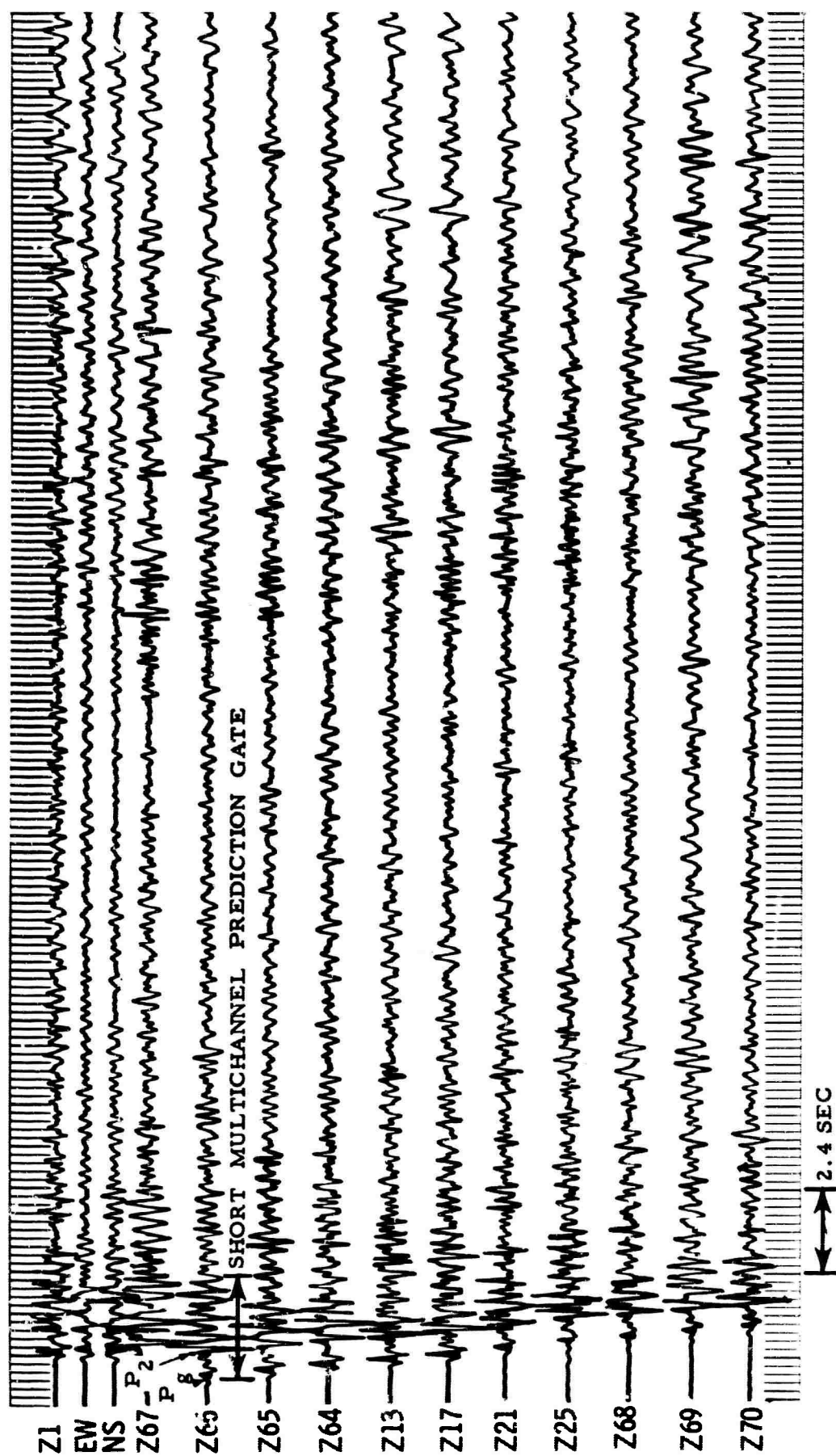


Figure 26. USGS Bylas Shot

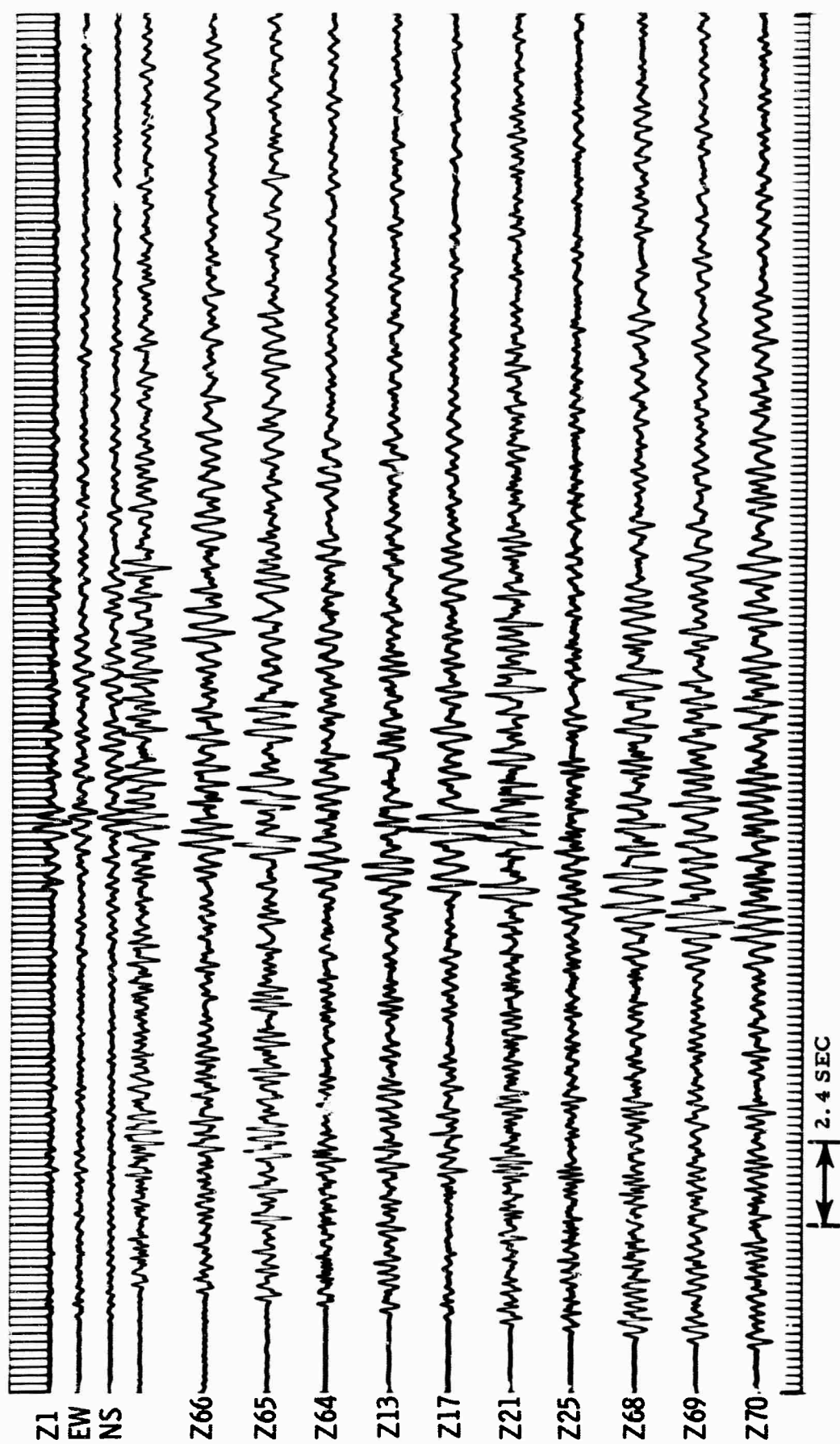


Figure 27. Clarkdale Quarry Blast

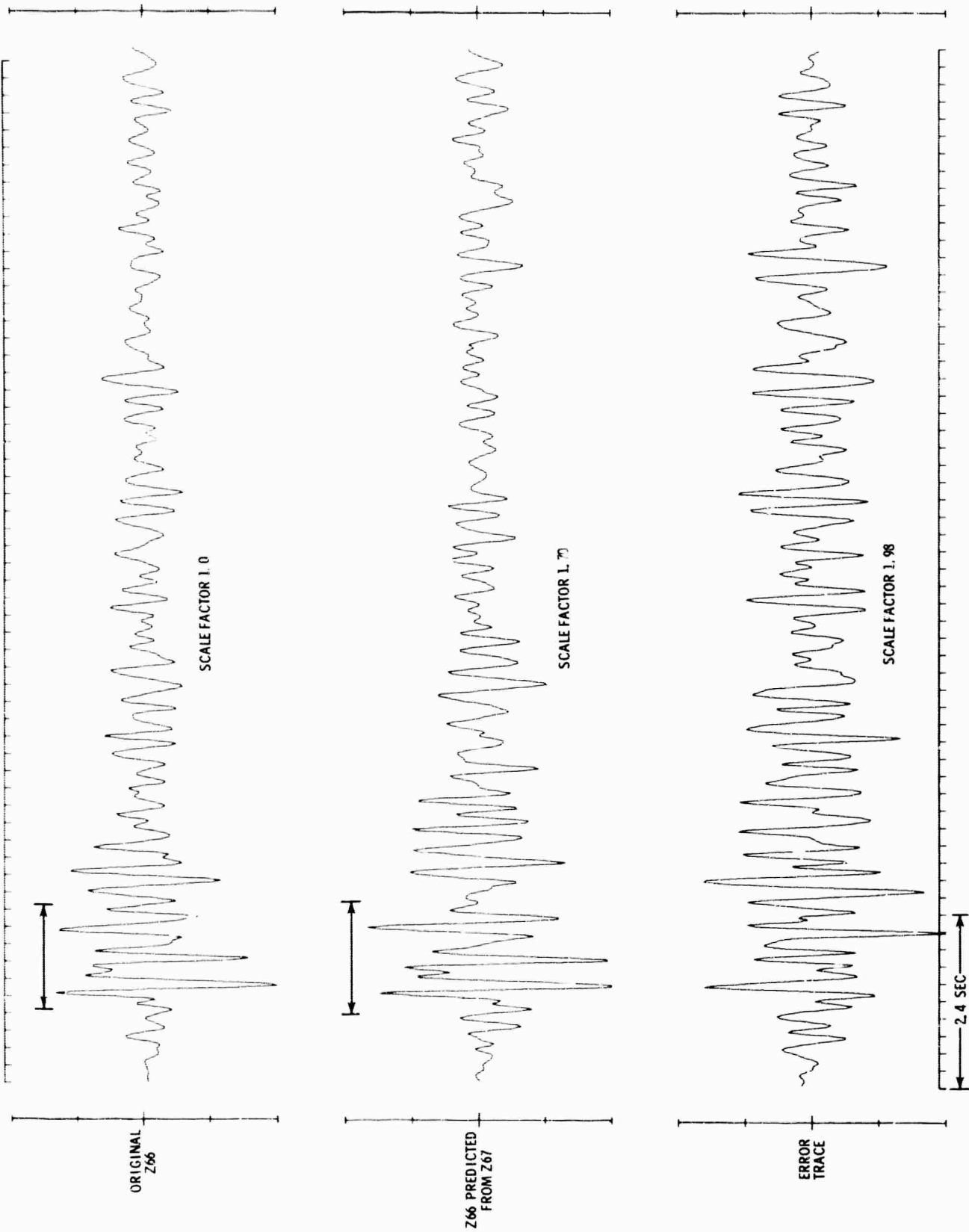


Figure 28. Original and Predicted Z-66 Output (for 'P' gate) and Error Trace

APPENDIX G

NEAR-SURFACE DISPERSION STUDIES AT TONTON FOREST SEISMOLOGICAL OBSERVATORY

by A. Frank Linville* and Stanley J. Laster*

ABSTRACT

Four local seismic events digitally recorded on a crossed-linear array have been analyzed to evaluate the representation of wave propagation in inhomogeneous earth models in terms of "local" dispersion. The analysis techniques studied are based primarily on the correlation properties of the signals at various receivers. Frequency-wavenumber spectra are computed for the events by various methods, and a comparison of the results indicates that the best method is a combination using averaged correlations computed from prewhitened data. The utility of computing dispersion curves from an estimation of the "transfer function" has been evaluated. The studies show the necessity of recording data directly "inline" in areas of rough topography between source and array if "local" dispersion is to be measured. Multi-channel prediction studies indicate that the signals are highly nonstationary in space.

*Texas Instruments Incorporated, Dallas, Texas

BLANK PAGE

APPENDIX G

NEAR-SURFACE DISPERSION STUDIES AT TONGO FOREST SEISMOLOGICAL OBSERVATORY

I. INTRODUCTION

This appendix deals with the analysis of four local seismic events recorded at Tonto Forest Seismological Observatory in Central Arizona. These events were small explosions detonated by the U.S. Geological Survey during a series of calibration shots for the Tonto Forest Observatory. Their distance, charge size and resultant frequency content were such that the propagation was controlled primarily by the upper 2 or 3 km of the earth's crust. The very rough topography of this area made conventional interpretation very difficult. The purpose of this study was to evaluate certain improved techniques for interpretation, based primarily on the correlation properties of the signals at various receivers. In addition, it was desired to evaluate the representation of wave propagation in inhomogeneous earth models in terms of "local" dispersion. Some information was gained concerning the actual near-surface earth structure at Tonto Forest but this was a byproduct rather than a primary aim of this study. Needless to say, the results obtained are not unique and it would be unrealistic to attempt a detailed interpretation with only four pieces of data.

II. DESCRIPTION OF ARRAY

The seismograms described in this appendix were recorded by the 21-element crossed-linear array at Tonto Forest Seismological Observatory (TFO).

Figure 1 shows the array configuration and locations of the short-period Johnson-Matheson vertical seismometers. The locations are shown on a topographic map to point out elevation variations of 800 ft or more within this array. It will be seen later that this variation is a considerable percentage of the layer thickness which is being estimated by dispersion analysis of Rayleigh waves. Variations of this nature may also result in scattering of seismic waves within the array. Table 1 gives elevations, rock types at the seismometer vault and coordinates for the 21-elements of the cross array.

Each arm of the array consisted of 11 inline elements with 21 common to both arms. The spacing between inline elements was 1 km with variations to ± 20 percent.

Table 1

ELEVATIONS, ROCK TYPES AND COORDINATES

Seismometer No.	Elevation (ft)	Rock Type	N. Latitude	W. Longitude
Z63	5074	Granite	34° 14' 54"	111° 18' 07"
Z62	4969	Granite	34 15 21	111 17 42
Z61	4890	Weathered Granite	34 15 49	111 17 17
Z60	4947	Granite	34 16 08	111 16 52
Z 9	4998	Granite	34 16 40	111 16 32
Z21	5294	Sandstone	34 17 12	111 16 03
Z31	5254	Limestone	34 17 44	111 15 35
Z71	5319	Limestone	34 18 07	111 15 15
Z72	5323	Limestone	34 18 34	111 14 48
Z73	5583	Limestone	34 19 02	111 14 23
Z74	5694	Limestone	34 19 29	111 13 58
Z67	4952	Weathered Granite	34 15 08	111 12 43
Z66	4868	Granite	34 15 29	111 13 16
Z65	4832	Weathered Granite	34 15 44	111 13 53
Z64	4850	Granite	34 16 10	111 14 22
Z13	4838	Granite	34 16 31	111 14 56
Z17	4969	Granite	34 16 50	111 15 28
Z21	5294	Sandstone	34 17 12	111 16 03
Z25	5204	Limestone	34 17 53	111 16 40
Z68	5080	Limestone	34 17 53	111 17 09
Z69	4900	Limestone	34 18 13	111 17 42
Z70	4833	Limestone	34 18 34	111 18 16

A major feature in the area is the Diamond Rim fault, shown in Figure 1. This fault, with a displacement of from 1000 to 1500 ft, trends roughly northwest-southeast across the northeast part of the array. A large variation in the thickness of the sedimentary layer will, of course, be associated with this fault.

III. DESCRIPTION OF DATA

The seismograms analyzed in this appendix were four USGS calibration series shots of April-May 1964 — Strawberry, Rye Creek, Kohl's Ranch, and Chase Ranch shotpoints. Shot locations with respect to the array are shown in Figure 1 on a topographic map. A major feature in the immediate area is the sedimentary Mogollon Rim which trends roughly northwest-southeast and rises 2500 ft above the array. Table 2 gives origin times and coordinates for each shot.

Table 2

ORIGIN TIMES AND COORDINATES FOR EACH SHOT

Shot	N. Latitude Degrees	W. Longitude Degrees	Origin Time	Date
Strawberry (1035)	34.369	111.434	14:15:00.19	4-30-64
Rye Creek	34.137	111.360	20:30:00.23	4-23-64
Kohl's Ranch	34.323	111.066	14:30:00.19	4-22-64
Chase Ranch	34.392	111.287	21:00:00.02	4-23-64

The shots were recorded on the Texas Instruments Digital Field System (DFS)* at 24-msec sampling giving an alias frequency of 21 cps, well outside the frequency band of interest.

Table 3 gives the channel number, seismometer number and distance from each shot to each receiver. Seismograms of the four shots are shown in variable area display in Figures 2, 3 and 4. The recordings show the "inline" and "crossline" arms of the array; the traces from the inline arm have been equalized on a mean (absolute) amplitude basis.

*Trademark of Texas Instruments Incorporated

Table 3
CHANNEL IDENTIFICATION AND DISTANCE FROM
EACH SHOT TO EACH RECEIVER

Channel No.	Seismometer No.	Distance (km)			
		Strawberry	Rye Creek	Chase Ranch	Kohl's Ranch
1	Horizontal N-S	—	—	—	—
2	Horizontal E-W	—	—	—	—
3	Z63	18.125	13.527	16.021	23.275
4	Z62	17.975	14.539	15.149	22.389
5	Z61	17.587	15.601	14.266	21.508
6	Z60	17.992	16.412	13.727	20.751
7	Z 9	17.857	17.533	12.817	19.995
8	Z21	17.924	18.732	11.913	19.036
9	Z31	18.075	19.934	11.045	18.159
10	Z71	18.192	20.780	10.513	17.550
11	Z72	18.537	21.843	10.013	16.794
12	Z73	18.828	22.882	9.454	16.040
13	Z74	19.225	23.940	9.063	15.406
14	Z67	24.241	18.748	16.990	15.620
15	Z66	23.199	18.635	16.115	16.058
16	Z65	22.131	18.291	15.288	16.686
17	Z64	21.097	18.472	14.329	17.097
18	Z13	20.025	18.488	13.460	17.687
19	Z17	19.004	18.554	12.722	18.341
20	Z21	17.924	18.732	11.913	19.036
21	Z25	16.740	18.988	11.072	19.813
22	Z68	15.831	19.194	10.513	20.472
23	Z69	14.876	19.475	9.922	21.226
24	Z70	13.749	19.974	9.422	22.049

Records from the Strawberry and Rye Creek shotpoints are generally more interpretable than those from Kohl's Ranch and Chase Ranch. By this, we mean that pulse-like events are found which can be traced across the record and that a given peak or trough in the surface wavetrain can be traced across several traces. The Chase Ranch record is the worst, showing large changes in pulse shape from trace to trace. Three events are apparent on most of the recordings, i. e., P (compressions), S (shear) and Rayleigh waves. The dominant event is the dispersed Rayleigh wave, which is best seen in Figure 3 where high-cut filtering at 3.1 cps has been employed. The higher frequency P- and S-events are best seen in Figure 4 where low-cut filtering at 2.9 cps has been employed. The P-wave events are pulse-like and are assumed to be critically refracted events propagated along some interface or through some zone of increasing velocity at depth. In certain seismograms such as those recorded from the Kohl's Ranch shotpoint, events following the initial P-arrival are seen. These appear to have the same velocity and are probably multiples of the first event with reflection taking place between the surface and the refracting zone. The S-wave events are not so clearly defined, and a normal mode description may be more appropriate than a ray (pulse) interpretation. In any case, these events are contaminated by scattered surface waves generated locally by the earlier-arriving P-waves.

Table 4 gives the P- and S-velocity measurements which were obtained directly from the recordings. The average P-refraction velocity is 5.71 km/sec and the average S-refraction velocity is 3.32 km/sec. These velocities are thought to be characteristic of the granite material underlying the array site. The travel-time curves show no systematic dependence of these velocities upon distance or azimuth; however, with only four shotpoints, the lack of any such indication is certainly not significant. Reflections or refractions which could be associated with the deeper velocity discontinuities such as the Conrad and Mohorovicic are not seen on these records.

IV. FREQUENCY-WAVENUMBER ANALYSIS

Propagating waves have traditionally been interpreted in terms of plane waves and this has become a more powerful tool with the advent of electronic computers. The technique is to decompose the seismic disturbance into a large number of sinusoidal plane waves, each with a different frequency-wavenumber pair. Amplitudes of the plane waves, considered as a function of frequency and wavenumber, are just the well-known 2-dimensional Fourier transform of the seismic event. In these studies, we considered only a 1-dimensional inline array. Many practical difficulties may arise in computing the transform. One could simply compute numerically the 2-dimensional Fourier transform of the input data. However, because of the presence of noise in the data, we have preferred to estimate the 2-dimensional correlation

Table 4

P- AND S-VELOCITY MEASUREMENTS

Shot	P-Velocity (km/sec)	S-Velocity (km/sec)
Strawberry	5.46	(3.21)
Rye Creek	5.87	3.36
Kohl's Ranch	5.83	(3.39)
Chase Ranch	(5.68)	?

function and then compute its transform (numerically). This requires computation of an autocorrelation function and crosscorrelation between receivers with increasing separation. These correlations can be chosen in a number of ways, the exact choice strongly affecting the result. Spectra were computed for the four shots using the nearest to inline arm of the array for each. The correlations were computed over a 14.4-sec gate on Rye Creek and Kohl's Ranch data, a 15.6-sec gate on the Strawberry data and a 19.2-sec gate on the Chase Ranch data. As above, the data sample period was 0.024 sec.

In computing the frequency-wavenumber (f - k) spectrum for the Strawberry event, a single nonredundant set of auto- and crosscorrelation functions was used. This results from assuming that the seismic disturbance is space-stationary, i. e., that the crosscorrelation function between two receivers depends on their separation but not on their absolute location. Figure 5 shows the correlations. They are very smooth, well-behaved functions but show the energy to be concentrated in a narrow frequency band. To show this more clearly, the frequency spectrum of the autocorrelation function is presented in Figure 6. The energy is strongly peaked between 1 and 2 cps. This band corresponds to the Rayleigh wave energy. The compressional and shear arrivals show higher frequencies but contain little energy.

The f - k spectrum for this event is shown in Figure 7. It is well-known that events traveling with a definite velocity (V) are represented in f - k spectra by energy distributed along the line $f = kV$. If dispersion is present (i. e., V is a function of frequency), the line has curvature. In the present case, most of the energy lies along a line corresponding to a velocity of 2.8 km/sec. We interpret this to mean that the 1- to 2-cps Rayleigh

energy at TFO travels at this velocity. Although this energy band has considerable width, there is some slight indication of dispersion as shown by the fact that the 2.8-km/sec line actually crosses the energy band at an angle to its axis. No good evidence is seen in the spectrum for other velocities. Some sidelobe structure due to the length of the array (10 km) is seen. The spacing between receivers is about 1 km, which would suggest an alias point in wavenumber at about 1 cycle/km. (However, since the spacing varies by several percent, there is a "pseudo-alias" instead of a true alias.) This accounts for the high energy levels at low wavenumber above 2 cps.

Similar computations were performed for the Rye Creek event. The correlations are shown in Figure 8 and the f-k spectrum in Figure 9. The velocity of Rayleigh waves is again near 2.8 km/sec. Evidence for dispersion is again slight, but some appears to be present. No evidence for other velocities is seen. However, both compressional and shear waves are seen on the seismic record. Since these have a higher frequency content than the Rayleigh wave, it seems likely that the significant portion of the high-frequency energy is being overlooked simply because it is so much smaller than the Rayleigh energy.

An attempt to overcome this was made by prewhitening the data. The spectrum of the autocorrelation function used in the f-k computation is shown in Figure 10(A). The spectra for several other traces were also computed and averaged, giving the result shown in Figure 10(B). Next, a time-domain filter operator was designed to bring up the averaged power spectrum to a uniform level at all frequencies (i. e., whiten it). Figure 10(C) shows the frequency response of this filter. (Note that it would be difficult to achieve this result with simple bandpass filtering.) The filter operator was applied to all traces in the Rye Creek record and the correlations computed for the same traces as before. Figure 10(D) shows the spectrum of the autocorrelation after whitening. The spectrum contains much more energy at high frequencies than the spectra at the top of the figures; however, it cannot be called uniform or white because several large peaks are present. The whitening filter has overcompensated. The reason lies in the fact that the filter was computed from an average spectrum, while none of the traces has exactly this spectrum. Nevertheless, the filter has performed adequately as can be seen from the prewhitened record shown in Figure 11. The Rayleigh wave is still readily observable, but the compressional and shear arrivals have been greatly enhanced. The correlations for the whitened data are shown in Figure 12 and the f-k spectrum in Figure 13.

The most obvious change in the f-k spectrum is the abundant energy at frequencies above 2 cps as would be expected from the prewhitened seismograms. The Rayleigh wave is at least as well-defined as in the raw data — but its alias, though fragmentary, can now be traced to frequencies

above 4 cps. One interesting feature is a suggestion of energy with velocities of 3.5 to 4.5 km/sec at frequencies below 1 cps, which would fall at the low-frequency end of the Rayleigh mode. This could represent low-frequency energy from the source or it could be ambient-noise energy present within the correlation gate. Such ambient-noise energy is readily observed in the absence of a signal. However, it is unlikely that a significant portion of the ambient noise would be traveling in a direction parallel to the inline arm of the array, which might rule out the latter explanation of the low-frequency energy.

No direct evidence is found for other velocities; however, the high energy region at 4.2 cps and low wavenumber has a somewhat higher velocity than the Rayleigh wave and may represent aliased shear-wave energy. The P-wave still cannot be observed on the f-k spectrum.

The assumption of space-stationarity, which has been used above, is known to be somewhat in error — partly because of the presence of scattered energy and partly because of the correlation coupling between the P-, S- and Rayleigh waves. To evaluate the effect of this nonstationarity upon the f-k spectrum of the Rye Creek seismogram, ensemble averaging was applied to the correlation functions. Under the assumption that the nonstationary behavior varies randomly as one looks at the correlation function for various pairs of receivers, it is seen that averaging over correlations representing the same space separation will eliminate these effects. By our definitions of space stationarity, the stationarity behavior will not be affected. We have computed the averaged correlations even though there is some variation in spacing of the receiver. This will cause a small amount of degradation in the result, but this is expected to be a minor problem. The ensemble average correlations are shown in Figure 14 and the f-k spectrum in Figure 15. The averaging process is more effective for the correlations of small space lag than those of large space lag because a finite array such as that used at TFO yields more distinct correlations for small lags.

The frequency-wavenumber spectrum obtained by this averaging technique gave a better definition of the Rayleigh mode than any other method. The dispersion characteristic can be continuously traced over the frequency range of 1 to 3 cps. One paradoxical feature is the small hump in the curve between wavenumbers of 0.8 and 0.9 cycles/km. Evidence also may be seen for this in the original f-k spectrum and the prewhitened spectrum. This appears to indicate an increase in phase velocity with frequency, which is an impossibility for any simple plane-layered model. One possible interpretation is that much of the Rayleigh energy in this wavenumber range is scattered or laterally refracted so that it arrives at the array from a slightly offside direction. In that case, its phase velocity would appear to be higher than for events arriving from an inline direction. There are many difficulties with such an explanation — principally, the problem of explaining

why such a process is wavenumber-selective. For lack of evidence, we do not consider this problem further in this appendix.

The computation of frequency-wavenumber spectra for the Kohl's Ranch and Chase Ranch seismograms presented a problem. These shotpoints were not inline with either arm of the cross array; however, in the interest of analyzing the data, it was decided in each case to use the arm of the array which was nearest inline. The seismometer positions were projected (by using circular arcs) onto a linear array inline with the shot. It is not difficult to show that this is valid for an earth model consisting of plane parallel layers. Two results were immediate: first, since the spacing of this hypothesized array was smaller than for the original array, the alias point occurred at a larger wavenumber; and second, the new array had a shorter total length so the resolution was less and the sidelobes were more of a problem.

Because of the good results obtained by averaging the Rye Creek correlation functions, the same technique was used here. However, one must bear in mind that the variation in spacing was greater here, and this results in more degradation when the correlations are averaged. The correlation functions, frequency spectrum and f-k spectrum for Kohl's Ranch are shown in Figures 16, 17 and 18 while those for Chase Ranch are shown in Figures 19, 20 and 21. In each case, there is very little correlation between the various receivers as compared to the Rye Creek and Strawberry seismograms. Not even a well-defined Rayleigh pulse is seen. The f-k spectra in the case of Kohl's Ranch shows some evidence of the Rayleigh velocity, while that for Chase Ranch is uninterpretable. This is not too surprising when one looks back at the original records (Figures 2 and 3). The Rayleigh wave can be visually correlated between some traces on the Kohl's Ranch seismogram, but shows large changes in pulse shape from trace to trace on the Chase Ranch record. This may be partially attributed to the higher frequency content of the Chase record. However, most of the difficulty can be traced to the use of a noninline array in an area of very rough topography. This is discussed in more detail at the end of the next section.

V. DISPERSION ANALYSIS

Group velocities were determined by picking peaks and troughs of the Rayleigh wave at each seismometer for the Strawberry event (Figure 22) and for the Rye Creek event (Figure 23). These events are in line with the arm of the array from which the measurements were taken, and the points show little scatter; however, the group velocities measured from Kohl's Ranch and Chase Ranch were uninterpretable due to the scatter between the points. It will be shown later in this section that this scatter is expected with changes in layer thickness due to different paths from the source to each seismometer for the Kohl's Ranch and Chase Ranch event. When the path

from source to seismometers is the same, the group velocity measurements show little scatter; however, the group velocity curve that has been measured is for the averaged crustal configuration that exists over the entire path from source to seismometer so these curves cannot be interpreted in terms of local dispersion due to crustal structure under the array.

The frequency-wavenumber analysis just discussed has given a rough estimate of the velocity of Rayleigh waves in the near-surface material underlying Tonto Forest Observatory. Therefore, an attempt is made to measure more precisely the slight dispersion of Rayleigh waves (i.e., the dependence of phase velocity upon frequency) and the possible variation of the phase velocity across the array. From this information, a crude estimate of the layered structures may be made.

As a first attempt to measure the dispersion of the Rayleigh wavetrain, the seismograms for Rye Creek and Kohl's Ranch shotpoints were filtered with high-cut filters; then, measurable peaks and troughs were visually correlated between traces. This allowed a direct measurement of the phase velocity. The apparent frequencies were determined by measuring the time intervals between successive peaks and trough. The results are shown in Figures 24 and 25. (Note that results are obtained only in the frequency band of 1.5 to 2.5 cps.) Although the Rye Creek records were considered good and the Kohl's Ranch records were considered poor, there was no significant difference between the results since both showed significant scatter. It was found that on one end of the array the energy from Kohl's Ranch shotpoint could be easily traced, while on the other end the signal varied drastically from trace to trace. Only the results from the traceable end of the array are shown. Two problems occur in measuring dispersion in this manner: first, the events (peaks or trough) must be identifiable from receiver to receiver; and second, it must be possible to measure the frequency with sufficient accuracy. Other methods, particularly those based on the Fourier transform, tend to minimize these effects. These will be discussed in succeeding paragraphs.

In a plane-layered material, dispersion of normal modes corresponds simply to a frequency-dependent phase shift (Laster, Foreman and Linville, 1965). One can determine a "transfer function" which operates on a given mode to propagate it from one receiver to a second receiver a unit distance away, independent of the initial source-receiver distance. The Fourier transform of this operator has unit amplitude and phase response simply related to the dispersion function of the mode considered. In models where the layer thicknesses are slowly varying functions of horizontal distance, the transfer function is still a useful concept. Its phase response depends on dispersion due to local structure under the receivers but is relatively independent of complications in the path between the source and near receiver.

Determination of local dispersion curves thus reduces to the problem of estimating the transfer function between two receivers. If only a single mode is present in a received seismogram, a single-channel spatial prediction filter is equivalent to the transfer function. This approach is used in this study because the Rayleigh mode is the dominant arrival and can be assumed to be the only mode present.

Computation of prediction filters in the time domain requires an estimation of the auto- and crosscorrelation functions for the two traces considered. As above, the results obtained depend strongly on the methods used to estimate these correlations.

The inline arrays for each of the four events were divided into two groups of five channels each, the center seismometer being discarded in each case. One trace in each set was chosen as a reference trace. Then, the autocorrelation for this trace and its crosscorrelation with the other traces in the set were computed. Using these correlations, filter operators were computed to predict each of the other four traces in the set, using the reference trace as input data. The Fourier transform of these filters was computed and the phase velocity determined from phase angle. In instances when consistent results were obtained, there were attempts to fit a simple single-layered model to the dispersion results. A solution of this kind is far from unique but should indicate the gross near-surface structures.

Figure 26 shows the correlation functions and prediction filters for the Strawberry seismogram, using the northwest arm of the array. The time gates used to compute these correlations contained only the Rayleigh arrival. As before, these correlations are seen to be very strongly peaked in frequency. On the other hand, the prediction filters encompass a much wider frequency band. This is true for two reasons. First, the prediction filter performs adequately at frequencies for which the power in both the reference trace and the trace to be predicted is very small but coherent. This means that reasonable dispersion curves may be obtained over much broader frequency bands by this method than by peak picking. Second, at frequencies for which the reference trace has no power, the filter design process places no effective restrictions on the response of the filter. At such frequencies, the response may be very large. The large endpoints on the filters are due primarily to this cause.

Figure 27 shows dispersion points obtained from these data. The points are coded to show the pairs of receivers from which the computations were made. Three sets of the data lie very closely together. The somewhat lower values for the pair of seismometers Z70 and Z21 probably agree with the other data within the limits of experimental error. The presence of dispersion is evident. (Note also that good results are obtained

over the frequency band of 1 to 3.5 cps.) If a single layer over half-space model is assumed, the half-space Rayleigh velocity would extrapolate to about 2.95 km/sec. The dashed line gives the theoretical curve for one such model which seems to give an adequate fit. Table 5 gives the parameters for this model.

Figures 28 and 29 show correlation, prediction filters and dispersion points for the southeast arm of the array from the Strawberry shot. The gross features of the correlations and prediction filters are similar to those for the northwest arm; however, dispersion results show somewhat more scatter. The dispersion curve has a steeper slope than that for the northwest arm and this difference is probably significant. The dashed line is a theoretical curve giving an adequate fit to these data. The corresponding layered model is shown in Table 6. (Note that we have held the layer thickness constant and lowered the average velocity.) We could have fitted the upper end of the curve by increasing the layer thickness and holding the velocity constant; however, the phase-velocity values of about 2.1 km/sec near 3.5 cps require a lower velocity near the surface. In any event, the solution given is not unique.

Since the data seemed to fall into two well-defined groups, there was an attempt to reduce the scatter by averaging correlations representing the same space lags within each group. This required computation of all possible correlations within each set of traces. The averaged correlation, prediction filters and dispersion points for the northwest arm are shown in Figures 30 and 31. Similar results for the southeast arm are shown in Figures 32 and 33. The scatter of the points is reduced somewhat, but the results for neither arm are greatly affected. The models in Tables 5 and 6 still provide an adequate fit to the experimental data as shown by the dashed lines in Figures 31 and 33.

Some improvement was obtained by averaging the Strawberry data; however, this technique was not applied to the other shots. For each of the remaining groups of data (two groups for each of the Rye Creek, Chase Ranch and Kohl's Ranch shots), only one correlation was computed for each space lag. The correlations, prediction filters and dispersion points obtained from the Rye Creek shot are shown in Figures 34 and 35 for the southwest arm of the array and in Figures 36 and 37 for the northeast arm. Dispersion results for the two arms of the array are in much closer agreement for the Rye Creek seismogram than for the Strawberry seismogram. There is some indication that the phase velocity (at a given frequency) is slightly lower on the northeast end than on the southwest end, but the model in Table 5 is a reasonable fit to either set of data. The model of Table 6 certainly fits neither data set.

Table 5

PARAMETERS FOR SINGLE-LAYER OVER HALF-SPACE MODEL

Layer	P-Velocity (km/sec)	S-Velocity	Layer Thickness (km)	Density Ratio
1	4.8	2.6	0.5	1.0
2	5.9	3.2	∞	—

Table 6

PARAMETERS FOR SINGLE-LAYER OVER HALF-SPACE MODEL

Layer	P-Velocity (km/sec)	S-Velocity	Layer Thickness (km)	Density Ratio
1	4.5	2.3	0.5	1.0
2	5.9	3.2	∞	—

Before discussing the Kohl's Ranch and Chase Ranch results, it is worthwhile to mention that for both Rye Creek and Strawberry shot-points only about 50 to 70 percent of the energy present is predictable on a single-channel basis. Some of the remaining energy may be recording system noise, but probably a great deal of it is scattered energy generated locally by the earlier arriving P- and S-waves. This level of predictability is reasonable if a number of distinct scattering centers are present. Attempts were made also to measure shear-mode dispersion, but no reasonable results were obtained. However, by looking at the seismograms, one can determine that the shear velocity is about 3.2 km/sec and the shear frequency is about 4 cps. Both of these results are compatible with the first shear mode for the models in Tables 5 and 6.

Again, the Kohl's Ranch and Chase Ranch shotpoints required special consideration because they were not inline with either arm of the array. As in the previous discussion dealing with f-k spectra, we constructed a hypothetical inline array with smaller spacing for each shotpoint. As mentioned before, this would be valid for plane-layered earth models. However, it was found that reasonable dispersion curves could not be obtained for the Chase Ranch shot and that only a few reasonable points could be obtained for Kohl's Ranch, these being from the northwest end of the array.

In the interest of brevity, the computed results are not shown, but the cross-correlation between adjacent traces was found to be small for these shots. All these results are in agreement with the frequency-wavenumber analysis.

Considerable effort was expended to find the cause for the behavior of the Kohl's Ranch and Chase Ranch data. The answer seems to be a combination of two effects. First, the topography between any of the shots and the receiver array is very rough. Approximate elevation profiles between seismometer Z21 and each of the shotpoints are shown in Figures 38, 39, 40, and 41. However, since reasonable results were obtained for Strawberry and Rye Creek, this alone is not sufficient to cause the difficulty. Second, it is quite significant that both these shots are almost in line with the array. In spite of the elevation differences between shot and array, the phase difference between two receivers depends only on the part of the path between the two receivers; the signals at these receivers have in common the badly dissected part of the path. For the Kohl's Ranch and Chase Ranch shots, this is not true. The elevation profiles from Chase Ranch to Z74 and Z21 are strikingly different (comparison shown in Figure 38). The same is true for Kohl's Ranch to Z67 and Z21 (comparison shown in Figure 39). In these cases, the signals on the two receivers have no part of the path in common and the phase differences depend on the whole path. In areas of rough topography, it is absolutely necessary to use inline arrays for measuring dispersion. However, if severe elevation change exists between receivers even this is not sufficient, because the earth model probably cannot be represented by a layered model and "dispersion" is no longer a useful concept.

VI. MULTICHANNEL PREDICTION

In the time domain, the system of n -prediction filters which yield the minimum mean-square-error for fixed filter length r is given by the solutions $y_j(t)$ of the equation:

$$\begin{bmatrix} \phi_{ij}(\tau) \end{bmatrix} \begin{bmatrix} y_j(\tau) \end{bmatrix} = \begin{bmatrix} \phi_{io}(\tau) \end{bmatrix}$$

where $\begin{bmatrix} \phi_{ij}(\tau) \end{bmatrix}$ is the $rn \cdot rn$ matrix of crosscorrelations of the input channels, $\begin{bmatrix} y_j(\tau) \end{bmatrix}$ is the $rn \cdot 1$ matrix of prediction filter operator points and $\begin{bmatrix} \phi_{io}(\tau) \end{bmatrix}$ is the $rn \cdot 1$ matrix of crosscorrelations between the input channels and the channel being predicted. A set of 5-channel prediction filters was designed using the Rye Creek prewhitened data. The information contained in channels 1 through 5 will be used to predict the information contained in channel 6. The correlation functions used to solve the preceding matrix equation and the filter solutions are shown in Figure 42. The left-hand matrix

consists of all crosscorrelations between the five input channels Z63, Z62, Z61, Z60, and Z9. The right-hand matrix consists of the crosscorrelations between the channel being predicted (Z21) and the five input channels. Each prediction filter channel is convolved with the appropriate input channel and the five filtered outputs summed to give the predicted channel. Short filter operators (49 points) were designed by taking advantage of the fact that the predominate energy was moving across the array at Rayleigh velocity. The seismogram traces were shifted to align the Rayleigh wave before the correlation functions were computed. Then, the filters designed were applied to the shifted seismograms. The gate length used to compute the correlation was 600 samples (14.4 sec) which included the P-, S- and Rayleigh arrivals on each trace.

It is interesting to note that the forms of the prediction filters are very complicated and that no direct physical interpretation can be attached to them. Obviously, the filters are working hardest to predict the Rayleigh-wave energy since this dominates the seismogram. However, if this were the only mechanism at work, one would expect the filters to be pulse-like with the pulses aligned on each channel (because of the shift in the original data to align the Rayleigh wave). The rather diffuse form of the filters is probably due, in part, to the fact that the power spectra of the traces are not identical.

Figure 43(A) shows the results of applying the filters to the channels from which they were designed. The top trace is Z21, the middle trace is the predicted Z21 and the bottom trace is the prediction error obtained by subtracting the predicted trace from the actual trace. It is not surprising that the prediction error within the correlation gate (600 samples) is very small. Information outside the gate was not used in the correlation process so, of course, the prediction error is large before the P-arrival and after the Rayleigh arrival. The largest error within the correlation gate appears to be in the P-arrival. This is almost certainly due to the time shift applied to the data to align the Rayleigh wave. After this shift is applied, the P-waves appear to arrive earlier on the trace being predicted than on the traces used in the prediction. Although the filter operators are 2-sided in time, they do not span the apparent moveout of the P-waves and, as a result, the more distant traces are not actually used in predicting the P-wave section of the output trace. The filter design technique used here gives directly the expected power in the error trace. For the present example, 90 percent of the power is predictable on the average.

Next, this set of filters was applied to the channels 1 km farther away from the source; i. e., filters 1 through 5 were applied to Z62, Z61, Z60, Z9, and Z21 to predict Z31. Figure 43(B) shows the results. The top trace is Z31, the middle trace is the predicted Z31 and the bottom trace is the prediction error. The error appears larger than the actual trace.

This is attributed to nonstationarity in its broadest sense. If we define signal and noise to be space-stationary, this implies that the crosscorrelations depend only on the channel separations and not the absolute channel locations. Two-dimensional spreading of the normal modes and leakage of the PL modes will appear as nonstationarity. Trace equalization will minimize nonstationarity due to 2-dimensional spreading but not to PL mode leakage. Local signal-generated noise may be one important reason for the large error trace. This local noise contributes to the spatial nonstationarity in two ways. First, the scattering centers are so close to the receivers that the noise correlations change drastically from one pair of receivers to the next. An extreme case of this would occur when scattering centers actually lie between receivers. Second, crosscorrelation coupling between the local noise and energy directly from the source is a form of nonstationarity because this correlation depends on the absolute location of the source and receivers as well as on receiver separation.

Another possible cause of the large error trace is the fact that receiver spacing is not exactly 1 km but varies about this by as much as 10 percent.

VII. CONCLUSIONS

Results of the present study are very encouraging. The frequency-wavenumber analysis and dispersion studies have shown the usefulness of the "local" dispersion representation — even in very rough topography — subject to the limitations that (1) an inline recording array be used and (2) the topography within the recording array itself be fairly smooth. The first of these conditions is required because interpretation is possible only if the difference in the signals recorded at two receivers depends only on the subsurface between the receivers. This obviously will not be true for a noninline array. The second condition is necessary in order that the subsurface at the recording array be adequately represented by a sequence of layered models.

The frequency-wavenumber spectra showed the Rayleigh wavetrain very well but gave little or no indication of the P- and S-waves. Also, there was only slight indication of dispersion in the Rayleigh wave. Upon comparing the various methods used to compute these spectra, the best method seems to be a combination of averaged correlations computed from prewhitened data. It also appears necessary to design the prewhitening filter on the basis of the data to which it is to be applied.

The prediction studies showed that the signal is about 50 to 60 percent predictable on a single-channel basis but almost completely predictable on a multichannel basis. This is true despite the fact that the signal

is highly nonstationary in space. A set of multichannel prediction filters designed from a given set of traces actually makes use of the nonstationarity to achieve a lower prediction error. When this set of filters is applied to a different set of traces, prediction results are very poor. All of these results suggest that the recorded seismograms contain a significant amount of energy generated at a number of local scattering centers.

The dispersion studies resulted in a crude model of the Tonto Forest near-surface structure; however, the model is not unique. On the northwest and southwest sides of the array, the indicated surficial layer has a P-velocity of 4.8 km/sec and a layer thickness of 0.5 km. On the northeast side of the array, the layer velocity is slightly lower. On the southeast side, the surficial P-velocity is about 4.5 km/sec and the layer thickness was taken to be 0.5 km, though it may be somewhat greater than this. Surface outcrop maps show the southwest and southeast array arms to be on exposed granite, while the northwest and northeast arms are mostly on sediments of Cambrian and Devonian age, so one would expect the southwest and southeast arms to show higher layer velocity than the northwest and northeast arms. This appears to be in direct disagreement with the single-layer model we have fitted to the measured dispersion points; however, it is felt that the measured dispersion curves are reliable and that the changes seen in the dispersion curves between the southwest and southeast area have a real physical significance. An understanding of the cause of disagreement is still lacking.

The P-velocity of the underlying material, treated here as a half-space, is 5.9 km/sec. This is in good agreement with a velocity of 6.0 to 6.05 km/sec seen on refraction records from greater distances. Thus, the velocity of this material probably remains relatively constant to a depth of several kilometers. Unfortunately, no evidence of deeper-crust events was seen on these records.

VIII. ACKNOWLEDGMENT

The authors wish to thank Lyle Atkins and Gerald Shockey who processed data and prepared illustrations for this paper, and Renner B. Hofmann, who performed the early editing on these seismograms. The cooperation of the U.S. Geological Survey during its shooting program also is appreciated. This work was supported by the Air Force Office of Scientific Research under Contract AF 49(638)-1244.

IX. REFERENCE

Laster, S.E., J.G. Foreman and A.F. Linville, 1965, Theoretical investigation of modal seismograms for a layer over a half-space: *Geophysics*, v. 30, Aug., p. 571-596.

FIGURE CAPTIONS

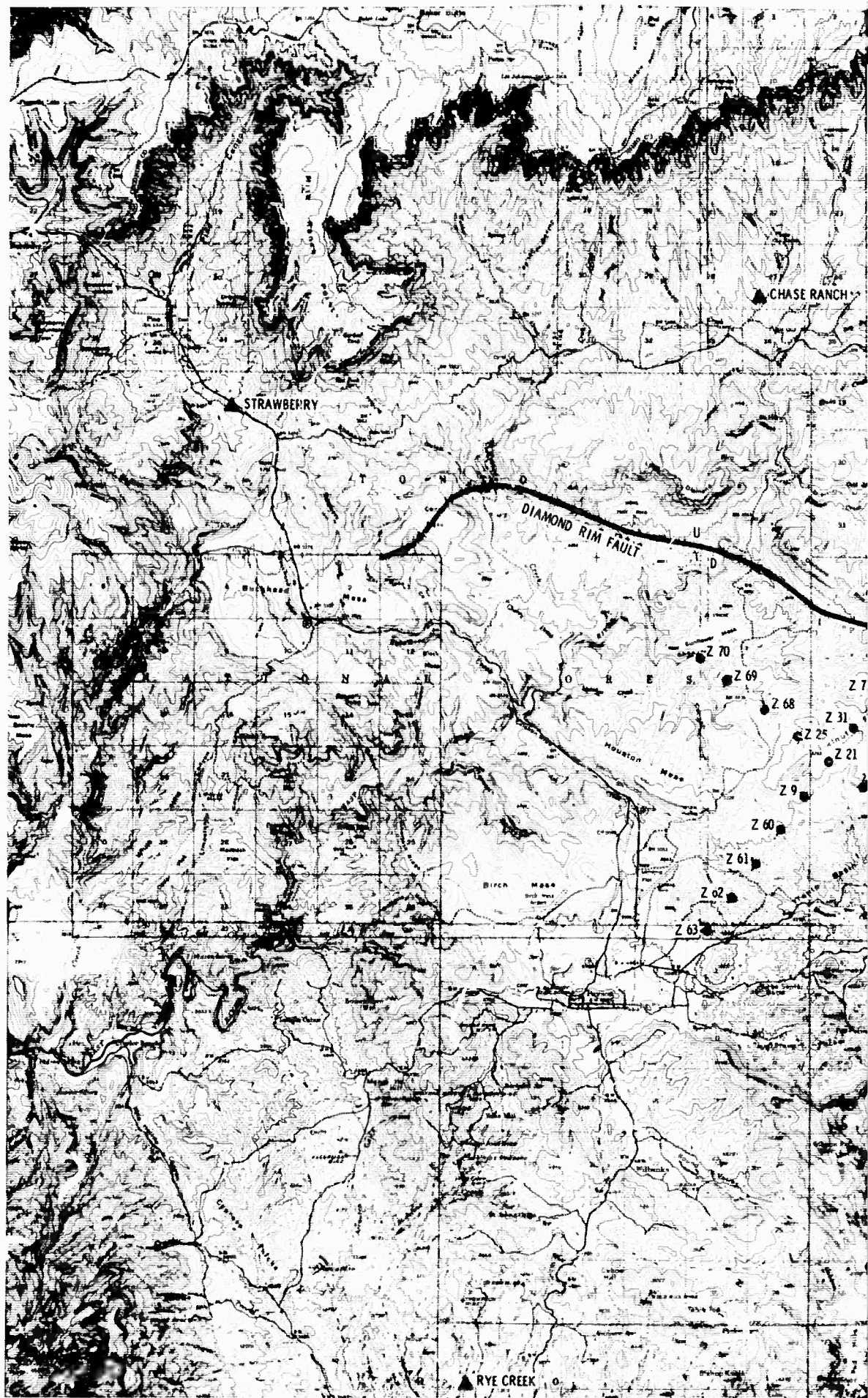
<u>Figure</u>	<u>Title</u>
1	Geometric Configuration of TFO 21-Element Crossed-Linear Array and Shot Locations
2	Seismograms of Strawberry, Rye Creek, Chase Ranch, and Kohl's Ranch Shots. Filter: low-out, high-out
3	Seismograms of Strawberry, Rye Creek, Chase Ranch, and Kohl's Ranch Shots. Filter low-out, high-3.1 cps
4	Seismograms of Strawberry, Rye Creek, Chase Ranch, and Kohl's Ranch Shots. Filter: low-2.9 cps, high-out
5	Auto- and Crosscorrelation Functions Used To Compute Frequency-Wavenumber Spectrum for Strawberry Event
6	Frequency Spectrum of Autocorrelation $Z_{70} \times Z_{70}$ for Strawberry Event
7	Frequency-Wavenumber Spectrum for Strawberry Event Using Single Nonredundant Set of Correlation Functions. (Numbers within contours represent db down from maximum amplitude)
8	Single Nonredundant Set of Auto- and Crosscorrelations Computed from Rye Creek Data
9	Frequency-Wavenumber Spectrum for Rye Creek Event Using Single Nonredundant Set of Correlation Functions. (Numbers within contours represent db down from maximum amplitude)
10 (A)	Frequency Spectrum of Autocorrelation $Z_{63} \times Z_{63}$ for Rye Creek before Whitening
10(B)	Frequency Spectrum of Averaged Autocorrelations for Rye Creek before Whitening
10(C)	Frequency Response of Whitening Filter for Rye Creek
10(D)	Frequency Spectrum of Autocorrelation $Z_{63} \times Z_{63}$ for Rye Creek after Whitening
11	Rye Creek Inline Arm before (A) and after (B) Prewhitening
12	Single Nonredundant Set of Auto- and Crosscorrelations Computed from Rye Creek Whitened Data

<u>Figure</u>	<u>Title</u>
13	Frequency-Wavenumber Spectrum for Rye Creek Event Using Single Nonredundant Set of Correlation Functions Computed from Whitened Data. (Numbers within contours represent db down from maximum amplitude)
14	Ensemble Average Correlations Computed from Rye Creek Data. Correlation space lags denote averaging over all correlations with that particular space separation.
15	Frequency-Wavenumber Spectrum for Rye Creek Event Using Ensemble Average Correlations. (Numbers within contours represent db down from maximum amplitude)
16	Ensemble Average Correlations Computed from Kohl's Ranch Data. Correlation space lags denote averaging over all correlations with that particular space separation
17	Frequency Spectrum of Ensemble Average Autocorrelations for Kohl's Ranch Event
18	Frequency-Wavenumber Spectrum for Kohl's Ranch Event Using Ensemble Average Correlations. (Numbers within Contours represent db down from maximum amplitude)
19	Ensemble Average Correlations Computed from Chase Ranch Data. Correlation space lags denote averaging over all correlations with that particular space separation
20	Frequency Spectrum of Ensemble Average Autocorrelation for Chase Ranch Event
21	Frequency-Wavenumber Spectrum for Chase Ranch Event Using Ensemble Average Correlations. (Numbers within contours represent db down from maximum amplitude)
22	Rayleigh Group Velocities from Inline Arm for Strawberry Event
23	Rayleigh Group Velocities from Inline Arm for Rye Creek Event
24	Rayleigh Phase Velocities Determined from Peak and Trough Method for Rye Creek Event
25	Rayleigh Phase Velocities Determined from Peak and Trough Method for Kohl's Ranch Event Using Only NW Arm of Array
26	(A) Correlation Functions from Strawberry Event Using NW Arm of Array; (B) Single-Channel Prediction Filters

<u>Figure</u>	<u>Title</u>
27	Rayleigh Phase Velocity Points from Strawberry Event Using NW Arm of Array. (Dashed curve is phase velocity for theoretical model given in Table 5)
28	(A) Correlation Functions from Strawberry Event Using SE Arm of the Array; (B) Single-Channel Prediction Filters
29	Rayleigh Phase Velocity Points from Strawberry Event Using SE Arm of Array. (Dashed curve is phase velocity for theoretical model given in Table 6)
30	(A) Averaged Correlation Function from Strawberry Event Using NW Arm of Array; (B) Single-Channel Prediction Filters
31	Rayleigh Phase Velocity Points from Strawberry Event Using Averaged Correlations of NW Arm of Array. (Dashed curve is phase velocity for theoretical model given in Table 5)
32	(A) Averaged Correlation Functions From Strawberry Event Using SE Arm of Array; (B) Single-Channel Prediction Filters
33	Rayleigh Phase Velocity Points from Strawberry Event Using Averaged Correlations of SE Arm of Array. (Dashed curve is phase velocity for theoretical model given in Table 6)
34	Correlation Functions from Rye Creek Event Using SW Arm of Array; (B) Single-Channel Prediction Filters
35	Rayleigh Phase Velocity Points from Rye Creek Event Using SW Arm of Array. (Dashed curve is phase velocity for theoretical model given in Table 5)
36	(A) Correlation Functions from Rye Creek Event Using NE Arm of Array; (B) Single-Channel Filters
37	Rayleigh Phase Velocity Points from Rye Creek Event Using SW Arm of Array. (Dashed curve is phase velocity for theoretical model given in Table 5)
38	(A) Elevation Profile from Chase Ranch to Z21; (B) Elevation Profile from Chase Ranch to Z74
39	(A) Elevation Profile from Kohl's Ranch to Z21; (B) Elevation Profile from Kohl's Ranch to Z67

FigureTable

- | | |
|----|--|
| 40 | Elevation Profile from Rye Creek to Z21 |
| 41 | Elevation Profile from Strawberry to Z21 |
| 42 | (A) Correlation Functions between 5-Input Channels;
(B) Correlation Functions between Predicted Channel
and 5-Input Channels; (C) 5-Channel Prediction Filter
Operators |
| 43 | (A) Top Trace -- Actual Trace to be Predicted (Z21);
Middle Trace -- Predicted Trace; Bottom Trace --
Prediction Error Trace; (B) Top Trace -- Actual Trace
to be Predicted (Z31); Middle Trace -- Predicted Trace;
Bottom Trace -- Prediction Error Trace |



Figur

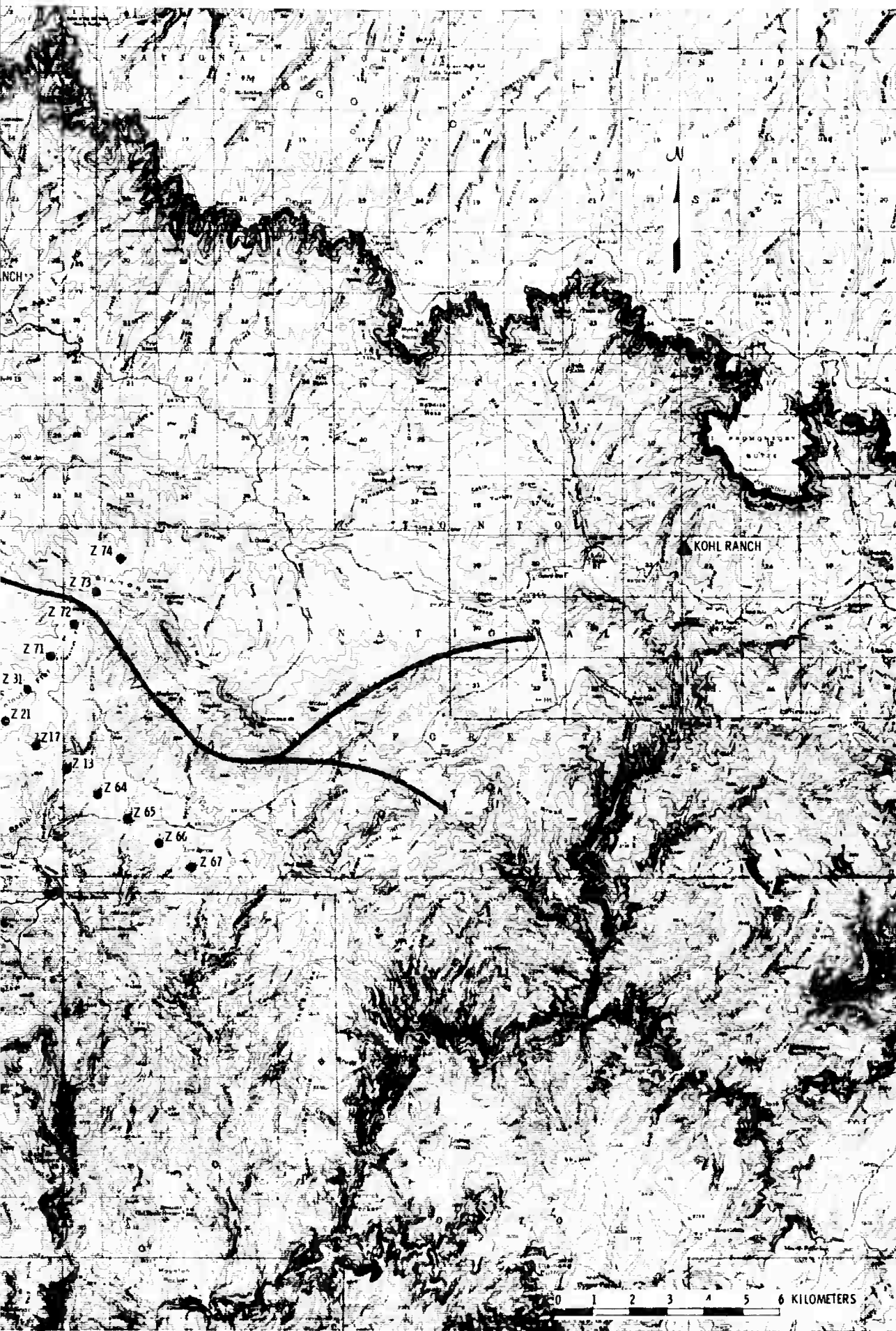


Figure 1. Geometric Configuration of TFO 21-Element Crossed-Linear Array and Shot Locations

BLANK PAGE

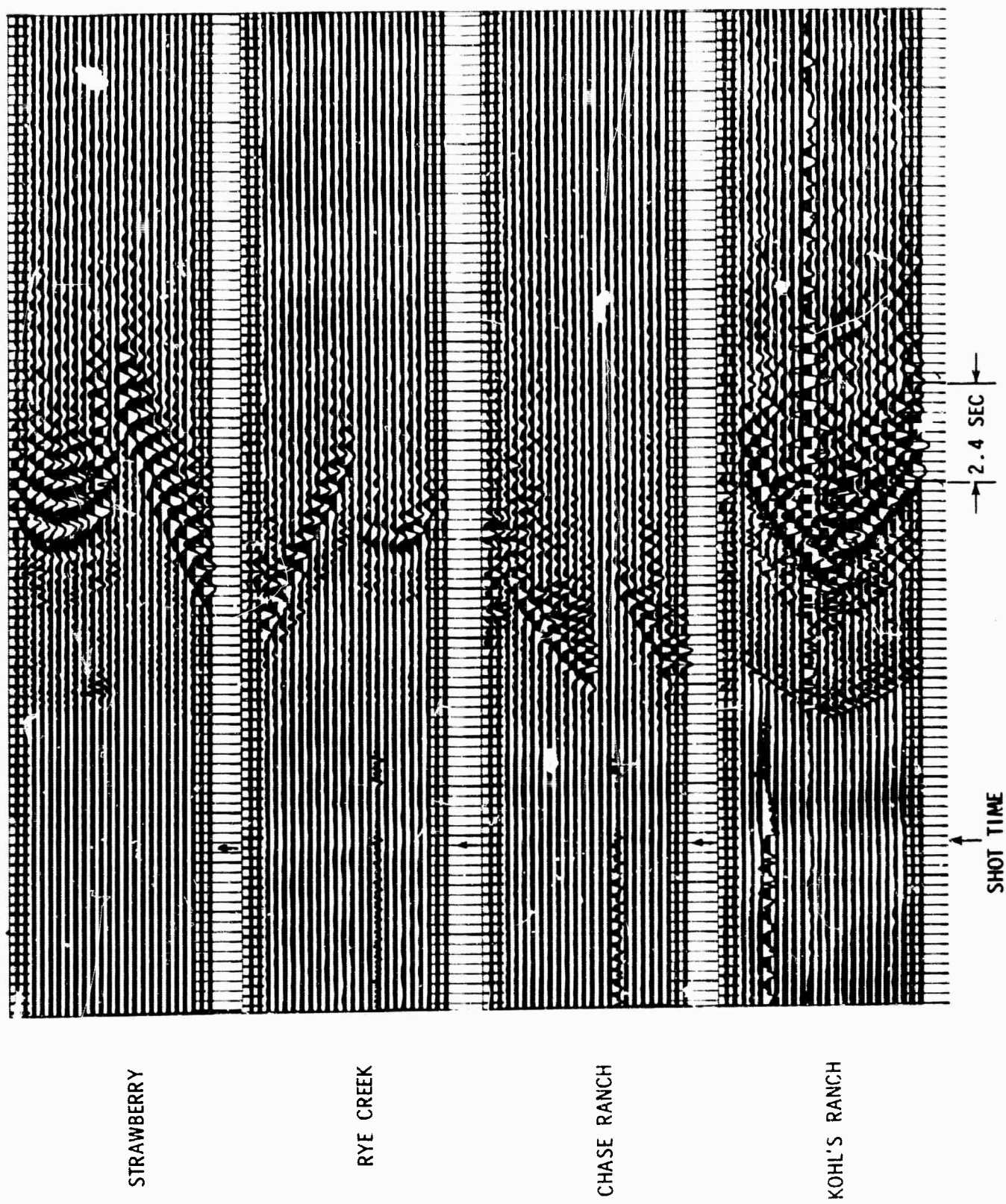


Figure 2. Seismograms of Strawberry, Rye Creek, Chase Ranch, and Kohl's Ranch Shots.
Filter: low-out, high-out

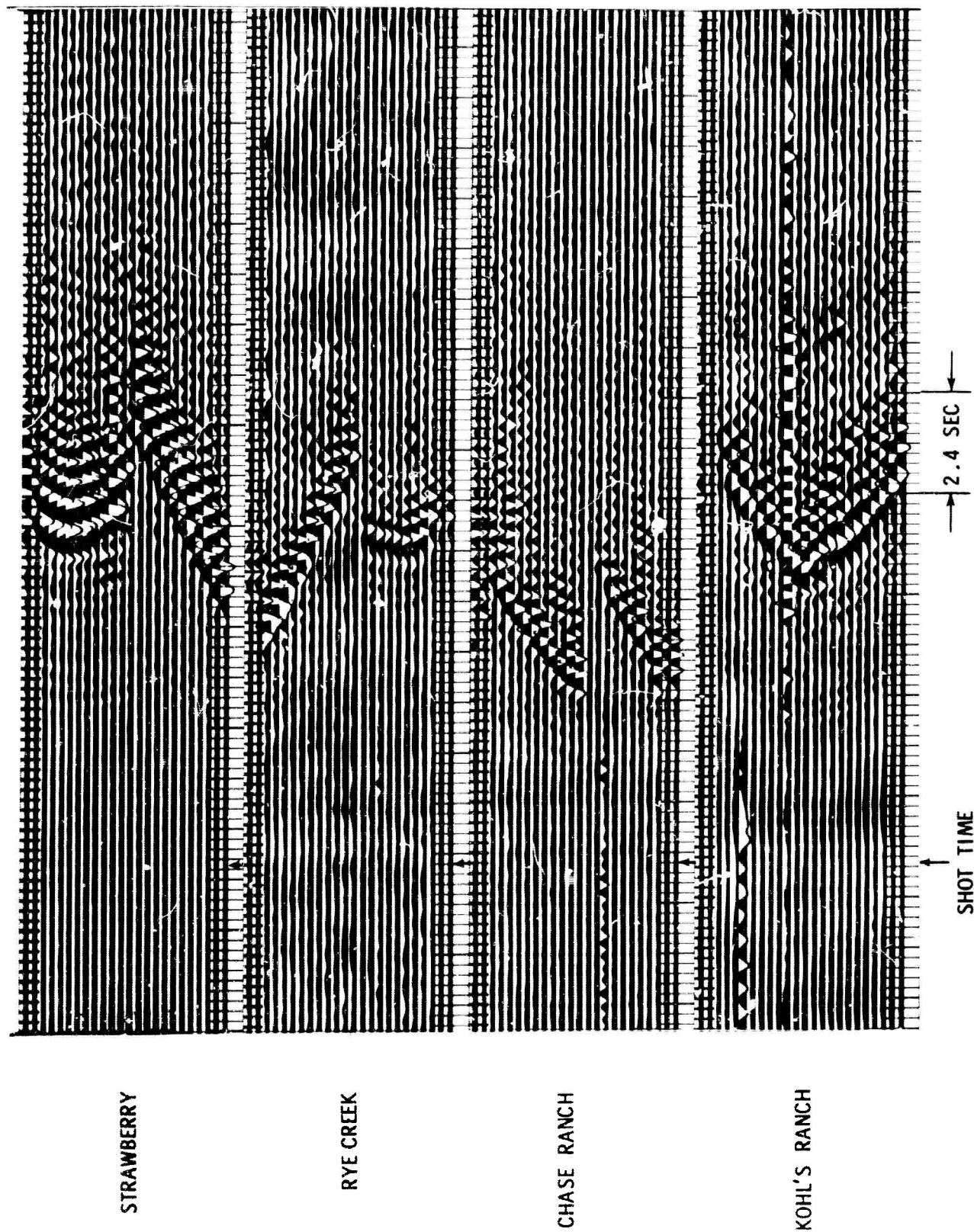


Figure 3. Seismograms of Strawberry, Rye Creek, Chase Ranch, and Kohl's Ranch
 Shots. Filter: low-out, high-out

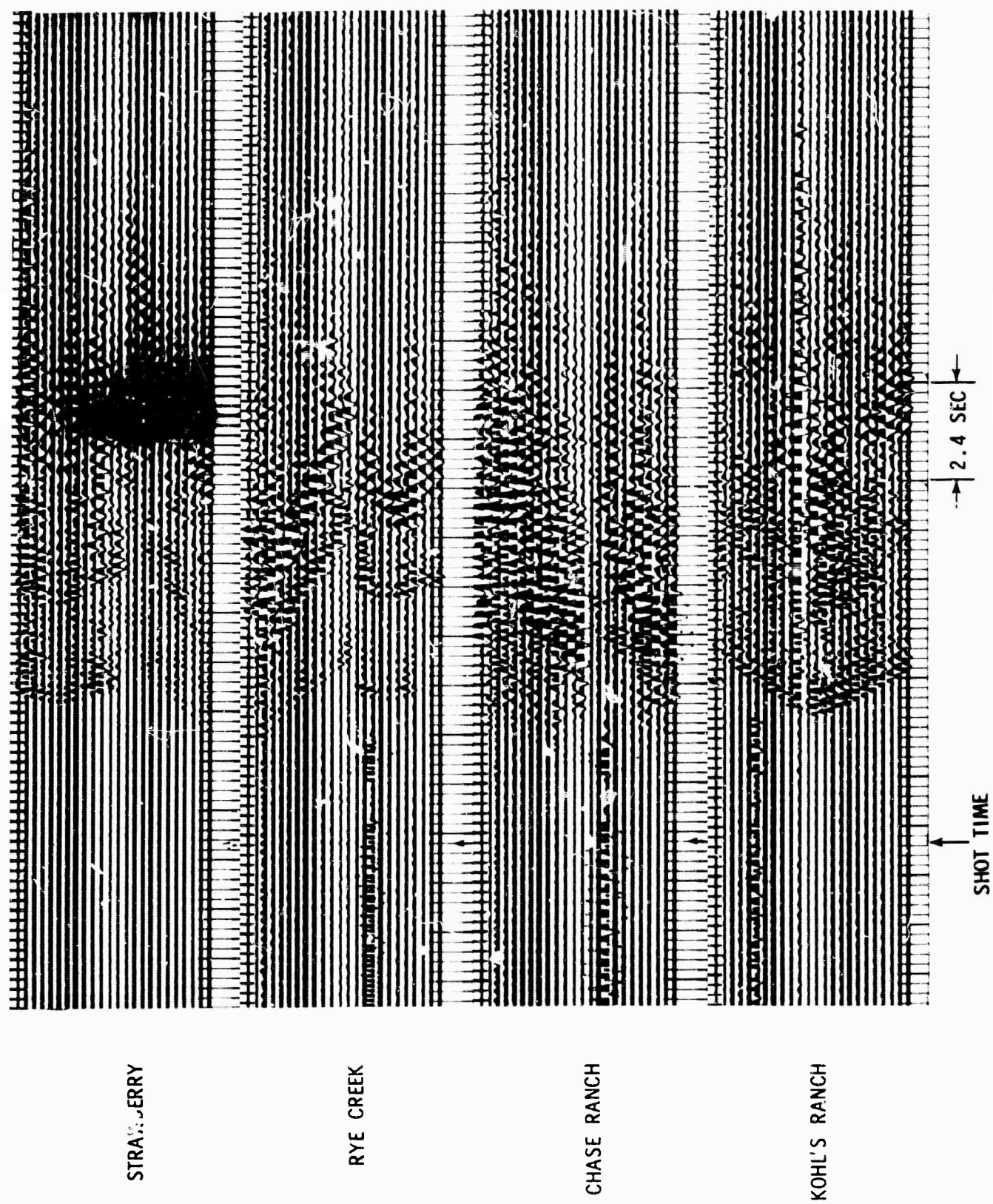


Figure 4. Seismograms of Stawberry, Rye Creek, Chase Ranch, and Kohl's Ranch Shots. Filter: low-2.9 cps, high-out

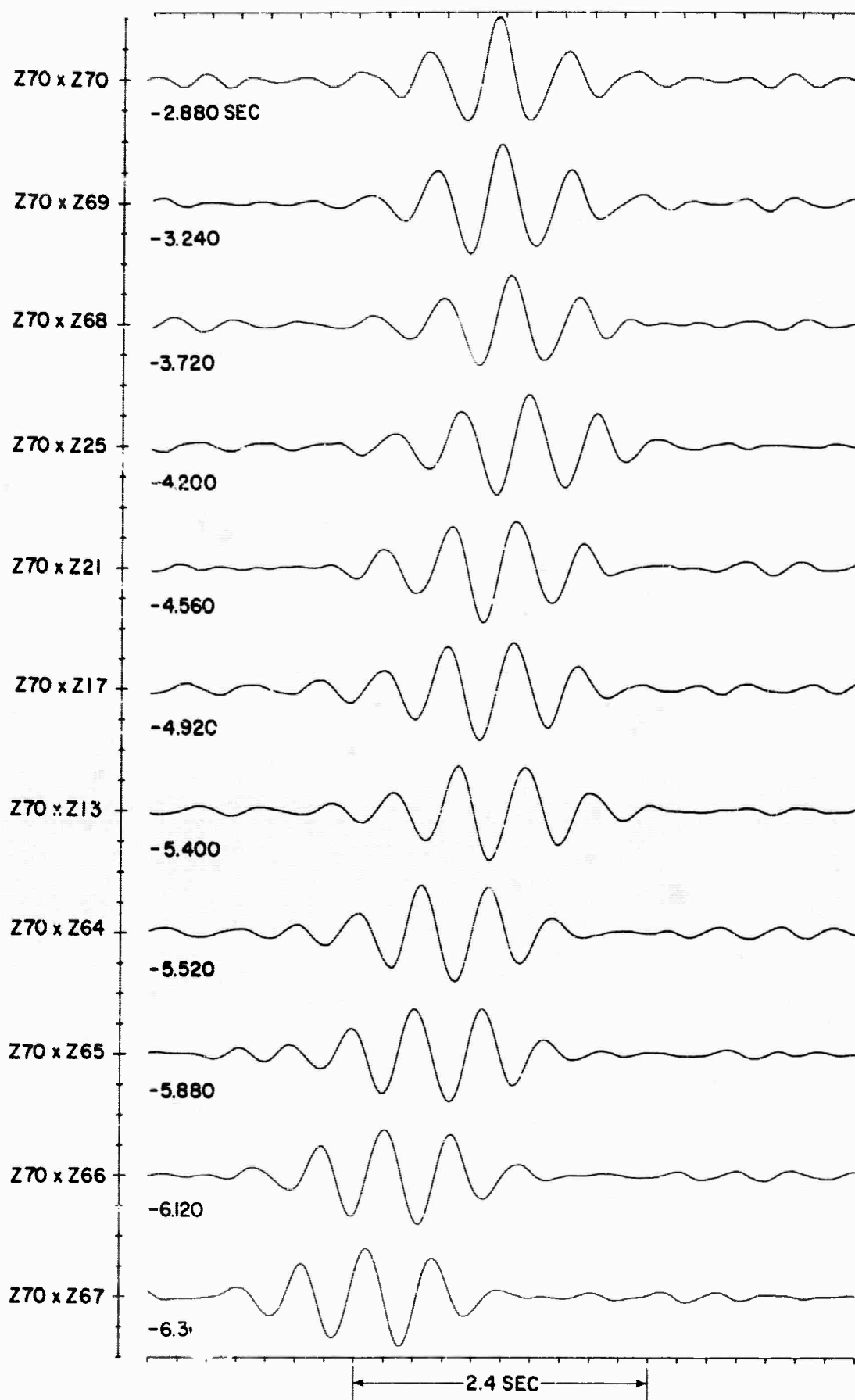


Figure 5. Auto- and Crosscorrelation Functions Used To Compute Frequency-Wavenumber Spectrum for Strawberry Event

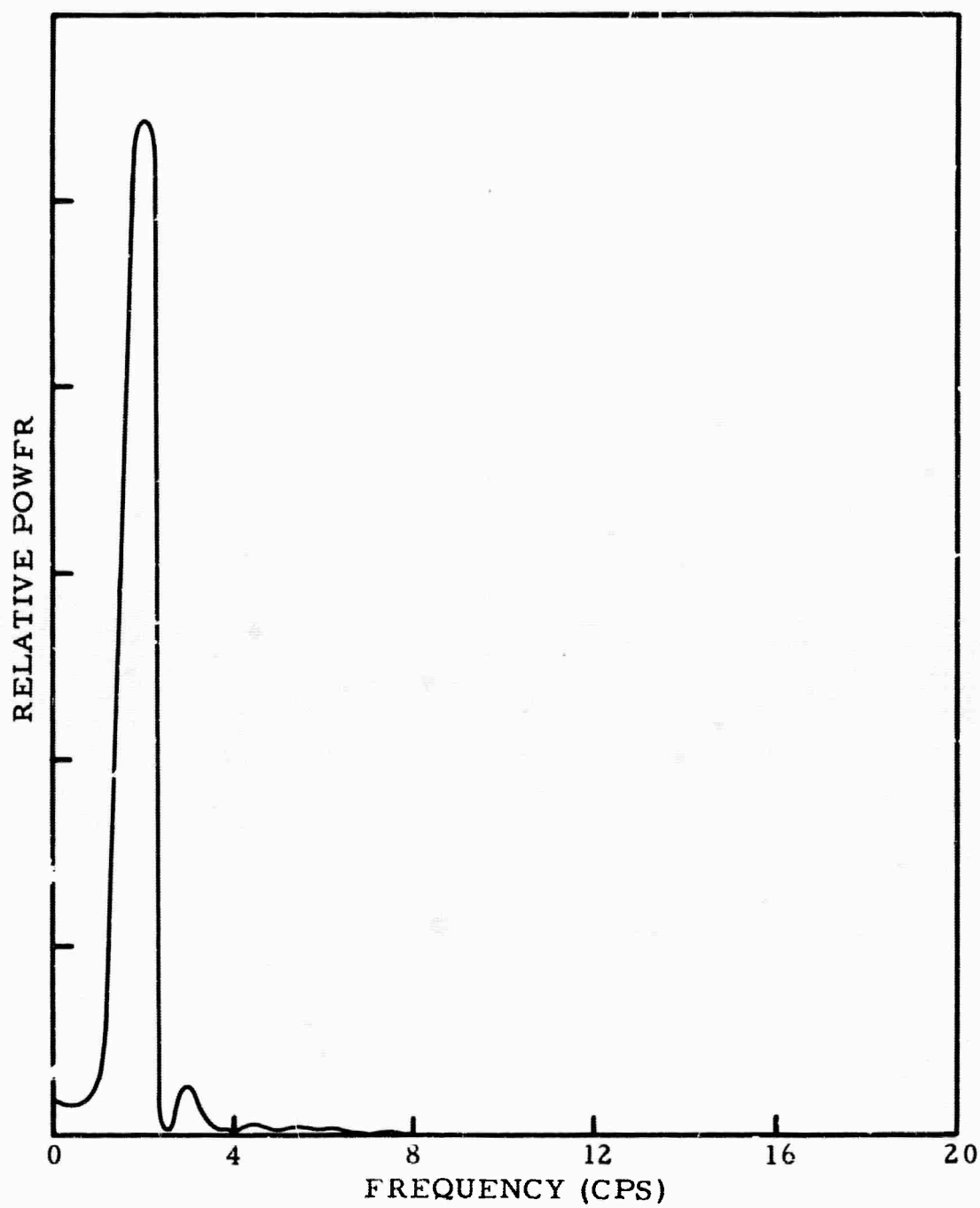


Figure 6. Frequency Spectrum of Autocorrelation Z 70 x Z 70 for Strawberry Event

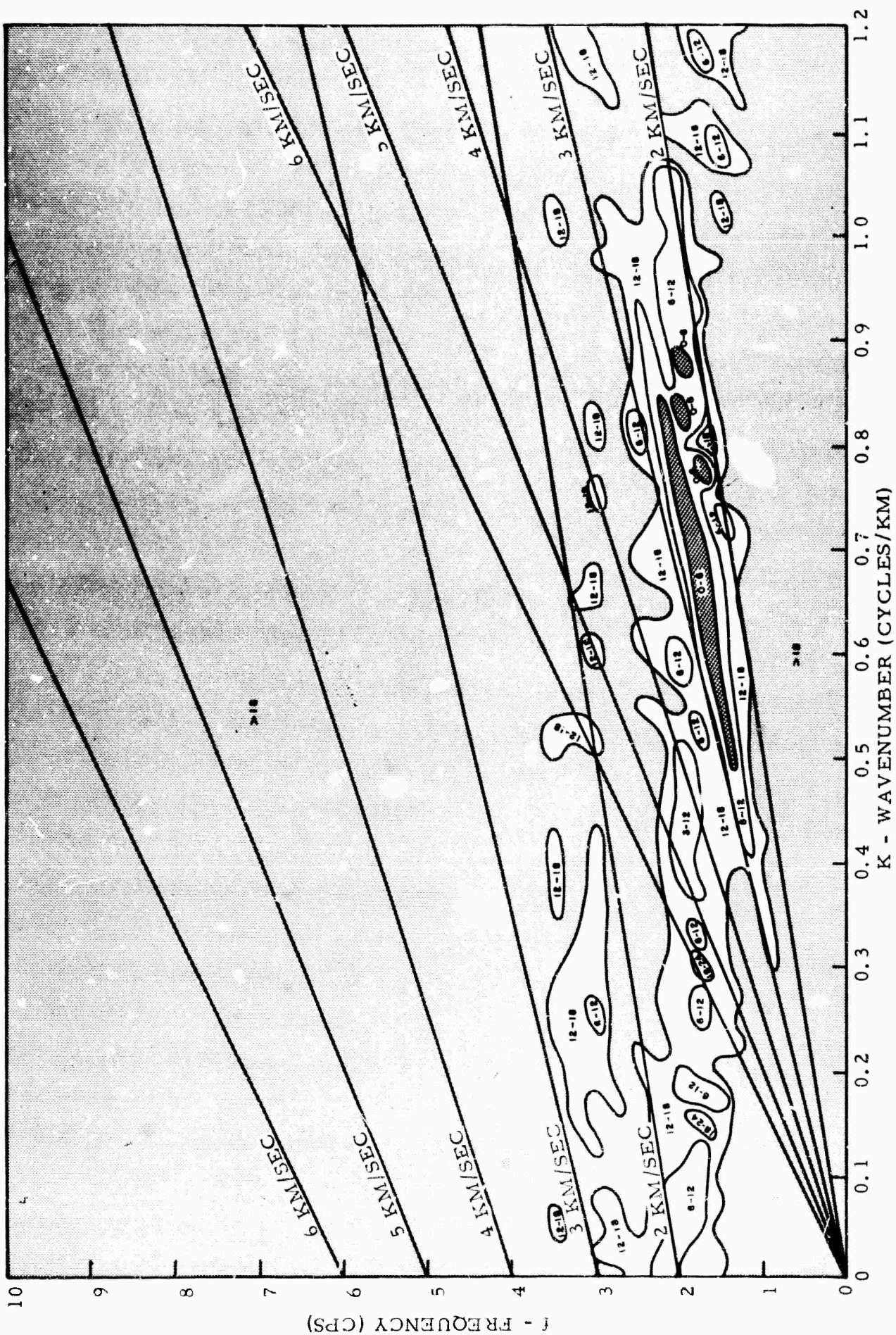


Figure 7. Frequency-Wavenumber Spectrum for Strawberry Event Using Single Nonredundant Set of Correlation Functions. (Numbers within contours represent db down from maximum amplitude)

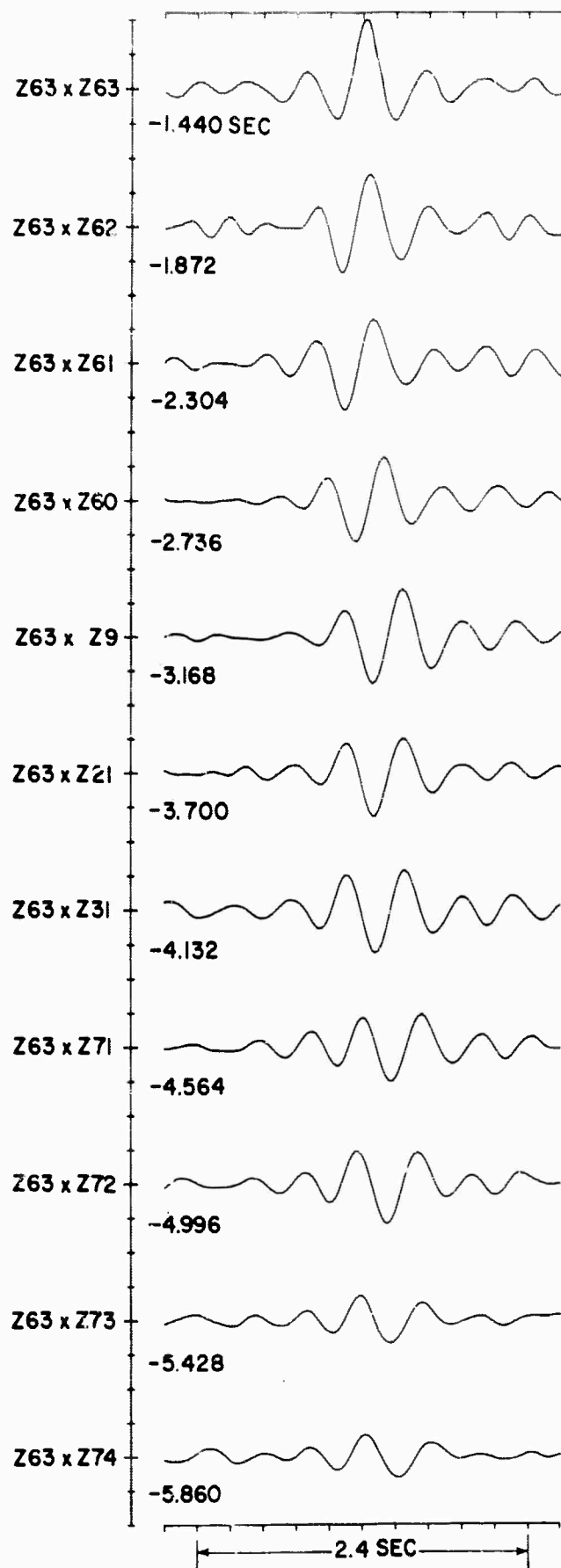


Figure 8. Single Nonredundant Set of Auto- and Crosscorrelations Computed from Rye Creek Data

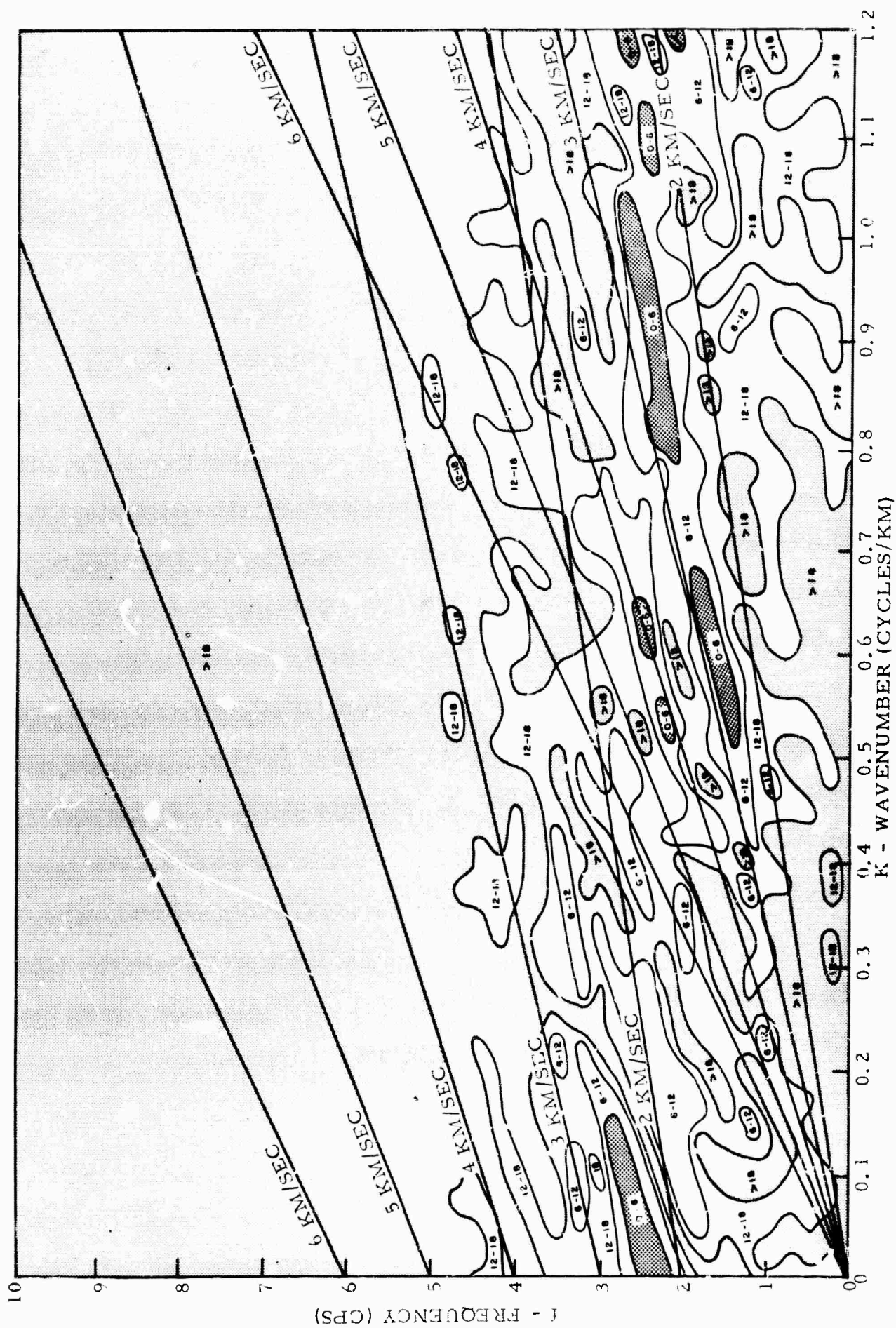


Figure 9. Frequency-Wavenumber Spectrum for Rye Creek Event Using Single Nonredundant Set of Correlation Functions. (Numbers within contours represent db down from maximum amplitude)

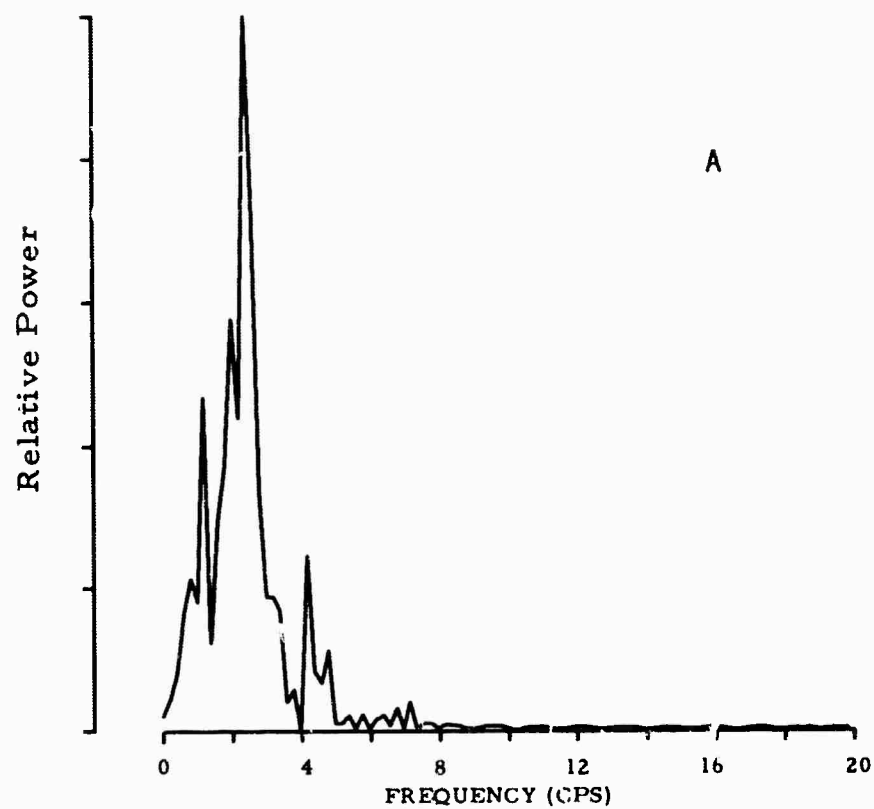


Figure 10(A) Frequency Spectrum of Autocorrelation $Z_{63} \times Z_{63}$ for Rye Creek before Whitening

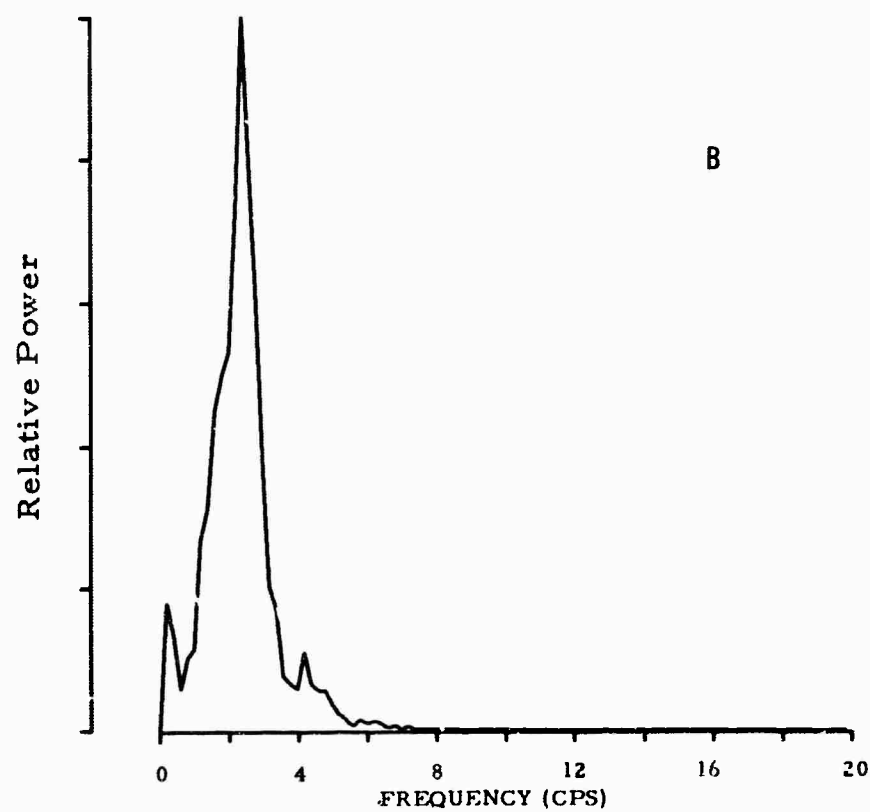


Figure 10(B) Frequency Spectrum of Averaged Autocorrelations for Rye Creek before Whitening

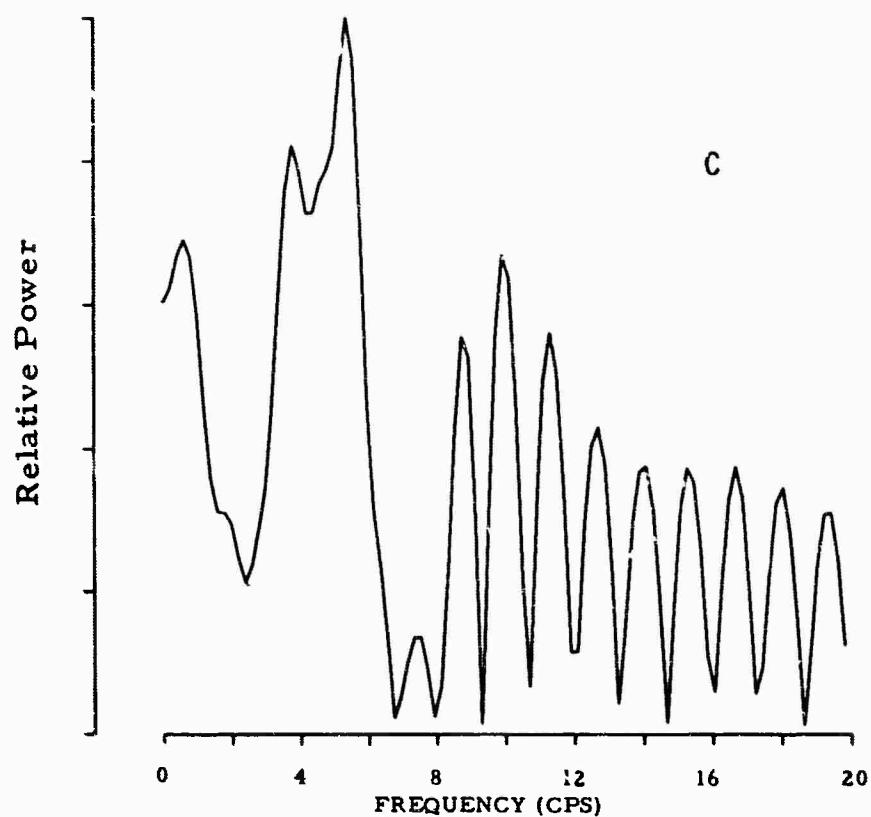


Figure 10(C) Frequency Response of Whitening Filter for Rye Creek

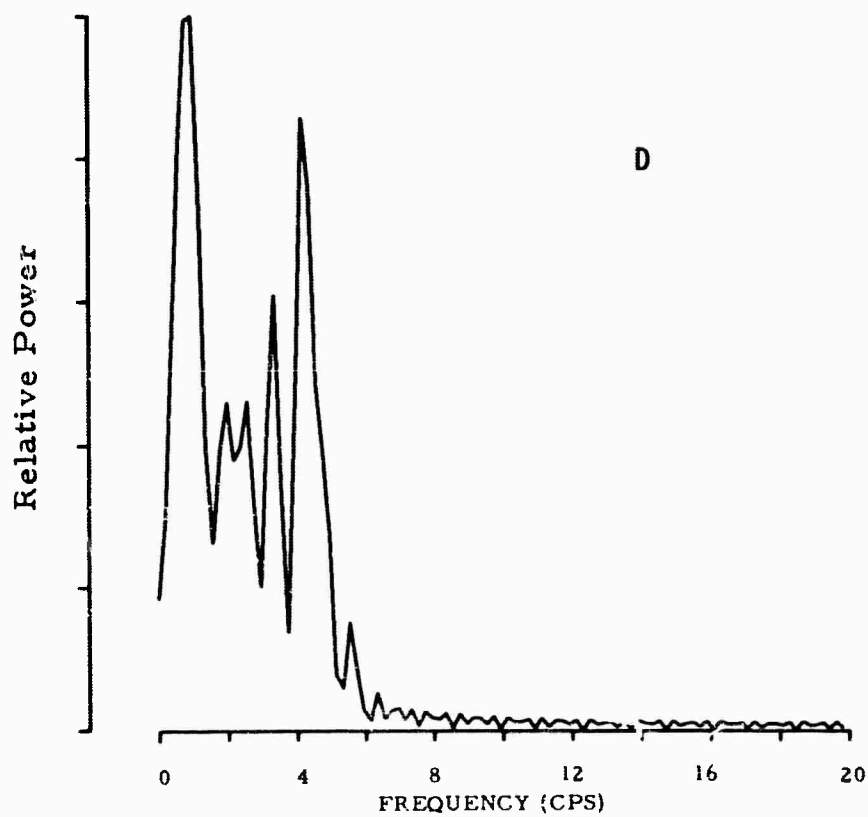


Figure 10(D) Frequency Spectrum of Autocorrelation $Z_{63} \times Z_{63}$ for Rye Creek after Whitening

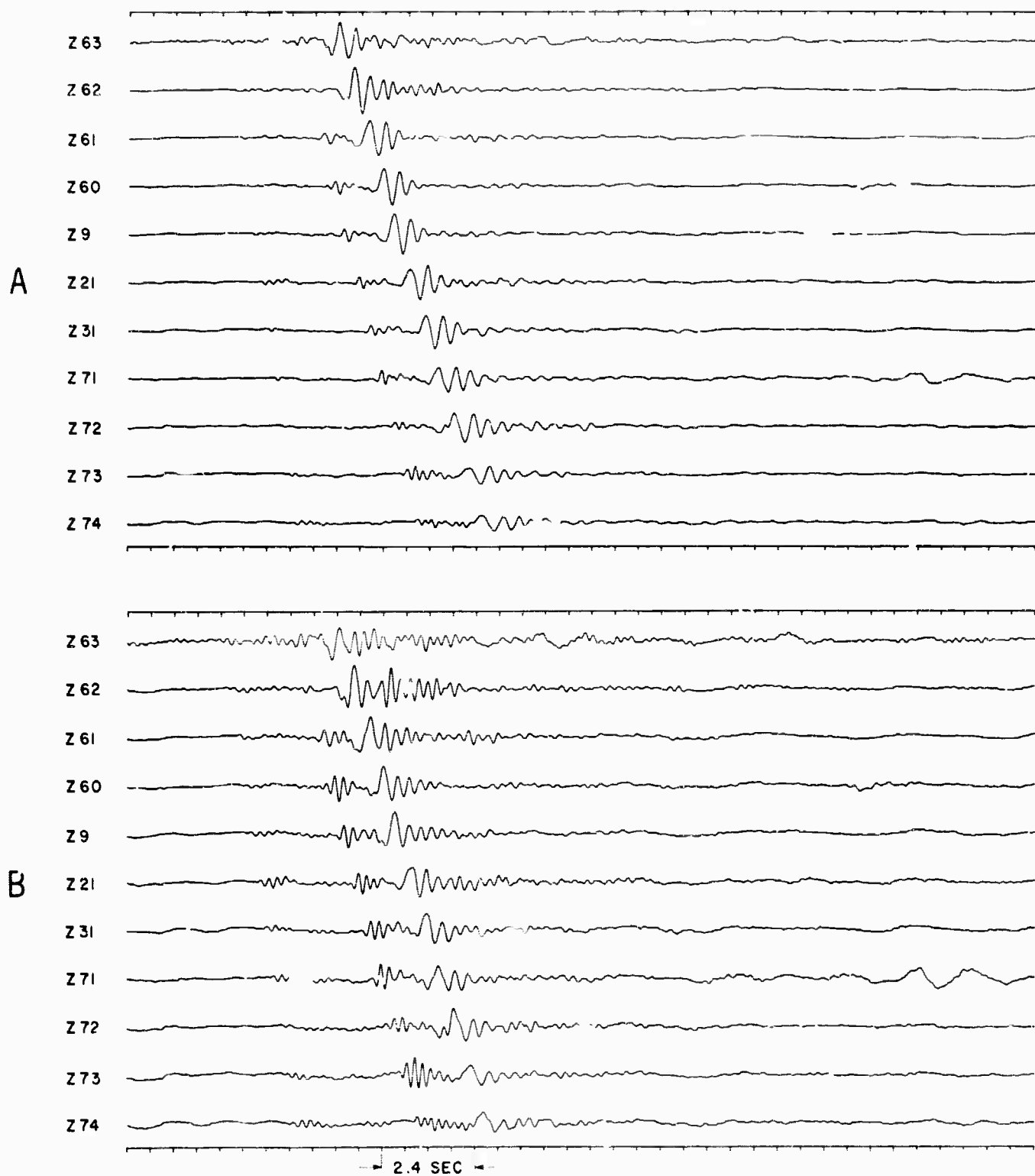


Figure 11. Rye Creek Inline Arm before (A) and after (B) Prewhitening

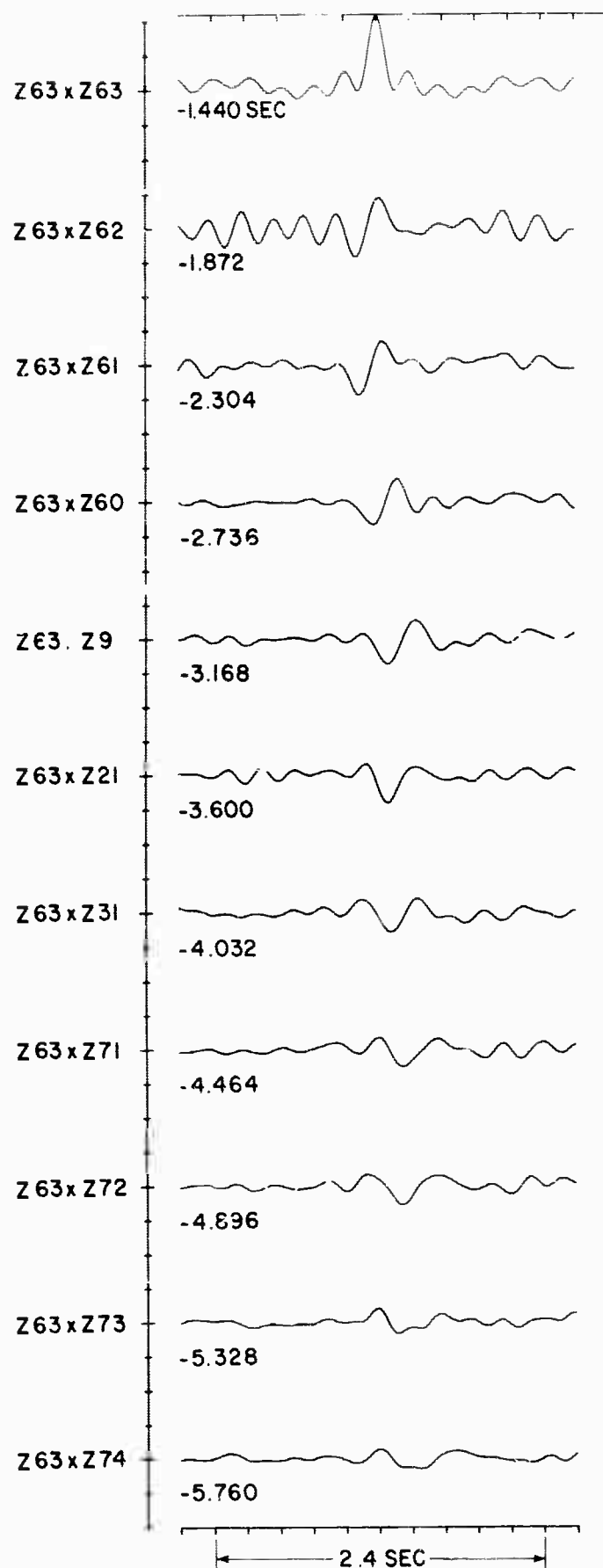


Figure 12. Single Nonredundant Set of Auto- and Crosscorrelations
Computed from Rye Creek Whitened Data

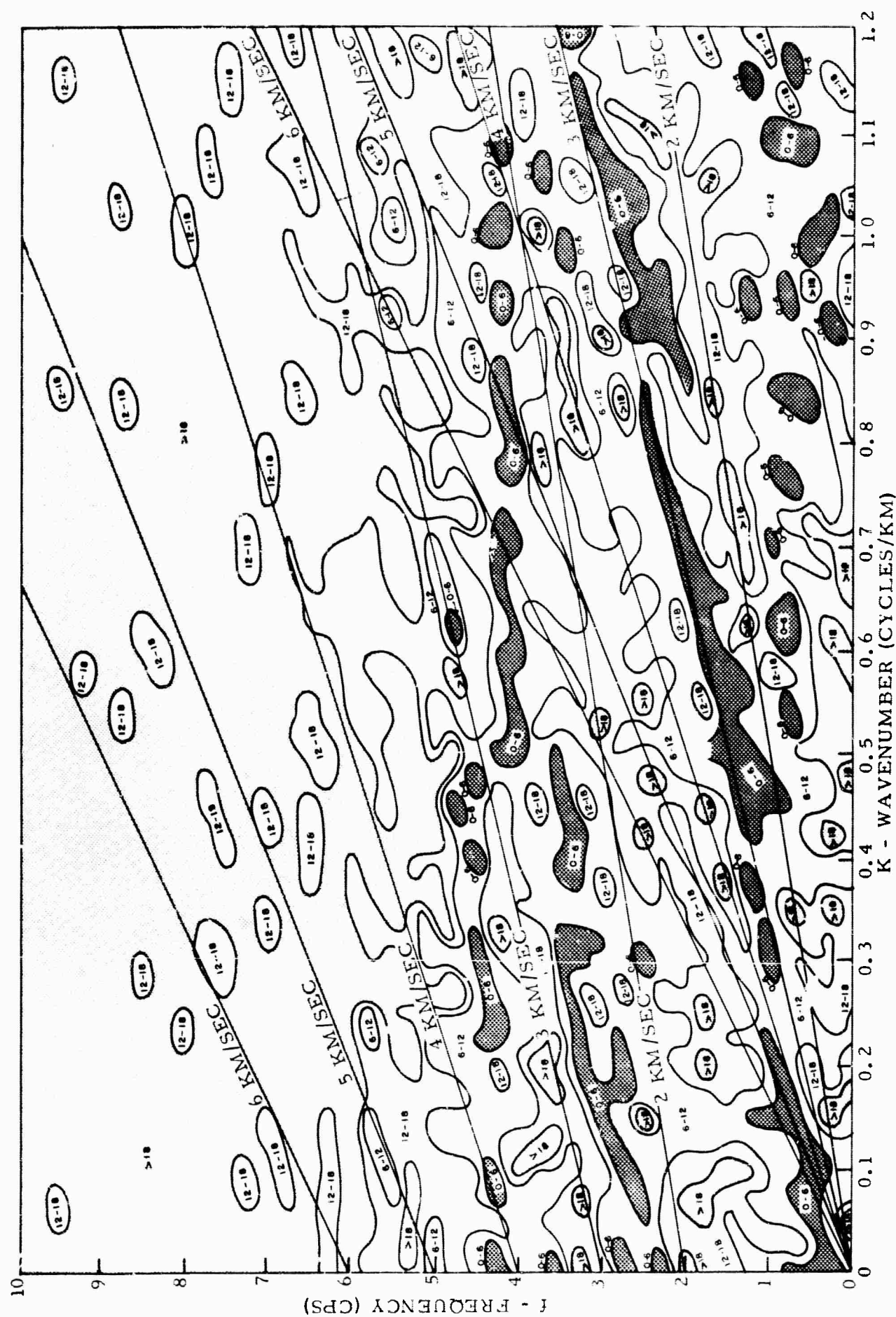


Figure 13. Frequency-Wavenumber Spectrum for Rye Creek Event Using Single Nonredundant Set of Correlation Functions Computed from Whiten Data. (Numbers within contours represent db down from maximum amplitude)

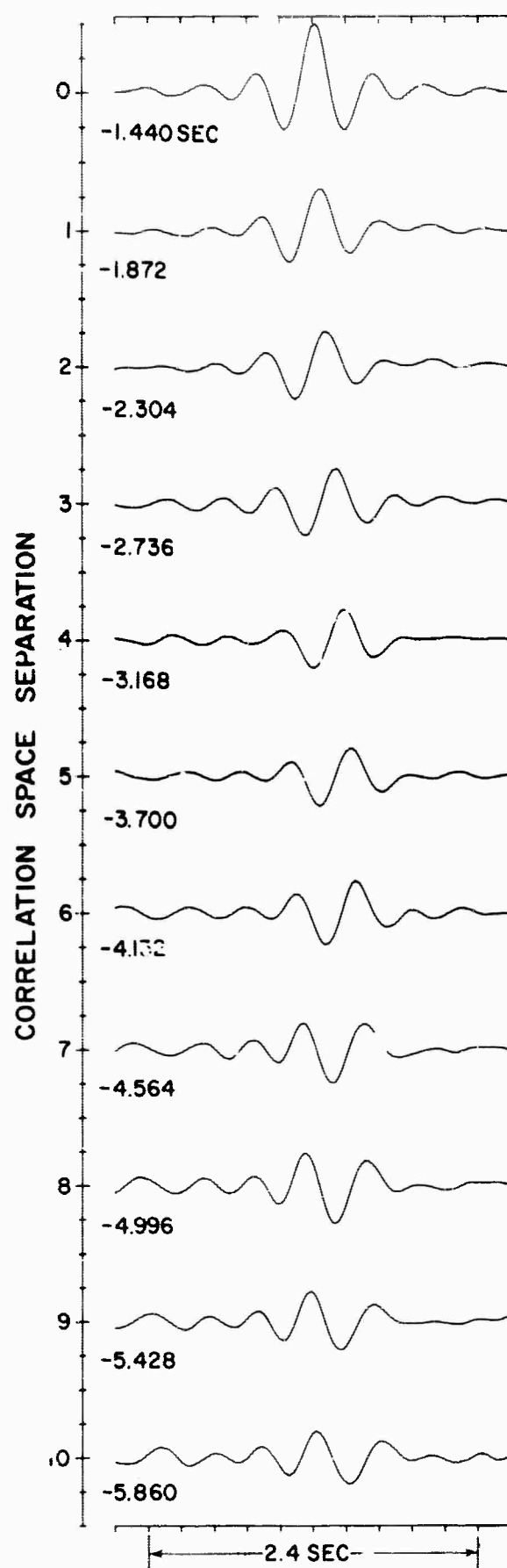


Figure 14. Ensemble Average Correlations Computed from Rye Creek Data. Correlation space lags denote averaging over all correlations with that particular space separation.

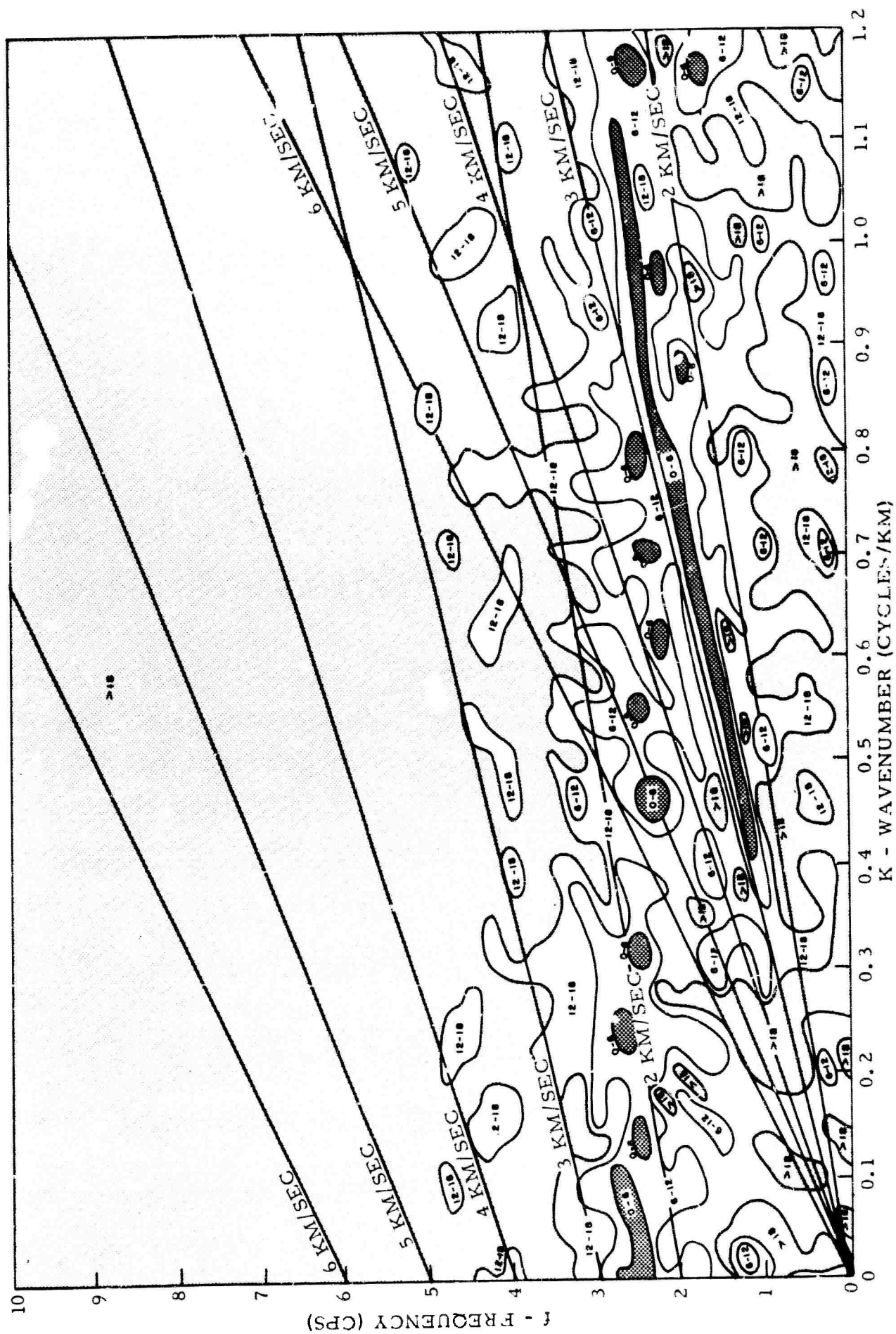


Figure 15. Frequency-Wavenumber Spectrum for Rye Creek Event Using Ensemble Average Correlations. (Numbers within contours represent db from maximum amplitude)

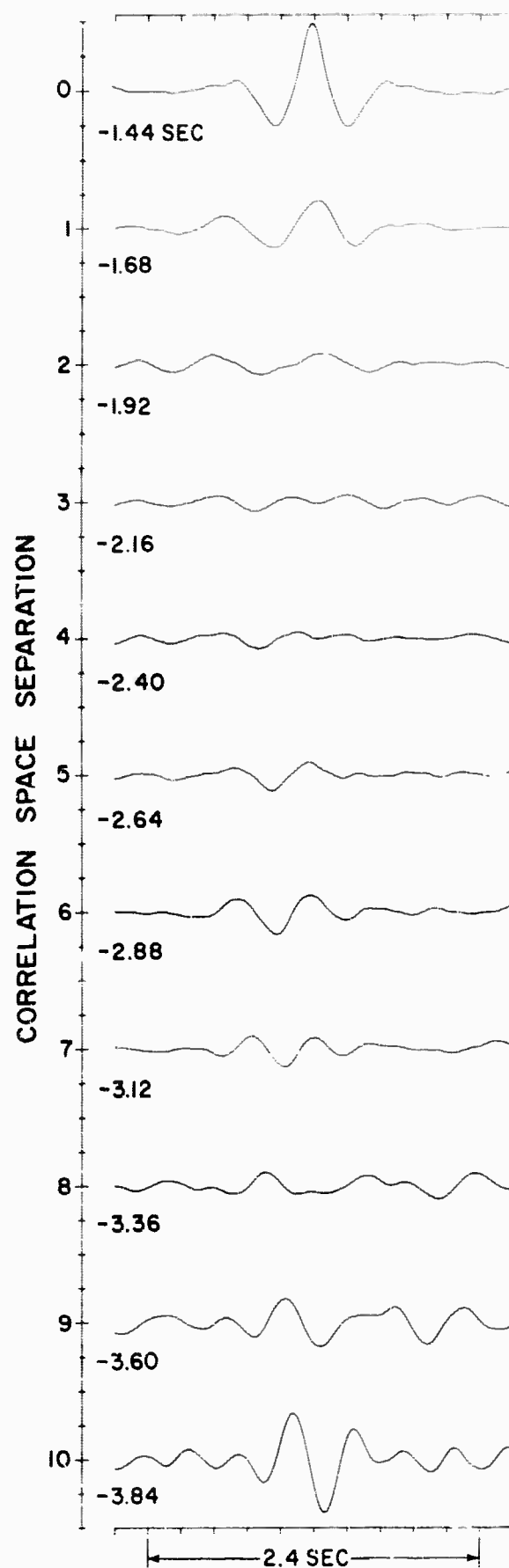


Figure 16. Ensemble Average Correlations Computed from Kohl's Ranch Data. Correlation space lags denote averaging over all correlations with that particular space separation

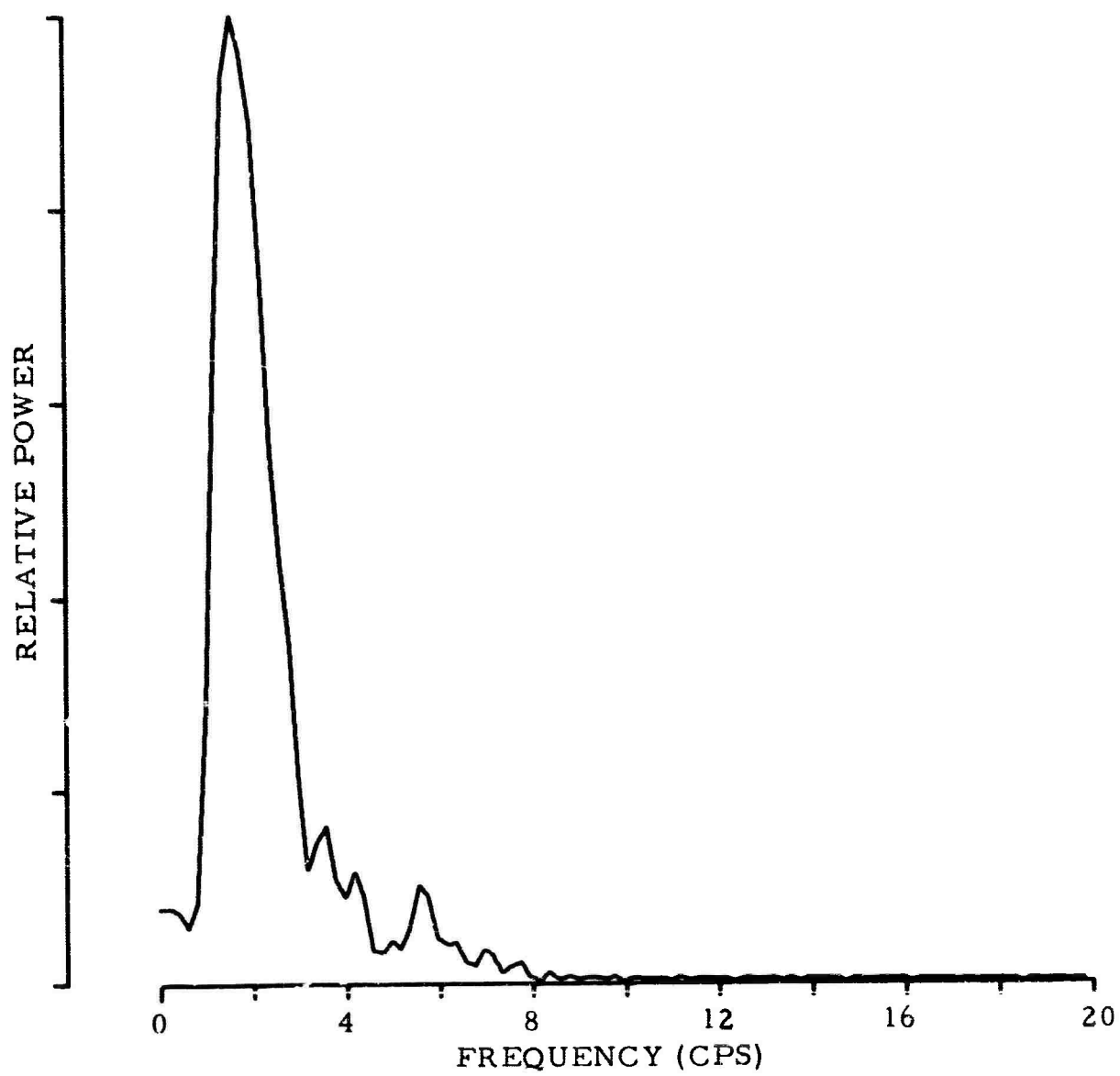


Figure 17. Frequency Spectrum of Ensemble Average Autocorrelations for Kohl's Ranch Event

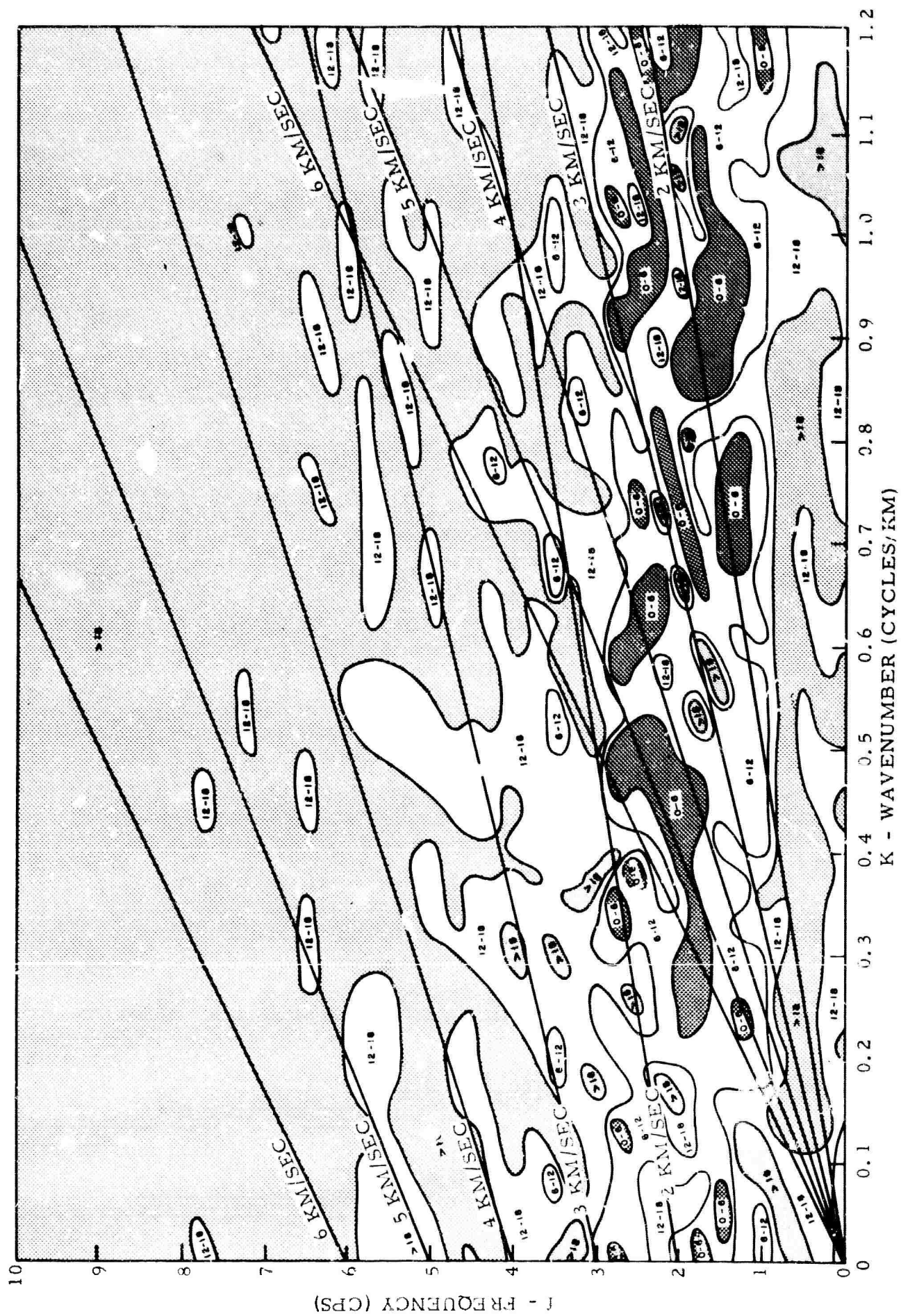


Figure 18. Frequency-Wavenumber Spectrum for Kohl's Ranch Event Using Ensemble Average Correlations. (Numbers within Contours represent db down from maximum amplitude)

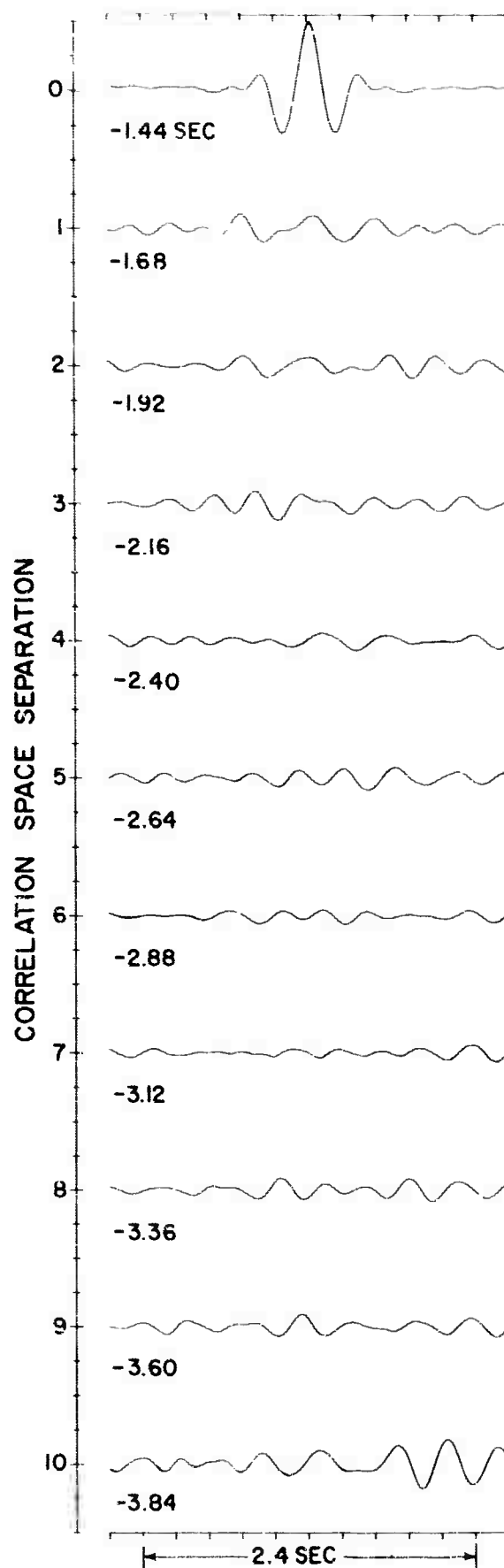


Figure 19. Ensemble Average Correlations Computed from Chase Ranch Data. Correlation space lags denote averaging over all correlations with that particular space separation

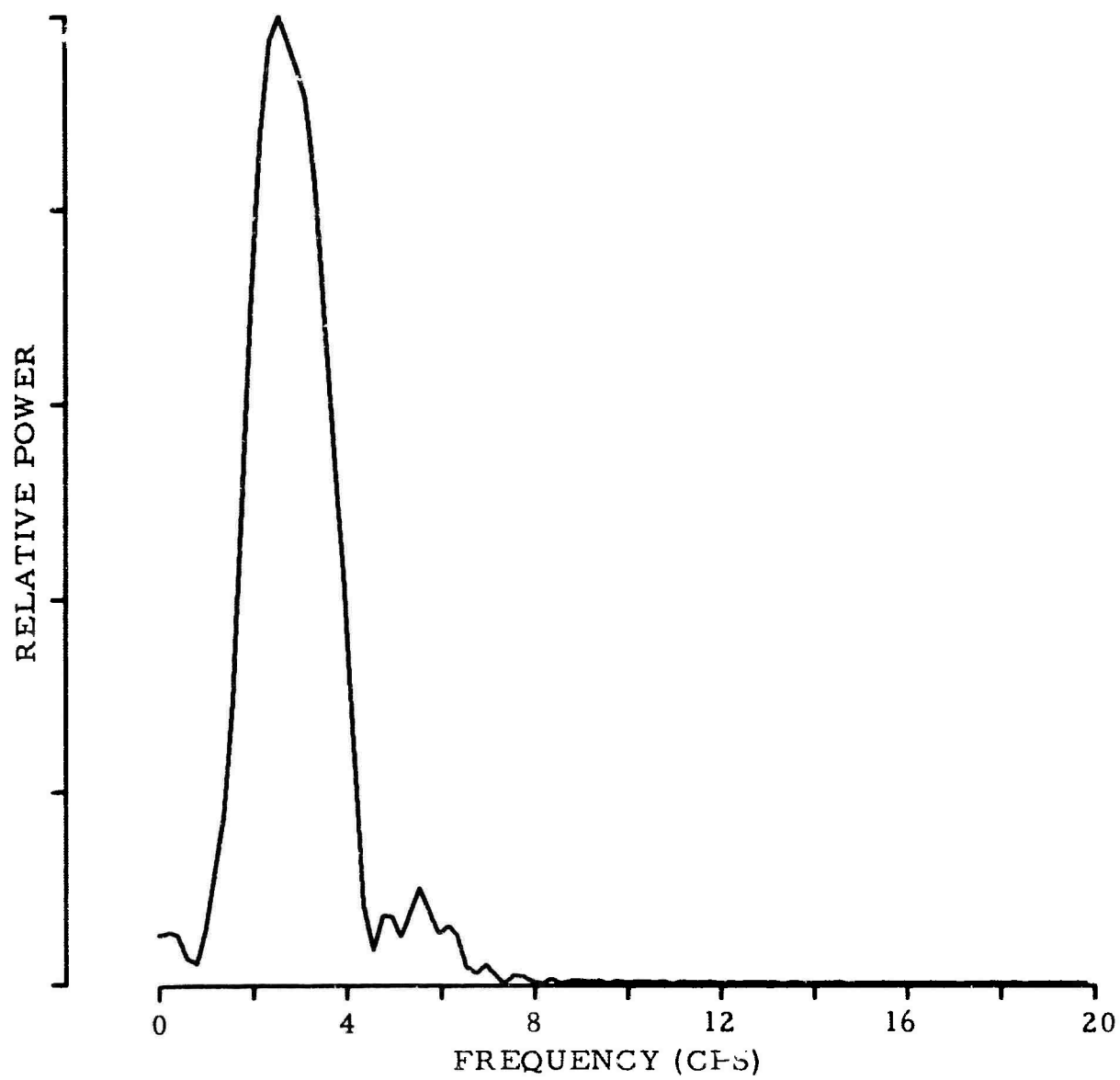


Figure 20. Frequency Spectrum of Ensemble Average Autocorrelation for Chase Ranch Event

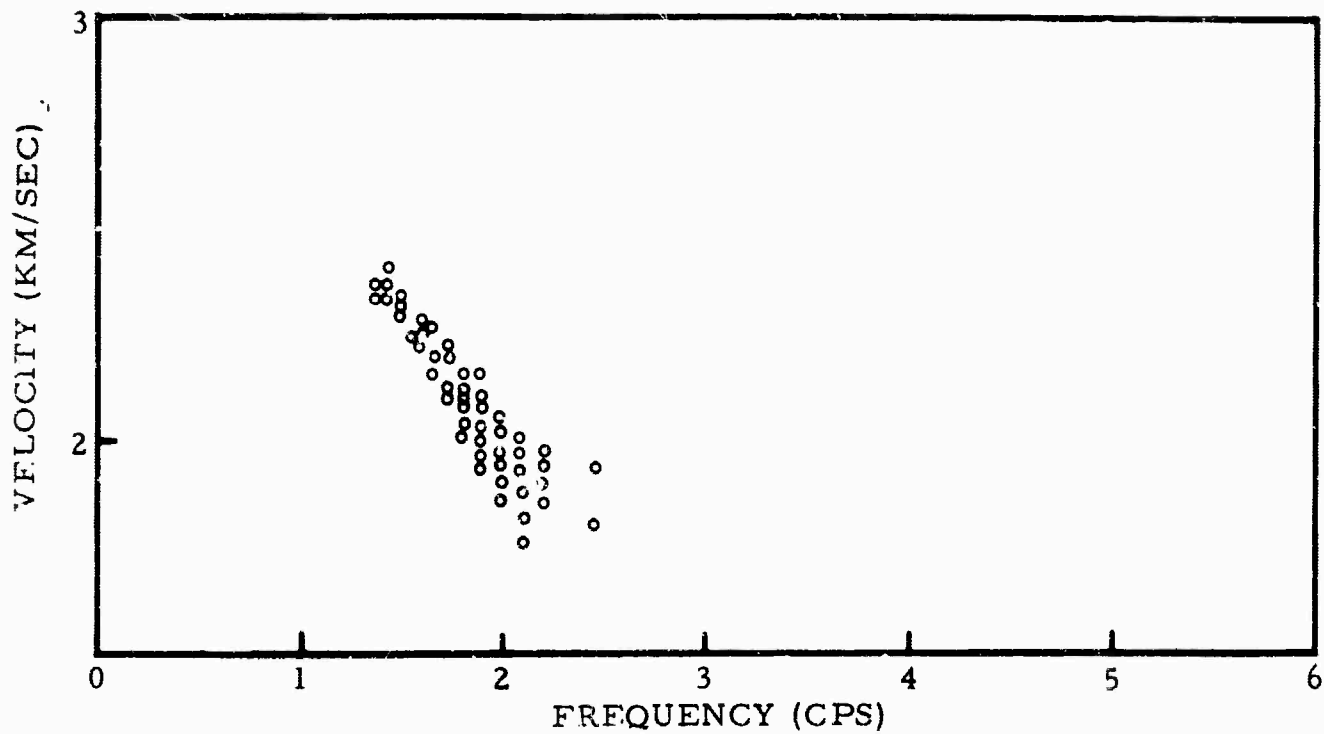


Figure 22. Rayleigh Group Velocities from Inline Arm for Strawberry Event

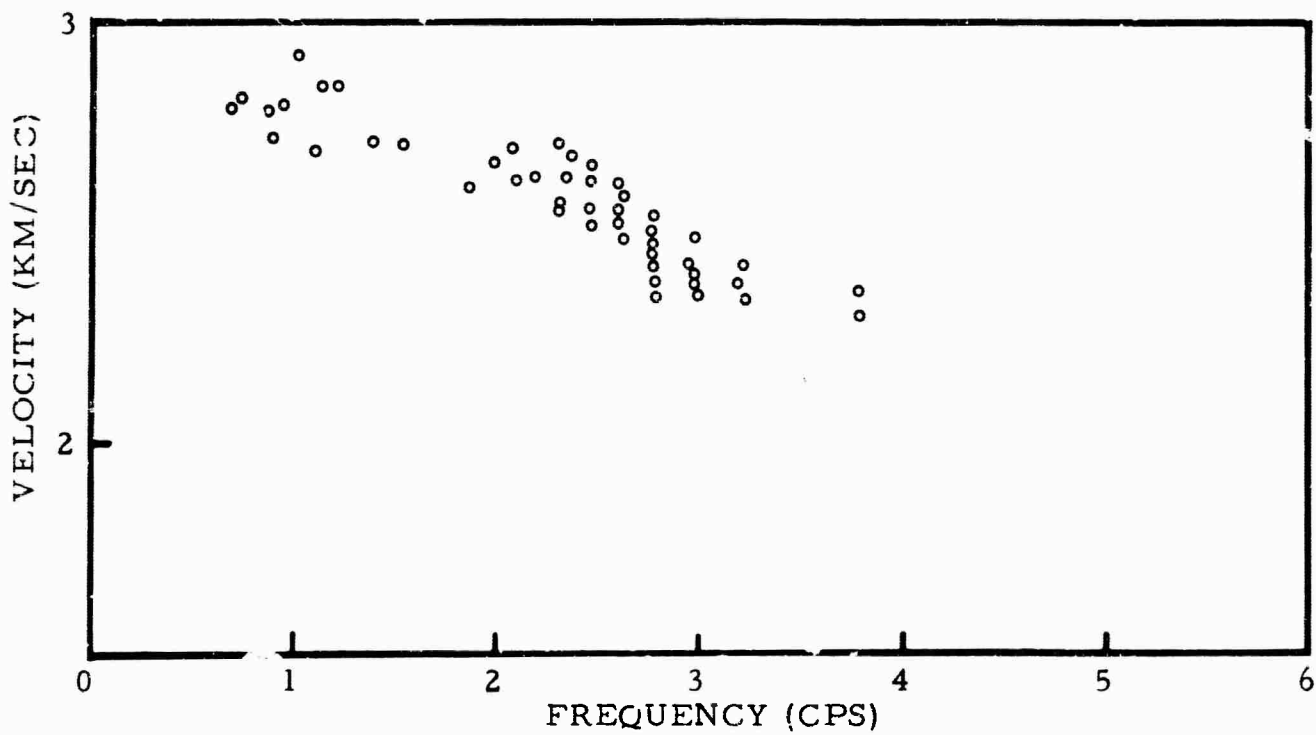


Figure 23. Rayleigh Group Velocities from Inline Arm for Rye Creek Event

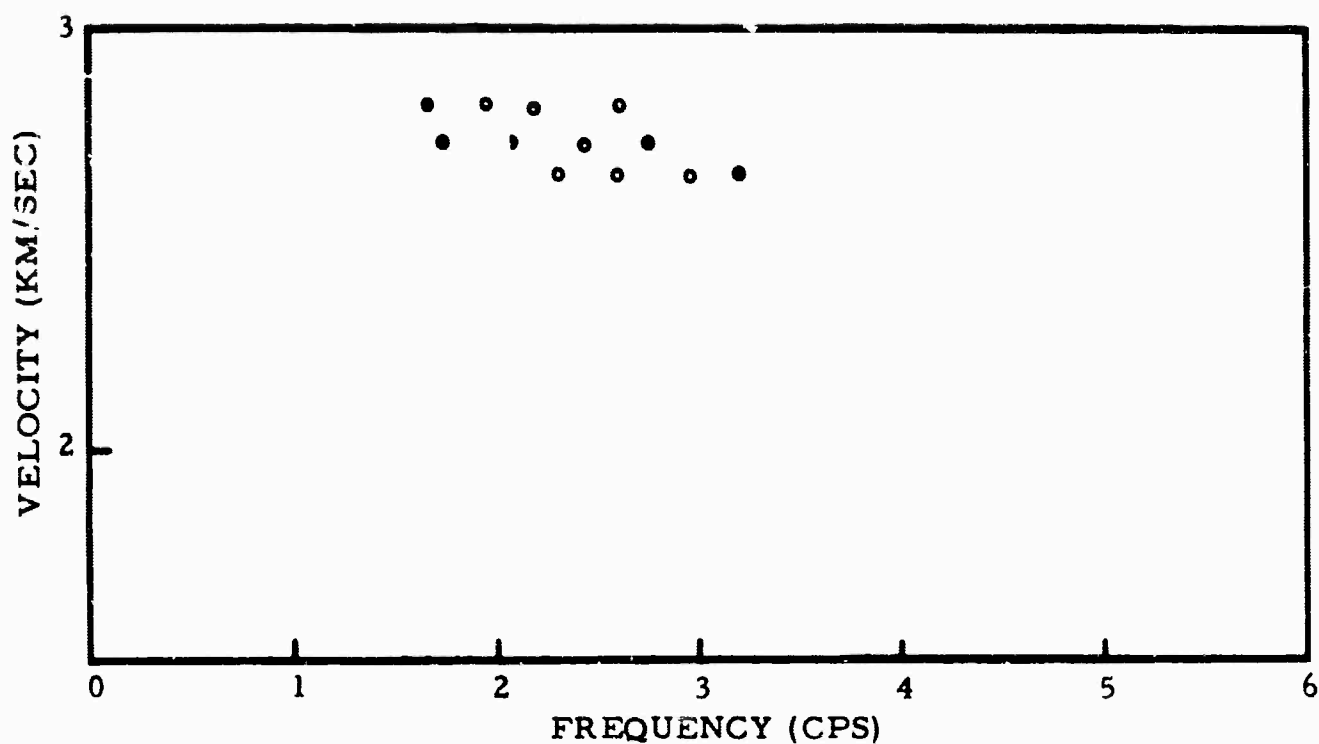


Figure 24. Rayleigh Phase Velocities Determined from Peak and Trough Method for Rye Creek Event

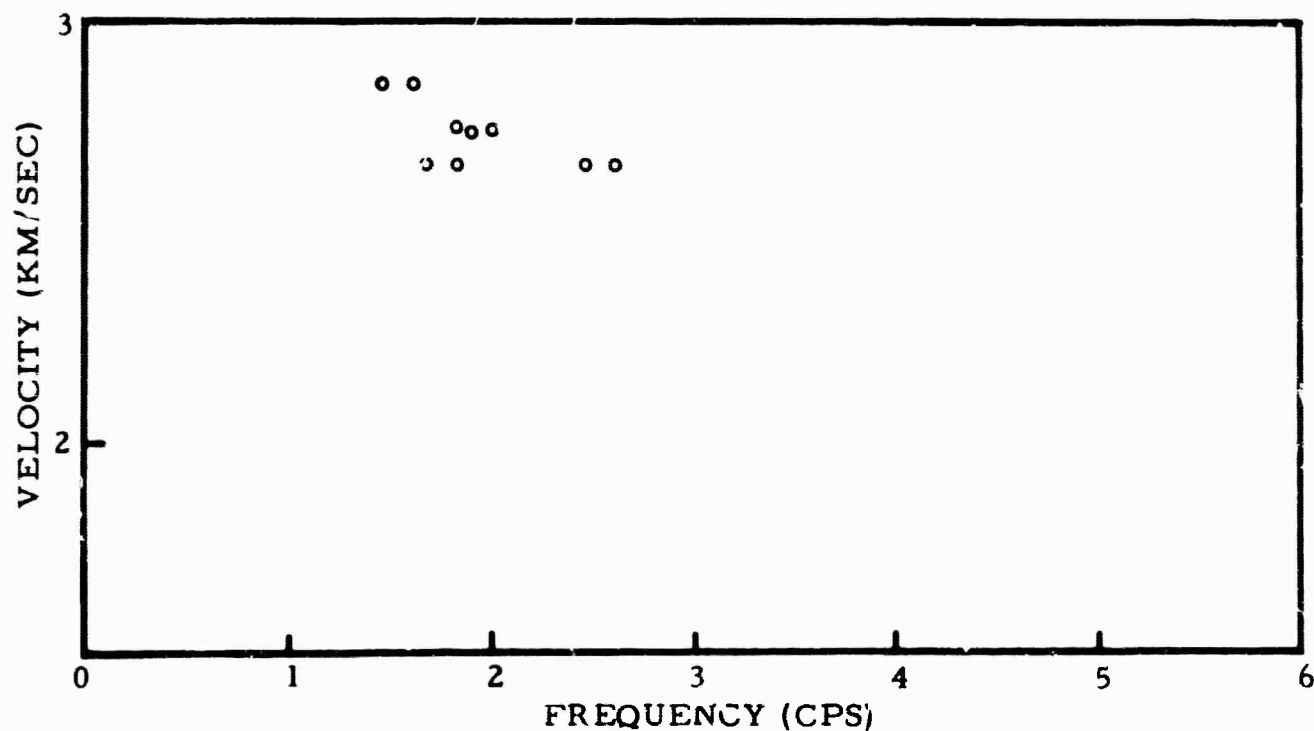


Figure 25. Rayleigh Phase Velocities Determined from Peak and Trough Method for Kohi's Ranch Event Using Only NW Arm of Array

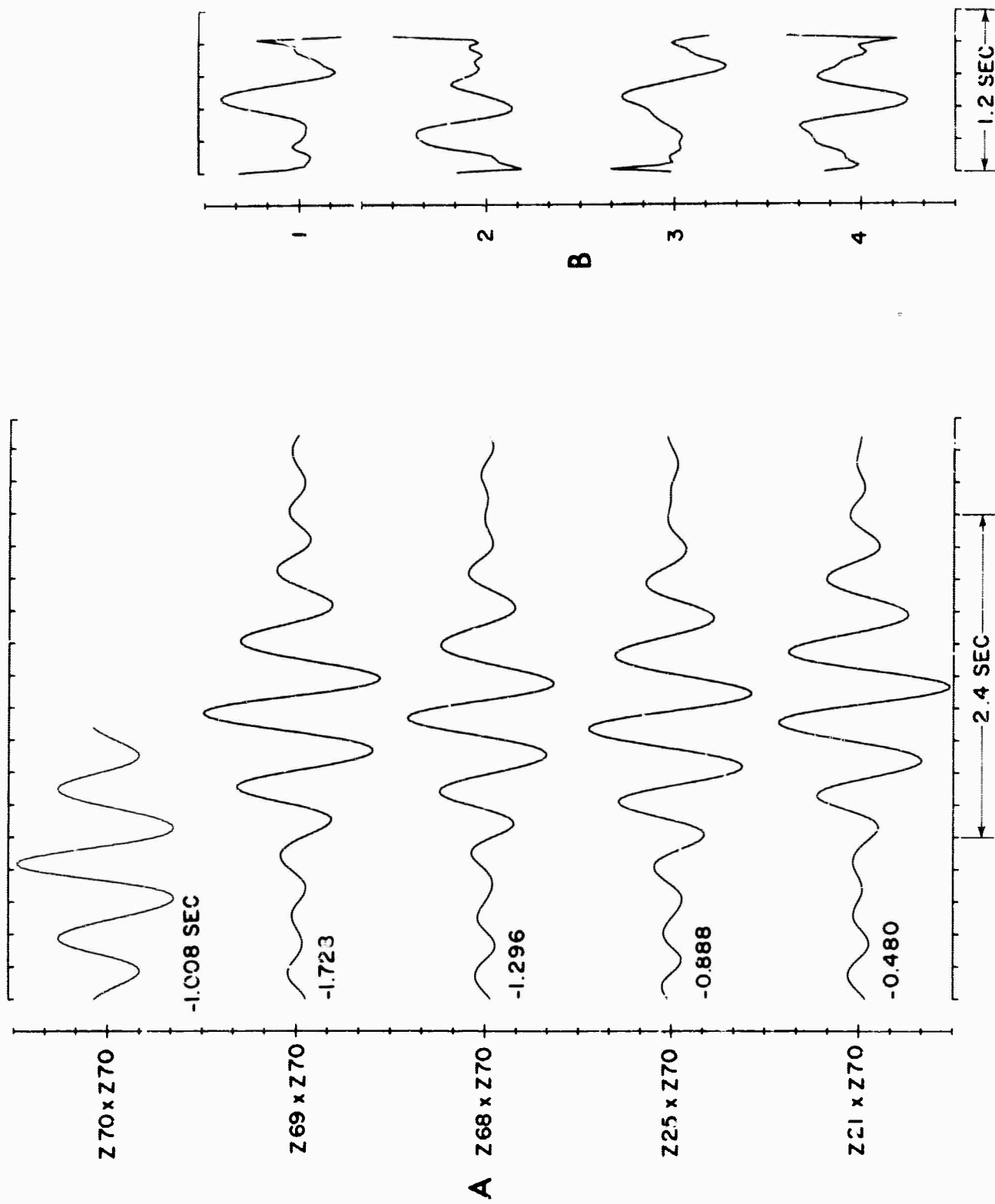


Figure 26(A) Correlation Functions from Strawberry Event Using NW Array of Array;
(B) Single-Channel Prediction Filters

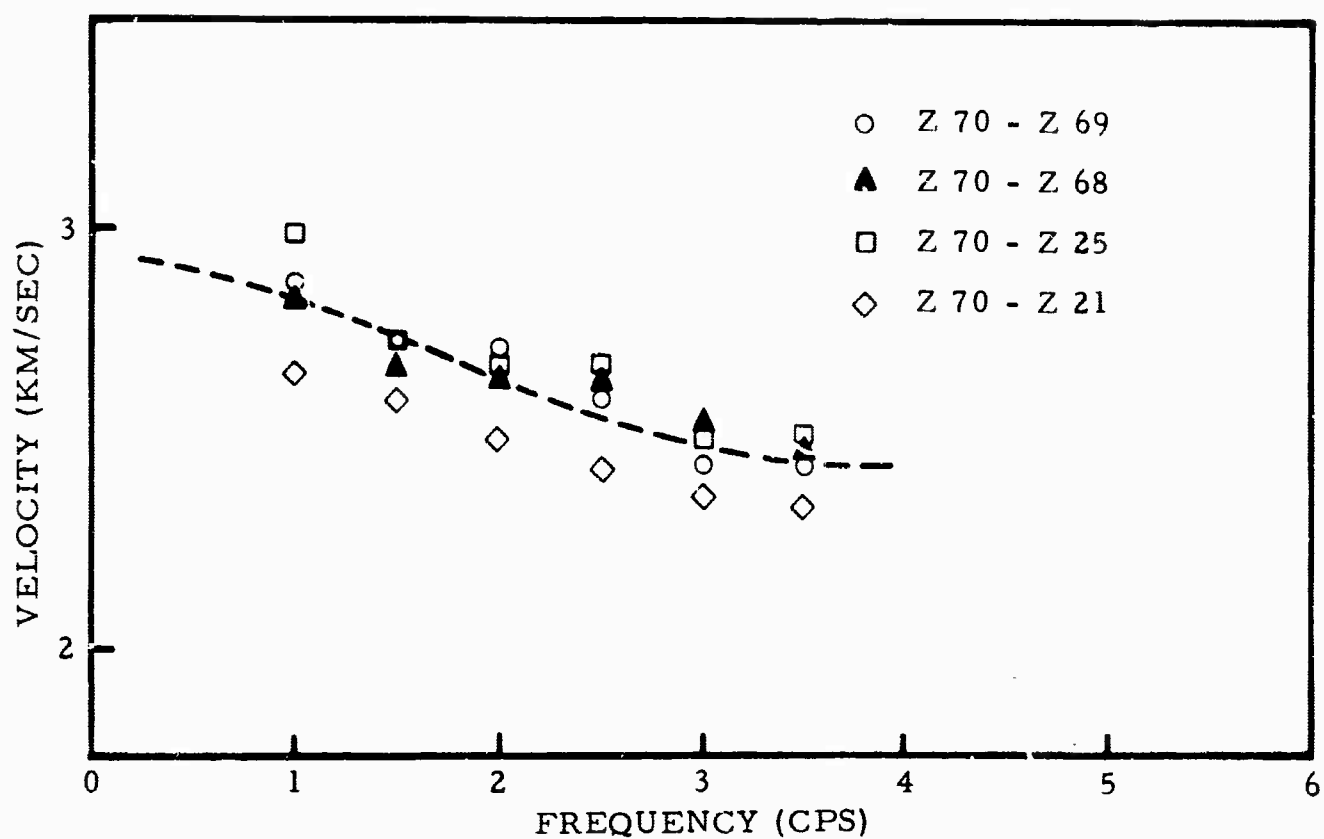


Figure 27. Rayleigh Phase Velocity Points from Strawberry Event Using NW Arm of Array. (Dashed curve is phase velocity for theoretical model given in Table 5)

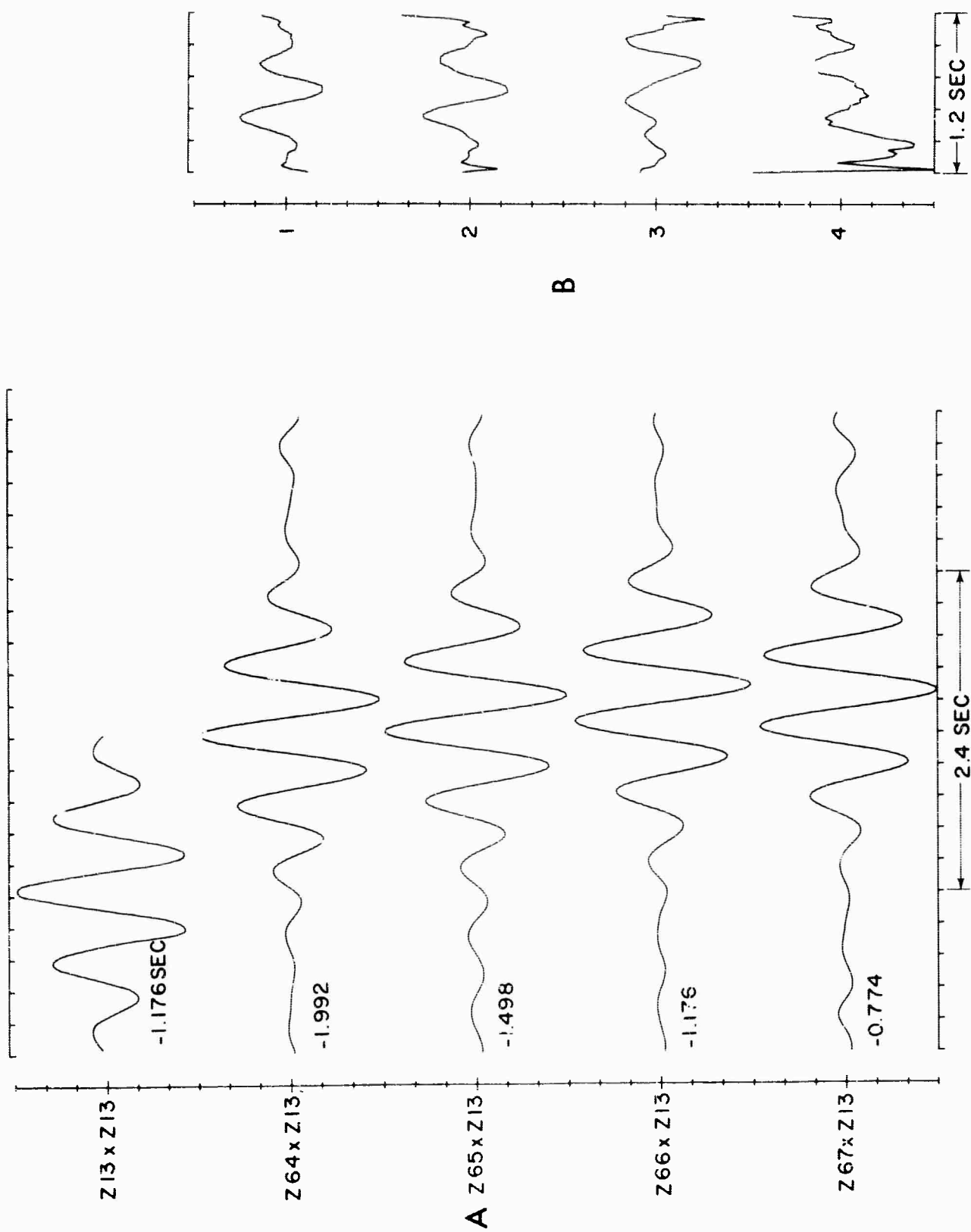


Figure 28(A) Correlation Functions from Strawberry Event Using SE Arm of the Array ;
 (B) Single-Channel Prediction Filters

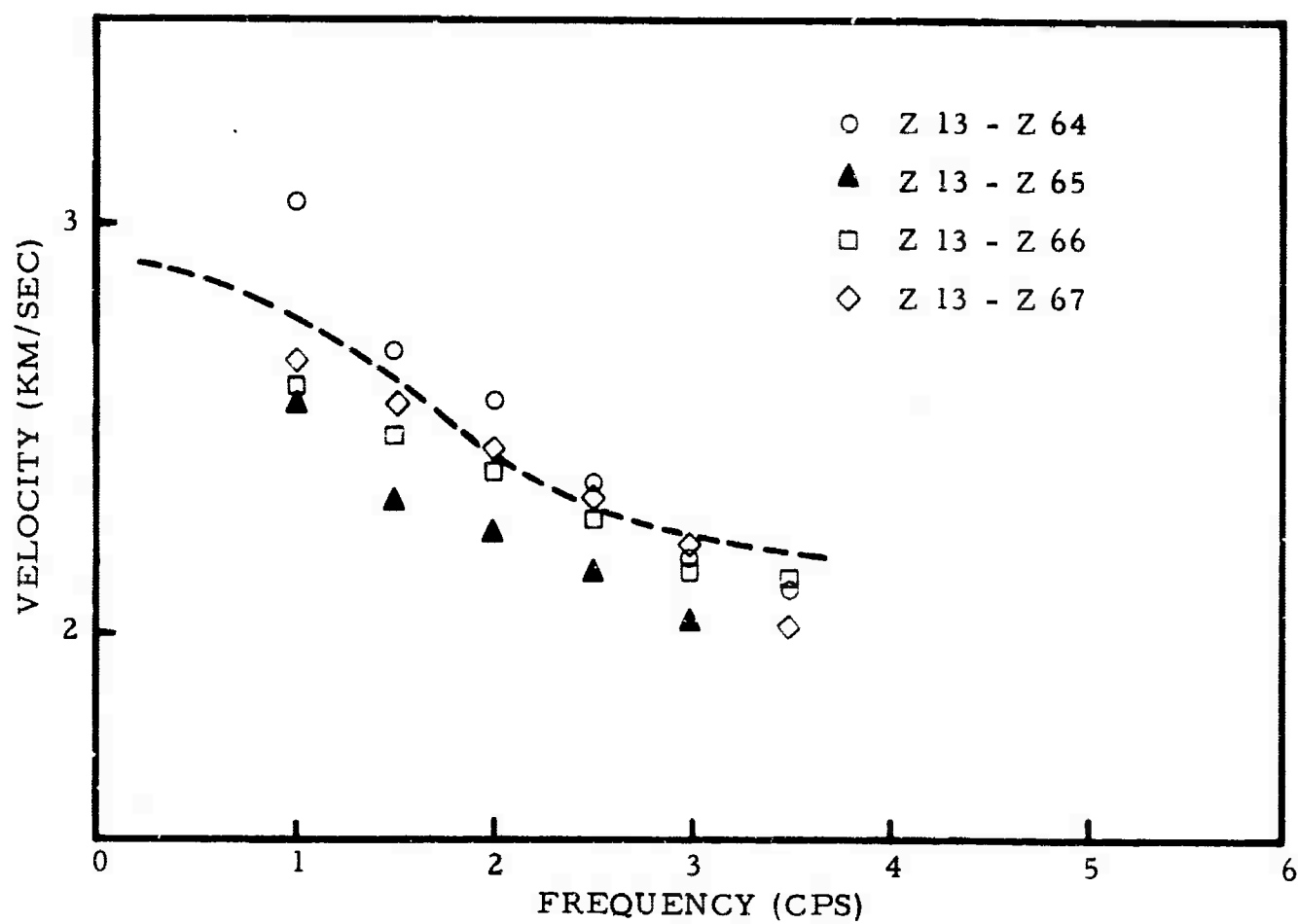


Figure 29. Rayleigh Phase Velocity Points from Strawberry Event Using SE Arm of Array. (Dashed curve is phase velocity for theoretical model given in Table 6)

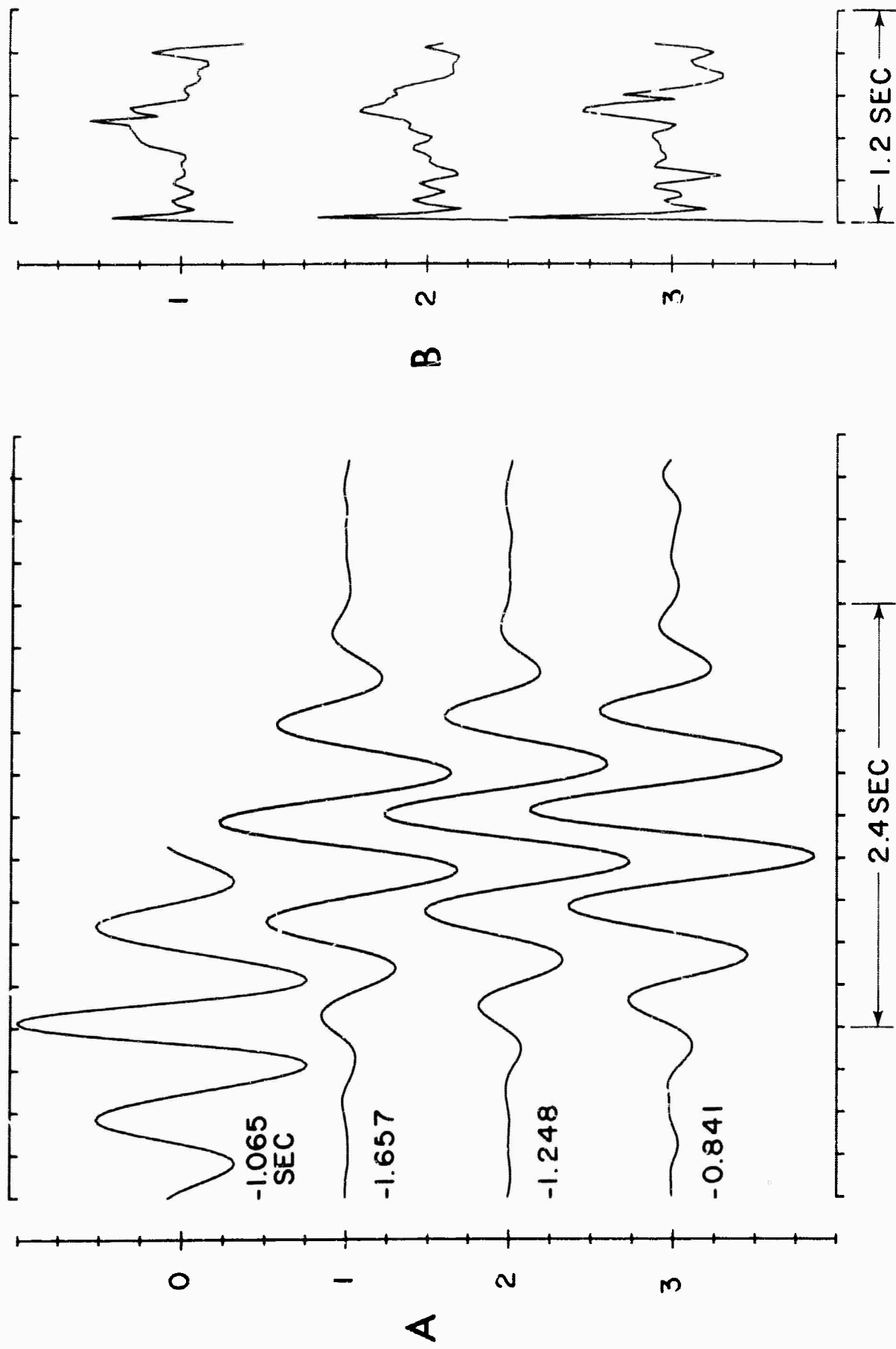


Figure 30(A) Averaged Correlation Function from Strawberry Event Using NW Arm of Array;
(B) Single-Channel Prediction Filters

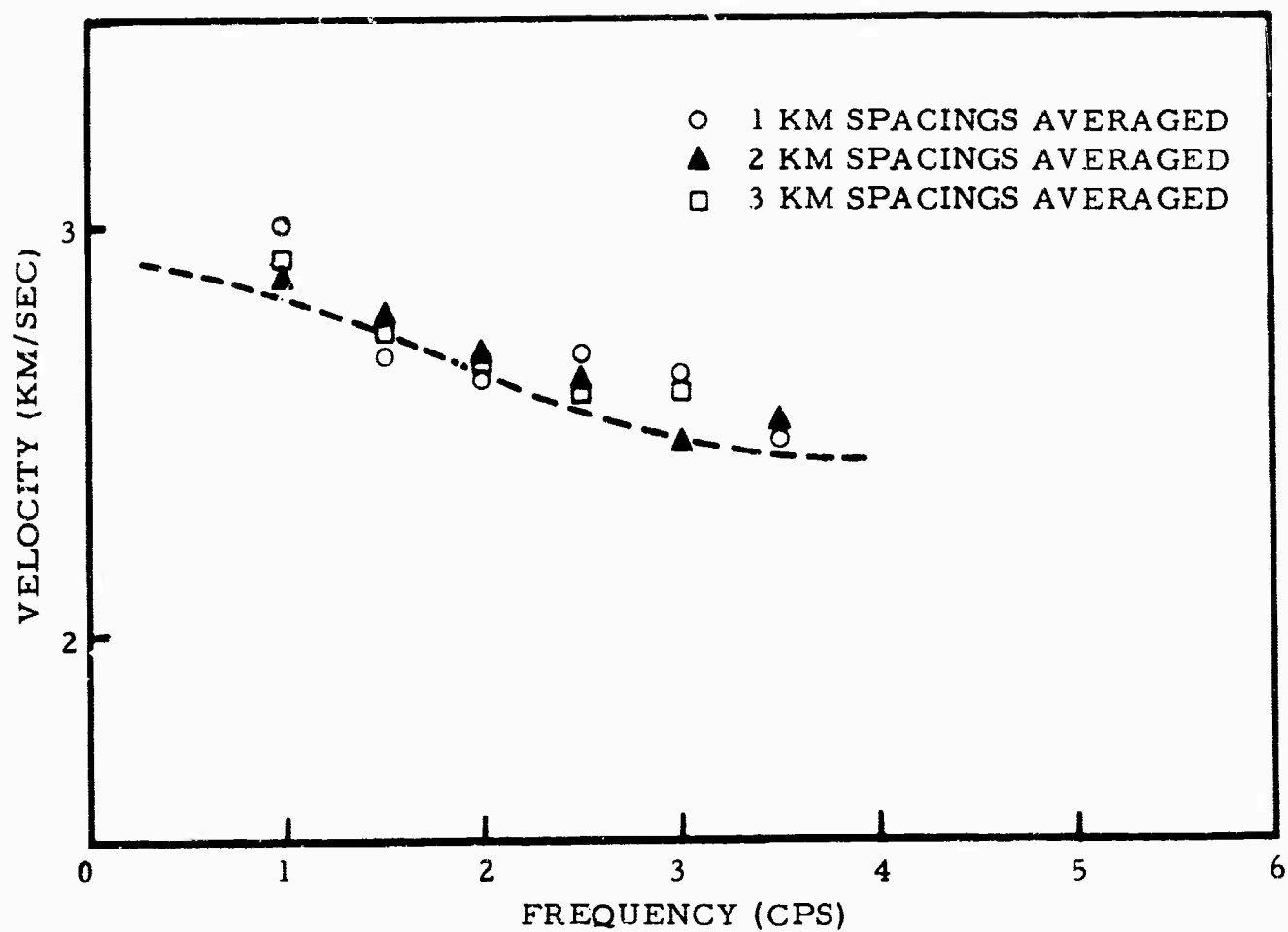


Figure 31. Rayleigh Phase Velocity Points from Strawberry Event Using Averaged Correlations of NW Arm of Array. (Dashed curve is phase velocity for theoretical model given in Table 5)

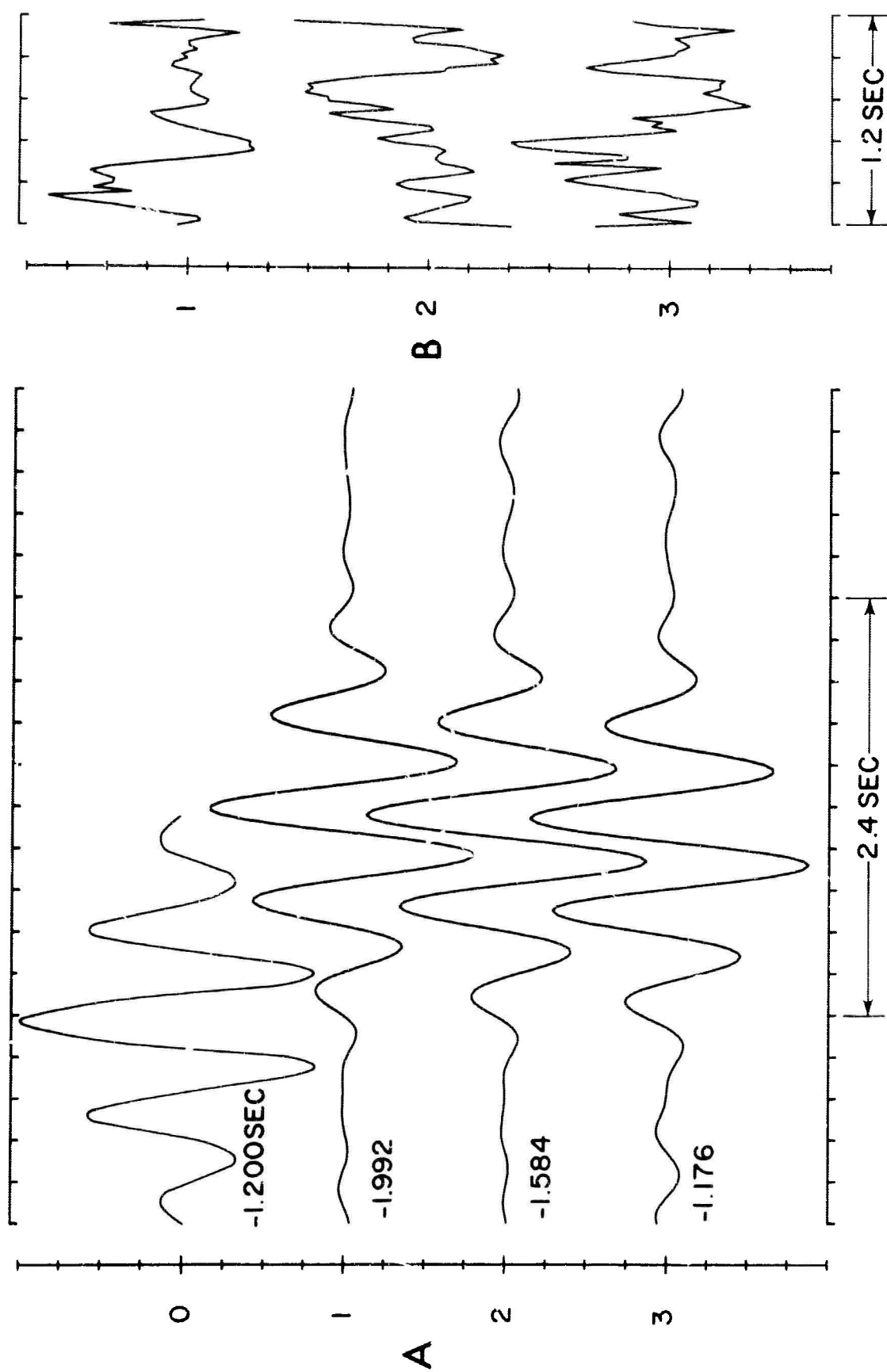


Figure 32(A) Averaged Correlation Functions From Strawberry Event Using SE Arm of Array ;
 (B) Single-Channel Prediction Filters

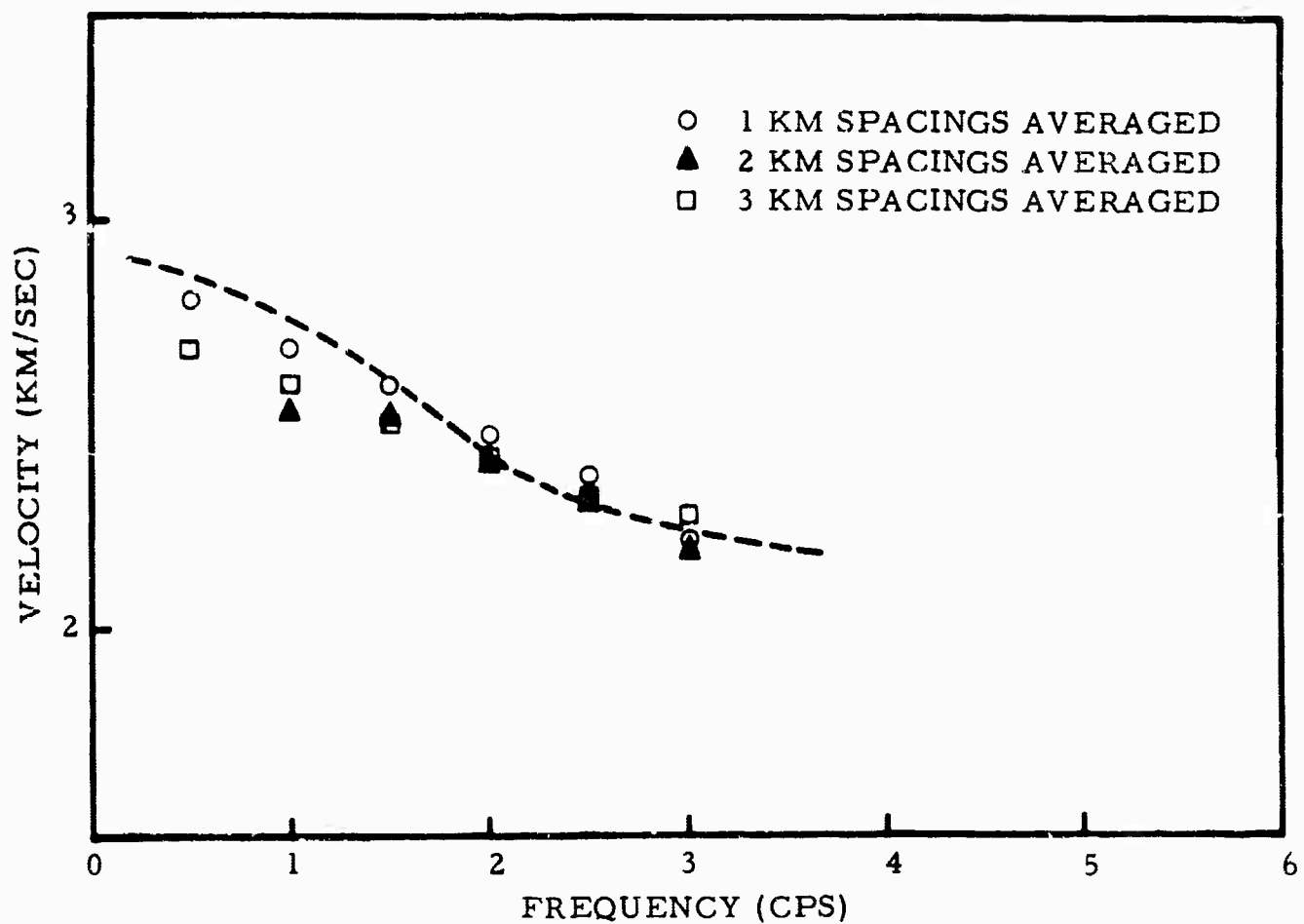


Figure 33. Rayleigh Phase Velocity Points from Strawberry Event Using Averaged Correlations of SE Arm of Array. (Dashed curve is phase velocity for theoretical model given in Table 6)

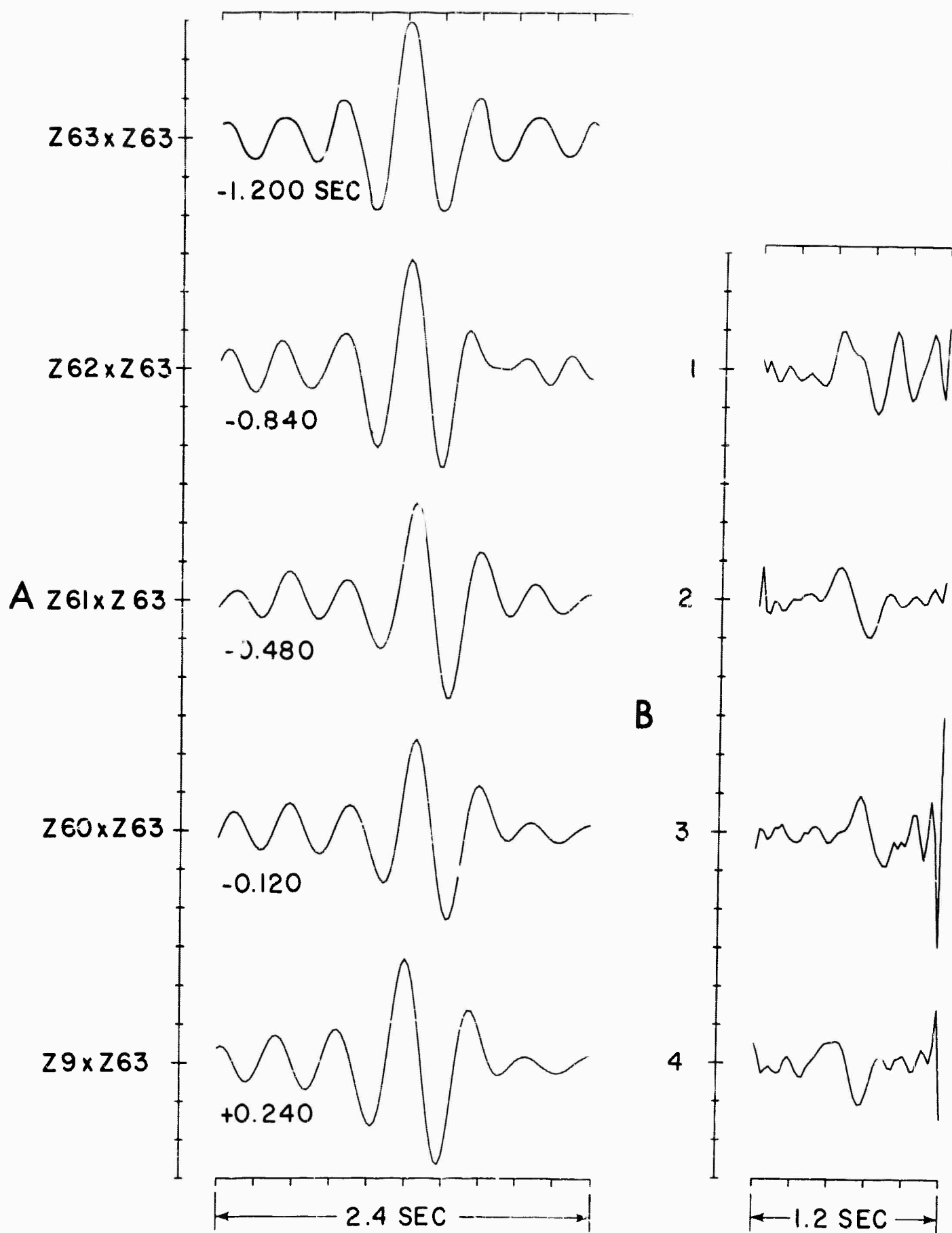


Figure 34(A) Correlation Functions from Rye Creek Event Using SW Arm of Array; (B) Single-Channel Prediction Filters

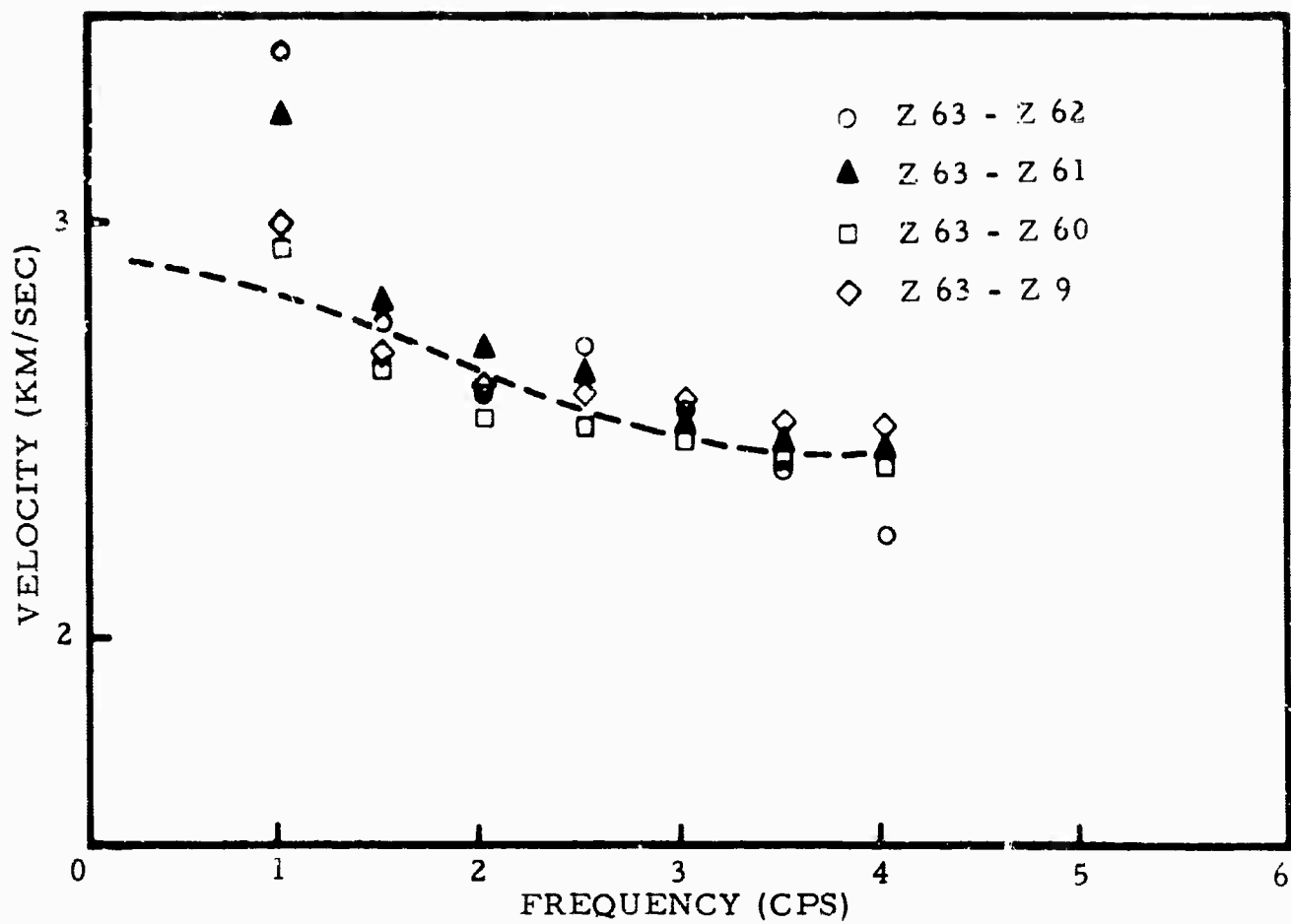


Figure 35. Rayleigh Phase Velocity Points from Rye Creek Event Using SW Arm of Array. (Dashed curve is phase velocity for theoretical model given in Table 5)

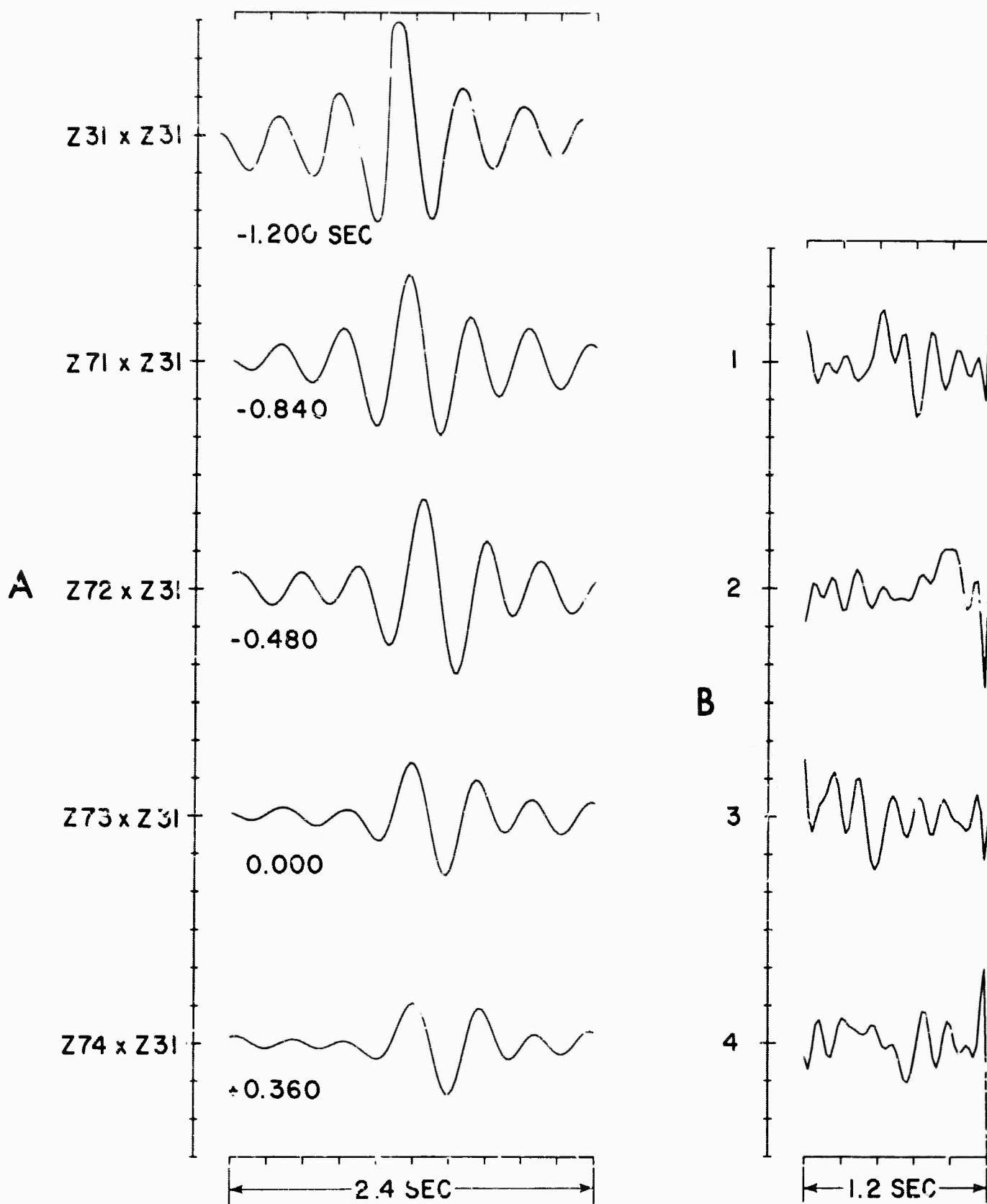


Figure 35 (A) Correlation Functions from Rye Creek Event Using NE Arm of Array; (B) Single-Channel Filters

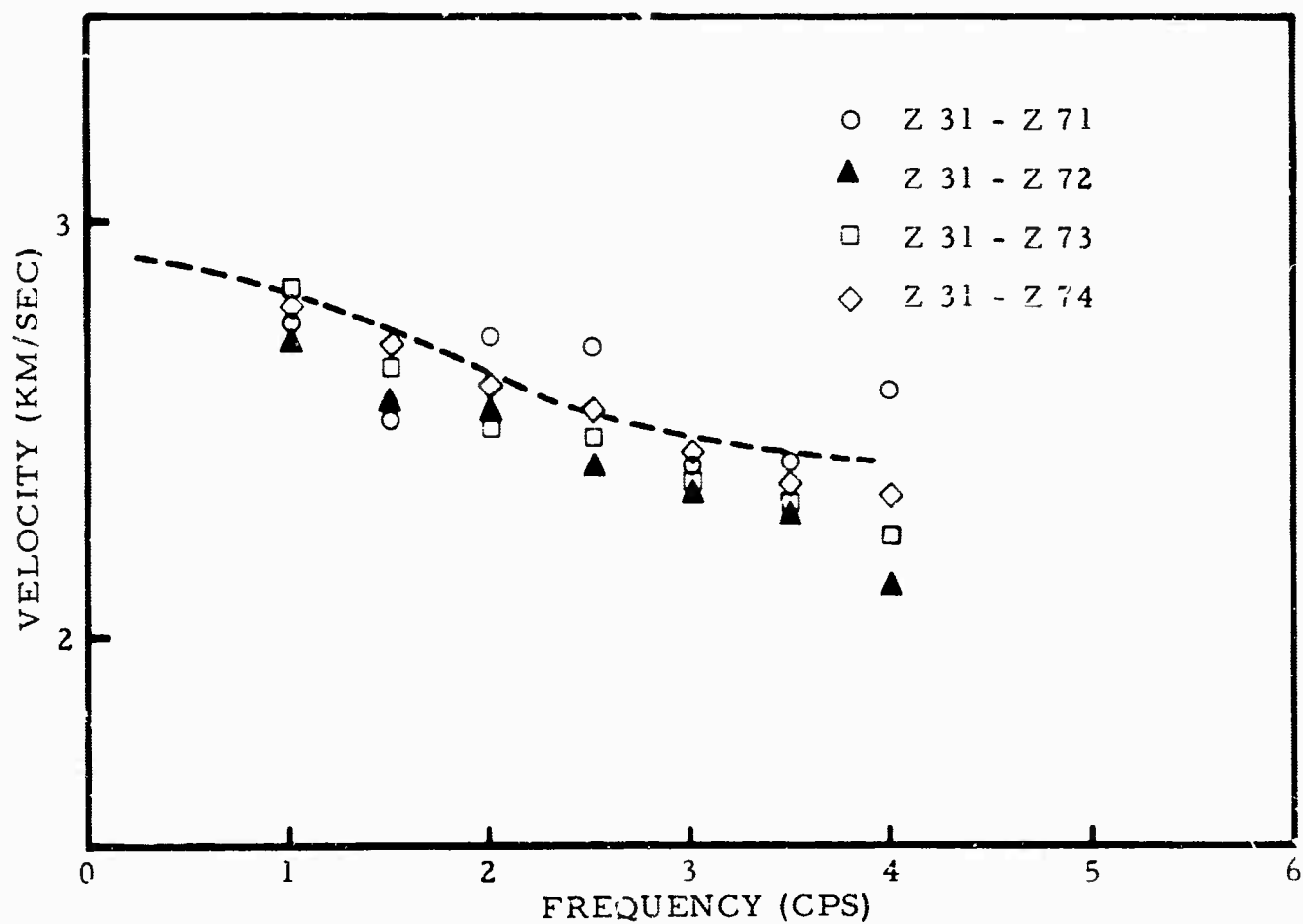


Figure 37. Rayleigh Phase Velocity Points from Rye Creek Event Using SW Arm of Array. (Dashed curve is phase velocity for theoretical model given in Table 5)

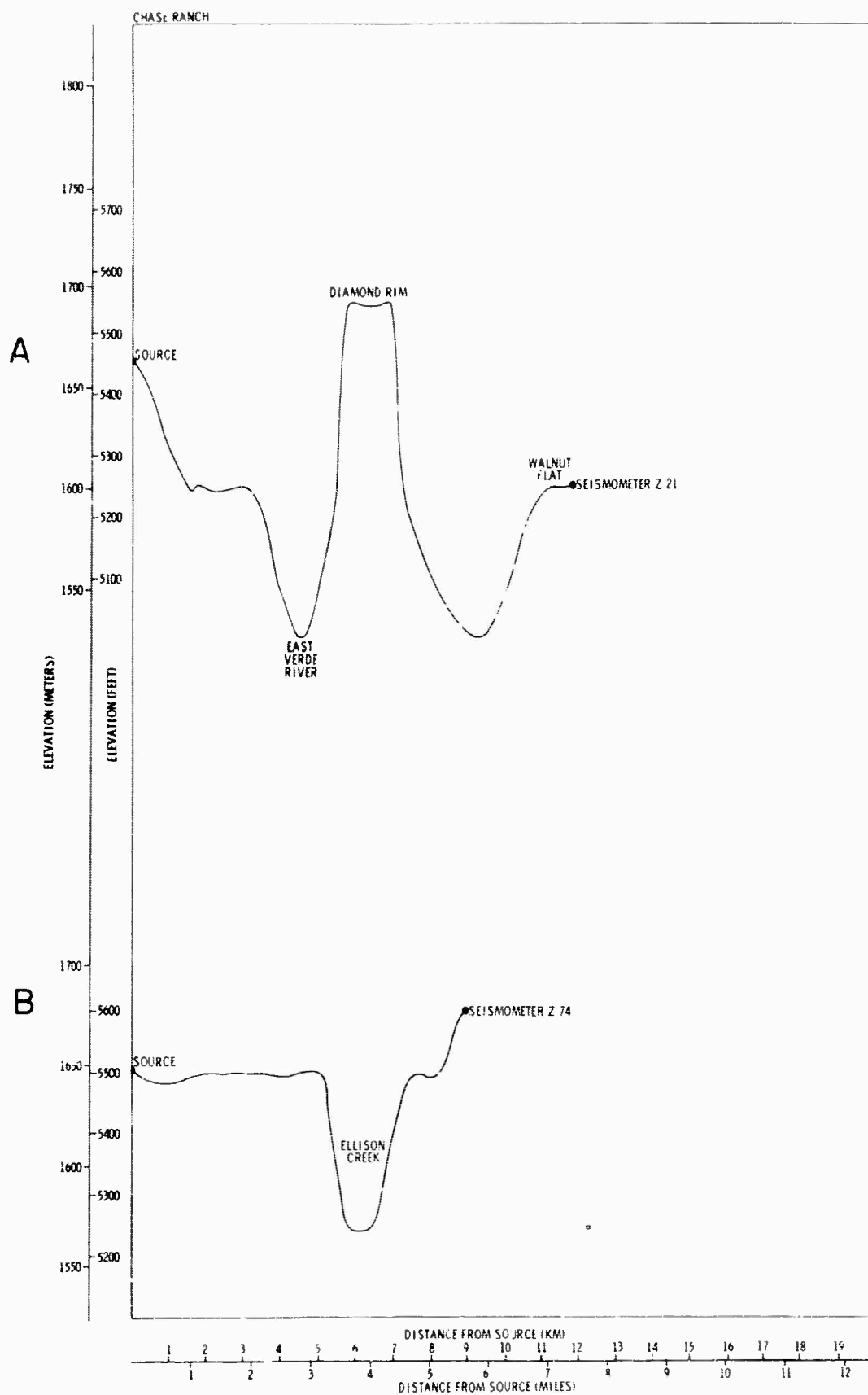


Figure 38 (A) Elevation Profile from Chase Ranch to Z21
(B) Elevation Profile from Chase Ranch to Z74

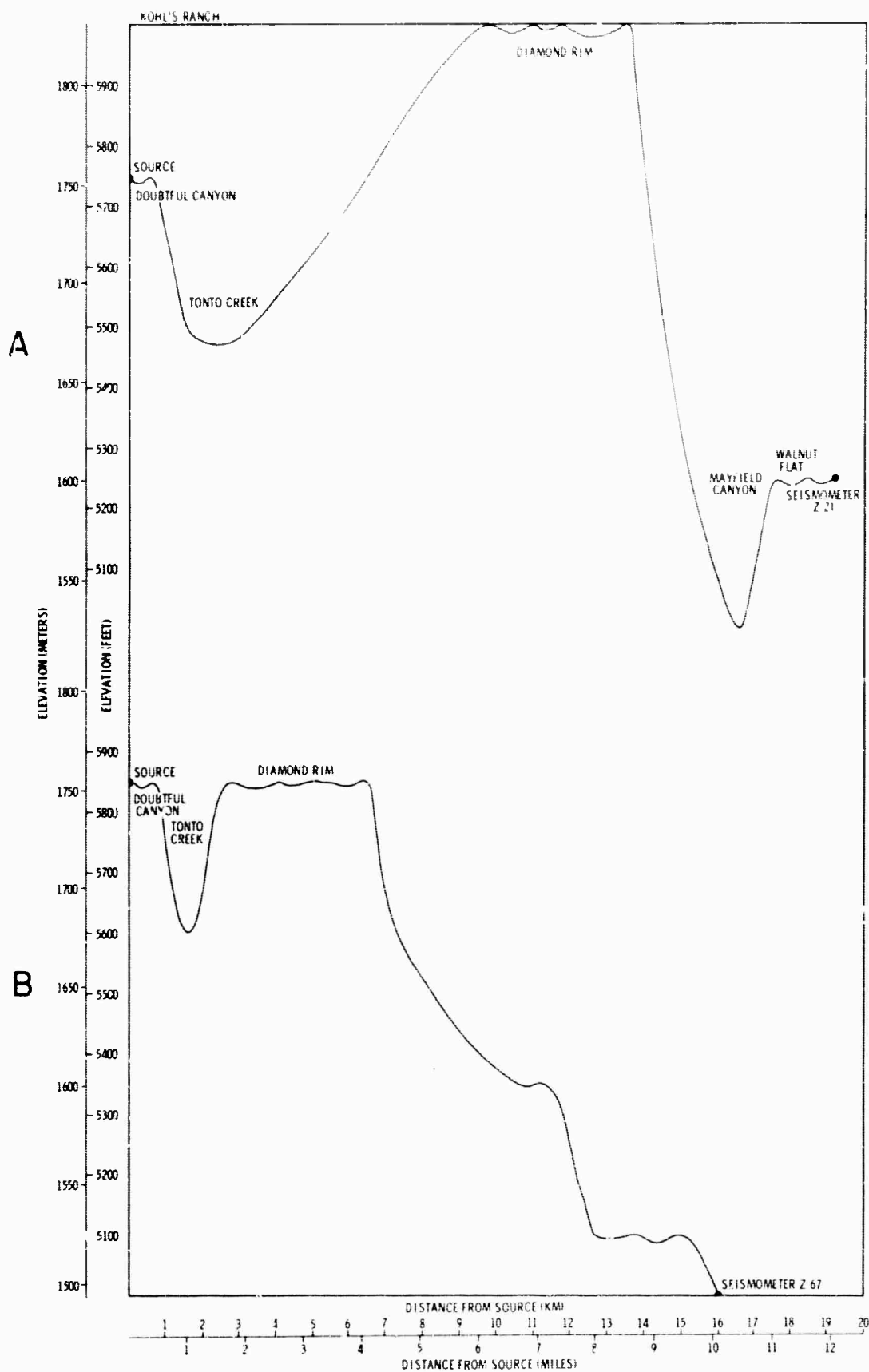


Figure 39 (A) Elevation Profile from Kohl's Ranch to Z21
(B) Elevation Profile from Kohl's Ranch to Z67

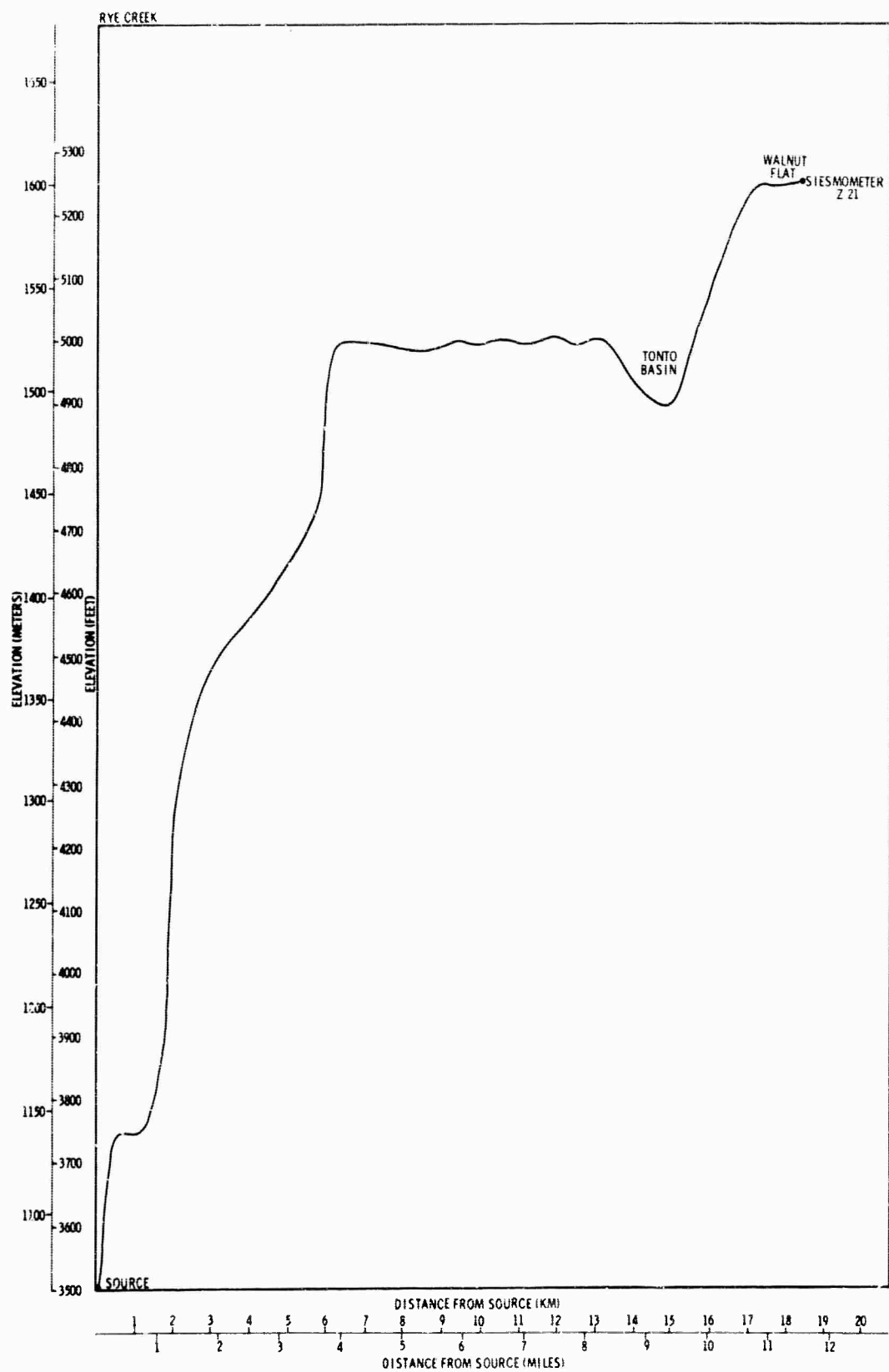


Figure 40. Elevation Profile from Rye Creek to Z21

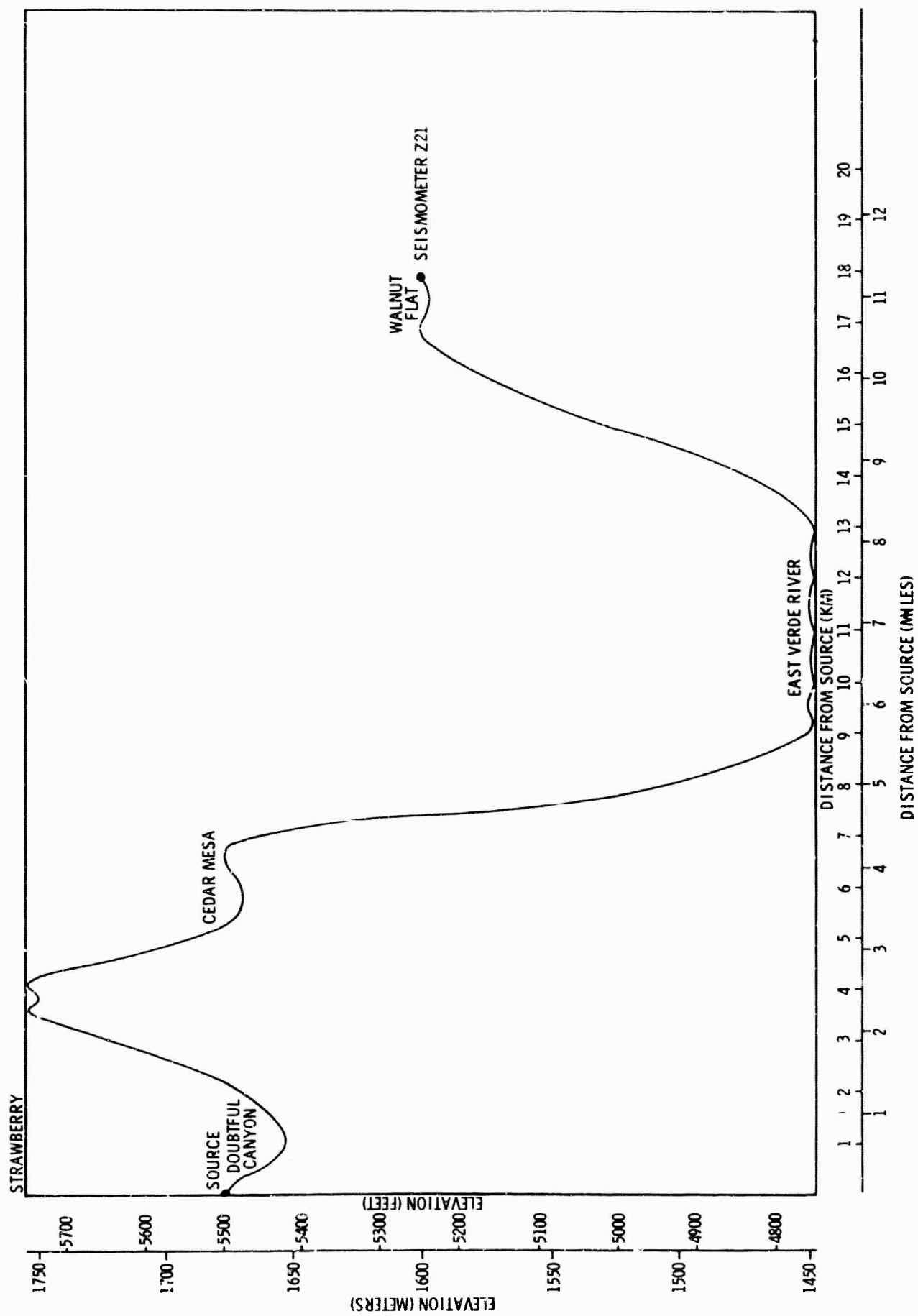


Figure 41. Elevation Profile from Strawberry to Z21

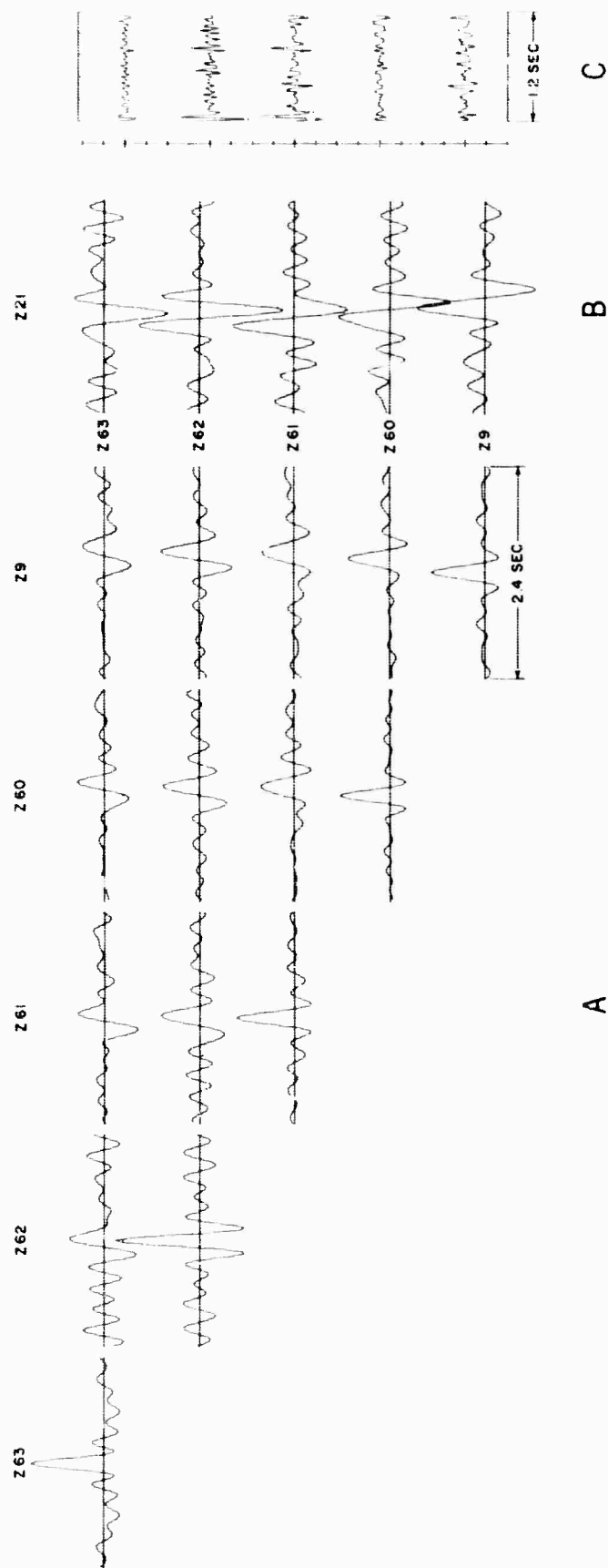


Figure 42 (A) Correlation Functions between 5-Input Channels; (B) Correlation Functions between Channel to be Predicted and 5-Input Channels; (C) 5-Channel Prediction Filter Operators

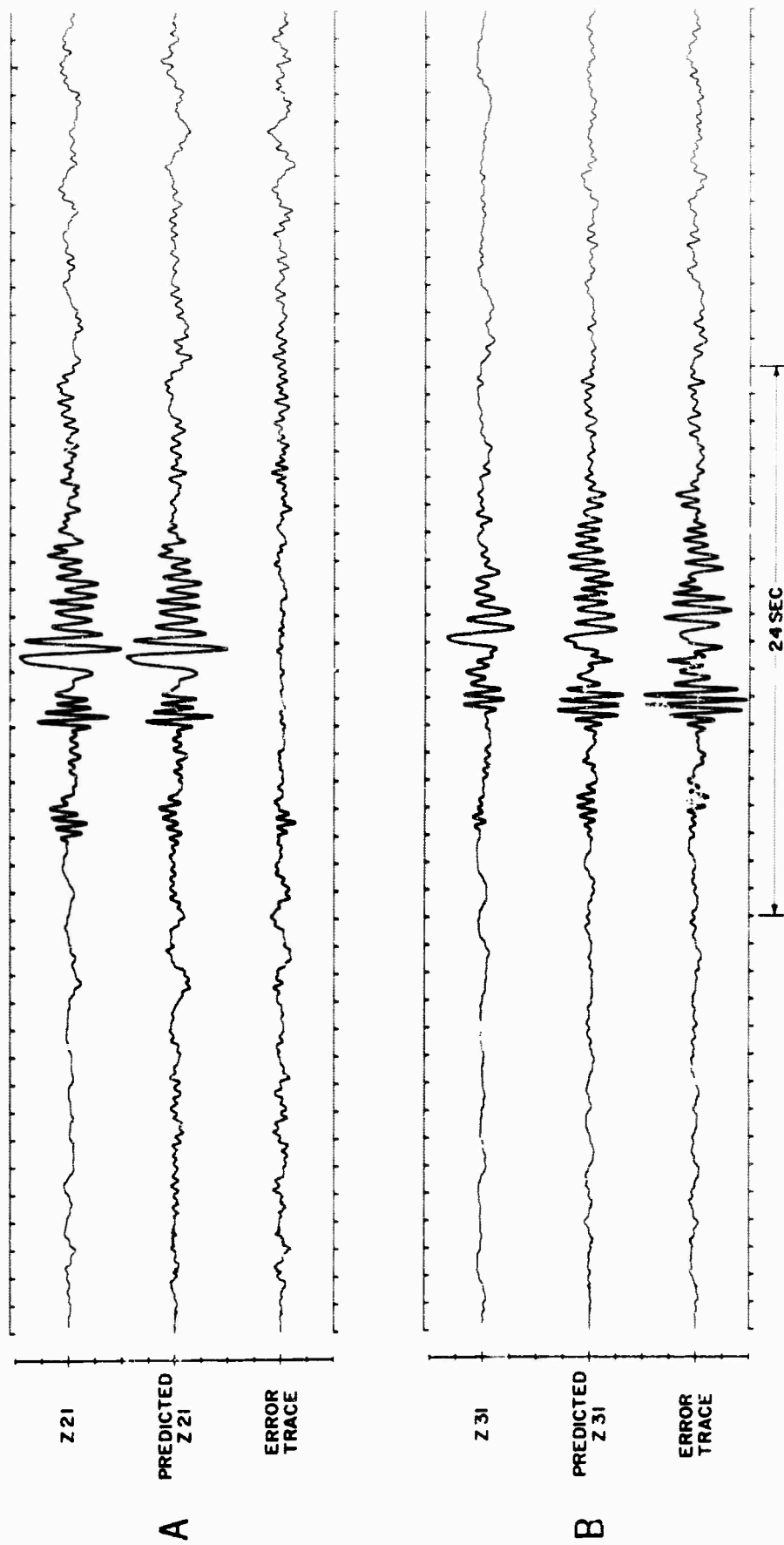


Figure 43 (A) Top Trace—Actual Trace to be Predicted (Z21); Middle Trace—Predicted Trace; Bottom Trace—Prediction Error Trace; (B) Top Trace—Actual Trace to be Predicted (Z31); Middle Trace—Predicted Trace; Bottom Trace—Prediction Error Trace

BLANK PAGE

DOCUMENT CONTROL DATA - R&D

(Security classification of title, body of abstract and indexing annotation must be entered when the overall report is classified)

1 ORIGINATING ACTIVITY (Corporate author) Texas Instruments, Inc. Science Services Division P.O. Box 5621, Dallas, Texas 75222		2a REPORT SECURITY CLASSIFICATION Unclassified	
		7b GROUP	
3 REPORT TITLE Basis Research in Crustal Studies			
4 DESCRIPTIVE NOTES (Type of report and inclusive dates) Final Report Sept. 1, 1963 to Dec. 31, 1965			
5 AUTHOR(S) (Last name, first name, initial) Backus, Milo M. Laster, Stanley J.			
6. REPORT DATE Dec. 31, 1965	7a. TOTAL NO. OF PAGES 401	7b. NO. OF REFS 24	
8a. CONTRACT OR GRANT NO. AF 49(638)-1244	8a. ORIGINATOR'S REPORT NUMBER(S)		
b. PROJECT NO.			
c.	8b OTHER REPORT NO(S) (Any other numbers that may be assigned this report)		
d.			
10. AVAILABILITY/LIMITATION NOTES Qualified requestors may obtain copies of this report from DDC. Other persons or organizations should apply to the Clearinghouse for Federal Scientific and Technical Information (CFSTI), Sills Building, 5285 Port Royal Road, Springfield, Virginia 22151.			
11. SUPPLEMENTARY NOTES ARPA Order 292-63 This research was sponsored by Advanced Research Projects Agency		12. SPONSORING MILITARY ACTIVITY Air Force Office of Scientific Research Washington, D.C.	

13. ABSTRACT

The work performed under Contract AF 49(638)-1244 falls into four tasks: (1) single-layer models; (2) multilayer models; (3) models with layer thickness variation; and (4) experimental studies using field data.

The single-layer studies included theoretical investigation of normal and leaking modes, studies of the practical aspects of frequency-wavenumber analysis and investigation of mode separation by multichannel filtering. The importance of leaking modes has been well-established and their use for interpretation greatly enhanced by mode separation to obtain detailed dispersion curves.

Theoretical and analog model investigations for two layers over a half-space showed the difficulty in directly observing an intermediate velocity layer using frequencies of 0.5 cps or less. However, such a layer implicitly affects the dispersion curves for low-order modes. Direct evidence (refractions, plateaus in the dispersion curves) becomes important near 1.0 cps.

Analog model investigations of a model having a dipping M-discontinuity showed a wide range of phase velocities for ray events, as predicted. The true refraction velocity, was measured using phase velocity differences and was found to be in agreement with known values. Measurement of leaking-mode dispersion curves at various points in the model showed the utility of the "local" dispersion representation. These curves may be used to measure average dip.

Experimental studies of field data showed the usefulness of velocity filtering as an interpretive aid. Correlation statistics for small events showed that only about 50 percent of the energy arriving between the first arrival and surface waves is predictable. For events at small distance ($\Delta < 30$ km), Rayleigh-mode dispersion curves were measured. These suggested low near-surface velocities extending to a depth of 1/2 km. It was found that receiving arrays inline with the shot are necessary for adequate dispersion measurements.

14 KEY WORDS	LINK A		LINK B		LINK C	
	ROLE	WT	ROLE	WT	ROLE	WT
Crustal Studies						
Leaking Mode						
Mode Separation						
Frequency-Wavenumber Spectra						
Multichannel Filtering						
Local Dispersion						
Dipping Interface						

INSTRUCTIONS

1. ORIGINATING ACTIVITY: Enter the name and address of the contractor, subcontractor, grantee, Department of Defense activity or other organization (*corporate author*) issuing the report.

2a. REPORT SECURITY CLASSIFICATION: Enter the overall security classification of the report. Indicate whether "Restricted Data" is included. Marking is to be in accordance with appropriate security regulations.

2b. GROUP: Automatic downgrading is specified in DoD Directive 5200.10 and Armed Forces Industrial Manual. Enter the group number. Also, when applicable, show that optional markings have been used for Group 3 and Group 4 as authorized.

3. REPORT TITLE: Enter the complete report title in all capital letters. Titles in all cases should be unclassified. If a meaningful title cannot be selected without classification, show title classification in all capitals in parenthesis immediately following the title.

4. DESCRIPTIVE NOTES: If appropriate, enter the type of report, e.g., interim, progress, summary, annual, or final. Give the inclusive dates when a specific reporting period is covered.

5. AUTHOR(S): Enter the name(s) of author(s) as shown on or in the report. Enter last name, first name, middle initial. If military, show rank and branch of service. The name of the principal author is an absolute minimum requirement.

6. REPORT DATE: Enter the date of the report as day, month, year, or month, year. If more than one date appears on the report, use date of publication.

7a. TOTAL NUMBER OF PAGES: The total page count should follow normal pagination procedures, i.e., enter the number of pages containing information.

7b. NUMBER OF REFERENCES: Enter the total number of references cited in the report.

8a. CONTRACT OR GRANT NUMBER: If appropriate, enter the applicable number of the contract or grant under which the report was written.

8b, 8c, & 8d. PROJECT NUMBER: Enter the appropriate military department identification, such as project number, subproject number, system numbers, task number, etc.

9a. ORIGINATOR'S REPORT NUMBER(S): Enter the official report number by which the document will be identified and controlled by the originating activity. This number must be unique to this report.

9b. OTHER REPORT NUMBER(S): If the report has been assigned any other report numbers (*either by the originator or by the sponsor*), also enter this number(s).

10. AVAILABILITY/LIMITATION NOTICES: Enter any limitations on further dissemination of the report, other than those

imposed by security classification, using standard statements such as:

- (1) "Qualified requesters may obtain copies of this report from DDC."
- (2) "Foreign announcement and dissemination of this report by DDC is not authorized."
- (3) "U. S. Government agencies may obtain copies of this report directly from DDC. Other qualified DDC users shall request through _____."
- (4) "U. S. military agencies may obtain copies of this report directly from DDC. Other qualified users shall request through _____."
- (5) "All distribution of this report is controlled. Qualified DDC users shall request through _____."

If the report has been furnished to the Office of Technical Services, Department of Commerce, for sale to the public, indicate this fact and enter the price, if known.

11. SUPPLEMENTARY NOTES: Use for additional explanatory notes.

12. SPONSORING MILITARY ACTIVITY: Enter the name of the departmental project office or laboratory sponsoring (*paying for*) the research and development. Include address.

13. ABSTRACT: Enter an abstract giving a brief and factual summary of the document indicative of the report, even though it may also appear elsewhere in the body of the technical report. If additional space is required, a continuation sheet shall be attached.

It is highly desirable that the abstract of classified reports be unclassified. Each paragraph of the abstract shall end with an indication of the military security classification of the information in the paragraph, represented as (TS), (S), (C) or (U).

There is no limitation on the length of the abstract. However, the suggested length is from 150 to 225 words.

14. KEY WORDS: Key words are technically meaningful terms or short phrases that characterize a report and may be used as index entries for cataloging the report. Key words must be selected so that no security classification is required. Identifiers, such as equipment model designation, trade name, military project code name, geographic location, may be used as key words but will be followed by an indication of technical context. The assignment of links, rules, and weights is optional.